

Methods in
Molecular Biology 2785

Springer Protocols

Robert Pernecky *Editor*

Biomarkers for Alzheimer's Disease Drug Development

Second Edition

 Humana Press

METHODS IN MOLECULAR BIOLOGY

Series Editor

John M. Walker

School of Life and Medical Sciences

University of Hertfordshire

Hatfield, Hertfordshire, UK

For further volumes:

<http://www.springer.com/series/7651>

For over 35 years, biological scientists have come to rely on the research protocols and methodologies in the critically acclaimed *Methods in Molecular Biology* series. The series was the first to introduce the step-by-step protocols approach that has become the standard in all biomedical protocol publishing. Each protocol is provided in readily-reproducible step-by-step fashion, opening with an introductory overview, a list of the materials and reagents needed to complete the experiment, and followed by a detailed procedure that is supported with a helpful notes section offering tips and tricks of the trade as well as troubleshooting advice. These hallmark features were introduced by series editor Dr. John Walker and constitute the key ingredient in each and every volume of the *Methods in Molecular Biology* series. Tested and trusted, comprehensive and reliable, all protocols from the series are indexed in PubMed.

Biomarkers for Alzheimer's Disease Drug Development

Second Edition

Edited by

Robert Perneczky

*Department of Psychiatry and Psychotherapy, LMU Hospital, Ludwig-Maximilians-University Munich,
Munich, Germany*

 **Humana Press**

Editor

Robert Perneczky
Department of Psychiatry and Psychotherapy
LMU Hospital, Ludwig-Maximilians-University Munich
Munich, Germany

ISSN 1064-3745 ISSN 1940-6029 (electronic)
Methods in Molecular Biology
ISBN 978-1-0716-3773-9 ISBN 978-1-0716-3774-6 (eBook)
<https://doi.org/10.1007/978-1-0716-3774-6>

© The Editor(s) (if applicable) and The Author(s), under exclusive license to Springer Science+Business Media, LLC, part of Springer Nature 2024

This work is subject to copyright. All rights are solely and exclusively licensed by the Publisher, whether the whole or part of the material is concerned, specifically the rights of translation, reprinting, reuse of illustrations, recitation, broadcasting, reproduction on microfilms or in any other physical way, and transmission or information storage and retrieval, electronic adaptation, computer software, or by similar or dissimilar methodology now known or hereafter developed.

The use of general descriptive names, registered names, trademarks, service marks, etc. in this publication does not imply, even in the absence of a specific statement, that such names are exempt from the relevant protective laws and regulations and therefore free for general use.

The publisher, the authors, and the editors are safe to assume that the advice and information in this book are believed to be true and accurate at the date of publication. Neither the publisher nor the authors or the editors give a warranty, expressed or implied, with respect to the material contained herein or for any errors or omissions that may have been made. The publisher remains neutral with regard to jurisdictional claims in published maps and institutional affiliations.

This Humana imprint is published by the registered company Springer Science+Business Media, LLC, part of Springer Nature.

The registered company address is: 1 New York Plaza, New York, NY 10004, U.S.A.

Paper in this product is recyclable.

Preface

Alzheimer's disease is a devastating neurodegenerative disorder that affects millions of people worldwide. Despite significant progress in understanding the underlying biology of the disease, developing effective treatments for Alzheimer's disease remains a major challenge. In recent years, there have been several promising developments in the field of Alzheimer's disease drug development, including the discovery of new drug targets and the development of novel therapeutic approaches.

One exciting development is the approval of new disease-modifying drugs targeting amyloid in several countries. These first-generation drugs represent a new era in Alzheimer's disease drug development, with the potential for greater benefits for affected individuals and society. For example, aducanumab is a human immunoglobulin G1 monoclonal antibody that binds to the linear epitope formed by amino acids 3–7 of the A β peptide, with a higher affinity for fibrillar aggregates as compared with monomers. It has become the first amyloid-targeting antibody to be approved in the United States for Alzheimer's disease patients with mild cognitive impairment or the mild dementia stage of the disease.

This second edition of our textbook provides an up-to-date and comprehensive overview of the current state of technologies helping to accelerate Alzheimer's disease drug development. We cover the latest advances in preclinical and clinical research, including new insights into the molecular mechanisms of Alzheimer's disease and emerging therapeutic strategies. We also discuss the challenges and opportunities in Alzheimer's disease drug development, including the need for improved biomarkers and diagnostic tools, as well as the importance of collaboration and data sharing among researchers. Our laboratory protocols help researchers to use cutting-edge methods in their work. This book also includes emerging new approaches such as digital biomarkers and advanced neuroimaging analysis since those tools will transform how clinical trials in the Alzheimer's disease field are performed.

Our goal with this textbook is to provide students, researchers (both from academia and industry), and clinicians with a valuable resource for understanding the complexities of Alzheimer's disease drug development. We hope that this book will inspire and inform future efforts to develop effective treatments for this devastating disease. Our expectation is that this book will complement other excellent volumes and monographs on Alzheimer's disease that cover the basic science or clinical aspects of the disease.

Munich, Germany

Robert Perneczky

Contents

<i>Preface</i>	<i>v</i>
<i>Contributors</i>	<i>ix</i>

PART I STRATEGIES TO IMPROVE ALZHEIMER'S DISEASE BIOMARKERS

1 Blood-Based Biomarkers for Early Alzheimer's Disease Diagnosis in Real-World Settings	3
<i>Robert Perneczky, Niels Hansen, Anna Hofmann, Christoph Laske, Josef Priller, Timo Grimmer, Lutz Frölich, Emrah Düzel, Frank Jessen, and Jens Wiltfang</i>	
2 Alzheimer's Disease Prevention and Treatment Based on Population-Based Approaches	15
<i>Robert Perneczky</i>	

PART II INNOVATIVE FLUID BIOMARKERS

3 CSF N-Glycomics Using High-Throughput UPLC-ESI Techniques in Alzheimer's Disease	37
<i>Angela Messina, Rita Barone, Luisa Sturiale, Mario Zappia, Angelo Palmigiano, and Domenico Garozzo</i>	
4 CSF N-Glycomics Using MALDI MS Techniques	49
<i>Angela Messina, Donata Agata Romeo, Rita Barone, Luisa Sturiale, Angelo Palmigiano, Mario Zappia, and Domenico Garozzo</i>	
5 Optimized Pre-analytical Handling Protocol for Blood-Based Biomarkers of Alzheimer's Disease	67
<i>Alexander Jethwa and Laura Stöckl</i>	
6 Mass Spectrometry-Based Metabolomics Multi-platform for Alzheimer's Disease Research	75
<i>Álvaro González-Domínguez, Ana Sayago, Ángeles Fernández-Recamales, and Raúl González-Domínguez</i>	

PART III MAGNETIC RESONANCE IMAGING METHODS

7 Analysis of Resting-State Functional Magnetic Resonance Imaging in Alzheimer's Disease	89
<i>Ersin Ersözülü and Boris-Stephan Rauchmann</i>	
8 Diffusion Tensor Imaging in Alzheimer's Studies	105
<i>Adriana L. Ruiz-Rizzo, Kathrin Finke, and Mario E. Archila-Meléndez</i>	
9 Magnetic Resonance Spectroscopy (MRS) in Alzheimer's Disease	115
<i>Nasim Sheikh-Babaei</i>	

10 Neuroimaging Methods for MRI Analysis in CSF Biomarkers Studies 143
*Carles Falcon, Grégory Operto, José Luis Molinuevo,
and Juan Domingo Gispert*

PART IV MOLECULAR IMAGING APPROACHES

11 Amyloid PET Imaging: Standard Procedures and Semiquantification. 165
Francesca D’Amico, Luca Sofia, Matteo Bauckneht, and Silvia Morbelli

12 PET Imaging to Measure Neuroinflammation In Vivo 177
Maura Malpetti, Nicolai Franzmeier, and Matthias Brendel

13 Imaging Neuroinflammation: Quantification of Astrocytosis
in a Multitracer PET Approach 195
*Elena Rodriguez-Vicitez, Amit Kumar, Mona-Lisa Malarte,
Konstantinos Ioannou, Filipa M. Rocha, and Konstantinos Chiotis*

PART V NEUROPATHOLOGY

14 High-Throughput Lipidomic and Metabolomic Profiling for Brain
Tissue and Biofluid Samples in Neurodegenerative Disorders..... 221
Bonne M. Thompson and Giuseppe Astarita

15 Neuropathological Assessment as an Endpoint in Clinical Trial Design 261
Steve M. Gentleman and Alan King Lun Liu

16 Noninvasive Visualization of Amyloid-Beta Deposits in Alzheimer’s
Amyloidosis Mice via Fluorescence Molecular Tomography
Using Contrast Agent 271
Wuwei Ren and Ruiqing Ni

17 Brain Banking in Dementia Studies 287
Abmet Turan Isik, Derya Kaya, and Murat Gokden

PART VI DIGITAL BIOMARKERS AND IN SILICO METHODS

18 Speech-Based Digital Biomarkers for Alzheimer’s Research 299
*Simona Schäfer, Janna Herrmann, Sol Tovar,
Nicklas Linz, and Johannes Tröger*

19 cCOG Web-Based Cognitive Assessment Tool..... 311
Hanneke F. M. Rhodius-Meester, Teemu Paaajanen, and Jyrki Lötjönen

20 In Silico Models to Validate Novel Blood-Based Biomarkers 321
Angélique Sadlon

Index 345

Contributors

- MARIO E. ARCHILA-MELÉNDEZ • *Department of Neurosurgery, Jena University Hospital, Jena, Germany*
- GIUSEPPE ASTARITA • *Department of Biochemistry and Molecular & Cellular Biology, Georgetown University, Washington, DC, USA*
- RITA BARONE • *CNR, Istituto per i Polimeri, Compositi e i Biomateriali Catania, Catania, Italy; Pediatric Neurology Unit, Department of Pediatrics, University of Catania, Catania, Italy*
- MATTEO BAUCKNEHT • *Nuclear Medicine Unit, Department of Health Sciences, University of Genoa, Genoa, Italy; IRCCS Ospedale Policlinico San Martino, Genoa, Italy*
- MATTHIAS BRENDEL • *Munich Cluster for Systems Neurology (SyNergy), Munich, Germany; Department of Nuclear Medicine, LMU University Hospital, LMU Munich, Munich, Germany; German Center for Neurodegenerative Diseases (DZNE), Munich, Germany*
- KONSTANTINOS CHIOTIS • *Division of Clinical Geriatrics, Center for Alzheimer Research, Department of Neurobiology, Care Sciences and Society, Karolinska Institutet, Stockholm, Sweden; Department of Neurology, Karolinska University Hospital, Stockholm, Sweden*
- FRANCESCA D'AMICO • *Nuclear Medicine Unit, Department of Health Sciences, University of Genoa, Genoa, Italy; IRCCS Ospedale Policlinico San Martino, Genoa, Italy*
- EMRAH DÜZEL • *Institute of Cognitive Neurology and Dementia Research (IKND), Otto-von-Guericke University, Magdeburg, Germany; German Center for Neurodegenerative Diseases (DZNE) Magdeburg, Magdeburg, Germany*
- ERSIN ERSÖZLÜ • *Department of Psychiatry and Psychotherapy, University Hospital, LMU Munich, Munich, Germany; Department of Geriatric Psychiatry and Developmental Disorders, kbo-Isar-Amper-Klinikum Munich East, Academic Teaching Hospital of LMU Munich, Munich, Germany*
- CARLES FALCON • *Barcelonaβeta Brain Research Center, Pasqual Maragall Foundation, Barcelona, Spain; Centro de Investigación Biomédica en Red de Bioingeniería, Biomateriales y Nanomedicina (CIBER-BBN), Madrid, Spain*
- ÁNGELES FERNÁNDEZ-RECAMALES • *Department of Chemistry, Faculty of Experimental Sciences, University of Huelva, Huelva, Spain; International Campus of Excellence CeiA3, University of Huelva, Huelva, Spain*
- KATHRIN FINKE • *Department of Neurology, Jena University Hospital, Jena, Germany*
- NICOLAI FRANZMEIER • *Institute for Stroke and Dementia Research, LMU University Hospital, LMU Munich, Munich, Germany; Munich Cluster for Systems Neurology (SyNergy), Munich, Germany; Department of Psychiatry and Neurochemistry, Institute of Neuroscience and Physiology, University of Gothenburg, Mölndal and Gothenburg, Sweden*
- LUTZ FRÖLICH • *Department of Geriatric Psychiatry, Central Institute of Mental Health, Medical Faculty Mannheim, University of Heidelberg, Mannheim, Germany*
- DOMENICO GAROZZO • *CNR, Istituto per i Polimeri, Compositi e i Biomateriali Catania, Catania, Italy*
- STEVE M. GENTLEMAN • *Department of Brain Sciences, Imperial College London, London, UK*

- JUAN DOMINGO GISPERT • *BarcelonaBeta Brain Research Center, Pasqual Maragall Foundation, Barcelona, Spain; Centro de Investigación Biomédica en Red de Bioingeniería, Biomateriales y Nanomedicina (CIBER-BBN), Madrid, Spain*
- MURAT GOKDEN • *Division of Neuropathology, Department of Pathology, University of Arkansas for Medical Sciences, Little Rock, AR, USA*
- ÁLVARO GONZÁLEZ-DOMÍNGUEZ • *Instituto de Investigación e Innovación Biomédica de Cádiz (INiBICA), Hospital Universitario Puerta del Mar, Universidad de Cádiz, Cádiz, Spain*
- RAÚL GONZÁLEZ-DOMÍNGUEZ • *Instituto de Investigación e Innovación Biomédica de Cádiz (INiBICA), Hospital Universitario Puerta del Mar, Universidad de Cádiz, Cádiz, Spain*
- TIMO GRIMMER • *Department of Psychiatry and Psychotherapy, Klinikum rechts der Isar, Technical University Munich, Munich, Germany*
- NIELS HANSEN • *Department of Psychiatry and Psychotherapy, University Medical Center Göttingen, Göttingen, Germany*
- JANNA HERRMANN • *ki:elements GmbH, Saarbrücken, Germany*
- ANNA HOFMANN • *Hertie Institute for Clinical Brain Research, University of Tuebingen, Tuebingen, Germany; Department of Neurology, University Hospital Tuebingen, Tuebingen, Germany; German Center for Neurodegenerative Diseases (DZNE) Tuebingen, Tuebingen, Germany*
- KONSTANTINOS IOANNOU • *Division of Clinical Geriatrics, Center for Alzheimer Research, Department of Neurobiology, Care Sciences and Society, Karolinska Institutet, Stockholm, Sweden*
- AHMET TURAN ISIK • *Unit for Aging Brain and Dementia, Department of Geriatric Medicine, Faculty of Medicine, Dokuz Eylul University, Izmir, Turkey*
- FRANK JESSEN • *Department of Psychiatry and Psychotherapy, University of Cologne, Medical Faculty, Cologne, Germany; German Center for Neurodegenerative Diseases (DZNE) Bonn, Bonn, Germany; Excellence Cluster on Cellular Stress Responses in Aging-Associated Diseases (CECAD), University of Cologne, Cologne, Germany*
- ALEXANDER JETHWA • *Roche Diagnostics GmbH, Penzberg, Germany*
- DERYA KAYA • *Unit for Aging Brain and Dementia, Department of Geriatric Medicine, Faculty of Medicine, Dokuz Eylul University, Izmir, Turkey*
- AMIT KUMAR • *Division of Clinical Geriatrics, Center for Alzheimer Research, Department of Neurobiology, Care Sciences and Society, Karolinska Institutet, Stockholm, Sweden*
- CHRISTOPH LASKE • *German Center for Neurodegenerative Diseases (DZNE) Tuebingen, Tuebingen, Germany; Section for Dementia Research, Hertie Institute for Clinical Brain Research, University of Tuebingen, Tuebingen, Germany; Department of Psychiatry and Psychotherapy, University of Tuebingen, Tuebingen, Germany*
- NICKLAS LINZ • *ki:elements GmbH, Saarbrücken, Germany*
- ALAN KING LUN LIU • *Nuffield Department of Clinical Neurosciences, University of Oxford, Oxford, UK*
- JYRKI LÖTJÖNEN • *Combinostics Oy, Tampere, Finland*
- MONA-LISA MALARTE • *Division of Clinical Geriatrics, Center for Alzheimer Research, Department of Neurobiology, Care Sciences and Society, Karolinska Institutet, Stockholm, Sweden*
- MAURA MALPETTI • *Department of Clinical Neurosciences, University of Cambridge, Cambridge, UK*
- ANGELA MESSINA • *CNR, Istituto per i Polimeri, Compositi e i Biomateriali Catania, Catania, Italy*

- JOSÉ LUIS MOLINUEVO • *Barcelonaβeta Brain Research Center, Pasqual Maragall Foundation, Barcelona, Spain; CIBER Fragilidad y Envejecimiento Saludable (CIBERFES), Madrid, Spain*
- SILVIA MORBELLI • *Nuclear Medicine Unit, Department of Health Sciences, University of Genoa, Genoa, Italy; IRCCS Ospedale Policlinico San Martino, Genoa, Italy*
- RUIQING NI • *Institute for Regenerative Medicine, University of Zurich, Zurich, Switzerland; Institute for Biomedical Engineering, ETH Zurich & University of Zurich, Zurich, Switzerland*
- GRÉGORIO OPERTO • *Barcelonaβeta Brain Research Center, Pasqual Maragall Foundation, Barcelona, Spain*
- TEEMU PAAJANEN • *Work ability and Working Careers, Finnish Institute of Occupational Health, Helsinki, Finland*
- ANGELO PALMIGIANO • *CNR, Istituto per i Polimeri, Compositi e i Biomateriali Catania, Catania, Italy*
- ROBERT PERNECZKY • *Department of Psychiatry and Psychotherapy, LMU Hospital, Ludwig-Maximilians-University Munich, Munich, Germany; German Center for Neurodegenerative Diseases (DZNE) Munich, Munich, Germany; Munich Cluster for Systems Neurology (SyNergy), Munich, Germany; Ageing Epidemiology (AGE) Research Unit, School of Public Health, Imperial College London, London, UK; Sheffield Institute for Translational Neuroscience (SITraN), University of Sheffield, Sheffield, UK*
- JOSEF PRILLER • *Department of Psychiatry and Psychotherapy, Klinikum rechts der Isar, Technical University Munich, Munich, Germany; German Center for Neurodegenerative Diseases (DZNE) Berlin, Berlin, Germany; Department of Psychiatry and Psychotherapy, Charite University Medicine, Berlin, Germany; Dementia Research Institute, University of Edinburgh, Edinburgh, UK*
- BORIS-STEPHAN RAUCHMANN • *Department of Psychiatry and Psychotherapy, University Hospital, LMU Munich, Munich, Germany; Department of Neuroradiology, University Hospital, LMU Munich, Munich, Germany; German Center for Neurodegenerative Diseases (DZNE) Munich, Munich, Germany; Sheffield Institute for Translational Neuroscience (SITraN), University of Sheffield, Sheffield, UK*
- WUWEI REN • *School of Information Science and Technology, ShanghaiTech University, Shanghai, China*
- HANNEKE F. M. RHODIUS-MEESTER • *Alzheimer Center Amsterdam, Neurology, Vrije Universiteit Amsterdam, Amsterdam UMC location VUmc, Amsterdam, The Netherlands; Amsterdam Neuroscience, Neurodegeneration, Amsterdam, The Netherlands; Department of Internal medicine, Geriatric Medicine section, Vrije Universiteit Amsterdam, Amsterdam UMC, Amsterdam, the Netherlands; Department of Geriatric Medicine, The Memory Clinic, Oslo University Hospital, Oslo, Norway*
- FILIPA M. ROCHA • *Division of Clinical Geriatrics, Center for Alzheimer Research, Department of Neurobiology, Care Sciences and Society, Karolinska Institutet, Stockholm, Sweden*
- ELENA RODRIGUEZ-VIEITEZ • *Division of Clinical Geriatrics, Center for Alzheimer Research, Department of Neurobiology, Care Sciences and Society, Karolinska Institutet, Stockholm, Sweden; Division of Neurogeriatrics, Center for Alzheimer Research, Department of Neurobiology, Care Sciences and Society, Karolinska Institutet, Stockholm, Sweden*
- DONATA AGATA ROMEO • *CNR, Istituto per i Polimeri, Compositi e i Biomateriali Catania, Catania, Italy*

- ADRIANA L. RUIZ-RIZZO • *Department of Neurology, Jena University Hospital, Jena, Germany*
- ANGÉLIQUE SADLON • *Department of Clinical Chemistry, Pharmacogenomics Research Group, Bern University Hospital & University of Bern, Bern, Switzerland*
- ANA SAYAGO • *Department of Chemistry, Faculty of Experimental Sciences, University of Huelva, Huelva, Spain; International Campus of Excellence CeiA3, University of Huelva, Huelva, Spain*
- SIMONA SCHÄFER • *ki:elements GmbH, Saarbrücken, Germany*
- NASIM SHEIKH-BAHAEI • *Department of Radiology, Keck School of Medicine of USC, Los Angeles, CA, USA*
- LUCA SOFIA • *Nuclear Medicine Unit, Department of Health Sciences, University of Genoa, Genoa, Italy; IRCCS Ospedale Policlinico San Martino, Genoa, Italy*
- LAURA STÖCKL • *Roche Diagnostics GmbH, Penzberg, Germany*
- LUISA STURIALE • *CNR, Istituto per i Polimeri, Compositi e i Biomateriali Catania, Catania, Italy*
- BONNE M. THOMPSON • *Arkuda Therapeutics, Watertown, MA, USA*
- SOL TOVAR • *ki:elements GmbH, Saarbrücken, Germany*
- JOHANNES TRÖGER • *ki:elements GmbH, Saarbrücken, Germany*
- JENS WILTFANG • *Department of Psychiatry and Psychotherapy, University Medical Center Göttingen, Göttingen, Germany; German Center for Neurodegenerative Diseases (DZNE) Goettingen, Goettingen, Germany; Neurosciences and Signaling Group, Institute of Biomedicine (iBiMED), Department of Medical Sciences, University of Aveiro, Aveiro, Portugal*
- MARIO ZAPPÀ • *Section of Neurosciences-Department GF Ingrassia, University of Catania, Catania, Italy*

Part I

Strategies to Improve Alzheimer's Disease Biomarkers



Chapter 1

Blood-Based Biomarkers for Early Alzheimer's Disease Diagnosis in Real-World Settings

Robert Perneczky, Niels Hansen, Anna Hofmann, Christoph Laske, Josef Priller, Timo Grimmer, Lutz Frölich, Emrah Düzel, Frank Jessen, and Jens Wiltfang
and for the German Network Memory Clinics – Diagnostic Tools Working Group

Abstract

As our knowledge about the biology of Alzheimer's disease (AD) expands and we recognize the significance of early intervention for effective treatment, there is a shift in focus toward detecting the disease at an early stage. AD is characterized by the accumulation of misfolded amyloid- β (A β) and phosphorylated tau proteins in the brain, leading to the formation of senile plaques and neurofibrillary tangles. While a definitive diagnosis of AD can only be confirmed through autopsy by examining these pathological features, there are now reliable methods available for diagnosing the disease in living individuals. These methods involve analyzing cerebrospinal fluid and using positron emission tomography to accurately assess the presence of A β and tau proteins. While these diagnostic markers have shown high accuracy in memory-clinic populations, they do have limitations such as the requirement for invasive lumbar puncture or exposure to ionizing radiation. Additionally, they are not easily accessible outside of specialized healthcare settings. Blood-based biomarkers of the core pathological features of AD are being developed, showing promise for less invasive, scalable identification of AD cases in the community. The advantages for the healthcare systems of this development are obvious, but the diagnostic performance of blood-based biomarkers in broader, non-selected populations outside of retrospective analyses and research cohorts still requires further investigation, including the combination with more effective neuropsychological assessments such as digital cognitive test solutions.

Key words Early diagnosis of Alzheimer's disease and dementia, Subjective cognitive impairment and mild cognitive impairment, Scalable diagnostic technologies, Patient and service user value, Early and targeted treatment and prevention of neurodegeneration

1 A Global Dementia Pandemic

Modern societies have achieved longer life expectancies, which is a significant accomplishment. However, the aging global population

has led to a rapid increase in the number of individuals affected by dementia. This has had a profound negative impact on the lives of affected families and national budgets. In 2018, the global cost of dementia was estimated to be US\$1 trillion, and it is projected to reach US\$2 trillion by 2030. Among various causes of dementia, Alzheimer's disease (AD) is the most prevalent, currently affecting approximately 55 million individuals worldwide. This number is expected to rise to 132 million by 2050 [1].

To address this global challenge, the World Health Organization (WHO) developed a dementia plan in 2017, outlining priorities for action. These priorities include enhancing dementia diagnosis, treatment, and care [2]. Similar national strategies, such as the 2020 German National Dementia Strategy [3], have also been implemented. However, a recent study indicates that healthcare systems are not adequately equipped to effectively detect cognitive decline, accurately diagnose early-stage disease, and determine the most suitable interventions or deliver disease-modifying treatments in the future [4].

2 A Paradigm Shift Toward Early Disease Detection

As our understanding of the biology of AD increases and we recognize the importance of early intervention for effective treatment, there is a shift in focus toward early disease detection. Pathologically, AD is characterized by the accumulation of misfolded amyloid- β ($A\beta$) and phosphorylated tau proteins in the brain, forming senile plaques and neurofibrillary tangles, respectively. While a definite diagnosis of AD requires confirmation of these pathological features through autopsy, there are now reliable methods available for diagnosing AD in living individuals. This is made possible through the use of cerebrospinal fluid (CSF) and positron emission tomography (PET) measures, which accurately assess the burden of $A\beta$ and tau proteins. These diagnostic markers have shown high accuracy in memory-clinic populations, but they do have limitations such as the need for invasive lumbar puncture or exposure to ionizing radiation. Additionally, they are not readily accessible outside of specialized healthcare settings [5]. Furthermore, their diagnostic performance in broader, non-selected populations still requires further investigation.

3 Targeting the Early Diagnostic Window with Therapies

AD exhibits a prolonged presymptomatic stage that can last for many years. Recent advancements in imaging and fluid marker technologies have enabled the detection of increasing biological abnormalities during this stage. Once AD pathology surpasses a

specific threshold determined by an individual's resilience against neurodegeneration [6], cognitive symptoms begin to manifest. The terms mild cognitive impairment (MCI) or prodromal AD are used to describe cases where cognitive performance falls below the expected norm for age and education, while basic daily activities remain mostly unaffected [7, 8].

Recent evidence suggests that concerns regarding cognitive decline could be an indication of early AD, even in the absence of objective below-average results on psychometric tests required for an MCI diagnosis [9]. When AD-related biomarker changes are present during this stage of subjective cognitive decline (SCD), the risk of progressing to MCI and dementia significantly increases [10]. The accurate identification of individuals with AD in the SCD stage is crucial as it offers a window of opportunity for early intervention and disease prevention. It is important to identify individuals in the community who have cognitive complaints and subtle deficits before their condition progresses to more severe stages. However, in most countries worldwide, there is currently a lack of infrastructure to accurately identify individuals with very early AD outside of specialized clinics, leading to low diagnostic rates [11]. Despite evidence showing that structured screening programs can significantly improve the detection of dementia cases [12], such programs are not widely implemented.

The implementation of financial incentives aimed at increasing specialist referrals by primary care physicians has not yielded improved diagnostic rates for early cognitive decline in the UK [13]. Likewise, in Germany a significant number of dementia cases still go undiagnosed [14], and primary care physicians' motivation to conduct cognitive screening is limited due to the absence of effective disease-modifying treatments [15]. Similar challenges are observed in other high-income countries. On the contrary, previous research suggests that community-based screening programs targeting memory concerns and minor cognitive deficits are both feasible and efficient in various settings [16]. A recent systematic review conducted for the US Preventive Services Task Force indicated that screening instruments can adequately detect cognitive impairment, but it remains uncertain whether systematic screening for cognitive impairment improves outcomes for patients and caregivers [17]. Therefore, further research is urgently needed to investigate the acceptance, effectiveness, and costs of community-based cognitive evaluations. Additionally, exploring the attitudes of seniors and primary care physicians toward opportunistic cognitive screening is crucial for developing an acceptable approach that can drive changes in current healthcare practices.

4 The Benefits of Digital Cognitive Testing

Standardized questionnaires like the SCD-Q [18] are available for assessing subjective complaints, but their validity and usefulness outside of specialized memory clinics still need to be determined. Objective psychometric tests such as the Mini-Mental-State Examination (MMSE) [19] or the Montreal Cognitive Assessment (MoCA) [20] can enhance diagnostic accuracy. Digital cognitive tests may offer significant advantages over traditional paper-and-pencil assessments, particularly in community settings and primary care. They can be self-administered without requiring extensive involvement from healthcare professionals, potentially reducing rater bias and improving the reliability of longitudinal assessments. This could make early intervention more feasible [21]. However, it is yet to be determined whether self-administered tests provide enough additional diagnostic value to justify their integration into routine clinical care. Only if the test results offer actionable information for healthcare professionals will digital testing have a tangible impact on patient care.

5 Complementary Digital and Fluid Biomarkers

To enhance the accuracy of population-based cognitive screening, one potential approach is to integrate digital cognitive tests with pathophysiological biomarkers. Recent advancements in the identification of blood biomarkers provide a unique opportunity for noninvasive and scalable targeted diagnostics, which can inform decisions regarding specialist referral in primary care medicine. By combining precise blood protein assays with digital cognitive tests, it could be possible to create a robust screening tool that reduces errors in identifying preclinical or prodromal AD. However, the real-world effectiveness, cost-efficiency, and acceptance of this innovative approach still need to be fully explored.

The development of a blood-based biomarker algorithm holds critical importance due to its ease of measurement and cost-effectiveness compared to the current gold standard assessments using CSF and PET. Recent studies have shown promising results in clinical and population-based cohorts, utilizing new ultrasensitive assay technology to measure blood concentrations of various AD biomarkers. These biomarkers include p-tau 181 and p-tau 217 (but not total tau) and neurofilament light chain (NfL) [22], although there have been conflicting results for A β 42/40 [23].

An analysis of the US healthcare system indicated that integrating cognitive screening tests with blood-based biomarkers could eliminate wait lists for specialist assessments within the first 3 years and potentially reduce annual costs by US\$400–700 million.

Additionally, it could lead to an increase of approximately 120,000 correctly identified cases per year [24]. In cases of SCD or MCI, the most effective prediction model for AD appears to be a combination of plasma pTau-181/217, *APOE* genotype, and a brief cognitive assessment of memory and executive function [25]. However, it is important to conduct a real-world evaluation of triage strategies, as genetic analyses have their own limitations, including increased requirements for patient consent and data protection.

6 Defining Appropriate Reference Ranges for Blood Biomarkers

Previous studies have demonstrated that concentrations of biomarkers in CSF [26] and blood [27, 28] are influenced not only by neurodegeneration but also by age. As a result, it is necessary to establish age-specific normal ranges for prodromal AD to ensure accurate diagnostic assessments. A recent study aimed to define reference ranges for plasma neurofilament light chain (NfL) in healthy individuals ranging from 5 to 90 years of age [29], and similar efforts will be required for other blood biomarkers and early symptomatic stages of AD. Adjusted reference ranges for NfL have also been proposed, taking into account factors such as renal function and body mass index [30], and there is some evidence suggesting higher NfL levels in men compared to women, although the clinical significance of this difference remains to be determined [31]. Plasma markers such as A β 42, A β 40, t-tau, and p-tau can be influenced by comorbidities such as chronic kidney disease, hypertension, hyperlipidemia, diabetes, myocardial infarction, and stroke [32]. Ethnicity [33] and food intake (postprandial vs fasting) [34] may also impact blood protein levels, and if these factors are not appropriately addressed, the proportion of misdiagnosed individuals may increase, especially in non-specialized settings and early stages of the disease.

Another important consideration is determining the optimal blood compartment for analysis, as concentrations in plasma and serum may provide similar diagnostic information but may differ in certain situations. For instance, studies have shown comparable diagnostic performance and strong correlations between serum and plasma pairs, suggesting that p-tau analysis can be extended to healthcare settings with a preference for serum over other blood matrices. However, it should be noted that absolute biomarker concentrations may not be interchangeable, indicating that plasma and serum samples should be used independently [35]. Standardized values may prove helpful when combining results from different blood matrices, as demonstrated for NfL [36].

7 Lessons from Familial Alzheimer's Disease

Familial AD exhibits distinct characteristics from the sporadic form, including different associated genes and comorbidities. However, genetic AD cohorts still provide a valuable model system for studying biomarkers relevant to individuals with late symptom onset. Longitudinal biomarker analyses spanning up to 15 years are available for participants in the Dominantly Inherited AD Network (DIAN), and published data demonstrates a strong correlation and elevated levels of NfL in both CSF and blood at the presymptomatic stages of familial AD. Longitudinal analysis of NfL dynamics in serum revealed the ability to differentiate mutation carriers from non-carriers almost a decade earlier than cross-sectional absolute NfL levels [37]. Thus, serum NfL dynamics can predict disease progression and brain neurodegeneration in the early presymptomatic stages of familial AD, indicating its potential utility as a clinically useful biomarker, even in early sporadic disease.

In the University College London Longitudinal Study of Familial AD, plasma p-tau181 concentrations were found to be elevated in both symptomatic and presymptomatic mutation carriers compared to non-carriers [38]. Despite significant intra-individual variability, individual values of plasma p-tau181 effectively discriminated symptomatic and presymptomatic carriers from non-carriers of the same age and sex. P-tau181 concentrations were higher in mutation carriers compared to non-carriers as early as 16 years before the estimated symptom onset, supporting its value as an early marker of AD.

The same University College London longitudinal study also revealed increased levels of glial fibrillary acidic protein (GFAP) in plasma of both presymptomatic and symptomatic mutation carriers compared to non-carriers, as well as in symptomatic carriers compared to presymptomatic carriers [39]. These differences were observed up to 16 years prior to symptom onset, consistent with findings of elevated plasma GFAP concentrations in A β -positive compared to A β -negative cognitively normal older individuals [40]. Overall, these findings support plasma GFAP as a potential biomarker for early AD and highlight the involvement of activated astrocytes in the early stages of the disease.

8 Performance of Blood Biomarkers Across the Alzheimer's Continuum

Molecular blood biomarkers show promise in optimizing diagnostic approaches and potentially enabling early diagnoses of AD. These markers can also assist in stratifying patients by predicting the progression from early stages, such as SCD or MCI, to manifest stages of AD dementia. Several blood biomarker

candidates are currently being investigated for diagnosing AD and assessing prognosis. Markers related to A β pathology, which are part of current CSF and A β -PET biomarkers, are of significant interest for blood-based diagnostics in AD.

A recent study compared plasma biomarkers across two independent cohorts, BioFINDER and the AD Neuroimaging Initiative. The study demonstrated that combining immunoprecipitation with mass spectrometry analysis platform was superior to standard immunoassays for detecting A β , particularly by relying on the A β -42/A β -40 ratio within the brain [41]. Immunoprecipitation plasma assays with mass spectrometry exhibited moderate to good diagnostic accuracy in detecting brain amyloidosis in large AD cohorts, both in cognitively unimpaired and impaired individuals [42]. The diagnostic accuracy of this analysis platform improved further when considering the *APOE* status [42]. Automated analysis of the A β -42/A β -40 ratio [43] (and p-tau181 [44]) using the Lumipulse platform was also shown to provide high accuracy in AD diagnosis. However, other measurement methods such as SIMOA technology [45] or using carbon nanotubes for detecting A β -42/A β -40 in plasma samples did not yield convincing results in detecting brain amyloidosis [46].

In addition to measuring A β peptides, p-tau forms such as p-tau181, p-tau217, and p-tau231 are currently under intense investigation as promising biomarkers for early diagnosis and disease progression in AD. These markers have shown utility in diagnosing AD early, differentiating AD from other neurodegenerative diseases, and predicting cognitive decline and neurodegenerative processes in AD [41, 47–53]. A comprehensive retrospective study presented evidence that p-tau217 outperforms p-tau181 in distinguishing AD from other neurodegenerative conditions such as frontotemporal dementia [49] (Thijssen, La Joie et al., 2021), and p-tau217 has been highlighted as a potential marker for preclinical and prodromal stages of AD [54].

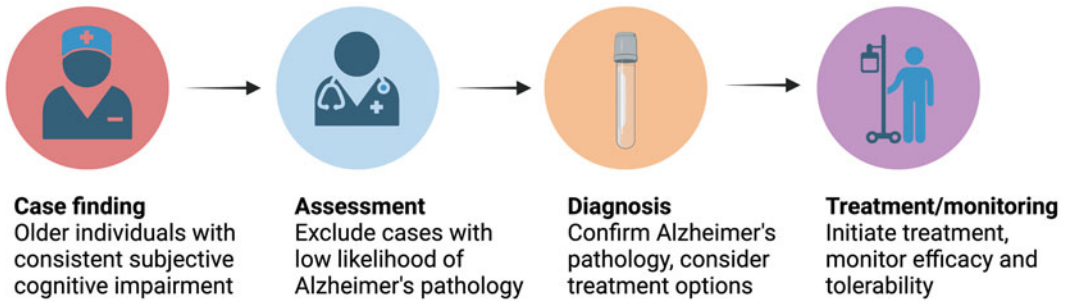
In the preclinical stage, another blood biomarker of interest is GFAP, a marker of astroglial inflammation. GFAP has shown potential for detecting A β pathology in preclinical stages and predicting the progression from MCI to dementia [50, 55]. Furthermore, a cytoskeleton marker of axonal neurodegeneration in blood has demonstrated a close correlation with CSF concentration [56]. Plasma NfL has been explored to predict the disease course and cognitive outcome in AD [50, 57]. Currently available tests have shortcomings in access, throughput, and scalability that limit widespread implementation. A high-throughput and fully automated Lumipulse plasma p-tau181 assay for the detection of AD has been evaluated and showed robust performance in differentiating AD from control participants [44]. However, the Lumipulse technique needs to be validated in multicenter cohorts and for other AD biomarkers.

In larger multicenter cohorts, there is a need to explore ultrasensitive assays capable of covering the full biomarker-based classification of AD using blood biomarkers, offering a less invasive approach than CSF. A recent study [58] demonstrated a strong correlation between CSF and blood markers, suggesting the feasibility of implementing biomarker-based classification in blood. However, a limitation of A β -42/A β -40 is that its levels in blood are considerably lower than in CSF [59]. Developing composite marker panels that provide higher diagnostic accuracy than individual biomarkers may prove beneficial. In the future, the range of blood biomarkers for AD is expected to expand. For example, serum β -synuclein has emerged as a novel candidate for indicating synaptic degeneration in the temporal lobe in AD [60]. These studies and considerations underscore the increasing importance of blood biomarkers in the future early and differential diagnosis of AD.

9 Outlook and Next Steps Required

Ensuring the long-term effectiveness of any new diagnostic algorithm is crucial to create tangible benefits to the older population. It is essential to develop tailored approaches that align with the specific requirements of local healthcare systems, thus ensuring their sustained commitment. The availability and coverage of various interventions vary significantly across different regions worldwide. In this regard, employing low-cost assessments like digital and blood biomarkers may offer advantages over more expensive alternatives such as PET scans. Currently, one of the primary challenges in identifying early-stage cognitive decline cases is the limited preparedness of healthcare systems to offer proactive screening visits and specialist assessments following initial check-ups in primary care settings. As soon as AD-modifying drug will be available more broadly, the demand for accurate early diagnostics will dramatically increase, necessitating the readiness of healthcare systems to address this need. Objective digital tests can provide valuable information to healthcare professionals for making better care decisions, while enabling primary care doctors to make informed decisions about specialist referrals at an earlier stage can alleviate the burden on the general practitioner sector. To support coverage decisions, it is important to gather more quantitative data on the diagnostic yield and cost per identified patient associated with combined digital and blood biomarkers, as this information will be vital for payers. The envisioned diagnostic and care pathways will include close collaboration across different healthcare sectors, and specialized specialist memory clinics will play an increasingly important role in verifying early AD diagnoses, making treatment decisions and monitoring drug efficacy and safety [61] (Fig. 1).

Care pathway



Healthcare sector

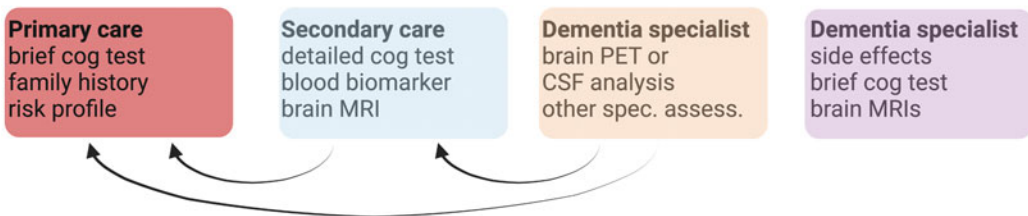


Fig. 1 Potential pathway for case identification, diagnostic ascertainment, and treatment initiation/monitoring in early Alzheimer's disease (reprinted with permission from [61]). A proposed model has been suggested for a care pathway aimed at identifying older individuals who exhibit minor cognitive complaints or deficits in primary care. This would be followed by a secondary care step where subjects with a very low likelihood of Alzheimer's disease pathology would be excluded, possibly through the use of blood-based biomarkers. Diagnostic confirmation would then be conducted by a dementia specialist, potentially employing positron emission tomography and cerebrospinal fluid markers. Following a careful evaluation of potential risks and benefits, including the monitoring of side effects, disease-modifying treatment would be initiated. It is important to note that individuals may also move backward in this model if they fail to meet the criteria for progressing to the next stage, such as having a negative blood biomarker for Alzheimer's disease

Acknowledgments

R.P. is supported by the German Center for Neurodegenerative Disorders (Deutsches Zentrum für Neurodegenerative Erkrankungen, DZNE), the Deutsche Forschungsgemeinschaft (DFG, 1007 German Research Foundation) under Germany's Excellence Strategy within the framework of 1008 the Munich Cluster for Systems Neurology (EXC 2145 SyNergy – ID 390857198), the Davos Alzheimer's Collaborative, the VERUM Foundation, the Robert-Vogel-Foundation, the National Institute for Health and Care Research (NIHR) Sheffield Biomedical Research Centre (NIHR203321), the University of Cambridge – Ludwig-Maximilians-University Munich Strategic Partnership within the

framework of the German Excellence Initiative and Excellence Strategy, and the European Commission under the Innovative Health Initiative program (project 101132356).

Conflicts of Interest R.P. has received honoraria for advisory boards and speaker engagements from Roche, Eisai, Eli Lilly, Biogen, Janssen-Cilag, Astra Zeneca, Schwabe, Grifols, Novo Nordisk, and Tabuk. J. W. has been an honorary speaker for Actelion, Amgen, Beeijing Yibai Science and Technology Ltd., Gloryren, Janssen Cilag, Med Update GmbH, Pfizer, and Roche Pharma and has been a member of the advisory boards of Abbott, Biogen, Boehringer Ingelheim, Lilly, MSD Sharp & Dohme, and Roche Pharma and receives fees as a consultant for Immunogenetics, Nose-lab, and Roboscreen and holds the following patents: PCT/EP 2011 001724 and PCT/EP 2015 052945.

References

1. Prince M et al (2015) World Alzheimer report – the global impact of dementia
2. WHO (2017) Global action plan on the public health response to dementia 2017–2025
3. Nationale Demenzstrategie (2020)
4. Hlavka JP, Mattke S, Liu JL (2019) Assessing the preparedness of the health care system infrastructure in six European countries for an Alzheimer's treatment. *Rand Health Q* 8(3):2
5. Simonsen AH et al (2017) Recommendations for CSF AD biomarkers in the diagnostic evaluation of dementia. *Alzheimers Dement* 13(3): 274–284
6. Perneczky R et al (2019) Translational research on reserve against neurodegenerative disease: consensus report of the international conference on cognitive reserve in the Dementias and the Alzheimer's Association reserve, resilience and protective factors professional interest area working groups. *BMC Med* 17(1):47
7. Perneczky R et al (2006) Complex activities of daily living in mild cognitive impairment: conceptual and diagnostic issues. *Age Ageing* 35(3):240–245
8. Perneczky R et al (2006) Impairment of activities of daily living requiring memory or complex reasoning as part of the MCI syndrome. *Int J Geriatr Psychiatry* 21(2):158–162
9. Jessen F et al (2020) The characterisation of subjective cognitive decline. *Lancet Neurol* 19(3):271–278
10. Jessen F et al (2022) Subjective cognitive decline and stage 2 of Alzheimer disease in patients from memory centers. *Alzheimers Dement*
11. Strohmaier U et al (2018) Patients with dementia in primary care: who is referred to a neurologist/psychiatrist and what patient-oriented factors are associated with the visit? *J Alzheimers Dis* 64(3):925–932
12. Eichler T et al (2015) Rates of formal diagnosis of dementia in primary care: the effect of screening. *Alzheimers Dement (Amst)* 1(1): 87–93
13. Bell S et al (2015) A diagnosis for pound55: what is the cost of government initiatives in dementia case finding. *Age Ageing* 44(2): 344–345
14. Wangler J, Fellgiebel A, Jansky M (2018) Dementia diagnosis in general practitioner care - attitudes, procedures and challenges from the perspective of general practitioners in Rhineland-Palatinate. *Dtsch Med Wochenschr* 143(19):e165–e171
15. Sannemann L et al (2021) General practitioners' attitude toward early and pre-dementia diagnosis of AD in five European countries-a MOPEAD project survey. *Alzheimers Dement (Amst)* 13(1):e12130
16. Scharre DW et al (2014) Community cognitive screening using the self-administered gerocognitive examination (SAGE). *J Neuropsychiatry Clin Neurosci* 26(4):369–375
17. Patnode CD et al (2020) Screening for cognitive impairment in older adults: updated evidence report and systematic review for the US

- preventive services task force. *JAMA* 323(8):764–785
18. Rami L et al (2014) The subjective cognitive decline questionnaire (SCD-Q): a validation study. *J Alzheimers Dis* 41(2):453–466
 19. Folstein MF, Folstein SE, McHugh PR (1975) “Mini-mental state”. A practical method for grading the cognitive state of patients for the clinician. *J Psychiatr Res* 12(3):189–198
 20. Nasreddine ZS et al (2005) The Montreal Cognitive Assessment, MoCA: a brief screening tool for mild cognitive impairment. *J Am Geriatr Soc* 53(4):695–699
 21. Ohman F et al (2021) Current advances in digital cognitive assessment for preclinical Alzheimer's disease. *Alzheimers Dement (Amst)* 13(1):e12217
 22. Cullen NC et al (2021) Plasma biomarkers of Alzheimer's disease improve prediction of cognitive decline in cognitively unimpaired elderly populations. *Nat Commun* 12(1):3555
 23. Pannee J et al (2021) The global Alzheimer's Association round robin study on plasma amyloid beta methods. *Alzheimers Dement (Amst)* 13(1):e12242
 24. Mattke S, Hanson M (2021) Expected wait times for access to a disease-modifying Alzheimer's treatment in the United States. *Alzheimers Dement*
 25. Palmqvist S et al (2021) Prediction of future Alzheimer's disease dementia using plasma phospho-tau combined with other accessible measures. *Nat Med* 27(6):1034–1042
 26. Yilmaz A et al (2017) Neurofilament light chain protein as a marker of neuronal injury: review of its use in HIV-1 infection and reference values for HIV-negative controls. *Expert Rev Mol Diagn* 17(8):761–770
 27. Khalil M et al (2020) Serum neurofilament light levels in normal aging and their association with morphologic brain changes. *Nat Commun* 11(1):812
 28. Kaeser SA et al (2021) A neuronal blood marker is associated with mortality in old age. *Nat Aging* 1(2):218–225
 29. Simren J et al (2022) Establishment of reference values for plasma neurofilament light based on healthy individuals aged 5–90 years. *Brain Commun* 4(4):fcac174
 30. Ladang A et al (2022) Neurofilament light chain concentration in an aging population. *Aging Clin Exp Res* 34(2):331–339
 31. Bridel C et al (2019) Diagnostic value of cerebrospinal fluid neurofilament light protein in neurology: a systematic review and meta-analysis. *JAMA Neurol* 76(9):1035–1048
 32. Syrjanen JA et al (2022) Associations of amyloid and neurodegeneration plasma biomarkers with comorbidities. *Alzheimers Dement* 18(6):1128–1140
 33. O'Bryant SE et al (2022) Medical comorbidities and ethnicity impact plasma Alzheimer's disease biomarkers: important considerations for clinical trials and practice. *Alzheimers Dement*
 34. Huber H et al (2023) Levels of Alzheimer's disease blood biomarkers are altered after food intake—a pilot intervention study in healthy adults. *Alzheimers Dement*
 35. Kac PR et al (2022) Diagnostic value of serum versus plasma phospho-tau for Alzheimer's disease. *Alzheimers Res Ther* 14(1):65
 36. Rubsamen N et al (2022) A method to combine neurofilament light measurements from blood serum and plasma in clinical and population-based studies. *Front Neurol* 13:894119
 37. Preische O et al (2019) Serum neurofilament dynamics predicts neurodegeneration and clinical progression in presymptomatic Alzheimer's disease. *Nat Med* 25(2):277–283
 38. O'Connor A et al (2021) Plasma phospho-tau181 in presymptomatic and symptomatic familial Alzheimer's disease: a longitudinal cohort study. *Mol Psychiatry* 26(10):5967–5976
 39. O'Connor A et al (2022) Plasma GFAP in presymptomatic and symptomatic familial Alzheimer's disease: a longitudinal cohort study. *J Neurol Neurosurg Psychiatry*
 40. Pereira JB et al (2021) Plasma markers predict changes in amyloid, tau, atrophy and cognition in non-demented subjects. *Brain* 144(9):2826–2836
 41. Janelidze S et al (2020) Plasma P-tau181 in Alzheimer's disease: relationship to other biomarkers, differential diagnosis, neuropathology and longitudinal progression to Alzheimer's dementia. *Nat Med* 26(3):379–386
 42. Li Y et al (2022) Validation of plasma amyloid-beta 42/40 for detecting Alzheimer disease amyloid plaques. *Neurology* 98(7):e688–e699
 43. Arranz J, Zhu N, Rubio-Guerra S, Rodríguez-Baz P, Carmona-Iragui M, Barroeta I, Illán-Gala I, Santos-Santos M, Fortea J, Lleó A, Tondo M, Alcolea D (2023) Diagnostic performance of plasma A β 1-42, A β 1-40 and pTau181 in the LUMIPULSE automated platform for the detection of Alzheimer disease. medRxiv
 44. Wilson EN et al (2022) Performance of a fully-automated Lumipulse plasma phospho-tau181

- assay for Alzheimer's disease. *Alzheimers Res Ther* 14(1):172
45. Zetterberg H et al (2011) Hypoxia due to cardiac arrest induces a time-dependent increase in serum amyloid beta levels in humans. *PLoS One* 6(12):e28263
 46. Kim K et al (2020) Clinically accurate diagnosis of Alzheimer's disease via multiplexed sensing of core biomarkers in human plasma. *Nat Commun* 11(1):119
 47. Karikari TK et al (2021) Diagnostic performance and prediction of clinical progression of plasma phospho-tau181 in the Alzheimer's Disease Neuroimaging Initiative. *Mol Psychiatry* 26(2):429–442
 48. Lantero Rodriguez J et al (2020) Plasma p-tau181 accurately predicts Alzheimer's disease pathology at least 8 years prior to post-mortem and improves the clinical characterisation of cognitive decline. *Acta Neuropathol* 140(3):267–278
 49. Thijssen EH et al (2021) Plasma phosphorylated tau 217 and phosphorylated tau 181 as biomarkers in Alzheimer's disease and frontotemporal lobar degeneration: a retrospective diagnostic performance study. *Lancet Neurol* 20(9):739–752
 50. Chatterjee P et al (2021) Diagnostic and prognostic plasma biomarkers for preclinical Alzheimer's disease. *Alzheimers Dement*
 51. Thijssen EH et al (2020) Diagnostic value of plasma phosphorylated tau181 in Alzheimer's disease and frontotemporal lobar degeneration. *Nat Med* 26(3):387–397
 52. Moscoso A et al (2021) Longitudinal associations of blood phosphorylated Tau181 and neurofilament light chain with neurodegeneration in Alzheimer disease. *JAMA Neurol* 78(4):396–406
 53. Palmqvist S et al (2020) Discriminative accuracy of plasma Phospho-tau217 for Alzheimer disease vs other neurodegenerative disorders. *JAMA* 324(8):772–781
 54. Leuzy A et al (2022) Blood-based biomarkers for Alzheimer's disease. *EMBO Mol Med* 14(1):e14408
 55. Cicognola C et al (2021) Plasma glial fibrillary acidic protein detects Alzheimer pathology and predicts future conversion to Alzheimer dementia in patients with mild cognitive impairment. *Alzheimers Res Ther* 13(1):68
 56. Alagaratnam J et al (2021) Correlation between CSF and blood neurofilament light chain protein: a systematic review and meta-analysis. *BMJ Neurol Open* 3(1):e000143
 57. Raket LL et al (2020) Utility of plasma neurofilament light and total tau for clinical trials in Alzheimer's disease. *Alzheimers Dement (Amst)* 12(1):e12099
 58. Alcolea D et al (2021) Use of plasma biomarkers for AT(N) classification of neurodegenerative dementias. *J Neurol Neurosurg Psychiatry* 92(11):1206–1214
 59. Nakamura A et al (2018) High performance plasma amyloid-beta biomarkers for Alzheimer's disease. *Nature* 554(7691):249–254
 60. Oeckl P et al (2023) Relationship of serum beta-synuclein with blood biomarkers and brain atrophy. *Alzheimers Dement* 19(4):1358–1371
 61. Perneczky R et al (2023) Anti-amyloid antibody therapies in Alzheimer's disease. *Brain* 146(3):842–849



Alzheimer's Disease Prevention and Treatment Based on Population-Based Approaches

Robert Pernecky

Abstract

The development of effective prevention and treatment strategies for Alzheimer's disease (AD) and dementia is hindered by limited knowledge of the underlying biological and environmental causes. While certain genetic factors have been associated with AD, and various lifestyle and environmental factors have been linked to dementia risk, the interactions between genes and the environment are not yet fully understood. To identify new avenues for dementia prevention, coordinated global efforts are needed to utilize existing cohorts and resources effectively and efficiently. This chapter provides an overview of current research on risk and protective factors for AD and dementia and discusses the opportunities and challenges associated with population-based approaches.

Key words Alzheimer's disease, Dementia, Drug development, Population-based, Cohort studies, Lifestyle, Environment, Genetics

1 Introduction

As the prevalence of Alzheimer's disease (AD) and its impact on healthcare and socioeconomic systems continue to grow worldwide, there is an urgent need to improve drug development success rates, and the approval of the first anti-amyloid- β ($A\beta$) targeting antibody drugs is initiating an exciting new era of AD treatment and prevention [1]. Successful drug discovery and development in other fields, such as cancer and infectious diseases, have demonstrated the potential of translational models that link epidemiological cohort and genetic data to potential drug targets and study endpoints [2]. Technology platforms, including neuroimaging, -omics, and biomarkers, have proven to be powerful tools in this process. To discover and develop novel disease-modifying treatments beyond the first generation of $A\beta$ -targeting compounds, as called for since the 2013 G8 Dementia Summit, a significant cultural shift must be initiated [3].

Increased life expectancy is a remarkable achievement of modern society, but it also brings with it the challenge of a growing prevalence of age-related disorders, placing a significant burden on global healthcare systems. Over the next 30–40 years, the number of people affected by late-onset neurodegenerative disorders such as AD and Parkinson’s disease is expected to increase three- to fourfold worldwide [4], with national and international dementia plans calling for immediate action, such as the 2017 WHO Action Plan [5]. The individual risk for these disorders varies greatly, and the development of effective prevention and treatment strategies is hindered by our incomplete understanding of the factors that influence vulnerability to neurodegeneration [6]. There is growing consensus among researchers that an individual’s susceptibility to AD is determined by a combination of biological and environmental factors, with important implications for the development of effective interventions. While AD has a significant hereditary component, monogenic familial forms caused by clearly pathogenic mutations in specific genes are extremely rare. Most AD cases are likely the result of complex interactions between common genetic variants and other factors. The biological mechanisms by which genes influence an individual’s vulnerability to AD are not yet fully understood, but recent discoveries of risk genes suggest the involvement of certain biological pathways, such as A β and tau processing, immune response, and lipid processing [7].

1.1 A Multicausal Model of Alzheimer’s Disease

An individual’s vulnerability to AD is influenced by a complex interplay of genetic and non-genetic factors, including environmental and epigenetic mechanisms. While genetic susceptibility is innate, the risk associated with certain environmental factors may be modifiable, offering opportunities for prevention or treatment through changes in lifestyle. Many known environmental risk factors are related to conditions such as obesity, diabetes, and vascular disease, which can potentially be modified. Protective environmental factors, such as a Mediterranean diet and cognitive and physical activity, can also be actively strengthened. An individual’s personality and inherent beliefs can influence their behavior and lifestyle choices, affecting their dementia risk. Additionally, factors outside an individual’s control, such as the healthcare system, air pollution, and the wider economy, can also impact their chronic disease risk [8] (Fig. 1).

2 Epidemiological Approaches to Alzheimer’s Disease Research

While the association between AD risk and certain environmental and lifestyle factors is well established, the underlying biological mechanisms are not yet fully understood. The use of high-throughput “omics” technologies in prospective cohort studies

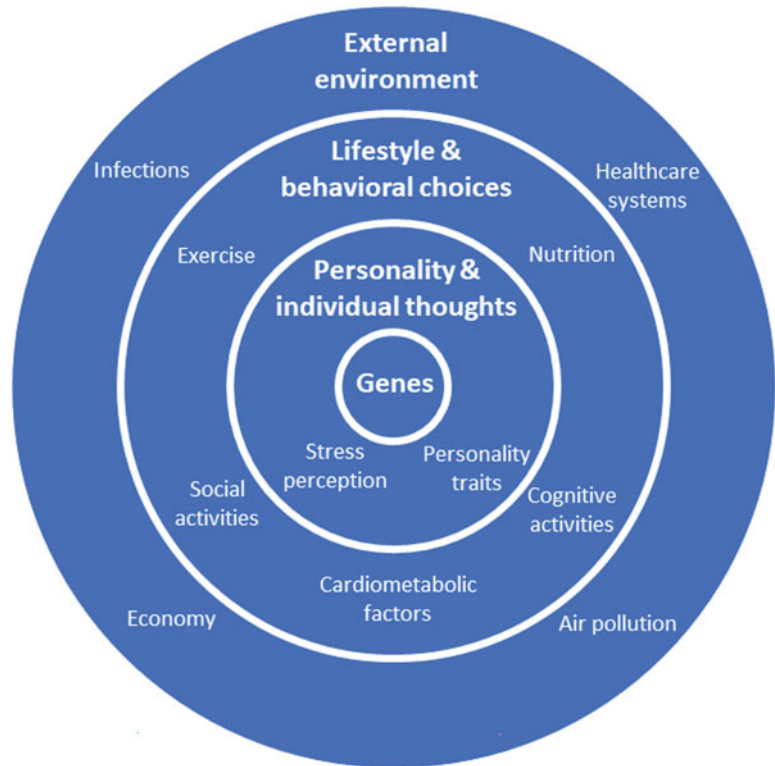


Fig. 1 A multicausal model of Alzheimer's disease

with stored biospecimens offers a unique opportunity to characterize individuals at the molecular level. Advanced technologies, such as epigenomics and metabolomics, can be applied to pre-diagnostic biosamples to identify early disease markers. By combining epidemiological and molecular data, with a focus on gene-environment interactions, etiological research can pave the way for the identification of etiopathogenetic pathways through systems biology approaches.

2.1 The Value of Established Global Infrastructures

In recent decades, several large-scale prospective cohort studies on aging and neurodegenerative disease have been established worldwide. These studies have collected detailed dietary, lifestyle, and clinical information, as well as biological samples and neuroimaging data, from many participants at various points in their lives. The continued follow-up of these existing infrastructures and the collection of additional detailed information from these aging populations is a highly efficient strategy for addressing existing knowledge gaps.

However, data analysis has mostly been restricted to individual cohorts due to differences in assessment procedures and methods between countries. As a result, there is an urgent need for

concerted action to facilitate the comprehensive analysis of large datasets and to increase knowledge transfer between experts in different countries. Standardized data analysis across global aging and neurodegeneration cohorts and effective networking activities between researchers in the field are crucial. The main goals of such networking activities are to develop harmonized measures for key outcomes used in different cohort studies (e.g., genome-wide data, environmental exposures, neuroimaging data, blood and cerebrospinal fluid proteins, etc.) and to facilitate knowledge transfer and expert exchanges between countries and institutions. This includes providing the best possible training and career opportunities for early-stage researchers. Examples of large-scale initiatives that effectively integrate information from diverse cohorts include the Dementias Platform UK (<http://www.dementiasplatform.uk/>) and the EU Joint Program for Neurodegenerative Disease Research (JPND) longitudinal cohort studies action group [9].

3 Gene-Environment Interaction Analyses

There is a growing consensus among researchers that AD and other forms of dementia result from a combination of genetic and environmental factors and their interactions [10, 11]. Subtle differences in DNA sequence composition, such as different allele status at polymorphic sites, can cause individuals to respond differently to the same environmental exposure. This partly explains why some individuals have a lower risk of developing the disease due to an environmental insult, while others are more vulnerable. For instance, not all carriers of the apolipoprotein (*APOE*) $\epsilon 4$ risk allele, the most significant genetic risk factor for AD, develop the disease or dementia even at an advanced age [12]. The presence of unknown gene-environment patterns may also contribute to the difficulties in identifying other major genetic effects besides *APOE*.

Population-based studies have consistently shown that 40–50% of individuals who reach the age of 90 are free of dementia, indicating that dementia is not an inevitable consequence of aging [13]. However, several important questions remain unanswered, including why some individuals escape dementia and what genetic and/or environmental factors distinguish them from those who develop the disease. Epidemiological studies have provided some insights into these questions, but the picture is still incomplete, particularly regarding the interactions among different factors at different stages of life.

Previous research has suggested interactions between genes and various environmental factors. For example, gene-diet interactions have been found between the *APOE* gene and nutrients such as n-3 polyunsaturated fatty acids, vitamin E, total fat, and energy intake in relation to the risk of AD and dementia [14]. Emerging

evidence also suggests that vascular changes can exacerbate preexisting A β pathology, increasing the risk of AD and dementia. Vascular pathology appears to amplify the risk of AD associated with the *APOE* ϵ 4 allele [15], and *APOE* ϵ 4 also seems to influence how certain lifestyle habits affect cognitive trajectories. For instance, the protective effect of regular leisure-time physical activity against AD and dementia appears to be more pronounced among carriers of the *APOE* risk allele [16]. Additionally, a low vascular burden and a healthy lifestyle seem to modulate genetic susceptibility [12]. However, evidence on gene-environment interactions beyond *APOE* is limited.

3.1 Diet and Nutrition

Diet is a major environmental factor that influences health throughout an individual's lifetime. In AD, the neurodegenerative process is accompanied by increased inflammation and oxidative stress, which can be partially alleviated by certain nutrients. Epidemiological studies have shown that higher intake or blood levels of several dietary components, including long-chain n-3 polyunsaturated fatty acids, antioxidant vitamins C and E, carotenoids, polyphenols, and vitamins B and D [17, 18], are associated with slower cognitive decline or lower risk of AD and dementia [19]. The potential role of fatty acids in AD was highlighted by the discovery of a set of phospholipids in peripheral blood that could predict the risk of amnesic mild cognitive impairment (MCI) or AD over a 2- to 3-year period with 90% accuracy [20]. However, the predictive validity of these biomarkers needs to be confirmed over a longer follow-up period to rule out reverse causality.

Healthy diets that provide a combination of nutrients, such as the Mediterranean diet, have been linked to a lower risk of dementia or cognitive decline [21]. This is supported by evidence from a limited number of controlled trials [22, 23]; however, most intervention studies with dietary supplements (e.g., n-3 polyunsaturated fatty acids, antioxidants, B vitamins) have been unsuccessful [24]. One possible explanation for this failure is that these studies did not adequately target individuals according to their genetic susceptibility to AD or to genetic characteristics linked to nutrient metabolism [11].

Although few epidemiological studies have investigated this domain, the most widely documented AD gene-diet interaction is related to the *APOE* genotype with n-3 polyunsaturated fatty acids (including a controlled trial [25]; see [14] for a review), vitamin E [26], and total fat and energy intake [27]. These studies have yielded conflicting results, showing a protective effect of diet in *APOE* ϵ 4 non-carriers only, in *APOE* ϵ 4 carriers only, or no effect at all. However, modest sample sizes in these studies have limited the ability to accurately investigate these nutrient-*APOE* interactions. More recently discovered genetic polymorphisms implicated in the risk of AD in large genome-wide association studies (GWAS; e.g.,

CLU, *CRI*, *BIN1*, *PICALM*, or *ABCA7*) could also be involved, but their interaction with diet has yet to be investigated.

There is biological plausibility for interactions between diet and several AD genes based on their involvement in common pathways. For example, dietary intake of nutrients with antioxidant properties such as vitamins C and E, carotenoids, and polyphenols influences the oxidative status of the body. Total antioxidant status and glutathione peroxidase activity are reduced in individuals carrying the *APOE* $\epsilon 4$ allele, suggesting reduced antioxidant defense mechanisms [28]. Furthermore, n-3 polyunsaturated fatty acids may modulate systemic inflammation. *CRI*, another locus for AD risk, encodes the main receptor of the protein complement C3b, involved in inflammatory processes [29]. Some AD genes might also interact with diet based on their role in nutrient bioavailability, particularly with lipids. For example, the *APOE* and *CLU* genes encode the ApoE and clusterin (ApoJ) apolipoproteins, respectively. These are the most abundantly expressed apolipoproteins in the central nervous system and important regulators of lipid metabolism in the brain. Both ApoE and ApoJ apolipoproteins are involved in the transport of cholesterol and phospholipids [30].

Healthy diets, such as the Mediterranean diet and the Dietary Approaches to Stop Hypertension (DASH) diet, provide combinations of nutrients that may impact inflammatory, metabolic, and oxidative status. Interactions between some of the novel loci associated with AD and the Mediterranean diet on cognitive function have been reported in a subsample from an intervention study [31]. These interactions need to be replicated in larger samples. Other potential candidate genes for gene-diet interactions in AD and dementia include variants associated with the metabolism of promising candidate nutrients for dementia prevention. These variants likely impact the bioavailability of these nutrients to the bloodstream and brain. For example, *FADS1/FADS2* [32] and *ELOVL2* encode fatty acid desaturases and elongases, respectively, which modify plasma levels of long-chain polyunsaturated fatty acids [33]. *BCMO1* encodes beta-carotene 15'-monooxygenase-1, which impacts blood levels of carotenoids [34]. It is possible that these genes modify the relationship between diet and AD risk. Finally, genes related to more general pathways linking diet to health, such as cholesterol or homocysteine metabolism [35, 36], might also be interesting modulators of the association between diet and AD.

3.2 Physical Activity and Other Active Lifestyles

Active lifestyles, which include physical, cognitive, and social activities, promote good overall and vascular health, increase functional capacity, and improve quality of life in all age groups. Epidemiological studies indicate that physical activity in midlife [16] or late-life [37] is associated with a reduced risk of cognitive impairment, AD, and dementia. Staying physically active or becoming more active

after midlife also contributes to lowering dementia risk, especially in people who are overweight or obese in midlife. These findings suggest that the window of opportunity for physical activity interventions to prevent dementia may extend from midlife to older ages [38]. Regular leisure time physical activity with at least moderate intensity was associated with a reduced risk for AD and dementia, but in some studies, even less intensive physical activity (e.g., walking) was protective.

Participation in cognitively stimulating activities [39, 40] and engagement in social activities [41] are linked to lower AD and dementia risk. Education and occupational status were shown to be important determinants of later life cognitive performance [42–44]. Many activities, occupational exposures, and hobbies include several active lifestyle domains (e.g., dancing has physical, mental, and social components), and it is important to explore further their relative importance and interactions. There is also regular co-occurrence with life habits and other lifestyle-related and psychosocial risk factors (e.g., unhealthy nutrition, smoking, and stress), and further work using large, long-term studies is needed to understand the interplay between these factors.

The cognitive reserve hypothesis (i.e., the capacity of the brain to cope with pathology to minimize or postpone the clinical expression of AD pathophysiology) was proposed to explain the disjunction between the degree of brain damage and its clinical presentation. Epidemiological studies suggest that lifelong experiences, including educational and occupational attainment, and leisure activities in later life are associated with a higher reserve [45]. However, several mechanisms may mediate the protective effect of an active lifestyle against dementia. Previous experimental studies suggested that physical activity can influence the aging brain through several mechanisms such as impact on A β burden, improving cerebral perfusion, increasing neurogenesis, induction of several gene transcripts, and central and peripheral growth factors such as brain-derived neurotrophic factor, which are relevant for the maintenance of cognitive functions [46–48]. Also, physical activity and engagement in cognitive and social activities were associated with both structural and functional brain changes [47].

There is only limited evidence about interactions between active lifestyles and genetic variants. It was reported that the protective effect of regular leisure time physical activity against AD and dementia may be more pronounced among *APOE* $\epsilon 4$ carriers vs non-carriers [12, 16]. The protective effect of higher education was also reported to be more pronounced in carriers of the *APOE* risk allele [49], and lifetime cognitive activity moderated the *APOE* genotype effect such that cortical A β pathology in positron emission tomography was lower in $\epsilon 4$ carriers that reported higher cognitive activity [50].

APOE has been linked to all the major features in AD pathogenesis, including A β generation and clearance, neurofibrillary tangle formation, oxidative stress, apoptosis, dysfunction in lipid transport and homeostasis, modulation of intracellular signaling, and synaptic plasticity. In all cases, the presence of the *APOE* $\epsilon 4$ allele has been shown to exacerbate these disturbances, in contrast to the protection seen with other *APOE* isoforms. Because of this and the relatively high frequency of the $\epsilon 4$ allele in the general population, possible *APOE*-lifestyle interactions may have relevance for dementia prevention (e.g., targeted/tailored interventions for *APOE* risk allele carriers) [51].

Some evidence also exists for AD risk genes other than *APOE*. It was suggested that individuals at high genetic risk (estimated by an integration of risk alleles within *PICALM*, *BINI*, and *CLU*) who maintain a physically active lifestyle show selective benefits in episodic memory performance [52]. However, these findings need to be validated in larger studies, and more research is needed to clarify potential gene-physical activity interactions.

3.3 Psychosocial Factors

There is increasing evidence that the development and clinical manifestation of AD in old age is not determined during a restricted period (e.g., old age), but rather it is a result of complex interactions between biological factors and environmental exposures over the life course. Psychosocial factors, defined as factors relating to the interrelationships of social variables and individual thoughts and behaviors, have recently emerged as determinants of dementia from several longitudinal population-based studies. There is growing evidence supporting the hypothesis that stress-related psychosocial factors experienced across the life course, such as negative life events during early life, midlife occupational stress, and late-life depression, sleep problems, and perception of psychological stress, play a role in the development of neuropsychiatric disorders such as AD and dementia [41].

The timing of a stressor may determine how much of an impact it will have on the brain. Experience of stress is thought to have a detrimental effect on the brain, especially during stages of life when the brain undergoes major changes (e.g., development in early life and deterioration in late life) [53, 54]. Although only a few studies have investigated such long-term associations, it was reported that people who experienced two or more stressful life events in early life had significantly smaller amygdala and hippocampal volumes in later life and those who experienced a late-life event had significantly larger amygdala volumes. In line with these findings, other studies have also shown that a history of early parental death or other negative events increases dementia risk [55].

Although the brain is more mature and stable in midlife and therefore should be less vulnerable to environmental insults, stress may still cause several physiological reactions in the central nervous,

endocrine, immune, and cardiovascular systems. All these factors may exacerbate cognitive deficits leading to dementia. Consistent with this notion, midlife occupation-related stress (low control at work and low job demands) was shown to be related to an increased dementia risk [56]. High job strain was related to an increased risk of late-life AD and dementia over a 6-year follow-up period [41]. In addition, it was reported that women who experienced midlife negative life events were at higher risk of AD and dementia over a 38-year follow-up period [57]. These findings suggest that midlife occupational stressors are relevant for AD and dementia risk and that there may be gender differences in terms of vulnerability to psychological stress from life events experienced in midlife.

During the aging process, the brain loses its plasticity, which is crucial to post-stress dendritic atrophy. Life after retirement may be viewed as a calm period when stressors such as workload and family responsibilities are no longer present; however, old age also encompasses powerful stressors due to important life changes, such as the loss of loved ones and the occurrence of new health problems. Therefore, these stressors and accompanying stress responses may affect functioning due to reduced plasticity of the aging brain [58]. To date, evidence on late-life stress in relation to the risk of AD and dementia is limited. Late-life depressive symptoms, stress-prone personality traits (high neuroticism in combination with low extraversion) [59], sleep problems [60], and stressful life events [61] were related to an increased risk of dementia.

Several genes have been implicated in stress response and stress-related disorders, including *IGF-1R*, *COMT*, *BDNF*, and *IDE*. However, it has not been sufficiently explored so far if these genes interact with known stressors and how they impact the related increased risk of AD and dementia. For example, individuals carrying the *APOE* $\epsilon 4$ allele may have less effective neural protection and repair mechanisms, and therefore they may be more vulnerable to the effects of environmental factors on cognitive function. Because of the common mechanisms shared by psychosocial factors and *APOE* $\epsilon 4$, it is plausible to hypothesize that these factors have interactive effects on the risk of AD and dementia.

3.4 Cardiometabolic Factors

It is well established that cardiovascular and metabolic pathology affect the risk of AD and dementia, with various studies showing an association with hypertension [62], arterial stiffness [63], diabetes mellitus [64], smoking [65], hypercholesterolemia [66], and cardiac diseases [67]. Importantly, this link is reported not only with vascular dementia but also with AD. Cardiometabolic factors have a direct effect on this association as well as serve as mediators for other factors, such as lifestyle and nutrition. For instance, physical activity leads to lower stiffness of the vasculature, better glycemic control, and less cardiac disease. Therefore, physical activity may lower the risk of dementia directly (e.g., via better brain perfusion

or improved neurogenesis), but may also exert its effect through any of the three mentioned cardiometabolic factors, all of which affect AD and dementia risk. Similarly, dietary factors can directly affect brain metabolism, but diet may also influence the cardiovascular system, which in turn can affect the brain.

Although cardiometabolic factors have been implicated in the development of all-cause dementia and AD, few studies have examined the association between subclinical atherosclerosis markers and prospective risk of dementia. High values of carotid intima-media thickness were associated with a significantly increased risk of dementia and AD during a 5-year follow-up [68]. Similarly, over a median follow-up of 9 years, the highest quintile of carotid intima-media thickness was related to prospective AD and dementia risk [69]. During up to 14 years of follow-up, multiple measures of carotid atherosclerosis were associated with a significant risk of AD and dementia [70]. All these findings suggest the possibility that early intervention to reduce atherosclerosis may help delay or prevent dementia onset.

Only a few studies have evaluated the association between MRI markers of cerebrovascular disease and prospective risk of AD and dementia, reporting that, compared with healthy controls, subjects with AD and MCI show white matter volumetric abnormalities suggestive of reduced white matter integrity [71]. These changes affect complex networks relevant to episodic memory and other cognitive processes, which characterize cognitive impairment and dementia. White matter abnormalities are also associated with an increased risk of progression from MCI to dementia [72]. Overall, the severity of white matter degeneration appears to be higher in advanced clinical stages of dementia, supporting the construct that these abnormalities are part of the relevant pathophysiological processes. Again, these findings may have relevant therapeutic implications because white matter lesions can be prevented through appropriate control of cardiometabolic factors.

Even though the association between cardiometabolic factors, alone or clustered within the concept of metabolic syndrome [73], and risk of AD and dementia are well established, it remains largely unclear how cardiometabolic pathology leads to cognitive impairment. There is evidence suggesting that this effect is at least partly exerted through interaction of cardiometabolic pathology with genetic factors. For instance, many studies have shown that vascular pathology and *APOE* $\epsilon 4$ have a multiplicative rather than an additive effect with regard to risk of AD and dementia [74]. Similar findings were reported regarding MRI markers of vascular disease and *APOE* $\epsilon 4$. Carriers of the $\epsilon 4$ allele, for example, have more subclinical brain lesions if they suffer from hypertension as well, which could reflect a diminished capacity for neuronal repair in the risk allele carrier group [75]. Conversely, several novel genes recently identified for AD are postulated to be involved in pathways

that involve lipid processing and vascular disease [76]. *ABCA7* is a member of a superfamily of cholesterol and phospholipid transporters that has been implicated in both lipid homeostasis and Alzheimer's disease (AD) risk [77]. This superfamily has been shown not only to influence lipids but also to directly affect the vessel wall [78]. However, putative interactions between cardiometabolic and genetic risk factors of AD and dementia largely remain to be investigated. Further research is needed to better understand the complex interplay between these factors and their impact on the risk of AD and dementia.

4 Conclusions

The availability of new antibody drugs for AD is the beginning of a new era of dementia prevention and treatment. At the same time, developing more effective treatment options for AD remains a major societal priority. The integration of existing cohort resources with advanced gene-environment analytical approaches may be an effective means to achieve this goal. After decades of intensive research on AD and other types of dementia, disease concepts with a stronger biological focus compared to the traditional clinically oriented classification systems have emerged. Consensus regarding these concepts is increasing among specialists in the field and diagnostic criteria will keep evolving as new evidence on the biology of AD becomes available.

Epidemiological research has shown that AD and dementia are predominantly disorders of older individuals. This means that aging and dementia are closely related processes and both are related to lifelong accumulation of biological alterations and organ damage. Although AD is the most common pathology underlying dementia in adults aged 65 years and older, studies suggest that the relationship between AD pathology and expression of dementia is attenuated in the oldest old [79]. The traditional diagnosis of dementia subtypes has been challenged by neuropathological and neuroimaging studies. These studies have revealed that AD-related lesions are often present in the brain of older adults with intact cognition and that more than half of the people with a clinical diagnosis of AD at autopsy have other neurodegenerative alterations and cerebrovascular injuries [80]. Moreover, epidemiological research strongly supports a relevant role of lifestyle and cardiovascular risk factors in the development of dementia. Most of these factors are especially relevant if present during middle age, and many of them are also related to cardiovascular disease [81]. Several studies report a decreasing trend of dementia incidence in Europe, possibly due to the decreased vascular burden during the last two to three decades [82, 83]. It is likely that after the age of 75 years, most dementia cases are due to both vascular and neurodegenerative disease of

different types. To improve dementia prevention worldwide, a closer collaboration of existing and planned population-based studies is required, and associations between biological and external factors should be scrutinized.

Acknowledgments

R.P. is supported by the German Center for Neurodegenerative Disorders (Deutsches Zentrum für Neurodegenerative Erkrankungen, DZNE), the Deutsche Forschungsgemeinschaft (DFG, 1007 German Research Foundation) under Germany's Excellence Strategy within the framework of 1008 the Munich Cluster for Systems Neurology (EXC 2145 SyNergy – ID 390857198), the Davos Alzheimer's Collaborative, the VERUM Foundation, the Robert-Vogel-Foundation, the German Center for Neurodegenerative Diseases (DZNE), the National Institute for Health and Care Research (NIHR) Sheffield Biomedical Research Centre (NIHR203321), the University of Cambridge – Ludwig-Maximilians-University Munich Strategic Partnership within the framework of the German Excellence Initiative and Excellence Strategy, and the European Commission under the Innovative Health Initiative program (project 101132356).

References

1. Perneczky R, Jessen F, Grimmer T, Levin J, Floel A, Peters O, Froelich L (2023) Anti-amyloid antibody therapies in Alzheimer's disease. *Brain* 146(3):842–849. <https://doi.org/10.1093/brain/awad005>
2. Hutter CM, Mechanic LE, Chatterjee N, Kraft P, Gillanders EM, Tank NCIG-ET (2013) Gene-environment interactions in cancer epidemiology: a National Cancer Institute Think Tank report. *Genet Epidemiol* 37(7): 643–657. <https://doi.org/10.1002/gepi.21756>
3. The Lancet N (2014) G8 dementia summit: a chance for united action. *Lancet Neurol* 13(1): 1. [https://doi.org/10.1016/S1474-4422\(13\)70275-8](https://doi.org/10.1016/S1474-4422(13)70275-8)
4. Prince M, Wimo A, Guerchet M, Ali G, Wu Y-T, Prina M (2015) World Alzheimer Report 2015 – the global impact of Dementia: an analysis of prevalence, incidence, cost and trends
5. WHO (2017) Global action plan on the public health response to dementia 2017–2025
6. Scheltens P, Blennow K, Breteler MM, de Strooper B, Frisoni GB, Salloway S, Van der Flier WM (2016) Alzheimer's disease. *Lancet* 388(10043):505–517. [https://doi.org/10.1016/S0140-6736\(15\)01124-1](https://doi.org/10.1016/S0140-6736(15)01124-1)
7. Bellenguez C, Kucukali F, Jansen IE, Kleiheidam L, Moreno-Grau S, Amin N, Naj AC, Campos-Martin R, Grenier-Boley B, Andrade V, Holmans PA, Boland A, Damotte V, van der Lee SJ, Costa MR, Kuulasmaa T, Yang Q, de Rojas I, Bis JC, Yaqub A, Prokic I, Chapuis J, Ahmad S, Giedraitis V, Aarsland D, Garcia-Gonzalez P, Abdelnour C, Alarcon-Martin E, Alcolea D, Alegret M, Alvarez I, Alvarez V, Armstrong NJ, Tsolaki A, Antunez C, Appollonio I, Arcaro M, Archetti S, Pastor AA, Arosio B, Athanasia L, Bailly H, Banaj N, Baquero M, Barral S, Beiser A, Pastor AB, Below JE, Bencheq P, Benussi L, Berr C, Besse C, Bessi V, Binetti G, Bizarro A, Blesa R, Boada M, Boerwinkle E, Borroni B, Boschi S, Bossu P, Brathen G, Bressler J, Bresner C, Brodaty H, Brookes KJ, Brusco LI, Buiza-Rueda D, Burger K, Burholt V, Bush WS, Calero M, Cantwell LB, Chene G, Chung J, Cuccaro ML, Carracedo A, Cecchetti R, Cervera-Carles L, Charbonnier C, Chen HH, Chillotti C, Ciccone S, Claassen J, Clark C, Conti E, Corma-Gomez A, Costantini E,

- Custodero C, Daian D, Dalmaso MC, Daniele A, Dardiotis E, Dartigues JF, de Deyn PP, de Paiva LK, de Witte LD, Debette S, Deckert J, Del Ser T, Denning N, DeStefano A, Dichgans M, Diehl-Schmid J, Diez-Fairen M, Rossi PD, Djurovic S, Duron E, Duzel E, Dufouil C, Eiriksdottir G, Engelborghs S, Escott-Price V, Espinosa A, Ewers M, Faber KM, Fabrizio T, Nielsen SF, Fardo DW, Farotti L, Fenoglio C, Fernandez-Fuertes M, Ferrari R, Ferreira CB, Ferri E, Fin B, Fischer P, Fladby T, Fliessbach K, Fongang B, Fornage M, Fortea J, Foroud TM, Fostinelli S, Fox NC, Franco-Macias E, Bullido MJ, Frank-Garcia A, Froelich L, Fulton-Howard B, Galimberti D, Garcia-Alberca JM, Garcia-Gonzalez P, Garcia-Madrona S, Garcia-Ribas G, Ghidoni R, Giegling I, Giorgio G, Goate AM, Goldhardt O, Gomez-Fonseca D, Gonzalez-Perez A, Graff C, Grande G, Green E, Grimmer T, Grunblatt E, Grunin M, Gudnason V, Guetta-Baranes T, Haapasalo A, Hadjigeorgiou G, Haines JL, Hamilton-Nelson KL, Hampel H, Hanon O, Hardy J, Hartmann AM, Hausner L, Harwood J, Heilmann-Heimbach S, Helisalmi S, Heneka MT, Hernandez I, Herrmann MJ, Hoffmann P, Holmes C, Holstege H, Vilas RH, Hulsman M, Humphrey J, Biessels GJ, Jian X, Johansson C, Jun GR, Kastumata Y, Kauwe J, Kehoe PG, Kilander L, Stahlbom AK, Kivipelto M, Koivisto A, Kornhuber J, Kosmidis MH, Kukull WA, Kuksa PP, Kunkle BW, Kuzma AB, Lage C, Laukka EJ, Launer L, Lauria A, Lee CY, Lehtisalo J, Lerch O, Lleo A, Longstreth W Jr, Lopez O, de Munain AL, Love S, Lovemark M, Luckcuck L, Lunetta KL, Ma Y, Macias J, MacLeod CA, Maier W, Mangialasche F, Spallazzi M, Marquie M, Marshall R, Martin ER, Montes AM, Rodriguez CM, Masullo C, Mayeux R, Mead S, Mecocci P, Medina M, Meggy A, Mehrabian S, Mendoza S, Menendez-Gonzalez M, Mir P, Moebus S, Mol M, Molina-Porcel L, Montreal L, Morelli L, Moreno F, Morgan K, Mosley T, Nothen MM, Muchnik C, Mukherjee S, Nacmias B, Ngandu T, Nicolas G, Nordestgaard BG, Olaus R, Orellana A, Orsini M, Ortega G, Padovani A, Paolo C, Papenberg G, Parnetti L, Pasquier F, Pastor P, Peloso G, Perez-Cordon A, Perez-Tur J, Pericard P, Peters O, Pijnenburg YAL, Pineda JA, Pinol-Ripoll G, Pisanu C, Polak T, Popp J, Posthuma D, Priller J, Puerta R, Quenez O, Quintela I, Thomassen JQ, Rabano A, Rainero I, Rajabli F, Ramakers I, Real LM, Reinders MJT, Reitz C, Reyes-Dumeyer D, Ridge P, Riedel-Heller S, Riederer P, Roberto N, Rodriguez-Rodriguez E, Rongve A, Allende IR, Rosende-Roca M, Royo JL, Rubino E, Rujescu D, Saez ME, Sakka P, Saltvedt I, Sanabria A, Sanchez-Arjona MB, Sanchez-Garcia F, Juan PS, Sanchez-Valle R, Sando SB, Sarnowski C, Satizabal CL, Scamosci M, Scarneas N, Scarpini E, Scheltens P, Scherbaum N, Scherer M, Schmid M, Schneider A, Schott JM, Selbaek G, Seripa D, Serrano M, Sha J, Shadrin AA, Skrobot O, Slifer S, Snijders GJL, Soinen H, Solfrizzi V, Solomon A, Song Y, Sorbi S, Sotolongo-Grau O, Spalletta G, Spottke A, Squassina A, Stordal E, Tartan JP, Tarraga L, Tesi N, Thalamuthu A, Thomas T, Tosto G, Traykov L, Tremolizzo L, Tybjaerg-Hansen A, Uitterlinden A, Ullgren A, Ulstein I, Valero S, Valladares O, Broeckhoven CV, Vance J, Vardarajan BN, van der Lugt A, Dongen JV, van Rooij J, van Swieten J, Vandenberghe R, Verhey F, Vidal JS, Vogelgsang J, Vyhnaek M, Wagner M, Wallon D, Wang LS, Wang R, Weinhold L, Wiltfang J, Windle G, Woods B, Yannakoulia M, Zare H, Zhao Y, Zhang X, Zhu C, Zulaica M, Eadb, Gr@Ace, Degesco, Eadi, Gerad, Demgene, FinnGen, Adgc, Charge, Farrer LA, Pstaty BM, Ghanbari M, Raj T, Sachdev P, Mather K, Jessen F, Ikram MA, de Mendonca A, Hort J, Tsolaki M, Pericak-Vance MA, Amouyel P, Williams J, Frikke-Schmidt R, Clarimon J, Deleuze JF, Rossi G, Seshadri S, Andreassen OA, Ingelsson M, Hiltunen M, Sleegers K, Schellenberg GD, van Duijn CM, Sims R, van der Flier WM, Ruiz A, Ramirez A, Lambert JC (2022) New insights into the genetic etiology of Alzheimer's disease and related dementias. *Nat Genet* 54(4):412–436. <https://doi.org/10.1038/s41588-022-01024-z>
8. Terracciano A, Sutun AR, An Y, O'Brien RJ, Ferrucci L, Zonderman AB, Resnick SM (2014) Personality and risk of Alzheimer's disease: new data and meta-analysis. *Alzheimers Dement* 10(2):179–186. <https://doi.org/10.1016/j.jalz.2013.03.002>
 9. JDP News (2013) Longitudinal cohort studies in neurodegeneration research: report of the JPND action group
 10. Elbaz A, Dufouil C, Alperovitch A (2007) Interaction between genes and environment in neurodegenerative diseases. *C R Biol* 330(4):318–328. <https://doi.org/10.1016/j.crv.2007.02.018>
 11. Barberger-Gateau P, Lambert JC, Feart C, Peres K, Ritchie K, Dartigues JF, Alperovitch A (2013) From genetics to dietetics: the contribution of epidemiology to understanding

- Alzheimer's disease. *J Alzheimers Dis* 33(Suppl 1):S457–S463. <https://doi.org/10.3233/JAD-2012-129019>
12. Ferrari C, Xu WL, Wang HX, Winblad B, Sorbi S, Qiu C, Fratiglioni L (2013) How can elderly apolipoprotein E epsilon4 carriers remain free from dementia? *Neurobiol Aging* 34(1):13–21. <https://doi.org/10.1016/j.neurobiolaging.2012.03.003>
 13. Yang Z, Slavin MJ, Sachdev PS (2013) Dementia in the oldest old. *Nat Rev Neurol* 9(7):382–393. <https://doi.org/10.1038/nrneuro.2013.105>
 14. Barberger-Gateau P, Samieri C, Feart C, Plourde M (2011) Dietary omega 3 polyunsaturated fatty acids and Alzheimer's disease: interaction with apolipoprotein E genotype. *Curr Alzheimer Res* 8(5):479–491
 15. Hofman A, Ott A, Breteler MM, Bots ML, Sliemers AJ, van Harskamp F, van Duijn CN, Van Broeckhoven C, Grobbee DE (1997) Atherosclerosis, apolipoprotein E, and prevalence of dementia and Alzheimer's disease in the Rotterdam Study. *Lancet* 349(9046):151–154. [https://doi.org/10.1016/S0140-6736\(96\)09328-2](https://doi.org/10.1016/S0140-6736(96)09328-2)
 16. Rovio S, Kareholt I, Helkala EL, Viitanen M, Winblad B, Tuomilehto J, Soininen H, Nissinen A, Kivipelto M (2005) Leisure-time physical activity at midlife and the risk of dementia and Alzheimer's disease. *Lancet Neurol* 4(11):705–711. [https://doi.org/10.1016/S1474-4422\(05\)70198-8](https://doi.org/10.1016/S1474-4422(05)70198-8)
 17. Clarke RJ, Bennett DA (2008) B vitamins for prevention of cognitive decline: insufficient evidence to justify treatment. *JAMA* 300(15):1819–1821. <https://doi.org/10.1001/jama.300.15.1819>
 18. Annweiler C, Montero-Odasso M, Llewellyn DJ, Richard-Devantoy S, Duque G, Beauchet O (2013) Meta-analysis of memory and executive dysfunctions in relation to vitamin D. *J Alzheimers Dis* 37(1):147–171. <https://doi.org/10.3233/JAD-130452>
 19. Cunnane SC, Plourde M, Pifferi F, Begin M, Feart C, Barberger-Gateau P (2009) Fish, docosahexaenoic acid and Alzheimer's disease. *Prog Lipid Res* 48(5):239–256. <https://doi.org/10.1016/j.plipres.2009.04.001>
 20. Mapstone M, Cheema AK, Fiandaca MS, Zhong X, Mhyre TR, MacArthur LH, Hall WJ, Fisher SG, Peterson DR, Haley JM, Nazar MD, Rich SA, Berlau DJ, Peltz CB, Tan MT, Kawas CH, Federoff HJ (2014) Plasma phospholipids identify antecedent memory impairment in older adults. *Nat Med* 20(4):415–418. <https://doi.org/10.1038/nm.3466>
 21. Feart C, Samieri C, Alles B, Barberger-Gateau P (2013) Potential benefits of adherence to the Mediterranean diet on cognitive health. *Proc Nutr Soc* 72(1):140–152. <https://doi.org/10.1017/S0029665112002959>
 22. Martinez-Lapiscina EH, Clavero P, Toledo E, San Julian B, Sanchez-Tainta A, Corella D, Lamuela-Raventos RM, Martinez JA, Martinez-Gonzalez MA (2013) Virgin olive oil supplementation and long-term cognition: the PREDIMED-NAVARRA randomized, trial. *J Nutr Health Aging* 17(6):544–552. <https://doi.org/10.1007/s12603-013-0027-6>
 23. Scheltens P, Twisk JW, Blesa R, Scarpini E, von Arnim CA, Bongers A, Harrison J, Swinkels SH, Stam CJ, de Waal H, Wurtman RJ, Wieggers RL, Vellas B, Kamphuis PJ (2012) Efficacy of Souvenaid in mild Alzheimer's disease: results from a randomized, controlled trial. *J Alzheimers Dis* 31(1):225–236. <https://doi.org/10.3233/JAD-2012-121189>
 24. Barberger-Gateau P, Feart C, Samieri C, Letenneur L (2013) Dietary patterns and dementia. In: Yaffe K (ed) *Chronic medical disease and cognitive aging: toward a healthy body and brain*. Oxford University Press, New York, pp 197–224
 25. Quinn JF, Raman R, Thomas RG, Yurko-Mauro K, Nelson EB, Van Dyck C, Galvin JE, Emond J, Jack CR Jr, Weiner M, Shinto L, Aisen PS (2010) Docosahexaenoic acid supplementation and cognitive decline in Alzheimer disease: a randomized trial. *JAMA* 304(17):1903–1911. <https://doi.org/10.1001/jama.2010.1510>
 26. Morris MC, Evans DA, Bienias JL, Tangney CC, Bennett DA, Aggarwal N, Wilson RS, Scherr PA (2002) Dietary intake of antioxidant nutrients and the risk of incident Alzheimer disease in a biracial community study. *JAMA* 287(24):3230–3237
 27. Luchsinger JA, Tang MX, Shea S, Mayeux R (2002) Caloric intake and the risk of Alzheimer disease. *Arch Neurol* 59(8):1258–1263
 28. Kharrazi H, Vaisi-Raygani A, Rahimi Z, Tavilani H, Aminian M, Pourmotabbed T (2008) Association between enzymatic and non-enzymatic antioxidant defense mechanism with apolipoprotein E genotypes in Alzheimer disease. *Clin Biochem* 41(12):932–936. <https://doi.org/10.1016/j.clinbiochem.2008.05.001>
 29. Lambert JC, Heath S, Even G, Campion D, Sleegers K, Hiltunen M, Combarros O, Zelenika D, Bullido MJ, Tavernier B, Letenneur L, Bettens K, Berr C, Pasquier F, Fievet N, Barberger-Gateau P, Engelborghs S,

- De Deyn P, Mateo I, Franck A, Helisalmi S, Porcellini E, Hanon O, European Alzheimer's Disease Initiative I, de Pancorbo MM, Lendon C, Dufouil C, Jaillard C, Leveillard T, Alvarez V, Bosco P, Mancuso M, Panza F, Nacmias B, Bossu P, Piccardi P, Annoni G, Seripa D, Galimberti D, Hannequin D, Licastro F, Soininen H, Ritchie K, Blanche H, Dartigues JF, Tzourio C, Gut I, Van Broeckhoven C, Alperovitch A, Lathrop M, Amouyel P (2009) Genome-wide association study identifies variants at *CLU* and *CR1* associated with Alzheimer's disease. *Nat Genet* 41(10):1094–1099. <https://doi.org/10.1038/ng.439>
30. Sleegers K, Lambert JC, Bertram L, Cruts M, Amouyel P, Van Broeckhoven C (2010) The pursuit of susceptibility genes for Alzheimer's disease: progress and prospects. *Trends Genet* 26(2):84–93. <https://doi.org/10.1016/j.tig.2009.12.004>
31. Martinez-Lapiscina EH, Galbete C, Corella D, Toledo E, Buil-Cosiales P, Salas-Salvado J, Ros E, Martinez-Gonzalez MA (2014) Genotype patterns at *CLU*, *CR1*, *PICALM* and *APOE*, cognition and Mediterranean diet: the PREDIMED-NAVARRA trial. *Genes Nutr* 9(3):393. <https://doi.org/10.1007/s12263-014-0393-7>
32. Harslof LB, Larsen LH, Ritz C, Hellgren LI, Michaelsen KF, Vogel U, Lauritzen L (2013) FADS genotype and diet are important determinants of DHA status: a cross-sectional study in Danish infants. *Am J Clin Nutr* 97(6):1403–1410. <https://doi.org/10.3945/ajcn.113.058685>
33. Lemaitre RN, Tanaka T, Tang W, Manichaikul A, Foy M, Kabagambe EK, Nettleton JA, King IB, Weng LC, Bhattacharya S, Bandinelli S, Bis JC, Rich SS, Jacobs DR Jr, Cherubini A, McKnight B, Liang S, Gu X, Rice K, Laurie CC, Lumley T, Browning BL, Psaty BM, Chen YD, Friedlander Y, Djousse L, Wu JH, Siscovick DS, Uitterlinden AG, Arnett DK, Ferrucci L, Fornage M, Tsai MY, Mozaffarian D, Steffen LM (2011) Genetic loci associated with plasma phospholipid n-3 fatty acids: a meta-analysis of genome-wide association studies from the CHARGE Consortium. *PLoS Genet* 7(7):e1002193. <https://doi.org/10.1371/journal.pgen.1002193>
34. Ferrucci L, Perry JR, Matteini A, Perola M, Tanaka T, Silander K, Rice N, Melzer D, Murray A, Cluett C, Fried LP, Albanes D, Corsi AM, Cherubini A, Guralnik J, Bandinelli S, Singleton A, Virtamo J, Walston J, Semba RD, Frayling TM (2009) Common variation in the beta-carotene 15,15'-monooxygenase 1 gene affects circulating levels of carotenoids: a genome-wide association study. *Am J Hum Genet* 84(2):123–133. <https://doi.org/10.1016/j.ajhg.2008.12.019>
35. Kathiresan S, Willer CJ, Peloso GM, Demissie S, Musunuru K, Schadt EE, Kaplan L, Bennett D, Li Y, Tanaka T, Voight BF, Bonnycastle LL, Jackson AU, Crawford G, Surti A, Guiducci C, Burt NP, Parish S, Clarke R, Zelenika D, Kubalanza KA, Morken MA, Scott LJ, Stringham HM, Galan P, Swift AJ, Kuusisto J, Bergman RN, Sundvall J, Laakso M, Ferrucci L, Scheet P, Sanna S, Uda M, Yang Q, Lunetta KL, Dupuis J, de Bakker PI, O'Donnell CJ, Chambers JC, Kooner JS, Hercberg S, Meneton J, Lakatta EG, Scuteri A, Schlessinger D, Tuomilehto J, Collins FS, Groop L, Altshuler D, Collins R, Lathrop GM, Melander O, Salomaa V, Peltonen L, Orho-Melander M, Ordovas JM, Boehnke M, Abecasis GR, Mohlke KL, Cupples LA (2009) Common variants at 30 loci contribute to polygenic dyslipidemia. *Nat Genet* 41(1):56–65. <https://doi.org/10.1038/ng.291>
36. van Meurs JB, Pare G, Schwartz SM, Hazra A, Tanaka T, Vermeulen SH, Cotlarciuc I, Yuan X, Malarstig A, Bandinelli S, Bis JC, Blom H, Brown MJ, Chen C, Chen YD, Clarke RJ, Dehghan A, Erdmann J, Ferrucci L, Hamsten A, Hofman A, Hunter DJ, Goel A, Johnson AD, Kathiresan S, Kampman E, Kiel DP, Kiemeny LA, Chambers JC, Kraft P, Lindemans J, McKnight B, Nelson CP, O'Donnell CJ, Psaty BM, Ridker PM, Rivadeneira F, Rose LM, Seedorf U, Siscovick DS, Schunkert H, Selhub J, Ueland PM, Vollenweider P, Waeber G, Waterworth DM, Watkins H, Witteman JC, den Heijer M, Jacques P, Uitterlinden AG, Kooner JS, Rader DJ, Reilly MP, Mooser V, Chasman DI, Samani NJ, Ahmadi KR (2013) Common genetic loci influencing plasma homocysteine concentrations and their effect on risk of coronary artery disease. *Am J Clin Nutr* 98(3):668–676. <https://doi.org/10.3945/ajcn.112.044545>
37. Scarmeas N, Luchsinger JA, Schupf N, Brickman AM, Cosentino S, Tang MX, Stern Y (2009) Physical activity, diet, and risk of Alzheimer disease. *JAMA* 302(6):627–637. <https://doi.org/10.1001/jama.2009.1144>
38. Tolppanen AM, Solomon A, Kulmala J, Kareholt I, Ngandu T, Rusanen M, Laatikainen T, Soininen H, Kivipelto M (2014) Leisure-time physical activity from mid- to late life, body mass index, and risk of dementia. *Alzheimers Dement*. <https://doi.org/10.1016/j.jalz.2014.01.008>

39. Wilson RS, Mendes De Leon CF, Barnes LL, Schneider JA, Bienias JL, Evans DA, Bennett DA (2002) Participation in cognitively stimulating activities and risk of incident Alzheimer disease. *JAMA* 287(6):742–748
40. Stern Y, Gurland B, Tatemichi TK, Tang MX, Wilder D, Mayeux R (1994) Influence of education and occupation on the incidence of Alzheimer's disease. *JAMA* 271(13):1004–1010
41. Paillard-Borg S, Fratiglioni L, Xu W, Winblad B, Wang HX (2012) An active lifestyle postpones dementia onset by more than one year in very old adults. *J Alzheimers Dis* 31(4):835–842. <https://doi.org/10.3233/JAD-2012-120724>
42. Liu Y, Julkunen V, Paajanen T, Westman E, Wahlund LO, Aitken A, Sobow T, Mecocci P, Tsolaki M, Vellas B, Muehlboeck S, Spenger C, Lovestone S, Simmons A, Soininen H, AddNeuroMed C (2012) Education increases reserve against Alzheimer's disease—evidence from structural MRI analysis. *Neuroradiology* 54(9):929–938. <https://doi.org/10.1007/s00234-012-1005-0>
43. Finkel D, Andel R, Gatz M, Pedersen NL (2009) The role of occupational complexity in trajectories of cognitive aging before and after retirement. *Psychol Aging* 24(3):563–573. <https://doi.org/10.1037/a0015511>
44. Karp A, Andel R, Parker MG, Wang HX, Winblad B, Fratiglioni L (2009) Mentally stimulating activities at work during midlife and dementia risk after age 75: follow-up study from the Kungsholmen Project. *Am J Geriatr Psychiatry* 17(3):227–236. <https://doi.org/10.1097/JGP.0b013e318190b691>
45. Stern Y (2012) Cognitive reserve in ageing and Alzheimer's disease. *Lancet Neurol* 11(11):1006–1012. [https://doi.org/10.1016/S1474-4422\(12\)70191-6](https://doi.org/10.1016/S1474-4422(12)70191-6)
46. Cotman CW, Berchtold NC (2002) Exercise: a behavioral intervention to enhance brain health and plasticity. *Trends Neurosci* 25(6):295–301
47. Rovio S, Spulber G, Nieminen LJ, Niskanen E, Winblad B, Tuomilehto J, Nissinen A, Soininen H, Kivipelto M (2010) The effect of midlife physical activity on structural brain changes in the elderly. *Neurobiol Aging* 31(11):1927–1936. <https://doi.org/10.1016/j.neurobiolaging.2008.10.007>
48. Komulainen P, Pedersen M, Hanninen T, Bruunsgaard H, Lakka TA, Kivipelto M, Hassinen M, Rauramaa TH, Pedersen BK, Rauramaa R (2008) BDNF is a novel marker of cognitive function in ageing women: the DR's EXTRA Study. *Neurobiol Learn Mem* 90(4):596–603. <https://doi.org/10.1016/j.nlm.2008.07.014>
49. Wang HX, Gustafson DR, Kivipelto M, Pedersen NL, Skoog I, Windblad B, Fratiglioni L (2012) Education halves the risk of dementia due to apolipoprotein epsilon4 allele: a collaborative study from the Swedish brain power initiative. *Neurobiol Aging* 33(5):1007 e1001–1007. <https://doi.org/10.1016/j.neurobiolaging.2011.10.003>
50. Wirth M, Villeneuve S, La Joie R, Marks SM, Jagust WJ (2014) Gene-environment interactions: lifetime cognitive activity, APOE genotype, and beta-amyloid burden. *J Neurosci* 34(25):8612–8617. <https://doi.org/10.1523/JNEUROSCI.4612-13.2014>
51. Maioli S, Puerta E, Merino-Serrais P, Fusari L, Gil-Bea F, Rimondini R, Cedazo-Minguez A (2012) Combination of apolipoprotein E4 and high carbohydrate diet reduces hippocampal BDNF and arc levels and impairs memory in young mice. *J Alzheimers Dis* 32(2):341–355. <https://doi.org/10.3233/JAD-2012-120697>
52. Ferencz B, Laukka EJ, Welmer AK, Kalpouzos G, Angleman S, Keller L, Graff C, Lovden M, Backman L (2014) The benefits of staying active in old age: physical activity counteracts the negative influence of PICALM, BIN1, and CLU risk alleles on episodic memory functioning. *Psychol Aging* 29(2):440–449. <https://doi.org/10.1037/a0035465>
53. Cohen RA, Grieve S, Hoth KF, Paul RH, Sweet L, Tate D, Gunstad J, Stroud L, McCaffery J, Hitsman B, Niaura R, Clark CR, McFarlane A, Bryant R, Gordon E, Williams LM (2006) Early life stress and morphometry of the adult anterior cingulate cortex and caudate nuclei. *Biol Psychiatry* 59(10):975–982. <https://doi.org/10.1016/j.biopsych.2005.12.016>
54. Wolkowitz OM, Epel ES, Reus VI, Mellon SH (2010) Depression gets old fast: do stress and depression accelerate cell aging? *Depress Anxiety* 27(4):327–338. <https://doi.org/10.1002/da.20686>
55. Savva GM, Wharton SB, Ince PG, Forster G, Matthews FE, Brayne C, Medical Research Council Cognitive F, Ageing S (2009) Age, neuropathology, and dementia. *New Engl J Med* 360(22):2302–2309. <https://doi.org/10.1056/NEJMoa0806142>
56. Seidler A, Nienhaus A, Bernhardt T, Kauppinen T, Elo AL, Frolich L (2004) Psychosocial work factors and dementia. *Occup Environ Med* 61(12):962–971. <https://doi.org/10.1136/oem.2003.012153>
57. Fratiglioni L, Qiu C (2011) Prevention of cognitive decline in ageing: dementia as the target, delayed onset as the goal. *Lancet Neurol* 10(9):

- 778–779. [https://doi.org/10.1016/S1474-4422\(11\)70145-4](https://doi.org/10.1016/S1474-4422(11)70145-4)
58. McEwen BS, Morrison JH (2013) The brain on stress: vulnerability and plasticity of the prefrontal cortex over the life course. *Neuron* 79(1):16–29. <https://doi.org/10.1016/j.neuron.2013.06.028>
 59. Wang HX, Karp A, Herlitz A, Crowe M, Kareholt I, Winblad B, Fratiglioni L (2009) Personality and lifestyle in relation to dementia incidence. *Neurology* 72(3):253–259. <https://doi.org/10.1212/01.wnl.0000339485.39246.87>
 60. Hahn EA, Wang HX, Andel R, Fratiglioni L (2013) A change in sleep pattern may predict Alzheimer disease. *Am J Geriatr Psychiatry*. <https://doi.org/10.1016/j.jagp.2013.04.015>
 61. Barnes DE, Yaffe K (2011) The projected effect of risk factor reduction on Alzheimer's disease prevalence. *Lancet Neurol* 10(9): 819–828. [https://doi.org/10.1016/S1474-4422\(11\)70072-2](https://doi.org/10.1016/S1474-4422(11)70072-2)
 62. Skoog I, Lernfelt B, Landahl S, Palmertz B, Andreasson LA, Nilsson L, Persson G, Oden A, Svanborg A (1996) 15-year longitudinal study of blood pressure and dementia. *Lancet* 347(9009):1141–1145
 63. Hanon O, Haulon S, Lenoir H, Seux ML, Rigaud AS, Safar M, Girerd X, Forette F (2005) Relationship between arterial stiffness and cognitive function in elderly subjects with complaints of memory loss. *Stroke* 36(10): 2193–2197. <https://doi.org/10.1161/01.STR.0000181771.82518.1c>
 64. Ott A, Stolk RP, van Harskamp F, Pols HA, Hofman A, Breteler MM (1999) Diabetes mellitus and the risk of dementia: the Rotterdam Study. *Neurology* 53(9):1937–1942
 65. Anstey KJ, von Sanden C, Salim A, O'Kearney R (2007) Smoking as a risk factor for dementia and cognitive decline: a meta-analysis of prospective studies. *Am J Epidemiol* 166(4): 367–378. <https://doi.org/10.1093/aje/kwm116>
 66. Anstey KJ, Lipnicki DM, Low LF (2008) Cholesterol as a risk factor for dementia and cognitive decline: a systematic review of prospective studies with meta-analysis. *Am J Geriatr Psychiatry* 16(5):343–354. <https://doi.org/10.1097/JGP.0b013e31816b72d4>
 67. de la Torre JC (2006) How do heart disease and stroke become risk factors for Alzheimer's disease? *Neurol Res* 28(6):637–644. <https://doi.org/10.1179/016164106X130362>
 68. Newman AB, Fitzpatrick AL, Lopez O, Jackson S, Lyketsos C, Jagust W, Ives D, Dekosky ST, Kuller LH (2005) Dementia and Alzheimer's disease incidence in relationship to cardiovascular disease in the Cardiovascular Health Study cohort. *J Am Geriatr Soc* 53(7): 1101–1107. <https://doi.org/10.1111/j.1532-5415.2005.53360.x>
 69. van Oijen M, de Jong FJ, Witteman JC, Hofman A, Koudstaal PJ, Breteler MM (2007) Atherosclerosis and risk for dementia. *Ann Neurol* 61(5):403–410. <https://doi.org/10.1002/ana.21073>
 70. Wendell CR, Waldstein SR, Ferrucci L, O'Brien RJ, Strait JB, Zonderman AB (2012) Carotid atherosclerosis and prospective risk of dementia. *Stroke* 43(12):3319–3324. <https://doi.org/10.1161/STROKEAHA.112.672527>
 71. Radanovic M, Pereira FR, Stella F, Aprahamian I, Ferreira LK, Forlenza OV, Busatto GF (2013) White matter abnormalities associated with Alzheimer's disease and mild cognitive impairment: a critical review of MRI studies. *Expert Rev Neurother* 13(5): 483–493. <https://doi.org/10.1586/ern.13.45>
 72. de Bruijn RF, Akoudad S, Cremers LG, Hofman A, Niessen WJ, van der Lugt A, Koudstaal PJ, Vernooij MW, Ikram MA (2014) Determinants, MRI correlates, and prognosis of mild cognitive impairment: the Rotterdam Study. *J Alzheimers Dis*. <https://doi.org/10.3233/JAD-132558>
 73. Eckel RH, Grundy SM, Zimmet PZ (2005) The metabolic syndrome. *Lancet* 365(9468): 1415–1428. [https://doi.org/10.1016/S0140-6736\(05\)66378-7](https://doi.org/10.1016/S0140-6736(05)66378-7)
 74. Skoog I, Kalaria RN, Breteler MM (1999) Vascular factors and Alzheimer disease. *Alzheimer Dis Assoc Disord* 13(Suppl 3):S106–S114
 75. de Leeuw FE, Richard F, de Groot JC, van Duijn CM, Hofman A, Van Gijn J, Breteler MM (2004) Interaction between hypertension, apoE, and cerebral white matter lesions. *Stroke* 35(5):1057–1060. <https://doi.org/10.1161/01.STR.0000125859.71051.83>
 76. Lambert JC, Ibrahim-Verbaas CA, Harold D, Naj AC, Sims R, Bellenguez C, DeStafano AL, Bis JC, Beecham GW, Grenier-Boley B, Russo G, Thornton-Wells TA, Jones N, Smith AV, Chouraki V, Thomas C, Ikram MA, Zelenika D, Vardarajan BN, Kamatani Y, Lin CF, Gerrish A, Schmidt H, Kunkle B, Dunstan ML, Ruiz A, Bihoreau MT, Choi SH, Reitz C, Pasquier F, Cruchaga C, Craig D, Amin N, Berr C, Lopez OL, De Jager PL, Deramecourt V, Johnston JA, Evans D, Lovestone S, Letenneur L, Moron FJ, Rubinsztein DC, Eiriksdottir G, Sleegers K, Goate AM, Fievet N, Huentelman MW,

- Gill M, Brown K, Kamboh MI, Keller L, Barberger-Gateau P, McGuinness B, Larson EB, Green R, Myers AJ, Dufouil C, Todd S, Wallon D, Love S, Rogaeva E, Gallacher J, St George-Hyslop P, Clarimon J, Lleo A, Bayer A, Tsuang DW, Yu L, Tsolaki M, Bossu P, Spalletta G, Proitsi P, Collinge J, Sorbi S, Sanchez-Garcia F, Fox NC, Hardy J, Deniz Naranjo MC, Bosco P, Clarke R, Brayne C, Galimberti D, Mancuso M, Matthews F, European Alzheimer's Disease I, Genetic, Environmental Risk in Alzheimer's D, Alzheimer's Disease Genetic C, Cohorts for H, Aging Research in Genomic E, Moebus S, Mecocci P, Del Zompo M, Maier W, Hampel H, Pilotto A, Bullido M, Panza F, Caffarra P, Nacmias B, Gilbert JR, Mayhaus M, Lannefelt L, Hakonarson H, Pichler S, Carrasquillo MM, Ingelsson M, Beekly D, Alvarez V, Zou F, Valladares O, Younkin SG, Coto E, Hamilton-Nelson KL, Gu W, Razquin C, Pastor P, Mateo I, Owen MJ, Faber KM, Jonsson PV, Combarros O, O'Donovan MC, Cantwell LB, Soininen H, Blacker D, Mead S, Mosley TH Jr, Bennett DA, Harris TB, Fratiglioni L, Holmes C, de Bruijn RF, Passmore P, Montine TJ, Bettens K, Rotter JJ, Brice A, Morgan K, Foroud TM, Kukull WA, Hannequin D, Powell JF, Nalls MA, Ritchie K, Lunetta KL, Kauwe JS, Boerwinkle E, Riemenschneider M, Boada M, Hiltunen M, Martin ER, Schmidt R, Rujescu D, Wang LS, Dartigues JF, Mayeux R, Tzourio C, Hofman A, Nothen MM, Graff C, Psaty BM, Jones L, Haines JL, Holmans PA, Lathrop M, Pericak-Vance MA, Launer LJ, Farrer LA, van Duijn CM, Van Broeckhoven C, Moskvina V, Seshadri S, Williams J, Schellenberg GD, Amouyel P (2013) Meta-analysis of 74,046 individuals identifies 11 new susceptibility loci for Alzheimer's disease. *Nat Genet* 45(12):1452–1458. <https://doi.org/10.1038/ng.2802>
77. Hollingworth P, Harold D, Sims R, Gerrish A, Lambert JC, Carrasquillo MM, Abraham R, Hamshere ML, Pahwa JS, Moskvina V, Dowzell K, Jones N, Stretton A, Thomas C, Richards A, Ivanov D, Widdowson C, Chapman J, Lovestone S, Powell J, Proitsi P, Lupton MK, Brayne C, Rubinsztein DC, Gill M, Lawlor B, Lynch A, Brown KS, Passmore PA, Craig D, McGuinness B, Todd S, Holmes C, Mann D, Smith AD, Beaumont H, Warden D, Wilcock G, Love S, Kehoe PG, Hooper NM, Vardy ER, Hardy J, Mead S, Fox NC, Rossor M, Collinge J, Maier W, Jessen F, Ruther E, Schurmann B, Heun R, Kolsch H, van den Bussche H, Heuser I, Kornhuber J, Wiltfang J, Dichgans M, Frolich L, Hampel H, Gallacher J, Hull M, Rujescu D, Giegling I, Goate AM, Kauwe JS, Cruchaga C, Nowotny P, Morris JC, Mayo K, Sleegers K, Bettens K, Engelborghs S, De Deyn PP, Van Broeckhoven C, Livingston G, Bass NJ, Gurling H, McQuillin A, Gwilliam R, Deloukas P, Al-Chalabi A, Shaw CE, Tsolaki M, Singleton AB, Guerreiro R, Muhleisen TW, Nothen MM, Moebus S, Jockel KH, Klopp N, Wichmann HE, Pankratz VS, Sando SB, Aasly JO, Barcikowska M, Wszolek ZK, Dickson DW, Graff-Radford NR, Petersen RC, Alzheimer's Disease Neuroimaging I, van Duijn CM, Breteler MM, Ikram MA, DeStefano AL, Fitzpatrick AL, Lopez O, Launer LJ, Seshadri S, consortium C, Berr C, Campion D, Epelbaum J, Dartigues JF, Tzourio C, Alperovitch A, Lathrop M, consortium E, Feulner TM, Friedrich P, Riehle C, Krawczak M, Schreiber S, Mayhaus M, Nicolhaus S, Wagenpfeil S, Steinberg S, Stefansson H, Stefansson K, Snaedal J, Bjornsson S, Jonsson PV, Chouraki V, Genier-Boley B, Hiltunen M, Soininen H, Combarros O, Zelenika D, Delepine M, Bullido MJ, Pasquier F, Mateo I, Frank-Garcia A, Porcellini E, Hanon O, Coto E, Alvarez V, Bosco P, Siciliano G, Mancuso M, Panza F, Solfrizzi V, Nacmias B, Sorbi S, Bossu P, Piccardi P, Arosio B, Annoni G, Seripa D, Pilotto A, Scarpini E, Galimberti D, Brice A, Hannequin D, Licastro F, Jones L, Holmans PA, Jonsson T, Riemenschneider M, Morgan K, Younkin SG, Owen MJ, O'Donovan M, Amouyel P, Williams J (2011) Common variants at ABCA7, MS4A6A/MS4A4E, EPHA1, CD33 and CD2AP are associated with Alzheimer's disease. *Nat Genet* 43(5):429–435. <https://doi.org/10.1038/ng.803>
78. Hovingh GK, Van Wijland MJ, Brownlie A, Bisioendial RJ, Hayden MR, Kastelein JJ, Groen AK (2003) The role of the ABCA1 transporter and cholesterol efflux in familial hypoalphalipoproteinemia. *J Lipid Res* 44(6):1251–1255. <https://doi.org/10.1194/jlr.M300080-JLR200>
79. Imhof A, Kovari E, von Gunten A, Gold G, Rivara CB, Herrmann FR, Hof PR, Bouras C, Giannakopoulos P (2007) Morphological substrates of cognitive decline in nonagenarians and centenarians: a new paradigm? *J Neurol Sci* 257(1-2):72–79. <https://doi.org/10.1016/j.jns.2007.01.025>
80. Serrano-Pozo A, Frosch MP, Masliah E, Hyman BT (2011) Neuropathological alterations in Alzheimer disease. *Cold Spring Harb Perspect Med* 1(1):a006189. <https://doi.org/10.1101/cshperspect.a006189>

81. Qiu C, Kivipelto M, von Strauss E (2009) Epidemiology of Alzheimer's disease: occurrence, determinants, and strategies toward intervention. *Dialogues Clin Neurosci* 11(2):111–128
82. Matthews FE, Arthur A, Barnes LE, Bond J, Jagger C, Robinson L, Brayne C, Medical Research Council Cognitive F, Ageing C (2013) A two-decade comparison of prevalence of dementia in individuals aged 65 years and older from three geographical areas of England: results of the Cognitive Function and Ageing Study I and II. *Lancet* 382(9902):1405–1412. [https://doi.org/10.1016/S0140-6736\(13\)61570-6](https://doi.org/10.1016/S0140-6736(13)61570-6)
83. Qiu C, von Strauss E, Backman L, Winblad B, Fratiglioni L (2013) Twenty-year changes in dementia occurrence suggest decreasing incidence in central Stockholm, Sweden. *Neurology* 80(20):1888–1894. <https://doi.org/10.1212/WNL.0b013e318292a2f9>

Part II

Innovative Fluid Biomarkers



CSF N-Glycomics Using High-Throughput UPLC-ESI Techniques in Alzheimer's Disease

Angela Messina, Rita Barone, Luisa Sturiale, Mario Zappia, Angelo Palmigiano, and Domenico Garozzo

Abstract

In this chapter, we will present a high-throughput method applied in our laboratory for the structural elucidation of the cerebrospinal fluid (CSF) N-glycome. This methodology is based on a commercial equipment developed by WATERS™ to speed up N-deglycosylation and N-glycan labeling of glycoproteins of pharmaceutical and biological interest such as monoclonal antibodies. This analytical kit is sold under the trade name of RapiFluor-MS (RFMS). We have slightly modified the methodology, increasing the glycosylation time and using a high-resolution mass analyzer for the analysis of CSF N-glycans, thus obtaining a high-throughput method (up to 96 samples simultaneously), mass accuracy better than 5 ppm, and the ability to separate and identify isomers.

Key words High-throughput N-glycomics, AD, Glyco-biomarkers, N-glycans

1 Introduction

N-glycosylation is a vital post-translational protein modification that plays a crucial role in many biological processes. The N-glycan moiety of glycoproteins strongly impacts on their physiological properties (such as solubility, half-life, protein folding) and biological functions (such as intercellular signaling, immunological regulation, receptor recognition) [1]. Consequently, detailed structural characterization of N-glycans is critical to understand physiological processes and to correlate changes in glycan structures with various pathological conditions.

Alzheimer's disease (AD) is the most common neurodegenerative disease [2]. The amyloid hypothesis of AD supports that polymerization of β -amyloid ($A\beta$) peptide in the brain is the patho-mechanism that occurs as a slow, progressive process along a protracted preclinical phase lasting almost two decades [3]. $A\beta$ peptide derives from the transmembrane amyloid precursor

protein (APP) through the action of β -secretase or BACE-1 and γ -secretase. BACE-1 produces a soluble fragment, APP β , and a C-terminal membrane-bound fragment. This is cleaved by γ -secretase into an APP intracellular fragment and further processed to form different A β peptides, including the A β -40 and A β -42 [4]. The identification of the factors that may act on APP processing, sorting, and secretion might be crucial to understand the initial mechanisms of the pathological cascade leading to neurotoxicity in AD brain.

Recently, high levels of bisecting GlcNAc in AD patients were found [5]. This is of pivotal importance because it was successively demonstrated that high levels of bisected N-glycans in BACE1 block its *lysosomal* degradation by increasing its concentration and, consequently, increasing the β -amyloid production [6]. These high levels of bisecting GlcNAc are already evident at the MCI state [5] and probably in the presymptomatic years opening the way to very early diagnoses and to new pharmaceutical targets. This being the case, high-throughput (HT) investigation methods to be able to analyze the highest number of samples in the shortest possible time are necessary. Here, we present our results on the N-glycomic analysis of CSF by applying a high-throughput method that allows to analyze 96 samples simultaneously in a 96-well plate. This procedure is based, with few modifications, on a commercial tool, *RapiFluor-MS*TM (RFMS), developed for HT monoclonal antibody N-glycans analysis. We have adapted the methodology to the N-glycomic of various substrates including CSF, brain tissue, serum, and other tissues [7], allowing N-glycans identification by molecular mass measurements within few ppm confidence and retention time, separation, and relative quantification of isomeric structures.

Figure 1 shows the overlapping total ion currents (TICs) of the N-glycans released by PNGase F, labeled by the *RapiFluor-MS*TM tag, and analyzed by HILIC UPLC ESI MS of a control CSF (blue line) and an Alzheimer's patient (AD1). We identified more than 90 structures, as shown in Table 1. Noticeable, all isomeric structures are chromatographically separated.

The two profiles in Fig. 1 show large quantitative differences in the peak at retention time 16.9 corresponding to FA2B, much more intense in the TIC corresponding to the AD patient. The opposite situation is observed for the peaks at RT 15.5 corresponding to FA2 and for the peaks at RT 27.4 and 28.6 corresponding to the disialylated biantennary structure. These peaks are more intense in the control chromatogram.

Figure 2a–d displays the EICs of the peak at m/z 1267.9861 corresponding to the disialylated biantennary glycans showing that this chromatographic technique is able to separate the three biantennary disialo N-glycans. The peak at RT 26.1 min corresponds to the structure with the two sialic acids linked 2–3, the peak at RT

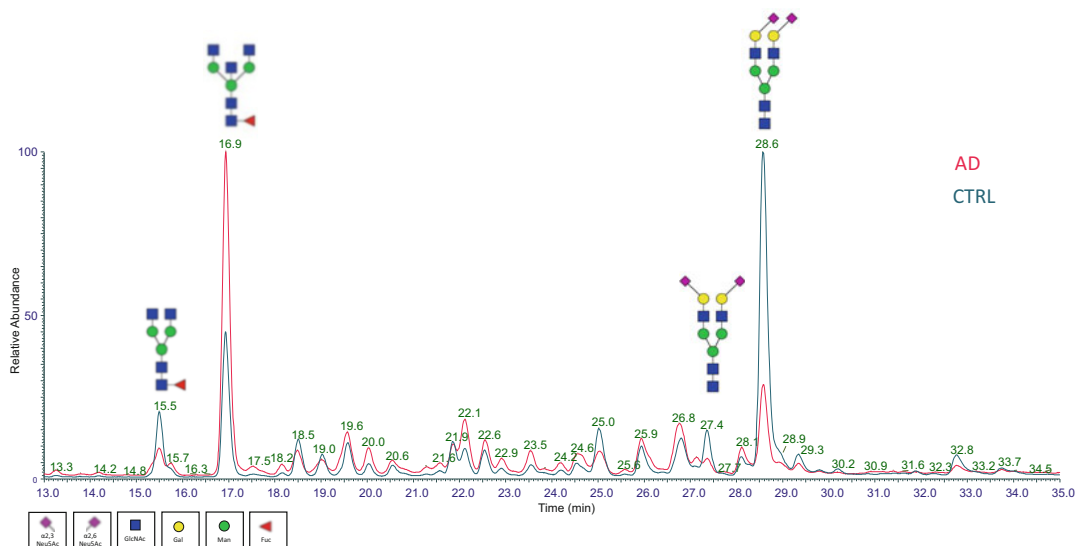


Fig. 1 Overlapping total ion currents (TICs) of the *N*-glycans released by PNGase F, labeled by the *RapiFluor-MS*[™] tag, and analyzed by HILIC UPLC ESI MS of a control cerebrospinal fluid (blue line) and an Alzheimer's patient (AD1)





















27.4 min relates to the *N*-glycan with a sialic acid linked 2,3 and one linked 2,6, and finally the most abundant peak at RT 28.6 min matches the biantennary-disialo *N*-glycan with both sialic acids linked 2,6. Furthermore, from the enlargements in Fig. 2c and d, it appears that the three peaks have different relative proportions in the AD patient and in the control patient, being the peak at 26.1 min more intense in the CSF of the AD patient. Although further investigations with large numbers of patients need to be conducted to confirm this finding, given that sialic acids are known to play a role in the pathogenesis of AD [8, 9], the knowledge on the relative abundance of sialic acids linked 2,3 or 2,6 can be very important.

2 Materials

2.1 Rapid Deglycosylation of Proteins: GlycoWorks Deglycosylation Module

1. Intact mAb Mass Check Standard.
2. MilliQ water.
3. 5x GlycoWorks Rapid Buffer
4. *RapiGest*[™] SF Powder Waters Corporation, 1 Pack of 10 mg vial.
Buffered solution. *RapiGest*[™] 5% (w/v). 10 mg *RapiGest*[™] in 200 μ L of 5x GlycoWorks Rapid Buffer (stable several months at -20 °C)
5. Sample Collection Module box.
6. Heating block (90 °C).

Table 1
Structures of CSF N-glycans identified

Matrix	Peak #	Structure	Composition	RT (min)	[M + 2H] ²⁺ Rapifluor		
					m/z (calc)	m/z (obs)	ppm
CSF	1		H5N2	17.05	773.8113	773.8105	-1.0338
CSF	2		H3N3F1	13.44	786.3271	786.3266	-0.6359
CSF	3		H4N3	15.23	794.3246	794.3226	-2.5179
CSF	4		H3N4	14.20	814.8378	814.8398	2.4545
CSF	5		H6N2	20.22	854.8377	854.8386	1.0528
CSF	5a		H6N2	20.62	854.8377	854.8364	-1.5208
CSF	6		H4N3F1	16.55	867.3535	867.3523	-1.3835
CSF	6a		H4N3F1	17.16	867.3535	867.3523	-1.3835
CSF	7		H3N4F1	15.53	887.8668	887.8665	-0.3379
CSF	8		H4N4	17.23	895.8643	895.8627	-1.7860
CSF	8a		H4N4	17.78	895.8643	895.8627	-1.7860
CSF	9		H3N5	15.76	916.3775	916.3798	2.5099
CSF	10		H4N3S1	20.86	939.8723	939.8718	-0.5320
CSF	11		H7N2	23.85	935.8641	935.8631	-1.0685
CSF	12		H3N4F2	18.72	960.8957	960.8973	1.6131
CSF	13		H4N4F1	18.53	968.8932	968.8926	-0.6193
CSF	13a		H4N4F1	19.05	968.8932	968.8926	-0.6193
CSF	14		H5N4	20.80	976.8907	976.8900	-0.7166
CSF	15		H3N5F1	16.93	989.4065	989.4055	-1.0107
CSF	16		H4N5	18.57	997.4039	997.4020	-1.9049
CSF	16a		H4N5	18.93	997.4039	997.4020	-1.9049







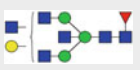
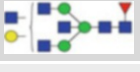








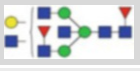


(continued)

Table 1
(continued)

Matrix	Peak #	Structure	Composition	RT (min)	[M + 2H] ²⁺ Rapifluor		ppm
					m/z (calc)	m/z (obs)	
CSF	17		H8N2	26.79	1016.8905	1016.8890	-1.4751
CSF	18		H4N3S1F1	22.10	1012.9012	1012.9035	2.2707
CSF	19		H3N6	18.42	1017.9172	1017.9189	1.6701
CSF	20		H4N4S1	21.76	1041.4120	1041.4105	-1.4404
CSF	20a		H4N4S1	22.46	1041.4120	1041.4105	-1.4404
CSF	21		H4N4F2	21.27	1041.9222	1041.9245	2.2075
CSF	21a		H4N4F2	21.59	1041.9222	1041.9245	2.2075
CSF	22		H5N4F1	21.26	1049.9196	1049.9188	-0.7620
CSF	22a		H5N4F1	21.86	1049.9196	1049.9188	-0.7620
CSF	23		H4N5F1	19.59	1070.4329	1070.4317	-1.1210
CSF	24		H4N5F1	20.04	1070.4329	1070.4317	-1.1210
CSF	25		H5N5	21.58	1078.4303	1078.4288	-1.3909
CSF	26		H3N6F1	18.42	1090.9462	1090.9483	1.9249
CSF	26a		H3N6F1	19.44	1090.9462	1090.9483	1.9249
CSF	27		H6N3S1	24.96	1101.9251	1101.9280	2.6318
CSF	27a		H6N3S1	26.45	1101.9251	1101.9278	2.4503
CSF	28		H9N2	28.90	1097.9169	1097.9186	1.5484
CSF	29		H4N4F1S1	22.90	1114.4409	1114.4395	-1.2562






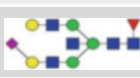
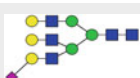

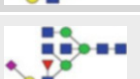







(continued)

Table 1
(continued)

Matrix	Peak #	Structure	Composition	RT (min)	[M + 2H] ²⁺ Rapifluor		
					m/z (calc)	m/z (obs)	ppm
CSF	29a		H4N4F1S1	23.54	1114.4409	1114.4395	-1.2562
CSF	30		H5N4S1	25.00	1122.4384	1122.4378	-0.5346
CSF	31		H4N5S1	23.72	1142.9516	1142.9545	2.5373
CSF	32		H4N5F2	22.12	1143.4618	1143.4644	2.2738
CSF	32a		H4N5F2	22.56	1143.4618	1143.4644	2.2738
CSF	33		H5N5F1	22.53	1151.4593	1151.4582	-0.9553
CSF	34		H4N6F1	21.30	1171.9726	1171.9747	1.7918
CSF	34a		H4N6F1	22.28	1171.9726	1171.9747	1.7918
CSF	35		H5N4F1S1	24.00	1195.4673	1195.4663	-0.8365
CSF	35a		H5N4F1S1	24.53	1195.4673	1195.4663	-0.8365
CSF	35b		H5N4F1S1	25.94	1195.4673	1195.4663	-0.8365
CSF	36		H5N4F3	26.67	1195.9775	1195.9800	2.0736
CSF	37		H4N5F1S1	21.86	1215.9806	1215.9833	2.2204
CSF	37a		H4N5F1S1	22.92	1215.9806	1215.9833	2.2204
CSF	37b		H4N5F1S1	24.67	1215.9806	1215.9837	2.5494
CSF	38		H5N5S1	26.00	1223.9781	1223.9786	0.4085
CSF	39		H6N5F1	26.45	1232.4857	1232.4873	1.2982
CSF	40		H4N6F2	24.22	1245.0015	1245.0039	1.9277
CSF	41		H5N4S2	26.08	1267.9861	1267.9862	0.0789










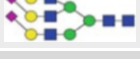

(continued)

Table 1
(continued)

Matrix	Peak #	Structure	Composition	RT (min)	[M + 2H] ²⁺ Rapifluor		ppm
					m/z (calc)	m/z (obs)	
CSF	41a		H5N4S2	27.38	1267.9861	1267.9850	-0.8675
CSF	41b		H5N4S2	28.59	1267.9861	1267.9850	-0.8675
CSF	42		H4N5S1F2	26.72	1289.0089	1289.0123	2.6377
CSF	43		H5N5F1S1	24.52	1297.0070	1297.0096	2.0046
CSF	43a		H5N5F1S1	25.10	1297.0070	1297.0097	2.0817
CSF	43b		H5N5F1S1	26.77	1297.0070	1297.0102	2.4672
CSF	44		H6N5S1	28.25	1305.0045	1305.0058	0.9962
CSF	44a		H6N5S1	28.97	1305.0045	1305.0070	1.9157
CSF	45		H4N6S1F1	23.56	1317.5203	1317.5227	1.8216
CSF	45a		H4N6S1F1	24.13	1317.5203	1317.5222	1.4421
CSF	46		H4N6S1	28.53	1325.5177	1325.5162	-1.1316
CSF	47		H5N6F2	23.53	1326.0279	1326.0265	-1.0558
CSF	47a		H5N6F2	23.81	1326.0279	1326.0262	-1.2820
CSF	47b		H5N6F2	24.18	1326.0279	1326.0264	-1.1312
CSF	48		H5N4F1S2	26.85	1341.0150	1341.0174	1.7897
CSF	49		H5N4F1S2	28.11	1341.0150	1341.0175	1.8643

(continued)

Table 1
(continued)

Matrix	Peak #	Structure	Composition	RT (min)	[M + 2H] ²⁺ Rapifluor		ppm
					m/z (calc)	m/z (obs)	
CSF	49a		H5N4F1S2	29.35	1341.0150	1341.0127	-1.7151
CSF	50		H5N5S2	29.14	1369.5258	1369.5260	0.1460
CSF	51		H5N5F1S2	26.98	1442.5547	1442.5589	2.9115
CSF	51a		H5N5F1S2	28.48	1442.5547	1442.5600	3.6740
CSF	51b		H5N5F1S2	29.80	1442.5547	1442.5580	2.2876
CSF	52		H5N6S1F2	27.33	1471.5757	1471.5779	1.4950
CSF	52a		H5N6S1F2	27.75	1471.5757	1471.5802	3.0579
CSF	53		H5N6S2F1	28.25	1544.0944	1544.0972	1.8134
CSF	54		H6N5S3	32.76	1596.0999	1596.1023	1.5037
CSF	55		H6N5S3F1	31.62	1669.1288	1669.1297	0.5392
CSF	55a		H6N5S3F1	33.75	1669.1288	1669.1311	1.3780

Linkages are not indicated on the cartoons, except for sialic acid linkages

7. GlycoWorks Rapid PNGase F.
8. Heating block (50 °C).

2.2 Rapid Labeling of Glycosylamines

1. GlycoWorks Reagent Solvent Anhydrous DMF.
2. GlycoWorks *Rapi*Fluor-MS™ Reagent Powder.
3. Acetonitrile (MeCN) UHPLC-MS, Scharlau-1 L.

2.3 HILIC SPE Clean-up of Labeled Glycosylamines

1. GlycoWorks HILIC μElution plate (included in the Sample Collection Module box).
2. Vacuum manifold.

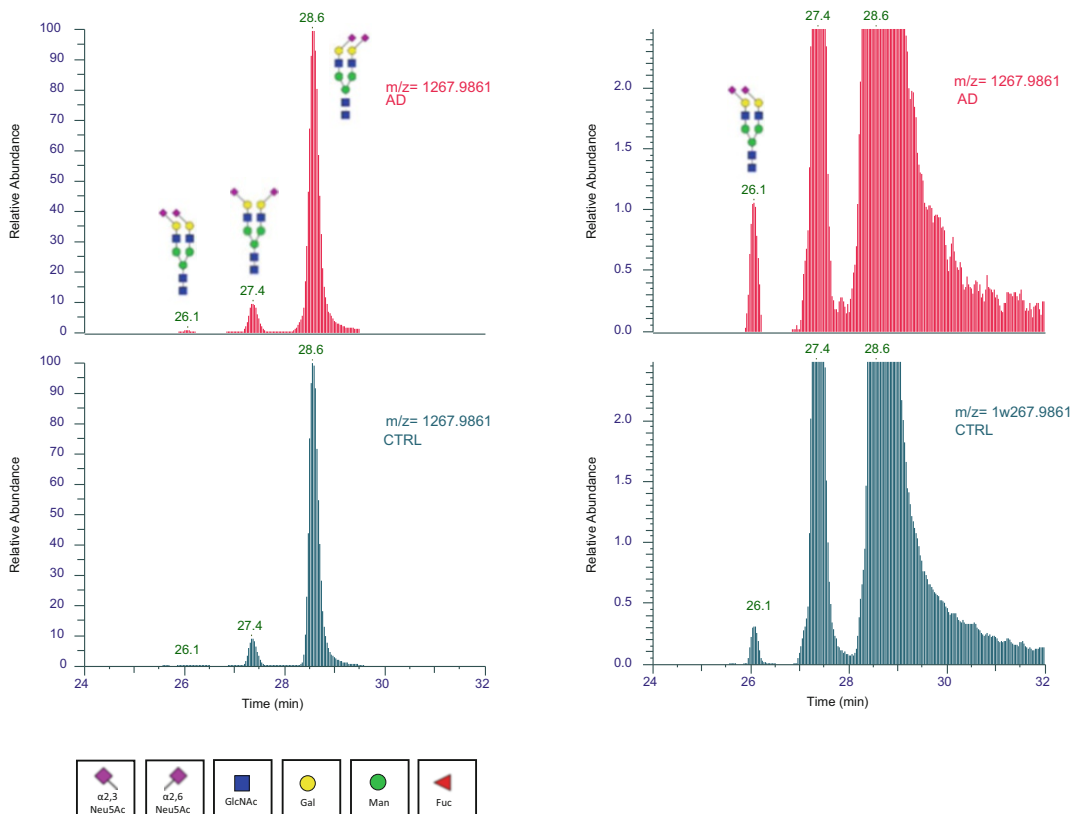


Fig. 2 EICs of the peak at m/z 1267.9861 corresponding to the disialylated biantennary glycans showing that this chromatographic technique is able to separate the three biantennary disialo N-glycans. The peak at RT 26.1 min corresponds to the structure with the two sialic acids linked 2–3, the peak at RT 27.4 min relates to the N-glycan with a sialic acid linked 2.3 and one linked 2.6, and finally the most abundant peak at RT 28.6 min matches the biantennary-disialo N-glycan with both sialic acids linked 2,6

3. Waste tray.
4. 96-well collection plate
5. 600 μ L Labeling Reaction tubes
6. MilliQ water.
 - Conditioning solution 1.* MilliQ water
7. Acetonitrile (MeCN) UHPLC-MS, Scharlau-1L.
 - Conditioning solution 2.* 15:85 (v/v) MilliQ water/MeCN
8. Formic acid LC-MS grade, Fluka Analytical.
 - Washing solution.* 1:9:90 (v/v/v) formic acid/MilliQ water/MeCN
9. GlycoWorks SPE Elution Buffer (200 mM ammonium acetate in 5% MeCN).
 - Eluting solution.* GlycoWorks SPE Elution Buffer.

2.4 HILIC-UPLC-ESI-MS Analysis for GlycoWorks RapiFluor-MS-Labeled N-Glycans

1. UHPLC THERMO system (Ultimate 3000 LPG3400SD) coupled to an Exactive Orbitrap HESI-II mass spectrometer (Thermo Fisher Scientific Inc., Bremen, Germany).
2. Hydrophilic interaction liquid chromatography (HILIC) column (ACQUITY UPLC Glycan BEH Amide 130 Å, Waters, 2.1 mm × 150 mm, 1.7 μm, Waters Corporation Milford, MA, USA).
3. Mobile phase A: 50 mM ammonium formate solution, pH 4.4 (Waters Ammonium Formate Soln-Glycan Analysis reconstituted in 1 L MilliQ water).
4. Mobile phase B: MeCN, UHPLC-MS, Scharlau-1L.

3 Methods

3.1 Rapid Deglycosylation of Proteins: GlycoWorks Deglycosylation Module

1. A volume of 7.5 μL of glycoprotein solution with a concentration of about 2 mg/mL is used. It is recommended not to exceed a total glycoprotein quantity of 15 μg, to not affect the PNGase F to substrate ratio.
2. Heat and equilibrate the two heat blocks to 50 °C and 90 °C, respectively, at least 30 min prior to beginning.
3. As a control standard, a vial (1 mg/vial) of Intact mAb Mass Check Standard is reconstituted in 500 μL of MilliQ water to obtain a 2 mg/mL IgG solution.
4. The contents of one vial (10 mg) *RapiGest*TM SF are dissolved in 200 μL of 5x GlycoWorks Rapid Buffer to prepare a buffered solution of 5% (w/v) *RapiGest*TM SF Surfactant. Vortex.
5. Add 15.3 μL of MilliQ water into a 1 mL tube.
6. Dispense 7.5 μL of the 2 mg/mL glycoprotein solution into above tube.
7. Add 6 μL of buffered solution of 5% (w/v) *RapiGest*TM SF Surfactant to each above tube.
8. Denature this mixture for 3 min in the heat block set at 90 °C.
9. Remove the tubes from the heat block and cool at room temperature for 3 min.
10. Dispense 1.2 μL of GlycoWorks Rapid PNGase F enzyme. Aspirate to mix.
11. Incubate the mixture for 30 min in the heat block set at 50 °C.
12. Remove the tubes from the heat block and cool at room temperature for 3 min.

3.2 Rapid Labeling of Glycosylamines

1. The content of one vial of 23 mg of the GlycoWorks *RapiFluor*-MS™ Reagent Powder is dissolved in 335 μL of the GlycoWorks Reagent Solvent Anhydrous DMF to prepare the Reagent solution. Mix and vortex to solubilize.
2. Dispense 12 μL of the *RapiFluor*-MS™ Reagent solution to the deglycosylation mixture in each 1 mL tube. Aspirate to mix at least five times.
3. Allow the labeling reaction at room temperature for 5 min.
4. Dilute each mixture with 358 μL of MeCN.

3.3 HILIC SPE Clean-up of Labeled Glycosylamines

1. Prepare a vacuum manifold with a set of three shims and set up on it the GlycoWorks HILIC $\mu\text{Elution}$ plate.
2. Add 200 μL of MilliQ water to condition each well.
3. Dispense 200 μL of 15:85 (v/v) MilliQ water/MeCN solution to equilibrate wells.
4. Load all ~ 400 μL of MeCN-diluted samples.
5. Add 600 μL (two times) of 1:9:90 (v/v/v) formic acid/MilliQ water/MeCN solution to wash wells.
6. Replace the waste tray with the 96-well collection plate fitted with 600 μL Labeling Reaction tubes.
7. Add 30 μL (three times) of GlycoWorks SPE Elution Buffer to elute glycans.

3.4 HILIC-UPLC-ESI-MS Analysis for GlycoWorks *RapiFluor*-MS-Labeled N-Glycans

Eluted RFMS-derivatized N-glycans, tagged at the glycosylamine residue of the terminal chitobiose epitope [10, 11], were separated by an UHPLC THERMO system (Ultimate 3000 LPG3400SD) coupled to an Exactive Orbitrap HESI-II mass spectrometer (Thermo Fisher Scientific Inc., Bremen, Germany). Analysis was performed by a hydrophilic interaction liquid chromatography (HILIC) column (ACQUITY UPLC Glycan BEH Amide 130 Å, Waters, 2.1 mm \times 150 mm, 1.7 μm , Waters Corporation Milford, MA, USA) at 60 °C. The separation was carried out at a flow rate of 0.4 mL/min, with 50 mM ammonium formate aqueous solution (pH 4.4) as solvent A and pure MeCN as solvent B [see Note 1]. Gradient conditions used were as follows: 0 min 25% A; 35 min 46% A; 36.5 min 100% A and flow rate of 0.2 ml/min; 39.5 min 100% A and flow rate of 0.2 ml/min; 43.1 min 25% A and flow rate of 0.2 ml/min; and 47.6 min 25% A and flow rate of 0.4 ml/min, which was kept constant for 17.4 min for column equilibration.

MS analyses were conducted under the following conditions: heater temperature 375 °C, capillary temperature 120 °C, spray voltage 1.90 kV, capillary voltage 120 V, tube lens voltage 120 V, and skimmer voltage, 50 V. Spectra were acquired in positive polarity, and resolution was adjusted at 70000 FWHM @200 m/z.

4 Notes

1. A 200 mM ammonium formate aqueous solution as solvent A provides better chromatographic resolution and tighter peaks.

References

1. Stanley P, Taniguchi N, Aebi M (2015-2017) N-glycans. In: Varki A, Cummings RD, Esko JD et al (eds) *Essentials of glycobiology*, 3rd edn. Cold Spring Harbor Laboratory Press, Cold Spring Harbor
2. Reitz C, Mayeux R (2014) Alzheimer disease: epidemiology, diagnostic criteria, risk factors and biomarkers. *Biochem Pharmacol* 88(4): 640–651
3. Villemagne VL, Burnham S, Bourgeat P, Brown B, Ellis KA, Salvado O, Szoek C, Macaulay SL, Martins R, Maruff P, Ames D (2013) Amyloid β deposition, neurodegeneration, and cognitive decline in sporadic Alzheimer's disease: a prospective cohort study. *Lancet Neurol* 12(4):357–367
4. Kowalska A (2004) Genetic aspects of amyloid beta-protein fibrillogenesis in Alzheimer's disease. *Folia Neuropathol* 42(4):235–237
5. Palmigiano A, Barone R, Sturiale L et al (2016) CSF N-glycoproteomics for early diagnosis in Alzheimer's disease. *J Proteome* 131:29–37
6. Kizuka Y, Kitazume S, Fujinawa R, Saito T, Iwata N, Saido TC, Nakano M, Yamaguchi Y, Hashimoto Y, Staufenbiel M, Hatsuta H (2015) An aberrant sugar modification of BACE 1 blocks its lysosomal targeting in Alzheimer's disease. *EMBO Mol Med* 7(2): 175–189
7. Messina A, Palmigiano A, Esposito F, Fiumara A, Bordugo A, Barone R, Sturiale L, Jaeken J, Garozzo D (2021) HILIC-UPLC-MS for high throughput and isomeric N-glycan separation and characterization in congenital disorders glycosylation and human diseases. *Glycoconj J* 38:201–211
8. Yang K, Yang Z, Chen X, Li W (2021) The significance of sialylation on the pathogenesis of Alzheimer's disease. *Brain Res Bull* 173: 116–123
9. Rawal P, Zhao L (2021) Sialometabolism in brain health and Alzheimer's disease. *Front Neurosci* 15:648617
10. Palmigiano A, Messina A, Sturiale L, Garozzo D (2018) Advanced LC-MS methods for N-glycan characterization. In: *Comprehensive analytical chemistry advances in the use of liquid chromatography mass spectrometry (LCMS): instrumentation developments and applications*, vol 79, pp 147–172
11. Zhou S, Veillon L, Dong X, Huang Y, Mechref Y (2017) Direct comparison of derivatization strategies for LC-MS/MS analysis of N-glycans. *Analyst* 142(23):4446–4455



CSF N-Glycomics Using MALDI MS Techniques

Angela Messina, Donata Agata Romeo, Rita Barone, Luisa Sturiale,
Angelo Palmigiano, Mario Zappia, and Domenico Garozzo

Abstract

In this chapter, we will present the methodology currently applied in our laboratory for the structural elucidation of the cerebrospinal fluid (CSF) N-glycome. N-glycans are released from denatured carboxymethylated glycoproteins by digestion with peptide-N-glycosidase F (PNGase F) and purified using both C18 Sep-Pak[®] and porous graphitized carbon (PGC) HyperSep[™] Hypercarb[™] solid phase extraction (SPE) cartridges. The glycan pool is subsequently permethylated to increase mass spectrometry sensitivity. Molecular assignments are performed through matrix-assisted laser desorption/ionization time-of-flight mass spectrometry (MALDI TOF MS) analysis considering either the protein N-linked glycosylation pathway or MALDI TOF MS/MS data. Each stage has been optimized to obtain high-quality mass spectra in reflector mode with an optimal signal-to-noise ratio up to m/z 4800. This method has been successfully adopted to associate specific N-glycome profiles to the early and the advanced phases of Alzheimer's disease (AD).

Key words AD, CSF, N-glycans, MALDI MS, MCI

1 Introduction

Although the role of N-glycosylation in the development and progression of AD is still to be elucidated [1], several findings show that it has a considerable impact on central nervous system (CNS) neurodegeneration processes [2–6]. Among all post-translational modifications that regulate protein processing, glycosylation is a common and versatile form that is vital for proper brain function. Glycans regulate how the proteins are processed and sorted inside the cells and play a role in cell adhesion, recognition, and signaling. Protein N-glycosylation is a highly ordered, sequential process that encompasses different cellular compartments. The nascent protein is glycosylated in the endoplasmic reticulum, where the precursor oligosaccharide Glc3Man9GlcNAc2 is first transferred en bloc to the polypeptide chain, and then processed in the Golgi [7]. Based on the last process, N-glycan structures are

distinguished in complex, hybrid, and high mannose types [7]. The huge variability of N-glycan structures basically relies on the type and position of attached sugars and branching.

CSF N-glycomics using MALDI MS techniques represents a reliable and a feasible approach for the characterization of brain glycoproteome enabling to identify possible alterations on different pathological processes affecting the CNS. Here we report the N-glycan CSF profile of a 79-year-old man with absence of neurological and cognitive concerns (obtained with the procedure briefly outlined in the summary) considered as a representative spectrum of a healthy reference control (see Fig. 1a). The developed protocol allowed us to pinpoint in human CSF a relevant incidence of biantennary N-glycans with bisecting GlcNAc and proximal fucosylation (α 1,6 fucosylation at the chitobiosyl core), the so-called brain-type N-glycosylation (Fig. 2a), whereas representative serum N-glycans are complex glycans with almost absent bisecting GlcNAc (Fig. 2b) [3, 8].

Our strategy led to a full identification of brain-type and serum-type glycoforms by MALDI TOF MS/MS analyses on representative (not-derivatized) model compounds, as the biantennary, bisected, fucosylated species FA2B and the isobaric triantennary fucosylated analogue FA3 (letter code described by Royle et al. [9]). The typical MS/MS fragmentation patterns of FA2B and FA3 glycoforms (precursor ion at m/z 1688.6, as sodium adduct) considered as model compounds for bisected and triantennary fucosylated N-glycoforms, respectively (see Fig. 3a, b), show B-type and Y-type ions due to glycoside bond cleavages (Domon and Costello nomenclature [10]). In addition, FA3 spectrum (Fig. 3b) is characterized by intense Z-type (m/z 1524.6) and C-type (m/z 1339.7) ion fragments, not present in the MS/MS spectrum of the bisected FA2B species (Fig. 2a). The fragmentation spectrum associated to FA2B, matched with those from the same precursor ion belonging to CSF profiles from healthy individuals and AD patients (Fig. 3c, d), thus suggesting the CSF glycoform at m/z 1688.6, and, consequently, the corresponding permethylated derivative at m/z 2080.9 (see Fig. 1a) are both associated to a bisected, core fucosylated structure [2].

N-glycans with bisecting GlcNAc, referred as bisected N-glycans, are synthesized by β 1,4-N-acetylglucosaminyltransferase III enzyme (GnT-III; EC 2.4.1.144) (encoded by *MGAT3*) that catalyzes GlcNAc attachment to the core β -mannose residue of N-glycans with β 1,4 linkage [11]. GnT-III is overexpressed in the brain of AD patients [12] and it has been found to modulate the innate immune response of blood monocytes to A β [12, 13]. Moreover, GnT-III plays a regulatory role of N-glycan biosynthesis, as bisecting GlcNAc, preventing the action of further GlcNAc transferases, leads to an overall reduction of the N-glycan branching [7, 14]. We have compared, in a recent study [2], the N-glycosylation profile of

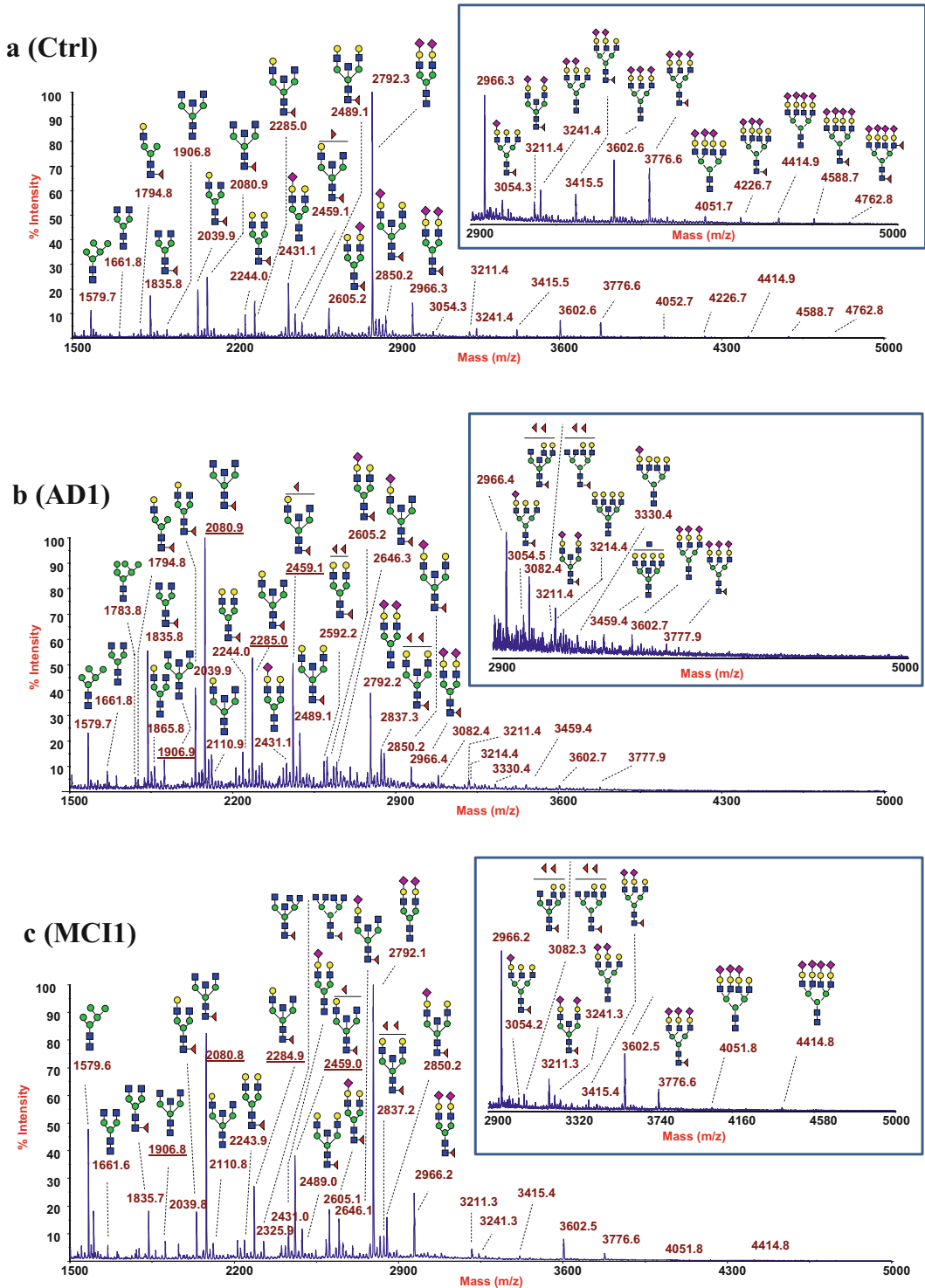


Fig. 1 MALDI-TOF spectra of permethylated CSF N-glycans from (a) healthy control (age 79 years), (b) AD1 patient (age 76 years), (c) MCI1 patient (age 75 years). Each figure inset highlights differences and/or similarities at high mass range between control, AD1, and MC1 profiles. N-acetylglucosamine (GlcNAc): blue square; mannose (Man): green circle; galactose (Gal): yellow circle; sialic acid (NeuAc): purple lozenge; fucose (Fuc): red triangle

CSF samples from patients with AD and mild cognitive impairment (MCI) and from healthy controls. Principal component analysis (PCA) showed all the 24 AD patients are classified into 2 groups, namely, AD1 (10 patients) characterized by an increase in brain-type glycoforms (bisected N-glycans) and AD2 group (14 patients) showing a reduction of the same species compared to healthy controls. Noteworthy, PCA revealed also two analogue MCI populations: MCI1 group (5 out of 11) with increased bisected N-glycans and MCI2, showing a lower amount of these species. Surprisingly, all MCI1 patients converted to AD within the clinical follow-up, whereas MCI2 patients remained unvaried, thus suggesting that CSF changes proceed the clinical onset providing useful biomarker for early AD diagnosis. Moreover, the reported findings suggest GnT-III as a possible target for the AD pharmaceuticals. N-glycan CSF profiles of AD1 and MCI1 patients are reported in Fig. 2b, c, respectively.

A database containing CSF N-glycans MALDI mass spectra from CTRL, MCI, AD1, and AD2 patients obtained with our procedure are downloadable at: <http://www.ipcb.ct.cnr.it/ct/spectra.jsp>.

Below, our procedure to profile N-glycans from 200 μ L of CSF samples will be described in detail. The same protocol has proved to be robust enough to achieve spectra with still satisfactory signal-to-noise ratio by employing up to only 20 μ L of CSF.

2 Materials

2.1 Denaturation of Proteins by Reduction and Alkylation

1. Ammonium bicarbonate (NH_4HCO_3), Sigma part # A6141-500 g.
Buffer solution. NH_4HCO_3 50 mM pH 7.8 in MilliQ water
2. RapiGest™ SF Powder Waters Corporation, 1 Pack of 1 mg vials, part # 186001860.
Denaturing buffer. RapiGest™ 0.1% (w/v). 1 mg RapiGest™ in 1 mL buffer solution (stable several months at -20°C)
3. Heating block (56°C).
4. Dithiothreitol (DTT), Sigma part # D9779-250 mg.
Reducing buffer. DTT 100 mM in buffer solution (always prepare fresh)
5. Iodoacetamide (IAA), Sigma part # I1149-5 g.
Alkylating buffer. IAA 100 mM in buffer solution (always prepare fresh. Light sensitive, keep in the dark).

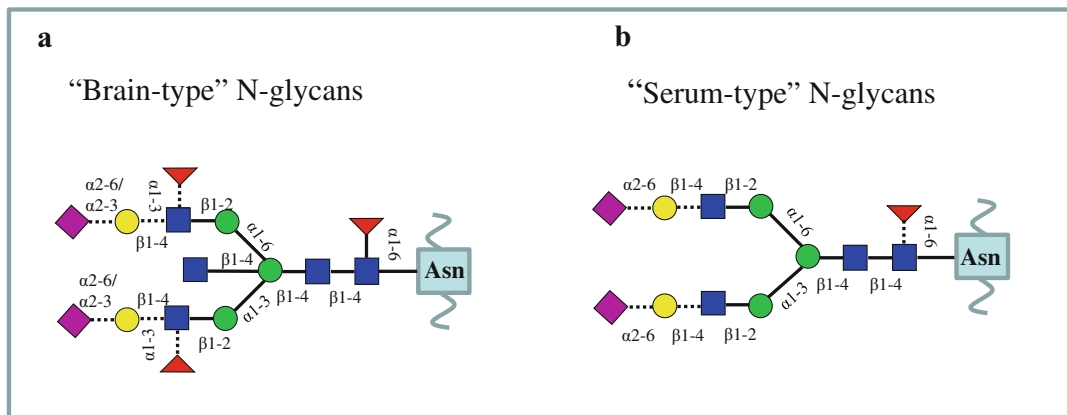


Fig. 2 Typical features of “brain-type” (a) and “serum-type” (b) complex biantennary N-glycans. Dotted linkages are related to additional “brain-type” and “serum-type” structural characteristics

2.2 PNGase F Digestion

1. N-glycosidase F (PNGase F, EC 3.5.1.52) of *Flavobacterium meningosepticum*, recombinant from *E. coli*, 250 units, 0.25 ml, solution in 50 mM sodium phosphate, 12.5 mM EDTA, 50% glycerol (v/v), pH 7.2, (Roche Molecular Biochemicals, Mannheim, Germany part # 11365177001) [see **Note 1**].

PNGase F is an amidase that cleaves the linkage between the innermost GlcNAc and the asparagine residues of high-mannose, hybrid, and complex N-glycans.

2. 500 mM hydrochloric acid (HCl) reagent grade 37%, Aldrich part # 25814–8-2-5 L, in MilliQ water.

2.3 C₁₈ Sep-Pak Purification of the Released N-Glycans

1. Sep-Pak[®] Vac tC18 1 cc, part # WAT036820 (Waters, Milford, MA).
2. SpeedVac[™] vacuum concentrator.
3. Methanol (MeOH) HPLC gradient grade, J.T. Baker[®] part # 8402-2.5 L.

Cleaning solution. MeOH

4. Acetic acid (HAc) ≥ 99.9%, Sigma Aldrich part # A6283-1 L.
Conditioning solution. 5% (v/v) HAc in MilliQ water.
Eluting solution. 5% (v/v) HAc in MilliQ water.

2.4 Solid Phase Extraction of the Released N-Glycans

1. HyperSep[™] Hypercarb[™] SPE cartridges 50 mg/1 mL part # 60106–303 (Thermo Scientific[™], Bellefonte, PA USA).
2. SpeedVac[™] vacuum concentrator.

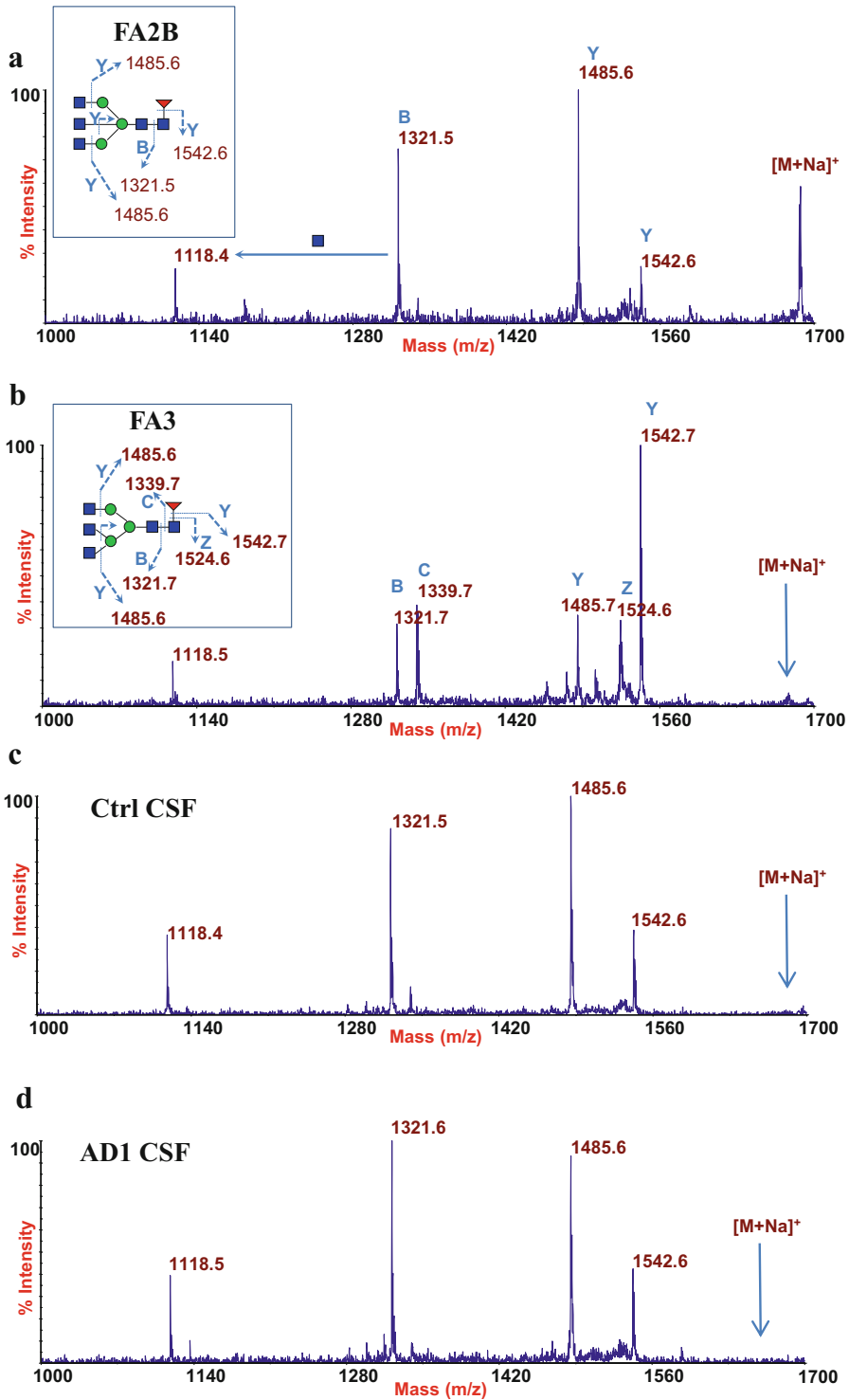


Fig. 3 MALDI-TOF/TOF fragmentation analysis of the parent ion at m/z 1688.6 from (a) FA2B model compound, (b) FA3 model compound, (c) healthy control CSF profile, and (d) AD1 CSF profile. N-acetylglucosamine (GlcNAc): blue square; mannose (Man): green circle; galactose (Gal): yellow circle; sialic acid (NeuAc): purple lozenge; fucose (Fuc): red triangle

3. NaOH, beads/pellets, 99.99% (metal basis), Alfa Aesar[®] part # 45780-100 g.
Basic priming solution. Sodium hydroxide (NaOH) 1 M in MilliQ water
4. Acetic acid (HAc) $\geq 99.9\%$, Sigma Aldrich part # A6283-1 L.
Acidic priming solution. 30% (v/v) HAc in MilliQ water
5. Trifluoroacetic acid (TFA) $\geq 99.9\%$ Purified B, Sigma Aldrich part # 299537-25 g.
6. Acetonitrile (MeCN) UHPLC-MS, Scharlau part # AC03911000-1 L.
Conditioning solution 1. 50% (v/v) MeCN in MilliQ water plus 0.1% (v/v) TFA.
Conditioning solution 2. 5% (v/v) MeCN in MilliQ water plus 0.1% (v/v) TFA.
Washing solution. 5% (v/v) MeCN, in MilliQ water plus 0.1% (v/v) TFA.
Eluting solution. 50% (v/v), MeCN, in MilliQ water plus 0.1% (v/v) TFA.

2.5 Glycan Permethylation

1. Permethylation is performed in PYREX screw cap culture tubes (13 × 100 mm, Corning[™]) with phenolic PTFE lined caps (Corning[™]).
2. Syringe Driven Filter Unit Millex[®]-HV 0.45 μm , PVDF, part # SLHVR04NL.
3. Freeze dryer.
4. NaOH, beads/pellets, 99.99% (metal basis), Alfa Aesar[®] part # 45780-100 g.
5. Methyl sulfoxide (DMSO) 99,7+% extra dry over molecular sieves, AcroSeal[™], ACROS Organics[™], part # 348441000-100 mL.
6. Iodomethane (ICH₃) contains copper as stabilizer, Reagent-Plus[®], 99.5%, Sigma Aldrich part # 289566-100 g [see Note 2].
7. Chloroform (CHCl₃) HPLC grade, $\geq 99.9\%$, Sigma Aldrich part # 528722-2 5 L.

2.6 MALDI MS Analysis of Permethylated Glycans

1. *MALDI TOF instrument.* 4800 Proteomic Analyzer (Applied Biosystems) equipped with a Nd:YAG laser operating at a wavelength of 355 nm with <500-ps pulse and 200-Hz firing rate.
2. *Calibration mixture.* The instrument is calibrated externally using the AB SCIEX TOF/TOF[™] 4700 Peptide Calibration Standard Mixture (TOF/TOF Calibration Mixture), containing des-Arg1-bradykinin ([MH]⁺ m/z 904.4681), angiotensin I ([MH]⁺ m/z 1296.6853), human [Glu1]-fibrinopeptide B

([MH]⁺ m/z 1570.6774), ACTH (adrenocorticotrophic hormone)-(1–17) ([MH]⁺ m/z 2093.0867), ACTH-(18–39) ([MH]⁺ m/z 2465.1989), and ACTH-(7–38) ([MH]⁺ m/z 3657.9294).

3. MeOH, HPLC gradient grade, J.T. Baker[®] part # 8402–2.5 L.
4. 5-Chloro-2-mercaptobenzothiazole (CMBT) technical grade, ≥90%, Aldrich part # 125571-5 g.
CMBT matrix solution. 10 mg/mL CMBT in 80/20 (v/v) MeOH/MilliQ water.
5. TFA ≥99.9% Purified B, Sigma Aldrich part # 299537-25 g.
6. MeCN, UHPLC-MS, Scharlau part # AC03911000-1 L.
7. 5α-cyano-4-hydroxycinnamic acid (CHCA) purum ≥99.0%, Fluka part # 28480-10 g.
CHCA matrix solution. 10 mg/mL solution of CHCA in 60/40 (v/v) 0.1% TFA/MeCN.

2.7 MALDI TOF/TOF MS/MS Differential Analysis of Bisected/Triantennary Glycans

1. FA2B model compound oligosaccharide, asialo, agalacto, bisected, fucosylated, biantennary N-linked glycan from Dextra Laboratories Ltd. part # C0840-20 µg.
2. Citric acid (C₆H₈O₇) 99 + %, Aldrich part # 240621-100 g.
3. Sodium phosphate dibasic heptahydrate (Na₂HPO₄ 7H₂O) Sigma part # S2429-250 g.
4. *Exoglycosidase digestion buffer.* Citrate/phosphate buffer 50 mM, pH 5. A 0.1 M citric acid solution is adjusted to pH 5 with 0.2 M Na₂HPO₄ 7H₂O solution and diluted 1:1 (v/v) with MilliQ water.
5. Neuraminidase (Sialidase, EC 3.2.1.18) from *Arthrobacter ureafaciens* 1 U (100 µL) in 10 mM sodium phosphate, 0.1% Micr-O-Protect (w/v), 0.25 mg/ml bovine serum albumin, pH 7 (Roche Molecular Biochemicals, Mannheim, Germany, part # 10269611001).
Neuraminidase is an exosialidase that cleaves the α-ketosidic linkage between sialic acid and an adjacent sugar residue.
6. β-Galactosidase from bovine testes (EC 3.2.1.23). Ammonium sulfate suspension, 1.0–3.0 units/mg protein (modified Warburg-Christian), 0.26 mL, 0.4 mg protein/mL (WC), 1.9 units/mg protein (Sigma part # G4142-.2UN).
β-galactosidase is a hydrolase enzyme that catalyzes the hydrolysis of β-galactosides into monosaccharides.
7. 2,5-Dihydroxybenzoic acid (DHB) Sigma part # G5254-10 g.
8. TFA ≥99.9% Purified B, Sigma Aldrich part # 299537-25 g.
9. MeCN, UHPLC-MS, Scharlau part # AC0.3911000-1 L.
10. MeOH, HPLC gradient grade, J.T. Baker[®] part # 8402–2.5 L.

DHB matrix solution. 50 mg/mL in 80/20 (v/v) 0.1% TFA/MeCN.

3 Methods

3.1 Denaturation of Proteins by Reduction and Alkylation

Denaturation of glycoproteins by reduction of disulfide bridges with DTT and subsequent alkylation of the free thiol groups with IAA is a crucial step to ensure a better availability of the glycosylation sites throughout PNGase F digestion. The use of *RapiGest*TM surfactant as denaturing agent provides a rapid and efficient sample deglycosylation.

1. A 200 μ L of CSF sample is freeze-dried and dissolved in 50 μ L of denaturing buffer, *RapiGest*TM 0.1% (w/v) in NH_4HCO_3 50 mM [*see Note 3*].
2. Add reducing buffer to the protein sample to obtain a final 5 mM DTT solution.
3. Incubate at 56 °C for 30 min.
4. Let cool sample at room temperature.
5. Add alkylating buffer to the protein sample to obtain a final 15 mM IAA solution.
6. Let react at room temperature in the dark for 40 min.

3.2 PNGase F Digestion

1. This step is carried out by adding 2 μ L PNGase F (2 U) [*see Note 4*].
2. Incubate at 37 °C overnight.
3. PNGase digestion is terminated by adding HCl 500 mM to a final concentration between 30 and 50 mM, pH \leq 2 [*see Note 5*].
4. Incubate at 37 °C for 45 min.
5. Dilute the sample with MilliQ water to a final volume of 500 μ L.

3.3 C₁₈ Sep-Pak Purification of the Released N-Glycans

N-glycans are separated from hydrophobic contaminants using a Sep-Pak[®] C18 cartridge. Impurities are adsorbed by the C18 stationary phase, whereas N-glycans elute with HAc 5%.

A vacuum manifold is employed to speed up this cleaning stage.

1. Clean the Sep-Pak[®] C18 cartridges with 3 mL of MeOH.
2. Condition the cartridge with 9 mL of HAc 5%.
3. Load the sample (500 μ L).
4. Elute with 3 mL HAc 5% and recover the sample.
5. Remove sample solvent in a SpeedVacTM vacuum concentrator.

3.4 Solid Phase Extraction of the Released N-Glycans

A further clean-up step using graphite cartridges is performed to remove salts and hydrophilic species. N-glycans are adsorbed by the hydrophilic graphite-based stationary phase, while impurities are discarded by washing solutions.

A vacuum manifold is employed to speed up this cleaning stage.

1. Wash the SPE cartridge with 1 mL of NaOH 1 M (basic priming solution), followed by 2 mL of MilliQ water, 1 mL of HAc 30% (acidic priming solution), and finally 1 mL of MilliQ water.
2. Condition the cartridge with 1 mL of 50% ACN in 0.1% TFA (conditioning solution 1) followed by 2 mL of 5% MeCN in 0.1% TFA (conditioning solution 2).
3. Load the sample (re-dissolved in 500 μ L of MilliQ water).
4. Wash with 1 mL of MilliQ water followed by 1 mL of 5% MeCN in 0.1% TFA (washing solution).
5. Elute the sample with 4×0.25 mL of 50% MeCN in 0.1% TFA (eluting solution) and collect in a unique Eppendorf™ tube.
6. Remove solvent in a SpeedVac™ vacuum concentrator.

3.5 Glycan Permethylation

Glycans are permethylated prior to MALDI mass spectrometry analysis. This derivatization method aims at reducing the high hydrophilic nature of the oligosaccharide sample, decreasing sample-to-sample and sample-to-matrix aggregation and enhancing about two order of magnitude signal sensitivity upon MALDI MS. Our permethylation protocol is performed according to Ciucanu and Kerek procedure [15]. All the reaction steps are accomplished in a fume hood because of the presence of iodomethane. The use of anhydrous DMSO and dry glassware is strictly recommended to reduce moisture absorption before permethylation.

1. Re-dissolve glycan sample in 400 μ L of MilliQ water.
2. Clarify sample solution by a 0.45 μ m filter unit. Put the filtered sample in a PYREX screw cap culture tube and add a magnetic stir bar [see Note 6].
3. Freeze-dry overnight.
4. About five pellets of NaOH are quickly crushed in a dry agate mortar, after the addition of 3 mL of anhydrous DMSO by a glass syringe, to obtain a NaOH slurry in DMSO.
5. With an end-broken Pasteur pipette, add 1 mL of the slurry solution into the glass tube containing the freeze-dried N-glycan pool.
6. Add about 400 μ L of ICH₃ with a Pasteur pipette, vortex, and let react in a magnetic stirrer at room temperature for 20 min.

7. Stop permethylation by adding, dropwise, 1 mL of MilliQ cold water [*see Note 7*].
8. Add 2 mL of chloroform.
9. Vortex and centrifuge at 2000 rpm for 2 min. Sample centrifugation allows the mixture to settle into two layers. Remove the upper water phase containing impurities and reagent excess.
10. Add 1 mL of MilliQ water and repeat **step 9**.
11. Transfer the chloroform phase into a clean screw capped glass tube.
12. Wash the sample chloroform solution with 1 mL of MilliQ water at least seven times or until the water phase has a neutral pH.
13. Transfer the final sample solution into another clean screw capped glass tube and let dry at room temperature under a gentle stream of nitrogen.

3.6 MALDI MS Analysis of Permethylated Glycans

1. Permethylated glycans are dissolved in MeOH to obtain a concentration of about 10 pmol/ μ L.
2. Prepare matrix solution by dissolving CMBT at a concentration of 10 mg/ml matrix in 80% MeOH [*see Note 8*]. Help CMBT dissolution by sonicating and then mild heating until matrix solution is clarified.
3. Mix 2–3 μ L of sample solution with the same quantity of matrix solution.
4. Put 1 μ L of the sample-matrix mixture on the cleaned stainless steel MALDI target allowing solvent evaporation and sample/matrix co-crystallization at room temperature and atmospheric pressure (dried drop method).

Spectra are acquired in positive ion reflectron mode allowing detection of monoisotopic masses. Each sample spot is submitted to multiple laser shots (1000–3000) and the extracted ions are detected by a TOF analyzer over a mass range of 1000–5000. Laser radiance is set slightly above the ion detection threshold. Typical voltage on the Sciex 4800 TOF/TOF mass spectrometer are as follows: source voltage, 20 kV; delayed extraction time, 500 ns; grid voltage, 16 kV; source 1 lens voltage, 10 kV; lens 1 voltage, 4.2 kV; and mirror 2 voltage, 20.494 kV.

External calibration is performed using 1 μ L of TOF/TOF Calibration Mixture in 24 μ L of CHCA matrix solution and putting 1 μ L of calibration mix/matrix on the MALDI target, thus allowing co-crystallization with the dried drop method [*see Note 9*]. Mass accuracy resulted better than 50 ppm. Data are processed using DataExplorer™ 4.9 software.

3.7 MALDI TOF/TOF MS/MS Differential Analysis of Bisected/Triantennary Glycans

To confirm the presence of bisected N-glycans in human CSF, we performed the differential MALDI TO/TOF MS/MS analysis on two isobaric compounds: FA2B as a representative model compound of bisected N-glycans (“brain-type” structures) and F3A as a representative model of complex triantennary glycoform (“serum-type” structures), and then we compared the MS/MS spectrum of the same precursor ion in the human CSF N-glycan profile(s) to those obtained from the models (see Fig. 2a–d).

FA2B glycan is a commercial compound purchased from Dextra Laboratories Ltd., whereas FA3 is obtained by serum treatment with neuraminidase and subsequently with β -galactosidase by the following method [*see Note 10*].

1. N-glycans are released and purified from 10 μ L of control human serum as described for CSF samples (Subheadings 3.1–3.4.).
2. The obtained glycan pool is dissolved in 200 μ L of citrate/phosphate buffer 50 mM, pH 5.
3. Add 4 μ L of neuraminidase (50 mU).
4. Incubate at 37 °C overnight.
5. Stop the reaction by deactivating the enzyme at 100 °C for 10 min.
6. Let cool sample at room temperature.
7. Add 13 μ L of β -galactosidase (10 mU).
8. Incubate at 37 °C overnight.
9. Stop the reaction by deactivating the enzyme at 100 °C for 10 min.
10. Let cool sample at room temperature.
11. Desalt glycan sample by SPE cartridge as described in Subheading 3.4.
MS analysis is finally performed on the obtained sample to confirm the presence of FA3 compound in the glycan mixture.
12. Prepare sample solution by adding 15 μ L di TFA 0.1% to the dried glycan pool.
13. Prepare matrix solution by dissolving DHB at a concentration of 50 mg/mL in 80/20 (v/v) 0.1% TFA/MeCN.
14. Mix 2 μ L of sample solution with the same quantity of matrix solution.
15. Put 1 μ L of the sample-matrix mixture on the cleaned stainless steel MALDI target allowing solvent evaporation and sample/matrix co-crystallization at room temperature and atmospheric pressure (dried drop method).

16. Once the spot is dried, recrystallize the sample by adding 0.3 μL of MeOH [*see* **Note 11**].
17. Spectra are acquired in positive reflector mode.

MS/MS analysis is performed on this same FA3 solution, on FA2B model compound, and on not-derivatized CSF samples (obtained as described from Subheadings 3.1 to 3.4.). Sample preparation for MS/MS analysis is the same as described for MS (from **steps 12 to 16**).

Typical voltage on the Sciex 4800 TOF/TOF mass spectrometer for MS/MS acquisitions are as follows: source 1 voltage, 4.2 kV; source 2 voltage, 15.0 kV; delayed extraction time 1330 ns; delayed extraction time 240,841 ns; source 1 lens voltage, 3.2 kV; lens 1 voltage, 2.525 kV; lens 2 voltage, 4.00 kV; lens 3 voltage, 2.1 kV; mirror 1 voltage, 10.256 kV; mirror 2 voltage, 17.4785 kV; metastable suppressor, 1.0 kV; time ion selector enabled; precursor mass window resolution, 400 (FWHM); and CID gas off.

Laser radiance is set higher (25–35%) above the threshold of ion detection.

External calibration is performed by using, as the precursor ion, the protonated molecular ion of the human [Glu1]-fibrinopeptide B at m/z 1570.6774 present in the Sciex TOF/TOF standard calibration mixture. The calibrant/matrix solution is loaded as for MALDI TOF MS.


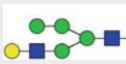






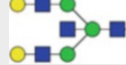




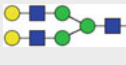









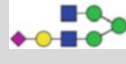



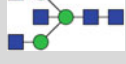
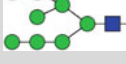



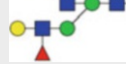




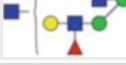




3.8 Assignments of Molecular Ions of Native and Permethylated Glycans

Glycans are detected in positive polarity by MALDI MS as sodiated ions $[M + \text{Na}]^+$. Structural assignments were primarily based on the knowledge of the accurate molecular weight and the N-glycan biosynthetic pathway. N-glycan species were also identified with the help of bioinformatics tools as those provided by the Consortium for Functional Glycomics (CFG; <http://www.functionalglycomics.org/>) and Glycoworkbench v2.1 [16]. For practical reasons, Fig. 1a–c shows only major CSF permethylated N-glycans. The complete peak assignments (a total of about 90 species for control CSF, ranging from m/z 1579 to m/z 4762.8) are reported in Table 1.

4 Notes

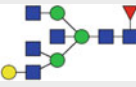

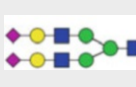
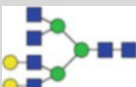
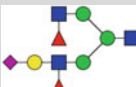


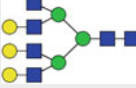
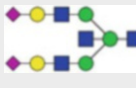
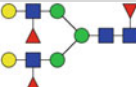

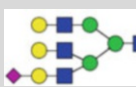

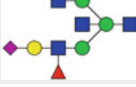
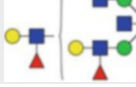

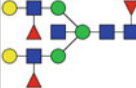

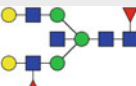
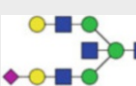


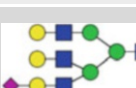
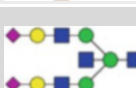
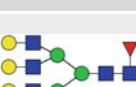

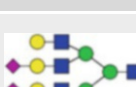
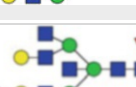
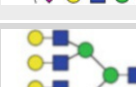
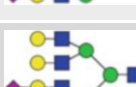



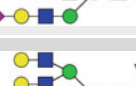



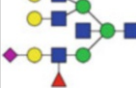

1. Some authors recommend the use of PNGase F in water (storage at 4 °C) because glycerol could inhibit matrix crystallization prior to MS. In our experience PNGase F storage in glycerol is preferable as it ensures a perfect enzyme stability for a longer period at –20 °C. Sample will be separated from the digestion buffer including glycerol through the subsequent clean-up steps.

Table 1
Structures of permethylated N-glycans from control CSF identified by MALDI-TOF MS

Structure	<i>m/z</i>	Structure	<i>m/z</i>	Structure	<i>m/z</i>
	1579.7		1999.0		2244.0
	1590.8		2010.0		2285.0
	1620.8		2029.0		2315.1
	1661.6		2039.9		2326.1
	1753.8		2069.9		2360.1
	1783.8		2081.0		2390.1
	1794.8		2110.9		2396.1
	1835.8		2152.0		2401.1
	1865.9		2156.0		2418.1
	1906.8		2192.0		2431.1
	1981.9		2214.0		2459.1
	1987.9		2227.0		2472.2
	2489.1		2704.2		2908.4
	2519.1		2717.2		2921.4

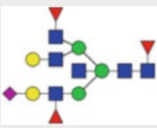
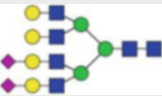
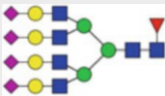
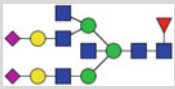

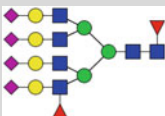
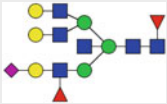
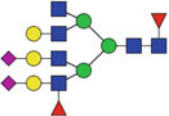
(continued)

Table 1
(continued)

Structure	<i>m/z</i>	Structure	<i>m/z</i>	Structure	<i>m/z</i>
	2530.1		2734.3		2966.3
	2560.2		2749.3		3024.4
	2564.2		2764.2		3037.4
	2592.2		2792.2		3054.4
	2605.1		2820.3		3082.4
	2646.2		2837.3		3140.5
	2663.2		2850.3		3198.4
	2676.2		2880.4		3211.4
	2693.2		2891.4		3241.4
	3269.5		3503.5		3864.7
	3282.5		3602.5		4051.7
	3299.5		3647.6		4226.7
	3415.5		3660.6		4414.8

(continued)

Table 1
(continued)

Structure	<i>m/z</i>	Structure	<i>m/z</i>	Structure	<i>m/z</i>
	3443.5		3690.6		4588.8
	3456.6		3776.6		4762.8
	3473.5		3834.7		

Linkages are not indicated on the cartoons; thus most structures may refer to two or more isomers as, for example, those due to different branching elongation or fucosylation at the three-linked or six-linked mannosyl residue of the core

2. All operations with ICH₃ should be performed in a fume hood.
3. All reagent amounts used for reduction and alkylation are calculated for 200 μL of CSF.
4. Proteolytic digestion before PNGase F addition is not necessary when utilizing *RapiGest*TM as denaturing agent.
5. Lowering the pH serves either to stop the reaction or to hydrolyze *RapiGest*TM whose by-products are easily removed from the sample by the subsequent clean-up steps.
6. Permethylation requires perfectly dry conditions; for this reason magnetic stir bar is added to sample before freeze-drying and is mandatory using anhydrous reagents and dry glasses.
7. As water addition has an exothermic effect, it should be accomplished by placing the reaction tube in an ice-cold bath and shaking frequently.
8. The most used matrix for permethylated glycans is DHB. We tested a number of matrices and found that CMBT gives much better results with remarkable increased sensitivity and resolution.
9. In general, it is a good practice to use the same matrix solution for the sample and the calibration mixture (in this case CMBT solution used as matrix for permethylated oligosaccharides). In our experience no improvement on accuracy of MS measurements was observed by performing calibration with the

standard SCIEX peptide mixture in CHCA, probably because the laser irradiation threshold is very similar for the two matrices.

10. This comparison can be performed by MS/MS analysis either on native or on permethylated glycans. The first choice is preferable as native (not-derivatized) glycans give a set of intense and well-defined ion fragments providing a clear-cut fingerprint identification.
11. Sample recrystallization with methanol or ethanol is sometimes useful, when using DHB as matrix, to redistribute sample and matrix crystals in a more homogeneous thin layer.

References

1. Schedin-Weiss S, Winblad B, Tjernberg LO (2014) The role of protein glycosylation in Alzheimer disease. *FEBS J* 281:46–62
2. Palmigiano A, Barone R, Sturiale L et al (2016) CSF N-glycoproteomics for early diagnosis in Alzheimer's disease. *J Proteome* 131:29–37
3. Barone R, Sturiale L, Palmigiano A et al (2012) Glycomics of pediatric and adulthood diseases of the central nervous system. *J Proteome* 75: 5123–5139
4. Kizuka Y, Kitazume S, Fujinawa R, Saito T, Iwata N, Saito T et al (2015) An aberrant sugar modification of BACE1 blocks its lysosomal targeting in Alzheimer's disease. *EMBO Mol Med* 7:175–189
5. Kizuka Y, Nakano M, Kitazume S, Saito T et al (2016) Bisecting GlcNAc modification stabilizes BACE1 protein under oxidative stress conditions. *Biochem J* 473(1):21–30
6. Kizuka Y, Kitazume S, Taniguchi N (2017) N-glycan and Alzheimer's disease. *Biochim Biophys Acta Gen Subj* 1861:2447. <https://doi.org/10.1016/j.bbagen.2017.04.012>
7. Stanley P, Schachter H, Taniguchi N (2009) N-Glycans. In: Varki A, Cummings R, Esko J, Freeze H, Stanley P, Bertozzi CR, Hart GW, Etzler ME (eds) *Essentials of Glycobiology*, 2nd edn. Cold Spring Harbor Laboratory Press, Cold Spring Harbor
8. Hoffmann A, Nimitz M, Getzlaff R, Conradt HS (1995) 'Brain-type' N-glycosylation of asialo-transferrin from human cerebrospinal fluid. *FEBS Lett* 359(2–3):164–168
9. Royle LI, Campbell MP, Radcliffe CM, White DM, Harvey DJ et al (2008) HPLC-based analysis of serum N-glycans on a 96-well plate platform with dedicated database software. *Anal Biochem* 376:1–12
10. Domon B, Costello CE (1988) A systematic nomenclature for carbohydrate fragmentations in FAB-MS/MS spectra of glycoconjugates. *Glycoconj J* 5:397–409
11. Schachter H (1986) Biosynthetic controls that determine the branching and microheterogeneity of protein-bound oligosaccharides. *Biochem Cell Biol* 64(3):163–181
12. Akasaka-Manyo K, Manyo H, Sakurai Y et al (2010) Protective effect of N-glycan bisecting GlcNAc residues on β -amyloid production in Alzheimer's disease. *Glycobiology* 20(1): 99–106
13. Avagyan H, Goldenson B, Tse E, Masoumi A et al (2009) Immune blood biomarkers of Alzheimer disease patients. *J Neuroimmunol* 210: 67–72
14. Ikeda Y, Ihara H, Tsukamoto H et al (2014) Mannosyl (Beta-1,4-)-glycoprotein Beta-1,4-N-Acetylglucosaminyltransferase (MGAT3); β 1,4-N-Acetylglucosaminyltransferase III (GnT-III, GlcNAcT-III). In: Taniguchi N et al (eds) *Handbook of glycosyltransferase and related genes*, 2nd edn. Springer Japan
15. Ciucanu I, Kerek F (1984) A simple and rapid method for the permethylation of carbohydrates. *Carbohydr Res* 131:209–217
16. Ceroni A, Maass K, Geyer H, Geyer R, Dell A, Haslam SM (2008) GlycoWorkbench: a tool for the computer-assisted annotation of mass spectra of glycans. *J Proteome Res* 7:1650–1659



Optimized Pre-analytical Handling Protocol for Blood-Based Biomarkers of Alzheimer's Disease

Alexander Jethwa and Laura Stöckl

Abstract

The therapeutic management of patients with Alzheimer's disease (AD) has been hindered by poor diagnostic accuracy. As such, there is an unmet clinical need for tools that can detect and diagnose the disease in its early stages. Compared with cerebrospinal fluid (CSF)-based biomarkers or positron emission tomography (PET), the use of reliable blood-based biomarkers could offer an accessible and minimally invasive method of streamlining diagnosis in the clinical setting. However, the influence of pre-analytical processing and sample handling parameters on the accurate measurement of protein biomarkers is well established, especially for AD CSF-based biomarkers. In this chapter, we provide recommendations for an optimal sample handling protocol for the analysis of blood-based biomarkers specifically for amyloid pathology in AD.

Key words Alzheimer's disease, Beta-amyloid, Blood-based biomarkers, Immunoassay, Phosphorylated tau (phospho-tau), Plasma, Pre-analytics, Protocol

1 Introduction

Alzheimer's disease (AD) is the most frequent form of dementia globally, accounting for 60–80% of cases, and is characterized by the deposition of β -amyloid ($A\beta$) peptides and tau pathology in the brain [1, 2]. Conventional treatment options for AD, including cholinesterase inhibitors and N-methyl-D-aspartate receptor antagonists, have offered only symptomatic relief without targeting the underlying disease pathology [2]. However, two novel disease-modifying therapies (DMTs) have now been granted accelerated approval by the US Food and Drug Administration: in June 2021, aducanumab was approved for the treatment of mild symptomatic AD [2], and this was followed in January 2023 by the approval of lecanemab for the treatment of mild cognitive impairment due to AD or mild AD with confirmed presence of $A\beta$ pathology [3].

Effective use of these novel DMTs requires early identification of patients with AD and cerebral amyloid and tau pathologies [4, 5]. Diagnosis of AD is usually based on a combination of validated biomarkers in cerebrospinal fluid (CSF), including A β , total tau, and phosphorylated tau (phospho-tau), and positron emission tomography (PET) imaging [6]. However, these invasive diagnostic tools could be supplemented or eventually even be replaced with reliable blood-based biomarkers of amyloid pathology and AD. Routine use of blood-based biomarkers would allow a more accessible, minimally invasive, and less expensive method of identifying patients who might benefit from DMTs [4, 7]. A strong correlation has previously been reported between a number of biomarkers found in both the CSF and blood [8–14]. For example, plasma β -amyloid 1–42/ β -amyloid 1–40 (A β 42/A β 40) and CSF phospho-tau/A β 42 ratios, which are reflective of amyloid pathology, have approximately 90% diagnostic accuracy compared with PET [12, 14–17].

Phospho-tau currently holds most promise as a blood-based biomarker. Phospho-tau concentrations have been shown to increase in blood as AD severity progresses and to predict changes in CSF and PET measures of A β , tau, and neurodegeneration [7]. As such, blood phospho-tau is cautiously recommended as a screening tool in clinical trials evaluating DMTs in AD and in non-AD trials to exclude patients who may have concomitant AD [18].

Considerable variation exists between institutions in pre-analytical handling processes and procedures for blood and CSF samples [19–21], and a number of studies have evaluated the impact of this on the measurement of blood-based biomarkers specifically for amyloid pathology and AD [4, 6, 22]. A standardized blood handling protocol is crucial for comparable and reliable results, especially when blood-based biomarkers are implemented in routine clinical care. Here, we present an optimized and straightforward pre-analytical handling protocol for the analysis of blood-based biomarkers of AD in fresh human blood samples for potential application in clinical practice.

2 Materials

1. Standard material for blood sampling according to the blood sampling system (e.g., vacuum extraction method): tourniquet, needle, disinfectant, and swab.
2. EDTA blood collection tubes (*see Note 1*).
3. Standard laboratory centrifuge suitable for centrifugation of blood collection tubes.
4. Polypropylene tubes for storage (*see Note 2*).

5. Freezer and boxes for storage at $-20\text{ }^{\circ}\text{C}$ or ideally at $-80\text{ }^{\circ}\text{C}$ (preferred for long-term storage).
6. Assay for biomarker of choice and corresponding diagnostic instrument.

3 Methods

The following protocol describes the recommended procedure for blood sample collection and processing according to previously described methods [4, 6]. A graphical summary of this procedure is shown in Fig. 1.

1. Perform venipuncture according to local standard operating procedures and/or manufacturer's instructions; allow free flow of blood with mild aspiration to avoid hemolysis.
2. Collect whole blood samples in EDTA blood collection tubes (*see Note 1*). To achieve the correct whole blood to anticoagulant ratio, fill each tube to the nominal volume according to the manufacturer's instructions (e.g., until the vacuum is exhausted).
3. To ensure sufficient mixing of the sample with the anticoagulant present in the tube, immediately invert the tubes five to ten times after sample collection or follow the tube manufacturer's instructions.
4. After blood draw, whole blood samples can be stored at $4\text{ }^{\circ}\text{C}$ for a maximum of 24 h, while storage at room temperature should be avoided or limited to a maximum of 2 h (*see Notes 3 and 4*).
5. Centrifuge the tubes according to the manufacturer's instructions (e.g., $2000\times g$ for 10 min) at room temperature in a swing bucket centrifuge.
6. After centrifugation, the plasma is stable for a maximum of 24 h when stored at $4\text{ }^{\circ}\text{C}$ or for a maximum of 2 h when stored at room temperature. Within that period, all remaining steps of the protocol must be completed (*see Notes 3 and 4*).
7. Transfer the separated plasma into a polypropylene tube (*see Notes 2 and 5*), invert several times to ensure sufficient mixing of the sample, and immediately proceed with the measurement using the biomarker assay of choice. Alternatively, aliquot into storage tubes and freeze at $-20\text{ }^{\circ}\text{C}$ or ideally at $-80\text{ }^{\circ}\text{C}$ (preferred for long-term storage) (*see Note 6*).
8. Samples remain stable for up to five tube transfers and up to two freeze/thaw cycles (at either $-20\text{ }^{\circ}\text{C}$ or $-80\text{ }^{\circ}\text{C}$) (*see Notes 7 and 8*).

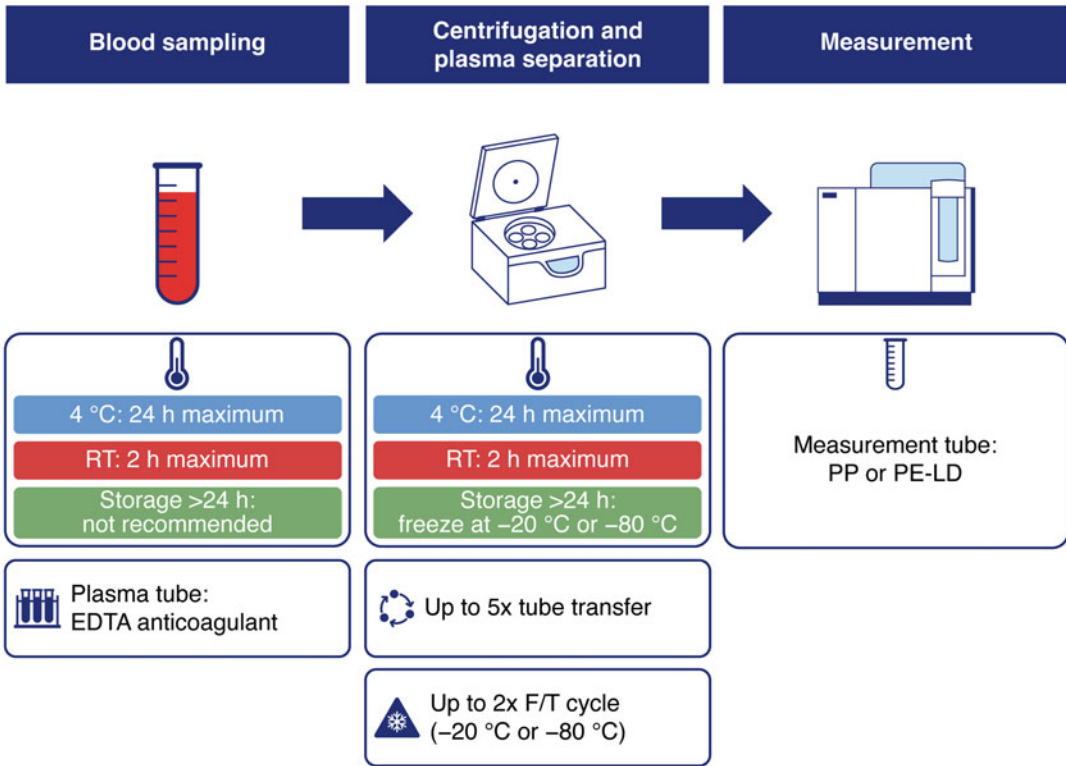


Fig. 1 Recommendations for blood collection and pre-analytical sample handling for the analysis of blood-based biomarkers of Alzheimer's disease. *EDTA* ethylenediaminetetraacetic acid, *F/T* freeze/thaw, *PE-LD* low-density polyethylene, *PP* polypropylene, *RT* room temperature. Reproduced and adapted from [6]

4 Notes

1. Both K2 and K3 EDTA blood collection tubes can be used. Also, tubes with or without separating gel can be used (*see* also **Note 5**). While EDTA plasma is the recommended anticoagulant and sample type, lithium heparin plasma, sodium citrate plasma, and serum may also be suitable for certain biomarkers (*see* Ref. [6]). It is recommended to test the stability of the biomarker of choice before using these sample types.
2. While polypropylene tubes are recommended, other plastic types may also be suitable (e.g., low-density polyethylene) [6].
3. **These are the most critical steps in the protocol; compliance with these specifications is extremely important to ensure reliable biomarker results.** Exceeding the recommended storage duration is not advised due to instability of certain biomarkers (e.g., A β 42 and A β 40) [6].
4. The blood-based biomarkers examined by Kurz et al. [6] have been shown to remain stable for up to 24 h at 4 °C in whole

blood and EDTA plasma, meaning that they can be stored in the fridge in their original blood collection tube without the need for immediate processing. Storage of samples for more than 24 h at 4 °C is not recommended due to the instability of some biomarkers [6]. Blood must be fully processed into plasma before freezing (i.e., whole blood cannot be frozen).

5. When transferring the plasma into a secondary storage or measuring tube, it must be ensured that no cellular components (e.g., erythrocytes, platelets) are included; therefore, the use of blood collection tubes with separating gel may be helpful. For tubes without separating gel, transfer must be carried out with particular care.
6. Plasma must be transferred to a fresh tube before freezing and cannot be frozen in the original blood collection tube, even if the cellular components of the blood are separated by a separation gel.
7. It is recommended to thaw samples by placing them on a roller mixer at room temperature for 15–30 min (or until the ice crystals have completely dissolved) and centrifuge samples containing precipitates before measurement. For larger volumes, the samples can also be thawed in a water bath at 25 °C and, afterward, homogenized on a roller mixer.
8. Previously frozen plasma may form clots when thawing and this effect intensifies after repeated freeze/thaw cycles. If clots are visible in the bottom of the tube after centrifugation, transfer the supernatant to a fresh measuring tube. Since certain diagnostic instruments are very sensitive to these clots, repeated centrifugation and transfer of the supernatant to a fresh measuring tube are recommended in the event of instrument errors.

Acknowledgments

This work was supported by Roche Diagnostics International Ltd. Alexander Jethwa and Laura Stöckl are full-time employees of Roche Diagnostics GmbH. The authors would like to thank Carolin Kurz, Isabelle Schrurs, Ivonne Suridjan, Selim Üstün Gürsel, Tobias Bittner, and Robert Perneczky for their contribution to this research. Third-party medical writing assistance, under the direction of the authors, was provided by Fiona Fernando, PhD, contract medical writer at Ashfield MedComms (Macclesfield, UK), an Inizio company, and was funded by Roche Diagnostics International Ltd. (Rotkreuz, Switzerland).

References

- DeTure MA, Dickson DW (2019) The neuropathological diagnosis of Alzheimer's disease. *Mol Neurodegener* 14:32. <https://doi.org/10.1186/s13024-019-0333-5>
- Esang M, Gupta M (2021) Aducanumab as a novel treatment for Alzheimer's disease: a decade of hope, controversies, and the future. *Cureus* 13:e17591. <https://doi.org/10.7759/cureus.17591>
- FDA (2023) FDA grants accelerated approval for Alzheimer's disease treatment. January 06, 2023. Available from: <https://www.fda.gov/news-events/press-announcements/fda-grants-accelerated-approval-alzheimers-disease-treatment>. Accessed 15 Feb 2023
- Rózga M, Bittner T, Batrla R, Karl J (2019) Preanalytical sample handling recommendations for Alzheimer's disease plasma biomarkers. *Alzheimers Dement (Amst)* 11:291–300. <https://doi.org/10.1016/j.dadm.2019.02.002>
- Rasmussen J, Langerman H (2019) Alzheimer's disease – why we need early diagnosis. *Degener Neurol Neuromuscul Dis* 9:123–130. <https://doi.org/10.2147/DNND.S228939>
- Kurz C, Stöckl L, Schürs I, Suridjan I, Gürsel SU, Bittner T, Jethwa A, Perneckzy R (2023) Impact of pre-analytical sample handling factors on plasma biomarkers of Alzheimer's disease. *J Neurochem* 165(1):95–105. <https://doi.org/10.1111/jnc.15757>
- Karikari TK, Ashton NJ, Brinkmalm G, Brum WS, Benedet AL, Montoliu-Gaya L, Lantero-Rodriguez J, Pascoal TA, Suárez-Calvet M, Rosa-Neto P et al (2022) Blood phospho-tau in Alzheimer disease: analysis, interpretation, and clinical utility. *Nat Rev Neurol* 18:400–418. <https://doi.org/10.1038/s41582-022-00665-2>
- Barthélemy NR, Horie K, Sato C, Bateman RJ (2020) Blood plasma phosphorylated-tau isoforms track CNS change in Alzheimer's disease. *J Exp Med* 217:e20200861. <https://doi.org/10.1084/jem.20200861>
- Blennow K, Dubois B, Fagan AM, Lewczuk P, de Leon MJ, Hampel H (2015) Clinical utility of cerebrospinal fluid biomarkers in the diagnosis of early Alzheimer's disease. *Alzheimers Dement* 11:58–69. <https://doi.org/10.1016/j.jalz.2014.02.004>
- Karikari TK, Pascoal TA, Ashton NJ, Janelidze S, Benedet AL, Rodriguez JL, Chamoun M, Savard M, Kang MS, Theriault J et al (2020) Blood phosphorylated tau 181 as a biomarker for Alzheimer's disease: a diagnostic performance and prediction modeling study using data from four prospective cohorts. *Lancet Neurol* 19:422–433. [https://doi.org/10.1016/S1474-4422\(20\)30071-5](https://doi.org/10.1016/S1474-4422(20)30071-5)
- Khoury R, Ghossoub E (2019) Diagnostic biomarkers of Alzheimer's disease: a state-of-the-art review. *Biomark Neuropsychiatry* 1:100005. <https://doi.org/10.1016/j.bionps.2019.100005>
- Ovod V, Ramsey KN, Mawuenyega KG, Bollinger JG, Hicks T, Schneider T, Sullivan M, Paumier K, Holtzman DM, Morris JC et al (2017) Amyloid β concentrations and stable isotope labeling kinetics of human plasma specific to central nervous system amyloidosis. *Alzheimers Dement* 13:841–849. <https://doi.org/10.1016/j.jalz.2017.06.2266>
- Tatebe H, Kasai T, Ohmichi T, Kishi Y, Kakeya T, Waragai M, Kondo M, Allsop D, Tokuda T (2017) Quantification of plasma phosphorylated tau to use as a biomarker for brain Alzheimer pathology: pilot case-control studies including patients with Alzheimer's disease and down syndrome. *Mol Neurodegener* 12:63. <https://doi.org/10.1186/s13024-017-0206-8>
- Zetterberg H (2019) Blood-based biomarkers for Alzheimer's disease – an update. *J Neurosci Methods* 319:2–6. <https://doi.org/10.1016/j.jneumeth.2018.10.025>
- Doecke JD, Ward L, Burnham SC, Villemagne VL, Li Q-X, Collins S, Fowler CJ, Manuilova E, Widmann M, Rainey-Smith SR et al (2020) Elecsys CSF biomarker immunoassays demonstrate concordance with amyloid-PET imaging. *Alzheimers Res Ther* 12:36. <https://doi.org/10.1186/s13195-020-00595-5>
- Nakamura A, Kaneko N, Villemagne VL, Kato T, Doecke J, Doré V, Fowler C, Li Q-X, Martins R, Rowe C et al (2018) High performance plasma amyloid- β biomarkers for Alzheimer's disease. *Nature* 554:249–254. <https://doi.org/10.1038/nature25456>
- Hansson O, Seibyl J, Stomrud E, Zetterberg H, Trojanowski JQ, Bittner T, Lifke V, Corradini V, Eichenlaub U, Batrla R et al (2018) CSF biomarkers of Alzheimer's disease concord with amyloid- β PET and predict clinical progression: a study of fully automated immunoassays in BioFINDER and ADNI cohorts. *Alzheimers Dement* 14:1470–1481. <https://doi.org/10.1016/j.jalz.2018.01.010>
- Hansson O, Edelmayer RM, Boxer AL, Carrillo MC, Mielke MM, Rabinovici GD,

- Salloway S, Sperling R, Zetterberg H, Teunissen CE (2022) The Alzheimer's association appropriate use recommendations for blood biomarkers in Alzheimer's disease. *Alzheimers Dement* 18:2669–2686. <https://doi.org/10.1002/alz.12756>
19. Hansson O, Batrla R, Brix B, Carrillo MC, Corradini V, Edelmayer RM, Esquivel RN, Hall C, Lawson J, Le Bastard N et al (2021) The Alzheimer's association international guidelines for handling of cerebrospinal fluid for routine clinical measurements of amyloid β and tau. *Alzheimers Dement* 17:1575–1582. <https://doi.org/10.1002/alz.12316>
20. Watt AD, Perez KA, Rembach AR, Masters CL, Villemagne VL, Barnham KJ (2012) Variability in blood-based amyloid-beta assays: the need for consensus on pre-analytical processing. *J Alzheimers Dis* 30:323–336. <https://doi.org/10.3233/JAD-2012-120058>
21. Snyder HM, Carrillo MC, Grodstein F, Henriksen K, Jeromin A, Lovestone S, Mielke MM, O'Bryant S, Sarasa M, Sjögren M et al (2014) Developing novel blood-based biomarkers for Alzheimer's disease. *Alzheimers Dement* 10:109–114. <https://doi.org/10.1016/j.jalz.2013.10.007>
22. Verberk IMW, Misdorp EO, Koelewijn J, Ball AJ, Blennow K, Dage JL, Fandos N, Hansson O, Hirtz C, Janelidze S et al (2021) Characterization of pre-analytical sample handling effects on a panel of Alzheimer's disease-related blood-based biomarkers: results from the standardization of Alzheimer's blood biomarkers (SABB) working group. *Alzheimers Dement* 18:1484–1497. <https://doi.org/10.1002/alz.12510>



Mass Spectrometry-Based Metabolomics Multi-platform for Alzheimer's Disease Research

Álvaro González-Domínguez, Ana Sayago,
Ángeles Fernández-Recamales, and Raúl González-Domínguez

Abstract

The integration of complementary analytical platforms is nowadays the most common strategy for comprehensive metabolomics analysis of complex biological systems. In this chapter, we describe methods and tips for the application of a mass spectrometry multi-platform in Alzheimer's disease research, based on the combination of direct mass spectrometry and orthogonal hyphenated approaches, namely, reversed-phase ultrahigh-performance liquid chromatography and gas chromatography. These procedures have been optimized for the analysis of multiple biological samples from human patients and transgenic animal models, including blood serum, various brain regions (e.g., hippocampus, cortex, cerebellum, striatum, olfactory bulbs), and other peripheral organs (e.g., liver, kidney, spleen, thymus).

Key words Metabolomics, Mass spectrometry, Multi-platform, Alzheimer's disease, Direct MS analysis, Ultrahigh-performance liquid chromatography, Gas chromatography

1 Introduction

Alzheimer's disease (AD) is recognized to be a multifactorial disorder encompassing a myriad of interrelated pathogenic events, including the well-known proteopathies associated with the deposition of β -amyloid plaques and the hyper-phosphorylation of protein tau, but also other cellular and metabolic perturbations involving oxidative stress, inflammation, energy-related and mitochondrial dysfunctions, disturbed neurotransmission, and abnormal metal homeostasis, among many others [1–3]. However, the exact causes behind the early onset of AD are still unknown, so diagnosis is currently performed via exclusion of other pathologies through a combination of neuropsychological and laboratory tests [4]. Furthermore, it should be noted that this neurodegenerative disorder presents great variability of complex clinical symptoms and a long presymptomatic period. Accordingly, the discovery of AD

biomarkers is crucial to develop novel reliable diagnostic and prognostic methods. In this vein, and considering the abovementioned multifaceted nature, metabolomics has emerged over the last years as a very powerful tool to characterize the molecular alterations behind the onset and progression of AD [4–6].

Metabolites are low-molecular-weight compounds (<1500 Da) that directly participate in enzyme-mediated endogenous metabolic reactions occurring in the organism, so their homeostasis is tightly regulated by upstream events in the central dogma of biology. Moreover, metabolites can also derive from exogenous exposure sources, such as diet or environmental pollution (i.e., the exposome), as well as from the gut microbiota [7]. Altogether, the metabolome can be regarded as the most reliable indicator of the organism's phenotype, reflecting changes downstream of the genomics, transcriptomics, and proteomics levels, and their interaction with the environment [8]. For this reason, and thanks to its ability for simultaneously and holistically analyzing a large number of biomolecules with diverse physicochemical nature, metabolomics has shown great potential in biomedical research for elucidating the molecular mechanisms underlying the pathogenesis and progression of diseases, investigating the involvement of potential risk factors, and studying the efficacy of pharmacological and nutritional treatments. However, the complexity and heterogeneity of the human metabolome considerably hinder the simultaneous determination of the entire set of these metabolites. Thus, the most common strategy in metabolomics research is applying analytical multi-platforms, based on the combination of complementary profiling techniques, with the aim of maximizing metabolome coverage [9].

Global nontargeted metabolomics fingerprinting is only affordable by using powerful analytical tools. To this end, mass spectrometry (MS) has become the most widely employed technique because of its sensitivity, selectivity, and broad coverage, thanks to the availability of multiple instrumental configurations. The simplest MS-based approach is direct MS analysis, based on direct introduction of sample extracts into the mass spectrometer without prior chromatographic or electrophoretic separation. This enables accomplishing fast and comprehensive metabolomics screenings, of great interest when dealing with large sample populations [10, 11]. Complementarily, the mass spectrometer can also be hyphenated with separation techniques to reduce the complexity of resulting metabolic profiles and thus facilitate the identification of individual metabolites. The interfacing of gas chromatography with mass spectrometry (GC-MS) is a robust tool that provides high sensitivity and resolution for determining low-molecular-weight metabolites [12, 13], including organic and amino acids, carbohydrates, amines, and fatty acids, among others. As an alternative, liquid chromatography (LC) is nowadays the main

workhorse in metabolomics because of its ability to deal with chemically diverse metabolites, from low-molecular-weight compounds to non-volatile and hydrophobic species, through the use of complementary retention mechanisms (e.g., reversed phase, RP; hydrophilic interaction liquid chromatography, HILIC) and ionization techniques (e.g., electrospray ionization, ESI; atmospheric pressure chemical ionization, APCI; atmospheric pressure photoionization, APPI) [14].

Herein, we provide some updates on our previous chapter [15], detailing methods and tips for comprehensive and high-throughput metabolomics analysis of different biological samples of interest in AD research through complementary MS-based analytical platforms.

2 Materials

High-purity solvents and reagents must be used for sample treatment and subsequent metabolomics analysis.

2.1 Collection and Extraction of Biological Samples

1. Saline solution: 9 g/L sodium chloride.
2. Extraction solvent for serum (polar extraction): 1:1 methanol/ethanol (v:v).
3. Reconstitution solvent for serum (polar extraction): 0.1% formic acid in 80:20 methanol/water (v:v).
4. Extraction solvent for serum (lipophilic extraction): 1:1 chloroform/methanol (v:v).
5. Reconstitution solvent for serum (lipophilic extraction): 0.1% formic acid, 10 mM ammonium formate, 60:40 dichloromethane/methanol (v:v).
6. Extraction solvent for tissues (polar extraction): 0.1% formic acid in methanol.
7. Extraction solvent for tissues (lipophilic extraction): 0.1% formic acid, 10 mM ammonium formate, 2:1 chloroform/methanol (v:v).
8. Cryogenic homogenizer: SPEX SamplePrep (Freezer/Mills 6770).
9. Pellet mixer.

2.2 Sample Derivatization

1. Methoxymation reagent: 20 mg/mL methoxyamine hydrochloride in pyridine.
2. Silylation reagent: N-methyl-N-trimethylsilyl-trifluoroacetamide (MSTFA).

2.3 Metabolomics Analyses

1. Instrumentation for metabolomics fingerprinting by direct MS analysis: QSTAR XL quadrupole-time-of-flight mass spectrometer (Sciex), equipped with ESI and APPI ionization sources, and with integrated syringe pump.
2. Instrumentation for metabolomics profiling by ultrahigh-performance liquid chromatography – mass spectrometry (UHPLC-MS): Accela LC system (Thermo Fisher Scientific) coupled to a QSTAR XL quadrupole-time-of-flight mass spectrometer (Sciex), equipped with ESI source.
3. Instrumentation for metabolomics profiling by gas chromatography – mass spectrometry (GC-MS): Trace GC ULTRA gas chromatograph coupled to ITQ 900 ion trap mass spectrometer detector (Thermo Fisher Scientific).
4. Flow injection solvent (APPI-MS analysis): methanol.
5. Photoionization dopant reagent (APPI-MS analysis): toluene.
6. Reversed-phase chromatographic column (UHPLC-MS analysis): Hypersil Gold C18, 2.1 × 50 mm, 1.9 μm (Thermo Fisher Scientific).
7. Mobile phase A (UHPLC-MS analysis): 0.1% formic acid, 10 mM ammonium formate in methanol.
8. Mobile phase B (UHPLC-MS analysis): 0.1% formic acid, 10 mM ammonium formate in water.
9. Gas chromatography column (GC-MS analysis): Factor Four capillary column VF-5MS 30 m × 0.25 mm ID, 0.25 μm film thickness.

3 Methods

3.1 Collection of Biological Samples

To collect serum blood samples from AD patients and healthy controls (*see Note 1*):

3.1.1 Human Blood Samples

1. Venipuncture the antecubital vein (*see Note 2*).
2. Withdraw the blood sample into a BD Vacutainer tube (*see Note 3*).
3. Put the blood tube in a refrigerator for 30 min to allow clot retraction (*see Note 4*).
4. Centrifuge at 1500 g for 10 min at 4 °C.
5. Aliquot the supernatant serum into cryotubes and store them at –80 °C until analysis (*see Note 5*).

3.1.2 Blood and Tissue Samples from APP × PS1 Transgenic Mice

1. Animals must be acclimated for 3 days after reception in rooms with a 12-h light/dark cycle at 20–25 °C, with water and food available ad libitum.
2. Anesthetize animals by isoflurane inhalation.

3. Extract blood samples by cardiac puncture. Put the blood tube in a refrigerator for 30 min to allow clot retraction (*see* **Notes 3 and 4**).
4. Centrifuge at 1500 g for 10 min at 4 °C.
5. Aliquot the supernatant serum into cryotubes and store them at –80 °C until analysis (*see* **Note 5**).
6. Remove the brain using surgical scissors, rinse with saline solution, and dissect it into hippocampus, cortex, cerebellum, striatum, and olfactory bulbs.
7. Remove other peripheral organs (liver, kidney, spleen, and thymus) and rinse with saline solution.
8. Snap-freeze the tissues in liquid nitrogen.
9. Store all the biological samples at –80 °C until analysis (*see* **Note 6**).

3.2 Extraction of Biological Samples

3.2.1 Extraction of Serum Samples

Serum samples are treated following a two-step extraction procedure to fractionate the serum metabolome in two extracts: (i) polar extract containing low-molecular-weight metabolites and phospholipids and (ii) lipophilic extract mainly composed by neutral lipids [16].

1. Mix 100 µL of serum with 400 µL of the polar extraction solvent.
2. Shake vigorously for 5 min using a vortex mixer to precipitate proteins.
3. Centrifuge samples at 4000 g for 10 min at 4 °C.
4. Transfer the supernatants to new tubes and keep the precipitates in cold for further treatment.
5. Take supernatants to dryness under a nitrogen stream (*see* **Note 7**).
6. Reconstitute the resulting residue with 100 µL of the polar reconstitution solvent (**polar extract**).
7. Add 400 µL of the lipophilic extraction solvent to the protein precipitates obtained in **step 4**.
8. Shake vigorously for 5 min using a vortex mixer.
9. Centrifuge at 10000 g for 10 min at 4 °C.
10. Take supernatants to dryness under a nitrogen stream (*see* **Note 7**).
11. Reconstitute the resulting residue with 100 µL of the lipophilic reconstitution solvent (**lipophilic extract**).
12. Store all the sample extracts at –80 °C until analysis.

3.2.2 Extraction of Tissue Samples

Tissue samples, including hippocampus, cortex, cerebellum, striatum, olfactory bulbs, liver, kidney, spleen, and thymus, are extracted following the methodology previously optimized by González-Domínguez et al. [17–19].

1. Using a cryogenic homogenizer, homogenize tissues for 30 s at a rate of 10 strokes per second (*see Note 8*).
2. Weight 30 mg of the homogenized tissue (or the entire sample for smaller organs) into 1.5 mL Eppendorf tubes.
3. Add 10 $\mu\text{L}/\text{mg}$ of the polar extraction solvent (pre-cooled at $-20\text{ }^{\circ}\text{C}$).
4. Use a pellet mixture for 2 min to homogenize the mixture and disrupt cells.
5. Centrifuge at 10000 g for 10 min at $4\text{ }^{\circ}\text{C}$.
6. Transfer the supernatant to a new tube (**polar extract**).
7. Add 10 $\mu\text{L}/\text{mg}$ of the lipophilic extraction solvent (pre-cooled at $-20\text{ }^{\circ}\text{C}$) to the pellet obtained in **step 5** (*see Note 9*).
8. Repeat **steps 4–6** to obtain the corresponding **lipophilic extracts**.
9. Store all the sample extracts at $-80\text{ }^{\circ}\text{C}$ until analysis.

3.2.3 Quality Control Samples

Prepare quality control (QC) samples by pooling equal volumes of each sample. These QC samples must be analyzed at the start of the run to equilibrate the analytical system as well as at intermittent points throughout the sequence to monitor system stability [20].

3.3 Sample Derivatization

Metabolomics profiling by GC-MS requires the application of a derivatization protocol to increase the volatility of target metabolites. For this purpose, polar extracts must be treated according to the following two-step methodology [21] (*see Note 10*):

1. Transfer 50 μL of the previously prepared polar extracts into a new tube and take to dryness under nitrogen stream (*see Note 7*).
2. Add 50 μL of the methoxymation reagent (*see Note 11*).
3. After briefly vortexing, incubate the sample at $80\text{ }^{\circ}\text{C}$ for 15 min using a water bath.
4. Add 50 μL of the silylation reagent (*see Note 11*).
5. Incubate at $80\text{ }^{\circ}\text{C}$ for 15 min using a water bath.
6. Centrifuge at 4000 g for 1 min and collect the supernatant for analysis (*see Note 12*).

Use the analytical conditions optimized elsewhere [16, 19, 22]:

3.4 Metabolomics Fingerprinting: Direct MS Analysis

3.4.1 Analysis by Direct Infusion Electrospray Mass Spectrometry (DI-ESI-MS)

1. Clean the ESI source before starting the analyses.
2. Tune the MS system to check the instrumental resolution and sensitivity (*see Note 13*).
3. Infuse sample extracts into the ESI-MS system using a syringe pump operating at 5 $\mu\text{L}/\text{min}$ flow rate.
4. Set the MS operating conditions as follows:
 - (a) Acquisition mode: full scan within the m/z range 50–1100 Da.
 - (b) Ion polarity: positive and negative ionization modes in separate runs.
 - (c) Scan time: 1.005 spectra per second.
 - (d) Total acquisition time: 0.2 min.
 - (e) Curtain gas: 1.13 L/min.
 - (f) Nebulizer gas: 1.56 L/min.
 - (g) Source temperature: 60 °C.
 - (h) Ion spray (IS) voltage: 3300 V in the positive ion mode and – 4000 V in the negative ion mode.
 - (i) Declustering potential (DP): 60 V in the positive ion mode and – 100 V in the negative ion mode.
 - (j) Focusing potential: 250 V in the positive ion mode and – 250 V in the negative ion mode.

3.4.2 Analysis by Flow Injection Atmospheric Pressure Photoionization Mass Spectrometry (FI- APPI-MS)

Use the analytical conditions optimized elsewhere [23, 24]:

1. Clean the APPI source before starting the analyses.
2. Tune the MS system to check the instrumental resolution and sensitivity (*see Note 13*).
3. Inject 10 μL of the sample extract by flow injection (i.e., no chromatographic column) using a LC system.
4. Set the flow rate of the injection solvent at 50 $\mu\text{L}/\text{min}$ for analysis under positive ion mode and at 100 $\mu\text{L}/\text{min}$ for analysis under negative ion mode.
5. Deliver the photoionization dopant reagent using a syringe pump.
6. Set the flow rate of the dopant reagent at 20 $\mu\text{L}/\text{min}$ for analysis under positive ion mode and at 40 $\mu\text{L}/\text{min}$ for analysis under negative ion mode.
7. Set the MS operating conditions as follows:
 - (a) Acquisition mode: full scan within the m/z range 50–1100 Da.
 - (b) Ion polarity: positive and negative ionization modes in separate runs.

- (c) Scan time: 1.005 spectra per second.
- (d) Total acquisition time: 0.5 min.
- (e) Curtain gas: 1.13 L/min.
- (f) Nebulizer gas: 1.56 L/min.
- (g) Heater gas: 3.00 L/min.
- (h) Lamp gas: 1.00 L/min.
- (i) Source temperature: 400 °C.
- (j) Ion spray (IS) voltage: 1500 V in the positive ion mode and – 23,000 V in the negative ion mode.
- (k) Declustering potential (DP): 50 V in the positive ion mode and – 50 V in the negative ion mode.
- (l) Focusing potential: 250 V in the positive ion mode and – 250 V in the negative ion mode.

3.5 Metabolomics Profiling: Hyphenated MS-Based Approaches

The combination of liquid and gas chromatography with mass spectrometry is nowadays the most common analytical strategy for comprehensive metabolomics analysis. The protocols described under this section are based on those previously optimized elsewhere [17, 25–27] (*see Note 14*).

3.5.1 Analysis by Ultrahigh-Performance Liquid Chromatography-Mass Spectrometry (UHPLC-MS)

1. Clean the ESI source before starting the analyses.
2. Tune the MS system to check the instrumental resolution and sensitivity (*see Note 13*).
3. Flush the LC system with mobile phase until pressure stabilization.
4. Set the UHPLC operating conditions as follows:
 - (a) Injection volume: 5 µL.
 - (b) Autosampler temperature: 4 °C.
 - (c) Column compartment temperature: 50 °C.
 - (d) Flow rate: 0.5 mL/min.
 - (e) Gradient program: 0–1 min, 95% B; 2.5 min, 25% B; 8.5–10 min, 0% B; 10.1–12 min, 95% B.
5. Set the QTOF-MS operating conditions as follows:
 - (a) Acquisition mode: full scan within the m/z range 50–1100 Da.
 - (b) Ion polarity: positive and negative ionization modes in separate runs.
 - (c) Scan time: 1.005 spectra per second.
 - (d) Curtain gas: 1.48 L/min.
 - (e) Nebulizer gas: 1.56 L/min.
 - (f) Heater gas: 6.25 L/min.

- (g) Source temperature: 400 °C.
- (h) Ion spray (IS) voltage: 5000 V in the positive ion mode and – 2500 V in the negative ion mode.
- (i) Declustering potential (DP): 100 V in the positive ion mode and – 120 V in the negative ion mode.
- (j) Focusing potential: 350 V in the positive ion mode and – 350 V in the negative ion mode.

3.5.2 Analysis by Gas Chromatography-Mass Spectrometry (GC-MS)

Set the operating conditions as follows:

1. Column temperature program: 0–0.5 min, 100 °C; 0.5–15.2 min, 100–320 °C; and 15.2–18 min, 320 °C.
2. Injector temperature: 280 °C.
3. Injection volume: 1 µL.
4. Injection mode: splitless.
5. Carrier gas: helium.
6. Carrier gas flow rate: 1 mL/min.
7. Electron ionization voltage: 70 eV.
8. Ion source temperature: 200 °C.
9. Acquisition mode: full scan spectra in the m/z range 35–650 Da.

4 Notes

1. Subjects affected by mild cognitive impairment (MCI) can also be enrolled to investigate metabolomics changes occurring in the early onset of neurodegenerative disorders, as previously reported [28, 29].
2. To minimize the influence of the circadian rhythm and diet, it is recommended to collect the samples in the morning and after, at least, 8 h of fasting.
3. Plasma samples can be used instead of serum. For this, blood must be collected in anticoagulant-containing tubes.
4. The pre-analytical phase (i.e., sample collection, pre-processing) must be standardized to minimize inter-sample variability factors and to maintain the metabolic integrity of the biological samples [30].
5. Discard hemolyzed samples, as this may strongly alter the circulating metabolomics profile.
6. The metabolomics procedures described in this chapter have been optimized for the analysis blood and tissue samples but

can easily be adapted for other biological matrices, such as urine [31].

7. The evaporation of sample extracts can also be carried out by using vacuum concentrators (e.g., SpeedVac), if available.
8. Smaller organs (e.g., hippocampus, striatum, olfactory bulbs) can be directly extracted without prior cryo-homogenization.
9. This second extraction step is of great interest for studying peripheral organs (i.e., liver, kidney, spleen, thymus) due to the high content of neutral lipid. However, **steps 7–8** can be omitted when brain tissues are analyzed, as previously reported [17, 22].
10. This derivatization protocol must only be accomplished in polar extracts containing low-molecular-weight metabolites. The low volatilities of neutral lipids that are present in lipophilic extracts impede their determination by GC-MS.
11. The derivatization reagents employed here (i.e., methoxyamine and MSTFA) are very sensitive to moisture. The methoxyamine solution in pyridine must be daily prepared. With regard to MSTFA, the authors recommend the purchase of sealed glass ampoules, which should be used within the day of its opening.
12. After derivatization, the sample extracts must immediately be analyzed to prevent degradation.
13. For accurate mass measurements, the TOF analyzer must daily be calibrated using renin and taurocholic acid solutions in positive and negative ion modes, respectively.
14. Metabolomics methods based on UHPLC-MS and GC-MS that are described in this chapter are only applicable for polar extracts. As previously stated in **Note 10**, lipophilic extracts are mainly composed by neutral lipids that are not readily analyzable by GC-MS due to their low volatilities. Moreover, the separation of these lipids by reversed-phase liquid chromatography requires the use of very long elution programs. For these reasons, lipophilic extracts are only fingerprinted by direct MS analysis.

References

1. Maccioni RB, Muñoz JP, Barbeito L (2001) The molecular bases of Alzheimer's disease and other neurodegenerative disorders. *Arch Med Res* 32:367–381
2. González-Domínguez R, García-Barrera T, Gómez-Ariza JL (2014) Characterization of metal profiles in serum during the progression of Alzheimer's disease. *Metallomics* 9:292–300
3. Dubois B, Feldman HH, Jacova C, Dekosky ST, Barberger-Gateau P, Cummings J, Delacourte A, Galasko D, Gauthier S, Jicha G, Meguro K, O'Brien J, Pasquier F, Robert P, Rossor M, Salloway S, Stern Y, Visser PJ, Scheltens P (2007) Research criteria for the diagnosis of Alzheimer's disease: revising the NINCDS-ADRDA criteria. *Lancet Neurol* 6: 734–746

4. González-Domínguez R, Sayago A, Fernández-Recamales Á (2017) Metabolomics in Alzheimer's disease: the need of complementary analytical platforms for the identification of biomarkers to unravel the underlying pathology. *J Chromatogr B Analyt Technol Biomed Life Sci* 1071:75–92
5. González-Domínguez R, González-Domínguez Á, Sayago A, González-Sanz JD, Lechuga-Sancho AM, Fernández-Recamales Á (2021) Mechanistic insights into Alzheimer's disease unveiled through the investigation of disturbances in central metabolites and metabolic pathways. *Biomedicine* 9:298
6. González-Domínguez R, Sayago A, Fernández-Recamales Á (2018) High-throughput direct mass spectrometry-based metabolomics to characterize metabolite fingerprints associated with Alzheimer's disease pathogenesis. *Meta* 8:52
7. González-Domínguez R, Jáuregui O, Queipo-Ortuño MI, Andrés-Lacueva C (2020) Characterization of the human exposome by a comprehensive and quantitative large-scale multianalyte metabolomics platform. *Anal Chem* 92:13767–13775
8. Dunn WB, Broadhurst DI, Atherton HJ, Goodacre R, Griffin JL (2011) Systems level studies of mammalian metabolomes: the roles of mass spectrometry and nuclear magnetic resonance spectroscopy. *Chem Soc Rev* 40:387–426
9. Gonzalez-Dominguez A, Duran-Guerrero E, Fernandez-Recamales A, Lechuga-Sancho AM, Sayago A, Schwarz M, Segundo C, Gonzalez-Dominguez R (2017) An overview on the importance of combining complementary analytical platforms in metabolomic research. *Curr Top Med Chem* 17:3289–3295
10. González-Domínguez R, Sayago A, Fernández-Recamales Á (2017) Direct infusion mass spectrometry for metabolomic phenotyping of diseases. *Bioanalysis* 9:131–148
11. González-Domínguez R, González-Domínguez Á, Segundo C, Schwarz M, Sayago A, Mateos RM, Durán-Guerrero E, Lechuga-Sancho AM, Fernández-Recamales Á (2019) High-throughput metabolomics based on direct mass spectrometry analysis in biomedical research. In: D'Alessandro A (ed) *High-throughput metabolomics*, Methods in molecular biology, vol 1978. Humana, New York, pp 27–38
12. Pasikanti KK, Ho PC, Chan EC (2008) Gas chromatography/mass spectrometry in metabolic profiling of biological fluids. *J Chromatogr B Analyt Technol Biomed Life Sci* 871:202–211
13. González-Domínguez R, González-Domínguez Á, Sayago A, Fernández-Recamales Á (2021) State-of-the-art mass spectrometry-based approaches to explore the polar metabolome: Alzheimer's disease as a case study. In: Ramautar R (ed) *Advanced mass spectrometry-based analytical separation techniques for probing the polar metabolome*. Royal Society of Chemistry, London, pp 219–241
14. Kuehnbaum NL, Britz-McKibbin P (2013) New advances in separation science for metabolomics: resolving chemical diversity in a post-genomic era. *Chem Rev* 113:2437–2468
15. González-Domínguez R, González-Domínguez Á, Sayago A, Fernández-Recamales Á (2018) Mass spectrometry-based metabolomic multiplatform for Alzheimer's disease research. In: Perneczky R (ed) *Biomarkers for Alzheimer's disease drug development*. Methods in molecular biology, vol 1750. Humana Press, New York, pp 125–137
16. González-Domínguez R, García-Barrera T, Gómez-Ariza JL (2014) Using direct infusion mass spectrometry for serum metabolomics in Alzheimer's disease. *Anal Bioanal Chem* 406:7137–7148
17. González-Domínguez R, García-Barrera T, Vitorica J, Gómez-Ariza JL (2014) Region-specific metabolic alterations in the brain of the APP/PS1 transgenic mice of Alzheimer's disease. *Biochim Biophys Acta* 1842:2395–2402
18. Gago-Tinoco A, González-Domínguez R, García-Barrera T, Blasco-Moreno J, Bebianno MJ, Gómez-Ariza JL (2014) Metabolic signatures associated with environmental pollution by metals in Doñana National Park using *P. clarkii* as bioindicator. *Environ Sci Pollut Res Int* 21:13315–13323
19. González-Domínguez R, García-Barrera T, Vitorica J, Gómez-Ariza JL (2015) High throughput multi-organ metabolomics in the APP/PS1 mouse model of Alzheimer's disease. *Electrophoresis* 36:2237–2249
20. Sangster T, Major H, Plumb R, Wilson AJ, Wilson ID (2006) A pragmatic and readily implemented quality control strategy for HPLC-MS and GC-MS-based metabolomic analysis. *Analyst* 131:1075–1078
21. González-Domínguez R, García-Barrera T, Gómez-Ariza JL (2015) Metabolite profiling for the identification of altered metabolic pathways in Alzheimer's disease. *J Pharm Biomed Anal* 107:75–81
22. González-Domínguez R, García-Barrera T, Vitorica J, Gómez-Ariza JL (2015) Metabolomic screening of regional brain alterations in the APP/PS1 transgenic model of Alzheimer's

- disease by direct infusion mass spectrometry. *J Pharm Biomed Anal* 102:425–435
23. González-Domínguez R, García-Barrera T, Gómez-Ariza JL (2015) Application of a novel metabolomic approach based on atmospheric pressure photoionization mass spectrometry using flow injection analysis for the study of Alzheimer's disease. *Talanta* 131:480–489
 24. González-Domínguez R, García-Barrera T, Vitorica J, Gómez-Ariza JL (2015) Application of metabolomics based on direct mass spectrometry analysis for the elucidation of altered metabolic pathways in serum from the APP/PS1 transgenic model of Alzheimer's disease. *J Pharm Biomed Anal* 107:378–385
 25. González-Domínguez R, García-Barrera T, Vitorica J, Gómez-Ariza JL (2015) Deciphering metabolic abnormalities associated with Alzheimer's disease in the APP/PS1 mouse model using integrated metabolomic approaches. *Biochimie* 110:119–128
 26. González-Domínguez R, García-Barrera T, Vitorica J, Gómez-Ariza JL (2015) Metabolomic investigation of systemic manifestations associated with Alzheimer's disease in the APP/PS1 transgenic mouse model. *Mol Biosyst* 11:2429–2440
 27. González-Domínguez R, García-Barrera T, Vitorica J, Gómez-Ariza JL (2015) Metabolomics reveals significant impairments in the immune system of the APP/PS1 transgenic mice of Alzheimer's disease. *Electrophoresis* 36:577–587
 28. González-Domínguez R, García A, García-Barrera T, Barbas C, Gómez-Ariza JL (2014) Metabolomic profiling of serum in the progression of Alzheimer's disease by capillary electrophoresis-mass spectrometry. *Electrophoresis* 35:3321–3330
 29. González-Domínguez R, Rupérez FJ, García-Barrera T, Barbas C, Gómez-Ariza JL (2016) Metabolomic-driven elucidation of pathological mechanisms associated with Alzheimer's disease and mild cognitive impairment. *Curr Alzheimer Res* 13:641–653
 30. González-Domínguez R, González-Domínguez Á, Sayago A, Fernández-Recamales Á (2020) Recommendations and best practices for standardizing the pre-analytical processing of blood and urine samples in metabolomics. *Meta* 10:229
 31. González-Domínguez R, Castilla-Quintero R, García-Barrera T, Gómez-Ariza JL (2014) Development of a metabolomic approach based on urine samples and direct infusion mass spectrometry. *Anal Biochem* 465:20–27

Part III

Magnetic Resonance Imaging Methods



Analysis of Resting-State Functional Magnetic Resonance Imaging in Alzheimer's Disease

Ersin Ersözlü and Boris-Stephan Rauchmann

Abstract

Alzheimer's disease (AD) has been characterized by widespread network disconnection among brain regions, widely overlapping with the hallmarks of the disease. Functional connectivity has been studied with an upward trend in the last two decades, predominantly in AD among other neuropsychiatric disorders, and presents a potential biomarker with various features that might provide unique contributions to foster our understanding of neural mechanisms of AD. The resting-state functional MRI (rs-fMRI) is usually used to measure the blood-oxygen-level-dependent signals that reflect the brain's functional connectivity. Nevertheless, the rs-fMRI is still underutilized, which might be due to the fairly complex acquisition and analytic methodology. In this chapter, we presented the common methods that have been applied in rs-fMRI literature, focusing on the studies on individuals in the continuum of AD. The key methodological aspects will be addressed that comprise acquiring, processing, and interpreting rs-fMRI data. More, we discussed the current and potential implications of rs-fMRI in AD.

Key words Alzheimer's disease, fMRI, Resting-state, Functional connectivity, Connectome, Intrinsic connectivity network, Graph theory

1 Introduction

Neuroimaging has evolved as a unique discipline over the last four decades, gaining massive importance in investigating neurobiological mechanisms of human behavior using two major modalities—positron emission tomography (PET) and functional magnetic resonance imaging (fMRI). However, the central concept of functional brain imaging via regional cerebral blood flow has been backed by the experiments of Roy and Sherrington in 1890 that showed the stimulation-induced alterations in cerebral circulation in mammals [1]. The required technical improvements needed almost a century before fMRI studies were developed, which was described as self-renewal for behavioral neurology since fMRI appeared less expensive and more accessible than PET [2]. Despite these expectations, fMRI currently counts as one of the costly and

complex imaging methods and remains still far from widespread clinical implementation and is suggested to be possibly underutilized likewise in clinical research [3, 4]. At the same time, alterations in functional connectivity (FC) may ultimately be an effective clinical biomarker for Alzheimer's disease (AD) continuum.

Fostering the understanding of intrinsic brain activity that might reflect the (patho-)physiology might be crucial, as cognitive functions are related to an efficient information transfer among distributed neuronal populations in functionally specialized brain areas [5]. With this in mind, the FC has been applied to examine cerebral network alterations in neurodegenerative and psychiatric diseases and is a potential biomarker [6, 7]. AD, the leading cause of dementia, has been the focus of fMRI studies [8–10]. Moreover, the established clinical biomarkers of amyloid and tau pathology overlap spatially and temporally with network FC alterations, revealing hub regions (i.e., highly connected regions) with higher vulnerability [5, 11, 12]. Therefore, FC may be a beneficial parameter that can detect, among other possible implications, the downstream effects of neurodegeneration due to AD on a circuit level [4].

The metabolic activity of the brain in the resting state has a special place in human physiology due to its relatively high energy consumption, estimated as approximately one-fifth of the body's energy consumption, accompanied by one-tenth of the cardiac output [13]. The majority (from 60% to 80%) of cerebral energy consumption is dedicated to intrinsic neuronal signaling, reflected by the large-scale brain networks, that is, intrinsic connectivity networks (ICN) [13, 14]. Interestingly, the change in energy consumption during an activity is estimated to be less than 5% compared to the resting state, which might suggest that the spontaneous activity in resting-state fMRI (rs-fMRI) is a rich source to explore the neural mechanisms [6].

We aim to describe the most commonly used methodology of fMRI that has been studied with a constant increase in the field of Alzheimer's disease research over the last two decades, which is reflected in the trajectory of the numbers of publications on resting state in general (Fig. 1), and to provide an overview of data acquisition and preparation approaches and the fMRI data analyses. With this aim, we present a (rather subjective) selection of standard methods and their rationale at a gross level, while the finer technical details are not included when possible.

2 The Brain Connectivity in Resting State

The most common fMRI analysis approach has been the blood-oxygen-level-dependent (BOLD) signal [15], possibly due to its high sensitivity and easy implementation [1], which measures brain

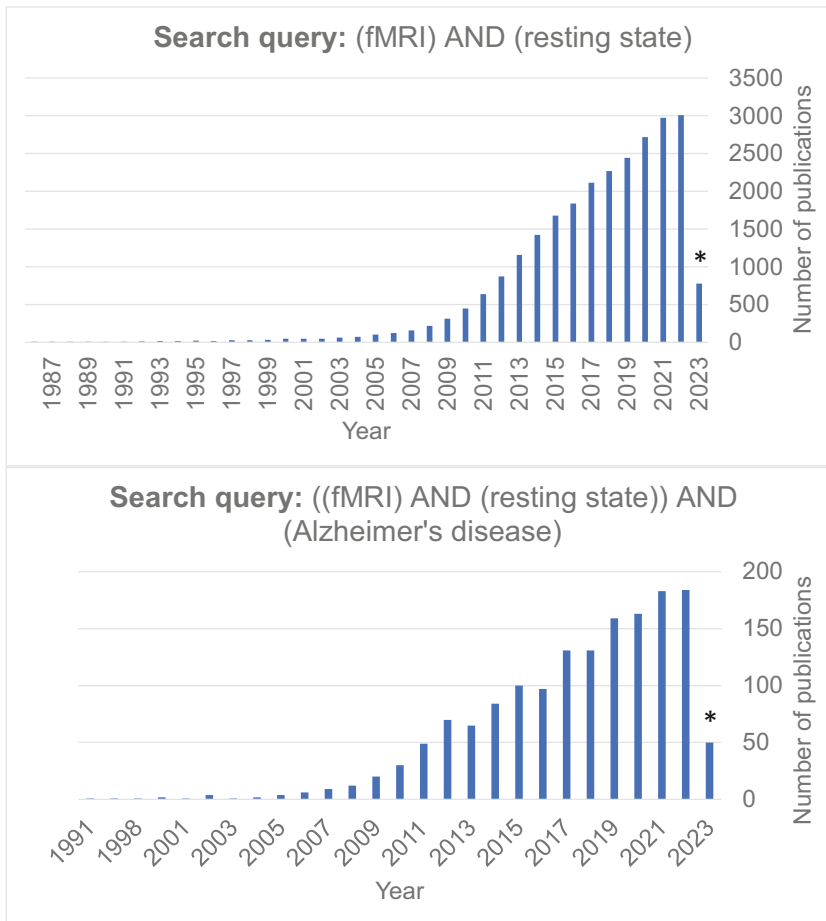


Fig. 1 Number of studies found with the given search queries on PubMed® (nih.gov) per year. *As at 25th of March 2023

activity indirectly by detecting associated changes in regional cerebral blood flow and oxygenation levels. The deoxygenated blood (paramagnetic effect) and oxygenated blood (diamagnetic effect) are modulated by cerebral blood flow, the cerebral metabolic rate of O₂, and cerebral blood volume. The paramagnetic and diamagnetic effects interfere with the T2* signal and change the signal intensity [14, 16, 17]. The rs-fMRI mainly measures the spontaneous low frequency (<0.08–0.1 Hz) fluctuations in the BOLD signal [18] that is specific to the gray matter and can reflect the spatial extent of temporally correlated networks [19]. These fluctuations occur through 3D variations in spatial frequencies that can be localized in x, y, and z directions concerning slice position, while several other factors modulate the signal, which is further elucidated below [16]. The BOLD signal is obtained continuously for a few minutes and provides an indirect marker of neuronal function on a spatial scale of 1–10 cm and a temporal scale of milliseconds to

minutes [3]. Temporal correlations of the BOLD signal between spatially distinct regions during the fMRI examination are defined as functional connectivity [18].

3 Image Preparation

Since the BOLD signal is affected by various confounders, such as anatomical, physiological, and image acquisition parameters [20], analyzing BOLD signal changes (i.e., functional connectivity) requires a certain level of expertise in image preparation. With this in mind, we present the commonly used steps from image acquisition and processing to statistical analyses in this section. A recent study addressed the importance of structured, optimally standardized data management and technical issues, which might shed light on throughout planning, including the analyses with fMRI data [21]. Since the most widely used method is single-shot echo planar imaging (EPI) in rs-fMRI studies, we focus on EPI in this chapter.

For the rs-fMRI examination, individuals are commonly instructed to lie supine and still with closed eyes with minimum head movements—for example, on foam padding and a restraining strap. The suitable magnetic resonance imaging protocol allows the measurement of the local cerebral oxygen concentrations and, in the end, the BOLD signal. The data will then be continuously recorded for 5–20 min as slices with a plane resolution of 1–3 mm thickness in less than 80 ms per slide [22], for example, an image every 2 s for 6 min for 180 three-dimensional images. The slices as time courses can then be represented in three-dimensional or four-dimensional (adding time, e.g., in NIfTi file format) datasets. The EPI images are usually acquired with other images, that is, T1 images for volume acquisition (preferentially with superior gray-white matter contrast—e.g., as in Magnetization Prepared-Rapid Gradient Echo (MP-RAGE) Sequence) [22, 23].

The MR signal is highly flexible since it depends on several tissue properties, which can be manipulated by adjusting pulse sequence parameters such as the repetition or echo times [23]. Additionally, the image resolution varies depending on the field strength systems from 1.5 to 3 and up to 7 Tesla (considered an ultra-high field with a resolution down to the micrometer) [16].

3.1 Image Processing: Preprocessing, Denoising, and Postprocessing

Image processing mainly consists of segmentation and registration methods to correct images for noise and sampling errors. As fMRI is generally implicated at a group level than on an individual level, that is, comparison between images of several subjects or imaging sessions, its analysis requires a variability reduction through image processing. The key image-processing steps are summarized below (Fig. 2), which might alter specific routines. The literature points to

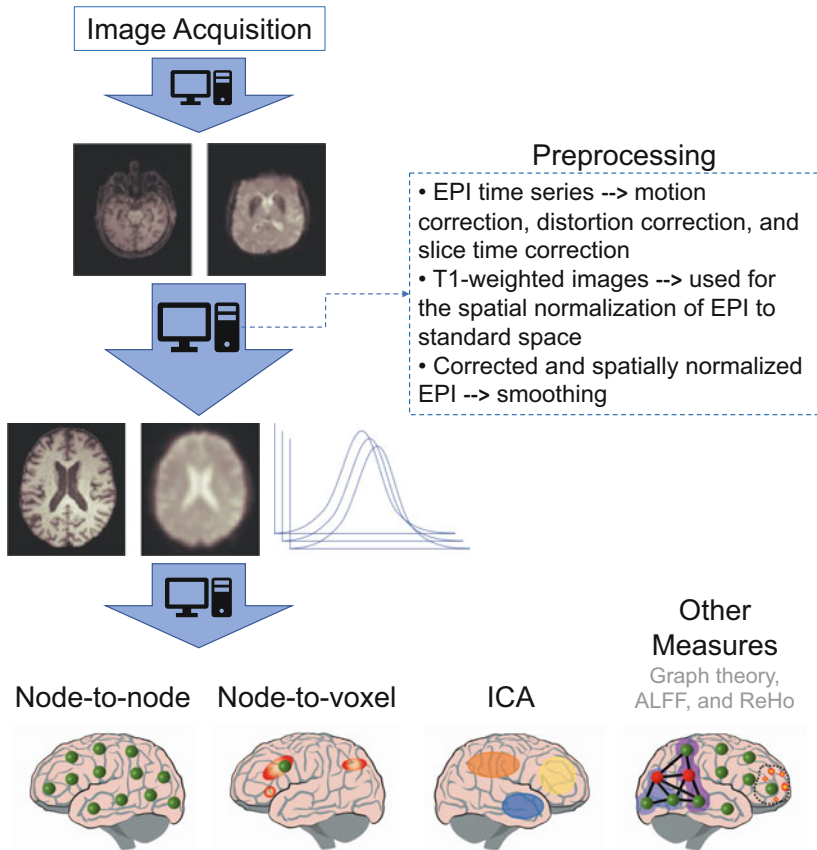


Fig. 2 Standard pipeline for image processing. Abbreviations: *EPI* echo-planar imaging, *ICA* independent component analysis, *ALFF* Amplitude of low-frequency fluctuations, *ReHo* Regional homogeneity

a general framework for image processing [24], albeit the researchers from different study groups have various approaches, causing high variability in the analysis of neuroimaging data [25]. Likewise, there are several alternative software packages based on freely available pipelines that are supposedly combinable with each other and interchangeably usable (Table 1). Quality control is required at each step, starting with inspecting the raw data [26].

3.1.1 Preprocessing

Preprocessing usually begins with realignment, which refers to reducing the effect of subject motion during the scan. A distortion correction might be employed to correct spatial distortions due to inhomogeneities in the magnetic field (e.g., due to the air–tissue interfaces). A slice timing correction refers to the correction for temporal differences in slice acquisition, as the timing of acquired slices varies. The latter allows plotting the time course of a voxel as a dotted line, of which the intensity value is combined among sampled frames to create a continuous curve.

Table 1
A list of some of the key software packages and respective functions

	Preprocessing	Denoising	Postprocessing – First-level analysis	Group statistics – Second-level analysis	Brain visualization ^a
Statistical parametric mapping (SPM) (ucl.ac.uk) [109]	✓	✓	✓	✓	✓
Analysis of functional neuroimages (AFNI) (nimh.nih.gov) [110]	✓	✓	✓	✓	
FMRIB Software Library (FSL) (ox.ac.uk) [111]	✓	✓	✓	✓	✓
NiLearn (github.io)		✓	✓	✓	✓
FreeSurfer Functional Analysis Stream (FsFast) (harvard.edu)	✓	✓	✓	✓	✓
CONN toolbox (conn-toolbox.org) ^b [112]	✓	✓	✓	✓	✓
fMRIPrep (fmriprep.org) ^b [113]	✓	✓			✓
GraphVar (nitrc.org) [114]			✓	✓	✓

^aAt least in one of the processing steps

^bAutomated pipelines for preprocessing and denoising

The normalization of the functional image by using the “coplanar” structural image as reference makes individual brains comparable by placing them into a reference frame (e.g., in Talairach space for landmark-based method) or in standard templates (e.g., in Montreal Neurological Institute (MNI) space for volume-based registration). Even when there is significant variability in the finer details in general, the gross structure shows a remarkable consistency [27]. The alignment provides a three-dimensional Cartesian coordinate space for later analysis.

Spatial smoothing (also called temporal filtering) refers to blurring the data in space, which can help reduce the mismatch and the spatial resolution [27]. With this, the spatial convolution

with a three-dimensional Gaussian filter (i.e., kernel) of 8–12 full-width half maximum (FWHM) depending on the voxel dimension—an FWHM of two to three times the voxel size—can be used [22, 24, 27].

The registration methods are considered sufficient in various populations, for example, older participants and patients with dementia [27]. However, efficient quality control for each step is even more critical when study participants are expected to present pathological structural changes, for example, brain atrophy or enlarged ventricles. Another practical challenge of rs-fMRI image analysis in patients with dementia is symptom related excessive motions during the image acquisition, requiring considerable caution.

3.1.2 Denoising

The denoising step is optionally implemented to preprocessed images using band-pass filtering (e.g., 0.008–0.09 HZ) and regression of temporal components that address additional noise sources, usually including cardiac, respiratory, and residual subject motion effects in the BOLD signal [28, 29]. The nuisance regressors are commonly derived from particular intracranial areas, such as white matter and ventricular cerebrospinal fluid signals, subject-motion parameters, and outlier scans [30–32].

3.1.3 Postprocessing and Statistical Analysis

Through the steps mentioned above, the processed images can be used to obtain subject activity maps representing single-subject FC between brain areas regarding synchronous activity (Biswal et al. 1995), corresponding to the so-called first level analysis. The analysis involves the correlation between the time course of cerebral regions, that is, voxel or a node [17]. The subject activity maps can be computed for later analysis concerning several analytic approaches—functional connectivity measure—described below.

In order to test a hypothesis, statistical models are utilized on a group level with the functional connectivity measure of interest using the subject activity maps. The general linear model is usually preferred to test FC as a dependent variable as it allows many types of analyses, for example, t-tests, analysis of variance analysis, and analysis of covariance [33]. As many statistical tests are usually needed due to simultaneously tested brain regions, adjustments should be made to avoid false-positive results (i.e., type I error) across voxels or regions. Adjustments can be made by utilizing Bonferroni, False Discovery Rate [34], and family-wise error, whereas the Bonferroni procedure might be too conservative in some circumstances because of spatial dependence among brain regions [16]. To address this, using the random field theory has been suggested [35], which is efficient but relies on many assumptions, such as heavy smoothing [22]. More, nonparametric thresholding solutions, such as permutation analysis [36] and threshold-

free cluster enhancement [37], can notably be advantageous for small sample sizes and noisy statistical images depending on the level of smoothing [38].

4 Analytic Approaches: Measures

4.1 *Intrinsic Connectivity Networks*

The studies identified consistent modules (called ICN) that show spatially independent and temporally highly correlated brain areas [15], for example, the default mode network (DMN), the salience network, the frontoparietal control network, and the dorsal attention network [39, 40]. The DMN has been one of the most extensively investigated RSNs in AD and is associated with internally focused tasks such as memory retrieval and remaining active during sensory tasks with minimal cognitive demand [41–43]. Despite the “resting” state in rs-fMRI, the extrinsic activity-related RSNs show FC, for example, in salience, dorsal attention, and frontoparietal networks [44, 45]. More, the ICNs are also characterized by anticorrelations (i.e., antagonistic activity), mainly between the DMN (as the task-negative network) and the rest of the ICNs (as task-positive networks) [46].

The network connectivity can be measured in rs-fMRI on node or voxel level. The main approaches to identifying network regions using voxel-wise FC are the independent component analysis and principal component analysis, which can generate group-level spatial maps. The spatial maps (or components) representing single RSNs can then estimate subject-specific measures by computing the FC among voxels of respective ICNs [22, 47, 48].

In contrast to data-driven methods, an alternative approach to analyze network FC is to consider a priori regions of a particular ICN. The reduction of node-to-node FC to composite measures to represent ICNs can be calculated as FC among brain regions that belong to a particular ICN using nodes [49–52] or voxels [53–55].

4.2 *Node Connectivity*

The functional connectome is principally a connectivity matrix [56], in which each row or column corresponds to a node that is a brain region as defined by the parcellation, that is, atlas regions (e.g., automated anatomical labeling [57], Brainnetome [58], and Schaefer [59]). The time courses across voxels are generally averaged to derive the time course of the corresponding node after masking the respective region. The matrix elements correspond to the functional connectivity values between two nodes, which are generally undirected or symmetrical, building edges (i.e., the connection between any pair of nodes) [15]. Another node-based approach is the seed-to-voxel connectivity, that is, the functional connectivity between a given node (as the seed) and all other brain voxels. The seed region choice depends on the goals of the analysis and is, therefore, hypothesis-driven [60]. The nodes are derived

from a priori templates, such as atlases, identified based on cytoarchitectonics, anatomical landmarks, or connectivity patterns [5].

4.3 Other Approaches to Analyze Functional Connectivity

The topological properties of a connectome, consisting of nodes and edges, can be analyzed using graph theory. The graph theory is usually analyzed after applying a threshold to remove spurious connections and to obtain sparsely connected connectivity matrices [61] that are expected to show higher randomness at less conservative threshold levels [62]. The connectivity matrices can be analyzed, depending on the research question, as weighted or binarized (linked or not) [5]. Thresholding may be applied using absolute (e.g., selecting correlation coefficients higher than 0.3) or relative (using density or network cost, e.g., selecting the highest 10% of correlation values in the matrix) values [61]. At the same time, different thresholding approaches have a notable impact on observed differences between control and disease groups [61, 63]. Since an overall consensus is lacking in the literature on the thresholding approach (likewise the parcellation) [62, 64, 65], researchers are encouraged to report their results at various thresholding levels and defined parameters [66]. Another methodological issue while defining the design of the graph analysis is that most studies exclude negative correlations, which might mistakeably discard neurobiologically valuable data [63, 67, 68]. The graph theoretical metrics can be summarized under integration and segregation terms, including (global/local) efficiency, clustering coefficient, and degree [56]. Also, primarily global metrics such as modularity and small-worldness have been frequently studied [63].

Some of the other central FC measures are the amplitude of low-frequency fluctuation (ALFF) and fractional ALFF (fALFF)—suggested as the improved ALFF—as well as regional homogeneity (ReHo) measures, which aim to detect regional abnormalities are reported in rs-fMRI studies, presenting high repeatability [69–71]. The ALFF/fALFF differ from the measures mentioned above because they consider amplitudes across voxels instead of the coherence between voxels [72]. At the same time, ReHo refers to the homogeneity of a local group of voxels by measuring the synchronization among one voxel and the nearby voxels [71].

An important alternative approach to the static description of FC is the dynamic FC, which refers to considering temporal variations in the BOLD signal among the time course instead of averaging the BOLD signal for later analysis [73]. Dynamic FC is not further elaborated in this chapter, preferentially focusing on approaches based on conventional static FC. However, this approach might bring additional value to the rs-fMRI data by considering time-varying changes in FC (i.e., brain activity within sub-portions of time series) [74].

5 Current and Potential Implications

The connectivity within and between specific networks has been related to the variability in cognitive and behavioral states [44, 75–77]. The functional network alterations are associated with cognitive decline in AD [8, 9, 78]. The studies showed that the network alterations present a wide overlap with the known neuropathological hallmarks of AD, that is, amyloid and tau pathologies, particularly in hub regions such as posteromedial components of DMN [5, 11, 79–81]. Network disruption in DMN and salience network have already been shown in the prodromal stages of AD in interaction with both amyloid and tau levels [11, 78, 82]. Moreover, the decreased DMN connectivity might be associated with disease progression from preclinical to clinical AD [8, 83]. More remarkably, reduced FC comprising posterior DMN regions might occur before amyloid PET becomes abnormal [8, 79]. Findings also suggest that network disruption in the dorsal attention network increases while AD progresses. The FC of salience and the frontoparietal networks are altered in AD when either within or between network connectivity is considered [49, 52, 84, 85], while anticorrelation between DMN and the frontoparietal network might alter first [79]. The FC within DMN, frontoparietal, and salience networks predicted the change in global cognitive performance while synergistically interacting with amyloid pathology [86]. Other brain areas with FC alterations are between the medial temporal lobe and DMN, which predicted variance in episodic memory functions at baseline and over an 8-year follow-up period [48]. Also relevantly, genetic factors such as *APOE* $\epsilon 4$ allele status [87] and family history of late-onset AD [88] was associated with network FC alterations.

The functional network alterations might underlie not only various disease entities among AD-related dementias (ADRD) [89, 90] but also the variance in clinical presentations of AD [53, 91, 92], including subtypes of AD—familial AD or early or late age at the onset [5]. The rs-fMRI may be thus used to contribute to the diagnostic while discriminating disease entities among ADRD.

The graph metrics revealed substantial alterations throughout life, most prominently before age 20 and late adulthood, and were associated with intelligence and cognitive functioning [60, 93]. Notably, segregation was also shown to be affected not only simply by age and sex [60, 94, 95] but also by educational years and fluid intelligence [96, 97]. Similarly, in the course of AD, the network FC can be affected by individual factors regarding education [98], fluid intelligence [99] and lifelong experiences [51].

The rs-fMRI may contribute to a noninvasive, efficient, and accurate diagnosis, which can be especially important in the earliest stages of AD, where clinical and neuropsychological assessments might be complicated [100]. Furthermore, a fine-tuned diagnostic and prognostic assessment might be possible through rs-fMRI, which may support clinicians who are not experts in the field, as well as patients and their relatives, in decision-making.

Considering the efficacy that may vary among individuals, rs-fMRI may provide a vast potential for investigating brain functioning while participants undergo an intervention. Less hypothetically, the previous studies utilized rs-fMRI that mainly focused on alterations in DMN while examining efficacy [101] or identifying participants responding to the treatment, for example, transcranial magnetic stimulation [102]. The former might be most suitable as a primary outcome for phase II studies and might also be appropriate as a potential secondary outcome in phase III trials [4, 103]. More importantly, the interventions are unlikely to show clinical efficacy without impacting network degradation [4], regardless of which form of intervention is studied—primary, secondary, or tertiary prevention.

FC-based identified hub regions have been recently used to predict regional tau propagation, suggesting that connectivity might predict up to 70% of the variance in the overall spatial spreading pattern of tau accumulation [12, 104]. A recent study also reported a remarkable spatial association between covariance in FC and microglial activation [105]. Considering individual connectomes in resting state may promote statistical power and reduce the number of participants.

In summary, rs-fMRI might contribute to clinical research and, ultimately, the clinical practices in the field of AD/ADRD in various ways, depending on the study design and hypothesis:

- I. Improving diagnosis.
 - Efficient diagnosis of AD (sensitivity).
 - Accurate diagnosis—discriminating AD from other neuropsychiatric disorders (specificity).
- II. Stratifying disease cohort.
 - Risk group.
 - Resilient and resistant individuals.
- III. Monitoring treatment strategies.
 - Efficacy—Primary/secondary outcome.
 - Estimation of response, for example, (endo-) phenotypes.

One of the critical concerns while considering rs-fMRI as a biomarker, which is supposed to detect fundamental changes in

biology with high precision, is that a critical variation in reproducibility, which might be affected by subject demographics, acquisition methods, scanning hardware, processing methods, and FC measures [106]. However, the computational methods and standardization efforts are constantly being improved. For example, researchers recently proposed an automated pipeline that integrates image processing with machine/deep learning approaches, aiming for a standardized methodology from preprocessing to interpreting the rs-fMRI data [107]. Furthermore, the validity of the BOLD signal was scrutinized as a measure of neuronal activity [108].

6 Conclusion

Near clinical assessments, surrogate biomarkers are essential to study neurobiological mechanisms in the natural disease course, especially while examining the effects of any observation or intervention. Imaging biomarkers have an additional feature compared to fluid or digital biomarkers, having a neuroanatomical dimension, and are commonly used in large multicenter clinical trials. The rs-fMRI, among other imaging biomarkers, provides numerous potentials, particularly for precision medicine aspects, while also bringing methodological challenges in clinical AD research. More research is needed to foster our understanding of the temporal and causal associations between AD hallmarks and brain functional network changes.

References

1. Kim S-G, Bandettini PA (2006) Principles of functional MRI. In: Functional MRI. Springer, New York, pp 3–23
2. Mesulam M-M (2000) Principles of behavioral and cognitive neurology. Oxford University Press
3. Hampel H, Gao P, Cummings J et al (2023) The foundation and architecture of precision medicine in neurology and psychiatry. *Trends Neurosci* 46:176–198
4. Cummings J (2019) The role of biomarkers in Alzheimer’s disease drug development. *Adv Exp Med Biol* 1118:29–61
5. Yu M, Sporns O, Saykin AJ (2021) The human connectome in Alzheimer disease — relationship to biomarkers and genetics. *Nat Rev Neurol* 17:545–563
6. Fox MD, Greicius M (2010) Clinical applications of resting state functional connectivity. *Front Syst Neurosci* 4:19
7. Filippi M, Spinelli EG, Cividini C et al (2023) The human functional connectome in neurodegenerative diseases: relationship to pathology and clinical progression. *Expert Rev Neurother* 23:59–73
8. Jones DT, Knopman DS, Gunter JL et al (2016) Cascading network failure across the Alzheimer’s disease spectrum. *Brain* 139:547–562
9. Dennis EL, Thompson PM (2014) Functional brain connectivity using fMRI in aging and Alzheimer’s disease. *Neuropsychol Rev* 24:49–62
10. Perovnik M, Rus T, Schindlbeck KA, Eidelberg D (2023) Functional brain networks in the evaluation of patients with neurodegenerative disorders. *Nat Rev Neurol* 19:73–90
11. Ingala S, Tomassen J, Collij LE et al (2021) Amyloid-driven disruption of default mode network connectivity in cognitively healthy individuals. *Brain Commun* 3:fcab201
12. Franzmeier N, Neitzel J, Rubinski A et al (2020) Functional brain architecture is

- associated with the rate of tau accumulation in Alzheimer's disease. *Nat Commun* 11:347
13. Raichle ME (2010) Two views of brain function. *Trends Cogn Sci* 14:180–190
 14. Lecrux C, Hamel E (2011) The neurovascular unit in brain function and disease. *Acta Physiol* 203:47–59
 15. Park H-J, Friston K (2013) Structural and functional brain networks: from connections to cognition. *Science* 342:1238411
 16. Sharma R (2012) Functional magnetic resonance imaging - advanced neuroimaging applications. INTECH
 17. Buxton RB (2009) Interpreting the BOLD response. In: *Introduction to functional magnetic resonance imaging*. Cambridge University Press, pp 400–424
 18. Fox MD, Raichle ME (2007) Spontaneous fluctuations in brain activity observed with functional magnetic resonance imaging. *Nat Rev Neurosci* 8:700–711
 19. Vemuri P, Jones DT, Jack CR Jr (2012) Resting state functional MRI in Alzheimer's disease. *Alzheimers Res Ther* 4:2
 20. Ogawa S, Menon RS, Kim SG, Ugurbil K (1998) On the characteristics of functional magnetic resonance imaging of the brain. *Annu Rev Biophys Biomol Struct* 27:447–474
 21. Gorgolewski KJ, Auer T, Calhoun VD et al (2016) The brain imaging data structure, a format for organizing and describing outputs of neuroimaging experiments. *Sci Data* 3:160044
 22. Poline JB, Ciuciu P, Roche A, Thirion B (2016) Intra and inter subject analyses of brain functional magnetic resonance images (fMRI). In: Paragios N, Ayache N, Duncan J (eds) *Handbook of biomedical imaging*. Springer, New York
 23. Buxton RB (2009) *Introduction to functional magnetic resonance imaging*, 2nd edn. Cambridge University Press, Cambridge
 24. Holiga S, Abdulkadir A, Klöppel S, Dukart J (2018) Functional magnetic resonance imaging in Alzheimer' disease drug development. *Methods Mol Biol* 1750:159–163
 25. Botvinik-Nezer R, Holzmeister F, Camerer CF et al (2020) Variability in the analysis of a single neuroimaging dataset by many teams. *Nature* 582:84–88
 26. Poldrack RA, Nichols T, Mumford J (2011) Preprocessing fMRI data. In: *Handbook of functional MRI data analysis*. Cambridge University Press, Cambridge, pp 34–52
 27. Poldrack RA, Mumford JA, Nichols TE (2011) *Handbook of functional MRI data analysis*. Cambridge University Press, Cambridge
 28. Morfini F, Whitfield-Gabrieli S, Nieto-Castañón A (2023) Functional connectivity MRI quality control procedures in CONN. *Front Neurosci* 17. <https://doi.org/10.3389/fnins.2023.1092125>
 29. Hallquist MN, Hwang K, Luna B (2013) The nuisance of nuisance regression: spectral misspecification in a common approach to resting-state fMRI preprocessing reintroduces noise and obscures functional connectivity. *NeuroImage* 82:208–225
 30. Caballero-Gaudes C, Reynolds RC (2017) Methods for cleaning the BOLD fMRI signal. *NeuroImage* 154:128–149
 31. Friston KJ, Williams S, Howard R et al (1996) Movement-related effects in fMRI time-series. *Magn Reson Med* 35:346–355
 32. Power JD, Mitra A, Laumann TO et al (2014) Methods to detect, characterize, and remove motion artifact in resting state fMRI. *NeuroImage* 84:320–341
 33. Poldrack RA, Nichols T, Mumford J (2011) A review of the general linear model. In: *Handbook of functional MRI data analysis*. Cambridge University Press, Cambridge, pp 191–200
 34. Benjamini Y, Hochberg Y (1995) Controlling the false discovery rate: a practical and powerful approach to multiple testing. *J R Stat Soc* 57:289–300
 35. Worsley KJ, Cao J, Paus T et al (1998) Applications of random field theory to functional connectivity. *Hum Brain Mapp* 6:364–367
 36. Bullmore ET, Suckling J, Overmeyer S et al (1999) Global, voxel, and cluster tests, by theory and permutation, for a difference between two groups of structural MR images of the brain. *IEEE Trans Med Imaging* 18:32–42
 37. Smith SM, Nichols TE (2009) Threshold-free cluster enhancement: addressing problems of smoothing, threshold dependence and localisation in cluster inference. *NeuroImage* 44:83–98
 38. Frackowiak RSJ, Friston KJ, Frith CD et al (2004) Chapter 13 – The Chronoarchitecture of the human brain: functional anatomy based on natural brain dynamics and the principle of functional Independence. In: *Human brain function (second edition)*. Academic Press, Burlington, pp 201–229
 39. Yeo BTT, Thomas Yeo BT, Krienen FM et al (2011) The organization of the human

- cerebral cortex estimated by intrinsic functional connectivity. *J Neurophysiol* 106: 1125–1165
40. Schultz AP, Chhatwal JP, Huijbers W et al (2014) Template based rotation: a method for functional connectivity analysis with a priori templates. *NeuroImage* 102(Pt 2): 620–636
 41. Greicius MD, Krasnow B, Reiss AL, Menon V (2003) Functional connectivity in the resting brain: a network analysis of the default mode hypothesis. *Proc Natl Acad Sci U S A* 100: 253–258
 42. Buckner RL, Andrews-Hanna JR, Schacter DL (2008) The brain's default network: anatomy, function, and relevance to disease. *Ann N Y Acad Sci* 1124:1–38
 43. Kim H, Daselaar SM, Cabeza R (2010) Overlapping brain activity between episodic memory encoding and retrieval: roles of the task-positive and task-negative networks. *NeuroImage* 49:1045–1054
 44. Seeley WW, Menon V, Schatzberg AF et al (2007) Dissociable intrinsic connectivity networks for salience processing and executive control. *J Neurosci* 27:2349–2356
 45. Fox MD, Corbetta M, Snyder AZ et al (2006) Spontaneous neuronal activity distinguishes human dorsal and ventral attention systems. *Proc Natl Acad Sci U S A* 103:10046–10051
 46. Fox MD, Snyder AZ, Vincent JL et al (2005) The human brain is intrinsically organized into dynamic, anticorrelated functional networks. *Proc Natl Acad Sci U S A* 102:9673–9678
 47. Erhardt EB, Rachakonda S, Bedrick EJ et al (2011) Comparison of multi-subject ICA methods for analysis of fMRI data. *Hum Brain Mapp* 32:2075–2095
 48. Berron D, van Westen D, Ossenkuppele R et al (2020) Medial temporal lobe connectivity and its associations with cognition in early Alzheimer's disease. *Brain* 143:1233–1248
 49. Brier MR, Thomas JB, Snyder AZ et al (2012) Loss of intranetwork and internetwork resting state functional connections with Alzheimer's disease progression. *J Neurosci* 32:8890–8899
 50. Rauchmann B-S, Ersoezlue E, Stoeklein S et al (2021) Resting-state network alterations differ between Alzheimer's disease atrophy subtypes. *Cereb Cortex* 31:4901–4915
 51. Ersoezlue E, Rauchmann B-S, Schneider-Axmann T et al (2023) Lifelong experiences as a proxy of cognitive reserve moderate the association between connectivity and cognition in Alzheimer's disease. *Neurobiol Aging* 122:33–44
 52. Wang P, Zhou B, Yao H et al (2015) Aberrant intra- and inter-network connectivity architectures in Alzheimer's disease and mild cognitive impairment. *Sci Rep* 5:14824
 53. Chhatwal JP, Schultz AP, Johnson KA et al (2018) Preferential degradation of cognitive networks differentiates Alzheimer's disease from ageing. *Brain* 141:1486–1500
 54. Schultz AP, Buckley RF, Hampton OL et al (2020) Longitudinal degradation of the default/saliency network axis in symptomatic individuals with elevated amyloid burden. *Neuroimage Clin* 26:102052
 55. Uddin LQ, Kelly AM, Biswal BB et al (2009) Functional connectivity of default mode network components: correlation, anticorrelation, and causality. *Hum Brain Mapp* 30: 625–637
 56. Bullmore E, Sporns O (2009) Complex brain networks: graph theoretical analysis of structural and functional systems. *Nat Rev Neurosci* 10:186–198
 57. Tzourio C, Benslamia L, Guillon B et al (2002) Migraine and the risk of cervical artery dissection: a case-control study. *Neurology* 59:435–437
 58. Fan L, Li H, Zhuo J et al (2016) The human Brainnetome atlas: a new brain atlas based on connectonal architecture. *Cereb Cortex* 26: 3508–3526
 59. Schaefer A, Kong R, Gordon EM et al (2018) Local-global parcellation of the human cerebral cortex from intrinsic functional connectivity MRI. *Cereb Cortex* 28:3095–3114
 60. Pievani M, de Haan W, Wu T et al (2011) Functional network disruption in the degenerative dementias. *Lancet Neurol* 10:829–843
 61. van den Heuvel MP, de Lange SC, Zalesky A et al (2017) Proportional thresholding in resting-state fMRI functional connectivity networks and consequences for patient-control connectome studies: issues and recommendations. *NeuroImage* 152:437–449
 62. Fornito A, Zalesky A, Bullmore ET (2010) Network scaling effects in graph analytic studies of human resting-state FMRI data. *Front Syst Neurosci* 4:22
 63. Hallquist MN, Hillary FG (2019) Graph theory approaches to functional network organization in brain disorders: a critique for a brave new small-world. *Netw Neurosci* 3:1–26

64. Lancichinetti A, Fortunato S (2012) Consensus clustering in complex networks. *Sci Rep* 2: 336
65. Murphy K, Fox MD (2017) Towards a consensus regarding global signal regression for resting state functional connectivity MRI. *NeuroImage* 154:169–173
66. Farahani FV, Karwowski W, Lighthall NR (2019) Application of graph theory for identifying connectivity patterns in human brain networks: a systematic review. *Front Neurosci* 13:585
67. Sporns O, Betzel RF (2016) Modular brain networks. *Annu Rev Psychol* 67:613–640
68. Rubinov M, Sporns O (2010) Complex network measures of brain connectivity: uses and interpretations. *NeuroImage* 52:1059–1069
69. Zang Y, Jiang T, Lu Y et al (2004) Regional homogeneity approach to fMRI data analysis. *NeuroImage* 22:394–400
70. Zou Q-H, Zhu C-Z, Yang Y et al (2008) An improved approach to detection of amplitude of low-frequency fluctuation (ALFF) for resting-state fMRI: fractional ALFF. *J Neurosci Methods* 172:137–141
71. Lyu D, Li T, Lyu X (2021) Resting-state functional reorganisation in Alzheimer's disease and amnesic mild cognitive impairment: protocol for a systematic review and meta-analysis. *BMJ Open* 11:e049798
72. Riedl V (2012) Intrinsic functional brain networks in health and disease. Graduate School of Systemic Neurosciences Ludwig-Maximilians Universität
73. Hutchison RM, Womelsdorf T, Allen EA et al (2013) Dynamic functional connectivity: promise, issues, and interpretations. *NeuroImage* 80:360–378
74. Filippi M, Spinelli EG, Cividini C, Agosta F (2019) Resting state dynamic functional connectivity in neurodegenerative conditions: a review of magnetic resonance imaging findings. *Front Neurosci* 13:657
75. Zhang D, Raichle ME (2010) Disease and the brain's dark energy. *Nat Rev Neurol* 6:15–28
76. Anticevic A, Cole MW, Murray JD et al (2012) The role of default network deactivation in cognition and disease. *Trends Cogn Sci* 16:584–592
77. Smith SM, Fox PT, Miller KL et al (2009) Correspondence of the brain's functional architecture during activation and rest. *Proc Natl Acad Sci U S A* 106:13040–13045
78. Palop JJ, Mucke L (2016) Network abnormalities and interneuron dysfunction in Alzheimer disease. *Nat Rev Neurosci* 17:777–792
79. Palmqvist S, Schöll M, Strandberg O et al (2017) Earliest accumulation of β -amyloid occurs within the default-mode network and concurrently affects brain connectivity. *Nat Commun* 8:1214
80. Hoenig MC, Bischof GN, Seemiller J et al (2018) Networks of tau distribution in Alzheimer's disease. *Brain* 141:568–581
81. Sheline YI, Raichle ME, Snyder AZ et al (2010) Amyloid plaques disrupt resting state default mode network connectivity in cognitively Normal elderly. *Biol Psychiatry* 67:584–587
82. Schultz AP, Chhatwal JP, Hedden T et al (2017) Phases of hyperconnectivity and hypoconnectivity in the default mode and salience networks track with amyloid and tau in clinically Normal individuals. *J Neurosci* 37: 4323–4331
83. Binnewijzend MAA, Schoonheim MM, Sanz-Arigita E et al (2012) Resting-state fMRI changes in Alzheimer's disease and mild cognitive impairment. *Neurobiol Aging* 33: 2018–2028
84. Elman JA, Madison CM, Baker SL et al (2016) Effects of beta-amyloid on resting state functional connectivity within and between networks reflect known patterns of regional vulnerability. *Cereb Cortex* 26:695–707
85. Zhou J, Greicius MD, Gennatas ED et al (2010) Divergent network connectivity changes in behavioural variant frontotemporal dementia and Alzheimer's disease. *Brain* 133: 1352–1367
86. Buckley RF, Schultz AP, Hedden T et al (2017) Functional network integrity presages cognitive decline in preclinical Alzheimer disease. *Neurology* 89:29–37
87. Chiesa PA, Cavedo E, Lista S et al (2017) Revolution of resting-state functional neuroimaging genetics in Alzheimer's disease. *Trends Neurosci* 40:469–480
88. Wang L, Roe CM, Snyder AZ et al (2012) Alzheimer disease family history impacts resting state functional connectivity. *Ann Neurol* 72:571–577
89. Seeley WW, Crawford RK, Zhou J et al (2009) Neurodegenerative diseases target large-scale human brain networks. *Neuron* 62:42–52
90. Tuovinen T, Rytty R, Moilanen V et al (2016) The effect of gray matter ICA and coefficient of variation mapping of BOLD data on the detection of functional connectivity changes in Alzheimer's disease and bvFTD. *Front Hum Neurosci* 10:680

91. Zhou J, Gennatas ED, Kramer JH et al (2012) Predicting regional neurodegeneration from the healthy brain functional connectome. *Neuron* 73:1216–1227
92. Amaefule CO, Dyrba M, Wolfsgruber S et al (2021) Association between composite scores of domain-specific cognitive functions and regional patterns of atrophy and functional connectivity in the Alzheimer's disease spectrum. *NeuroImage Clin* 29:102533
93. Filippi M, van den Heuvel MP, Fornito A et al (2013) Assessment of system dysfunction in the brain through MRI-based connectomics. *Lancet Neurol* 12:1189–1199
94. Chan MY, Park DC, Savalia NK et al (2014) Decreased segregation of brain systems across the healthy adult lifespan. *Proc Natl Acad Sci U S A* 111:E4997–E5006
95. Geerligs L, Renken RJ, Saliassi E et al (2015) A brain-wide study of age-related changes in functional connectivity. *Cereb Cortex* 25:1987–1999
96. Chan MY, Han L, Carreno CA et al (2021) Long-term prognosis and educational determinants of brain network decline in older adult individuals. *Nat Aging* 1:1053–1067
97. Mitchell DJ, Mousley ALS, Shafto MA et al (2023) Neural contributions to reduced fluid intelligence across the adult lifespan. *J Neurosci* 43:293–307
98. Bozzali M, Dowling C, Serra L et al (2015) The impact of cognitive reserve on brain functional connectivity in Alzheimer's disease. *J Alzheimers Dis* 44:243–250
99. Franzmeier N, Buerger K, Teipel S et al (2017) Cognitive reserve moderates the association between functional network anticorrelations and memory in MCI. *Neurobiol Aging* 50:152–162
100. Rodríguez-Gómez O, Rodrigo A, Iradier F et al (2019) The MOPEAD project: advancing patient engagement for the detection of "hidden" undiagnosed cases of Alzheimer's disease in the community. *Alzheimers Dement* 15:828–839
101. Blautzik J, Keeser D, Paolini M et al (2016) Functional connectivity increase in the default-mode network of patients with Alzheimer's disease after long-term treatment with Galantamine. *Eur Neuropsychopharmacol* 26:602–613
102. Lv T, You S, Qin R et al (2023) Distinct reserve capacity impacts on default-mode network in response to left angular gyrus-navigated repetitive transcranial magnetic stimulation in the prodromal Alzheimer disease. *Behav Brain Res* 439:114226
103. Cummings J, Zhong K, Cordes D et al (2017) Drug development in Alzheimer's disease—the role of default mode network assessment in phase II. *US Neurol* 13:67
104. Vogel JW, Iturria-Medina Y, Strandberg OT et al (2020) Spread of pathological tau proteins through communicating neurons in human Alzheimer's disease. *Nat Commun* 11:2612
105. Rauchmann B-S, Brendel M, Franzmeier N et al (2022) Microglial activation and connectivity in Alzheimer disease and aging. *Ann Neurol* 92:768–781
106. Clayton D, Coimbra A, Faraji F et al (2021) Resting-state functional magnetic resonance imaging in a randomized clinical trial for Alzheimer's disease. *Neuroimage Rep* 1:100055
107. Becker K, Brenner K, Gauß J, et al (2022) Pipeline for prediction and explanation of Alzheimer based on connectivity matrices with ML/DL methods. <https://github.com/JanaGauss/Connectome>. Accessed 1 Apr 2023
108. Chandra A, Dervenoulas G, Politis M, Alzheimer's Disease Neuroimaging Initiative (2019) Magnetic resonance imaging in Alzheimer's disease and mild cognitive impairment. *J Neurol* 266:1293–1302
109. Friston K (2007) A short history of SPM. In: *Statistical parametric mapping*. Elsevier, pp 3–9
110. Cox RW (1996) AFNI: software for analysis and visualization of functional magnetic resonance neuroimages. *Comput Biomed Res* 29:162–173
111. Jenkinson M, Beckmann CF, Behrens TEJ et al (2012) FSL. *Neuroimage* 62:782–790
112. Nieto-Castanon A, Whitfield-Gabrieli S (2022) CONN functional connectivity toolbox: RRID SCR_009550, release 22. Hilbert Press
113. Esteban O, Markiewicz CJ, Blair RW et al (2019) fMRIPrep: a robust preprocessing pipeline for functional MRI. *Nat Methods* 16:111–116
114. Kruschwitz JD, List D, Waller L et al (2015) GraphVar: a user-friendly toolbox for comprehensive graph analyses of functional brain connectivity. *J Neurosci Methods* 245:107–115



Diffusion Tensor Imaging in Alzheimer's Studies

Adriana L. Ruiz-Rizzo, Kathrin Finke, and Mario E. Archila-Meléndez

Abstract

In this chapter, we describe the use of quantitative metrics of white matter obtained from the diffusion tensor model based on diffusion-weighted imaging in Alzheimer's disease (AD). Our description synthesizes insights not only from patient populations with AD dementia but also from participants at risk for AD dementia (e.g., amnesic mild cognitive impairment, subjective cognitive decline, or familial AD mutation carriers). A reference to studies examining correlations with behavioral variables is also included. Our main message is to caution against the overinterpretation of diffusion metrics and to favor analyses that focus on regions of interest or major white matter tracts for biomarker studies in AD.

Key words Alzheimer's disease, DTI, Diffusion-weighted imaging, Diffusion metrics, Major tracts, Structural connectivity, White matter

1 Introduction

The diffusion tensor imaging (DTI) model [1] was introduced to provide quantitative information about the degree of anisotropy and the structural orientation of the diffusion of water molecules in the brain [2]. DTI is based on diffusion-weighted imaging (DWI), an inherently noise-sensitive magnetic resonance imaging (MRI) technique [2]. DWI uses the diffusion of water molecules to provide information about the microstructural properties of tissues, by measuring the random (Brownian) motion of water molecules.

White matter tracts are formed by large axon bundles. The diffusion of water in white matter is restricted (i.e., “anisotropic”) within the cellular walls of the axons composing the white matter tracts [2]. DTI uses the diffusion tensor to model the diffusion properties of tissues by estimating six parameters per voxel: three real eigenvalues and three orthogonal eigenvectors. A diffusion ellipsoid can be used as the diffusion tensor's reference frame. DTI parameters determine the primary diffusion direction and magnitude and can be reduced to scalar values and quantitative maps [2]—known as tensor-derived or DTI metrics. Commonly

estimated voxelwise DTI metrics include fractional anisotropy (FA: degree of asymmetry of diffusion), mean diffusivity (MD: average among the three orthogonal axes of the ellipsoid), radial diffusivity (RD, mean of the two minor axes of the ellipsoid), and axial diffusivity (AxD, diffusion along the principal diffusion direction of the ellipsoid) [3]. A novel DTI metric, the mode of anisotropy, has also been implemented in the context of AD. This index reflects shape differences in the diffusion tensor or type of anisotropy and is given from -1 to $+1$. The type of anisotropy can range from planar—as in regions with two fiber populations of similar density that cross each other, to linear—as in regions with one fiber orientation [4].

Most DTI metrics (e.g., RD, MD, and FA) have been shown to be associated with the gray matter of medial temporal lobe structures, such as hippocampal, parahippocampal, and entorhinal cortices [5]. Moreover, these metrics have been shown to predict cognitive decline in healthy older adults, older adults with subjective cognitive decline, and patients with mild cognitive impairment (MCI), as well as the conversion from MCI to AD dementia [5]. FA of the fornix, for example, correlates with memory decline and progression to AD both cross-sectionally and longitudinally [6]. Studies in early-onset autosomal-dominant inherited AD family members have reported selective white matter changes in the corpus callosum and long projecting fibers in MD that occur years before the expected symptom onset [7]. These findings underscore the relevance of DTI metrics as *noninvasive* biomarkers in the early stages of the course of AD.

A recent meta-analysis examined DTI metrics in amnesic MCI (aMCI) based on both region-of-interest (ROI, i.e., tracts selected prior to the analysis) and whole-brain-based (i.e., without prior tract selection) studies [8]. It revealed decreased FA of the fornix and uncinate fasciculus and increased MD in the parahippocampal cingulum, uncinate fasciculus, and corpus callosum (genu and splenium) in patients with aMCI versus healthy control participants. Using an activation likelihood estimation approach, this meta-analysis also showed decreased FA of the bilateral posterior corona radiata (connecting the cortex and the brain stem) in patients with aMCI relative to healthy control participants [8].

In patients with manifest AD dementia, DTI metrics of major white matter tracts such as the cingulum bundle, uncinate fasciculus, corpus callosum, anterior commissure, and superior longitudinal fasciculus II are altered [4]. Earlier findings already suggested the degeneration of a limbic-diencephalic network (i.e., temporoparietal white matter, posterior cingulum, splenium, and fornix) in AD dementia [9]. In comparison to healthy control participants, significant differences across all DTI metrics have been shown for the splenium of the corpus callosum, the left fornix, and the left hippocampal cingulum in patients with AD dementia

[10]. Increased MD of the forceps major (i.e., projections from the splenium of the corpus callosum [11]) and decreased FA of the posterior thalamic radiation have been found to best discriminate MCI from subjective cognitive decline [12]. DTI metrics of the left hippocampal cingulum and the left fornix have shown significant associations with the MiniMental State Examination; those of the corpus callosum and left hippocampal cingulum with the clinical dementia rating—sum of boxes; and those of the left hippocampal cingulum with the Alzheimer's Disease Assessment Scale [10]. Increased MD and reduced FA of the hippocampal cingulum, corpus callosum, uncinate fasciculus, tapetum, and posterior thalamic radiations have also been shown in patients with AD dementia after one-year follow-up [13].

2 Materials

1. Strong magnetic field gradient pulses during magnetic resonance imaging permit diffusion weighting, which includes imaging parameters such as diffusion magnitude (b -value), number and distribution of gradient directions, and the number of $b = 0$ images [2].
2. A three-dimensional diffusion model (the “tensor”) can be estimated by using those gradient pulses in multiple directions. White matter tracts will appear darker in the diffusion-weighted image if they are parallel to a particular gradient direction [14].
3. The tensor has three orthogonal eigenvectors and three positive eigenvalues, with the three eigenvalues ($\lambda_1, \lambda_2, \lambda_3$) giving the diffusivity in each eigenvector's direction, and the major eigenvector pointing in the principal diffusion direction [14].
4. Specialized software, such as FreeSurfer (<https://surfer.nmr.mgh.harvard.edu/fswiki>) [15] and FSL (<https://fsl.fmrib.ox.ac.uk/fsl/fslwiki>) [16]. Familiarity or experience working with a terminal or command window is desirable, as the use of scripting and command lines may be necessary.

3 Methods

1. A sensible analysis pipeline for DTI in AD studies can include an initial quality check (obvious artifacts); motion distortion/correction (volume co-registration), diffusion tensor fitting (e.g., ordinary linear least squares, weighted linear least squares, nonlinear least squares, etc.), computation of parametric maps (i.e., voxelwise maps of MD, FA, and a directionally encoded color map, and the corresponding eigenvectors

and eigenvalues), and final inspection of the results [17] (*see Note 1*).

2. White matter tracts can be delineated in 3D by DTI using fiber-tracking algorithms or “tractography,” which infer connections between neighboring voxels [2] (*see Note 2*). Fiber tractography pieces together each voxel’s single predominant local orientation to allow making inferences about the global fiber trajectories [18] (*see Note 3*).
3. With tractography, we can estimate the organization of white matter and study cross-sectional (one point in time, between individuals) and longitudinal (several points in time, between and/or within individuals) variations in the organization and properties of white matter pathways [19] (*see Note 4*).
4. An issue in tractography is that of “crossing fibers.” These refer to fiber bundles that exhibit two or more different orientations within the same voxel [2]. The impact of crossing fibers is most severe for nondominant tracts, as the orientation produced by DTI will likely reflect the largest contributing fiber direction [2].
5. Single-fiber clusters are mainly found in large tracts, for example, the corpus callosum, middle cerebellar peduncle, and the posterior limb of the internal capsule. At least two-fiber orientations can be found in almost half of the white matter voxels [20]. This characteristic might thus impact the reliability, robustness, and interpretation of the results found for particular tracts (*see Note 5*).
6. In cases where a *single* fiber population is studied (e.g., the corpus callosum), FA can reliably index axonal density (restricted volume fraction) and moderately correlate with myelination (myelin water fraction) metrics [21] (*see Notes 6 and 7*).
7. Both deterministic (unique fiber orientation for each voxel) and probabilistic (distribution of possible trajectories) tractography tend to reconstruct short and straight tracts that do not pass by regions of complex fiber configurations. This aspect makes the quantification of tractography results (e.g., “track density” or “connection strength”) particularly problematic [18] (*see Note 8*).
8. Differences in white matter between patients at-risk for AD dementia versus a reference group can be examined on ROIs defined a priori (e.g., manual tracing or tractography) or the whole-brain level (e.g., tract-based spatial statistics or voxel-based analysis) [8] (*see Note 9*).
9. Though informative, results derived from voxel-based analyses can be unspecific. Therefore, ROI analysis approaches might be

better suited for determining what regions are more sensitive for detecting group differences in AD [10], identifying correlations with measures of cognition and behavior, and/or establishing DTI-based biomarkers (*see Note 10*).

10. We have previously used TRACULA for identifying white matter tracts and analyzing their DTI metrics. TRACULA stands for “TRActs Constrained by UnderLYing Anatomy” and can be downloaded from <https://surfer.nmr.mgh.harvard.edu/fswiki/Tracula>. TRACULA is a method for the automated reconstruction of major white matter tracts. This method uses prior knowledge of the tract anatomy of a set of training participants (healthy subjects). This prior knowledge informs the probability of the pathway anatomy in the participant under analysis [22] (*see Note 11*).
11. The prior anatomical information of manually labeled tracts from the set of training participants helps TRACULA give the likelihood of a particular tract passing through or next to the different cortical and subcortical regions in the current (to-be-analyzed) data (i.e., a probabilistic distribution; [23]) (*see Note 12*).
12. TRACULA software comes as part of FreeSurfer and uses FSL functions, which makes it an easy-to-use and robust option (*see Note 13*).
13. DTI metrics within tracts of interest can be examined (i) to compare between AD-relevant (e.g., patients with AD dementia, patients with prodromal AD, AD mutation carriers, etc.) and control groups or pre- and post-treatment groups and/or (ii) to correlate with AD-relevant neural, cognitive, or behavioral variables (e.g., functional network connectivity, memory scores) (*see Note 14*).
14. The choice of white matter tracts of interest or ROIs can follow from the statistical correlation and/or theoretically plausible relationship between DTI metrics in a wide set of tracts and an already established AD biomarker. For example, an association between MD of major white matter tracts and hippocampal volume—a traditional marker of AD pathology—has been shown for cingulum-angular, cingulum-cingulate gyrus, and corticospinal tract bundles bilaterally in patients with AD dementia [23]. DTI metrics of the chosen tracts could then be used to analyze a concurrent variable or intervention (*see Notes 14 and 15*).
15. Caution should be exercised with regard to the interpretation of DTI metrics within tracts. For example, a decreased FA could be explained by the relative relationship among the tensor eigenvalues: a shortening in the longest axis of the diffusion ellipsoid (λ_1 , parallel diffusivity), enlargement of the

shortest axes (λ_2 and λ_3 , perpendicular diffusivity), or both [2] (see **Notes 6** and **16**).

16. The relative increase or decrease in DTI metrics can be linked to the particular tracts and groups under study. For example, patients with AD dementia have been reported to show *lower* mode of anisotropy values in the corpus callosum and cingulum bundle than patients with MCI or healthy control participants and in the superior longitudinal fasciculus when contrasted with controls only [4]. However, *higher* mode values can, in turn, be found in patients with MCI versus healthy control participants in regions of crossing fibers of the centrum semiovale [4] (see **Note 17**).
17. In considering the choice of particular DTI metrics, diffusivity measures (i.e., MD, RD, and AxD) can be more sensitive than anisotropy measures (i.e., FA) for detecting group differences [9], for example, in patients with aMCI compared to healthy control participants [10] (see **Note 18**).

4 Notes

1. A data-quality check (e.g., visual or quantitative) is strongly advised at each stage of the pipeline to ensure data robustness [17]. FSL visualization or mathematical tools are suitable for this purpose.
2. A clear boundary of a tract may be difficult to delineate because the axons that form it can merge and exit the tract at any point. Thus, there is no gold standard to judge the validity of tractography [2].
3. Different from the corresponding (physical) nerve fibers, the so-called “streamlines” or “fiber tracks” obtained from tractography are only virtual entities without a physical volume. Thus, fiber orientations are only *indirectly* obtained from the averaged diffusion patterns of water molecules [18].
4. A notable advantage of tractography is that it can be used to infer structural connectivity and thus help provide a functional parcellation of the brain [19]. However, tractography ought not to be used to provide a quantitative estimate of connection strength in an anatomical or physiological sense [24].
5. DTI-derived metrics have low specificity regarding a biological interpretation, given that complex fiber crossings can also explain them [20]. Moreover, any microstructural feature (e.g., cell size, density, permeability, and orientation distribution) can affect common DTI-derived metrics such as FA or MD [19]. Interpretations invoking the degree of myelination, axon density, or “white matter integrity” must be supported by

data from other sources or have strong theoretical foundations [24]. Thus, care is advised in interpreting observed increases and decreases in those metrics in a particular group versus another or in relation to a specific cognitive/behavioral variable. Interpretations should invoke the specific DTI metric used rather than any of the unknown sources for the differences/changes in the DTI metric.

6. Observing each eigenvalue ($\lambda_1, \lambda_2, \lambda_3$) can yield more precise information regarding the cause of decrease in FA [2]. Going beyond FA by exploring the full tensor behavior can prove even more informative [9].
7. FA should not be linearly equated to connectivity because FA is derived from the water molecules *within a voxel* whereas connectivity typically has a more extensive length [24].
8. Long-range “structural connectivity” *cannot* be reliably quantified by current fiber-tracking approaches. A higher-order model (e.g., the uncertainty orientation distribution function or the fiber orientation distribution function), the use of anatomical constraints (e.g., biological tissue priors), and the assessment of the fidelity of the reconstructed tracts to the DWI data (e.g., with global tracking or filtering approaches) could help increase the reliability of current fiber-tracking approaches [18].
9. Results from meta-analyses based on ROI and whole-brain approaches may not converge. Therefore, individual studies can attempt to include both [8] or explicitly consider, in their design or interpretation, the potential for false negatives or false positives with either approach.
10. A caveat is that predetermined ROIs, based on templates, can be problematic due to potential registration issues across brains and the inherent possibility of restricting the search space [10].
11. TRACULA is a global tractography approach, that is, it reconstructs a known connection between end regions. Thus, diffusion measures (e.g., FA) can be compared as a function of position along the length of a pathway and not just by looking at its grand average [22].
12. To obtain individual cortical and subcortical regions, TRACULA requires the T1-weighted anatomical volume, which is then processed with FreeSurfer.
13. Using other software of preference and experience for the reader is also possible. Our main point is to recommend software and/or processing pipelines that focus on anatomically defined white matter tracts for identifying DTI biomarkers in AD.

14. One issue is the definition of tracts of interest. In a recent study, for example, we used the statistical association with hippocampal volume, a well-known AD biomarker, to identify white matter tracts that could mediate the relationship between adherence to the Mediterranean diet and verbal memory scores [25]. We did it separately for each hippocampus by means of multiple linear regression. We adjusted for other variables potentially relevant to that relationship (i.e., diagnosis group, head motion in diffusion images, age, sex, education, global cognitive status, site (multicenter study), white matter hypointensities in the anatomical T1 image, total gray matter volume, and the contralateral hippocampal volume).
15. We recently found FA of white matter tracts to be associated with hippocampal volume in a heterogeneous sample including patients with AD dementia, patients with aMCI, healthy older adults with and without subjective cognitive decline, and healthy relatives of patients with dementia [25], namely, the superior longitudinal fasciculus, fornix, corticospinal tract, and hippocampal cingulum.
16. Using the volume fractions identified by mixture model approaches (e.g., FSL's *bedpostx*) as a quantitative index has been proposed as an alternative to DTI scalar metrics such as FA [20].
17. A further exploration by looking for a concurrent, counterintuitive increase in FA values in the same region and by using quantitative crossing-fiber tractography can allow determining which is the “spared” fiber and which is the “affected” fiber [4].
18. However, FA is one of the DTI-derived metrics that account for a third of the total variability and, thus, can be prioritized if there is no a priori information about the particular index that is most sensitive to the investigated condition [21].

References

1. Basser PJ, Mattiello J, LeBihan D (1994) MR diffusion tensor spectroscopy and imaging. *Biophys J* 66:259–267
2. Tournier J-D, Mori S, Leemans A (2011) Diffusion tensor imaging and beyond. *Magn Reson Med* 65:1532–1556
3. Tae W-S, Ham B-J, Pyun S-B et al (2018) Current clinical applications of diffusion-tensor imaging in neurological disorders. *J Clin Neurol* 14:129–140
4. Douaud G, Jbabdi S, Behrens TEJ et al (2011) DTI measures in crossing-fibre areas: increased diffusion anisotropy reveals early white matter alteration in MCI and mild Alzheimer's disease. *NeuroImage* 55:880–890
5. Selnes P, Aarsland D, Bjørnerud A et al (2013) Diffusion tensor imaging surpasses cerebrospinal fluid as predictor of cognitive decline and medial temporal lobe atrophy in subjective cognitive impairment and mild cognitive impairment. *J Alzheimers Dis* 33:723–736
6. Mielke MM, Okonkwo OC, Oishi K et al (2012) Fornix integrity and hippocampal volume predict memory decline and progression to Alzheimer's disease. *Alzheimers Dement* 8:105–113

7. Araque Caballero MÁ, Suárez-Calvet M, Duering M et al (2018) White matter diffusion alterations precede symptom onset in autosomal dominant Alzheimer's disease. *Brain* 141: 3065–3080
8. Yu J, Lam CLM, Lee TMC (2017) White matter microstructural abnormalities in amnesic mild cognitive impairment: a meta-analysis of whole-brain and ROI-based studies. *Neurosci Biobehav Rev* 83:405–416
9. Acosta-Cabronero J, Williams GB, Pengas G et al (2010) Absolute diffusivities define the landscape of white matter degeneration in Alzheimer's disease. *Brain* 133:529–539
10. Nir TM, Jahanshad N, Villalon-Reina JE et al (2013) Effectiveness of regional DTI measures in distinguishing Alzheimer's disease, MCI, and normal aging. *NeuroImage Clin* 3:180–195
11. Wakana S, Jiang H, Nagae-Poetscher LM et al (2004) Fiber tract-based atlas of human white matter anatomy. *Radiology* 230:77–87
12. Wen Q, Mustafi SM, Li J et al (2019) White matter alterations in early-stage Alzheimer's disease: a tract-specific study. *Alzheimers Dement Diagn Assess Dis Monit* 11:576–587
13. Mayo CD, Mazerolle EL, Ritchie L et al (2017) Longitudinal changes in microstructural white matter metrics in Alzheimer's disease. *NeuroImage Clin* 13:330–338
14. O'Donnell LJ, Westin C-F (2011) An introduction to diffusion tensor image analysis. *Neurosurg Clin N Am* 22:185–196
15. Fischl B (2012) FreeSurfer. *NeuroImage* 62: 774–781
16. Jenkinson M, Beckmann CF, Behrens TEJ et al (2012) FSL. *NeuroImage* 62:782–790
17. Jones DK, Leemans A (2011) Diffusion tensor imaging. In: Modò M, Bulte JWM (eds) *Magnetic resonance neuroimaging: methods and protocols*. Humana Press, Totowa, NJ, pp 127–144
18. Jeurissen B, Descoteaux M, Mori S et al (2019) Diffusion MRI fiber tractography of the brain. *NMR Biomed* 32:e3785
19. Assaf Y, Johansen-Berg H, Thiebaut de Schotten M (2019) The role of diffusion MRI in neuroscience. *NMR Biomed* 32:e3762
20. Jeurissen B, Leemans A, Tournier J-D et al (2013) Investigating the prevalence of complex fiber configurations in white matter tissue with diffusion magnetic resonance imaging. *Hum Brain Mapp* 34:2747–2766
21. De Santis S, Drakesmith M, Bells S et al (2014) Why diffusion tensor MRI does well only some of the time: variance and covariance of white matter tissue microstructure attributes in the living human brain. *NeuroImage* 89:35–44
22. Yendiki A, Panneck P, Srinivasan P et al (2011) Automated probabilistic reconstruction of white-matter pathways in health and disease using an atlas of the underlying anatomy. *Front Neuroinform* 5:23
23. Lee S-H, Coutu J-P, Wilkens P et al (2015) Tract-based analysis of white matter degeneration in Alzheimer's disease. *Neuroscience* 301: 79–89
24. Jones DK, Knösche TR, Turner R (2013) White matter integrity, fiber count, and other fallacies: the do's and don'ts of diffusion MRI. *NeuroImage* 73:239–254
25. Ruiz-Rizzo AL, Finke K, Damoiseaux JS, et al (2023) Fornix fractional anisotropy mediates the association between Mediterranean diet adherence and memory four years later in older adults without dementia, <https://www.biorxiv.org/content/10.1101/2023.03.31.534758v1>



Magnetic Resonance Spectroscopy (MRS) in Alzheimer's Disease

Nasim Sheikh-Bahaei

Abstract

MRS is a noninvasive technique to measure different metabolites in the brain. Changes in the levels of certain metabolites can be used as surrogate markers for Alzheimer's disease. They can potentially be used for diagnosis, prediction of prognosis, or even assessing response to treatment.

There are different techniques for MRS acquisitions including STimulated Echo Acquisition Mode (STEAM) and Point Resolved Spectroscopy (PRESS). In terms of localization, single or multi-voxel methods can be used. Based on current data:

1. NAA, marker of neuronal integrity and viability, reduces in AD with longitudinal changes over the time as the disease progresses. There are data claiming that reduction of NAA is associated with tau accumulation, early neurodegenerative processes, and cognitive decline. Therefore, it can be used as a stage biomarker for AD to assess the severity of the disease. With advancement of disease modifying therapies, there is a potential role for NAA in the future to be used as a marker of response to treatment.
2. mI, marker of glial cell proliferation and activation, is associated with AB pathology and has early changes in the course of the disease. The NAA/mI ratio can be predictive of AD development with high specificity and can be utilized in the clinical setting to stratify cases for further evaluation with PET for potential treatments.
3. The changes in the level of other metabolites such as Chol, Glu, Gln, and GABA are controversial because of the lack of standardization of MRS techniques, current technical limitations, and possible region specific changes.
4. Ultrahigh field MRS and more advanced techniques can overcome many of these limitations and enable us to measure more metabolites with higher accuracy.
5. Standardization of MRS techniques, validation of metabolites' changes against PET using PET-guided technique, and longitudinal follow-ups to investigate the temporal changes of the metabolites in relation to other biomarkers and cognition will be crucial to confirm the utility of MRS as a potential noninvasive biomarker for AD.

Key words Alzheimer's disease (AD), Amyloid beta (AB), Ascorbate (Asc), Choline (Chol), Creatine (Cr), γ -aminobutyric acid (GABA), Glucose, Glutamate (Glu), Glutamate + Glutamine (Glx), Glutamine (Gln), Glutathione (GSH), Magnetic resonance spectroscopy (MRS), Myoinositol (mI), N-acetylaspartate (NAA), Tau, Ultrahigh field

1 Basics

Magnetic resonance spectroscopy studies rely on the field of nuclear magnetic resonance (NMR) that studies the interaction between radiofrequency energy and atoms [1, 2]. Spectroscopy depends on a crucial property of the atomic nuclei, the spin, which is the particle's intrinsic angular momentum. Principles of quantum mechanics dictate that this nuclear spin occupies discrete states that are related to its characteristic frequency. This characteristic frequency for the nuclei is called the Larmor frequency and depends on the gyromagnetic ratio and the magnetic field strength. The Larmor resonance frequency can become independent of the magnetic field strength when expressed in parts-per-million (ppm) relative to a reference compound (chemical shift) (Fig. 1). Energy transitions between spin states give rise to specific frequency spectra associated with the energy level difference between the spin states. Understanding energy transitions between systems with different Larmor frequencies and different coupling magnitudes provides a good basis for resolving spectral lines in NMR spectra [3].

In a typical magnetic resonance experiment, we do not observe just one nucleus but a very large number of them. Protons are present in most tissues in the form of water or lipids. In the human brain, there are about 6×10^{19} proton spins in a small cubic volume of about $1 \times 1 \times 1$ mm [3]. When protons lie in a constant magnetic field B_0 , the presence of angular momentum makes the magnetic moment precess around the magnetic field. At a larger scale, when a large set of nuclei are placed in the magnetic field, the bulk macroscopic magnetization grows over time until a point that slightly favors the parallel to B_0 spin orientation. This so-called longitudinal magnetization is never detected directly as its small contribution can be overwhelmed by other contributions caused by electron currents within atoms and molecules. Thankfully, magnetization can be tilted away by applying a radiofrequency (RF) pulse through a transmitter coil. The simplest case to deal with is when the transmitter frequency is the same as the Larmor frequency ("on-resonance"). An application of such a pulse tilts the magnetization away from its axis and causes a rotating field B_1 in a different plane. By altering the time for which the pulse has been applied, we can alter the angle through which the magnetization is rotated. In many experiments, the commonly used flip angles are 90° or 180° . For example, for an on-resonance pulse of 90° , the effective field lies along the x axis and so the magnetization precesses in the yz-plane [4].

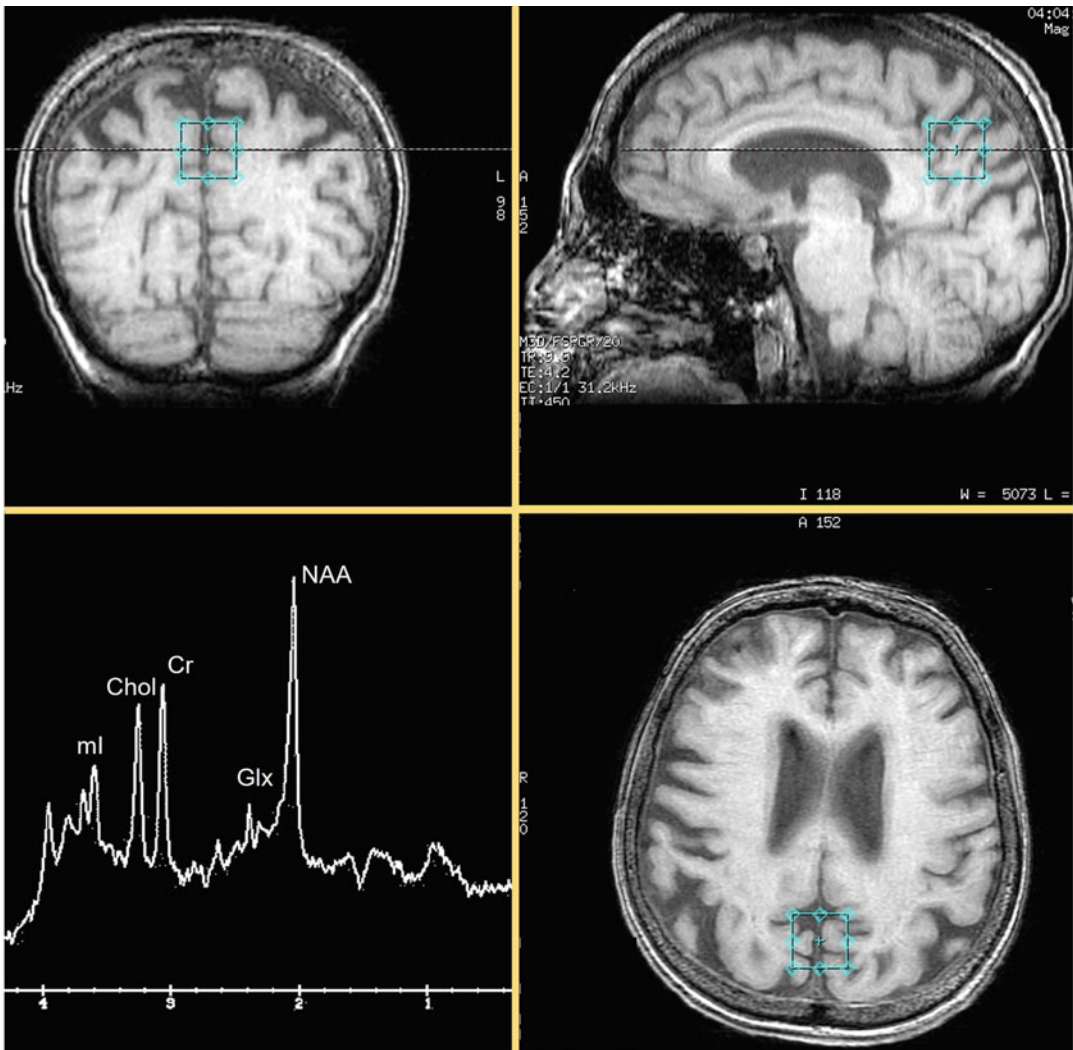


Fig. 1 Single voxel MR spectroscopy with region of interest selected on the posterior cingulate gyrus/precuneus region shown on three planes. The spectrum shows peaks of main metabolites: myoinositol (mI), choline (Chol), creatine (Cr), glutamate + glutamine (Glx), N-acetylaspartate (NAA)

2 Signal Detection

Suppose that we have managed, somehow, to tip the magnetization vector away from the z axis, such that it makes an angle β to that axis. After the RF power is switched off, the magnetic field starts to precess about the field. This rotating magnetization gives rise to the spectroscopy signal through electromagnetic induction into a nearby receiver coil. Note that the same RF coil used to transmit the RF pulse can be used to receive the signal. The magnetization tends to return to its equilibrium position (and size), a process

known as relaxation. This disappearance of macroscopic magnetization relates to loss of phase coherence due to random molecular processes (T_2) and loss of phase coherence due to magnetic field inhomogeneity (T_2^*). Thus, the signal undergoes what is called a free-induction decay (FID). Using mathematical tools, the magnetization components can be resolved as a function of time by solving the Bloch equations [3, 4].

One of the most basic and fundamental spectroscopy experiments is the spin echo experiment. A 90° RF pulse is applied followed by a 180° refocusing pulse. The 180° refocusing pulse rotates the transverse plane inverting the phase and separates the sequence into two equal periods, τ . The signal is acquired after the second delay τ , or 2τ from the beginning of the sequence (the time between the excitation pulse and the peak of the signal is called the echo time (TE)). In practical magnetic resonance spectroscopy experiments, we usually have several resonances in the spectrum that we want to detect, each of which has a different Larmor frequency. Hard excitation pulses can be used to excite several lines and Larmor frequencies with differential excitation of on-resonance and off-resonance spins. On the other hand, selective excitation pulses are pulses that excite a portion of the spectrum, while selective inversion pulses are pulses that invert the magnetization associated with just one resonance while leaving all the others in the spectrum unaffected. More advanced pulse shapes can be constructed by taking into consideration frequency selectivity, bandwidth (range of frequencies a pulse can capture), and RF power considerations and can be used accordingly depending on the experimental purpose [5]. Eventually, RF pulses make a precessing magnetization that can be detected to give a signal, which oscillates at a certain Larmor frequency, the free induction signal. This signal will eventually decay away due to the action of relaxation but can be captured and analyzed before magnetization returns back to equilibrium.

3 Methods

3.1 *Techniques of MRS Acquisition*

3.1.1 *Localization*

For most practical spectroscopy experiments, we are generally interested in a volume of interest where we need to localize certain metabolites. All localization methods rely on the selection of a spatially selective slice by the application of a frequency-selective RF pulse in the presence of a magnetic field gradient, a technique identical to slice selection in MRI. Following 1D slice selection, a second RF pulse is used to select a 2D column during a magnetic field gradient along an orthogonal spatial direction. Finally, a third RF pulse is used to reduce the 2D column to a 3D voxel along the remaining orthogonal gradient direction [6]. The combination of pulses while considering certain limitations in signal detection and

RF power limits have given rise to different acquisition methods. Here, we will briefly discuss the most representative (and perhaps most popular) techniques.

3.1.2 Acquisition Methods

STEAM

STimulated Echo Acquisition Mode (STEAM) is a localization method capable of complete 3D localization in a single acquisition [7, 8]. The signal is acquired during a sequence of three 90° RF pulses. Three FIDs, four spin echoes, and one stimulated echo (STE) are generated with the STE being the signal of interest generated after a delay following the last 90° pulse. By replacing the RF with slice selective pulses and refocusing gradients, one can localize STE within a volume of interest. STEAM is an appealing technique as it can make good spectroscopic acquisitions fast using short echo times.

PRESS

The Point Resolved Spectroscopy (PRESS) localization method [9, 10] is another popular spectroscopy acquisition method. In this sequence, one 90° RF excitation pulse and two 180° refocusing pulses are used. When the first 180° refocusing pulse is executed following the excitation pulse, a spin-echo is formed. The second 180° pulse refocuses this spin-echo during a delay period, and the final echo is formed at the PRESS at a certain echo time. Thus, PRESS looks at the spin-echo signals from the intersection of the three planes selected by the three pulses resulting in the desired volume locations. PRESS has a higher signal-to-noise ratio compared to STEAM. However, due to limits in the RF pulses that it uses, the PRESS refocusing 180° pulses have limited bandwidth that can cause increased chemical displacement (see next sections).

3.1.3 Adiabatic Localization

Fortunately, the adiabatic localization by adiabatic selective refocusing (LASER) and semi-LASER methods provide high bandwidth alternatives to PRESS for single voxel localization [11, 12]. The advantages of the LASER technique over STEAM and PRESS rely on the fact that they use adiabatic pulses while having higher bandwidth. With adiabatic pulses, spins having different resonant frequencies are inverted or manipulated at different times as the RF magnetic field can be written with a time-varying phase and time-varying amplitude [13]. This differs from canonical amplitude-modulated rectangular RF pulses where all spins are affected simultaneously. For adiabatic refocusing, there is a modulation of frequency and the amplitude of the RF pulse such that longitudinal magnetization is fully inverted at the end of the pulse, regardless of B1 inhomogeneity. This makes adiabatic pulses quite attractive as it makes them highly insensitive to B1 inhomogeneities. In addition, adiabatic pulses can offer large bandwidth RF

pulses via the use of large magnetic field gradients—something advantageous (as well shall see later) for minimizing chemical shift displacement. However, one limitation in using adiabatic pulses is the available maximum RF power that can be applied within acceptable limits.

In the LASER sequence, the entire sample is excited with a nonselective adiabatic excitation pulse after which three pairs of adiabatic inversion 180° pulses (AFP pulses) achieve 3D localization by selectively refocusing three orthogonal slices. The semi-LASER (sLASER) is similar; however, one pair of AFP pulses is replaced with a single slice-selective excitation pulse [14]. sLASER is a technique that is gaining high popularity for MRS due to its reliability and higher signal-to-noise ratio combined with the use of full adiabatic pulses.

3.2 Post Processing

Spectroscopy data can be degraded by multiple experimental artifacts. For example, line broadening, phase shifts due to RF errors, and signal amplitudes due to transmitter/receiver coil errors are only a few artifacts that can besmirch spectroscopy data. Thus, the experimenter needs to follow detailed post processing steps for data cleaning prior to metabolite quantification. These include (but not limited to) eddy current correction, motion correction, phase and frequency alignment, water removal, alignment, phasing, and zero filling. We will describe these shortly, but for a more comprehensive review, we refer the reader to the work by Near and colleagues [15]. Eddy currents are B_0 variations due to rapid gradient switching. These can be removed using an unsuppressed water spectrum, centered on the water resonance using identical gradient strengths and timings as in the water-suppressed dataset. Any time dependence in the frequency of the water signal will be observed as a nonlinearity in the phase of the FID signal. This nonlinearity can then be removed from the signal. Frequency and phase drifts are very common in spectroscopy as a result of B_0 instabilities and need to be corrected post acquisition. Several methods exist for retrospective correction of frequency and phase drifts depending on the acquisition method. For instance, certain methods use the residual water peak to estimate and correct the frequency and phase drift, while other methods use a reference spectrum for correction. Alignment of spectra is also important especially in subtraction data coming from edited sequence spectra. Methods for frequency and phase can also be used, but more dedicated techniques are required in certain cases. Additional post processing techniques are also mentioned. For example, due to its dominance in spectra, researchers might need to perform water removal from the spectra. There are several techniques with one prominent technique being HSVD, which is based on singular value decomposition of matrix representation of data [16]. Additional data cleaning can be done by using information from the “ideal” part of spectroscopy data and

applying it to the noisy part of data. Reference deconvolution is a powerful method that extracts the signal of a known reference material from the experimental data, compares it to the theoretically expected one, and constructs a correction mapping needed to convert the experimental data [17]. Zero filling is another technique that artificially lengthens the FID and increases digital resolution of the spectrum, without adding any noise. Phasing is also an important step in processing spectroscopy data. The phase of the complex spectral points depends on many factors including the receiver phase, RF pulse phase, voxel position, pulse sequence timing, and more. To correct for these phase abnormalities, techniques involve zero-order phasing (adding a linear phase) or first-order phasing (adding a linear phase shift as a function of frequency). Apodization is another process of denoising the signal and depends on the premise that the most interesting signal is at the beginning of the FID. Thus, the signal in the time domain is differentially weighted with early time points being assigned more important weights and later time points assigned less important weights. Finally, dimensionality reductions on the obtained data are necessary as different data samples might come from different runs, receiver channels, and more. For instance, one can combine MRS data across channels for example, using coil-based combination technique-based appropriate complex weights (phase and amplitude). Also, multiple runs can be averaged together to increase signal-to-noise ratio; however, more advanced techniques can also be applied that take into consideration the signal-to-noise ratio of each run (e.g., weighted average techniques).

3.3 Quantification

The final goal for the MRS post processing techniques is to quantify metabolite concentration. This is done by a process called fitting. Most techniques use a so-called linear combination model fitting, where each metabolite's contribution to the overall spectrum is modeled as a single response function called a "basis spectrum." This basis spectrum can be obtained either by using phantom data or simulations. For the latter, basis data can be simulated using the acquired parameters as the obtained data thus rendering this data highly accurate. For example, software such as FID-A [18] or SPINEVOLUTION [19] have been successfully used by researchers to produce basis sets based on the specification of the acquisition. After a basis set has been obtained, a fitting method is employed between the data and the basis. A constrained nonlinear least-squares analysis can be used to fit a linear combination of the basis spectra to the acquired MR spectrum by adjusting their individual amplitudes and frequencies, for example, as used in LCMo-del [20]. The goodness of fit can then be evaluated using Cramér-Rao bounds and confidence intervals.

3.4 Main Limitations

3.4.1 Chemical Shift Displacement

The application of a magnetic field gradient makes the spin Larmor frequency linearly dependent on the spatial position. This can result in a situation where, for example, a slice selective RF pulse can successfully select a slice with on resonance spins, but when off-resonance spins are present, the RF selects a slice with a certain offset. The selection of different spatial positions for spins with different Larmor frequencies is referred to as the chemical shift displacement artifact [6]. This is an important artifact to consider as it increases in the higher fields. This artifact is apparent in systems like N-acetyl aspartate (NAA), which has the most prominent signals among all other metabolites both in the amide and in the methyl parts of the spectrum. Optimized detection of the complete NAA spin system requires covering of the entire spectral range of all the metabolites in vivo and thus is more prone to CSDA. In general, higher bandwidth RF pulses (both refocusing and excitation) are needed to eliminate CSDA for the complete NAA spin system explaining the surge in adiabatic localization methods such as localization by (LASER) and semi-LASER. However, the use of sLASER at 3 Tesla for the amide region is also not optimal unless the excitation pulse has higher bandwidth. Thus, a design of new excitation pulses is required as explained later.

3.4.2 Metabolite Concentration and Macromolecules

One intrinsic limitation of spectroscopy data is that certain metabolites have low concentration and suffer from spectral overlap. For example, detection of γ -aminobutyric acid (GABA) is important due to its role in neurotransmission and its dysregulation in neurodegenerative diseases. However, due to its lower concentration and complicated peak pattern, its signal is difficult to reliably separate from more abundant metabolites such as creatine. This requires the usage of different pulses and higher fields (e.g., 7 Tesla) where spectra separation is more prominent. We will visit an example of this in the “Advancements” section.

Macromolecules (MMs) are broad signals upfield of tissue water (~0.5 to 4.5 ppm), can also affect the metabolite detection, and heavily depend on B_0 and TE. Thus, separation of broad MM signals from low-molecular-weight metabolites enables accurate determination of metabolite concentrations and is of primary interest in many studies especially in higher fields. A consensus from experts have recommended techniques for removing MMs using explicit modeling. For example, one can use a smooth approximation of spline or another type of mathematical fitting to remove these MMs from the signal although more research is required [21].

3.5 Advancements

3.5.1 Higher Magnetic Fields

Higher magnetic fields (7 Tesla and above) permit more accurate quantification of metabolites due to the increased spectral dispersion they provide. This provides an opportunity to researchers to utilize higher fields to detect “difficult” metabolites such as GABA

that would otherwise be undetectable in lower fields. New techniques have emerged that utilize ultrashort TE without editing. For example, certain techniques have used the stimulated echo acquisition signal from the STEAM sequence combined with ultrashort TE (≤ 8 ms) to detect GABA, thus avoiding SNR loss because of T2 relaxation [22]. Similar techniques have been implemented for detecting glucose [23] with fruitful applications in metabolic imaging. However, using higher fields comes with specific drawbacks that can heavily impact the signal (for example field inhomogeneities are exacerbated in higher fields). This requires careful tailoring of pulses and acquisition techniques that can mitigate these effects. One example that was mentioned before is the problem of CSDA for NAA detection that is apparent in higher fields. To this end, two novel selective excitation pulses have been recently developed that minimize CSDA [24]. The presented RF pulses improve slice selective excitation at higher magnetic fields not only for the amide region but also for the resonances within 1–4 ppm.

3.6 Additional Spectroscopy Techniques

1. Most discussed techniques talked referred to single voxel spectroscopy where metabolites are localized within a limited volume of interest. Magnetic resonance spectroscopic imaging (MRSI) is a powerful technique that provides localization of each spectrum over multiples regions the brain. Traditional MRSI uses phase encoding, in addition to volume pre-selection (e.g., as it comes from PRESS, STEAM, sLASER) to provide localization of each spectrum like classical MRI sequences. MRSI is a powerful technique for localizing spectra across the brain; however, the acquisition technique results in very long measurement times, since only a single-phase encoding step can be used. Ultrahigh field MRSI is also promising for obtaining whole-brain spectra. However, typical ultrahigh field effects (B0, B1 effects, presence of macromolecules/MMs) are exacerbated for MRSI, and thus, such methods require additional research.
2. Diffusion-weighted MRS (dMRS) is another spectroscopy method gaining traction. dMRS is based on sensitization of MRS to diffusion in a comparable manner to diffusion MRI. dMRS relies on previous MRS acquisition techniques (STEAM, PRESS, LASER) in combination with gradient pulses for diffusion sensitization [25, 26]. However, data acquisition in dMRS is long due to the diffusion aspect and prone to errors that come from phase and amplitude fluctuations. Eventually, dMRS can measure diffusion-weighted spectra acquired at different b-values. Because the diffusion properties of neuronal (e.g., NAA) and glial (e.g., choline) metabolites reflect the specific microstructural environment of their host cell type, dMRS has the potential to probe cell-specific compartmentalization [27].

3.7 *New Processing Techniques*

Besides acquisition techniques, exciting advancements are also related to processing the data and extracting meaningful information from noisy spectroscopy signals. One fruitful example where exciting new advancements are being made is fitting signals to basis sets. For instance, Borbath and colleagues provide a different approach where fitting is done in iterative fashion. In iteration 0, an optimization is done using only singlets in well-phased spectra, followed by additional iterations where fitting is done in the remaining metabolites in conjunction with spline modeling (B-spline) for baseline estimation [28]. Other advancements pertain to techniques related to metabolite quantification. For example, given its power in pattern recognition, deep learning has a potential to disambiguate spectral peaks and quantify metabolites in spectroscopy data. For example, researchers have successfully used convolutional neural networks on spectroscopy data for metabolite quantification. To train the model, the authors created a large set of synthetic data. This data was simulated to represent ideal metabolite spectra obtain using certain acquisition parameters (thus providing the ground truth for the model to learn) and later injected with various “noise” features [29]. The network was then tasked to learn to extract metabolites from this noisy data given the ground truth labels that were provided using the simulations. We expect more research in this area especially in metabolites that are to separate from baseline and MMs. In general, there are exciting new advancements regarding standardization of methods and sequences as well as discussion for integration of new features in acquisition or processing. The MRS community has started to curate a collection of open-access resources for magnetic resonance spectroscopy, including data, software code, and educational materials [30]. Consensus papers are also paving the way for providing guidelines for standardized acquisition [31, 32] and processing [15] methods. These initiatives provide an inclusive framework with the goal of standardization, reproducibility, and open access, thus paving the way for easier deployment of spectroscopy methods in research and clinical protocols.

4 Results

4.1 *Common Metabolites in MRS and Their Roles in Alzheimer’s Disease*

4.1.1 *N-acetylaspartate (NAA)*

NAA is a specific metabolite in the nervous system and synthesized by aspartic acid and acetyl-CoA in neuronal mitochondria, found predominantly in the neuronal cell body, axons, and dendrites but not the glial cells. It is often used as a marker of neuronal integrity, viability, and function in MRS studies [33–38]. It resonates at 2.01 ppm (Fig. 1), with a normal concentration of around 10–12 mmol/L [39, 40]. Typically, NAA concentrations are higher in gray matter regions due to densely packed neurons when

compared to white matter regions and decrease in both of these regions with age more consistently than do other metabolites such as choline, myo-inositol, and glutamate. Age-related decline may thus reflect decreases in neuronal density or function [41].

NAA and AD

NAA and the ratio of NAA over creatine (NAA/Cr) levels have been found to be reduced in various brain regions of patients with Alzheimer's disease (AD) (Fig. 2) compared to in healthy controls (HC) [42–44]. These regions include the hippocampus [42, 45–47], medial temporal lobe [45, 48], and posterior cingulate gyrus in particular [49–53]. These findings are consistent with known regions to be affected in AD and thus thought to reflect neuronal loss and dysfunction in these regions. Specifically, NAA/Cr values in the hippocampus have been reported as having the highest sensitivity and specificity for differentiating patients with AD from HC [50]. A study using serial MRS confirmed longitudinal reduction of NAA in the posterior cingulate gyrus of AD cases [43]. It has been claimed that the combination of NAA and [Cr + PCr] has a 74% accuracy in distinguishing AD from HC [42]. These changes in NAA can thus be used to detect early dementia due to high sensitivity to neuronal loss and damage prior to changes seen on structural MRI [54, 55]. Findings about NAA/Cr in other regions such as the medial temporal lobe (MTL) are more inconclusive, with some prior studies finding the ratio to be increased when compared to HC [56], and others finding markedly decreased levels in AD patients [48].

NAA and MCI

Additionally, some studies showed that NAA levels were significantly reduced in the hippocampus and posterior cingulate cortex of patients with mild cognitive impairment (MCI), before the onset of AD [57, 58]. These results are not as consistent as the known reduction of NAA in the later stages of AD. Some studies claim a more significant difference in the level of NAA in MCI cases compared to HC [43, 59, 60], while others found a difference between MCI and AD cases but not between MCI and HC [42]. In addition, there are reports claiming a more moderate reduction in the level of NAA at MCI stage not statistically significant from either AD patients [42] or controls [44].

A potential explanation for conflicting results in the literature could be the definition of MCI or the early versus late stages of MCI cases recruited in different studies. Some studies have shown that reduction of NAA in MCI cases may predict future conversion to AD [36, 39]. The converted MCI often had lower levels of NAA at baseline, followed by continued reductions in NAA in the posteromedial parietal cortex compared with patients with MCI who did not convert. The variation in the level of NAA changes in MCI might also be due to the length of follow-up, as some early MCI cases might not be followed for a long enough time [43]. Thus,

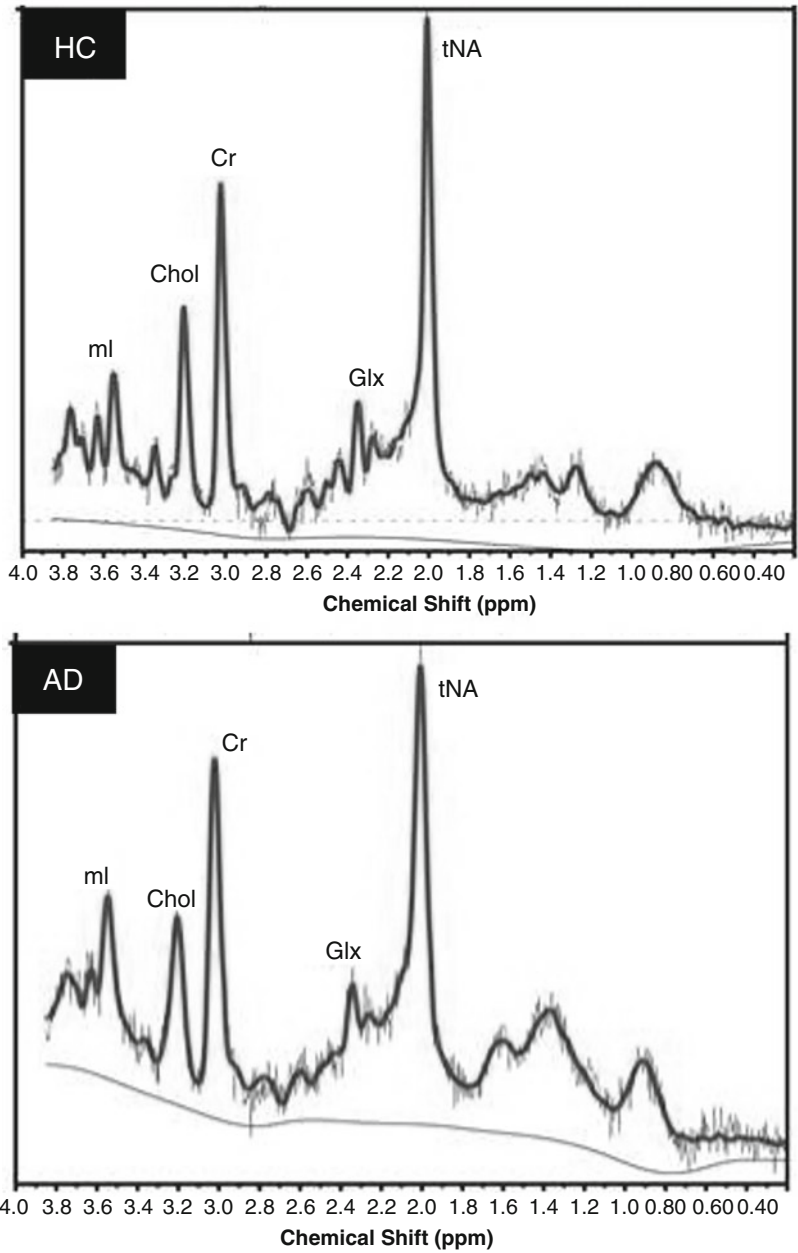


Fig. 2 Two MR spectra comparing a healthy control (top) with AD (bottom) demonstrate lower NAA and higher ml in the AD case. ml myo-inositol, Chol choline, Cr creatine, Glx glutamate + glutamine, tNA total N-acetyl group

given inconsistent observations of reduced NAA levels in MCI, diagnostic accuracy using this metabolite at early stages is somewhat unclear. More studies using homogeneous MCI cases with biomarker diagnosis are required to investigate the changes of NAA at the earliest stages of disease.

However, longitudinal reduction of NAA in the posterior cingulate gyrus has been observed in AD patients and has also been shown as correlating with cognitive deterioration. This allows for longitudinal reduction of NAA/Cr to be used as a marker of disease progression. Since these changes precede the structural MRI changes, they can be used as an early marker of conversion from MCI to AD, and more importantly, since it is a marker of neuronal density and activity, serial measurement of NAA can be used in the monitoring of treatment response [4, 61].

NAA and Other AD Pathology Biomarkers

NAA has a variety of correlations with other biomarkers when studied with patients with Alzheimer's disease. NAA reduction was also associated with memory impairment, with metabolic changes also having been shown to be correlated with degree of cognitive decline [62] and severity of both neurofibrillary tangle and amyloid plaque pathology (AB) [63]. Tau deposition in specifically the PCC and the medial temporal lobe was associated with decreased NAA levels, suggestive of neuronal and synaptic dysfunction in regions of tau accumulation [64]. Progressive accumulation of filamentous tau and subsequent neuronal death are central to the pathogenesis Alzheimer disease (AD), and this process begins years before the onset of clinical symptoms [65]. The presence of the APOE $\epsilon 4$ allele, a known AD risk factor, was associated with decreased levels of NAA in the posterior cingulate cortex. Decreased levels of NAA are also significantly associated with increased levels of t-tau and p-tau in the CSF in AD patients [66].

Furthermore, decreased levels of NAA are also significantly associated with decreased levels of CSF AB in AD patients [46, 66]. In cognitively normal older adults, however, no significant correlation was identified between global cortical AB and the level of NAA/Cr [67]. In autopsy samples, the NAA/Cr was associated with neurotic AB plaques [63] and also with reduction of the synaptic vesicle immunoreactivity and accumulation of early neuritic and pre-tangle tau in the posterior cingulate gyrus but not with the extracellular neurofibrillary tangle of tau. Based on these findings, it was suggested that NAA/Cr is a marker of early tau-mediated dynamic processes in AD [68].

Additionally, there is a significant correlation between reduced NAA levels and reduced glucose metabolism as indicated through FDG studies, indicating that these two markers are closely linked in the progression of AD [69]. In the first PET-guided MRS studies, Sheikh-Bahaei et al. found the level NAA/Cr was reduced not only in areas of amyloid deposition but also in the regions of neurodegeneration identified by hypometabolism on FDG PET. More importantly, they showed that there is a stepwise reduction in the level NAA from HC to MCI to AD. Based on their results, they suggested that NAA can be used a "disease stage biomarker" to improve the accuracy of diagnosis in the clinical setting [70].

4.1.2 *Myo-inositol (mI)*

mI is a precursor of both phosphatidylinositol (the major inositol-containing phospholipid) and phosphatidylinositol 4,5-bisphosphate (a key molecule in cellular signal transduction), which plays a role in the second messenger cycle and is generally regarded as a glial metabolite, found primarily in astrocytes [33, 57, 71]. It also plays a role in osmoregulation [71]. Elevation of the mI peak seen on MRS is related to glial proliferation and astrocytic and microglial activation or inflammation [72, 73]. The mI peak resonates at 3.5 ppm on the MRS spectrum (Fig. 1).

mI Changes and AD

Elevations in mI can be seen in early stages of AD (Fig. 2) and may be indicators of ongoing gliosis [55, 58, 74]. mI elevations usually precede the reductions in NAA that are more typically associated with later stages of AD [49, 58, 75]. Given the association of mI with glial activity in comparison to the correlation of NAA with cognitive decline and neural dysfunction, the timeframe of these metabolite changes indicates a possibility of glial proliferation occurring prior to neural dysfunction in the pathophysiology of AD [58, 74].

Prior studies showed that mI levels in MCI were increased in the right hippocampus relative to HC and additionally increased in patients with AD relative to both the MCI and control patients. mI levels slightly increased over time in the PCC for patients with AD but, interestingly, not in the control [76]. Another study showed AD patients had higher mI levels than amnesic MCI patients [57]. However, overall, in contrast to the longitudinal changes seen in NAA, mI increases do not exhibit continued increases in dementia stage, reaching a plateau fairly early in the progression of AD, which can indicate that mI elevation may also occur as an early change in AD [67].

mI and Other AD Pathology Biomarkers

The higher baseline mI levels in the PCC are associated with greater amyloid deposition and faster cognitive decline independent of age, sex, and APOE genotype. Increased levels of mI over time were also associated with increased amyloid deposition and cognitive decline [77]. In a population-based sample of cognitively normal individuals, the level of mI/Cr in the posterior cingulate gyrus (PCG) correlated with total cortical 11C-PiB uptake [67]. PET-guided MRS also confirmed association between with an increase in mI levels and degree of cortical amyloid deposition on PET [70]. Moreover, this study found mI/Cr increases in MCI compared to HC, with no significant difference between MCI and AD [70]. Based on multiple studies demonstrating the association between mI and AB particularly in autopsy and pathology studies demonstrating glial activation around the amyloid plaques

[62, 68], mI could be potentially considered as a surrogate marker for AB and used as a disease state marker [70].

Despite the strong association between mI and AB, there are controversial results regarding the association between mI and tau. No significant association was identified between mI concentration and in vivo total tau deposition in cognitively unimpaired older adults [64]. Also, others reported elevated mI levels in microtubule-associated protein tau (MAPT) mutation carriers, who may be in a more advanced state of tau pathology [78]. Moreover, mI/Cr increase and NAA/mI decrease in the posterior cingulate were associated with increased t-tau in the CSF [46]. In a recent systemic review on CSF AB, tau, and MRS metabolites, authors claimed that there is moderate evidence that mI and CSF tau are positively correlated [66]. Sheikh-Bahaei et al., using PET-guided MRS, did not find any association between mI/Cr and FDG PET [70].

Combination of NAA and mI in AD

Using a combination of NAA reduction and mI increase in patients with AD when compared to those with MCI and HC significantly improves the specificity and the accuracy of clinical diagnosis. Measurements of these two metabolites allow for comprehensive information about AD pathology, with the NAA/mI ratio having the strongest association with the underlying AD pathological changes [40, 63]. Prior studies have shown that NAA/mI ratio was significantly decreased in elderly MCI patients compared to the healthy elderly group. The level of NAA/mI in the PCC was significantly lower in individuals who later developed AD compared to those who remained cognitively normal. A follow-up study seven years later showed that individuals with lower NAA/mI ratio at baseline were more likely to have developed AD or progressed to a more severe stage of MCI, indicating NAA/mI ratio in PCC may be a potential risk marker for preclinical AD [79]. Thus, the NAA/mI ratio can be predictive of AD development with high specificity and can be utilized in the clinical setting as a prognostic biomarker.

4.1.3 Choline (Chol)

Chol is a precursor of acetylcholine (ACh) and a cell membrane component, which is commonly examined in MRS. It resonates at 3.2 ppm chemical shift (Fig. 1). Chol signal is associated with metabolism of cell membrane phosphatidylcholine, and thus, elevation in Chol signal reflects breakdown of cholinergic neurons cell membranes secondary to increased turnover, neural damage, and degeneration [33]. Alternatively, raised Chol peak could be due to a compensatory mechanism to overcome the deficit in the acetylcholine (ACh) production in AD by increasing in the catabolism of the phosphatidylcholine membrane to provide free Chol [80, 81]. Therefore, the level of Chol can serve as a proxy for

ACh activity, which cannot be measured *in vivo*. Chol is found in higher concentrations in gray matter compared to white matter [82]. The cortical ACh is crucial for cognitive processing, and its deficit is heavily involved with early AD and its cognitive symptoms [83, 84].

Chol Changes and AD

Elevation of Chol or Chol/Ct ratio in AD has been reported in many prior studies; however, no longitudinal changes were identified [40, 50, 58, 85]. Increased Chol levels have been observed in some studies in both hippocampus and PCC at various stages of the disease including MCI and AD [84, 86]. Many studies, on the other hand, did not find any differences between Chol/Cr level between AD patients and HC [47, 68, 87–89]. In a study investigating the level of Chol in MCI cases with longitudinal follow-ups, they found raised Chol/Cr in all MCI cases compared to HC with no difference between stable and converter MCI at the baseline. However, interestingly, the stable MCI cases showed more reduction in the level of Chol/Cr compared with converter MCI and control. It was hypothesized by authors that there is a compensatory mechanism in stable MCI cases with upregulation of the choline transferase to keep their cognitive function [43]. In another study, investigating changes in cholinergic neurotransmitter systems, specifically choline acetyltransferase (ChAT) activity, elderly individuals with MCI had higher levels of ChAT activity in the hippocampus and frontal cortex, which are regions implicated in learning and memory. These findings suggest a compensatory mechanism for the early stages of cognitive decline in MCI [90].

There are several explanations for conflicting results of Chol in AD. The variation in the region of interest can be a potential reason for the seemingly contradictory results between different studies [86]. The majority of studies not finding any difference in Chol/Cr levels between AD patients and HC measured it in the temporal lobe or hippocampi while studies finding increased Chol levels were mostly focused on the posterior cingulate gyrus. An anterior-posterior decline in the level of Cho in CN individuals has been reported previously [82, 91]. Autopsy data have also revealed the same pattern of change from anterior to posterior in the brain [92].

Chol and Other AD Pathology Biomarkers

The relationships between Chol and the level AB and tau have not been fully investigated. There are *in vitro* and animal studies claiming that impairment in cholinergic activity increases AB in mice [93] or the effect of cholinergic agonist on processing of AB precursor protein *in vitro* [94]. On the other hand, AB has an inhibitory effect on the cholinergic activity *in vitro* and in rat

models [95–97]. The associations between level Chol or Chol/Cr with AB PET in human are controversial with some studies showed increased Chol level in AB+ cases in HC and MCI [67, 76], while others found opposite results [98]. Based on reviewing different studies, it can be concluded that the association between Chol and AB might be stage and regional dependent, which needs further investigation as cholinergic changes are critical components of the AD and can potentially help future therapeutic targets.

4.1.4 Glutamate + Glutamine (Glx)

Glutamate (Glu) is the principal excitatory neurotransmitter in the central nervous system, and it is involved in glutamatergic neurotransmission through the Glu-glutamine (Glu-Gln) cycle between neurons and surrounding astrocytes [99, 100]. Glutamine (Gln) results from Glu conversion in presynaptic neurons [101]. These two metabolites are difficult to separate using low-field MRS and are thus often measured as a combined peak [86]. This combined peak resonates between 2.2 and 2.4 ppm on MRS (Fig. 1).

Glx Changes in AD

In some studies, Glx levels were found to be significantly decreased in individuals with AD, specifically in the hippocampus, anterior and posterior cingulate gyrus, and medial temporal lobe [102–104]. It has also been found to be moderately decreased in patients with MCI [103, 105]. However, other studies were unable to detect a significant difference in Glx levels between patients with AD and healthy controls [51]. Aforementioned limitations in current MRS techniques with combined peaks of Glu + Gln as well as difficulty even in separating Glx peak from other metabolites may explain these contradictory findings [86].

Glx levels were found to be more decreased in gray matter than in white matter [102], with disruption of gray matter microstructure associated with changes in Glx metabolism, thus making Glx concentration a potential biomarker for early detection of neurodegeneration [106]. Combining the level of Glx to NAA and mI as potential biomarkers in diagnosing AD greatly increased sensitivity of diagnosis [107].

Despite many *in vitro* and animal studies, demonstrating the critical role of Glu and Gln in synaptic homeostasis and cognitive function [108, 109], there is lack of *in vivo* data in human. Utilizing ultrahigh field MRS might overcome some of the current limitation and improve our understanding about the changed of Glx in AD. A recent study has shown that the level of Glx/Chol and Glu/Chol increased significantly in AD cases after treatment with acetylcholine esterase inhibitor. Therefore, accurate Glx levels might be suitable biomarkers for assessing the effect of treatment [110].

Glx and Other AD Pathology Biomarkers

There are some in vitro reports suggesting that AB might have some interaction with glutamatergic cycle through glutamate transport or glutamine synthetase [101]. However, an AB PET study did not show any relationship between the two [111]. It has been shown that Tau deposition in the PCC and MTL are associated with lower glutamate concentrations [64].

The association between Glx and FDG is reported in AD [112] and many conditions such as epilepsy [113], tumor [114], or behavior variant of frontotemporal dementia (bvFTD) [115]. Based on these results, Glx level can be used as a surrogate marker of neurodegeneration (tau pathology or hypometabolism) if measured accurately particularly in the future with the ultrahigh field MRS.

4.2 Novel MRS Metabolites and Their Roles in AD

Ultrahigh field (UHF) MRI can potentially change the role of MRS in AD diagnosis. It can overcome many of the current limitations for detection and quantification of the metabolites. The main advantages of UHF MRS are the significantly higher signal-to-noise ratio and capability of reducing the voxel size, in addition to the ability to detect many more metabolites peaks in the spectrum (up to 14–15) (Fig. 3). This will help to separate the Glu/Gln peaks and measure γ -aminobutyric acid (GABA) to investigate the excitatory and inhibitory neurotransmitters at various stages of AD. It will also help to measure some of the antioxidant markers in the brain such as ascorbate or glutathione. Many preclinical and in vitro studies have shown the role of neurotransmitters and antioxidant in AD pathologies, and measuring these changes noninvasively can revolutionize the future diagnosis of AD and play a critical role in assessing the response to treatment.

4.2.1 GABA

GABA is the most important inhibitory neurotransmitter in the mammalian brain. The GABA molecule contains three CH₂ groups, which resonate at 1.9, 2.3, and 3.0 ppm (Fig. 3). The role of GABA in many neurodegenerative disorders has been reported. Recent studies using UHF MRS have shown high reliability and reproducibility in measuring GABA in MRS [116].

There are some reports regarding changes in the level GABA in aging and the balance of excitatory-inhibitory system in AD and amnesic MCI [103, 111, 117]. And others have shown that GABA measured on MRS might largely represent pools of GABA that are linked to tonic rather than phasic inhibition. Therefore, it may contribute to the inhibitory tone of a brain area rather than GABAergic synaptic transmission [118]. To explore the role of GABA measured on MRS in neurodegenerative process, further studies using UHF MRS are needed with better characterization of cases and more standard techniques.

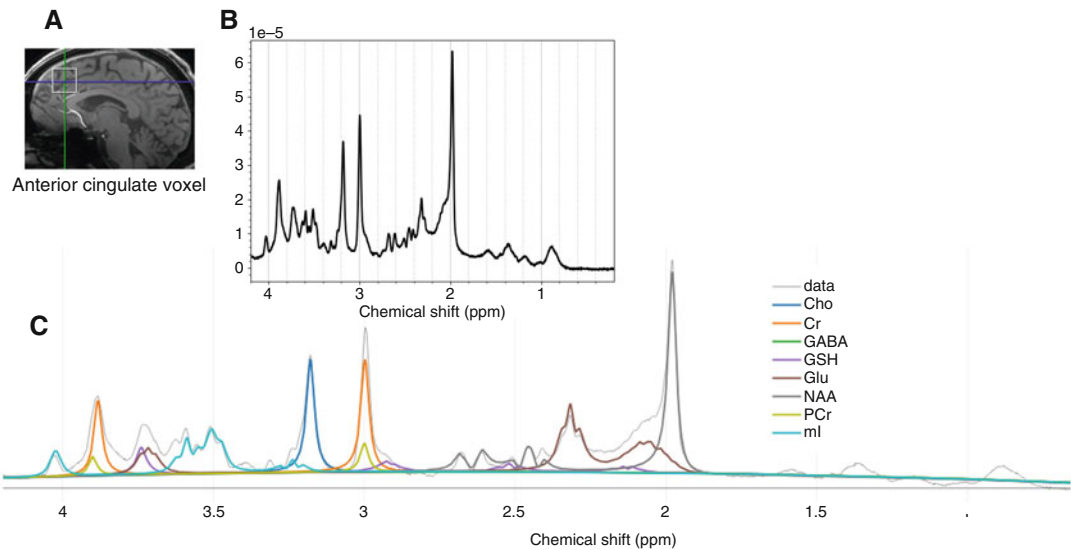


Fig. 3 Single voxel spectroscopy example at a 7 Tesla scanner. **(a)** Placement of voxel in the anterior cingulate. **(b)** Example of spectrum obtained after preprocessing. **(c)** Different metabolites can be quantified after fitting the spectrum to a basis. Cho: choline, Cr: creatine, GABA: γ -aminobutyric acid, GSH: glutathione, Glu: glutamate, ml: myoinositol, NAA: N-acetylaspartate, PCr: phosphocreatine

4.2.2 Glutathione

Glutathione (c-L-glutamyl-L-cysteinylglycine; GSH) is a major antioxidant in the human body particularly in major organs like brain, liver, and kidney. GSH is essential for detoxification of reactive oxygen species in brain cells. GSH also functions as a neuro-modulator/neurotransmitter mediating neuronal response via NMDA (N-Methyl-D-Aspartate) receptors and plays a role in the regulation of apoptosis, cell proliferation, and neuronal differentiation [119]. Oxidative stress plays a key role in different neurodegenerative disorders, in particular to AD. Detection of GSH at clinical field strengths of 1.5 or 3 T has been difficult due to its low concentration (1–5 mM) and overlap of its peak with N-acetylaspartate (NAA), creatine, glutamate, lipids, and macromolecular compounds. 7 T MRS can overcome these limitations. GSH resonances at different peaks including 2.3 and 4.7 ppm (Fig. 3).

There are some evidences showing the reduction in the level of GSH in AD compared to HC [119, 120]. However, data on MCI are slightly controversial as some studies showed reduction [120], while others found increase in the level of GSH [121]. Authors claimed that increased GSH in early MCI cases might be compensatory or neuroprotective response.

Further studies are required to delineate the role and changes of GSH in MCI and AD using UHF MRS. If future studies confirm the changes of GSH in areas of amyloid deposition with increase post anti-amyloid treatment, then measuring these metabolites can play a critical role in measuring treatment effects in the future.

4.2.3 Ascorbate

Ascorbate (Asc) is another potential antioxidant metabolites, which can be measured using UHF/7 T MRS. Prior studies have shown that Asc level is lower in the older adults [122]. Growing in vivo evidence supports the role of Asc linked to Alzheimer's disease (AD) pathogenesis, although evidence in humans yielded equivocal results. As an antioxidant, Asc can potentially protect brain through several mechanisms in addition to scavenging free radicals directly. Animal studies have shown that Asc modulates amyloid accumulation via a mechanism associated with the oxidative stress pathway and protects the endothelia from reactive oxygen species [123]. Additionally, Asc moderates glia-mediated inflammation, which is activated by oxidative stress [124].

Limited in vivo data on human are available regarding the changes in the level of Asc in AD and its potential role. One study showed that AD cases had higher level of Asc in their PCC compared to HC [125]. Since there are clinical trials and some data suggesting of potential protective role of vitamin C (ascorbate), then further investigation to detect the changes in the level of Asc using UHF MRS might be helpful for future treatment planning.

4.2.4 Glucose

Glucose metabolism impairment is one of the main hallmarks of AD and other neurodegenerative disorders. Currently, FDG-PET is the standard in vivo technique for assessing the brain hypometabolism. In the recent year with UHF MRS, there is a new opportunity to measure the amount of glucose in brain using noninvasive method [126]. Measuring glucose on MRS can be challenging particularly on lower magnetic field as the upfield glucose spectrum overlaps with other metabolites and the downfield glucose signal at 5.22 ppm is very close to the water resonance at 4.65 ppm, requiring good water suppression. Studies utilizing 7 T MRS have measured glucose peak as a possible biomarker for glucose quantification [127]. Further studies comparing MRS with FDG PET will be helpful to determine the correlation between the measures of glucose on MRS and PET and to validate it as potential biomarkers for future diagnostic or therapeutic studies.

References

1. Bloch F (1964) The principle of nuclear induction. In: Nobel lecturers in physics 1942–1962. Elsevier, New York, pp 203–216
2. Purcell EM, Torrey HC, Pound RV (1946) Resonance absorption by nuclear magnetic moments in a solid. *Phys Rev* 69:37–38. <https://doi.org/10.1103/PhysRev.69.37>
3. Graaf D (2019) Basic principles. In: *In Vivo NMR Spectroscopy*. John Wiley & Sons, Ltd, pp 1–42
4. Keeler J (2004) Understanding NMR spectroscopy. Available via [http://www-keelerchcamacuk/lectures/](http://www.keelerchcamacuk/lectures/). Accessed 15 June 2023
5. Graaf D (2019) Radiofrequency pulses. In: *In Vivo NMR Spectroscopy*. John Wiley & Sons, Ltd, pp 253–291
6. Graaf D (2019) Single volume localization and water suppression. In: *In Vivo NMR*

- Spectroscopy. John Wiley & Sons, Ltd, pp 293–334
7. Moonen CT, von Kienlin M, van Zijl PC, Cohen J, Gillen J, Daly P, Wolf G (1989) Comparison of single-shot localization methods (STEAM and PRESS) for in vivo proton NMR spectroscopy. *NMR Biomed* 2(5–6): 201–208. <https://doi.org/10.1002/nbm.1940020506>
 8. van Zijl PC, Moonen CT, Alger JR, Cohen JS, Chesnick SA (1989) High field localized proton spectroscopy in small volumes: greatly improved localization and shimming using shielded strong gradients. *Magn Reson Med* 10(2):256–265. <https://doi.org/10.1002/mrm.1910100210>
 9. Bottomley PA (1987) Spatial localization in NMR spectroscopy in vivo. *Ann N Y Acad Sci* 508:333–348. <https://doi.org/10.1111/j.1749-6632.1987.tb32915.x>
 10. Jung W-I (1996) Localized double spin echo proton spectroscopy part I: basic concepts. *Concepts Magn Reson* 8(1):1–15. [https://doi.org/10.1002/\(SICI\)1099-0534\(1996\)8:1<1::AID-CMR1>3.0.CO;2-2](https://doi.org/10.1002/(SICI)1099-0534(1996)8:1<1::AID-CMR1>3.0.CO;2-2)
 11. Conolly S, Glover G, Nishimura D, Macovski A (1991) A reduced power selective adiabatic spin-echo pulse sequence. *Magn Reson Med* 18(1):28–38. <https://doi.org/10.1002/mrm.1910180105>
 12. Scheenen TWJ, Heerschap A, Klomp DWJ (2008) Towards 1H-MRSI of the human brain at 7T with slice-selective adiabatic refocusing pulses. *MAGMA* 21(1–2):95–101. <https://doi.org/10.1007/s10334-007-0094-y>
 13. Sacolick LI, Rothman DL, de Graaf RA (2007) Adiabatic refocusing pulses for volume selection in magnetic resonance spectroscopic imaging. *Magn Reson Med* 57(3): 548–553. <https://doi.org/10.1002/mrm.21162>
 14. Oz G, Tkáč I (2011) Short-echo, single-shot, full-intensity 1H MRS for neurochemical profiling at 4T: validation in the cerebellum and brainstem. *Magn Reson Med* 65(4). <https://doi.org/10.1002/mrm.22708>
 15. Near J, Harris AD, Juchem C, Kreis R, Marjańska M, Öz G, Slotboom J, Wilson M, Gasparovic C (2021) Preprocessing, analysis and quantification in single-voxel magnetic resonance spectroscopy: experts' consensus recommendations. *NMR Biomed* 34(5): e4257. <https://doi.org/10.1002/nbm.4257>
 16. Pijnappel WWF, van den Boogaart A, de Beer R, van Ormondt D (1992) SVD-based quantification of magnetic resonance signals. *J Magn Reson* (1969) 97(1):122–134. [https://doi.org/10.1016/0022-2364\(92\)90241-X](https://doi.org/10.1016/0022-2364(92)90241-X)
 17. Gibbs A, Morris GA (1991) Reference deconvolution. Elimination of distortions arising from reference line truncation. *J Magn Reson* (1969) 91(1):77–83. [https://doi.org/10.1016/0022-2364\(91\)90409-M](https://doi.org/10.1016/0022-2364(91)90409-M)
 18. Simpson R, Devenyi GA, Jezard P, Hennessy TJ, Near J (2017) Advanced processing and simulation of MRS data using the FID appliance (FID-A)-an open source, MATLAB-based toolkit. *Magn Reson Med* 77(1): 23–33. <https://doi.org/10.1002/mrm.26091>
 19. Veshtort M, Griffin RG (2006) SPINEVOLUTION: a powerful tool for the simulation of solid and liquid state NMR experiments. *J Magn Reson* 178(2):248–282. <https://doi.org/10.1016/j.jmr.2005.07.018>
 20. Provencher SW (2001) Automatic quantitation of localized in vivo 1H spectra with LCModel. *NMR Biomed* 14(4):260–264. <https://doi.org/10.1002/nbm.698>
 21. Cudalbu C, Behar KL, Bhattacharyya PK, Bogner W, Borbath T, de Graaf RA, Gruetter R, Henning A, Juchem C, Kreis R, Lee P, Lei H, Marjańska M, Meikle R, Murali-Manohar S, Považan M, Rackayová V, Simicic D, Slotboom J, Soher BJ, Starčuk Z, Starčuková J, Tkáč I, Williams S, Wilson M, Wright AM, Xin L, Mlynárik V (2021a) Contribution of macromolecules to brain 1H MR spectra: experts' consensus recommendations. *NMR Biomed* 34(5):e4393. <https://doi.org/10.1002/nbm.4393>
 22. Genovese G, Deelchand DK, Terpstra M, Marjańska M (2023) Quantification of GABA concentration measured noninvasively in the human posterior cingulate cortex with 7 T ultra-short-TE MR spectroscopy. *Magn Reson Med* 89(3):886–897. <https://doi.org/10.1002/mrm.29514>
 23. Kaiser LG, Hirokazu K, Fukunaga M, Matson G (2016) Detection of glucose in the human brain with 1H MRS at 7 Tesla. *Magn Reson Med* 76(6):1653–1660. <https://doi.org/10.1002/mrm.26456>
 24. Kaiser LG, Veshtort M, Pappas I, Deelchand DK, Auerbach EJ, Marjańska M, Inglis BA (2022) Broadband selective excitation radiofrequency pulses for optimized localization in vivo. *Magn Reson Med* 87(5): 2111–2119. <https://doi.org/10.1002/mrm.29119>
 25. Ligneul C, Najac C, Döring A, Beaulieu C, Branzoli F, Clarke WT, Cudalbu C, Genovese G, Jbabdi S, Jelescu I, Karampinos D, Kreis R, Lundell H,

- Marjańska M, Möller HE, Mosso J, Mougél E, Posse S, Ruschke S, Simsek K, Szczepankiewicz F, Tal A, Tax C, Oeltzschner G, Palombo M, Ronen I, Valette J (2024) Diffusion-weighted MR spectroscopy: consensus, recommendations and resources from acquisition to modelling. *Magn Reson Med* 91(3):860–885
26. Genovese G, Marjańska M, Auerbach EJ, Cherif LY, Ronen I, Lehericy S, Branzoli F (2021) In vivo diffusion-weighted MRS using semi-LASER in the human brain at 3 T: methodological aspects and clinical feasibility. *NMR Biomed* 34(5):e4206. <https://doi.org/10.1002/nbm.4206>
27. Palombo M, Shemesh N, Ronen I, Valette J (2018) Insights into brain microstructure from in vivo DW-MRS. *NeuroImage* 182: 97–116. <https://doi.org/10.1016/j.neuroimage.2017.11.028>
28. Borbath T, Murali-Manohar S, Dorst J, Wright AM, Henning A (2021) ProFit-1D—A 1D fitting software and open-source validation data sets. *Magn Reson Med* 86(6): 2910–2929. <https://doi.org/10.1002/mrm.28941>
29. Lee HH, Kim H (2019) Intact metabolite spectrum mining by deep learning in proton magnetic resonance spectroscopy of the brain. *Magn Reson Med* 82(1):33–48. <https://doi.org/10.1002/mrm.27727>
30. Oeltzschner G (2020) MRSHub. In: MRSHub. <https://mrshub.netlify.com/>. Accessed 21 June 2023
31. Öz G, Deelchand DK, Wijnen JP, Mlynárik V, Xin L, Mekle R, Noeske R, Scheenen TWJ, Tkáč I, Mrs the EWG on ASV 1H (2021) Advanced single voxel 1H magnetic resonance spectroscopy techniques in humans: experts' consensus recommendations. *NMR Biomed* 34(5):e4236. <https://doi.org/10.1002/nbm.4236>
32. Deelchand DK, Berrington A, Noeske R, Joers JM, Arani A, Gillen J, Schär M, Nielsen J-F, Peltier S, Seraji-Bozorgzad N, Landheer K, Juchem C, Soher BJ, Noll DC, Kantarci K, Ratai EM, Mareci TH, Barker PB, Öz G (2021) Across-vendor standardization of semi-LASER for single-voxel MRS at 3T. *NMR Biomed* 34(5):e4218. <https://doi.org/10.1002/nbm.4218>
33. Liu H, Zhang D, Lin H, Zhang Q, Zheng L, Zheng Y, Yin X, Li Z, Liang S, Huang S (2021) Meta-analysis of neurochemical changes estimated via magnetic resonance spectroscopy in mild cognitive impairment and Alzheimer's disease. *Front Aging Neurosci* 13. <https://doi.org/10.3389/fnagi.2021.738971>
34. Miller BL (1991) A review of chemical issues in 1H NMR spectroscopy: N-acetyl-L-aspartate, creatine, and choline. *NMR Biomed* 4(2):47–52
35. Pfefferbaum A et al (1999) In vivo brain concentrations of N-acetyl compounds, creatine, and choline in Alzheimer disease. *Arch Gen Psychiatry* 56(2):185–192. <https://doi.org/10.1001/archpsyc.56.2.185>
36. Simmons ML, Frondoza C, Coyle JT (1991) Immunocytochemical localization of N-acetyl-aspartate with monoclonal antibodies. *Neuroscience* 45(1):37–45. [https://doi.org/10.1016/0306-4522\(91\)90101-S](https://doi.org/10.1016/0306-4522(91)90101-S)
37. Soares DP, Law M (2009) Magnetic resonance spectroscopy of the brain: review of metabolites and clinical applications. *Clin Radiol* 64(1):12–21. <https://doi.org/10.1016/j.crad.2008.07.002>
38. Tsai G, Coyle JT (1995) N-acetylaspartate in neuropsychiatric disorders. *Prog Neurobiol* 46:5. [https://doi.org/10.1016/0301-0082\(95\)00014-M](https://doi.org/10.1016/0301-0082(95)00014-M)
39. Frahm J, Michaelis T, Merboldt K-D, Hänicke W, Gyngell ML, Bruhn H (1991) On the N-acetyl methyl resonance in localized 1H NMR spectra of human brain In Vivo. *NMR Biomed* 4(4):201–204. <https://doi.org/10.1002/nbm.1940040408>
40. Valenzuela MJ, Sachdev P (2001) Magnetic resonance spectroscopy in AD. *Neurology* 56(5):592–598. <https://doi.org/10.1212/WNL.56.5.592>
41. Wiebenga OT, Klausner AM, Nagtegaal GJA, Schoonheim MM, Barkhof F, Geurts JGG, Pouwels PJW (2014) Longitudinal absolute metabolite quantification of white and gray matter regions in healthy controls using proton MR spectroscopic imaging. *NMR Biomed* 27(3):304–311. <https://doi.org/10.1002/nbm.3063>
42. Foy CML, Daly EM, Glover A, O'Gorman R, Simmons A, Murphy DGM, Lovestone S (2011) Hippocampal proton MR spectroscopy in early Alzheimer's disease and mild cognitive impairment. *Brain Topogr* 24(3–4):316–322. <https://doi.org/10.1007/s10548-011-0170-5>
43. Modrego PJ, Fayed N (2011) Longitudinal magnetic resonance spectroscopy as marker of cognitive deterioration in mild cognitive impairment. *Am J Alzheimers Dis Other Dement* 26(8):631–636. <https://doi.org/10.1177/1533317511433809>

44. Silveira de Souza A, de Oliveira-Souza R, Moll J, Tovar-Moll F, Andreiuolo PA, Bottino CMC (2011) Contribution of 1H spectroscopy to a brief cognitive-functional test battery for the diagnosis of mild Alzheimer's disease. *Dement Geriatr Cogn Disord* 32(5): 351–361. <https://doi.org/10.1159/000334656>
45. Ackl N, Ising M, Schreiber YA, Atiya M, Sonntag A, Auer DP (2005) Hippocampal metabolic abnormalities in mild cognitive impairment and Alzheimer's disease. *Neurosci Lett* 384(1–2):23–28
46. Bittner DM, Heinze HJ, Kaufmann J (2013) Association of 1H-MR spectroscopy and cerebrospinal fluid biomarkers in Alzheimer's disease: diverging behavior at three different brain regions. *J Alzheimers Dis* 36(1): 155–163. <https://doi.org/10.3233/JAD-120778>
47. Schuff N et al (1997) Changes of hippocampal N-acetyl aspartate and volume in Alzheimer's disease. A proton MR spectroscopic imaging and MRI study. *Neurology* 49(6): 1513–1521
48. Chao LL, Schuff N, Kramer JH, Du AT, Capizzano AA, O'Neill J, Wolkowitz OM, Jagust WJ, Chui HC, Miller BL, Yaffe K, Weiner MW (2005) Reduced medial temporal lobe N-acetylaspartate in cognitively impaired but nondemented patients. *Neurology* 64(2): 282–289. <https://doi.org/10.1212/01.WNL.0000149638.45635.FF>
49. Catani M et al (2001) (1)H-MR spectroscopy differentiates mild cognitive impairment from normal brain aging. *Neuroreport* 12(11): 2315–2317
50. Dixon RM, Bradley KM, Budge MM, Styles P, Smith AD (2002) Longitudinal quantitative proton magnetic resonance spectroscopy of the hippocampus in Alzheimer's disease. *Brain* 125(10):2332–2341. <https://doi-org.libproxy1.usc.edu/10.1093/brain/awf226>
51. Kantarci K, Reynolds G, Petersen RC, Boeve BF, Knopman DS, Edland SD, Smith GE, Ivnik RJ, Tangalos EG, Jack CR (2003) Proton MR spectroscopy in mild cognitive impairment and Alzheimer disease: comparison of 1.5 and 3 T. *AJNR Am J Neuroradiol* 24(5):843–849
52. Kantarci K (2013) Magnetic resonance spectroscopy in common dementias. *Neuroimaging Clin N Am* 23(3):393–406. <https://doi.org/10.1016/j.nic.2012.10.004>
53. Lim TS, Hong YH, Lee HY, Choi JY, Kim HS, Moon SY (2012) Metabolite investigation in both anterior and posterior cingulate gyri in Alzheimer's disease spectrum using 3-Tesla MR spectroscopy. *Dement Geriatr Cogn Disord* 33(2–3):149–155. <https://doi.org/10.1159/000338177>
54. Firbank MJ, Harrison RM, O'Brien JT (2002) A comprehensive review of proton magnetic resonance spectroscopy studies in dementia and Parkinson's disease. *Dement Geriatr Cogn Disord* 14(2):64–76. <https://doi.org/10.1159/000064927>
55. Shonk TK, Moats RA, Gifford P, Michaelis T, Mandigo JC, Izumi J, Ross BD (1995) Probable Alzheimer disease: diagnosis with proton MR spectroscopy. *Radiology* 195(1):65–72. <https://doi.org/10.1148/radiology.195.1.7892497>
56. Jessen F, Block W, Traber F, Keller E, Flacke S, Papassotiropoulos A, Lamerichs R, Heun R, Schild HH (2000) Proton MR spectroscopy detects a relative decrease of N-acetylaspartate in the medial temporal lobe of patients with AD. *Neurology* 55(5): 684–688. <https://doi.org/10.1212/WNL.55.5.684>
57. Watanabe T, Shiino A, Akiguchi I (2012) Hippocampal metabolites and memory performances in patients with amnesic mild cognitive impairment and Alzheimer's disease. *Neurobiol Learn Mem* 97(3):289–293. <https://doi.org/10.1016/j.nlm.2012.01.006>
58. Kantarci K, Jack CR, Xu YC, Campeau NG, O'Brien PC, Smith GE, Ivnik RJ, Boeve BF, Kokmen E, Tangalos EG, Petersen RC (2000) Regional metabolic patterns in mild cognitive impairment and Alzheimer's disease. *Neurology* 55(2):210–217. <https://doi.org/10.1212/WNL.55.2.210>
59. Hancu I, Zimmerman EA, Sailasuta N, Hurd RE (2005) 1H MR spectroscopy using TE averaged PRESS: a more sensitive technique to detect neurodegeneration associated with Alzheimer's disease. *Magn Reson Med* 53(4): 777–782. <https://doi.org/10.1002/mrm.20419>
60. Kantarci K, Xu Y, Shiung MM, O'Brien PC, Cha RH, Smith GE, Ivnik RJ, Boeve BF, Edland SD, Kokmen E, Tangalos EG, Petersen RC, Jack CR Jr (2002) Comparative diagnostic utility of different MR modalities in mild cognitive impairment and Alzheimer's disease. *Dement Geriatr Cogn Disord* 14(4): 198–207. <https://doi.org/10.1159/000066021>
61. Schott JM, Frost C, MacManus DG, Ibrahim F, Waldman AD, Fox NC (2010) Short echo time proton magnetic resonance spectroscopy in Alzheimer's disease: a

- longitudinal multiple time point study. *Brain* 133(11):3315–3322. <https://doi.org/10.1093/brain/awq208>
62. Rami L, Gómez-Ansón B, Bosch B, Sánchez-Valle R, Monte GC, Villar A, Molinuevo JL (2007) Cortical brain metabolism as measured by proton spectroscopy is related to memory performance in patients with amnesic mild cognitive impairment and Alzheimer's disease. *Dement Geriatr Cogn Disord* 24(4):274–279. <https://doi.org/10.1159/000107487>
 63. Kantarci K, Knopman DS, Dickson DW, Parisi JE, Whitwell JL, Weigand SD, Josephs KA, Boeve BF, Petersen RC, Jack CR (2008) Alzheimer disease: postmortem neuropathologic correlates of antemortem 1 H MR spectroscopy metabolite measurements 1. *Radiology* 248(1):210–220. <https://doi.org/10.1148/radiol.2481071590>
 64. Kara F, Joers JM, Deelchand DK, Park YW, Przybelski SA, Lesnick TG, Senjem ML, Zeydan B, Knopman DS, Lowe VJ, Vemuri P, Mielke MM, Machulda MM, Jack CR, Petersen RC, Öz G, Kantarci K (2022) 1H MR spectroscopy biomarkers of neuronal and synaptic function are associated with tau deposition in cognitively unimpaired older adults. *Neurobiol Aging* 112:16–26. <https://doi.org/10.1016/j.neurobiolaging.2021.12.010>
 65. Kantarci K, Boeve BF, Wszolek ZK, Rademakers R, Whitwell JL, Baker MC, Senjem ML, Samikoglu AR, Knopman DS, Petersen RC, Jack CR (2010) MRS in presymptomatic MAPT mutation carriers: a potential biomarker for tau-mediated pathology. *Neurology* 75(9):771–778. <https://doi.org/10.1212/WNL.0b013e3181f073c7>
 66. Piersson AD, Mohamad M, Rajab F, Suppiah S (2021) Cerebrospinal fluid amyloid beta, Tau levels, apolipoprotein, and 1H-MRS brain metabolites in Alzheimer's disease: a systematic review. *Acad Radiol* 28(10):1447–1463. <https://doi.org/10.1016/j.acra.2020.06.006>
 67. Kantarci K et al (2011) Magnetic resonance spectroscopy, beta-amyloid load, and cognition in a population-based sample of cognitively normal older adults. *Neurology* 77(10):951–958. <https://doi.org/10.1212/WNL.0b013e31822dc7e1>
 68. Murray ME, Przybelski SA, Lesnick TG, Liesinger AM, Spychalla A, Zhang B, Gunter JL, Parisi JE, Boeve BF, Knopman DS, Petersen RC, Jack CR, Dickson DW, Kantarci K (2014) Early Alzheimer's disease neuropathology detected by proton MR spectroscopy. *J Neurosci* 34(49):16247–16255. <https://doi.org/10.1523/JNEUROSCI.2027-14.2014>
 69. Mullins R, Reiter D, Kapogiannis D (2018) Magnetic resonance spectroscopy reveals abnormalities of glucose metabolism in the Alzheimer's brain. *Ann Clin Transl Neurol* 5(3):262–272. <https://doi.org/10.1002/acn3.530>
 70. Sheikh-Bahaei N, Sajjadi SA, Manavaki R, McLean M, O'Brien JT, Gillard JH (2018) Positron emission tomography-guided magnetic resonance spectroscopy in Alzheimer disease. *Ann Neurol* 83(4):771–778. <https://doi.org/10.1002/ana.25202>
 71. Fisher SK, Novak JE, Agranoff BW (2002) Inositol and higher inositol phosphates in neural tissues: homeostasis, metabolism and functional significance. *J Neurochem* 82(4):736–754. <https://doi.org/10.1046/j.1471-4159.2002.01041.x>
 72. Ross BD, Bluml S, Cowan R, Danielsen E, Farrow N, Gruetter R (1997) In vivo magnetic resonance spectroscopy of human brain: the biophysical basis of dementia. *Biophys Chem* 68(1–3):161–172. [https://doi.org/10.1016/S0301-4622\(97\)00032-X](https://doi.org/10.1016/S0301-4622(97)00032-X)
 73. Ross AJ, Sachdev PS (2004) Magnetic resonance spectroscopy in cognitive research. *Brain Res Rev* 44(2–3):83–102. <https://doi.org/10.1016/j.brainresrev.2003.11.001>
 74. Huang W, Alexander GE, Chang L, Shetty HU, Krasuski JS, Rapoport SI, Schapiro MB (2001) Brain metabolite concentration and dementia severity in Alzheimer's disease: a 1H MRS study. *Neurology* 57(4):626–632. <https://doi.org/10.1212/WNL.57.4.626>
 75. Miller BL, Moats RA, Shonk T, Ernst T, Woolley S, Ross BD (1993) Alzheimer disease: depiction of increased cerebral myo-inositol with proton MR spectroscopy. *Radiology* 187(2):433–437. <https://doi.org/10.1148/radiology.187.2.8475286>
 76. Voevodskaya O, Sundgren PC, Strandberg O, Zetterberg H, Minthon L, Blennow K, Wahlund LO, Westman E, Hansson O, Swedish BioFINDER study group (2016) Myo-inositol changes precede amyloid pathology and relate to APOE genotype in Alzheimer disease. *Neurology* 86(19):1754–1761. <https://doi-org.libproxy1.usc.edu/10.1212/WNL.0000000000002672>
 77. Voevodskaya O, Poulakis K, Sundgren P, Westin DV, Palmqvist S, Wahlund LO, Stomrud E, Hansson O, Westman E (2019) Brain myoinositol as a potential marker of amyloid-related pathology: a longitudinal study. *Neurology* 92(5):E395–E405.

- <https://doi.org/10.1212/WNL.0000000000006852>
78. Chen Q, Boeve BF, Tosakulwong N, Lesnick T, Brushaber D, Dheel C, Fields J, Forsberg L, Gavrilova R, Gearhart D, Haley D, Gunter JL, Graff-Radford J, Jones D, Knopman D, Graff-Radford N, Kraft R, Lapid M, Rademakers R, Syrjanen J, Wszolek ZK, Rosen H, Boxer AL, Kantarci K (2019) Frontal lobe 1 H MR spectroscopy in asymptomatic and symptomatic MAPT mutation carriers. *Neurology* 93(8):e758–e765. <https://doi.org/10.1212/WNL.0000000000007961>
 79. Waragai M, Moriya M, Nojo T (2017) Decreased N-acetyl aspartate/myo-inositol ratio in the posterior cingulate cortex shown by magnetic resonance spectroscopy may be one of the risk markers of preclinical Alzheimer's disease: a 7-year follow-up study. *J Alzheimers Dis* 60(4):1411–1427. <https://doi.org/10.3233/JAD-170450>
 80. MacKay S et al (1996) Alzheimer disease and subcortical ischemic vascular dementia: evaluation by combining MR imaging segmentation and H-1 MR spectroscopic imaging. *Radiology* 198(2):537–545. <https://doi.org/10.1148/radiology.198.2.8596863>
 81. Wurtman RJ, Blusztajn JK, Maire JC (1985) "Autocannibalism" of choline-containing membrane phospholipids in the pathogenesis of Alzheimer's disease-A hypothesis. *Neurochem Int* 7(2):369–372
 82. Doelken MT, Mennecke A, Stadlbauer A, Kloska S, Struffert T, Engelhorn T, Thuerauf N, Doerfler A, Stefan H, Hammen T (2009) Multi-voxel magnetic resonance spectroscopy of cerebral metabolites in healthy adults at 3 Tesla. *Acad Radiol* 16(12):1493–1501. <https://doi.org/10.1016/j.acra.2009.07.025>
 83. Muir JL (1997) Acetylcholine, aging, and Alzheimer's disease. *Pharmacol Biochem Behav* 56(4):687–696. [https://doi.org/10.1016/S0091-3057\(96\)00431-5](https://doi.org/10.1016/S0091-3057(96)00431-5)
 84. Song T, Song X, Zhu C, Patrick R, Skurla M, Santangelo I, Green M, Harper D, Ren B, Forester BP, Öngür D, Du F (2021) Mitochondrial dysfunction, oxidative stress, neuroinflammation, and metabolic alterations in the progression of Alzheimer's disease: a meta-analysis of in vivo magnetic resonance spectroscopy studies. *Ageing Res Rev* 72:101503. <https://doi.org/10.1016/j.arr.2021.101503>
 85. Adalsteinsson E, Sullivan EV, Kleinmans N, Spielman DM, Pfefferbaum A (2000) Longitudinal decline of the neuronal marker N-acetyl aspartate in Alzheimer's disease, *Lancet* 1696–1697. [https://doi.org.libproxy1.usc.edu/10.1016/s0140-6736\(00\)02246-7](https://doi.org.libproxy1.usc.edu/10.1016/s0140-6736(00)02246-7)
 86. Sheikh-Bahaei N (2020) MR spectroscopy in Alzheimer's disease. *Biomed Spectrosc Imaging* 9(1–2):13–21. <https://doi.org/10.3233/bsi-200194>
 87. Parnetti L, Tarducci R, Presciutti O, Lowenthal DT, Pippi M, Palumbo B, Gobbi G, Pelliccioli GP, Senin U (1997) Proton magnetic resonance spectroscopy can differentiate Alzheimer's disease from normal aging. *Mech Ageing Dev* 97(1):9–14. [https://doi.org/10.1016/S0047-6374\(97\)01877-0](https://doi.org/10.1016/S0047-6374(97)01877-0)
 88. Krishnan KR et al (2003) Randomized, placebo-controlled trial of the effects of donepezil on neuronal markers and hippocampal volumes in Alzheimer's disease. *Am J Psychiatry* 160(11):2003–2011. <https://doi.org/10.1176/appi.ajp.160.11.2003>
 89. Moats RA et al (1994) Abnormal cerebral metabolite concentrations in patients with probable Alzheimer disease. *Magn Reson Med* 32(1):110–115. <https://doi.org/10.1002/mrm.1910320115>
 90. Dekosky ST, Ikonomic MD, Styren SD, Beckett L, Wisniewski S, Bennett DA, Cochran EJ, Kordower JH, Mufson EJ (2002) Upregulation of choline acetyltransferase activity in hippocampus and frontal cortex of elderly subjects with mild cognitive impairment. *Ann Neurol* 51(2):145–155. <https://doi.org/10.1002/ana.10069>
 91. Pouwels PJ, Frahm J (1998) Regional metabolite concentrations in human brain as determined by quantitative localized proton MRS. *Magn Reson Med* 39:53–60
 92. Nitsch RM, Blusztajn JK, Doyle FM et al (1993) Phospholipid metabolite levels are altered in cerebral cortex of patients with dominantly inherited olivopontocerebellar atrophy. *Neurosci Lett* 161:191–194
 93. Liskowsky W, Schliebs R (2006) Muscarinic acetylcholine receptor inhibition in transgenic Alzheimer-like Tg2576 mice by scopolamine favors the amyloidogenic route of processing of amyloid precursor protein. *Int J Dev Neurosci* 24:149–156. <https://doi.org/10.1016/j.jdevneu.2005.11.010>
 94. Buxbaum JD, Oishi M, Chen HI et al (1992) Cholinergic agonists and interleukin 1 regulate processing and secretion of the Alzheimer beta/A4 amyloid protein precursor. *Proc Natl Acad Sci U S A* 89:10075–10078
 95. Nunes-Tavares N, Santos LE, Stutz B et al (2012) Inhibition of choline acetyltransferase

- as a mechanism for cholinergic dysfunction induced by amyloid-beta peptide oligomers. *J Biol Chem* 287(19377–19385):20. <https://doi.org/10.1074/jbc.m111.321448>
96. Zambrozcka A, Alberghina M, Strosznajder JB (2002) Effects of aging and amyloid-beta peptides on choline acetyltransferase activity in rat brain. *Neurochem Res* 27(277–281): 21. <https://doi.org/10.1023/a:1014951010834>
 97. Kar S, Issa AM, Seto D, Auld DS, Collier B, Quirion R (1998) Amyloid beta-peptide inhibits high-affinity choline uptake and acetylcholine release in rat hippocampal slices. *J Neurochem* 70:2179–2187
 98. Ikonomovic MD, Klunk WE, Abrahamson EE, Wu J, Mathis CA, Scheff SW, Mufson EJ, DeKosky ST (2011) Precuneus amyloid burden is associated with reduced cholinergic activity in Alzheimer disease. *Neurology* 77(1):39–47. <https://doi.org/10.1212/WNL.0b013e3182231419>
 99. Zhang Y, Shen J (2015) Regional and tissue-specific differences in brain glutamate concentration measured by in vivo single voxel MRS. *J Neurosci Methods* 239:94–99. <https://doi.org/10.1016/j.jneumeth.2014.09.021>
 100. Hertz L (2004) Intercellular metabolic compartmentation in the brain: past, present, and future. *Neurochem Int* 45(2–3):285–296. <https://doi.org/10.1016/j.neuint.2003.08.016>
 101. Walton HS, Dodd PR (2007) Glutamate-glutamine cycling in Alzheimer's disease. *Neurochem Int* 50(7-8):1052–1066. <https://doi.org/10.1016/j.neuint.2006.10.007>. Epub 2006 Dec 1
 102. Hattori N, Abe K, Sakoda S, Sawada T (2002) Proton MR spectroscopic study at 3 Tesla on glutamate/glutamine in Alzheimer's disease. *Neuroreport* 13(1):183–186. <https://doi.org/10.1097/00001756-200201210-00041>
 103. Huang D, Liu D, Yin J, Qian T, Shrestha S, Ni H (2017) Glutamate-glutamine and GABA in brain of normal aged and patients with cognitive impairment. *Eur Radiol* 27(7): 2698–2705. <https://doi.org/10.1007/s00330-016-4669-8>
 104. Walecki J, Barcikowska M, Ćwikła JB, Gabryelewicz T (2011) N-acetylaspartate, choline, myoinositol, glutamine and glutamate (glx) concentration changes in proton MR spectroscopy (1H MRS) in patients with mild cognitive impairment (MCI). *Med Sci Monit* 17(12):MT105–MT111. <https://doi.org/10.12659/MSM.882112>
 105. Fayed N, Modrego PJ, Rojas-Salinas G, Aguilar K (2011) Brain glutamate levels are decreased in Alzheimer's disease. *Am J Alzheimer's Dis Other Dementias* 26(6): 450–456. <https://doi.org/10.1177/1533317511421780>
 106. Zeydan B, Kantarci K (2021) Decreased glutamine and glutamate: an early biomarker of neurodegeneration. *Int Psychogeriatr* 33(1): 1–2. <https://doi.org/10.1017/S1041610219001807>
 107. Antuono PG, Jones JL, Wang Y, Li S-J (2001) Decreased glutamate + glutamine in Alzheimer's disease detected in vivo with 1H-MRS at 0.5 T. *Neurology* 56(6):737–742. <https://doi.org/10.1212/WNL.56.6.737>
 108. Andersen JV, Markussen KH, Jakobsen E, Schousboe A, Waagepetersen HS, Rosenberg PA, Aldana BI (2021) Glutamate metabolism and recycling at the excitatory synapse in health and neurodegeneration. *Neuropharmacology* 196:108719. <https://doi.org/10.1016/j.neuropharm.2021.108719>. Epub 2021 July 15
 109. Andersen JV, Schousboe A, Verkhratsky A (2022) Astrocyte energy and neurotransmitter metabolism in Alzheimer's disease: integration of the glutamate/GABA-glutamine cycle. *Prog Neurobiol* 217:102331. <https://doi.org/10.1016/j.pneurobio.2022.102331>. Epub 2022 Jul 21. PMID: 35872221
 110. Cho SH, Rhee HY, Oh J, Lee JS, Park S, Shin WC, Paik JW, Ryu CW, Park KC, Jahng GH (2021) Longitudinal functional magnetic resonance spectroscopy study in subjects with mild cognitive impairment and Alzheimer's disease. *Curr Alzheimer Res* 18(4):335–346. <https://doi.org/10.2174/1567205018666210708145924>
 111. Riese F, Gietl A, Zölch N, Henning A, O'Gorman R, Kälin AM, Leh SE, Buck A, Warnock G, Edden RA, Luechinger R, Hock C, Kollias S, Michels L (2015) Posterior cingulate γ -aminobutyric acid and glutamate/glutamine are reduced in amnesic mild cognitive impairment and are unrelated to amyloid deposition and apolipoprotein E genotype. *Neurobiol Aging* 36(1):53–59. <https://doi.org/10.1016/j.neurobiolaging.2014.07.030>. Epub 2014 July 29. PMID: 25169676; PMCID: PMC5531169
 112. Sheikh-Bahaei N (2018) The effect of voxel position and tissue composition on MR Spectroscopy in Alzheimer's disease, paper presented at the “Western Neuroradiological Society”, Dana Point, Oct 2018

113. Pfund Z, Chugani DC, Juhász C, Muzik O, Chugani HT, Wilds IB, Seraji-Bozorgzad N, Moore GJ (2000) Evidence for coupling between glucose metabolism and glutamate cycling using FDG PET and 1H magnetic resonance spectroscopy in patients with epilepsy. *J Cereb Blood Flow Metab* 20(5): 871–878. <https://doi.org/10.1097/00004647-200005000-00014>
114. Sai KKS, Zachar Z, Bingham PM, Mintz A (2017) Metabolic PET imaging in oncology. *AJR Am J Roentgenol* 209(2):270–276. <https://doi.org/10.2214/AJR.17.18112>. Epub 2017 May 2
115. Leuzy A, Zimmer ER, Dubois J, Pruessner J, Cooperman C, Soucy JP, Kostikov A, Schirmaccher E, Désautels R, Gauthier S, Rosa-Neto P (2016) In vivo characterization of metabotropic glutamate receptor type 5 abnormalities in behavioral variant FTD. *Brain Struct Funct* 221(3):1387–1402. <https://doi.org/10.1007/s00429-014-0978-3>. Epub 2015 Jan 18
116. Völzke Y, Pracht ED, Hattingen E, Tse DH Y, Stöcker T (2021) On the reproducibility of hippocampal MEGA-sLASER GABA MRS at 7T using an optimized analysis pipeline. *MAGMA* 34(3):427–436. <https://doi.org/10.1007/s10334-020-00879-9>. Epub 2020 Aug 31. PMID: 32865653; PMCID: PMC8154804
117. Fujihara K, Narita K, Suzuki Y, Takei Y, Suda M, Tagawa M, Ujita K, Sakai Y, Narumoto J, Near J, Fukuda M (2015) Relationship of γ -aminobutyric acid and glutamate+glutamine concentrations in the perigenual anterior cingulate cortex with performance of Cambridge Gambling Task. *Neuroimage* 109:102–108. <https://doi.org/10.1016/j.neuroimage.2015.01.014>. Epub 2015 Jan 9
118. Dyke K, Pépés SE, Chen C, Kim S, Sigurdsson HP, Draper A, Husain M, Nachev P, Gowland PA, Morris PG, Jackson SR (2017) Comparing GABA-dependent physiological measures of inhibition with proton magnetic resonance spectroscopy measurement of GABA using ultra-high-field MRI. *Neuroimage* 152:360–370. <https://doi.org/10.1016/j.neuroimage.2017.03.011>. Epub 2017 Mar 9. PMID: 28284797; PMCID: PMC5440178
119. Mandal PK, Tripathi M, Sugunan S (2012) Brain oxidative stress: detection and mapping of anti-oxidant marker 'Glutathione' in different brain regions of healthy male/female, MCI and Alzheimer patients using non-invasive magnetic resonance spectroscopy. *Biochem Biophys Res Commun* 417(1):43–48. <https://doi.org/10.1016/j.bbrc.2011.11.047>. Epub 2011 Nov 19. PMID: 22120629
120. Shukla D, Mandal PK, Tripathi M, Vishwakarma G, Mishra R, Sandal K (2020) Quantitation of in vivo brain glutathione conformers in cingulate cortex among age-matched control, MCI, and AD patients using MEGA-PRESS. *Hum Brain Mapp* 41(1):194–217. <https://doi.org/10.1002/hbm.24799>. Epub 2019 Oct 4. PMID: 31584232; PMCID: PMC7268069
121. Duffy SL, Lagopoulos J, Hickie IB, Diamond K, Graeber MB, Lewis SJ, Naismith SL (2014) Glutathione relates to neuropsychological functioning in mild cognitive impairment. *Alzheimers Dement* 10(1): 67–75. <https://doi.org/10.1016/j.jalz.2013.01.005>. Epub 2013 May 18
122. Marjańska M, McCarten JR, Hodges J, Hemmy LS, Grant A, Deelchand DK, Terpstra M (2017) Region-specific aging of the human brain as evidenced by neurochemical profiles measured noninvasively in the posterior cingulate cortex and the occipital lobe using 1H magnetic resonance spectroscopy at 7 T. *Neuroscience* 354:168–177. <https://doi.org/10.1016/j.neuroscience.2017.04.035>. Epub 2017 May 3. PMID: 28476320; PMCID: PMC5516630
123. Monacelli F, Acquarone E, Giannotti C, Borghi R, Nencioni A (2017) Vitamin C, aging and Alzheimer's disease. *Nutrients* 9(7):670. <https://doi.org/10.3390/nu9070670>. PMID: 28654021; PMCID: PMC5537785
124. Wang JY, Wen LL, Huang YN, Chen YT, Ku MC (2006) Dual effects of antioxidants in neurodegeneration: direct neuroprotection against oxidative stress and indirect protection via suppression of glia-mediated inflammation. *Curr Pharm Des* 12(27):3521–3533. <https://doi.org/10.2174/138161206778343109>. PMID: 17017945
125. Marjańska M, McCarten JR, Hodges JS, Hemmy LS, Terpstra M (2019) Distinctive neurochemistry in Alzheimer's disease via 7 T in vivo magnetic resonance spectroscopy. *J Alzheimers Dis* 68(2):559–569. <https://doi.org/10.3233/JAD-180861>. PMID: 30775983; PMCID: PMC6481537
126. Kuribayashi H, Urushibata Y, Imai H, Ahn S, Seethamraju RT, Isa T, Okada T (2023) Quantification of cerebral glucose concentrations via detection of the H1- α -glucose peak in 1 H MRS at 7T. *J Magn Reson Imaging*

- (Jun 1). <https://doi.org/10.1002/jmri.28834>. Epub ahead of print
127. Veeraiah P, Jansen JFA (2023) Multinuclear magnetic resonance spectroscopy at ultra-high-field: assessing human cerebral

metabolism in healthy and diseased states. *Metabolites* 13(4):577. <https://doi.org/10.3390/metabo13040577>. PMID: 37110235; PMCID: PMC10143499



Neuroimaging Methods for MRI Analysis in CSF Biomarkers Studies

Carles Falcon, Grégory Operto, José Luis Molinuevo, and Juan Domingo Gispert

Abstract

Among others, the existence of pathophysiological biomarkers such as cerebrospinal fluid (CSF) A β -42, t-tau, and p-tau preceding the onset of Alzheimer's disease (AD) symptomatology has shifted the conceptualization of AD as a *continuum*. In addition, magnetic resonance imaging (MRI) enables the study of structural and functional cross-sectional correlates and longitudinal changes in vivo, and therefore, the combination of CSF data and imaging analyses emerges as a synergistic approach to understand the structural correlates related with specific AD-related biomarkers. In this chapter, we describe the methods used in neuroimaging that will allow researchers to combine data on CSF metabolites with imaging analyses.

Key words Magnetic resonance imaging, ROI-based analysis, Voxel-based morphology, Diffusion tensor imaging, Structural and functional connectivity, Functional MRI, Imaging biomarkers, Alzheimer's disease

1 Introduction

A promising approach to increase the accuracy in the diagnosis of Alzheimer's disease (AD) and improve the prognosis of persons with cognitive decline or impairment is the use of AD cerebrospinal fluid (CSF) biomarkers [1]. Furthermore, as the well-established AD CSF biomarkers (A β -42, t-tau and p-tau) represent proxies of pathology, they may be incorporated in research studies to know the underlying biology of a given cohort. An interest approach is combining several of them as a normalized index enabling researchers to study the AD *continuum* even in cross-sectional samples [2, 3]. On the other hand, analysis and interpretation of neuroimaging data are often carried out to investigate on intraindividual

Carles Falcon and Grégory Operto contributed equally with all other contributors.

longitudinal changes and/or intersubject/group differences, in particular in the context of AD. Magnetic resonance imaging (MRI) allows the study of structural and functional cross-sectional correlates and longitudinal changes in vivo, and therefore, the combination of CSF data and imaging analyses in AD research stands as a synergistic approach to understand the structural correlates related with specific disease-related biomarkers.

During the last decade, we have followed this approach for studying cerebral correlates of AD biomarkers along the disease *continuum*. In order to do it, the first step was to develop a normalized biomarker index, the AD CSF index, which allowed us to estimate the degree of pathology. This endorsed us to conclude that changes in different brain areas follow a nonlinear pattern along the AD *continuum* also occurring with different degrees of pathological load [4]. This approach also allowed us to study the impact of inflammation, through the study of astroglial and microglial markers, on the structure of the brain along the *continuum* [5, 6]. Furthermore, the use of different MRI sequences enables us not only to define macroscopic structural changes but also to delve into the cerebral microstructure through diffusion tensor imaging (DTI), which allows us to hypothesize on their physiopathology.

In this chapter, we describe the methods used in neuroimaging in order to combine data on CSF metabolites with imaging analyses. Specifically, we discuss different MRI analysis modalities, which are as follows: (1) volumetric region of interest (ROI)-based analysis: As hypotheses are frequently stated in terms of brain structures or ROIs, ROI-based analysis allows to focus data analysis over a number of parcels with homogeneous characteristics. (2) Voxel-based morphology (VBM): The aim of VBM is to assess for intergroup morphological differences using a voxel by voxel statistical analysis. (3) Parametric maps from diffusion tensor imaging (DTI): DTI has gained interest in AD for its ability to characterize white matter integrity. (4) Structural and functional connectivity: Parametric maps give quantitative measures about white matter integrity but hides anatomical and topological information. With respect to this, recent tractography techniques are now able to extract models of the fiber tracts connecting nuclei of the central nervous system, giving detailed descriptions of the structural connectome and opening the way to their analysis at the group level. (5) Functional MRI (fMRI): The goal of fMRI is to detect the voxels in the brain related to the task the subject performs during the scanning time [7–9].

2 Materials

2.1 Magnetic Resonance Imaging Modalities

MRI combines radiofrequency (RF) pulses and magnetic gradients to explore magnetic properties of tissues, such as the longitudinal (T1) and transversal (T2) magnetic relaxation times [10]. Each particular combination of RF pulses and gradients is referred to as MRI sequence and provides different information about the morphology, physiology, and functionality of tissues [11]. The main sequences used in neuroimaging are three-dimensional T1-weighted structural images (3dT1w), BOLD-contrast images (fMRI), and diffusion tensor imaging (DTI).

2.1.1 Three-Dimensional T1-Weighted (3dT1w) Images

A 3dT1w sequence provides detailed information about the morphology of the brain, offering a good contrast between gray and white matter. It accounts for differences in longitudinal relaxation parameter T1 across the brain (Fig. 1a). Analyses benefit from the voxel (contraction of “*volume*” and “*elements*”) to be isotropic (i.e., with the same size in all three spatial directions). Voxel size depends on the scanner capability and the time to spend on the acquisition. Standard value ranges from 0.5 to 1.2 mm, and values tend to get lower as scanner technology improves. Other important parameters to be fixed are repetition time (TR), echo time (TE), inversion time (TI), and flip-angle. Their optimal values depend on the scanner and image resolution. The acquisition time extends from 3 to 9 min.

2.1.2 Blood Oxygenation Level-Dependent (BOLD) Contrast Imaging

The echo planar imaging (EPI) sequence is an ultrafast sequence that can be sensitive to the oxyhemoglobin-deoxyhemoglobin ratio in blood, the so-called blood oxygenation level-dependent (BOLD) signal, which is related to the brain function. Images are acquired while the subject is performing a cognitive-sensitive task (fMRI, functional MRI) or during a rest period (rs-fMRI, resting-state functional MRI). Neural activation cannot be detected itself but its physiological effects: a local increase of perfusion, which does not entail an increase in oxygen consumption that produces a rise of the oxyhemoglobin-deoxyhemoglobin ratio, the so-called hemodynamic response function (HRF). The whole brain is scanned in 1 to 4 s (TR) (Fig. 1b). As the change in contrast due to brain activation is very low (below 3%), images are noisy, and the intensity of each voxel also depends on other uncontrolled variables, several images have to be acquired (from 60 to few hundreds) during a scan period that ranges from 3 to 30 min, and posterior statistical analyses should be done to determine the voxels related to the brain function in study. Relevant acquisition parameters, apart from TR, are TE, flip-angle, voxel size, and slice thickness and inter-slice gap. To correct for geometrical distortion of EPI due to eddy currents and field inhomogeneity related to different

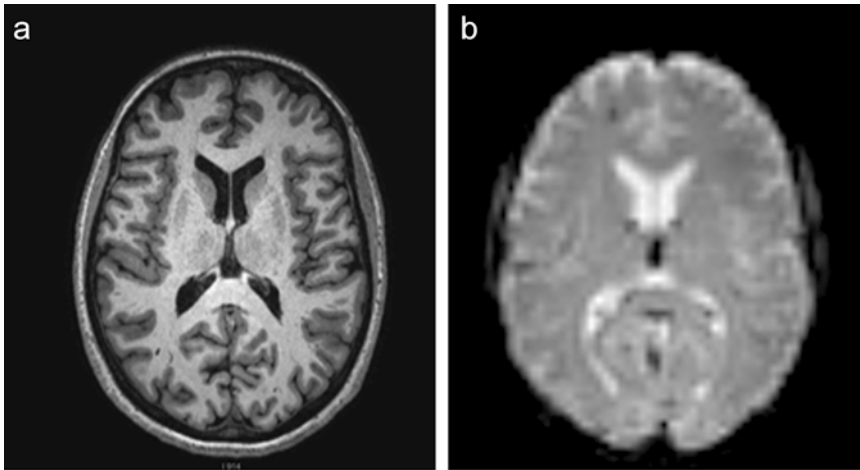


Fig. 1 Example of 3dT1w (a) and fMRI (b) images from the same subject

magnetic susceptibility of tissues, it is necessary to acquire a B0-map or few images with reverse phase encoding direction [12].

2.1.3 Diffusion Tensor Imaging (DTI)

DTI is a processed image derived from a T2-weighted image, referred to as b_0 (Fig. 2a) and a set of diffusion weighted images with the same geometrical prescription. Diffusion-weighted images are obtained by adding two opposite gradients between the magnetic excitation and the signal readout to the b_0 image. The double gradient produces a drop of signal, with respect to b_0 image, proportional to the amount of water diffusion in its direction (Fig. 2b). From DTI, data can be derived various diffusivity parametric maps, for example, mean diffusivity (MD) (Fig. 2c), radial diffusivity (RD), fractional anisotropy (FA) (Fig. 2d), and axial diffusivity (AD). These parameters measure specific microstructural alterations that are related to relevant biological factors such as cytotoxic edema (cell swelling) that is associated to restricted water diffusivity or demyelination (axonal loss) that reduces FA. On top of this, it must be noted that the direction of higher diffusion follows the main direction of the axons since myelin bands restrict diffusion across them. This property enables the tracking of white matter fibers in the so-called “fiber-tracking” (Fig. 2e) (*see Note 1*). The main acquisition parameters for DTI are TR, TE, flip-angle, voxel size (must be cubic with inter-slice gap zero to perform tractography), and the intensity of the diffusion weighting monitored by the parameter b . Like BOLD-contrast images, DTI is an EPI sequence. Therefore, B0-map or a b_0 image with reverse phase encoding directions can be useful to correct for image distortion that highly improves the quality of the derived images.

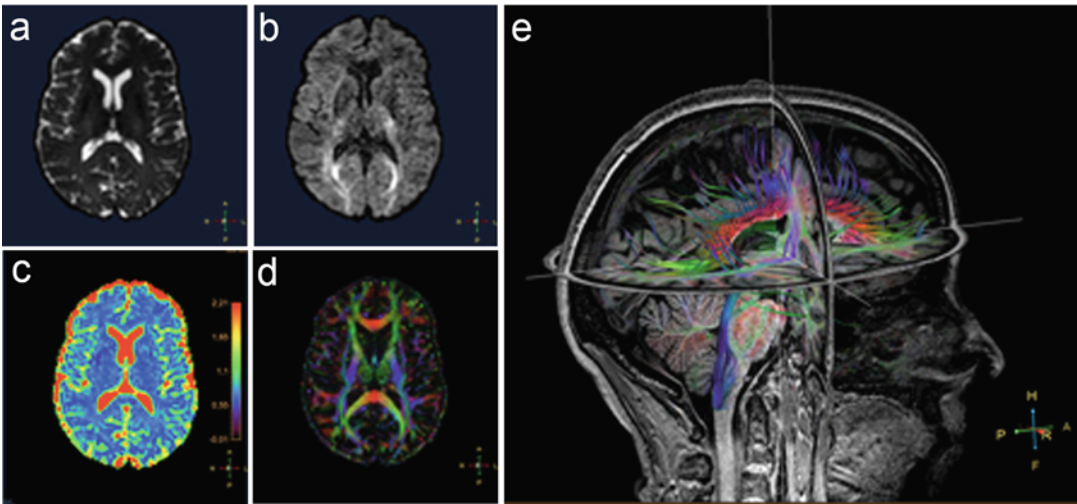


Fig. 2 b0 image (a), diffusion weighted image (b), mean diffusivity map (c), fractional anisotropy map (d) from the same subject. Partial tractography of white matter bundles through corpus callosum and cortico-spinal path overlaid on a 3dT1w image (e)

2.2 Fundamental Neuroimaging Processing Tools

2.2.1 Segmentation

The raw signal in images is presented as a three-dimensional grid of voxels that provide local measures related to structure or function. Signal variations can be analyzed at either the region level (3.1 and 3.5) or at the *voxel* level (3.2–3.4).

Segmentation techniques are used to identify voxels that belong to the same tissue (typically, gray matter, white matter, and cerebrospinal fluid) or brain structure. By doing so, volume and other morphometric features of these tissues or structures can be obtained and analyzed. The partitioning of the voxels can be “hard” (i.e., each voxel is assigned a single label) or “probabilistic” (i.e., each voxel is assigned a probability of belonging to one label). Tissue probability maps are extracted from structural images by means of tissue segmentation algorithms. This step converts 3dT1w images, which have arbitrary units and scaling factor, to 0 to 1 maps (Fig. 3). Voxel values can be interpreted as the probability of the voxel belonging to the mapped tissue and account for its gray level, location, and partial volume effects (edge voxels containing more than one tissue). Sometimes, the outcome of the segmentation is the boundary separating the different tissues or brain regions. Segmentation algorithms may be specialized and focus on a specific structure or may cover a full range of regions (e.g., FSL, FreeSurfer, SPM, volBrain), and the nature of their results can vary from voxel-based clusters for volumetric structures to cortical surface 3D meshes or patches, fiber bundles, cortical folds models, among many others. Resulting objects are likely to be closer to the individual anatomical truth, and by focusing on the signal of interest tends to improve sensitivity [13]. Depending on

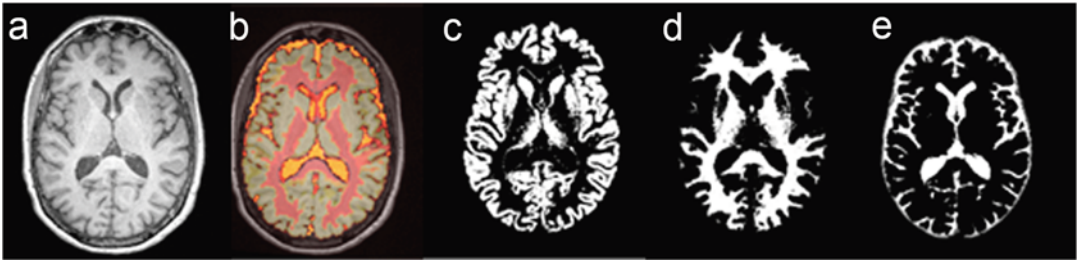


Fig. 3 Segmentation of a 3dT1w images (a): labeling voxels according their gray level and position in the brain (b), and creating a 0–1 tissue probabilistic map of GM (c), WM (d) and CSF (e)

the accuracy of the method, this opens the way to shape analysis techniques or object-based morphometry as opposed to standard voxel-based methods. As a logical consequence, using individually segmented structures rather than warping data onto a reference atlas is advocated for the study of intersubject variability.

2.2.2 Coregistration and Spatial Normalization

Coregistration is the process of geometrically aligning two images: one is defined as the “target” or “reference” image (i.e., the one that defines the target geometrical space) and the other the “moving” image (i.e., the one that is going to be spatially transformed to be aligned with the target image). Depending on whether the two images belong to the same modality and/or subject different algorithms apply. The easiest situation is intersubject registration of images of the same modality. For instance, in fMRI acquisitions, slight head movements can be corrected using these techniques by aligning all the images in the series to the first or to the mean image. In these cases, the algorithm first estimates the “rigid” spatial transformation (three rotations and three displacements along the x , y , and z directions) so that the matching of the two images is optimal. Then, two options are normally available: the moving image can be resampled to the voxel size and dimensions of the target image, or the transformation can be stored in the header of the moving image for displaying purposes but without altering the actual data in the images. Images of different modalities can also be aligned using multimodal registration techniques. A typical example would be to coregister a 3dT1w image with a PET image of the same individual. The first image conveys detailed structural information on the brain anatomy, and the PET image provides the functional information.

Coregistration can also be performed between images of different individuals. Generally, this step is referred to as spatial normalization or warping, since the moving image needs to be distorted to match the target image. In spatial normalization, the target image is usually a “template,” that is, a representative image, which can be provided by the normalization method or computed from the sample under study. On a first instance, spatial

normalization enables the voxel-wise analysis of the images. Since individual morphological features are removed, the same anatomical locations fall into the same voxels and group comparisons or correlation analyses can be implemented without having to define regions of interest a priori. But spatial normalization techniques also enable morphometric studies by analyzing the different deformation fields that characterize the individual anatomy. Deformation fields establish a mapping between each voxel of the moving image to their corresponding location in the reference space. Therefore, they can be analyzed as three-dimensional mappings (i.e., tensor or deformation based morphometry), or a spatially varying scalar property of the deformation can be computed to drive the morphometric analysis. This is the case in voxel-based morphometry, where the relative changes in volume are computed by calculating the Jacobian determinants or the divergence of the individual deformation maps. Many normalization methods exist and differ in nature and degree of the applied spatial transformation. Many reference templates are also available; the mostly used is MNI stereotactic frame. Selecting the right one amounts to finding the most representative of the population under study, for example, in the context of the ageing brain [14]. Diffeomorphic transformations have been shown to provide the best performance among non-affine transformations [15].

The warping of images of different modalities across different individuals is not straightforward at all and does not constitute a typical requirement of brain image processing pipelines. Thus, it exceeds the scope of this chapter.

2.2.3 Smoothing and Denoising

Smoothing solves three problems. First, it reduces noise and increases the correlation across neighboring voxels. From the physiological point of view, it makes no sense one voxel showing a significant difference and not the surrounding ones. There is an implicit prior that involved brain areas should have a minimum extension. Secondly, it makes the information on the voxels being slightly expanded to ensure certain degree of interaction of misaligned voxels due to subtle normalization inaccuracies. Third, the main one, it ensures parametric statistics can be applied in the voxel-based statistical analysis. Under certain assumptions, not always verified, a smoothed map behaves as a Gaussian field, and then, random field theory can be used to determine statistical thresholds of significance.

MR images come with signal properties/quality that depend on the type and parameters of the acquisition sequence. Some algorithms are efficient at improving the signal-to-noise ratio of the images and as such form part of the analysis pipeline as standard preprocessing steps. Such techniques generally rely on a distribution model of the noise (e.g., Rician) and apply corrections based

on the information found either locally around every voxel [16] or on similar patches elsewhere in the image [17].

3 Methods

3.1 Region of Interest (ROI)-Based Volumetric Analysis

ROI-based analysis allows focusing the analysis over a number of parcels with homogeneous characteristics. ROIs are thus often defined over anatomical data and then used to filter the signal from other modalities.

Two approaches are generally available, as two opposite ways of addressing the core obstacle represented by anatomical variability. The first one consists in warping all the subjects to a common reference space and using ROIs defined from a brain atlas (*see Note 2*). The other one consists in delineating ROIs individually in every subject, for example, using segmentation algorithms. Countless methods are able to perform automatic or semiautomatic segmentation of an exhaustive variety of brain structures, which may then be used as ROIs on any individual data. The following section gives a template of a standard ROI-based analysis workflow.

3.1.1 ROI-Based Analysis Using an Atlas

1. Coregister the image of interest (image modality, parametric map) with a structural image (3dT1w) for every subject.
2. Perform spatial normalization on every subject's 3dT1w, save the registration parameters, and calculate the inverse transformation. Select a brain atlas of ROIs in standard space matching the interest of the study and apply the *inverse* transformation to the brain atlas in order to warp the atlas to the subject's native space.
3. Alternatively to (2), select a segmentation method of a specific or a variety of structure(s) and run it on every subject's anatomy to obtain subject-matched ROIs.
4. Alternatively to (2) and (3), perform the spatial normalization and apply the parameters to the image of interest to match it to the atlas in the standard space.
5. Extract numerical features from every ROI over every image of interest in the subject's native space.
6. Perform statistical analyses on these features.

3.1.2 Alternatives

It is possible also to perform shape and other geometrical property analyses of regions themselves, not on their content [18].

3.2 Voxel-Based Morphology (VBM)

Prior to statistical analysis, images should be processed to normalize their intensity (tissue segmentation) and morphometry (spatial normalization) and to ensure parametric statistics could be applied

(smoothing). Pre-processing steps are slightly different for cross-sectional and longitudinal studies.

3.2.1 Cross-Sectional VBM Processing Pipeline

1. Segmentation of 3dT1w image in tissues: Gray matter (GM), white matter (WM), and cerebrospinal fluid (CSF) maps, and, optionally, others.
2. Spatial normalization of tissue maps.
3. Normalized maps are multiplied by the Jacobian determinant of the spatial normalization (modulation), which encodes the differences of volume on the original images as differences on intensity on normalized images.
4. Smoothing images by convolution with a Gaussian kernel. The standard range of size of the kernel is 6–12 mm FWHM (full width at half maximum).

3.2.2 Longitudinal Studies Processing Pipeline

1. Linear and nonlinear registration of pre and post images. Linear registration helps nonlinear registration to converge. Nonlinear registration results in the pre-post average, Jacobian determinant (JD) (or alternatively divergence of deformations) images.
2. Pre-post average images are segmented.
3. From GM, WM, and CSF maps, the subject's GM/WM mask (depending on the tissue in study) is obtained by selecting those voxels whose probability of belonging to GM/WM is bigger to the probability of being part of any other tissue.
4. GM/WM mask are applied to JD map.
5. Spatial normalization of average images is performed. The modulation of spatial normalization to template is not applied to avoid mixing cross and longitudinal effects.
6. Smoothing of normalized JD images with a 6–12 mm FWHM Gaussian Kernel.

3.2.3 Getting Statistical Mappings

Once preprocessed, the proper statistical test to accept or reject the hypothesis in study is performed voxel by voxel (Fig. 4a) resulting in a statistical parametric map (T or F value for all the voxels on analysis). After choosing a statistical criterion to determine what difference is considered as significant (Fig. 4b), surviving voxels can be overlaid to an anatomical template or an anatomically labeled atlas to report the affected regions (Fig. 4c). It is important to note the high risk of false positives, due to massive number of analyses, and the way to deal with it.

3.2.4 Alternatives

There are several other alternative analyses of 3dT1w images, for instance, cortical thickness analysis [19], shape analysis of substructures [18, 20], analysis of sulci [21] or machine learning, and other multivariate methods [22, 23].

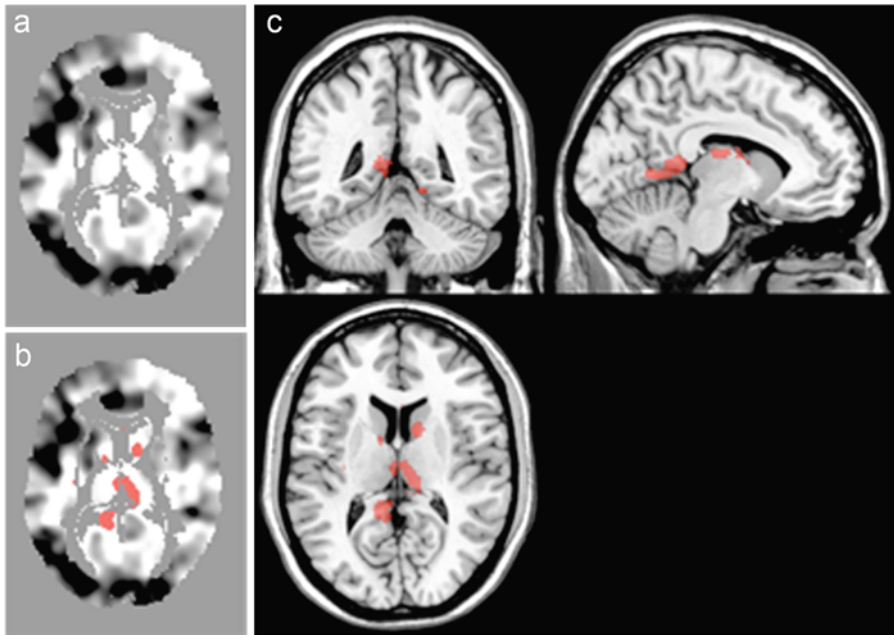


Fig. 4 Statistical parametric map of a voxel-wise T-test (T-value of the T-test performed voxel by voxel) (a), significant voxels in red (T-value over the statistical threshold of significance) (b) and overlaid of significant areas over a 3dT1w image as reference (c)

3.3 Parametric Diffusion Tensor Imaging (DTI) Analysis

The typical workflow includes the processing in parallel of DTI data and 3dT1w images. 3dT1w images provide structural anatomical resolution at a higher resolution than DTI and therefore are used both for intersubject normalization and by some methods to guide the processing of DTI data. Yet, some integrated software solutions, for example, Tract-Based Spatial Statistics (TBSS) from FSL toolbox, drive the intersubject spatial matching based on pure DTI data and rely on no other modality. In particular, this approach applies nonlinear registration across subjects on diffusion data and then perform a group-level analysis along skeletons modeling the main fiber tracts [24].

3.3.1 Preprocessing and Generation of Parametric Maps from DTI Data

1. Apply denoising algorithm on both the 3dT1w and the DTI data, for example, a nonlocal means (NL-means) Rician denoising method on all DTI and 3dT1w to increase image quality.
2. Apply bias correction on 3dT1w.
3. Apply eddy current correction to adjust the DTI data for distortion and motion using affine registration to the non-weighted diffusion volume (B_0 map).
4. Run model estimation on corrected DTI data. This will generate red-green-blue (RGB) color-coded maps showing diffusion

local directions as well as maps of the first eigenvalues of every local model.

5. Generate parametric maps MD, FA, RD, and AD obtained from the local combination of the various eigenvalues.

3.3.2 Spatial Normalization Through Anatomical Images and Statistical Analyses

The following part of the workflow warps every subject into a normalized space to then allow an exploratory whole-brain voxel-level group analysis. Anatomical normalization is applied to all subjects' anatomical data (e.g., 3dT1w). This solves the core problem of localization [25] and spatial correspondence between subjects at the cost of geometric distortion. A number of reference templates or atlases are available. Selecting the right one amounts to finding the most representative of the population under study, for example, in the context of the ageing brain [14]. As a result of this step combined by the previous one, DTI data undergo a two-step transformation, first from native DTI space to the subject's 3dT1w space and then from the subject's 3dT1w space to reference space (*see* Subheading 3.2 for this last step).

1. Perform a segmentation task to extract the brain mask out from the b0 image.
2. Perform a segmentation task to extract a mask of the white matter from the b0 image.
3. Repeat these two operations on the 3dT1w to get a brain mask and a white matter mask map from 3dT1w.
4. Apply coregistration from the b0-image white matter mask to the 3dT1w white matter mask and save registration parameters.
5. Apply transformation to every parametric map using these same registration parameters in order to warp it to the 3dT1w space.
6. Normalize 3dT1w as described in Subheading 3.2 and apply the transformation to DTI maps.
7. Standard ROI-based analyses are applicable from this step on. It is also possible to run a voxel-based statistical analysis on every set of smoothed normalized parametric maps (FA, MD, RD, AD), for example, based on general linear models using the standard Statistical Parametric Mapping software for neuroimaging.

3.4 Structural Connectivity

Structural connectivity between cortical areas and subcortical structures can be represented as a non-oriented graph made of nodes (i.e., the whole set of areas and structures) and edges (i.e., connections, or the absence thereof, between two areas/structures) with a weight measuring the strength of connection (i.e., in numbers of fibers) between any two nodes. Such a graph has an equivalent matrix representation, called adjacency matrix in graph theory, and connectivity matrix in the neuroimaging context (Fig. 5).

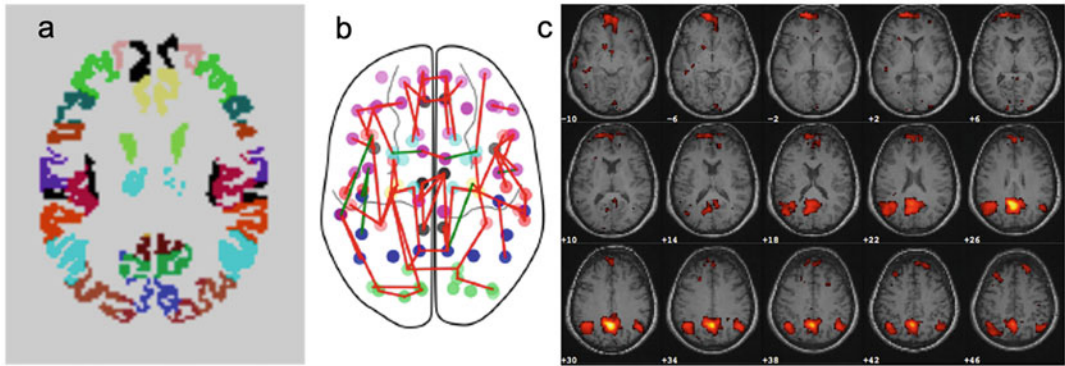


Fig. 5 Atlas adapted to the subject's anatomy (a), structural connectivity graph (b) and map of regions correlated with precuneus in a resting-state functional connectivity study (c)

The first step consists in generating parametric maps, which was described in section Parametric DTI analysis. In this context actually, parametric maps are essentially used for quality assurance purposes after the preprocessing steps. The following pipeline describes how to achieve a structural connectivity analysis using tractography and automatic segmentation of anatomical structures:

1. Generate parametric maps (FA maps in particular) for every subject in their native DTI space, following section *Parametric DTI analysis*.
2. Visually inspect FA and RGB maps for quality control. This step is crucial to ensure the right orientations of the fibers and possibly spot errors in the gradients used for the modeling. It is especially recommended to check for any possible axis swap from one subject to another.
3. Run anatomical segmentation pipeline on every subject's anatomy. Maps of the interface between gray and white matter (GM maps) and/or CSF are generally helpful to create constraints and boundaries for the tractography. A large variety of algorithmic tools provide such representations as segmentation maps or triangulated meshes. Besides, any other segmented structure may be used as a *seed* by the tractography step. Such seeds correspond to ROIs from/to which the streamlines will start/end, be either cortical or subcortical structures. The resulting information about structural connectivity hence depends on the definition of such cortical or subcortical ROIs to be taken as nodes of the connectome.
4. Check the quality of the resulting segmentation maps by overlaying these over the subject's anatomy.
5. Warp the segmentation maps (GM, CSF, and *seeds*) to the subject's DTI space using the same 3dT1w-to-b0 image

coregistration parameters estimated during the prior generation of parametric maps (Fig. 5a).

6. Run the tractography step taking the segmentation map as *seed map* to generate both the streamline tracks and the connectivity matrix. Provide GM and CSF masks as constraints to guide the process (fibers do not cross the ventricles or sulci) (Fig. 5b).
7. Estimate a connectivity matrix with respect to the ROIs used as *seeds*, measuring the number of existing connecting fibers for each pair. According to the study and the corresponding ROIs, the matrix hence describes cortico-cortical and/or cortico-subcortical connections. It may be symmetrical, of size the number of seed regions: in this case, each row/column would give the estimated numbers of connections from every seed to any other.
8. Perform statistical analysis on the connectivity matrices. Statistical analysis can be performed at the group level over the entire set of matrices once estimated for every subject. It is important to check for normality in order to properly apply parametric or nonparametric statistical tests.

3.5 Functional Connectivity (fMRI)

fMRI pre-processing pipeline is different in fMRI and rs-fMRI studies. fMRI requires a model of the expected activation pattern (task/stimulus onset and duration convolved with the HRF) and to check, voxel by voxel, if temporal variations of intensity are independent (random/physiological) or related to the task. rs-fMRI looks for inter-region correlations of the spurious activity of the brain when no specific task is performed.

3.5.1 Processing fMRI

1. If available, BOLD images are corrected for EPI distortions.
2. The set of fMRI-volumes are aligned to correct for involuntary small movements during the acquisition. The mean image of the fMRI series is created.
3. Mean fMRI image is registered to structural anatomical image 3dT1w, and the transformation is applied to the rest of volumes.
4. 3dT1w images are spatially normalized to a standard template (mainly in MNI stereotactic space) using affine and non-affine transformations. fMRI images are spatially normalized by applying the transformation calculated during the 3dT1w spatial normalization
5. fMRI images are smoothed with a Gaussian filter (6–12 mm FWHM kernel),
6. GLM statistical analyses are performed to check voxel by voxel if its temporal evolution is related to the model. That results in a statistical parametric mapping (T-value voxel a voxel) that

provides activated areas once a proper statistical threshold is applied.

3.5.2 Processing of rs-fMRI

It is not as fixed as in fMRI. Depending on the images characteristics and the posterior statistical analyses to be performed, it could be convenient to add, suppress, or change the order of the steps to get more reliable results. Next, a standard pipeline is shown

1. Slice-timing correction (*see Note 3*).
2. Correction for EPI distortions, realign of time series, register to 3dT1w and spatially normalization, as done in fMRI.
3. Detection of outliers, bad volumes, or dark slices, due to sudden movements of the subject during the exploration (e.g., due to cough).
4. Detrending the time series (up to third-order polynomials) to flattener the baseline and to make next step more efficient.
5. Regress out the mean WM and CSF signal, the values obtained in the realign procedure (three rotations and three translations for each volume to correct for involuntary head movements during the scanning time), the mean value of the image (optional), and the nulling regressors to avoid the effect of the outliers [26].
6. Smoothing of images with a Gaussian Kernel of 8–12 mm (FWHM).
7. Band-pass filtering images to remove nonrelevant intensity variations. The frequencies of interest, from the physiological point of view, are in the range of 0.1–0.01 Hz. Each study can use customized cutoff frequencies to select the appropriate information to answer specific questions.
8. Voxel-based analysis of functional connectivity, that is, determination of functional networks of areas of the brain working conjointly, requires the selection of the area (ROI) whose functional connectivity is investigated, to take the mean value of the image and evaluate the correlation, voxel by voxel, and the correlation of its time series with the ROI time series (first order analysis, seed-based connectivity) (Fig. 5c).

3.5.3 Second-Order Statistics, Group Comparison

Both fMRI and seed-based functional connectivity studies allow a second-order analysis to determine differences of statistical maps between groups. The main second-order analysis is the random effects analysis (RFX) (*see Note 4*).

3.5.4 Functional Connectivity

Alternatively, GM can be parceled as described previously. Then, the correlation of the temporal series of each ROI with the rest of ROI's time series will result in a functional connectivity matrix for each subject [27]. Fisher transformation is used to convert

correlation coefficients to z-scores to make possible the parametric statistical analysis of functional connectivity matrices between groups (*see Note 5*).

3.5.5 Alternatives

There are alternatives to fMRI analyses, mainly the free-model multivariate analyses such as principal component analysis (PCA) and independent component analysis (ICA). Functional connectivity can be also assessed by alternative analyses such as matching learning or neural networks methods [28].

3.6 Conclusions

Neuroimaging techniques are increasingly being used in scientific areas (epidemiology, population genetics, etc.) other than the traditional research fields where neuroimaging used to play a central role (neurology, psychiatry, neuroscience, etc.). Noteworthy, these research fields are characterized by conducting research with much higher sample sizes. This has fostered the interest in neuroimaging-derived outcome variables, neuroimaging modalities, and analytical methods. It has also spurred the development of technological solutions for acquiring, storing, transferring, analyzing, and sharing large neuroimaging datasets. Neuroimaging analysis is a highly “technified” field with analytical tools and software suites that have been developed and used for decades, which have created their own scientific environments and user communities. It falls beyond the scope of this text to recommend any of the publicly available tools for a particular application or to perform a detailed analysis of their characteristics. On the other hand, we intended to present and describe the most common image processing tools and pipelines for investigators from outside the neuroimaging field to better understand the way images are processed and analyzed and common pitfalls and limitations in neuroimaging analyses.

In this regard, we would like to put the emphasis on three aspects: (1) knowing what the “hidden” algorithms do is critical for the correct interpretation of the results, (2) quality control of the images is mandatory, and (3) pitfalls and limitations in the statistical analysis of neuroimages.

It is necessary to have an intimate understanding the image processing tools in order to correctly interpret the results of a neuroimaging analysis. Even though the neuroimaging software tools are progressively easier to use, the implications of the technical underpinnings of the underlying algorithms are critical for correctly interpreting the results. For this reason, we intentionally avoided to take one particular neuroimaging analysis suite and provide step-by-step instructions to make typical analyses. Novel users may find several of these “recipes” online. On the other hand, we intended to present the rationale under some standard pipelines for novel users to better understand interpret neuroimaging results on their labs or on the literature. For instance, in VBM analyses, knowing whether images have been modulated to code for changes

in volume and whether the modulation takes into account global brain volume or it has to be regressed out in the design matrix or the way variance is partitioned in an SPM design matrix where columns are orthogonalized to the previous ones are common examples that have triggered endless discussions, even among experts. All the major neuroimaging platforms have supporting forums that gather users and developers. In case of doubt, it is strongly recommended to consult these forums. Even in the event of not having any concerns on a particular study, regular consultation of these forums may help identifying pitfalls in our own analyses.

State-of-the-art automatic imaging processing tools are highly robust and refined. However, users have to be aware that there is no guarantee that the result of the processing will be of sufficient quality for the ensuing analysis. Therefore, quality control of the raw and intermediate images is mandatory. Unfortunately, quality control have not received the same amount of attention as the development of novel analytical or processing tools. Development of aids to streamline the quality control of the images and the adoption of common quality control standards are impending needs to improve the reproducibility of neuroimaging results. Examples in the good direction are quantitative quality control tools and metrics developed for monitoring raw images on the XNAT platform (<http://cbs.fas.harvard.edu/science/core-facilities/neuroimaging/information-investigators/qc>) or, for processed images, the Quality Assessment (QA) tool in the Computational Anatomy Toolbox for SPM (<http://www.neuro.uni-jena.de/cat/index.html#QA>).

Of course, a preliminary consideration is the detection of incidental findings that may constitute exclusion criteria for the study or compromise the correct processing or analysis of the image. Depending on the age, the acquired image modalities, and other clinical characteristics of the study participants, a significant percentage of incidental findings have been reported in the literature even when scanning asymptomatic individuals and up to 15% of them may actually require referral for clinical follow-up [29]. In this regard, neuroradiological review of all the images should be mandatory, but unfortunately, it is not as commonly performed for research studies, as it probably should.

Finally, voxel-wise statistical analysis of neuroimages present with some limitations that are important to bear in mind for interpreting our own results or those in the literature. The most notorious pitfall is the multiple comparisons problem. Typically, an unbiased, whole-brain voxel-wise analysis simultaneously tests hundreds of thousands of voxels. In this scenario, the probability of detecting some false positives is almost certain. However, some features in the images alleviate this situation. First, neighboring voxels present with very similar information that originally stem

from the inherent limitation the spatial extent of the homologies that can be established between the brain anatomies of different individuals. Based on this assumption, spatial normalization algorithms implement regularization terms that penalize gross fine-detail deformations, and smoothing algorithms are applied to remove high spatial frequency noise while not affecting the signal to the same extent. The correlation observed among neighboring voxels makes the Bonferroni correction far too conservative for neuroimaging analyses, and several methods have been developed to estimate the actual number of independent observations in the images, taking into account the cumulative effect of all preprocessing steps. Please note that the degree of smoothing in the preprocessing step will have a critical impact on this estimation and, hence, on the corrected p-value of the analysis. Larger smoothing kernels result in more significant corrected p-values at the cost of decreased sensitivity to detect small-localized effects. Therefore, a trade-off between statistical power and the spatial resolution of the analysis is inherently being performed. However, even though the impact on the expected number of false positives under the null hypothesis is estimated by the multiple comparison correction, the loss of sensitivity to detect regionally small effects is only controlled indirectly through the size of the smoothing kernel as no Type-II error (false-negative) estimation is performed. In addition, it is typical to establish a minimum cluster size in order for a positive result to be considered as significant. Several of these strategies have been put into question recently [30], but it must be noted that the major neuroimaging analysis suites have improved their methods accordingly. Some of them implement Monte-Carlo permutation strategies that minimize the assumptions in the correction for multiple comparisons.

Other general statistical considerations are also prominent sources of worry in the analyses of neuroimages: dealing with outliers, overfitting, highly correlated predictor variables, the impact of the order of their inclusion, and the way that different software packages deal with this situation. In this regard, it must be noted that neuroimaging analysis packages are generally not equipped with diagnostic tools to neither check the validity of the statistical assumptions nor implement nonparametric alternatives in the event that these are not met in certain cases. They do not include either tools to estimate the attained statistical power of the analysis.

In conclusion, neuroimaging analysis suites provide with an armory of state-of-the-art tools to render high-quality and reliable data and analyses. Their continuous development and testing by thousands of researches over the last decades result in extremely robust open-source algorithms and highly specialized user communities that welcome and are eager to help novel users. In addition, the standardization of the major processing steps, analytical criteria, and even algorithmic implementations has a positive impact on the

comparability of different studies. Since the analysis can be scripted, source data and analytical methods can be stored for future reference or shared with the community for additional analyses and meta-analyses. Together with publicly available datasets, enabling the access of proprietary data together with the batch codes used for attaining published results greatly contributes to enhance the reproducibility of neuroimaging research. No particular analytical platform or algorithm can be regarded as superior to the rest in general terms, and comparison studies are required to rationally selecting one implementation for a particular application. Overall, users should be aware of the implications and limitations of the different processing and analysis options for a correct interpretation of their own results and that of the existing literature.

4 Notes

1. Tractography techniques produce streamlines paths that model anatomical tracts found in the white matter. The validation of these (millions of) streamlines is a tough problem due to factors such as the difficult access to ground truth or some complex patterns, for example, fanning and crossing fibers. White matter tractography is generally done either with a method known as “deterministic” tractography or with a “probabilistic” method. Advantages of the probabilistic method include the ability to explicitly represent uncertainty in the data and a higher reliable reconstruction of crossing fibers at higher computational costs [31]. In both approaches, prior knowledge of the anatomy of fiber tracts is important for distinguishing between fiber tracts of interest and streamline tracks that follow improbable routes or suggest nonexistent connections between brain areas.
2. In this context, *brain atlases* come into play to provide a set of ROIs that cover the brain volume. However, an atlas provides regions that generally account for a certain state of the current knowledge, while the targeted effect of the study might not fit the grain of the atlas ROIs. Moreover, an atlas is constructed and used to represent a certain population, therefore possibly failing at capturing individual anatomical traits. The most widely used atlas is AAL [32].
3. Statistical analyses require each volume to be scanned at once, in the same time point. However, slices are acquired sequentially and in an interleaved way. Slices-timing correction uses temporal interpolation to guess the slice intensity as it was acquired at the same time of a reference slice. It is necessary to know the order of slice acquisition beforehand.

4. RFX performs a voxel by voxel analyses on contrast images (difference of intensity among rest and activation in fMRI and degree of correlation in rs-fMRI) with the hypothesis that, if the difference in a voxel is random (false positive), it would not appear in the other subjects, and the mean value among subjects should tend to zero. If the mean value of the contrast in one voxel is significantly different of zero, it can be concluded that there is an effect of interest. The surrounding hypothesis is that all subjects use the same network (strategy) to perform the cognitive task. It is fundamental a good experiment design to ensure that happens.
5. It is important to note that both signal and noise can be correlated. Image artifacts can derive in great correlations values that don't reveal real functional connectivity. A good quality assurance of rs-fMRI images is mandatory to get reliable functional matrices [33, 34].

References

1. Balasa M, Sánchez-Valle R, Antonell A et al (2014) Usefulness of biomarkers in the diagnosis and prognosis of early-onset cognitive impairment. *J Alzheimers Dis* 40:919–927. <https://doi.org/10.3233/JAD-132195>
2. Molinuevo JL, Gispert JD, Dubois B et al (2013) The AD-CSF-index discriminates Alzheimer's disease patients from healthy controls: a validation study. *J Alzheimers Dis* 36:67–77. <https://doi.org/10.3233/JAD-130203>
3. Struyfs H, Molinuevo JL, Martin J-J et al (2014) Validation of the AD-CSF-index in autopsy-confirmed Alzheimer's disease patients and healthy controls. *J Alzheimers Dis* 41:903–909. <https://doi.org/10.3233/JAD-131085>
4. Gispert JD, Rami L, Sánchez-Benavides G et al (2015) Nonlinear cerebral atrophy patterns across the Alzheimer's disease continuum: impact of APOE4 genotype. *Neurobiol Aging* 36:2687–2701. <https://doi.org/10.1016/j.neurobiolaging.2015.06.027>
5. Gispert JD, Monté GC, Suárez-Calvet M et al (2017) The APOE ε4 genotype modulates CSF YKL-40 levels and their structural brain correlates in the continuum of Alzheimer's disease but not those of sTREM2. *Alzheimer's Dement: Diagn Assess Dis Monit* 6:50–59. <https://doi.org/10.1016/j.dadm.2016.12.002>
6. Gispert JD, Suárez-Calvet M, Monté GC et al (2016) Cerebrospinal fluid sTREM2 levels are associated with gray matter volume increases and reduced diffusivity in early Alzheimer's disease. *Alzheimers Dement* 12:1259–1272. <https://doi.org/10.1016/j.jalz.2016.06.005>
7. Friston K, Ashburner J (1994) Statistical parametric mapping. *Funct Neuroimaging Tech Found* 1–74
8. Mazziotta JC, Toga AW (2002) *Brain mapping: the methods*. Academic Press
9. Toga AW, Mazziotta JC (2000) *Brain mapping: the systems*, volume 2. Academic Press
10. Stark DD, Bradley WG (1999) *Magnetic Resonance Imaging*. Mosby
11. Bernstein MA, King KE, Zhou XJ, Fong W (2005) Handbook of MRI pulse sequences. *Med Phys* 10(1118/1):1904597
12. Hutton C, Bork A, Josephs O et al (2002) Image distortion correction in fMRI: a quantitative evaluation. *NeuroImage* 16:217–240. <https://doi.org/10.1006/nimg.2001.1054>
13. Mangin JF, Rivière D, Cachia A et al (2004) Object-based morphometry of the cerebral cortex. *IEEE Trans Med Imaging* 23:968–982
14. Samanez-Larkin GR, D'Esposito M (2008) Group comparisons: imaging the aging brain. *Soc Cogn Affect Neurosci* 3:290–297. <https://doi.org/10.1093/scan/nsn029>
15. Klein A, Andersson J, Ardekani BA et al (2009) Evaluation of 14 nonlinear deformation algorithms applied to human brain MRI registration. *NeuroImage* 46:786–802. <https://doi.org/10.1016/j.neuroimage.2008.12.037>
16. Manjón JV, Coupé P, Concha L et al (2013) Diffusion weighted image denoising using

- overcomplete local PCA. *PLoS One* 8:e73021. <https://doi.org/10.1371/journal.pone.0073021>
17. Coupe P, Yger P, Prima S et al (2008) An optimized blockwise nonlocal means denoising filter for 3-D magnetic resonance images. *IEEE Trans Med Imaging* 27:425–441. <https://doi.org/10.1109/TMI.2007.906087>
 18. Scher AI, Xu Y, Korf ESC et al (2007) Hippocampal shape analysis in Alzheimer's disease: a population-based study. *NeuroImage* 36:8–18. <https://doi.org/10.1016/j.neuroimage.2006.12.036>
 19. Fischl B (2012) *FreeSurfer Neuroimage* 62: 774–781. <https://doi.org/10.1016/j.neuroimage.2012.01.021>
 20. Tondelli M, Wilcock GK, Nichelli P et al (2012) Structural MRI changes detectable up to ten years before clinical Alzheimer's disease. *Neurobiol Aging* 33:825.e25–825.e36. <https://doi.org/10.1016/j.neurobiolaging.2011.05.018>
 21. Rametti G, Junqué C, Bartrés-Faz D et al (2010) Anterior cingulate and paracingulate sulci morphology in patients with schizophrenia. *Schizophr Res* 121:66–74. <https://doi.org/10.1016/j.schres.2010.05.016>
 22. Habeck CG (2010) Basics of multivariate analysis in neuroimaging data. *J Vis Exp* 1–6. <https://doi.org/10.3791/1988>
 23. Ziegler G, Dahnke R, Gaser C (2012) Models of the aging brain structure and individual decline. *Front Neuroinform* 6:3. <https://doi.org/10.3389/fninf.2012.00003>
 24. Smith SM, Jenkinson M, Johansen-Berg H et al (2006) Tract-based spatial statistics: Voxelwise analysis of multi-subject diffusion data. *NeuroImage* 31:1487–1505. <https://doi.org/10.1016/j.neuroimage.2006.02.024>
 25. Devlin JT, Poldrack RA (2007) In praise of tedious anatomy. *NeuroImage* 37:1033–1041. <https://doi.org/10.1016/j.neuroimage.2006.09.055>
 26. Lemieux L, Salek-Haddadi A, Lund TE et al (2007) Modelling large motion events in fMRI studies of patients with epilepsy. *Magn Reson Imaging* 25:894–901. <https://doi.org/10.1016/j.mri.2007.03.009>
 27. Van Dijk KRA, Hedden T, Venkataraman A et al (2010) Intrinsic functional connectivity as a tool for human connectomics: theory, properties, and optimization. *J Neurophysiol* 103:297–321. <https://doi.org/10.1152/jn.00783.2009>
 28. Mourão-Miranda J, Bokde ALW, Born C et al (2005) Classifying brain states and determining the discriminating activation patterns: support vector machine on functional MRI data. *NeuroImage* 28:980–995. <https://doi.org/10.1016/j.neuroimage.2005.06.070>
 29. Brugulat-Serrat A, Rojas S, Bargalló N et al (2017) Incidental findings on brain MRI of cognitively normal first-degree descendants of patients with Alzheimer's disease: a cross-sectional analysis from the ALFA (Alzheimer and Families) project. *BMJ Open* 7:e013215. <https://doi.org/10.1136/bmjopen-2016-013215>
 30. Eklund A, Nichols TE, Knutsson H (2016) Cluster failure: why fMRI inferences for spatial extent have inflated false-positive rates. *Proc Natl Acad Sci U S A* 113:7900–7905. <https://doi.org/10.1073/pnas.1602413113>
 31. Hagler DJ, Ahmadi ME, Kuperman J et al (2009) Automated white-matter tractography using a probabilistic diffusion tensor atlas: application to temporal lobe epilepsy. *Hum Brain Mapp* 30:1535–1547. <https://doi.org/10.1002/hbm.20619>
 32. Tzourio-Mazoyer N, Landeau B, Papathanassiou D et al (2002) Automated anatomical labeling of activations in SPM using a macroscopic anatomical parcellation of the MNI MRI single-subject brain. *NeuroImage* 15:273–289. <https://doi.org/10.1006/nimg.2001.0978>
 33. van Dijk KRA, Sabuncu MR, Buckner RL (2012) The influence of head motion on intrinsic functional connectivity MRI. *NeuroImage* 59:431–438. <https://doi.org/10.1016/j.neuroimage.2011.07.044>
 34. Cole DM et al (2010) Advances and pitfalls in the analysis and interpretation of resting-state FMRI data. *Front Syst Neurosci* 4:1459. <https://doi.org/10.3389/fnsys.2010.00008>

Part IV

Molecular Imaging Approaches



Amyloid PET Imaging: Standard Procedures and Semiquantification

Francesca D'Amico, Luca Sofia, Matteo Bauckneht, and Silvia Morbelli

Abstract

Amyloid plaques are a neuropathologic hallmark of Alzheimer's disease (AD), which can be imaged through positron emission tomography (PET) technology using radiopharmaceuticals that selectively bind to the fibrillar aggregates of amyloid- β plaques (Amy-PET). Several radiotracers for amyloid PET have been validated (^{11}C -Pittsburgh compound B and the ^{18}F -labeled compounds such as ^{18}F -florbetaben, ^{18}F -florbetapir, and ^{18}F -flutemetamol). Images can be interpreted by means of visual/qualitative, semi-quantitative, and quantitative criteria. Here, we summarize the main differences between the available radiotracers for Amy-PET, the proposed interpretation criteria, and main proposed quantification methods.

Key words Amyloid PET, Biomarkers, Alzheimer's disease, Early perfusion amyloid PET imaging, Centiloids

1 Introduction

Over the past two decades, one of the major breakthroughs for the approach to Alzheimer's disease (AD) patients both in the clinical and research settings has been represented by the validation of diagnostic biomarkers able to demonstrate the presence of pathological mechanisms of AD and to predict further cognitive decline and dementia onset since the stage of mild cognitive impairment (MCI) [1, 2]. In this setting, amyloidosis biomarkers are able to identify the molecular/neuropathological feature of AD. In the present clinical setting, this class of biomarkers includes cerebrospinal fluid (CSF) amyloid- β_{1-42} reduction and brain amyloid accumulation as imaged through PET technology using radiopharmaceuticals that selectively bind to the fibrillar aggregates of amyloid- β plaques (AMY-PET) [2]. In the last ten years, pathological validity and potential clinical usefulness of AMY-PET have been repeatedly reported, and its use has entered the clinical routine in many European countries [3]. At the moment, amyloid PET can be

considered a second biomarkers with respect to CSF biomarkers. In more recent years, blood-based biomarkers have also been developed, and in the research setting, they have demonstrated to be useful to identify the core pathologies in Alzheimer's disease, such as amyloid- β and phosphorylated tau (p-tau) deposition second biomarker [4]. When blood biomarkers will be available in the clinical settings, they might serve as first biomarker in the flowchart for the etiological diagnosis of AD. In this regard, AMY-PET might again serve as second biomarker in case of inconclusive results [5]. Similarly, there's an emerging role of AMY (and TAU) PET technology in clinical trials, and this role might affect the use of AMY-PET once disease-modifying drugs will be approved for clinical use also in Europe [6, 7]. For both, these emerging role of AMY-PET, interpretation criteria, and signal quantification might be even more crucial that for the present "diagnosis-oriented" use (based on visual qualitative criteria). Accordingly, in this second edition of the present chapter, we will more deeply discuss on semiquantification methods for AMY-PET reading and reporting [8, 9].

2 Materials

Several radiotracers for amyloid PET have been investigated. The largest body of evidence was originally available for ^{11}C -Pittsburgh compound B (PiB). In the last decade, several lines of evidence have been made available also on the ^{18}F -labeled compounds for amyloid PET imaging [10]. In fact, three fluorinated tracers, ^{18}F -florbetaben (NeuraCeq), ^{18}F -florbetapir (Amyvid), and ^{18}F -flutemetamol (Vizamyl), have been approved by both the United States and the European authorities [10]. Although these tracers share a common imaging target and similar imaging characteristics, A β radiopharmaceuticals differ in their tracer kinetics, target-to-background ratio, and specific binding ratios. These differences impact on recommended imaging parameters such as injected doses, uptake time after tracer administration, and scan durations (details are reported in Table 1).

2.1 Patients' Preparation and Tracer Injection

1. There is no known evidence of drug interactions between amyloid radiotracers and common drugs prescribed for dementia patients.
2. No drug withdrawal is recommended, except for anti-A β antibodies administered in the context of experimental studies.
3. No rest condition is needed before the tracer injection. For patients requiring sedation, ^{18}F -labeled radiopharmaceuticals should be injected before the administration of sedation to

Table 1
Recommended dose, uptake time, and scan duration for Amyloid PET tracers

Tracer	Recommended dose (MBq)	Uptake time (minutes)	Scan duration (minutes)
[18F]F-Florbetaben	300	90	20
[18F]F-Florbetapir	370	30–50	10
[18F]F-Flutemetamol	185	90	20

minimize any theoretic effects of sedatives on cerebral blood flow and radiotracer delivery.

4. The dose must be assayed in a suitable calibrator before administration. Tracers must be injected using aseptic technique through a short intravenous catheter (approximately 4 cm/1.5 in or less, to minimize the potential for adsorption of substantial amounts of the drug to the catheter) in a single intravenous bolus in a total volume of 10 mL or less, followed by the injection with an intravenous flush of 0.9% sterile sodium chloride solution. The injection site should be routinely inspected for dose infiltration.

2.2 Scan Acquisition

1. After a delay depending on the injected radiotracer, the scan acquisition time usually lasts 10–20 min (*see* Table 1).
2. Images should be acquired in three-dimensional mode with appropriate data corrections and reconstructed using attenuation correction with typical trans-axial pixel sizes of 2–3 mm and a slice thickness of 2–4 mm. A dynamic scan can also be performed, lasting 60 or 90 min from the time of injection in order to calculate binding and to provide a distribution volume ratio.

2.3 Early Perfusion Amyloid PET and Dual Point Dynamic Imaging

Several studies has shown that the early time frames of dynamic PIB PET (as well as of the fluorinated AMY-PET tracers) are closely related to the first-pass influx rate (KI), which is strongly correlated to cerebral blood flow (CBF) because of a high extraction fraction of lipophilic radiotracers into the brain. In this regard, a “dual-phase brain PET” might be performed through the acquisition of a short image lasting around 5 min immediately after injection, providing information on CBF. This acquisition will be followed by the late “standard” acquisition at equilibrium. Indeed, it is well known that regional cerebral perfusion is coupled to cerebral metabolism, which, on turn, is coupled with synaptic function [11, 12]. Accordingly, early phase amyloid PET imaging can act as a surrogate for ¹⁸F-FDG-PET imaging, thus providing information on neurodegeneration [13]. This approach is certainly of great

interest and potentially cost-effective. However, large-scale validation studies are needed in order to validate and allow the introduction of this approach into the routine clinical practice (which at the moment still represent an off label acquisition protocol). Finally, recently, new methods of semiquantification imply the use of early scans to provide semiquantitative metrics with innovative approaches (cfr. The time-delayed ratio. See the paragraph on semiquantification).

2.4 Dynamic Acquisition

While visual/qualitative and semiquantitative approaches have been implemented in the clinical setting for diagnostic purpose. More precise quantification methods can be suitable to fully capture the complexity of amyloid PET signal in the framework of longitudinal studies. In this regard, absolute quantification and parametric analysis of tracer uptake requires a dynamic acquisition. In fact, it has been shown that SUV ratio overestimates amyloid burden compared with quantitative non-displaceable binding potential (BPND) [14, 15].

However, the long standard time duration of a dynamic acquisition (up to 90 min) may result in lower patient comfort and lesser efficient use of both scanner and tracer batch, in addition to an increased risk of motion artifacts.

Recent studies aimed to evaluate the reliability of shorter duration dynamic acquisitions [16] or dual point dynamic imaging [17]. The latter consists in a dual-time-window protocol (also called “coffee-break” protocol) in which data are acquired separately for early (0–30 min post injection) and late phases (90–110 min).

2.5 A β Radiotracers

2.5.1 ^{11}C -PiB

PiB is a derivative of a fluorescent amyloid dye, thioflavin T, and has been shown to possess high affinity and high specificity for fibrillar A β in plaques and in other A β containing lesions. PiB also displays a much lower affinity toward other misfolded proteins with a similar-sheet secondary structure such as α -synuclein and tau [18]. However, the 20-min radioactive decay half-life of ^{11}C limits the use of ^{11}C -PiB to centers with an on-site cyclotron and ^{11}C radiochemistry expertise, making routine clinical use very expensive.

2.5.2 ^{18}F -Florbetaben

^{18}F -florbetaben (^{18}F -AV-1, ^{18}F -BAY-94-9172, Neuraceq®) binds with high affinity to A β in plaques and cerebral amyloid angiopathy in postmortem brain tissue sections with lack of binding to Lewy bodies or NFT at low nanomolar concentrations [19]. It received Food and Drug Administration (FDA) and European Medicines Agency (EMA) approval for clinical use in February/March 2014.

2.5.3 ^{18}F -Florbetapir

^{18}F -florbetapir (^{18}F -AV-45, Amyvid®) is a stilbene derivative, developed by Avid Radiopharmaceuticals (a wholly owned subsidiary of Lilly). Initial in vitro evaluation showed binding to A β

plaques in AD brain sections [20]. ^{18}F -Florbetapir was the first radiotracer—and the first ^{18}F labeled radiotracer approved by FDG—approved by FDA in April 2012 and EMA in January 2013. Florbetapir is characterized by its rapid reversible binding characteristics allowing scanning at just 30–50 min after injection, similar to ^{11}C -PiB [20].

2.5.4 ^{18}F -Flutemetamol

^{18}F -flutemetamol (GE-067, Vizamy®) is a fluoro derivative of ^{11}C -PiB developed by GE Healthcare. ^{18}F -flutemetamol brain retention is highly correlated with ^{11}C -PiB and with A β burden as measured immunohistochemical assessment of brain biopsy tissue [21]. ^{18}F -flutemetamol received FDA approval in October 2013 and EMA approval in September 2014.

3 Methods

After the tracer is injected in the patient, it rapidly enters the brain by passive diffusion through the blood–brain barrier and reaches the sites of interest in a time-interval mainly from the bloodstream. The lipophilic nature of the tracer, combined with a high lipid content in the white matter, leads to a nonspecific binding in brain white matter. By contrast, the high affinity binding to the amyloid fibrils results in a significantly slower clearance of the tracer bound to amyloid plaques in the gray matter [10]. Amyloid radiotracers have been compared *ex vivo* [18], finding that both the retention in the gray and white matter is slightly different for different ligands, whereas binding sites are substantially the same. This latter point ensures that all the radiopharmaceuticals may be used similarly and in reliable way to determine the density of cerebral amyloid plaques. In fact, the objective of AMY-PET image interpretation is to provide an estimate of the brain β -amyloid plaque density [10]. Accordingly, a positive AMY-PET scan identifies the presence of brain amyloidosis and not necessarily the presence of AD (the results but must be considered in the context of the person’s medical history, physical examination, and cognitive testing) [1, 2, 9, 10]. In fact, while all AMY-PET tracers have high affinity and selectively for β -amyloid plaques and not for other pathological proteins such as TAU pathology and alpha-synuclein deposits, the high affinity is paralleled by limited specificity for different amyloid type [1, 2, 9, 10, 22]. In fact, all AMY-PET tracers are able to bind classic (“AD-type”) neuritic plaques, diffuse extracellular plaques (nonspecific for AD) as well as vascular amyloid typical of cerebral amyloid angiopathy [6]. By contrast given the repeatedly proven high negative predictive value of AMY-PET imaging, a negative amyloid PET scan is able to identify among cognitive impaired patients, subjects unlikely to be affected by AD.

3.1 *Visual/ Qualitative Images Evaluation*

1. Specific in vitro studies have demonstrated that all AMY-PET tracers share similar binding to a nanomolar high affinity site, and thus, these amyloid ligands can be used in a comparable and reliable manner to assess brain amyloid density [18].
2. The specific criteria for amyloid PET image visual interpretation differ among available radiotracers, and qualitative evaluation of images acquired with a given amyloid tracer should be performed using the instructions provided by the manufacturers. Some general principles should be considered when interpreting AMY-PET scans [10]. A suitable image scaling should be employed: a 16-bit scale is recommended for image display [10]. For 18F-Florbetaben and 18F-Florbetapir, PET images should be displayed using gray scale and inverse gray scale, respectively, while color scales (such as “cool” or “spectrum”) are recommended for 18F-Flutemetamol. First evaluation should be in transversal orientation. Coronal and sagittal planes as well as PET/CT fused images can also be evaluated and can be of help especially to inspect specific brain regions (posterior cingulate in sagittal view) and to clarify doubtful cases in the presence of atrophy or noisy images. Visual criteria for 18F-Flutemetamol reading also include the inspection of the striatum (while this is not the case for all the other tracers). Image size should be optimized for a clear differentiation between nonspecific/physiologic white matter and pathologic gray matter uptake.
3. The cerebellar cortex is expected to be free of amyloid deposition even in subjects with cerebral cortical amyloid deposition. For this reason, white/gray matter contrast at cerebellar level is used as reference for 18F-Florbetapir scan evaluation. Conversely, the white matter maximum has been suggested as a reference for AMY-PET scan when 18F-Florbetaben is used, and for 18F-Flutemetamol, it is recommended to set the scale intensity to a level of about 90% in the pons region [10].
4. The typical appearance of a negative AMY-PET scans is nonspecific white matter uptake and little or no binding in the gray matter. Thus, negative scans have a clear gray/white matter contrast.
5. The evidence of radiotracer uptake extending to the edge of the cerebral cortex and forming a smooth, regular boundary reflects the presence of gray matter amyloidosis and thus a positive AMY-PET scan. Figure 1 shows the typical appearance of a negative (A) and a positive (B) AMY-PET scan.

3.2 *Semiquantitative Approaches*

Most amyloid-PET images are rather easily evaluated by a trained eye, and the reliability of amyloid PET binary reads across different sites has been demonstrated to be high even in the multicenter

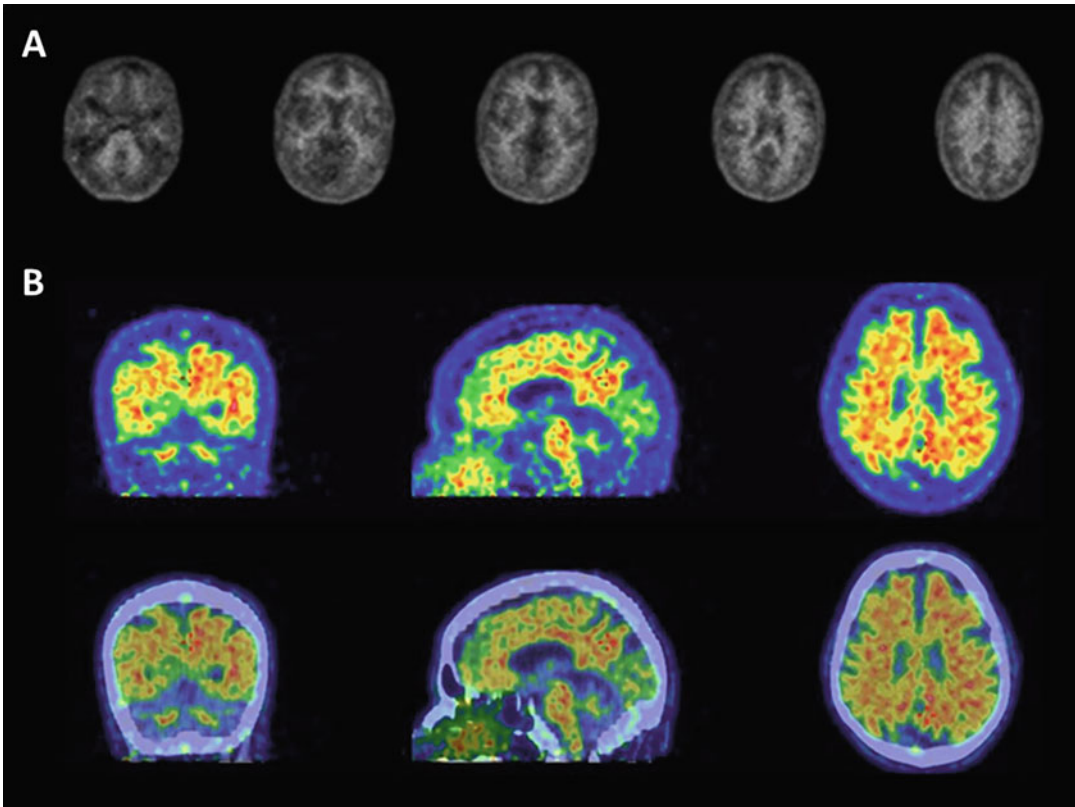


Fig. 1 Examples of positive and negative Amy PET scan. Panel (a) shows the typical appearance of a negative Amy PET scan acquired with 18F-Florbetaben in which the contrast between white and gray matter is well evident in all brain areas, as in the cerebellum. Conversely, panel (b) represents a positive scan acquired with 18F-Flutemetamol in which the radiotracer is widely distributed in all cortical areas (no contrast between white and gray matter uptake). Notably, in the lower panel (1b), a PET/CT-fused images are included. In these images, it is well evident that some small cortical regions (i.e., posterior cingulate in sagittal view), apparently characterized by preserved contrast between white and gray matter, are actually regions with more marked atrophy (low uptake corresponds to larger subarachnoideal component)

settings [23]. However, as amyloid-PET becomes a widespread tool, uncertain instances are going to be met more frequently. Accordingly, more sophisticated approaches has been proposed and extensively evaluated with the aim of providing semiquantification of AMY-PET data both regional and whole brain level.

1. Commercially semiquantification software are already available, and they generally rely on the numerical estimation of the Standardized Uptake Value ratio (SUVr) [23] or reference-based z-scores [24]. SUVr procedure calculates the ratio of PET counts between a number of target regions of interest (ROI) versus a reference one. ROI number, placement, and size vary among implementations, and they often require reader's feedback. SUVr was validated by histopathological studies

of density of neuritic amyloid- β plaques and compared with CSF results with good agreement [25]. Very few studies provided a head-to-head comparison of SUVR results and correspondent cutoffs in the same patients with all the AMY-PET tracers [26, 27]. Moreover SUVR values, and thus thresholds for discrimination between positive and negative scans, depend on the choice of the reference region (more often the cerebellum brain stem or cerebellar gray matter). In fact, the upper limit of normal binding varies per size and placement of cortical and reference regions of interest (generally between 1.3 and 1.6 for neocortical SUVR). On the other side, Z-scores represent the number of standard deviations from the mean of a reference or control group and are generally based on SUVR values. Published studies are based on scans classification threshold of $z = 2.0$ demonstrating high concordance with visual read and an autopsy cohort [22].

2. Centiloids: Given the use of different amyloid PET tracers both in clinical and research settings, intertracer standardization of the SUVR metric has become a clinical and research need (especially in multicenter collaborations). A working group has been formed within the Alzheimer's Imaging Consortium in 2012 with the aim of standardizing quantitative amyloid imaging measures by scaling the outcome of each particular analysis method or tracer to a 0–100 scale, anchored by young controls (≤ 45 years) and typical AD patients [8]. The units of this scale have been named "Centiloids." This approach aims to define "standard" method for analyzing PiB PET data and then a method for scaling any "nonstandard" method of Amy-PET analysis to the Centiloid scale. A key component of the optimal use of the Centiloid method is related to free access to all necessary data on a public database and all of the scan data used in this initial report that has been deposited on the Global Alzheimer's Association Information Network (GAAIN; <http://www.gaain.org>) for free public access. More recent studies validated the use of centiloids with the other amyloid tracers, such as florbetaben, flutemetamol, and florbetapir. Applying a common scale will thus aid in the diagnosis and prognosis of Alzheimer's disease (AD) and in monitoring anti-amyloid therapeutic interventions [28]. The most recent trials investigating the efficacy of anti-amyloid therapies, like the TRAILBLAZER-ALZ [7], use centiloids not only as inclusion criteria but also as a secondary outcome of efficacy. For example, in the abovementioned trial evaluating the use of donanemab versus placebo in early AD patients, only subjects with more than 37 centiloids were included. Longitudinal changes in the amyloid burden were evaluated with centiloids: patients were defined as amyloid-negative if centiloids were below

25, leading to a reduction of the drug doses. The therapy was switched to placebo if centiloids were below 11 in one scan or below 25 in two consecutive scans.

3. Other methods: Other methods have been proposed to overcome the difficulties of image reading and the possible shortcomings of the SUVr-based methods. A SUVr-Independent Evaluation of Brain Amyloidosis named Evaluation of Brain Amyloidosis (ELBA) has been developed to deliver a geometrical/intensity score to be used for ranking and dichotomic assessment [22]. ELBA does not rely on small, specific ROIs as it evaluates the whole brain and ELBA demonstrated to perform with area under the roc curve (AUC) = 0.997 versus the visual assessment. The longitudinal analysis estimated a test/retest error of 2.3%, and longitudinal analysis suggests that the ELBA method accurately ranks the brain amyloid burden [22]. TDr (time-delayed ratio) is based on tracer kinetics information. The TDr method requires two static scans per subject: one early (~ 0–10 min after the injection) and one late (typically 50–70 min or 90–100 min after the injection, depending on the tracer) [29]. High perfusion regions are delineated on the early scan and applied onto the late scan. A SUVr-like ratio is calculated between the average intensities in the high perfusion regions and the late scan hotspot. TDr requires minimal image processing; it is independent on predefined regions of interest and does not require MR registration. With the aim of increasing sensitivity for detecting change and therefore statistical power in clinical trials, the A β load metric was developed by Invicro (<https://invicro.com/casestudies/amyloid-load/>) as a novel approach to quantify global A β burden using [18F]florbetapir as the test ligand [30]. The A β load metric is then generated based on spatio-temporal modeling work as a linear combination of images: (i) nonspecific binding of the tracer and (ii) “A β carrying capacity,” which is the greatest possible A β concentration for a specific region.

3.3 Integration Between Amyloid PET Data and Other AD Biomarkers

1. The use of AD biomarkers in routine clinical practice should take into account not only the diagnostic performances of a test but also cost-effectiveness estimates [3]. In 2010, to guide clinicians on how best to apply amyloid PET in the clinical evaluation of people with cognitive decline, a working group convened by the Alzheimer’s Association and the Society of Nuclear Medicine and Molecular Imaging (SNMMI) developed appropriate use criteria for brain amyloid PET scans [30]. According to this criteria, amyloid PET should only be considered in patients with clear, measurable cognitive deficits when there is substantial diagnostic uncertainty after a

comprehensive evaluation by a dementia specialist. The Amyloid Imaging Task Force did not consider other proposed diagnostic biomarkers for AD and therefore did not draw any conclusions with regard to the relative value of amyloid PET compared with CFS, MRI, and FDG-PET. However, besides the clinical neuropsychological assessment, a comprehensive evaluation should certainly include an MRI scan while it is still to be clarified the cost-effectiveness of a flowchart proposing (or laying against) the use of FDG and/or CSF biomarkers before AMY-PET [9].

2. In more recent years, other initiatives have faced the issue of the most appropriate flowcharts for the etiological diagnosis of MCI and dementia. In the present scenario, in which information about the presence of brain amyloidosis can be either provided by CSF biomarkers or amy-PET evaluation, it is likely that for costs-related reasons CSF biomarkers will be considered the first line of diagnostic in the suspect of AD. Indeed, CSF biomarkers also provide information on T and N.

However, around 30% of patients may have contraindication to CSF analysis or may receive CSF inconclusive results. Amyloid-PET will be then needed when CSF amyloid readings are not available or borderline, but the diagnosis of AD is still the most likely. In these cases, if amyloid-PET is positive, a final etiologic diagnosis of AD can be made. In the next future, the availability of blood biomarkers, especially of in the presence of disease-modifying drugs, will probably further change the AD diagnostic flowchart and thus the role of amyloid PET in the clinical setting.

References

1. Albert MS, DeKosky ST, Dickson D et al (2011) The diagnosis of mild cognitive impairment due to Alzheimer's disease: recommendations from the National Institute on Aging and Alzheimer's Association workgroup. *Alzheimers Dement* 7:270–279
2. Dubois B, Feldman HH, Jacova C et al (2014) Advancing research diagnostic criteria for Alzheimer's disease: the IWG-2 criteria. *Lancet Neurol* 13:614–629
3. Teipel S, Drzezga A, Grothe MJ et al (2015) Multimodal imaging in Alzheimer's disease: validity and usefulness for early detection. *Lancet Neurol* 14:1037–1353
4. Teunissen CE, Verberk IMW, Thijssen EH et al (2022) Blood-based biomarkers for Alzheimer's disease: towards clinical implementation. *Lancet Neurol* 21:66–77
5. Caprioglio C, Garibotto V, Jessen F et al (2022) The clinical use of Alzheimer's disease biomarkers in patients with mild cognitive impairment: a European Alzheimer's disease consortium survey. *J Alzheimers Dis* 89:535–551
6. van Dyck CH, Swanson CJ, Aisen P et al (2023) Lecanemab in early Alzheimer's disease. *N Engl J Med* 388:9–21
7. Mintun MA, Lo AC, Duggan Evans C et al (2021) Donanemab in early Alzheimer's disease. *N Engl J Med* 384:1691–1704
8. Klunk WE, Koeppe RA, Price JC et al (2015) The Centiloid project: standardizing quantitative amyloid plaque estimation by PET. *Alzheimers Dement* 11:11–15
9. Guerra UP, Nobili FM, Padovani A et al (2015) Recommendations from the Italian

- Interdisciplinary Working Group (AIMN, AIP, SINDEM) for the utilization of amyloid imaging in clinical practice. *Neurol Sci* 36:1075–1081
10. Minoshima S, Drzezga AE, Barthel H et al (2016) SNMMI procedure standard/EANM practice guideline for amyloid PET imaging of the brain 1.0. *J Nucl Med* 57:1316–1322
 11. Garibotto V, Morbelli S, Pagani M (2016) Erratum to: dual-phase amyloid PET: hitting two birds with one stone. *Eur J Nucl Med Mol Imaging* 43:1747
 12. Magistretti PJ (2000) Cellular bases of functional brain imaging: insights from neuron-glia metabolic coupling. *Brain Res* 886:108–112
 13. Boccalini C, Peretti DE, Ribaldi F et al (2022) Early-phase 18F-Florbetapir and 18F-Flutemetamol images as proxies of brain metabolism in a memory clinic setting. *J Nucl Med* 64:266–273
 14. van Berckel BN, Ossenkoppele R, Tolboom N et al (2013) Longitudinal amyloid imaging using 11C-PiB: methodologic considerations. *J Nucl Med* 54:1570–1576
 15. Collij LE, Konijnenberg E, Reimand J et al (2019) Assessing amyloid pathology in cognitively normal subjects using 18F-Flutemetamol PET: comparing visual reads and quantitative methods. *J Nucl Med* 60:541–547
 16. Oliveira FP, Ferreira SM, Silva MG et al (2022) Patlak plot based on the first 30 minutes post-injection dynamic 18F-florbetaben positron emission tomography scan separates amyloid- β positive from negative studies. *Br J Radiol* 95(1139):20211023
 17. Yoon HJ, Kim BS, Jeong JH et al (2021) Dual-phase 18F-florbetaben PET provides cerebral perfusion proxy along with beta-amyloid burden in Alzheimer's disease. *Neuroimage Clin* 31:102773
 18. Ni R, Gillberg PG, Bergfors A et al (2013) Amyloid tracers detect multiple binding sites in Alzheimer's disease brain tissue. *Brain* 136:2217–2227
 19. Hsiao IT, Huang CC, Hsieh CJ et al (2012) Correlation of early-phase 18F-florbetapir (AV-45/Amyvid) PET images to FDG images: preliminary studies. *Eur J Nucl Med Mol Imaging* 39:613–620
 20. Koole M, Lewis DM, Buckley C et al (2009) Whole-body biodistribution and radiation dosimetry of 18F-GE067: a radioligand for in vivo brain amyloid imaging. *J Nucl Med* 50:818–822
 21. O'Keefe GJ, Saunders TH, Ng S et al (2009) Radiation dosimetry of beta-amyloid tracers 11C-PiB and 18F-BAY94-9172. *J Nucl Med* 50:309–315
 22. Chincarini A, Sensi F, Rei L et al (2016) Alzheimer's Disease Neuroimaging Initiative. Standardized uptake value ratio-independent evaluation of brain amyloidosis. *J Alzheimers Dis* 54:1437–1457
 23. Kinahan PE, Fletcher JW (2010) Positron emission tomography-computed tomography standardized uptake values in clinical practice and assessing response to therapy. *Semin Ultrasound CT MR* 31:496–505
 24. Thurfjell L, Lilja J, Lundqvist R et al (2014) Automated quantification of 18F-flutemetamol PET activity for categorizing scans as negative or positive for brain amyloid: concordance with visual image reads. *J Nucl Med* 55:1623–1628
 25. Clark CM, Pontecorvo MJ, Beach TG et al (2012) Cerebral PET with florbetapir compared with neuropathology at autopsy for detection of neuritic amyloid- β plaques: a prospective cohort study. *Lancet Neurol* 11:669–678
 26. Landau SM, Thomas BA, Thurfjell L et al (2014) Alzheimer's Disease Neuroimaging Initiative. Amyloid PET imaging in Alzheimer's disease: a comparison of three radiotracers. *Eur J Nucl Med Mol Imaging* 41:1398–1407
 27. Bischof GN, Bartenstein P, Barthel H et al (2021) Toward a universal readout for 18F-labeled amyloid tracers: the CAPTAINS study. *J Nucl Med* 62:999–1005
 28. Battle MR, Pillay LC, Lowe VJ et al Centiloid scaling for quantification of brain amyloid with [18F]flutemetamol using multiple processing methods. *EJNMMI Res* 8(1):107
 29. Chincarini A, Peira E, Corosu M et al (2020) A kinetics-based approach to amyloid PET semi-quantification. *Eur J Nucl Med Mol Imaging* 47(9):2175–2185
 30. Johnson KA, Minoshima S, Bohnen NI et al (2013) Appropriate use criteria for amyloid PET: a report of the Amyloid Imaging Task Force, the Society of Nuclear Medicine and Molecular Imaging, and the Alzheimer's Association. *Alzheimers Dement* 9:e-1–e-16



PET Imaging to Measure Neuroinflammation In Vivo

Maura Malpetti, Nicolai Franzmeier, and Matthias Brendel

Abstract

This paper provides an overview of the role of neuroinflammation in Alzheimer's disease and other neurodegenerative diseases, highlighting the potential of anti-inflammatory treatments to slow or prevent decline. This research focuses on the use of positron emission tomography (PET) imaging to visualize and quantify molecular brain changes in patients, specifically microglial activation and reactive astrogliosis. We discuss the development and application of several PET radioligands, including first-generation ligands like PK11195 and Ro5-4864, as well as second- and third-generation ligands such as [11C]PBR28, [18F]DPA-714, [18F]GE-180, and [11C]ER176. These ligands target the 18-kDa translocator protein (TSPO), which is overexpressed in activated microglia and upregulated in astrocytes. We also address the limitations of these ligands, such as low brain uptake, poor penetration of the blood-brain barrier, short half-life, and variable kinetic behavior. Furthermore, we demonstrate the impact of genetic polymorphisms on ligand binding.

Key words Neuroinflammation, Alzheimer's disease, Positron Emission Tomography (PET), Microglial activation, 18-kDa Translocator Protein (TSPO)

1 Introduction

Considerable progress has been made in understanding some of the lifelong risk factors and brain changes associated with dementia and related conditions. Growing evidence from epidemiology, genetics, animal models, and postmortem studies indicates neuroinflammation as a key process in Alzheimer's disease and other neurodegenerative diseases. In people with these conditions, a range of anti-inflammatory treatments could be helpful to slow or prevent decline. Postmortem and animal model studies reveal increased levels of activated microglia in disease-specific regions that topographically mirror neurodegeneration. Radioligands for positron emission tomography (PET) have been developed to visualize and quantify molecular brain changes in vivo in patients. In this chapter, we provide an overview on PET imaging of

microglial activation and reactive astrogliosis, including PET radioligands and achieved key results.

2 TSPO PET Tracers

Several PET radioligands have been developed to quantify and localize in vivo brain inflammation. Ligands targeting the 18-kDa translocator protein (TSPO), which is overexpressed on the mitochondrial membrane in activated microglia and upregulated in astrocytes, have been widely used to study neuroinflammation in dementia. First-generation ligands targeting TSPO were radiolabeled with carbon-11, including PK11195 (1-(2-chlorophenyl)-N-methyl-N-(1-methylpropyl)-3-isoquinoline carboxamide) and Ro5-4864 (4'-chlorodiazepam). Ro5-4864 is part of the benzodiazepine family, and its binding affinity varies due to temperature and species, while [^{11}C]PK11195 is a carboxamide isoquinoline and has been proven to have high affinity and selectivity to TSPO. [^{11}C]PK11195 is one of the most widely used TSPO PET ligands to study neuroinflammation; however, some limitations, such as low brain uptake, poor penetration of the blood-brain barrier, a short half-life, and highly variable kinetic behavior, have pushed the field to develop second- and third-generation TSPO ligands. Among others, these include [^{11}C]PBR28, [^{18}F]DPA-714, [^{18}F]GE-180, and [^{11}C]ER176.

[^{11}C]PBR28 showed promising use to image microglial activation, with its reduced lipophilicity but still retaining good blood-brain barrier penetration. However, as for [^{11}C]PK11195, [^{11}C]-labeled tracers are difficult to implement at large-scale studies or in clinical routine because of their short half-life (~20 min). Promising next-generation TSPO tracers that have radiolabeled with fluorine-18 have been developed, which are characterized by longer half-life (~110 min) and lower positron energy. In particular, we will discuss main findings with [^{18}F]DPA-714, which is a [^{18}F]-labeled compound with a pyrazolopyrimidine group, and with [^{18}F]GE-180, a third-generation tetrahydrocarbazole TSPO tracer. Although [^{11}C]PK11195 has a lower signal-to-noise ratio than next-generation TSPO PET radioligands, it has the advantage over alternative ligands that it is minimally affected by common genetic polymorphisms (i.e., the single nucleotide polymorphism (SNP) rs6971) substantially affecting ligand binding in Caucasian populations [1–3]. For second- and third-generation tracers, depending on the SNP they carry, participants can be high-, mixed-, or low-affinity binders; the low signal in the latter category precludes meaningful use of these tracers [4].

2.1 TSPO PET in Alzheimer's Disease

TSPO PET tracers have been widely used to quantify and localize activated microglia *in vivo* in people on the Alzheimer's disease spectrum, in particular by applying PK11195 and PBR28 PET. Across different studies, increased TSPO PET uptake has been found in medial temporal regions, including the entorhinal cortex, temporoparietal cortex including the precuneus, and the cingulate cortex of patients with Alzheimer's dementia (Fig. 1). At the clinical stage of Alzheimer's disease, microglial activation co-localizes and correlates negatively with brain metabolism, as assessed with FDG PET [5]. Longitudinal studies with [¹⁸F]DPA-714 and [¹¹C]PBR28 PET have suggested a linear increasing trajectory of microglial activation across the aging Alzheimer's continuum, triggered by amyloid- β deposition and then continued by tau accumulation [6–8]. However, recent work indicated that elevated TSPO PET signals in humans may rather depend on microglia proliferation than on altered gene expression levels [9].

Nonetheless, *in vivo* PET tracers to evaluate inflammation have made it possible to assess how neuroinflammation may affect cognitive decline in Alzheimer's disease and how neuroinflammation may interact with other hallmark pathological processes, such as tau accumulation and atrophy. Regional patterns of microglial activation match clinical syndromes [5], while the degree of TSPO uptake correlates with worse cognitive performance [10–13]. Importantly, in patients with symptomatic Alzheimer's disease, elevated microglial activation in the anterior temporal regions predicts longitudinal cognitive decline over 3 years over and above atrophy [14]. Multimodal analyses have characterized that tau pathology and microglial activation show an interaction, which mediates the effect of neuronal loss on cognition [15]. Empowered by multi-tracer studies, it has also been possible to map the spatial progression trajectories of microglial activation, as measured by [¹¹C]PK11195 or [¹¹C]PBR28, and tau accumulation trajectories (as assessed with Flortaucipir or [¹⁸F]MK-6240 PET) [16–19]. Microglial activation and tau accumulation show parallel spatial progression trajectories from medial temporal lobe to associative/transmodal neocortical areas, corroborating the hypotheses that were developed in postmortem contexts [20, 21]. In typical and atypical Alzheimer's disease, regional tau has been described more frequently associated with microglial activation when compared to regional amyloid- β pathology [22]. In addition, baseline microglial activation patterns have been found to be associated with propagation trajectories of tau over time – and amyloid levels may catalyze microglial activation effects on tau spreading [18].

Along the spectrum of Alzheimer's disease, the interaction between amyloid- β deposition, tau accumulation, and microglial activation has been associated with functional and structural connectivity and cognitive impairment. Higher regional TSPO PET signal is associated with white matter changes (Low et al. 2020) and

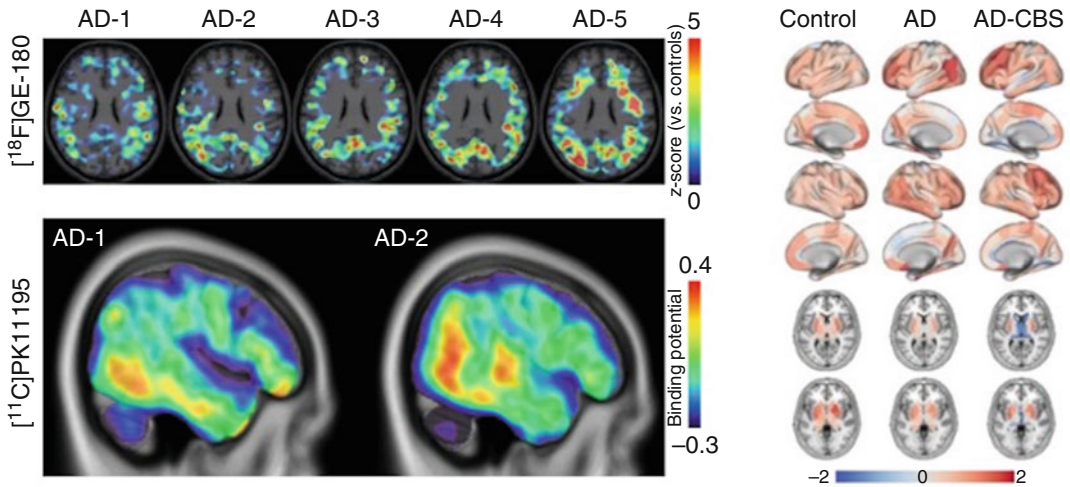


Fig. 1 TSPO PET imaging with $[^{18}\text{F}]\text{GE-180}$ and $[^{11}\text{C}]\text{PK11195}$ in patients with Alzheimer's disease. Z-score maps and binding potential maps on the left show individual patterns of elevated TSPO PET signals in individual patients of the Alzheimer's disease continuum. Surface projections on the right show regional TSPO PET signal intensities (z-scores -2 to 2) in controls and patients with typical and atypical Alzheimer's disease (modified from [22]). AD-CBS = Alzheimer's disease with corticobasal syndrome phenotype. Individual cases are unpublished data from the LMU University Hospital and University of Cambridge

disruption in large-scale functional connectivity of the medial temporal lobe, as such that neuroinflammation-associated connectivity changes mediate cognitive impairments [12, 23]. Cross-modality work with fMRI and PET imaging indicated that interregional covariance in TSPO PET signal is preferentially distributed along functionally highly connected brain regions, with MRI structural connectivity showing a weaker association with microglial activation [23]. Taken together, these studies suggest that inflammation and tau pathology critically drive the pathogenesis cascade of Alzheimer's disease, linking neurodegeneration to cognitive decline.

2.2 TSPO PET in Preclinical Models of Alzheimer's Disease

TSPO PET imaging in mouse models of Alzheimer's disease is an excellent tool to understand trajectories of neuroinflammation signals during disease development [24–26] and upon immunomodulation [27]. The combination of TSPO PET imaging with in-depth ex vivo analyses or behavioral testing revealed saturation effects of microglial activation with increasing amyloidosis [28] (Fig. 2), higher levels of TSPO expression in female mice with amyloidosis [29], and predictive power of TSPO PET signals as a microglia response index [30]. Importantly, preclinical models can also be used to understand regional sources of TSPO PET signals at the cellular level and highlighted strong selectivity of TSPO PET signals in Alzheimer's disease models to glial cells [31, 32]. Recently, the understanding of the skull-meninges-brain axis in Alzheimer's disease was strongly accelerated by exploiting TSPO PET signals through beyond brain analysis [33].

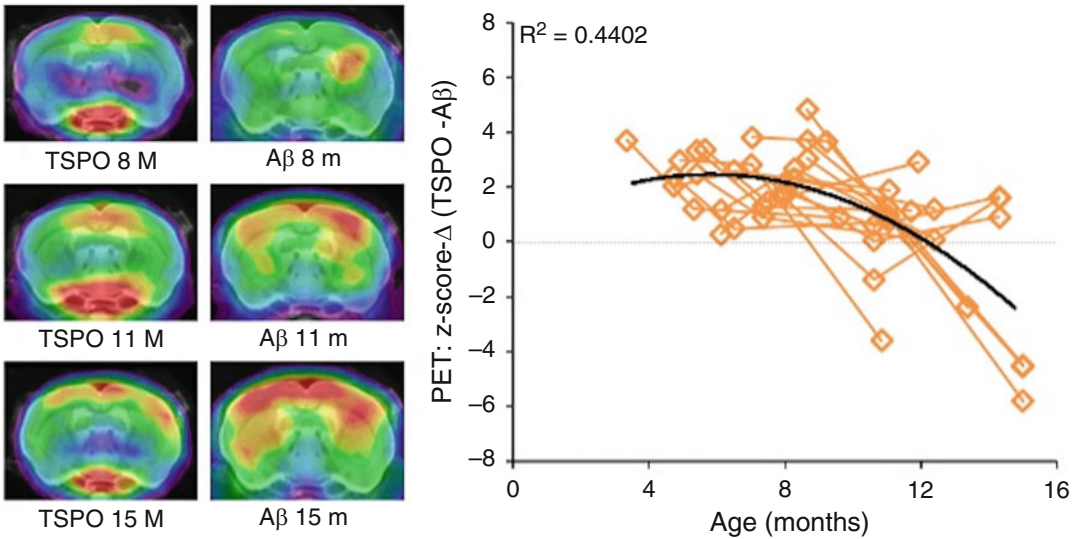


Fig. 2 Longitudinal trajectories of TSPO PET and amyloid- β PET signals in an amyloidosis mouse model. Graph shows the changes of TSPO PET relative to changes in amyloid- β ($A\beta$) PET as a function of age

2.3 TSPO PET in Non-Alzheimer's Tauopathies

Neuroinflammation has been described as a key pathogenic factor in non-Alzheimer's primary tauopathies, such as Pick's disease associated with frontotemporal dementia, progressive supranuclear palsy, and corticobasal degeneration. In fact, postmortem human studies reported microglial activation and other inflammatory processes (i.e., astrocyte activation, T cell infiltration) across all these diseases [34–37], and genome wide association studies implicated inflammatory pathways in their etiology [38–42]. In particular, genome wide association studies have identified *LRRK2* genetic variants related to neuroinflammation as risk factors for developing PSP [43, 44].

Despite extensive applications of TSPO PET tracers in Alzheimer's disease, only few studies have been conducted on the non-Alzheimer's primary tauopathies. In patients with progressive supranuclear palsy, TSPO PET binding has been found to be increased not only in subcortical regions (basal ganglia, striatum, and midbrain) but also in the frontal cortex and cerebellum [12, 45–47] (Fig. 3). In these regions, higher TSPO PET binding strongly correlates with clinical severity [46] and predicts a faster rate of clinical decline [48]. Reports with TSPO PET in patients with corticobasal degeneration are limited, but coherently showing elevated TSPO labeling in subcortical brain regions, especially basal ganglia, and stronger signal in the forebrain [47, 49], corresponding well with the known distribution of neuropathological changes.

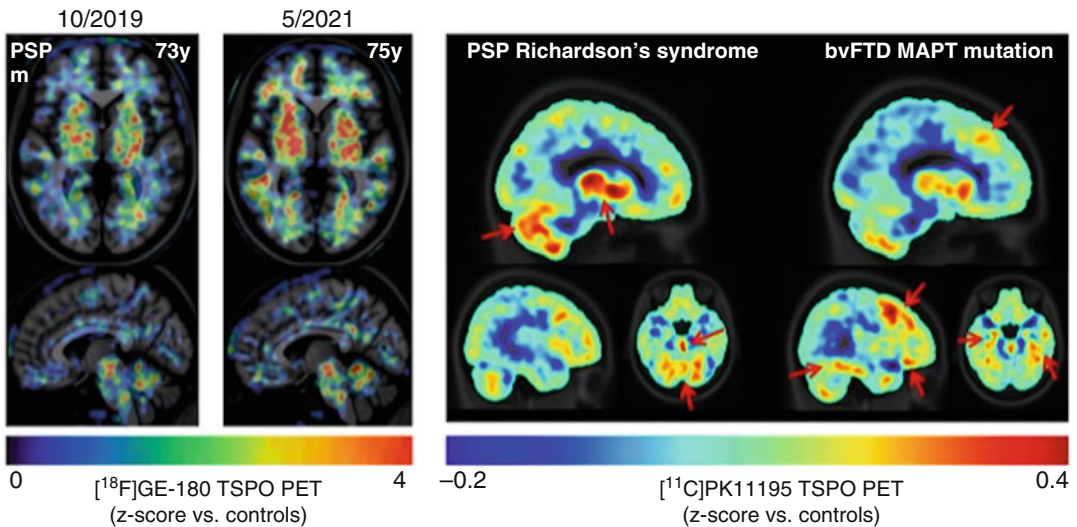


Fig. 3 TSPO PET in non-AD tauopathies. Left: longitudinal TSPO PET imaging in a patient with progressive supranuclear palsy (PSP) Richardson syndrome using [^{18}F]GE-180. Images show regional z-score differences against an age-matched in-house cohort. Right: examples of [^{11}C]PK11195 binding potential (BP) maps highlighting the key regions where a patient with PSP Richardson syndrome and a MAPT mutation carrier with bvFTD display high levels of activated microglia and are associated with their clinical symptoms. Images derived from individual cases are unpublished data from the LMU University Hospital and University of Cambridge

Across the frontotemporal dementia spectrum, higher regional inflammation indexed by TSPO is associated with specific clinical syndromes and correlates with severity [18, 50]. Importantly, in a recent study, faster cognitive decline in people with sporadic and genetic frontotemporal dementia was found to be associated with reduced baseline gray matter volume and increased microglial activation in frontal regions, bilaterally. In frontal regions, microglial activation and gray matter volume were negatively correlated but provided independent information, with inflammation being a stronger predictor of the rate of cognitive decline [51]. In frontotemporal dementia cases associated with autosomal dominant mutations in the microtubule-associated protein tau (MAPT) gene, TSPO PET has revealed neuroinflammation in frontotemporal regions across all symptomatic cases [52], reflecting the individual's clinical syndrome [48]. Furthermore, TSPO PET studies in presymptomatic cases carrying the genetic mutation showed that neuroinflammation occurs early and at a comparable extent to symptomatic patients with the same mutations, preceding PET identification of other molecular pathologies such as tau, brain atrophy, and the development of the full syndrome [53, 54]. Altogether, these studies strongly support the role of central nervous system inflammation in accelerating disease progression in these conditions, across different pathologies and clinical syndromes.

3 Alternative Targets for Microglia Activation

Although TSPO PET has been so widely adopted to assess neuroinflammation, TSPO overexpression constitutes only one of various processes involved in neuroinflammation in dementia – and TSPO tracers are not well suited to differentiate pro-inflammatory and anti-inflammatory glial phenotypes. Furthermore, expression of TSPO in several cell types hampers the interpretation of imaging signals in healthy brain and brain diseases [55]. To allow such characterizations, alternative ligands aimed at other parts of the inflammatory cascade have been and are being developed. Such ligands for alternative targets may help to clarify the inflammatory mechanisms and responses – including pro- vs anti-inflammatory processes – and support the development of diverse therapeutic strategies. These new ligands center around various non-TSPO targets to bind.

Both microglia and neurons express the enzyme cyclooxygenase, in its two isoforms COX1 and COX2. These have been suggested to play a role in neuroinflammation cascades and thus also as putative novel targets for PET ligands. Tracers for the respective isoforms include [^{11}C]KTP-Me and [^{11}C]PS13 for COX1 and [^{11}C]MC1 for COX2. Among them, [^{11}C]KTP-Me has demonstrated increased signal in preclinical studies, and also in patients with Alzheimer's disease, surrounding especially amyloid- β plaques [56, 57]. Another potential target is the colony-stimulating factor 1 receptor (CSF1R), which is a tyrosine kinase receptor subtype which has been demonstrated to moderate/mediate microglial proliferation, survival, and activation and as such to be involved in the initiation of broader pro-inflammatory responses. Alzheimer's neuropathology is associated with CSF1R upregulation [58]. Tracers that bind CSF1R, such as [^{11}C]CPPC and [^{11}C]GW2580, have demonstrated binding specificity and in validation work that utilized preclinical and postmortem human Alzheimer's disease tissue, respectively; increased binding of both of these radioligands was observed [59, 60]. Finally, another target that is being evaluated is the cannabinoid receptor type 2 (CB2R). This receptor is mainly expressed on cells of the immune system, including microglia. While under normal physiological circumstances, CB2R expression is low, and preclinical mouse work has shown that amyloidosis strongly increase its abundance [61]. Among various CB2R radioligands that have been produced, [^{11}C]NE40 has shown reduced signal in Alzheimer's disease compared to healthy controls – but the contribution of amyloid burden remains to be established [62].

One promising alternative target to image activated microglia is the P2X7 receptor, which is a purinergic receptor that sits on the outer cell membrane, and its signaling is involved in microglial

activation. Correspondingly, modulating and altering signaling via this receptor as well as its abundance could provide a novel treatment strategy for neurodegenerative diseases – and their efficacy could be evaluated best with ligands binding to this receptor. While P2X7R is dominantly expressed on the surface of microglia, it is to less extent also found on the surfaces of astrocytes and oligodendrocytes. P2X7 overexpression has been linked to neuroinflammatory conditions and indicates microglial activation and proliferation, being involved in pro-inflammatory signaling with upregulation of the inflammasome and cytokine release [63]. Pre-clinical work in Alzheimer's disease models has characterized that elevated P2X7R expression is associated with amyloid- β burden [64, 65], suggesting a broader physiological relevance to the dementia disease process. Various promising radioligands to bind P2X7R have been developed, including [^{11}C]JNJ-54173717 (JNJ-717), [^{18}F]JNJ-64413739, and [^{11}C]SMW139. In particular, [^{18}F]JNJ-64413739 has shown favorable kinetics in healthy control participants with good test-retest variability [66]. Nevertheless, increased binding of these ligands in patients with dementia remains to be assessed and confirmed. Further work and systematic evaluations are needed to establish the confounds and nuisance factors that may alter binding affinity for any of these tracers.

4 PET Imaging of Reactive Astrogliosis

In line with the requirement to distinguish microglial against other glial contributions to neuroinflammation, there are various ongoing research efforts to develop radioligands that are selective for the measurement of astrocyte-related inflammatory responses. These ligands may hold the key to disentangle the disease-relevant contributions of microglia- versus astrocyte-mediated inflammatory processes, across many different neurodegenerative disorders.

Tracers have been developed targeting the monoamine oxidase B (MAO-B), which is an enzyme located on mitochondrial membranes within astrocytes and serotonin-releasing neurons. In several neurodegenerative diseases, MAO-B upregulation has been linked to further astrogliosis markers, such as glial fibrillary acidic protein (GFAP) levels. An early development in this direction was the tracer [^{11}C]deuterium-L-deprenyl (DED), which is an irreversible MAO-B inhibitor allowing the visualization of early astrogliosis in sporadic and autosomal dominant Alzheimer's disease [67–71]. In particular, a recent study compared the [^{11}C]DED tracer with plasma levels of GFAP levels in presymptomatic and symptomatic participants with autosomal dominant Alzheimer's disease and patients with sporadic Alzheimer's disease [72]. In this cohort, [^{11}C]DED PET binding and plasma GFAP concentration levels followed divergent trajectories, showing negative cross-sectional

associations. In presymptomatic mutation carriers, regional [^{11}C]DED binding concentrations were high in the very early phase of the disease – decades before symptom onset – and decreased over time. On the other hand, plasma GFAP levels increased approaching the symptom onset. These markers may detect different states and/or subtypes of astrogliosis. To allow imaging at centers without onsite cyclotrons, [^{18}F]F-DED was developed and showed promising translational results in a mouse model and first pilot patients with Alzheimer's disease pathology [73] (Fig. 4). Other tracers, including [^{11}C]Cou, [^{11}C]SL25, and [^{18}F]SMBT-1, have been developed toward better reversible binding properties and more selective binding, avoiding undesirable active metabolites, as compared to [^{11}C]DED. In particular, [^{18}F]SMBT-1 PET has shown increased astrocytic activation in mediotemporal and cortical brain areas of patients with Alzheimer's disease when compared to healthy controls [74] and higher *in vivo* signals in patients with Alzheimer's disease when compared to healthy controls [75].

Another putative target for radioligands that have been the mitochondrial imidazole binding sites (I_2BS) are composed of a group of proteins and have been suggested to moderate GFAP expression and be co-expressed with MAO-B on astrocytic mitochondrial membranes. In both patients with Parkinson's [76] and Alzheimer's disease [77], the I_2BS tracer [^{11}C]BU99008 has characterized increases in reactive astroglia, in the latter case especially in areas with greater amyloid burden. Studies using [^3H]BU99008 in human postmortem Alzheimer's disease tissue have suggested binding specificity for I_2BS expressing astrocytes and revealed [^3H]DED and [^3H]BU99008 may have divergent binding properties/behaviors. The [^3H]BU99008 binding distribution also confirmed co-localization with GFAP expression and other astrogliosis markers [78].

5 Conclusions

Across the neurodegenerative disease spectrum, TSPO PET has been instrumental in characterizing that increased inflammation occurs not just in symptomatic participants with Alzheimer's and non-Alzheimer's tauopathies but also presymptomatic and prodromal dementias. In these conditions, TSPO binding is associated with the functional anatomy of the cognitive deficit and specific clinical syndromes and correlates with functional and structural neurodegeneration. Most importantly, *in vivo* imaging study with TSPO PET in humans indicates that neuroinflammation levels predict how fast patients clinically decline. This linkage to clinical outcomes has motivated a variety of drug development pipelines aimed at utilizing immunomodulatory strategies in neurodegenerative diseases. PET imaging can be an indispensable tool for

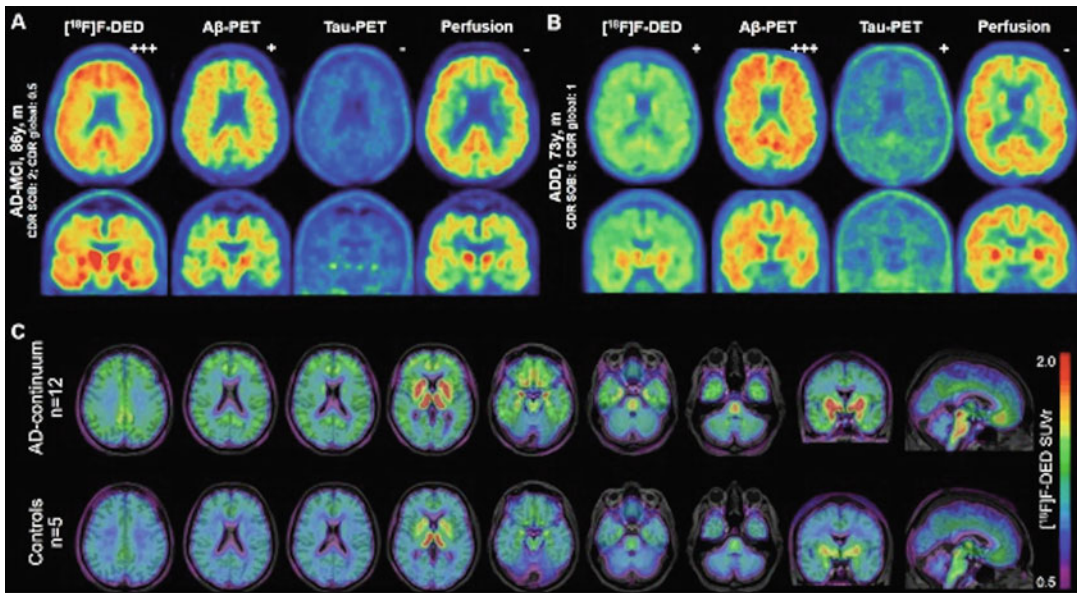


Fig. 4 Preliminary experience with $[^{18}\text{F}]\text{F-DED}$ at the LMU University Hospital (unpublished data). Individual patient examples with multimodal PET imaging show (a) very high $[^{18}\text{F}]\text{F-DED}$ signal in the presence of mild cognitive impairment and A + T-N- status as well as (b) moderate $[^{18}\text{F}]\text{F-DED}$ signal in the presence of mild dementia and A + T + N- status. (c) Group average $[^{18}\text{F}]\text{F-DED}$ images (standardized uptake value ratios, parietal white matter reference) show axial, coronal, and sagittal slices throughout the brain upon an MRI template for 12 patients of the AD-continuum (age: 69 ± 5 years; 5 females; 2 AD-SMC, 6 AD-MCI, 4 ADD) and 5 cognitively healthy controls (age: 68 ± 6 ; 2 females)

immunomodulatory clinical trials, with diagnostic prognostic and treatment-monitoring uses. However, a better understanding of the source of TSPO PET signal and the utility of PET tracers targeting alternative targets is needed for a full implementation of these methods in clinical trials. In particular, to fully realize its potential for the purposes, it will be necessary to resolve the longitudinal progression and timeline of inflammation that is observable in vivo. Additionally, further antemortem PET and postmortem histopathological comparative analyses are required to substantiate the specificity of the PET ligands and the linkage of in vivo inflammation measures with immunohistochemical molecular pathology.

References

1. Guo Q, Owen DR, Rabiner EA, Turkheimer FE, Gunn RN (2012) Identifying improved TSPO PET imaging probes through biomathematics: the impact of multiple TSPO binding sites in vivo. *NeuroImage* 60(2):902–910. <https://doi.org/10.1016/j.neuroimage.2011.12.078>
2. Kobayashi M, Jiang T, Telu S, Zoghbi SS, Gunn RN, Rabiner EA, Owen DR, Guo Q, Pike VW, Innis RB, Fujita M (2018) (11)C-DPA-713 has much greater specific binding to translocator protein 18 kDa (TSPO) in human brain than (11)C-(R)-PK11195. *J Cereb Blood Flow Metab* 38(3):393–403. <https://doi.org/10.1177/0271678X17699223>

3. Owen DR, Yeo AJ, Gunn RN, Song K, Wadsworth G, Lewis A, Rhodes C, Pulford DJ, Bennacef I, Parker CA, StJean PL, Cardon LR, Mooser VE, Matthews PM, Rabiner EA, Rubio JP (2012) An 18-kDa translocator protein (TSPO) polymorphism explains differences in binding affinity of the PET radioligand PBR28. *J Cereb Blood Flow Metab* 32(1):1–5. <https://doi.org/10.1038/jcbfm.2011.147>
4. Vettermann FJ, Harris S, Schmitt J, Unterrainer M, Lindner S, Rauchmann BS, Palleis C, Weidinger E, Beyer L, Eckenweber F, Schuster S, Biechele G, Ferschmann C, Milenkovic VM, Wetzel CH, Rupprecht R, Janowitz D, Buerger K, Pernecky R, Höglinger GU, Levin J, Haass C, Tonn JC, Niyazi M, Bartenstein P, Albert NL, Brendel M (2021) Impact of TSPO receptor polymorphism on [(18)F]GE-180 binding in healthy brain and pseudo-reference regions of Neurooncological and neurodegenerative disorders. *Life (Basel)* 11(6). <https://doi.org/10.3390/life11060484>
5. Tondo G, Iaccarino L, Caminiti SP, Presotto L, Santangelo R, Iannaccone S, Magnani G, Perani D (2020) The combined effects of microglia activation and brain glucose hypometabolism in early-onset Alzheimer's disease. *Alzheimers Res Ther* 12(1):50. <https://doi.org/10.1186/s13195-020-00619-0>
6. Hamelin L, Lagarde J, Dorothee G, Potier MC, Corlier F, Kuhnast B, Caille F, Dubois B, Fillon L, Chupin M, Bottlaender M, Sarazin M (2018) Distinct dynamic profiles of microglial activation are associated with progression of Alzheimer's disease. *Brain* 141(6):1855–1870. <https://doi.org/10.1093/brain/awy079>
7. Kreisl WC, Lyoo CH, Liow JS, Wei M, Snow J, Page E, Jenko KJ, Morse CL, Zoghbi SS, Pike VW, Turner RS, Innis RB (2016) (11)C-PBR28 binding to translocator protein increases with progression of Alzheimer's disease. *Neurobiol Aging* 44:53–61. <https://doi.org/10.1016/j.neurobiolaging.2016.04.011>
8. Zou J, Tao S, Johnson A, Tomljanovic Z, Polly K, Klein J, Razlighi QR, Brickman AM, Lee S, Stern Y, Kreisl WC (2020) Microglial activation, but not tau pathology, is independently associated with amyloid positivity and memory impairment. *Neurobiol Aging* 85: 11–21. <https://doi.org/10.1016/j.neurobiolaging.2019.09.019>
9. Nutma E, Fancy N, Weinert M, Tsartsalis S, Marzin MC, Muirhead RCJ, Falk I, Breur M, de Bruin J, Hollaus D, Pieterman R, Anink J, Story D, Chandran S, Tang J, Trolese MC, Saito T, Saido TC, Wiltshire KH, Beltran-Lobo P, Phillips A, Antel J, Healy L, Dorion M-F, Galloway DA, Benoit RY, Amossé Q, Ceyzériat K, Badina AM, Kövari E, Bendotti C, Aronica E, Radulescu CI, Wong JH, Barron AM, Smith AM, Barnes SJ, Hampton DW, van der Valk P, Jacobson S, Howell OW, Baker D, Kipp M, Kaddatz H, Tournier BB, Millet P, Matthews PM, Moore CS, Amor S, Owen DR (2023) Translocator protein is a marker of activated microglia in rodent models but not human neurodegenerative diseases. *Nat Commun* 14(1):5247. <https://doi.org/10.1038/s41467-023-40937-z>
10. Edison P, Archer HA, Gerhard A, Hinze R, Pavese N, Turkheimer FE, Hammers A, Tai YF, Fox N, Kennedy A, Rossor M, Brooks DJ (2008) Microglia, amyloid, and cognition in Alzheimer's disease: an [11C](R)PK11195-PET and [11C]PIB-PET study. *Neurobiol Dis* 32(3):412–419. <https://doi.org/10.1016/j.nbd.2008.08.001>
11. Fan Z, Aman Y, Ahmed I, Chetelat G, Landeau B, Ray Chaudhuri K, Brooks DJ, Edison P (2015) Influence of microglial activation on neuronal function in Alzheimer's and Parkinson's disease dementia. *Alzheimers Dement* 11(6):608–621 e607. <https://doi.org/10.1016/j.jalz.2014.06.016>
12. Passamonti L, Tsvetanov KA, Jones PS, Bevan-Jones WR, Arnold R, Borchert RJ, Mak E, Su L, O'Brien JT, Rowe JB (2019) Neuroinflammation and functional connectivity in Alzheimer's disease: interactive influences on cognitive performance. *J Neurosci* 39(36): 7218–7226. <https://doi.org/10.1523/JNEUROSCI.2574-18.2019>
13. Yokokura M, Mori N, Yagi S, Yoshikawa E, Kikuchi M, Yoshihara Y, Wakuda T, Sugihara G, Takebayashi K, Suda S, Iwata Y, Ueki T, Tsuchiya KJ, Suzuki K, Nakamura K, Ouchi Y (2011) In vivo changes in microglial activation and amyloid deposits in brain regions with hypometabolism in Alzheimer's disease. *Eur J Nucl Med Mol Imaging* 38(2): 343–351. <https://doi.org/10.1007/s00259-010-1612-0>
14. Malpetti M, Passamonti L, Rittman T, Jones PS, Vazquez Rodriguez P, Bevan-Jones WR, Hong YT, Fryer TD, Aigbirhio FI, O'Brien JT, Rowe JB (2020) Neuroinflammation and Tau colocalize in vivo in progressive supranuclear palsy. *Ann Neurol* 88(6):1194–1204. <https://doi.org/10.1002/ana.25911>
15. Nicastro N, Malpetti M, Mak E, Williams GB, Bevan-Jones WR, Carter SF, Passamonti L, Fryer TD, Hong YT, Aigbirhio FI, Rowe JB,

- O'Brien JT (2020) Gray matter changes related to microglial activation in Alzheimer's disease. *Neurobiol Aging* 94:236–242. <https://doi.org/10.1016/j.neurobiolaging.2020.06.010>
16. Dani M, Wood M, Mizoguchi R, Fan Z, Walker Z, Morgan R, Hinz R, Biju M, Kuruvilla T, Brooks DJ, Edison P (2018) Microglial activation correlates in vivo with both tau and amyloid in Alzheimer's disease. *Brain* 141(9):2740–2754. <https://doi.org/10.1093/brain/awy188>
 17. Ismail R, Parbo P, Madsen LS, Hansen AK, Hansen KV, Schaldemose JL, Kjeldsen PL, Stokholm MG, Gottrup H, Eskildsen SF, Brooks DJ (2020) The relationships between neuroinflammation, beta-amyloid and tau deposition in Alzheimer's disease: a longitudinal PET study. *J Neuroinflammation* 17(1):151. <https://doi.org/10.1186/s12974-020-01820-6>
 18. Pascoal TA, Benedet AL, Ashton NJ, Kang MS, Theriault J, Chamoun M, Savard M, Lussier FZ, Tissot C, Karikari TK, Ottoy J, Mathotaarachchi S, Stevenson J, Massarweh G, Scholl M, de Leon MJ, Soucy JP, Edison P, Blennow K, Zetterberg H, Gauthier S, Rosa-Neto P (2021) Microglial activation and tau propagate jointly across Braak stages. *Nat Med* 27(9):1592–1599. <https://doi.org/10.1038/s41591-021-01456-w>
 19. Terada T, Yokokura M, Obi T, Bunai T, Yoshikawa E, Ando I, Shimada H, Suhara T, Higuchi M, Ouchi Y (2019) In vivo direct relation of tau pathology with neuroinflammation in early Alzheimer's disease. *J Neurol* 266(9):2186–2196. <https://doi.org/10.1007/s00415-019-09400-2>
 20. Serrano-Pozo A, Mielke ML, Gomez-Isla T, Betensky RA, Growdon JH, Frosch MP, Hyman BT (2011) Reactive glia not only associates with plaques but also parallels tangles in Alzheimer's disease. *Am J Pathol* 179(3):1373–1384. <https://doi.org/10.1016/j.ajpath.2011.05.047>
 21. Sheffield LG, Marquis JG, Berman NE (2000) Regional distribution of cortical microglia parallels that of neurofibrillary tangles in Alzheimer's disease. *Neurosci Lett* 285(3):165–168. [https://doi.org/10.1016/s0304-3940\(00\)01037-5](https://doi.org/10.1016/s0304-3940(00)01037-5)
 22. Finze A, Biechele G, Rauchmann BS, Franzmeier N, Palleis C, Katzdobler S, Weidinger E, Guersel S, Schuster S, Harris S, Schmitt J, Beyer L, Gnorich J, Lindner S, Albert NL, Wetzel CH, Rupprecht R, Rominger A, Danek A, Burow L, Kurz C, Tato M, Utecht J, Papazov B, Zaganjori M, Trappmann LK, Goldhardt O, Grimmer T, Haeckert J, Janowitz D, Buerger K, Keeser D, Stoecklein S, Dietrich O, Morenas-Rodriguez E, Barthel H, Sabri O, Bartenstein P, Simons M, Haass C, Hoglinger GU, Levin J, Perneczky R, Brendel M (2023) Individual regional associations between Abeta-, tau- and neurodegeneration (ATN) with microglial activation in patients with primary and secondary tauopathies. *Mol Psychiatry*. <https://doi.org/10.1038/s41380-023-02188-8>
 23. Rauchmann BS, Brendel M, Franzmeier N, Trappmann L, Zaganjori M, Ersoezlue E, Morenas-Rodriguez E, Guersel S, Burow L, Kurz C, Haeckert J, Tato M, Utecht J, Papazov B, Pogarell O, Janowitz D, Buerger K, Ewers M, Palleis C, Weidinger E, Biechele G, Schuster S, Finze A, Eckenweber F, Rupprecht R, Rominger A, Goldhardt O, Grimmer T, Keeser D, Stoecklein S, Dietrich O, Bartenstein P, Levin J, Hoglinger G, Perneczky R (2022) Microglial activation and connectivity in Alzheimer disease and aging. *Ann Neurol* 92(5):768–781. <https://doi.org/10.1002/ana.26465>
 24. Hu W, Pan D, Wang Y, Bao W, Zuo C, Guan Y, Hua F, Yang M, Zhao J (2020) PET imaging for dynamically monitoring Neuroinflammation in APP/PS1 mouse model using [(18)F] DPA714. *Front Neurosci* 14:810. <https://doi.org/10.3389/fnins.2020.00810>
 25. James ML, Belichenko NP, Nguyen TV, Andrews LE, Ding Z, Liu H, Bodapati D, Arksey N, Shen B, Cheng Z, Wyss-Coray T, Gambhir SS, Longo FM, Chin FT (2015) PET imaging of translocator protein (18 kDa) in a mouse model of Alzheimer's disease using N-(2,5-dimethoxybenzyl)-2-18F-fluoro-N-(2-phenoxyphenyl)acetamide. *J Nucl Med* 56(2):311–316. <https://doi.org/10.2967/jnumed.114.141648>
 26. Liu B, Le KX, Park MA, Wang S, Belanger AP, Dubey S, Frost JL, Holton P, Reiser V, Jones PA, Trigg W, Di Carli ME, Lemere CA (2015) In vivo detection of age- and disease-related increases in Neuroinflammation by 18F-GE180 TSPO MicroPET imaging in wild-type and Alzheimer's transgenic mice. *J Neurosci* 35(47):15716–15730. <https://doi.org/10.1523/jneurosci.0996-15.2015>
 27. Biechele G, Blume T, Deussing M, Zott B, Shi Y, Xiang X, Franzmeier N, Kleinberger G, Peters F, Ochs K, Focke C, Sacher C, Wind K, Schmidt C, Lindner S, Gildehaus FJ, Eckenweber F, Beyer L, von Ungern-Sternberg B, Bartenstein P, Baumann K, Dorostkar MM, Rominger A, Cumming P,

- Willem M, Adelsberger H, Herms J, Brendel M (2021) Pre-therapeutic microglia activation and sex determine therapy effects of chronic immunomodulation. *Theranostics* 11(18): 8964–8976. <https://doi.org/10.7150/thno.64022>
28. Blume T, Focke C, Peters F, Deussing M, Albert NL, Lindner S, Gildehaus FJ, von Ungern-Sternberg B, Ozmen L, Baumann K, Bartenstein P, Rominger A, Herms J, Brendel M (2018) Microglial response to increasing amyloid load saturates with aging: a longitudinal dual tracer in vivo muPET-study. *J Neuroinflammation* 15(1):307. <https://doi.org/10.1186/s12974-018-1347-6>
 29. Biechele G, Franzmeier N, Blume T, Ewers M, Luque JM, Eckenweber F, Sacher C, Beyer L, Ruch-Rubinstein F, Lindner S, Gildehaus FJ, von Ungern-Sternberg B, Cumming P, Bartenstein P, Rominger A, Hoglinger GU, Herms J, Brendel M (2020) Glial activation is moderated by sex in response to amyloidosis but not to tau pathology in mouse models of neurodegenerative diseases. *J Neuroinflammation* 17(1):374. <https://doi.org/10.1186/s12974-020-02046-2>
 30. Focke C, Blume T, Zott B, Shi Y, Deussing M, Peters F, Schmidt C, Kleinberger G, Lindner S, Gildehaus FJ, Beyer L, von Ungern-Sternberg B, Bartenstein P, Ozmen L, Baumann K, Dorostkar MM, Haass C, Adelsberger H, Herms J, Rominger A, Brendel M (2019) Early and longitudinal microglial activation but not amyloid accumulation predicts cognitive outcome in PS2APP mice. *J Nucl Med* 60(4):548–554. <https://doi.org/10.2967/jnumed.118.217703>
 31. Tournier BB, Tsartsalis S, Ceyzériat K, Fraser BH, Grégoire MC, Kövari E, Millet P (2020) Astrocytic TSPO upregulation appears before microglial TSPO in Alzheimer's disease. *J Alzheimers Dis* 77(3):1043–1056. <https://doi.org/10.3233/jad-200136>
 32. Bartos LM, Kunte ST, Beumers P, Xiang X, Wind K, Ziegler S, Bartenstein P, Choi H, Lee DS, Haass C, von Baumgarten L, Tahirovic S, Albert NL, Lindner S, Brendel M (2022) Single cell radiotracer allocation via immunomagnetic sorting (scRadiotracing) to disentangle PET signals at cellular resolution. *J Nucl Med* 63:1459. <https://doi.org/10.2967/jnumed.122.264171>
 33. Kolabas ZI, Kuemmerle LB, Perneczky R, Förstera B, Ulukaya S, Ali M, Kapoor S, Bartos LM, Büttner M, Caliskan OS, Rong Z, Mai H, Höher L, Jeridi D, Molbay M, Khalin I, Deligiannis IK, Negwer M, Roberts K, Simats A, Carofiglio O, Todorov MI, Horvath I, Ozturk F, Hummel S, Biechele G, Zatcepin A, Unterrainer M, Gnörich J, Roodselaar J, Shrouder J, Khosravani P, Tast B, Richter L, Díaz-Marugán L, Kaltenecker D, Lux L, Chen Y, Zhao S, Rauchmann BS, Sterr M, Kunze I, Stanic K, Kan VWY, Besson-Girard S, Katzdobler S, Palleis C, Schädler J, Paetzold JC, Liebscher S, Hauser AE, Gokce O, Lickert H, Steinke H, Benakis C, Braun C, Martinez-Jimenez CP, Buerger K, Albert NL, Höglinger G, Levin J, Haass C, Kopczak A, Dichgans M, Havla J, Kümpfel T, Kerschensteiner M, Schifferer M, Simons M, Liesz A, Krahrmer N, Bayraktar OA, Franzmeier N, Plesnila N, Erener S, Puelles VG, Delbridge C, Bhatia HS, Hellal F, Elsner M, Bechmann I, Ondruschka B, Brendel M, Theis FJ, Erturk A (2023) Distinct molecular profiles of skull bone marrow in health and neurological disorders. *Cell* 186(17):3706–3725.e3729. <https://doi.org/10.1016/j.cell.2023.07.009>
 34. Hartnell IJ, Woodhouse D, Jasper W, Mason L, Marwaha P, Graffeuil M, Lau LC, Norman JL, Chatelet DS, Buee L, Nicoll JAR, Blum D, Dorothee G, Boche D (2023) Glial reactivity and T cell infiltration in frontotemporal lobar degeneration with tau pathology. *Brain*. <https://doi.org/10.1093/brain/awad309>
 35. Ishizawa K, Dickson DW (2001) Microglial activation parallels system degeneration in progressive supranuclear palsy and corticobasal degeneration. *J Neuropathol Exp Neurol* 60(6):647–657. <https://doi.org/10.1093/jnen/60.6.647>
 36. Lant SB, Robinson AC, Thompson JC, Rollinson S, Pickering-Brown S, Snowden JS, Davidson YS, Gerhard A, Mann DM (2014) Patterns of microglial cell activation in frontotemporal lobar degeneration. *Neuropathol Appl Neurobiol* 40(6):686–696. <https://doi.org/10.1111/nan.12092>
 37. Woollacott IOC, Toomey CE, Strand C, Courtney R, Benson BC, Rohrer JD, Lashley T (2020) Microglial burden, activation and dystrophy patterns in frontotemporal lobar degeneration. *J Neuroinflammation* 17(1): 234. <https://doi.org/10.1186/s12974-020-01907-0>
 38. Broce I, Karch CM, Wen N, Fan CC, Wang Y, Tan CH, Kouri N, Ross OA, Hoglinger GU, Muller U, Hardy J, International FTDGC, Momeni P, Hess CP, Dillon WP, Miller ZA, Bonham LW, Rabinovici GD, Rosen HJ, Schellenberg GD, Franke A, Karlsen TH, Veldink JH, Ferrari R, Yokoyama JS, Miller BL, Andreassen OA, Dale AM, Desikan RS, Sugrue

- LP (2018) Immune-related genetic enrichment in frontotemporal dementia: an analysis of genome-wide association studies. *PLoS Med* 15(1):e1002487. <https://doi.org/10.1371/journal.pmed.1002487>
39. Ferrari R, Hernandez DG, Nalls MA, Rohrer JD, Ramasamy A, Kwok JB, Dobson-Stone C, Brooks WS, Schofield PR, Halliday GM, Hodges JR, Piguet O, Bartley L, Thompson E, Haan E, Hernandez I, Ruiz A, Boada M, Borroni B, Padovani A, Cruchaga C, Cairns NJ, Benussi L, Binetti G, Ghidoni R, Forloni G, Galimberti D, Fenoglio C, Serpente M, Scarpini E, Clarimon J, Lleo A, Blesa R, Waldo ML, Nilsson K, Nilsson C, Mackenzie IR, Hsiung GY, Mann DM, Grafman J, Morris CM, Attems J, Griffiths TD, McKeith IG, Thomas AJ, Pietrini P, Huey ED, Wassermann EM, Baborie A, Jaros E, Tierney MC, Pastor P, Razquin C, Ortega-Cubero S, Alonso E, Pernecky R, Diehl-Schmid J, Alexopoulos P, Kurz A, Rainero I, Rubino E, Pinessi L, Rogaeva E, St George-Hyslop P, Rossi G, Tagliavini F, Giaccone G, Rowe JB, Schlachetzki JC, Uphill J, Collinge J, Mead S, Danek A, Van Deerlin VM, Grossman M, Trojanowski JQ, van der Zee J, Deschamps W, Van Langenhove T, Cruts M, Van Broeckhoven C, Cappa SF, Le Ber I, Hannequin D, Golfer V, Vercelletto M, Brice A, Nacmias B, Sorbi S, Bagnoli S, Piaceri I, Nielsen JE, Hjerlmind LE, Riemenschneider M, Mayhaus M, Ibach B, Gasparoni G, Pichler S, Gu W, Rossor MN, Fox NC, Warren JD, Spillantini MG, Morris HR, Rizzu P, Heutink P, Snowden JS, Rollinson S, Richardson A, Gerhard A, Bruni AC, Maletta R, Frangipane F, Cupidi C, Bernardi L, Anfossi M, Gallo M, Conidi ME, Smirne N, Rademakers R, Baker M, Dickson DW, Graff-Radford NR, Petersen RC, Knopman D, Josephs KA, Boeve BF, Parisi JE, Seeley WW, Miller BL, Karydas AM, Rosen H, van Swieten JC, Dopper EG, Seelaar H, Pijnenburg YA, Scheltens P, Logroscino G, Capozzo R, Novelli V, Puca AA, Franceschi M, Postiglione A, Milan G, Sorrentino P, Kristiansen M, Chiang HH, Graff C, Pasquier F, Rollin A, Deramecourt V, Lebert F, Kapogiannis D, Ferrucci L, Pickering-Brown S, Singleton AB, Hardy J, Momeni P (2014) Frontotemporal dementia and its subtypes: a genome-wide association study. *Lancet Neurol* 13(7):686–699. [https://doi.org/10.1016/S1474-4422\(14\)70065-1](https://doi.org/10.1016/S1474-4422(14)70065-1)
 40. Hoglinger GU, Melhem NM, Dickson DW, Sleiman PM, Wang LS, Klei L, Rademakers R, de Silva R, Litvan I, Riley DE, van Swieten JC, Heutink P, Wszolek ZK, Uitti RJ, Vandrovicova J, Hurtig HI, Gross RG, Maetzler W, Goldwurm S, Tolosa E, Borroni B, Pastor P, Group PSPGS, Cantwell LB, Han MR, Dillman A, van der Brug MP, Gibbs JR, Cookson MR, Hernandez DG, Singleton AB, Farrer MJ, Yu CE, Golbe LI, Revesz T, Hardy J, Lees AJ, Devlin B, Hakonarson H, Muller U, Schellenberg GD (2011) Identification of common variants influencing risk of the tauopathy progressive supranuclear palsy. *Nat Genet* 43(7):699–705. <https://doi.org/10.1038/ng.859>
 41. Pottier C, Ren Y, Perkerson RB 3rd, Baker M, Jenkins GD, van Blitterswijk M, DeJesus-Hernandez M, van Rooij JGJ, Murray ME, Christopher E, McDonnell SK, Fogarty Z, Batzler A, Tian S, Vicente CT, Matchett B, Karydas AM, Hsiung GR, Seelaar H, Mol MO, Finger EC, Graff C, Oijerstedt L, Neumann M, Heutink P, Synofzik M, Wilke C, Prudlo J, Rizzu P, Simon-Sanchez J, Edbauer D, Roeber S, Diehl-Schmid J, Evers BM, King A, Mesulam MM, Weintraub S, Geula C, Bieniek KF, Petrucelli L, Ahern GL, Reiman EM, Woodruff BK, Caselli RJ, Huey ED, Farlow MR, Grafman J, Mead S, Grinberg LT, Spina S, Grossman M, Irwin DJ, Lee EB, Suh E, Snowden J, Mann D, Ertekin-Taner N, Uitti RJ, Wszolek ZK, Josephs KA, Parisi JE, Knopman DS, Petersen RC, Hodges JR, Piguet O, Geier EG, Yokoyama JS, Rissman RA, Rogaeva E, Keith J, Zinman L, Tartaglia MC, Cairns NJ, Cruchaga C, Ghetti B, Kofler J, Lopez OL, Beach TG, Arzberger T, Herms J, Honig LS, Vonsattel JP, Halliday GM, Kwok JB, White CL 3rd, Gearing M, Glass J, Rollinson S, Pickering-Brown S, Rohrer JD, Trojanowski JQ, Van Deerlin V, Bigio EH, Troakes C, Al-Sarraj S, Asmann Y, Miller BL, Graff-Radford NR, Boeve BF, Seeley WW, Mackenzie IRA, van Swieten JC, Dickson DW, Biernacka JM, Rademakers R (2019) Genome-wide analyses as part of the international FTLT-DTP whole-genome sequencing consortium reveals novel disease risk factors and increases support for immune dysfunction in FTLT. *Acta Neuropathol* 137(6):879–899. <https://doi.org/10.1007/s00401-019-01962-9>
 42. Respondek G, Levin J, Hoglinger GU (2018) Progressive supranuclear palsy and multiple system atrophy: clinicopathological concepts and therapeutic challenges. *Curr Opin Neurol* 31(4):448–454. <https://doi.org/10.1097/WCO.0000000000000581>
 43. Jabbari E, Koga S, Valentino RR, Reynolds RH, Ferrari R, MMX T, Rowe JB, Dalgard CL, Scholz SW, Dickson DW, Warner TT,

- Revesz T, Hoglinger GU, Ross OA, Ryten M, Hardy J, Shoaib M, Morris HR, Group PSPG (2021) Genetic determinants of survival in progressive supranuclear palsy: a genome-wide association study. *Lancet Neurol* 20(2): 107–116. [https://doi.org/10.1016/S1474-4422\(20\)30394-X](https://doi.org/10.1016/S1474-4422(20)30394-X)
44. Moehle MS, Webber PJ, Tse T, Sukar N, Standaert DG, DeSilva TM, Cowell RM, West AB (2012) LRRK2 inhibition attenuates microglial inflammatory responses. *J Neurosci* 32(5):1602–1611. <https://doi.org/10.1523/JNEUROSCI.5601-11.2012>
 45. Gerhard A, Trender-Gerhard I, Turkheimer F, Quinn NP, Bhatia KP, Brooks DJ (2006) In vivo imaging of microglial activation with [11C](R)-PK11195 PET in progressive supranuclear palsy. *Mov Disord* 21(1):89–93. <https://doi.org/10.1002/mds.20668>
 46. Malpetti M, Kievit RA, Passamonti L, Jones PS, Tsvetanov KA, Rittman T, Mak E, Nicastrò N, Bevan-Jones WR, Su L, Hong YT, Fryer TD, Aigbirhio FI, O'Brien JT, Rowe JB (2020) Microglial activation and tau burden predict cognitive decline in Alzheimer's disease. *Brain* 143(5):1588–1602. <https://doi.org/10.1093/brain/awaa088>
 47. Palleis C, Sauerbeck J, Beyer L, Harris S, Schmitt J, Morenas-Rodriguez E, Finze A, Nitschmann A, Ruch-Rubinstein F, Eckenweber F, Biechele G, Blume T, Shi Y, Weidinger E, Prix C, Botzel K, Danek A, Rauchmann BS, Stocklein S, Lindner S, Unterrainer M, Albert NL, Wetzels C, Rupprecht R, Rominger A, Bartenstein P, Herms J, Pernecky R, Haass C, Levin J, Hoglinger GU, Brendel M (2021) In vivo assessment of Neuroinflammation in 4-repeat Tauopathies. *Mov Disord* 36(4):883–894. <https://doi.org/10.1002/mds.28395>
 48. Malpetti M, Passamonti L, Jones PS, Street D, Rittman T, Fryer TD, Hong YT, Vasquez Rodriguez P, Bevan-Jones WR, Aigbirhio FI, O'Brien JT, Rowe JB (2021) Neuroinflammation predicts disease progression in progressive supranuclear palsy. *J Neurol Neurosurg Psychiatry* 92(7):769–775. <https://doi.org/10.1136/jnnp-2020-325549>
 49. Gerhard A, Watts J, Trender-Gerhard I, Turkheimer F, Banati RB, Bhatia K, Brooks DJ (2004) In vivo imaging of microglial activation with [11C](R)-PK11195 PET in corticobasal degeneration. *Mov Disord* 19(10): 1221–1226. <https://doi.org/10.1002/mds.20162>
 50. Bevan-Jones WR, Cope TE, Jones PS, Kaalund SS, Passamonti L, Allinson K, Green O, Hong YT, Fryer TD, Arnold R, Coles JP, Aigbirhio FI, Larner AJ, Patterson K, O'Brien JT, Rowe JB (2020) Neuroinflammation and protein aggregation co-localize across the frontotemporal dementia spectrum. *Brain* 143(3): 1010–1026. <https://doi.org/10.1093/brain/awaa033>
 51. Malpetti M, Cope TE, Street D, Jones PS, Hezemans FH, Mak E, Tsvetanov KA, Rittman T, Bevan-Jones WR, Patterson K, Passamonti L, Fryer TD, Hong YT, Aigbirhio FI, O'Brien JT, Rowe JB (2023) Microglial activation in the frontal cortex predicts cognitive decline in frontotemporal dementia. *Brain* 146(8):3221–3231. <https://doi.org/10.1093/brain/awad078>
 52. Malpetti M, Rittman T, Jones PS, Cope TE, Passamonti L, Bevan-Jones WR, Patterson K, Fryer TD, Hong YT, Aigbirhio FI, O'Brien JT, Rowe JB (2021) In vivo PET imaging of neuroinflammation in familial frontotemporal dementia. *J Neurol Neurosurg Psychiatry* 92(3):319–322. <https://doi.org/10.1136/jnnp-2020-323698>
 53. Bevan-Jones WR, Cope TE, Jones PS, Passamonti L, Hong YT, Fryer T, Arnold R, Coles JP, Aigbirhio FI, O'Brien JT, Rowe JB (2019) In vivo evidence for pre-symptomatic neuroinflammation in a MAPT mutation carrier. *Ann Clin Transl Neurol* 6(2):373–378. <https://doi.org/10.1002/acn3.683>
 54. Miyoshi M, Shinotoh H, Wszolek ZK, Strongosky AJ, Shimada H, Arakawa R, Higuchi M, Ikoma Y, Yasuno F, Fukushi K, Irie T, Ito H, Suhara T (2010) In vivo detection of neuropathologic changes in presymptomatic MAPT mutation carriers: a PET and MRI study. *Parkinsonism Relat Disord* 16(6):404–408. <https://doi.org/10.1016/j.parkreldis.2010.04.004>
 55. Bartos LM, Kirchleitner SV, Kolabas ZI, Quach S, Blobner J, Mueller SA, Ulukaya S, Hoehner L, Horvath I, Wind-Mark K, Holzgreve A, Ruf VC, Gold L, Kunze LH, Kunte ST, Beumers P, Antons M, Zatcepin A, Briel N, Hoermann L, Messerer D, Bartenstein P, Riemenschneider MJ, Lindner S, Ziegler S, Herms J, Lichtenthaler SF, Ertürk A, Tonn JC, Baumgarten LV, Albert NL, Brendel M (2023) Deciphering sources of PET signals in the tumor microenvironment of glioblastoma at cellular resolution. *bioRxiv*. <https://doi.org/10.1101/2023.01.26.522174>
 56. Ohnishi A, Senda M, Yamane T, Mikami T, Nishida H, Nishio T, Akamatsu G, Ikari Y, Kimoto S, Aita K, Sasaki M, Shinkawa H, Yamamoto Y, Shukuri M, Mawatari A, Doi H, Watanabe Y, Onoe H (2016) Exploratory

- human PET study of the effectiveness of (11)C-ketoprofen methyl ester, a potential biomarker of neuroinflammatory processes in Alzheimer's disease. *Nucl Med Biol* 43(7): 438–444. <https://doi.org/10.1016/j.nucmedbio.2016.04.005>
57. Shukuri M, Mawatari A, Ohno M, Suzuki M, Doi H, Watanabe Y, Onoe H (2016) Detection of Cyclooxygenase-1 in activated microglia during amyloid plaque progression: PET studies in Alzheimer's disease model mice. *J Nucl Med* 57(2):291–296. <https://doi.org/10.2967/jnumed.115.166116>
 58. Lodder C, Scheyltjens I, Stancu IC, Botella Lucena P, Gutierrez de Rave M, Vanherle S, Vanmierlo T, Cremers N, Vanrusselt H, Brone B, Hanseeuw B, Octave JN, Bottelbergs A, Movahedi K, Dewachter I (2021) CSF1R inhibition rescues tau pathology and neurodegeneration in an A/T/N model with combined AD pathologies, while preserving plaque associated microglia. *Acta Neuropathol Commun* 9(1):108. <https://doi.org/10.1186/s40478-021-01204-8>
 59. Horti AG, Naik R, Foss CA, Minn I, Misheneva V, Du Y, Wang Y, Mathews WB, Wu Y, Hall A, LaCourse C, Ahn HH, Nam H, Lesniak WG, Valentine H, Pletnikova O, Troncoso JC, Smith MD, Calabresi PA, Savonenko AV, Dannals RF, Pletnikov MV, Pomper MG (2019) PET imaging of microglia by targeting macrophage colony-stimulating factor 1 receptor (CSF1R). *Proc Natl Acad Sci U S A* 116(5):1686–1691. <https://doi.org/10.1073/pnas.1812155116>
 60. Zhou X, Ji B, Seki C, Nagai Y, Minamimoto T, Fujinaga M, Zhang MR, Saito T, Saido TC, Suhara T, Kimura Y, Higuchi M (2021) PET imaging of colony-stimulating factor 1 receptor: a head-to-head comparison of a novel radioligand, (11)C-GW2580, and (11)C-CPPC, in mouse models of acute and chronic neuroinflammation and a rhesus monkey. *J Cereb Blood Flow Metab* 41(9):2410–2422. <https://doi.org/10.1177/0271678X211004146>
 61. Savonenko AV, Melnikova T, Wang Y, Ravert H, Gao Y, Koppel J, Lee D, Pletnikova O, Cho E, Sayyida N, Hiatt A, Troncoso J, Davies P, Dannals RF, Pomper MG, Horti AG (2015) Cannabinoid CB2 receptors in a mouse model of abeta amyloidosis: immunohistochemical analysis and suitability as a PET biomarker of neuroinflammation. *PLoS One* 10(6): e0129618. <https://doi.org/10.1371/journal.pone.0129618>
 62. Ahmad R, Postnov A, Bormans G, Versijpt J, Vandenbulcke M, Van Laere K (2016) Decreased in vivo availability of the cannabinoid type 2 receptor in Alzheimer's disease. *Eur J Nucl Med Mol Imaging* 43(12): 2219–2227. <https://doi.org/10.1007/s00259-016-3457-7>
 63. Illes P (2020) P2X7 receptors amplify CNS damage in neurodegenerative diseases. *Int J Mol Sci* 21(17). <https://doi.org/10.3390/ijms21175996>
 64. Martin E, Amar M, Dalle C, Youssef I, Boucher C, Le Duigou C, Bruckner M, Prigent A, Sazdovitch V, Halle A, Kanellopoulos JM, Fontaine B, Delatour B, Delarasse C (2019) New role of P2X7 receptor in an Alzheimer's disease mouse model. *Mol Psychiatry* 24(1):108–125. <https://doi.org/10.1038/s41380-018-0108-3>
 65. McLarnon JG, Ryu JK, Walker DG, Choi HB (2006) Upregulated expression of purinergic P2X(7) receptor in Alzheimer disease and amyloid-beta peptide-treated microglia and in peptide-injected rat hippocampus. *J Neuro-pathol Exp Neurol* 65(11):1090–1097. <https://doi.org/10.1097/01.jnen.0000240470.97295.d3>
 66. Koole M, Schmidt ME, Hijzen A, Ravenstijn P, Vandermeulen C, Van Weehaeghe D, Serdons K, Celen S, Bormans G, Ceusters M, Zhang W, Van Nueten L, Kolb H, de Hoon J, Van Laere K (2019) (18)F-JNJ-64413739, a novel PET ligand for the P2X7 Ion Channel: radiation dosimetry, kinetic modeling, test-retest variability, and occupancy of the P2X7 antagonist JNJ-54175446. *J Nucl Med* 60(5): 683–690. <https://doi.org/10.2967/jnumed.118.216747>
 67. Carter SF, Scholl M, Almkvist O, Wall A, Engler H, Langstrom B, Nordberg A (2012) Evidence for astrocytosis in prodromal Alzheimer disease provided by 11C-deuterium-L-deprenyl: a multitracer PET paradigm combining 11C-Pittsburgh compound B and 18F-FDG. *J Nucl Med* 53(1):37–46. <https://doi.org/10.2967/jnumed.110.087031>
 68. Rodriguez-Vieitez E, Carter SF, Chiotis K, Saint-Aubert L, Leuzy A, Scholl M, Almkvist O, Wall A, Langstrom B, Nordberg A (2016) Comparison of early-phase 11C-deuterium-L-Deprenyl and 11C-Pittsburgh compound B PET for assessing brain perfusion in Alzheimer disease. *J Nucl Med* 57(7): 1071–1077. <https://doi.org/10.2967/jnumed.115.168732>
 69. Rodriguez-Vieitez E, Saint-Aubert L, Carter SF, Almkvist O, Farid K, Scholl M, Chiotis K, Thordardottir S, Graff C, Wall A, Langstrom B,

- Nordberg A (2016) Diverging longitudinal changes in astrogliosis and amyloid PET in autosomal dominant Alzheimer's disease. *Brain* 139(Pt 3):922–936. <https://doi.org/10.1093/brain/awv404>
70. Scholl M, Carter SF, Westman E, Rodriguez-Vieitez E, Almkvist O, Thordardottir S, Wall A, Graff C, Langstrom B, Nordberg A (2015) Early astrogliosis in autosomal dominant Alzheimer's disease measured in vivo by multi-tracer positron emission tomography. *Sci Rep* 5:16404. <https://doi.org/10.1038/srep16404>
 71. Vilaplana E, Rodriguez-Vieitez E, Ferreira D, Montal V, Almkvist O, Wall A, Lleo A, Westman E, Graff C, Fortea J, Nordberg A (2020) Cortical microstructural correlates of astrogliosis in autosomal-dominant Alzheimer disease. *Neurology* 94(19):e2026–e2036. <https://doi.org/10.1212/WNL.0000000000009405>
 72. Chiotis K, Johansson C, Rodriguez-Vieitez E, Ashton NJ, Blennow K, Zetterberg H, Graff C, Nordberg A (2023) Tracking reactive astrogliosis in autosomal dominant and sporadic Alzheimer's disease with multi-modal PET and plasma GFAP. *Mol Neurodegener* 18(1):60. <https://doi.org/10.1186/s13024-023-00647-y>
 73. Ballweg A, Klaus C, Vogler L, Katzdobler S, Wind K, Zatcepin A, Ziegler SI, Secgin B, Eckenweber F, Bohr B, Bernhardt A, Fietzek U, Rauchmann BS, Stoecklein S, Quach S, Beyer L, Scheifele M, Simmet M, Joseph E, Lindner S, Berg I, Koglin N, Mueller A, Stephens AW, Bartenstein P, Tonn JC, Albert NL, Kumpfel T, Kerschensteiner M, Perneczky R, Levin J, Paeger L, Herms J, Brendel M (2023) [(18)F]F-DED PET imaging of reactive astrogliosis in neurodegenerative diseases: preclinical proof of concept and first-in-human data. *J Neuroinflammation* 20(1):68. <https://doi.org/10.1186/s12974-023-02749-2>
 74. Harada R, Hayakawa Y, Ezura M, Lertsirisuk P, Du Y, Ishikawa Y, Iwata R, Shidahara M, Ishiki A, Kikuchi A, Arai H, Kudo Y, Yanai K, Furumoto S, Okamura N (2021) (18)F-SMBT-1: a selective and reversible PET tracer for monoamine oxidase-B imaging. *J Nucl Med* 62(2):253–258. <https://doi.org/10.2967/jnumed.120.244400>
 75. Villemagne VL, Harada R, Doré V, Furumoto S, Mulligan R, Kudo Y, Burnham S, Krishnadas N, Bozinovski S, Huang K, Lopresti BJ, Yanai K, Rowe CC, Okamura N (2022) First-in-humans evaluation of (18)F-SMBT-1, a novel (18)F-labeled monoamine oxidase-B PET tracer for imaging reactive Astrogliosis. *J Nucl Med* 63(10):1551–1559. <https://doi.org/10.2967/jnumed.121.263254>
 76. Wilson H, Dervenoulas G, Pagano G, Tyacke RJ, Polychronis S, Myers J, Gunn RN, Rabiner EA, Nutt D, Politis M (2019) Imidazoline 2 binding sites reflecting astroglia pathology in Parkinson's disease: an in vivo 11C-BU99008 PET study. *Brain* 142(10):3116–3128. <https://doi.org/10.1093/brain/awz260>
 77. Calsolaro V, Matthews PM, Donat CK, Livingston NR, Femminella GD, Guedes SS, Myers J, Fan Z, Tyacke RJ, Venkataraman AV, Perneczky R, Gunn R, Rabiner EA, Gentleman S, Parker CA, Murphy PS, Wren PB, Hinz R, Sastre M, Nutt DJ, Edison P (2021) Astrocyte reactivity with late-onset cognitive impairment assessed in vivo using (11)C-BU99008 PET and its relationship with amyloid load. *Mol Psychiatry* 26(10):5848–5855. <https://doi.org/10.1038/s41380-021-01193-z>
 78. Kumar A, Koistinen NA, Malarte ML, Nennesmo I, Ingelsson M, Ghetti B, Lemoine L, Nordberg A (2021) Astroglial tracer BU99008 detects multiple binding sites in Alzheimer's disease brain. *Mol Psychiatry* 26(10):5833–5847. <https://doi.org/10.1038/s41380-021-01101-5>



Imaging Neuroinflammation: Quantification of Astrocytosis in a Multitracer PET Approach

Elena Rodriguez-Vieitez, Amit Kumar, Mona-Lisa Malarte, Konstantinos Ioannou, Filipa M. Rocha, and Konstantinos Chiotis

Abstract

The recent progress in the development of in vivo biomarkers is rapidly changing how neurodegenerative diseases are conceptualized and diagnosed and how clinical trials are designed today. Alzheimer's disease (AD) – the most common neurodegenerative disorder – is characterized by a complex neuropathology involving the deposition of extracellular amyloid- β ($A\beta$) plaques and intracellular neurofibrillary tangles (NFTs) of hyperphosphorylated tau proteins, accompanied by the activation of glial cells, i.e., astrocytes and microglia, and neuroinflammatory response, leading to neurodegeneration and cognitive dysfunction. An increasing diversity of positron emission tomography (PET) imaging radiotracers is available to selectively target the different pathophysiological processes of AD. Along with the success of $A\beta$ PET and the more recent tau PET imaging, there is a great interest to develop PET tracers to image glial reactivity and neuroinflammation. While most research to date has focused on imaging microgliosis, there is an upsurge of interest in imaging reactive astrocytes in the AD *continuum*. There is increasing evidence that reactive astrocytes are morphologically and functionally heterogeneous, with different subtypes that express different markers and display various homeostatic or detrimental roles across disease stages. Therefore, multiple biomarkers are desirable to unravel the complex phenomenon of reactive astrocytosis. In the field of in vivo PET imaging in AD, the research concerning reactive astrocytes has predominantly focused on targeting monoamine oxidase B (MAO-B), most often using either ^{11}C -deuterium-L-deprenyl (^{11}C -DED) or ^{18}F -SMBT-1 PET tracers. Additionally, imidazoline₂ binding (I_2BS) sites have been imaged using ^{11}C -BU99008 PET. Recent studies in our group using ^{11}C -DED PET imaging suggest that astrocytosis may be present from the early stages of disease development in AD. This chapter provides a detailed description of the practical approach used for the analysis of ^{11}C -DED PET imaging data in a multitracer PET paradigm including ^{11}C -Pittsburgh compound B (^{11}C -PiB) and ^{18}F -fluorodeoxyglucose (^{18}F -FDG). The multitracer PET approach allows investigating the comparative regional and temporal patterns of in vivo brain astrocytosis, fibrillar $A\beta$ deposition, glucose metabolism, and brain structural changes. It may also contribute to understanding the potential role of novel plasma biomarkers of reactive astrocytes, in particular the glial fibrillary acidic protein (GFAP), at different stages of disease progression. This chapter attempts to stimulate further research in the field, including the development of novel PET tracers that may allow visualizing different aspects of the complex astrocytic and microglial response in neurodegenerative diseases. Progress in the field will contribute to the incorporation of PET imaging of glial reactivity and neuroinflammation as biomarkers with clinical application and motivate further investigation on glial cells as therapeutic targets in AD and other neurodegenerative diseases.

Key words Alzheimer's disease, Amyloid, Astrocytosis, ^{11}C -deuterium-L-deprenyl, ^{18}F -fluorodeoxyglucose (^{18}F -FDG), ^{11}C -Pittsburgh compound B (^{11}C -PiB), Neuroinflammation, Multitracer PET imaging, Positron emission tomography

1 Introduction

Clinical practice in the field of neurodegenerative diseases is evolving toward an increasing reliance on in vivo biomarkers that may contribute to more accurate and differential diagnoses and help provide individualized care. No disease-modifying treatments are yet widely available for Alzheimer's disease (AD) – the most common cause of dementia – but research on in vivo biomarkers is rapidly advancing our understanding of the disease pathophysiology and progression. Biomarkers that can capture the earliest brain pathophysiological changes are needed for early diagnosis and as outcome measures in clinical trials of novel therapies at early stages [1], when they have the greatest chance to be efficacious.

Pathological hallmarks of AD include the abnormal deposition of extracellular amyloid- β ($\text{A}\beta$) plaques and intracellular aggregates of hyperphosphorylated tau proteins in the form of neurofibrillary tangles (NFTs) [2]. A commonly accepted model assumes that $\text{A}\beta$ plaque deposition is an initiating event [3], followed by deposition of NFTs, neurodegeneration, and cognitive decline [4]. Alternatively, $\text{A}\beta$ deposition and neurodegeneration may arise independently [5], and $\text{A}\beta$ may interact with tau NFTs to accelerate downstream pathological changes leading to cognitive dysfunction [6]. Furthermore, there is increasing evidence that AD is complex and multifactorial including glial reactivity and neuroinflammation [7, 8] involving microglia and astrocytes, which may play beneficial and/or detrimental roles from early stages [9–11] and may even be drivers of synapse loss, synaptic dysfunction, and cognitive impairment [12]. There is also increasing evidence for heterogeneity in the clinical presentation and cognitive phenotypes of AD patients [13]. Thus, the availability of multiple in vivo biomarkers reflecting the diverse pathophysiological features of AD will help characterize patients, apply more individualized treatments, and stratify participants for enrichment of clinical trials.

Continuously evolving neuroimaging techniques enable the investigation of in vivo regional brain changes including structural, molecular, and pathophysiological changes along disease progression. Positron emission tomography (PET) is a molecular imaging technique that allows visualization and absolute quantification of different brain pathophysiological alterations at the molecular level [14]. Different modalities of PET imaging are currently used to track $\text{A}\beta$, tau NFTs, glucose metabolism, brain perfusion, glial reactivity, and neuroinflammatory changes in AD. The ongoing development of new PET modalities is greatly expanding the

range of in vivo PET biomarkers that will become available in the near future.

PET imaging is based on the tracer concept. A tracer – labeled with a radioactive isotope and thus referred to as “radiotracer” – is injected into the individual’s bloodstream, eventually entering the brain and interacting selectively with a given target in a predictable way, without altering the brain homeostasis [14]. Table 1 lists the properties of a good radiotracer [15, 16]. As the radiotracer reaches the target in the brain, the attached radioactive isotope – most frequently fluorine-18 (half-life of 110 min) or carbon-11 (half-life of 20 min) – decays by the emission of a positron. After traveling a distance of about 1–3 mm, the positron combines with an electron in the brain tissue, resulting in the emission of two oppositely directed (at approximately 180°) photons (511 keV γ -rays), which are detected in temporal coincidence by a ring of scintillator detectors in the PET scanner. The reconstruction of all such simultaneous γ -ray detection events allows generating 3D brain images for visual assessment by clinicians, which are also amenable of absolute quantification characterized by high sensitivity – typically able to quantify biochemical properties at the nanomolar concentration range. While the spatial resolution of PET (1–2 mm) is lower than that of other brain imaging techniques such as magnetic resonance imaging (MRI), the strength of PET imaging is that it provides quantitative information on brain functional and molecular biology alterations.

The criteria for diagnosis of AD are continuously evolving toward a greater reliance on in vivo biomarkers including PET imaging [17, 18]. Recently, the PET A β tracers ¹⁸F-florbetapir, ¹⁸F-flutemetamol, and ¹⁸F-florbetaben were approved by the European Medicines Agency and by the US Food and Drug Administration for assessing the presence of A β pathology in individuals with early memory disorders.

Along with the success of A β PET, and the more recent tau PET imaging [19], there is also a great interest to develop PET tracers to image glial reactivity and neuroinflammation in AD and other neurodegenerative diseases [20–22]; Fig. 1 illustrates some of the most common PET tracers that have been applied in human studies to track different pathophysiological features of AD. Glial reactivity is meant to maintain homeostasis, both in aging and neurodegeneration, by surveying the brain environment for signs of harmful processes and then undergoing changes aimed at limiting the harm and repairing damage [23]. It is commonly accepted that a certain degree of glial reactivity is beneficial but that chronic and excess reactivity may instigate neuroinflammatory responses that trigger further damage and therefore may contribute to pathology [24]. While it is not well known whether microglia or astrocytes are activated first, both undergo different stages of anti-inflammatory or pro-inflammatory reactivity, and they interact

Table 1
Properties of a good PET radiotracer

Properties
High sensitivity: able to detect substances at the nanomolar concentration range
Enters the brain: adequate lipophilicity, adequate ability to cross the blood-brain barrier
High in vivo affinity and selectivity for a target
Low nonspecific binding
Suitable pharmacokinetic properties within the time interval of the PET scan
Limited plasma binding and peripheral metabolism
Low contamination from radioactive metabolites in the brain: radioactive metabolites do not significantly cross the blood-brain barrier
High specific activity that allows for reasonably low injected volumes

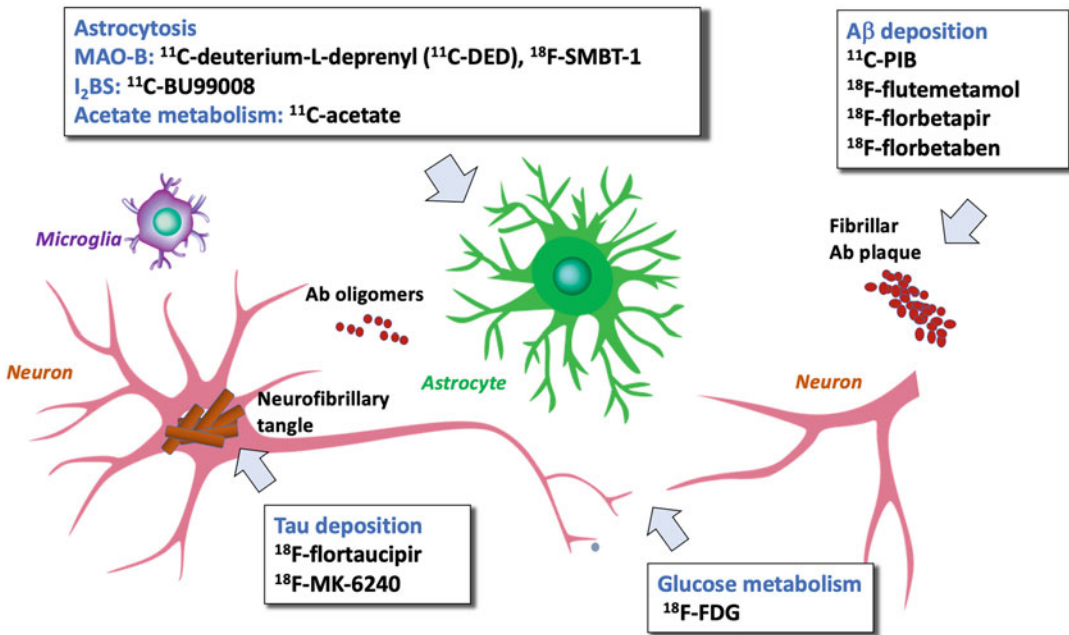


Fig. 1 Pathological features of Alzheimer's disease and selected PET tracers that have been applied in human PET studies

with each other to promote further neuroinflammatory responses [7].

Currently, PET imaging of neuroinflammation is not regarded as an in vivo biomarker for clinical diagnosis or to evaluate disease progression, but it may help in the future to diagnose neurodegenerative diseases and to test novel therapeutic agents targeting glial cells [25]; therefore, there is a significant interest to develop novel

biomarkers for glial reactivity and neuroinflammation [1]. Most studies on PET imaging of neuroinflammation in AD have aimed at visualizing microglial reactivity, as measured by elevated expression of translocator protein 18 kDa (TSPO), a five transmembrane domain protein mainly located in the outer mitochondrial membrane of microglia; for comprehensive reviews on this topic, please see [20, 21, 26]. While few studies claim that TSPO is also overexpressed in reactive astrocytes [27, 28], the overall agreement is that TSPO is mostly a marker of microglial reactivity. ^{11}C -PK11195 is the most widely used TSPO PET tracer, although it has relatively low brain penetrance and high nonspecific binding [29]. Second-generation TSPO PET tracers that have been already applied in human include ^{11}C -PBR28, ^{18}F -DPA-714, ^{18}F -FEPPA, ^{11}C -DAA1106, ^{18}F -PBR06, ^{18}F -PBR111, and ^{18}F -GE180, and novel tracers targeting alternative microglial targets are under development [21].

1.1 Current Status of PET Imaging Tracers for Astrocytosis

In neurodegenerative diseases, astrocytes adopt distinct state(s) and phenotypic changes in response to pathological damage and are termed “reactive astrocytes” – as defined in a recent consensus paper [30]. There is mounting evidence that there are diverse subtypes of reactive astrocytes that are morphologically and functionally heterogeneous. Reactive astrocytes may express different markers across subtypes and display beneficial or detrimental roles at different disease stages [24]. Therefore, multiple biomarkers are desirable to understand the complex phenomenon of astrocytosis, including both fluid and neuroimaging biomarkers, as reported in a recent review [31] and meta-analysis [32].

Very few PET tracers have been applied to investigate in vivo astrocyte reactivity, with monoamine oxidase B (MAO-B) being the prevalent target, most commonly measured using ^{11}C -deuterium-L-deprenyl (^{11}C -DED) [33]. Other emerging PET tracers to target MAO-B have been recently reviewed [22, 33]. Among these, several have already been successfully applied in human participants, with ^{18}F -SMBT-1 emerging as particularly promising [34, 35]. Advantages of ^{18}F -SMBT-1 include its potential for clinical use due to the fluorine-18 labeling, high specificity for MAO-B, and reversible kinetics. The uptake of ^{18}F -SMBT-1 was found to be elevated in patients with AD compared with controls [35]. Of note, while both ^{11}C -DED and ^{18}F -SMBT-1 tracers target MAO-B, results from the respective studies might not be fairly comparable due to differences in quantification methodologies. In particular, while the dynamic ^{11}C -DED PET images have been quantified using the modified reference Patlak model using the cerebellar gray matter as reference [36], the static ^{18}F -SMBT-1 images were evaluated using the standardized uptake value ratio (SUVr) with respect to the white matter used as reference region. These methodological differences highlight the need for further studies to

validate the respective findings using similar quantification methodologies.

Beyond MAO-B, novel PET tracers are under development to target other features of reactive astrocytes in AD [22]. A relevant target is imidazole binding sites (I₂BS), prominently expressed on the outer mitochondrial membrane of reactive astrocytes [37]. Only five PET tracers have been explored for targeting I₂BS so far [38], and only one of them (BU99008) has reached studies in human brain. In vitro studies showed higher uptake of ³H-BU99008 in the brains of AD patients compared with healthy controls [39]. Consistent with these in vitro findings, the ¹¹C-BU99008 tracer showed higher in vivo uptake in AD patients compared with controls [40].

Finally, there are efforts to investigate metabolic changes in astrocytes in vivo, using tracers to image acetate metabolism. In a recent translational study [41], the authors demonstrated that reactive astrocytes had an increased rate of acetate absorption via elevated monocarboxylate transporter-1 in mouse models and that AD patients had higher acetate uptake measured with in vivo ¹¹C-acetate PET compared with healthy controls in temporoparietal cortical regions, in coincidence with reduced glucose uptake as measured by ¹⁸F-FDG PET in the same regions. Higher ¹¹C-acetate PET was also reported in prodromal AD patients compared with healthy controls [42], providing further evidence that astrocytes become reactive from early stages of AD.

1.2 PET Imaging of Astrocytosis Using ¹¹C-Deuterium-L-Deprenyl

This chapter will focus in particular on the practical procedures to investigate PET imaging of in vivo astrocyte reactivity, also known as astrocytosis or astrogliosis, using the PET tracer ¹¹C-deuterium-L-deprenyl (¹¹C-DED). ¹¹C-DED binds specifically to MAO-B [43, 44], which is overexpressed in reactive astrocytes and serotonergic neurons [45–47]. Autoradiography studies using ³H-L-deprenyl and the commonly used in vitro marker for tracking astrocytosis, namely, glial fibrillary acidic protein (GFAP) immunohistochemistry, have demonstrated that ³H-L-deprenyl binding was co-localized with GFAP staining in the brain tissue from patients with amyotrophic lateral sclerosis (ALS) [45, 46, 48] and AD [49–51], indicating an overall moderate correlation between MAO-B and GFAP. An autoradiography study using ¹¹C-L-deprenyl in AD brain tissue showed the highest tracer binding in early Braak stages, thus suggesting an early involvement of astrocytes in the progression of the disease [52]. The laminar distribution of ³H-L-deprenyl had a different pattern than that of Aβ deposition as measured by ³H-PiB [50]. In contrast, the laminar pattern of ³H-L-deprenyl was more similar to that of tau deposits as measured by ³H-THK5117 [49].

In vivo PET investigations of MAO-B were initiated with a previously developed ¹¹C-L-deprenyl tracer (without deuterium

in its formulation) [43], which showed too high affinity and irreversible binding. The deuterated version of the tracer (^{11}C -deuterium-L-deprenyl) had lower rate of radiotracer trapping in the human brain compared to ^{11}C -L-deprenyl, indicating improved pharmacokinetic properties, in particular a lower influence of brain perfusion on tracer binding [53, 54]. Thus, the deuterated formulation resulted in improved sensitivity to detect proliferation of glial cells in neurodegenerative disease [53].

1.3 Association of ^{11}C -Deuterium-L-Deprenyl PET with $\text{A}\beta$, Tau, Glucose Metabolism, and Brain Structure: Review of Multitracer Studies

^{11}C -deuterium-L-deprenyl (^{11}C -DED) PET imaging has been used to investigate astrocytosis in neurodegenerative diseases including AD [55–57], ALS [36], and Creutzfeldt-Jakob disease (CJD) [58, 59]. A multitracer PET imaging paradigm has been applied in recent studies, whereby each individual undergoes dynamic PET imaging scans using three radiotracers: ^{11}C -DED, ^{11}C -Pittsburgh compound B (^{11}C -PiB), and ^{18}F -fluorodeoxyglucose (^{18}F -FDG). In these studies, significantly increased ^{11}C -DED binding was found in prodromal stages of AD in comparison with healthy controls or to patients with AD dementia [55], and ^{11}C -DED binding in prodromal AD patients was negatively correlated with gray matter density [60]. In addition, the early-phase uptake of ^{11}C -DED was demonstrated to be a surrogate marker for brain perfusion, allowing the tracer to have dual-use properties as a marker of both perfusion and astrocytosis [61]. The study of familial autosomal dominant AD (ADAD), in which mutation carriers develop clinical AD at a predictable age of onset, has allowed investigating brain pathophysiological and cognitive changes from early presymptomatic stages. By applying multitracer PET imaging in ADAD, the first in vivo observation of astrocytosis at early presymptomatic stages using the PET tracer ^{11}C -DED was reported [62], as well as diverging longitudinal trajectories showing increasing $\text{A}\beta$ plaque deposition (^{11}C -PiB), while declining levels of both astrocytosis (^{11}C -DED) and glucose metabolism (^{18}F -FDG) [57, 63]. Furthermore, ^{11}C -DED binding was associated with microstructural changes as quantified in the gray matter using diffusion-weighted imaging [64]. Early astrocytosis preceding $\text{A}\beta$ plaque deposition was also replicated in a transgenic mouse model of AD [65]. Thus, early elevation in astrocytosis suggested promising therapeutic potential [66].

1.4 Relationship of ^{11}C -Deuterium-L-Deprenyl PET with Plasma Glial Fibrillary Protein (GFAP)

GFAP is part of the astrocyte cytoskeleton, and it is the most common marker for tracking reactive astrocytes at autopsy using in vitro investigations. There are recent advances in assays used to quantify GFAP both in the CSF and in plasma [67]. However, the association of peripheral GFAP levels with astrocyte reactivity remains to be explored. With the advent of plasma biomarkers in neurodegenerative diseases, there are numerous recent studies that investigate plasma GFAP in relation to other biomarkers in the AD

continuum and other neurodegenerative diseases [67, 68]. It has been suggested that reactive astrocytes release GFAP into the bloodstream via the astrocyte end-feet surrounding the brain capillaries, and plasma GFAP was found to be closely associated with A β deposition in the AD *continuum* [67]. However, further comparative biomarker studies are needed to verify whether plasma GFAP reflects brain astrocytosis. Two studies have addressed the association between astrocytosis using PET imaging versus plasma GFAP [56, 69], presenting with contrasting results. In a multimodal cross-sectional study of ADAD, ^{11}C -DED declined in mutation carriers from presymptomatic stages of ADAD toward symptomatic stages, while plasma GFAP showed an opposite trend of continuously increasing values [56]. The observed divergent patterns can be interpreted to suggest that astrocytosis measured with ^{11}C -DED may reflect a different subtype or state of reactive astrocytes compared with that measured by plasma GFAP [56]. In contrast, a cross-sectional study in the AD *continuum* has reported a positive association of plasma GFAP with brain ^{18}F -SMBT-1 PET retention in brain regions that have early A β accumulation, although the association was reported as low-to-moderate [69]. The differences observed between these studies may be partly attributed to the different cohort and PET image quantification methods, along with the selected reference regions. For example, although ^{18}F -SMBT-1 is quantified using the white matter as reference, the white matter is not entirely devoid of MAO-B uptake, which may influence the interpretation of the findings, underscoring the need for further validation studies.

1.5 Summary

In summary, the findings of early astrocytosis using ^{11}C -DED motivate further research on PET imaging of glial reactivity. This chapter provides a detailed description of the practical approach used for the analysis of ^{11}C -DED PET imaging data in a multitracer PET paradigm including ^{11}C -PiB and ^{18}F -FDG. The multitracer PET approach has shown great value to investigate the comparative regional and temporal patterns of in vivo brain astrocytosis, fibrillar A β deposition, and glucose metabolism in patients with sporadic or familial AD. In this chapter, the illustration of the multitracer PET imaging paradigm attempts to motivate further research in this field, including the development of novel PET tracers targeting a wider array of markers to visualize different stages of astrocytic and microglial reactivity. Advancements in longitudinal, multimodal imaging and fluid biomarkers will contribute to characterizing the complex heterogeneity (multiple states/subtypes) of reactive astrocytes in different brain diseases. Progress in the field will promote the future integration of PET imaging of glial reactivity and neuroinflammation as biomarkers with clinical application in AD and other neurodegenerative diseases and to further explore glial cells as promising therapeutic targets.

2 Materials

2.1 MRI Scanners

1. MRI imaging scans are performed in a 3 Tesla (T) Siemens Trio scanner.

2.2 PET Scanners

1. PET imaging scans are performed at the Uppsala PET Center (Uppsala, Sweden) on ECAT EXACT HR+ (Siemens/CTI) and GE discovery ST PET/CT scanners.

2.3 Image Analysis Software

1. The **Statistical Parametric Mapping (SPM)** software was developed by Friston and colleagues at the University College London [70–72]. The SPM8 software version and its associated toolboxes can be freely downloaded (<http://www.fil.ion.ucl.ac.uk/spm/>), and it requires MATLAB (www.mathworks.com/products/matlab/).
2. **VINCI** (“Volume Imaging in Neurological Research, Co-Registration and ROIs included”) is a software tool that was designed for the visualization and analysis of volume data generated by medical tomographical systems, with a special focus on the needs for data analysis in PET imaging (<http://vinci.sf.mpg.de>).
3. **VOIager** is an imaging software tool developed by GE Healthcare (<https://www.ge.com/digital/industries/healthcare>).
4. The **Hammers brain atlas** is a freely available adult brain maximum probability map in Montreal Neurological Institute (MNI) space (<http://brain-development.org/brain-atlases/adult-brain-maximum-probability-map-hammers-mith-atlas-n30r83-in-mni-space/>). In our studies, PET uptake has been quantified with either the Hammers atlas version with 29 regions of interest (ROIs) [57] or with an in-house volumetric MNI space version of the Desikan-Killiany atlas [56].
5. **Imlook4d** (<https://dicom-port.com/product/imlook4d/>) is a free advanced medical imaging analysis software tool, which can be used for scripting and algorithm development, and is easily extended using MATLAB.
6. The **Biological Parametric Mapping (BPM)** software is a toolbox for multimodal image analysis based on a voxel-wise application of the general linear model (<https://www.nitrc.org/projects/rbpm/>). The BPM toolbox has been developed in MATLAB, it incorporates a user-friendly interface for performing voxel-wise correlation and regression analyses, and it relies on the SPM software for visualization and statistical inference [73].

3 Methods

This section illustrates the practical procedures for multitracer PET imaging, as applied in previously published studies by our group [55–57, 74]. In summary, each participant receives, on the same day, three dynamic PET scans using the radiotracers ^{11}C -PiB, ^{11}C -DED, and ^{18}F -FDG. The description below includes the procedures for the recruitment of participants, MRI image acquisition, PET radiotracer synthesis, PET image acquisition, reconstruction and analysis, and PET quantification. For ^{11}C -DED PET, full quantitative analysis is performed using a graphical approach based on the modified reference Patlak model [36, 75], which was previously validated against a model using arterial sampling [76]. For ^{11}C -PiB and ^{18}F -FDG, semiquantitative analyses are performed by means of the SUVr, using either the cerebellar gray matter or the pons as a reference region. Figure 2 presents an overview of the experimental setup for PET image scanning, image acquisition, processing, and quantification.

3.1 Participants

1. Patients, referred for memory problems to the Department of Geriatric Medicine, Karolinska University Hospital, Huddinge, Sweden, are recruited for the study.
2. Healthy elderly individuals, who may be recruited from advertising in the community, do not deviate from clinically normal in a physical examination and have normal MRI findings.
3. All participants sign a written informed consent to participate in the study, which is conducted according to the declaration of Helsinki and subsequent revisions. Prior to the study initiation, ethical approval is obtained from the regional Human Ethics Committee of Stockholm and the Faculty of Medicine and Radiation Hazard Ethics Committee of Uppsala University Hospital, Sweden.
4. Patients undergo a comprehensive clinical and imaging examination including medical history, neurological and psychiatric examination, MRI, apolipoprotein E (*APOE*) genotyping from blood, neuropsychological assessment, and cerebrospinal fluid (CSF) analysis.
5. Diagnoses are made during a consensus meeting where a geriatrician/neurologist, a neuropsychologist, and a nurse discuss the outcome of the assessment of the patients.
6. Patients are diagnosed as either mild cognitive impairment (MCI) or probable AD dementia.
7. The diagnosis of mild cognitive impairment (MCI) is based on Petersen's criteria [77].

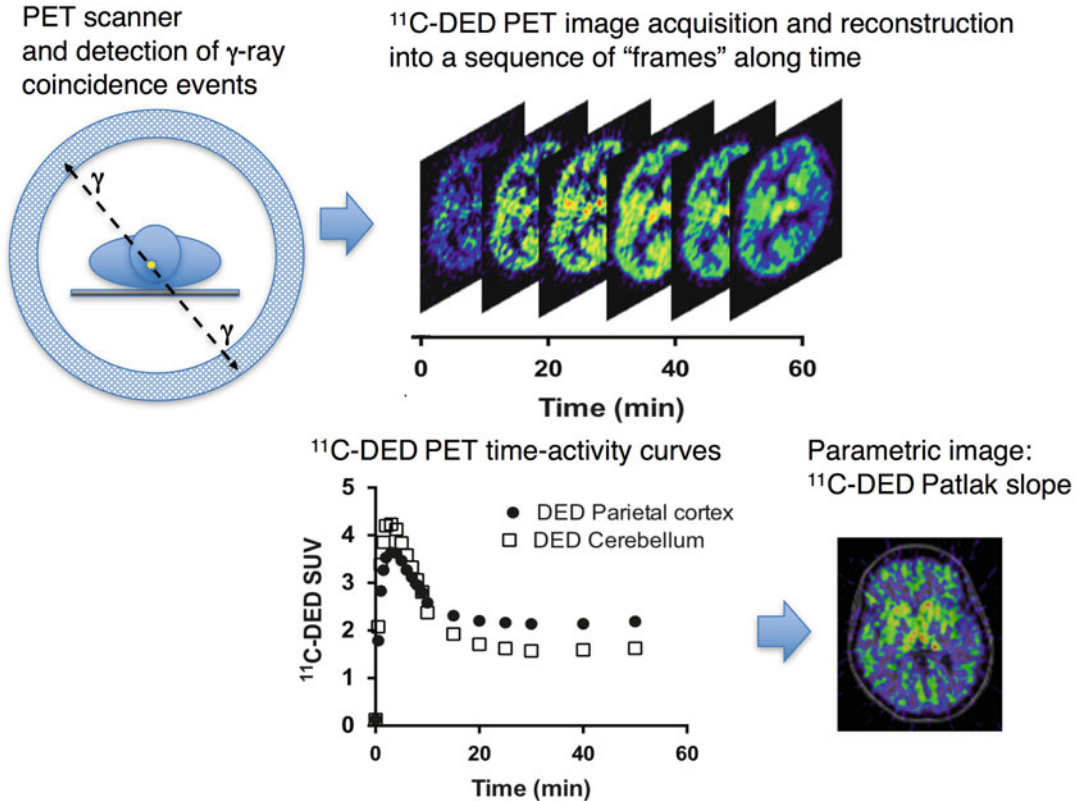


Fig. 2 Schematic diagram of PET imaging experimental setup for data acquisition, processing, and quantification. *DED* ^{11}C -deuterium-L-deprenyl, *PET* positron emission tomography, *SUV* standardized uptake value (PET radiotracer uptake normalized to injected dose and body weight)

8. Probable AD dementia is diagnosed according to the National Institute of Neurologic and Communication Disorders, Alzheimer Disease and Related Disorders Association (NINCDS-ADRDA) criteria [78].
9. MCI patients are further divided into PiB-positive and PiB-negative groups using a cutoff value of 1.41 neocortical SUV_r with reference to the cerebellar gray matter, as previously described [79]. The subgroup of PiB-positive MCI patients fulfills the diagnostic criteria for prodromal AD [18].

3.2 MRI

1. All participants undergo a structural 3D T_1 magnetization-prepared rapid-acquisition gradient-echo (MPRAGE) sequence on a 3 Tesla (T) Siemens Trio MRI scanner.
2. MRI images are acquired with a matrix size of $192 \times 256 \times 256$ and voxel size of $1.0 \times 0.98 \times 0.98$ mm and are reconstructed to $1.0 \times 1.0 \times 1.0$ mm isometric voxels, with an echo time of 3.42 ms, repetition time of 1780 ms, inversion time of 900 ms, and flip angle of 9° .

3. To exclude patients with non-AD-related brain abnormalities and to examine possible brain abnormalities in healthy controls, fluid-attenuated inversion recovery T₂ and diffusion-weighted images are also acquired.
4. The structural T₁ MRI image for Subject 01 (as an example) is labeled: **01_T1_MRI.nii**. (*see Note 1*).

3.3 Radiotracer Synthesis and Preparation

1. Production of ¹¹C-PiB, ¹¹C-DED, and ¹⁸F-FDG is carried out according to the standard good manufacturing process at Uppsala University PET Centre.
2. Radiotracer synthesis procedures are reported elsewhere [[36](#), [54](#), [76](#), [80](#), [81](#)].

3.4 PET Image Acquisition

1. Each participant undergoes three PET imaging scans on the same day, using three PET tracers in the following order: ¹¹C-PiB, ¹¹C-DED, and ¹⁸F-FDG.
2. PET scans are acquired at the Uppsala PET Center (Uppsala, Sweden) on either ECAT EXACT HR+ (Siemens/CTI) or GE discovery ST PET/CT scanners.
3. Participants are injected each radiotracer by intravenous injection. The mean injected doses for each tracer are 211 ± 65 MBq for ¹¹C-DED, 227 ± 76 MBq for ¹¹C-PiB, and 229 ± 42 MBq for ¹⁸F-FDG, as previously reported [[57](#)].
4. Patients fast for 4 h preceding the ¹⁸F-FDG scan.
5. The orbitomeatal line is used to center the head of the participants.
6. The PET data are acquired as the patient lies in the scanner during 60 min (for each of ¹¹C-PiB and ¹¹C-DED scans) and 45 min for the ¹⁸F-FDG scan.
7. The PET data are acquired in three-dimensional mode, yielding a 155 mm field of view.

3.5 PET Image Reconstruction

1. All emission data are reconstructed with filtered back projection using a 4 mm Hanning filter, resulting in a transaxial spatial resolution of 5 mm in the field of view. The matrix includes 128×128 pixels, and a zoom factor of 2.5 is used.
2. The ¹¹C-PiB acquisitions consist of 24 time frames (4×30 , 9×60 , 3×180 , and 8×300 s) over 60 min. The ¹¹C-DED reconstructed acquisitions consist of 19 frames (4×30 , 8×60 , 4×300 , and 3×600 s), with a total duration of 60 min. For each ¹⁸F-FDG acquisition, 21 frames (4×30 , 9×60 , 3×180 , and 4×300 s) are acquired over 45 min.

3.6 Within-Subject Realignment and Summation of PET Images

1. All reconstructed frames are realigned to correct for subject motion during each PET scan.
2. Using VOIager software, the dynamic PET data are processed to perform intra-subject realignment, by aligning each successive frame to the previous frame to correct for possible motion of the subject during the scan.
3. For each of the tracers, the realigned dynamic series of each PET tracer is subsequently uploaded into VOIager, which is used to create average images of the late-frame PET uptake, also called “summation images.” More specifically, the following late-frame time-weighted averaged (or “summation”) images are created: a 50-min static image for ^{11}C -DED, corresponding to 10–60 min; a 20-min static image for ^{11}C -PiB, corresponding to 40–60 min; and a 15-min static image for ^{18}F -FDG, corresponding to 30 to 45 min. These images are labeled as follows (for Subject 01): **01_DED_late_sum.nii**; **01_PiB_late_sum.nii**; **01_FDG_late_sum.nii**.
4. In addition, frames 3 to 6 of ^{11}C -DED, corresponding to 1- to 4-min tracer uptake, are summed to obtain a measure of brain perfusion: **01_DED_early_sum.nii**; this optimum early-phase time frame duration was previously reported as a proxy for brain perfusion based on its close correlation with glucose metabolism as measured by ^{18}F -FDG in the same subjects [61].

3.7 Within-Subject Co-Registration Procedures

1. Figure 3 illustrates the within-subject co-registration procedures for Subject 01, involving one structural MRI scan and three PET images using ^{11}C -DED, ^{11}C -PiB, and ^{18}F -FDG, respectively.
2. After the ^{11}C -DED PET data had been reconstructed and realigned and the late frames were summed, the ^{11}C -DED images are not transformed any further. Therefore, in this protocol, all the steps for the PET image analysis of one individual are performed in the subject’s native ^{11}C -DED PET space.
3. For each participant, the T_1 MRI image (**01_T1_MRI.nii**) is co-registered onto the individual’s ^{11}C -DED late-sum image in native ^{11}C -DED space (**01_DED_late_sum.nii**) using SPM8 (Functional Imaging Laboratory, Wellcome Department of Imaging Neuroscience, University College London) (*see Note 2*).
4. To perform this co-registration step, the function “Coregister (Estimate & Reslice)” is applied using the VBM/PET SPM8 module. The reference image (which remains static) is **01_DED_late_sum.nii**, and the source image (the image that is moved onto the space of the reference image) is **01_T1_MRI.nii**. As a result of the procedure, the

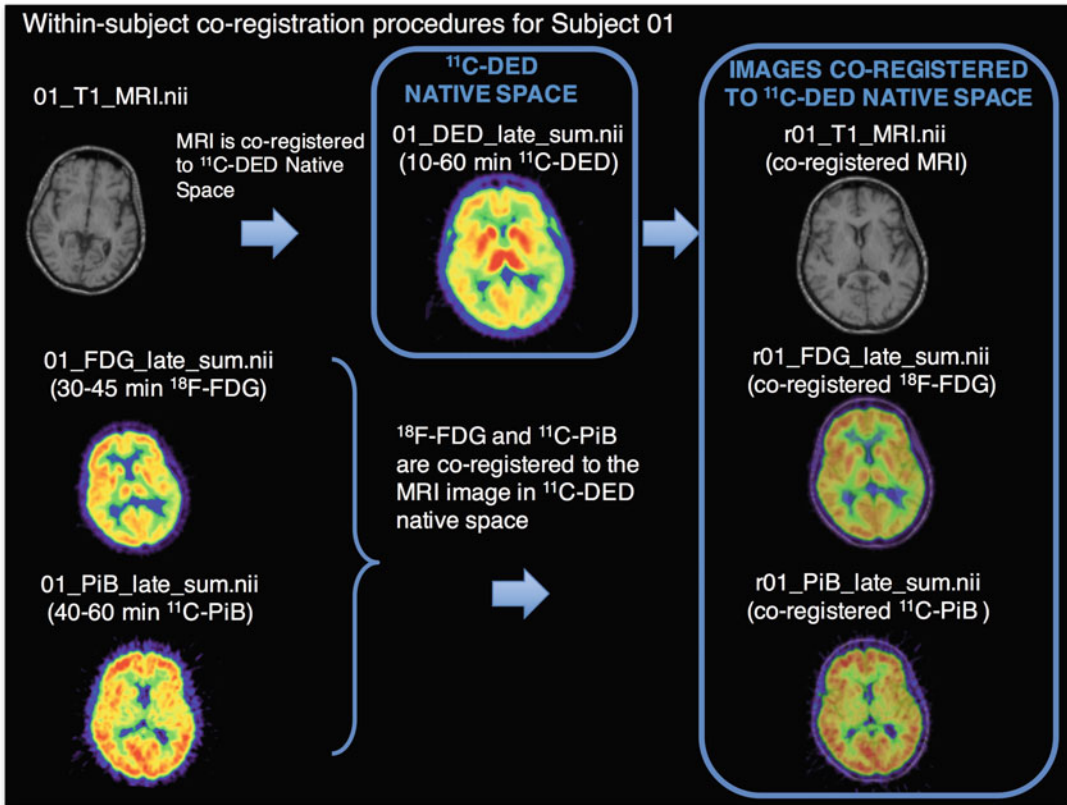


Fig. 3 Within-subject co-registration procedures for MRI and PET images, illustrated for an AD dementia patient

co-registered T₁ MRI image is automatically labeled with an r prefix, thus labelled: **r01_T1_MRI.nii** (see Note 3).

5. Also for each participant, the SPM8 function “Coregister (Estimate & Reslice)” is used to co-register the ¹¹C-PiB and ¹⁸F-FDG late-sum images (**01_PiB_late_sum.nii** and **01_FDG_late_sum.nii**, used as “Source Images”) onto the individual T₁ MRI image (**r01_T1_MRI.nii**, used as “Reference image”). As a result, the co-registered ¹¹C-PiB and ¹⁸F-FDG late-sum images are labeled: **r01_PiB_late_sum.nii** and **r01_FDG_late_sum.nii** (see Note 4).

3.8 Subject-Specific Gray Matter Atlas for PET Image Quantification

1. Figure 4 illustrates the steps for within-subject PET image quantification (for Subject 01), which involves the creation of a subject-specific gray matter atlas, using the Hammers atlas as a basis.
2. After the individual T₁ MRI image was co-registered to native DED space (**r01_T1_MRI.nii**, described in Subheading 3.7, step 4), the MRI image is segmented into gray matter and white matter tissue classes using the unified segmentation

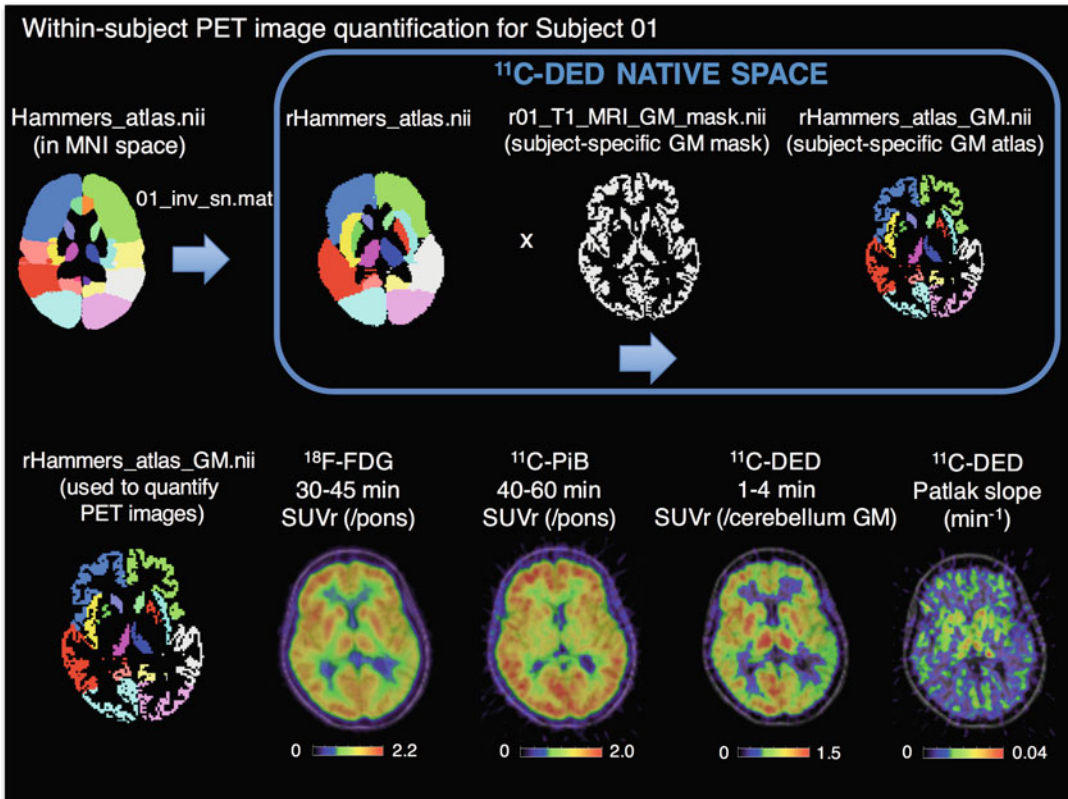


Fig. 4 Within-subject quantification of PET images, illustrated for an AD dementia patient. *GM* gray matter, *SUVr* standardized uptake value ratio

algorithm of SPM8 [82]; the subject-specific probabilistic gray matter map for Subject 01 is saved as **r01_T1_MRI_GM_map.nii**. For this step, the “Segment” function of SPM8 is used with the default parameters. This segmentation step results in two matrices: a direct matrix **01_sn.mat** that transforms images from native $^{11}\text{C-DED}$ space into MNI space and the corresponding inverse matrix **01_inv_sn.mat** that transforms images in the reverse direction: from MNI into native $^{11}\text{C-DED}$ space.

3. The inverse nonlinear transformation matrix from SPM8’s segmentation algorithm (**01_inv_sn.mat**) is then used to warp the simplified digital probabilistic Hammers atlas (**Hammers_atlas.nii**) [83] consisting of 29 cortical and subcortical ROIs, as well as a hand-drawn whole pons region (**Pons_atlas.nii**) – both in MNI space – into the $^{11}\text{C-DED}$ native space of Subject 01 (**rHammers_atlas.nii** and **rPons_atlas.nii**, respectively). To perform this step, the “Normalise (write)” function from SPM8 is applied to the atlas and pons images in MNI

space, using the **01_inv_sn.mat** matrix as the parameter file (*see Note 5*).

4. A threshold of 0.5 is applied to the subject-specific probabilistic gray matter map (**r01_T1_MRI_GM_map.nii**), whereby voxels with a probability greater than 50% of being gray matter are assigned a value of 1 and 0 otherwise. This step results in a subject-specific gray matter mask in native ^{11}C -DED space and is saved as **r01_T1_MRI_GM_mask.nii** (*see Note 6*).
5. The subject-specific Hammers atlas in ^{11}C -DED native space (**rHammers_atlas.nii**) is multiplied by the corresponding binary gray matter mask (**r01_T1_MRI_GM_mask.nii**), which generates a gray matter specific digital atlas for Subject 01, saved as **rHammers_atlas_GM.nii** (*see Note 7*).

3.9 Model for Quantification of ^{11}C -DED PET Image Data

1. For ^{11}C -DED quantification, a modified reference Patlak model [36, 75] is applied to the ^{11}C -DED dynamic PET data from 20 to 60 min, as previously described [55, 57] (*see Note 8*).
2. The modified reference Patlak model belongs to a group of graphical analysis techniques, in this case based on the Patlak linearization approach [75]. Following the Patlak approach, a scatter plot is created where the y axis is the measured PET activity in a target ROI divided by that in the reference tissue, and the x axis is a “normalized time” (integral of the reference time-activity curve from the injection point to the current time point and divided by the reference tissue PET activity at the current time point). The scatter plot is fitted by linear regression after an equilibration time t^* , and the slope of the regression line is the estimate of radiotracer binding in the target ROI (*see Note 9*).
3. The cerebellar gray matter is selected here as “modified reference,” based on that it has the lowest specific binding of all brain regions, as reported in a previous autoradiography study using ^{11}C -DED in brain tissue from AD patients and healthy controls [52]. The cerebellar gray matter also showed the lowest ^{11}C -DED binding of all investigated regions in the present studies [55, 57].
4. The modified reference Patlak model assumes a cerebellar gray matter slope value of 0.01 min^{-1} , to take into account the fact that this region is not completely devoid of specific binding.
5. The graphical approach generates individual 3D parametric Patlak slope images, which are thus the estimates of ^{11}C -DED binding (units: min^{-1}). An individual Patlak slope parametric image for Subject 01 is illustrated in Fig. 4.

3.10**Semiquantitative Method for ^{11}C -PiB and ^{18}F -FDG PET Image Data**

1. The previously co-registered and resliced ^{11}C -PiB and ^{18}F -FDG images for each participant, both in native ^{11}C -DED space (**r01_PiB_late_sum.nii** and **r01_FDG_late_sum.nii**), are sampled using the created individual gray matter atlas (**r01_Hammers_GM.nii**) and the individual pons atlas (**r01_pons.nii**), both having been previously co-registered to native ^{11}C -DED space.
2. Either the whole pons or the cerebellar gray matter has been reported as suitable reference regions for both ^{11}C -PiB and ^{18}F -FDG PET quantification in sporadic AD. The whole pons is used as example in this protocol, because it was found to be preserved from pathology in both ADAD and sporadic AD [84, 85] (*see Note 10*).
3. Using the individual gray matter atlas, the ratios of average ^{11}C -PiB and ^{18}F -FDG uptake are calculated for each atlas ROI with respect to the respective average uptake in the reference region, which are called standardized uptake value ratios (SUVr) and are thus dimensionless. Images displaying PET quantification using SUVr are illustrated in Fig. 4 (*see Note 11*).

3.11 Statistical Approaches for Comparison of PET Uptake Between Diagnostic Groups

1. A cross-sectional PET imaging study typically aims at comparing PET uptake between a diagnostic group (e.g., a group of prodromal AD or of AD dementia patients) and a group of healthy controls. A study will typically perform region-of-interest (ROI) and/or voxel-wise types of analyses, which may provide complementary information.

3.12 Region-of-Interest (ROI) Based Analyses

1. A number of brain ROIs are selected based on a hypothesis to be tested. Alternatively, an exploratory analysis over wide brain regions may be justified when investigating novel tracers, for which little previous information is available.
2. Parametric or nonparametric statistical tests are applied as appropriate to compare PET uptake in the selected ROIs between a diagnostic and a control group (*see Note 12*).
3. Due to the multiple ROIs analyzed, appropriate methods for the correction for multiple comparisons are applied. For PET data analysis, a procedure controlling for false discovery rate as implemented in the Benjamini-Hochberg method [86] using p-plot software [87] may be applied to correct for multiple regional tests.

3.13 Voxel-Wise Analyses

1. Voxel-wise analyses may be performed to compare the PET uptake between a diagnostic and a control group.
2. Prior to voxel-wise analyses, individual PET uptake images from different subjects need to be spatially normalized to

MNI space, to allow for comparisons across individuals. The normalization step is performed using SPM8 “Normalize (write)” using the previously obtained transformation matrix (**01_matrix_sn.mat**) as parameter file, for conversion of the individual PET uptake images from native ^{11}C -DED space to MNI space.

3. Normalized images are smoothed by an 8 mm full width at half maximum (FWHM) Gaussian filter using the VBM/PET SPM8 “Smooth” function and masked using a gray matter mask to allow for sampling of only gray matter regions.
4. A voxel-wise comparison between PET uptake in a diagnostic vs. a control group is performed using SPM8 two-sample t-test function for group comparisons.
5. A voxel-wise correlation analysis between two PET imaging modalities in a given diagnostic group is performed using Biological Parametric Mapping (BPM, v3.3) [73].
6. BPM correlation maps and SPM8 T-maps are thresholded at $p < 0.001$ (uncorrected, ≥ 20 -voxel cluster extent) and projected onto a template cortical surface using FreeSurfer (v5.3, surfer.nmr.harvard.edu) or BrainNet Viewer (a toolbox for SPM8; <https://www.nitrc.org/projects/bnv/>). Clusters that remain significant after family-wise error (FWE, $p < 0.05$) correction for multiple comparisons are tabulated.

4 Notes

1. Brain images are typically in the format NIfTI (Neuroimaging Informatics Technology Initiative) and have an extension .nii. Other widely used formats for medical images include DICOM (Digital Imaging and Communications in Medicine), Analyze, ECAT, and Interfile.
2. Alternatively, a subject’s static MRI scan may be used as template (native space), and the individual’s PET image (or images) is co-registered to the MRI template, as in the recently published multimodal study from our group involving ^{11}C -DED PET imaging [56], which also used more recently developed SPM12 version of Statistical Parametric Mapping. In the protocol described in this chapter, the intention was to preserve the ^{11}C -DED image quality as closely as possible to as the original image data to allow for modeling and quantification of this tracer using the Imlook4d software.
3. Given that this co-registration is an intermodal within-subject registration procedure, a six-parameter rigid-body transformation is applied using the “Coregistration (Estimate & Reslice)” option in SPM8 and Normalised Mutual Information as

Objective Function. Reslice options are trilinear interpolation, no wrapping, and no masking of images.

4. When performing multiple image processing steps in SPM8 for a cohort of participants, it is useful to develop MATLAB scripts that allow for automatization of the processes (https://en.wikibooks.org/wiki/SPM/Programming_intro).
5. The SPM8 “Normalise (write)” function is applied using the Nearest Neighbour Interpolation option, no wrapping, and preserving concentrations (all parameters for bounding box and voxel sizes are entered as NaN).
6. This thresholding step can be performed using “ImCal” option in SPM8, or other imaging software tools such as VINCI, using the Threshold Tool, and Image Volume Arithmetics.
7. The segmented gray matter from the MRI is used to restrict the sampling to gray matter areas within each region-of-interest in the Hammers atlas. This multiplication step can be performed using “ImCal” option in SPM8.
8. Ideally, a reference region has virtually no specific binding of the tracer. A “modified reference” is a region with a relatively low specific binding of the tracer, and lower than that in the remaining brain regions, and which can thus be used as modified reference.
9. The modified reference Patlak graphical approach can be applied in two ways: to fit time-activity curves extracted from each of the ROIs of the atlas or by fitting the dynamic ^{11}C -DED PET data pixel-by-pixel and thus obtaining parametric images of the ^{11}C -DED binding. Both approaches are implemented in MATLAB scripts using Imlook4d. More recently [56], we have applied the modified reference Patlak model to ^{11}C -DED PET data using the open source QModeling toolbox [88].
10. If the study involves familial ADAD participants, it is important to note that the cerebellar gray matter has been found to contain A β plaque deposits, and it is thus typically not used as a reference region in ADAD [84]; instead, the pons may be used. The pons has been used as reference for both ^{11}C -PiB and ^{18}F -FDG in sporadic or familial forms of AD [57, 89].
11. The semi-quantification of ^{11}C -PiB and ^{18}F -FDG in terms of SUVr is very common in the literature and has the advantage of simplicity and thus ease of application in the clinic. Previous studies have validated these SUVr semiquantitative approach for ^{11}C -PiB and ^{18}F -FDG PET against other available fully quantitative modeling approaches [90, 91].

12. Statistical analyses are performed using SPSS (IBM SPSS Statistics, version 22.0) and R (v. 3.1.2, R Foundation for Statistical Computing, Vienna, Austria).

Acknowledgments

We are grateful to the staff at the Uppsala PET Center. E.R-V. received funding from the Stockholm County Council-Karolinska Institutet regional agreement on medical training and clinical research (ALF grant), Neurofonden, Swedish Dementia Association (Demenfonden), Åhlén Foundation, Swedish Alzheimer Foundation (Alzheimerfonden), Gamla Tjänarinnor foundation, Gun and Bertil Stohne's Foundation, and the Karolinska Institutet Foundation for Medical Research (KI Fonder). A.K. received funding from Swedish Dementia Association (Demenfonden), Åhlén Foundation, Swedish Alzheimer Foundation (Alzheimerfonden), Gamla Tjänarinnor Foundation, Gun and Bertil Stohne's Foundation, the Karolinska Institutet Foundation for Medical Research (KI Fonder), Magnus Bergvalls Stiftelse, Tore Nilsons Stiftelse, and the Alzheimer Association USA (AARF-21-848395). K. I. received funding from the Swedish Dementia Association (Demensfonden). K.C. was supported by Region Stockholm (clinical postdoctoral appointment).

References

1. Mattsson N, Carrillo MC, Dean RA et al (2015) Revolutionizing Alzheimer's disease and clinical trials through biomarkers. *Alzheimers Dement (Amst)* 1:412–419. <https://doi.org/10.1016/j.dadm.2015.09.001>
2. Braak H, Braak E (1991) Neuropathological staging of Alzheimer-related changes. *Acta Neuropathol* 82:239–259. <https://doi.org/10.1007/BF00308809>
3. Hardy J, Selkoe DJ (2002) The amyloid hypothesis of Alzheimer's disease: progress and problems on the road to therapeutics. *Science* 297:353–356. <https://doi.org/10.1126/science.1072994>
4. Jack CR, Knopman DS, Jagust WJ et al (2013) Tracking pathophysiological processes in Alzheimer's disease: an updated hypothetical model of dynamic biomarkers. *Lancet Neurol* 12:207–216. [https://doi.org/10.1016/S1474-4422\(12\)70291-0](https://doi.org/10.1016/S1474-4422(12)70291-0)
5. Jack CR, Wiste HJ, Weigand SD et al (2013) Amyloid-first and neurodegeneration-first profiles characterize incident amyloid PET positivity. *Neurology* 81:1732–1740. <https://doi.org/10.1212/01.wnl.0000435556.21319.e4>
6. Sperling R, Mormino E, Johnson K (2014) The evolution of preclinical Alzheimer's disease: implications for prevention trials. *Neuron* 84:608–622. <https://doi.org/10.1016/j.neuron.2014.10.038>
7. Heneka MT, Carson MJ, Khoury JE et al (2015) Neuroinflammation in Alzheimer's disease. *Lancet Neurol* 14:388–405. [https://doi.org/10.1016/S1474-4422\(15\)70016-5](https://doi.org/10.1016/S1474-4422(15)70016-5)
8. De Strooper B, Karran E (2016) The cellular phase of Alzheimer's disease. *Cell* 164:603–615. <https://doi.org/10.1016/j.cell.2015.12.056>
9. Thal DR (2012) The role of astrocytes in amyloid β -protein toxicity and clearance. *Exp Neurol* 236:1–5. <https://doi.org/10.1016/j.expneurol.2012.04.021>
10. Acosta C, Anderson HD, Anderson CM (2017) Astrocyte dysfunction in Alzheimer disease: astrocytes in Alzheimer's disease. *J Neurosci Res* 95:2430–2447. <https://doi.org/10.1002/jnr.24075>
11. Verkhratsky A, Marutle A, Rodríguez-Arellano JJ, Nordberg A (2015) Glial asthenia and functional paralysis: a new perspective on

- neurodegeneration and Alzheimer's disease. *Neuroscientist* 21:552–568. <https://doi.org/10.1177/1073858414547132>
12. Chung W-S, Welsh CA, Barres BA, Stevens B (2015) Do glia drive synaptic and cognitive impairment in disease? *Nat Neurosci* 18: 1539–1545. <https://doi.org/10.1038/nn.4142>
 13. Murray ME, Graff-Radford NR, Ross OA et al (2011) Neuropathologically defined subtypes of Alzheimer's disease with distinct clinical characteristics: a retrospective study. *Lancet Neurol* 10:785–796. [https://doi.org/10.1016/S1474-4422\(11\)70156-9](https://doi.org/10.1016/S1474-4422(11)70156-9)
 14. Jones T, Townsend D (2017) History and future technical innovation in positron emission tomography. *J Med Imaging* 4:011013. <https://doi.org/10.1117/1.JMI.4.1.011013>
 15. Turkheimer F, Dunn J (2014) Experimental design and practical data analysis in positron emission tomography. Published independently, London, London
 16. Pike VW (2009) PET radiotracers: crossing the blood–brain barrier and surviving metabolism. *Trends Pharmacol Sci* 30:431–440. <https://doi.org/10.1016/j.tips.2009.05.005>
 17. McKhann GM, Knopman DS, Chertkow H et al (2011) The diagnosis of dementia due to Alzheimer's disease: recommendations from the National Institute on Aging-Alzheimer's Association workgroups on diagnostic guidelines for Alzheimer's disease. *Alzheimer's Dement* 7:263–269. <https://doi.org/10.1016/j.jalz.2011.03.005>
 18. Dubois B, Feldman HH, Jacova C et al (2014) Advancing research diagnostic criteria for Alzheimer's disease: the IWG-2 criteria. *Lancet Neurol* 13:614–629. [https://doi.org/10.1016/S1474-4422\(14\)70090-0](https://doi.org/10.1016/S1474-4422(14)70090-0)
 19. Leuzy A, Chiotis K, Lemoine L et al (2019) Tau PET imaging in neurodegenerative tauopathies—still a challenge. *Mol Psychiatry* 24:1112–1134. <https://doi.org/10.1038/s41380-018-0342-8>
 20. Albrecht DS, Granziera C, Hooker JM, Loggia ML (2016) In vivo imaging of human neuroinflammation. *ACS Chem Neurosci* 7:470–483. <https://doi.org/10.1021/acschemneuro.6b00056>
 21. Boche D, Gerhard A, Rodriguez-Vieitez E, Faculty MINC (2019) Prospects and challenges of imaging neuroinflammation beyond TSPO in Alzheimer's disease. *Eur J Nucl Med Mol Imaging* 46:2831–2847. <https://doi.org/10.1007/s00259-019-04462-w>
 22. Fontana IC, Scarpa M, Malarte M-L et al (2023) Astrocyte signature in Alzheimer's disease continuum through a multi-PET tracer imaging perspective. *Cell* 12:1469. <https://doi.org/10.3390/cells12111469>
 23. Burda JE, Sofroniew MV (2014) Reactive gliosis and the multicellular response to CNS damage and disease. *Neuron* 81:229–248. <https://doi.org/10.1016/j.neuron.2013.12.034>
 24. Kumar A, Fontana IC, Nordberg A (2023) Reactive astrogliosis: a friend or foe in the pathogenesis of Alzheimer's disease. *J Neurochem* 164:309–324. <https://doi.org/10.1111/jnc.15565>
 25. Hamby ME, Sofroniew MV (2010) Reactive astrocytes as therapeutic targets for CNS disorders. *Neurotherapeutics* 7:494–506. <https://doi.org/10.1016/j.nurt.2010.07.003>
 26. Stefaniak J, O'Brien J (2015) Imaging of neuroinflammation in dementia: a review. *J Neurol Neurosurg Psychiatry* 87:21. <https://doi.org/10.1136/jnnp-2015-311336>
 27. Cosenza-Nashat M, Zhao M-L, Suh H-S et al (2009) Expression of the translocator protein of 18 kDa by microglia, macrophages and astrocytes based on immunohistochemical localization in abnormal human brain. *Neuropathol Appl Neurobiol* 35:306–328. <https://doi.org/10.1111/j.1365-2990.2008.01006.x>
 28. Lavis S, Guillermier M, Hérard A-S et al (2012) Reactive astrocytes overexpress TSPO and are detected by TSPO positron emission tomography imaging. *J Neurosci* 32:10809–10818. <https://doi.org/10.1523/JNEUROSCI.1487-12.2012>
 29. Turkheimer FE, Rizzo G, Bloomfield PS et al (2015) The methodology of TSPO imaging with positron emission tomography. *Biochem Soc Trans* 43:586–592. <https://doi.org/10.1042/BST20150058>
 30. Escartin C, Galea E, Lakatos A et al (2021) Reactive astrocyte nomenclature, definitions, and future directions. *Nat Neurosci* 24:312–325. <https://doi.org/10.1038/s41593-020-00783-4>
 31. Carter SF, Herholz K, Rosa-Neto P et al (2019) Astrocyte biomarkers in Alzheimer's disease. *Trends Mol Med* 25:77–95. <https://doi.org/10.1016/j.molmed.2018.11.006>
 32. Bellaver B, Ferrari-Souza JP, Uglione Da Ros L et al (2021) Astrocyte biomarkers in Alzheimer disease: a systematic review and meta-analysis. *Neurology* 96:e2944–e2955. <https://doi.org/10.1212/WNL.0000000000012109>
 33. Rodriguez-Vieitez E (2021) Chapter 20: PET imaging of monoamine oxidase B. In: PET and

- SPECT of neurobiological systems, 2nd edn. Springer Nature, pp 521–545
34. Villemagne VL, Harada R, Doré V et al (2022) First-in-humans evaluation of 18F-SMBT-1, a novel 18F-labeled monoamine oxidase-B PET tracer for imaging reactive Astrogliosis. *J Nucl Med* 63:1551–1559. <https://doi.org/10.2967/jnumed.121.263254>
 35. Villemagne VL, Harada R, Doré V et al (2022) Assessing reactive Astrogliosis with ¹⁸F-SMBT-1 across the Alzheimer disease Spectrum. *J Nucl Med* 63:1560–1569. <https://doi.org/10.2967/jnumed.121.263255>
 36. Johansson A, Engler H, Blomquist G et al (2007) Evidence for astrocytosis in ALS demonstrated by [¹¹C](l)-deprenyl-D2 PET. *J Neurol Sci* 255:17–22. <https://doi.org/10.1016/j.jns.2007.01.057>
 37. Li J-X (2017) Imidazoline I 2 receptors: an update. *Pharmacol Ther* 178:48–56. <https://doi.org/10.1016/j.pharmthera.2017.03.009>
 38. Parker CA, Nutt DJ, Tyacke RJ (2023) Imidazoline-I2 PET Tracers in Neuroimaging. *IJMS* 24:9787. <https://doi.org/10.3390/ijms24129787>
 39. Kumar A, Koistinen NA, Malarte M-L et al (2021) Astroglial tracer BU99008 detects multiple binding sites in Alzheimer’s disease brain. *Mol Psychiatry* 26:5833–5847. <https://doi.org/10.1038/s41380-021-01101-5>
 40. Calsolaro V, Matthews PM, Donat CK et al (2021) Astrocyte reactivity with late-onset cognitive impairment assessed in vivo using 11C-BU99008 PET and its relationship with amyloid load. *Mol Psychiatry* 26:5848–5855. <https://doi.org/10.1038/s41380-021-01193-z>
 41. Nam M-H, Ko HY, Kim D et al (2023) Visualizing reactive astrocyte-neuron interaction in Alzheimer’s disease using 11C-acetate and 18F-FDG. *Brain* 146:2957–2974. <https://doi.org/10.1093/brain/awad037>
 42. Duong MT, Chen YJ, Doot RK et al (2021) Astrocyte activation imaging with 11C-acetate and amyloid PET in mild cognitive impairment due to Alzheimer pathology. *Nucl Med Commun* 42:1261–1269. <https://doi.org/10.1097/MNM.0000000000001460>
 43. Fowler JS, MacGregor RR, Wolf AP et al (1987) Mapping human brain monoamine oxidase a and B with ¹¹C-labeled suicide Inactivators and PET. *Science* 235:481–485. <https://doi.org/10.1126/science.3099392>
 44. Fowler JS, Logan J, Volkow ND, Wang G-J (2005) Translational neuroimaging: positron emission tomography studies of monoamine oxidase. *Mol Imaging Biol* 7:377–387. <https://doi.org/10.1007/s11307-005-0016-1>
 45. Ekblom J, Jossan SS, Orelund L et al (1994) Reactive gliosis and monoamine oxidase B. In: Tipton KF, Youdim MBH, Barwell CJ et al (eds) *Amine oxidases: function and dysfunction*. Springer Vienna, Vienna, pp 253–258
 46. Ekblom J, Jossan SS, Bergström M et al (1993) Monoamine oxidase-B in astrocytes. *Glia* 8: 122–132. <https://doi.org/10.1002/glia.440080208>
 47. Levitt P, Pintar JE, Breakefield XO (1982) Immunocytochemical demonstration of monoamine oxidase B in brain astrocytes and serotonergic neurons. *Proc Natl Acad Sci U S A* 79:6385–6389. <https://doi.org/10.1073/pnas.79.20.6385>
 48. Jossan SS, Ekblom J, Aquilonius S-M, Orelund L (1994) Monoamine oxidase-B in motor cortex and spinal cord in amyotrophic lateral sclerosis studied by quantitative autoradiography. In: Tipton KF, Youdim MBH, Barwell CJ et al (eds) *Amine oxidases: function and dysfunction*. Springer Vienna, Vienna, pp 243–248
 49. Lemoine L, Saint-Aubert L, Nennesmo I et al (2017) Cortical laminar tau deposits and activated astrocytes in Alzheimer’s disease visualised by 3H-THK5117 and 3H-deprenyl autoradiography. *Sci Rep* 7:45496. <https://doi.org/10.1038/srep45496>
 50. Marutle A, Gillberg P-G, Bergfors A et al (2013) 3H-Deprenyl and 3H-PIB autoradiography show different laminar distributions of astroglia and fibrillar β -amyloid in Alzheimer brain. *J Neuroinflammation* 10:861. <https://doi.org/10.1186/1742-2094-10-90>
 51. Saura J, Luque JM, Cesura AM et al (1994) Increased monoamine oxidase B activity in plaque-associated astrocytes of Alzheimer brains revealed by quantitative enzyme radiography. *Neuroscience* 62:15–30. [https://doi.org/10.1016/0306-4522\(94\)90311-5](https://doi.org/10.1016/0306-4522(94)90311-5)
 52. Gulyás B, Pavlova E, Kása P et al (2011) Activated MAO-B in the brain of Alzheimer patients, demonstrated by [¹¹C]-l-deprenyl using whole hemisphere autoradiography. *Neurochem Int* 58:60–68. <https://doi.org/10.1016/j.neuint.2010.10.013>
 53. Fowler JS, Wang GJ, Logan J et al (1995) Selective reduction of radiotracer trapping by deuterium substitution: comparison of carbon-11-L-deprenyl and carbon-11-deprenyl-D2 for MAO B mapping. *J Nucl Med* 36:1255–1262
 54. Fowler JS, Wolf AP, MacGregor RR et al (1988) Mechanistic positron emission tomography studies: demonstration of a deuterium

- isotope effect in the monoamine oxidase-catalyzed binding of [¹¹C]L-deprenyl in living baboon brain. *J Neurochem* 51:1524–1534. <https://doi.org/10.1111/j.1471-4159.1988.tb01121.x>
55. Carter SF, Schöll M, Almkvist O et al (2012) Evidence for Astrocytosis in prodromal Alzheimer disease provided by ¹¹C-deuterium-L-Deprenyl: a multitracer PET paradigm combining ¹¹C-Pittsburgh compound B and ¹⁸F-FDG. *J Nucl Med* 53:37–46. <https://doi.org/10.2967/jnumed.110.087031>
 56. Chiotis K, Johansson C, Rodriguez-Vieitez E et al (2023) Tracking reactive astrogliosis in autosomal dominant and sporadic Alzheimer's disease with multi-modal PET and plasma GFAP. *Mol Neurodegener* 18:60. <https://doi.org/10.1186/s13024-023-00647-y>
 57. Rodriguez-Vieitez E, Saint-Aubert L, Carter SF et al (2016) Diverging longitudinal changes in astrocytosis and amyloid PET in autosomal dominant Alzheimer's disease. *Brain* 139:922–936. <https://doi.org/10.1093/brain/awv404>
 58. Engler H, Lundberg P, Ekblom K et al (2003) Multitracer study with positron emission tomography in Creutzfeldt-Jakob disease. *Eur J Nucl Med Mol Imaging* 30:85–95. <https://doi.org/10.1007/s00259-002-1008-x>
 59. Engler H, Nennesmo I, Kumlien E et al (2012) Imaging astrocytosis with PET in Creutzfeldt-Jakob disease: case report with histopathological findings. *Int J Clin Exp Med* 5:201–207
 60. Choo IH, Carter SF, Schöll ML, Nordberg A (2014) Astrocytosis measured by ¹¹C-deprenyl PET correlates with decrease in gray matter density in the parahippocampus of prodromal Alzheimer's patients. *Eur J Nucl Med Mol Imaging* 41:2120–2126. <https://doi.org/10.1007/s00259-014-2859-7>
 61. Rodriguez-Vieitez E, Carter SF, Chiotis K et al (2016) Comparison of early-phase ¹¹C-deuterium-L-Deprenyl and ¹¹C-Pittsburgh compound B PET for assessing brain perfusion in Alzheimer disease. *J Nucl Med* 57:1071–1077. <https://doi.org/10.2967/jnumed.115.168732>
 62. Schöll M, Carter SF, Westman E et al (2015) Early astrocytosis in autosomal dominant Alzheimer's disease measured in vivo by multitracer positron emission tomography. *Sci Rep* 5:16404. <https://doi.org/10.1038/srep16404>
 63. Carter SF, Chiotis K, Nordberg A, Rodriguez-Vieitez E (2019) Longitudinal association between astrocyte function and glucose metabolism in autosomal dominant Alzheimer's disease. *Eur J Nucl Med Mol Imaging* 46:348–356. <https://doi.org/10.1007/s00259-018-4217-7>
 64. Vilaplana E, Rodriguez-Vieitez E, Ferreira D et al (2020) Cortical microstructural correlates of astrocytosis in autosomal-dominant Alzheimer disease. *Neurology* 94:e2026–e2036. <https://doi.org/10.1212/WNL.00000000000009405>
 65. Rodriguez-Vieitez E, Ni R, Gulyás B et al (2015) Astrocytosis precedes amyloid plaque deposition in Alzheimer APPsw transgenic mouse brain: a correlative positron emission tomography and in vitro imaging study. *Eur J Nucl Med Mol Imaging* 42:1119–1132. <https://doi.org/10.1007/s00259-015-3047-0>
 66. Schott JM, Fox NC (2016) Inflammatory changes in very early Alzheimer's disease: friend, foe, or don't know? *Brain* 139:647–650. <https://doi.org/10.1093/brain/awv405>
 67. Benedet AL, Milà-Alomà M, Vrillon A et al (2021) Differences between plasma and cerebrospinal fluid glial fibrillary acidic protein levels across the Alzheimer disease continuum. *JAMA Neurol* 78:1471. <https://doi.org/10.1001/jamaneurol.2021.3671>
 68. Johansson C, Thordardottir S, Laffita-Mesa J et al (2023) Plasma biomarker profiles in autosomal dominant Alzheimer's disease. *Brain* 146:1132–1140. <https://doi.org/10.1093/brain/awac399>
 69. Chatterjee P, Doré V, Pedrini S et al (2023) Plasma glial fibrillary acidic protein is associated with ¹⁸F-SMBT-1 PET: two putative astrocyte reactivity biomarkers for Alzheimer's disease. *JAD* 92:615–628. <https://doi.org/10.3233/JAD-220908>
 70. Acton PD, Friston KJ (1998) Statistical parametric mapping in functional neuroimaging: beyond PET and fMRI activation studies. *Eur J Nucl Med* 25:663–667
 71. Friston KJ (1995) Commentary and opinion: II. Statistical parametric mapping: ontology and current issues. *J Cereb Blood Flow Metab* 15:361–370. <https://doi.org/10.1038/jcbfm.1995.45>
 72. Kiebel SJ, Ashburner J, Poline J-B, Friston KJ (1997) MRI and PET Coregistration—a cross validation of statistical parametric mapping and automated image registration. *NeuroImage* 5:271–279. <https://doi.org/10.1006/nimg.1997.0265>
 73. Casanova R, Srikanth R, Baer A et al (2007) Biological parametric mapping: a statistical toolbox for multimodality brain image analysis. *NeuroImage* 34:137–143. <https://doi.org/10.1016/j.neuroimage.2006.09.011>

74. Farid K, Carter SF, Rodriguez-Vieitez E et al (2015) Case report of complex amyotrophic lateral sclerosis with cognitive impairment and cortical amyloid deposition. *JAD* 47:661–667. <https://doi.org/10.3233/JAD-141965>
75. Patlak CS, Blasberg RG (1985) Graphical evaluation of blood-to-brain transfer constants from multiple-time uptake data. Generalizations. *J Cereb Blood Flow Metab* 5:584–590. <https://doi.org/10.1038/jcbfm.1985.87>
76. Bergström M, Kumlien E, Lilja A et al (1998) Temporal lobe epilepsy visualized with PET with 11C-L-deuterium-deprenyl – analysis of kinetic data. *Acta Neurol Scand* 98:224–231. <https://doi.org/10.1111/j.1600-0404.1998.tb07300.x>
77. Petersen RC (2004) Mild cognitive impairment as a diagnostic entity. *J Intern Med* 256:183–194. <https://doi.org/10.1111/j.1365-2796.2004.01388.x>
78. McKhann G, Drachman D, Folstein M et al (1984) Clinical diagnosis of Alzheimer’s disease: report of the NINCDS-ADRDA Work Group* under the auspices of Department of Health and Human Services Task Force on Alzheimer’s disease. *Neurology* 34:939–939. <https://doi.org/10.1212/WNL.34.7.939>
79. Nordberg A, Carter SF, Rinne J et al (2013) A European multicentre PET study of fibrillar amyloid in Alzheimer’s disease. *Eur J Nucl Med Mol Imaging* 40:104–114. <https://doi.org/10.1007/s00259-012-2237-2>
80. Klunk WE, Engler H, Nordberg A et al (2004) Imaging brain amyloid in Alzheimer’s disease with Pittsburgh Compound-B: imaging amyloid in AD with PIB. *Ann Neurol* 55:306–319. <https://doi.org/10.1002/ana.20009>
81. Mathis CA, Wang Y, Holt DP et al (2003) Synthesis and evaluation of ¹¹C-labeled 6-substituted 2-Arylbenzothiazoles as amyloid imaging agents. *J Med Chem* 46:2740–2754. <https://doi.org/10.1021/jm030026b>
82. Ashburner J, Friston KJ (2005) Unified segmentation. *NeuroImage* 26:839–851. <https://doi.org/10.1016/j.neuroimage.2005.02.018>
83. Hammers A, Allom R, Koeppe MJ et al (2003) Three-dimensional maximum probability atlas of the human brain, with particular reference to the temporal lobe. *Hum Brain Mapp* 19:224–247. <https://doi.org/10.1002/hbm.10123>
84. Lippa CF, Saunders AM, Smith TW et al (1996) Familial and sporadic Alzheimer’s disease: neuropathology cannot exclude a final common pathway. *Neurology* 46:406–412. <https://doi.org/10.1212/WNL.46.2.406>
85. Minoshima S, Frey KA, Foster NL, Kuhl DE (1995) Preserved pontine glucose metabolism in Alzheimer disease: a reference region for functional brain image (PET) analysis. *J Comput Assist Tomogr* 19:541–547. <https://doi.org/10.1097/00004728-199507000-00006>
86. Benjamini Y, Hochberg Y (1995) Controlling the false discovery rate—a practical and powerful approach to multiple testing. *J R Stat Soc Ser B (Methodological)* 57(1):289–300
87. Turkheimer FE, Smith CB, Schmidt K (2001) Estimation of the number of “true” null hypotheses in multivariate analysis of neuroimaging data. *NeuroImage* 13:920–930. <https://doi.org/10.1006/nimg.2001.0764>
88. López-González FJ, Paredes-Pacheco J, Thurnhofer-Hemsi K et al (2019) QModeling: a multiplatform, easy-to-use and open-source toolbox for PET kinetic analysis. *Neuroinformatics* 17:103–114. <https://doi.org/10.1007/s12021-018-9384-y>
89. Edison P, Hinz R, Ramackhansingh A et al (2012) Can target-to-pons ratio be used as a reliable method for the analysis of [¹¹C]PIB brain scans? *NeuroImage* 60:1716–1723. <https://doi.org/10.1016/j.neuroimage.2012.01.099>
90. Herholz K (2010) Cerebral glucose metabolism in preclinical and prodromal Alzheimer’s disease. *Expert Rev Neurother* 10:1667–1673. <https://doi.org/10.1586/ern.10.136>
91. Lopresti BJ, Klunk WE, Mathis CA et al (2005) Simplified quantification of Pittsburgh Compound B amyloid imaging PET studies: a comparative analysis. *J Nucl Med* 46:1959–1972

Part V

Neuropathology



High-Throughput Lipidomic and Metabolomic Profiling for Brain Tissue and Biofluid Samples in Neurodegenerative Disorders

Bonne M. Thompson and Giuseppe Astarita

Abstract

Recent research has revealed the potential of lipidomics and metabolomics in identifying new biomarkers and mechanistic insights for neurodegenerative disorders. To contribute to this promising area, we present a detailed protocol for conducting an integrated lipidomic and metabolomic profiling of brain tissue and biofluid samples. In this method, a single-phase methanol extraction is employed for extracting both nonpolar and highly polar lipids and metabolites from each biological sample. The extracted samples are then subjected to liquid chromatography-mass spectrometry-based assays to provide relative or semiquantitative measurements for hundreds of selected lipids and metabolites per sample. This high-throughput approach enables the generation of new hypotheses regarding the mechanistic and functional significance of lipid and metabolite alterations in neurodegenerative disorders while also facilitating the discovery of new biomarkers to support drug development.

Key words Lipidomics, Metabolomics, Lipids, Neurodegeneration, Drug discovery, Drug development, Omics, Biomarker

1 Introduction

Metabolites and lipids are essential components of biological systems, playing critical roles in energy metabolism, membrane structure, and signaling pathways [1, 2]. Dysregulation of these molecules has been linked to various diseases, including neurodegenerative disorders [2, 3]. While metabolomics aims to identify and quantify the composition of metabolites, lipidomics is a subset of metabolomics that focuses specifically on lipid metabolites [2, 4]. Lipidomic and metabolomic profiling of biological samples provides a comprehensive snapshot of the physiological and pathological status of the system and aids in identifying altered biochemical pathways in various diseases.

Lipidomics and metabolomics are powerful tools in functional genomics that can provide valuable insights into gene function and identify potential biomarkers for diseases and drug development. A discovery lipidomics and metabolomics approach involves screening as many metabolites as possible in a biological sample without bias, generating hypotheses about the potential roles of lipids, metabolites, or biochemical pathways in disease and drug mechanisms. Statistical tools can then compare molecular profiles between different groups, such as healthy versus diseased, control versus treated, or wild-type versus genetically modified, providing insights into disease mechanisms and drug effects [1, 5].

Recent studies have employed discovery lipidomics and metabolomics approaches to investigate the function of the *GRN* gene [6, 7], mutations in which result in a deficiency of progranulin (PGRN). PGRN plays a crucial role in lysosomal function and ultimately in the proper functioning of the nervous system, but its exact function remains unclear. PGRN deficiency is a cause of frontotemporal dementia (FTD) in humans and is also linked to an increased risk for developing other neurodegenerative disorders such as amyotrophic lateral sclerosis (ALS), Parkinson's disease (PD), and Alzheimer's disease (AD) [8]. Unbiased lipidomics and metabolomics approaches have revealed that bis (monoacylglycero)phosphate (BMP) was deficient, and glucosyl sphingosine and gangliosides were accumulated in brain tissues and biofluids from *Grn*^{-/-} mice [6, 7]. The alterations in BMP and glycosphingolipids were found to be defining molecular features of the lysosomal dysfunction resulting from *GRN* deficiency and could potentially serve as target engagement biomarkers for drug development [6, 7].

This chapter outlines a high-throughput lipidomics and metabolomics approach for brain tissues and biofluids. The workflow begins with a single-phase extraction method for extracting both nonpolar and highly polar lipids and metabolites from the same biological sample [9]. The extracted samples are then analyzed using multiplexed lipidomics and metabolomics mass spectrometry-based assays, with reversed-phase chromatography for lipid separation and hydrophilic interaction liquid chromatography (HILIC) for polar metabolite separation. Multiplexed assays can be performed with triple quadrupole mass spectrometers to enable high-throughput, semiquantitative measurements of hundreds of selected lipids and metabolites per sample using only a few nonnatural internal standards, providing relative or semiquantitative measurements of lipids and metabolites. This protocol can also be applied to analyze lipids and metabolites from various other animal tissues and cells with minor modifications [9]. This approach has been widely adopted in both academic and industry research laboratories and has demonstrated success in translational research and biomarker discovery, particularly pertaining to neurodegenerative disorders [6, 7, 10–15].

2 Materials

2.1 Equipment

1. TripleQuad 7500 electrospray mass spectrometer equipped with an ExionLC liquid chromatography system and SCIEX OS 3.1 software.
2. FastPrep-24™ 5G bead beating grinder and lysis system for tissue homogenization (*see Note 1*).
3. CoolPrep™ adapter 24 × 2 mL tube holder for the FastPrep-24™ 5G bead beating grinder and lysis system.
4. Refrigerated microcentrifuge, such as Eppendorf Centrifuge 5425 R – Microcentrifuge.
5. Rack vortexer, such as VWR multitube vortex mixer.
6. Nitrogen evaporator system for MTP format, such as Organomation MICROVAP Microplate Evaporator.
7. A set of pipettes capable of handling volumes from 1 to 1000 µL, such as Gilson PIPETMAN (*see Note 2*).

2.2 Solvents and Chemicals

1. Methanol (MS-grade).
2. Acetonitrile (MS-grade).
3. Isopropyl alcohol (MS-grade).
4. Water (MS-grade).
5. Ammonium formate (MS-grade).
6. Ammonium acetate (MS-grade).
7. Formic acid (MS-grade).

2.3 Supplies

1. Preloaded tubes for homogenizer system: Lysing Matrix D, 2 mL tubes preloaded with zirconium-silicate beads for tissue homogenization.
2. 1.5 mL polypropylene microcentrifuge tubes, such as Eppendorf™ LoBind Microcentrifuge Tubes: Protein.
3. Microvette® 500 K3 EDTA blood collection tubes.
4. 8 mL glass vials with PTFE-lined screw caps, such as Thermo Scientific™ Screw Vial Convenience Kit, 8 mL clear glass vial with open top septa caps.
5. 40 mL glass vials with PTFE-lined screw caps, such as Thermo Scientific™ Screw Vial Convenience Kit, 8 mL clear glass vial with open top septa caps.
6. 96-well LCMS plate with silanized conical glass inserts.
7. PTFE/silicone cap mat for LCMS plates.
8. ACQUITY Premier BEH C18 1.7 µm, 2.1 × 100 mm column.

9. ACQUITY Premier BEH amide 1.7 μm , 2.1 \times 150 mm column.
10. HALO HILIC 2.0 μm , 3.0 \times 150 mm column.

2.4 Internal Standard Mixtures

Internal standards, which are non-endogenous lipids and metabolites, are added to the biological samples prior to extraction. They serve as reference compounds to normalize for extraction efficiency and instrument response during the subsequent lipidomics and metabolomics analysis. The components and concentrations of internal standard mixtures are listed in Tables 1–6.

Prepare the six internal standard mixtures as follows:

1. Mix 1: SPLASH[®] LIPIDOMIX[®] Mass Spec Standard (Table 1). This standard mix is sold in solution, which is used directly without further dilution. Transfer the solution into an 8 mL glass vial with PTFE-lined screw cap and store at $-20\text{ }^{\circ}\text{C}$.
2. Mix 2: an in-house prepared internal standard mixture of individually purchased lipid standards dissolved in MS-grade methanol (Table 2). Prepare the solution in an 8 mL glass vial with PTFE-lined screw cap and store at $-20\text{ }^{\circ}\text{C}$.
3. Mix 3: deuterated primary COX and LOX LCMS mixture (Table 3). This standard mix is sold in solution, which is used directly without further dilution. Transfer the solution into an 8 mL glass vial with PTFE-lined screw cap and store at $-20\text{ }^{\circ}\text{C}$.
4. Mix 4: labeled amino acids standards (Table 4). This standard mix is sold in a dry form and should be prepared for use by dissolving it in 1 mL of MS-grade water. Store the solution in its original vial at a temperature of $-20\text{ }^{\circ}\text{C}$.
5. Mix 5: labeled carnitines standards (Table 5). This standard mix is sold in a dry form and should be prepared for use by dissolving it in 1 mL of MS-grade water. Store the solution in its original vial at a temperature of $-20\text{ }^{\circ}\text{C}$.
6. Mix 6: an in-house prepared internal standard mixture of individually purchased metabolites dissolved in MS-grade methanol (Table 6). Prepare the solution in an 8 mL glass vial with PTFE-lined screw cap and store at $-20\text{ }^{\circ}\text{C}$.

3 Methods

3.1 Collection of Brain Tissue

1. Record how animals have been anesthetized because this could affect the final results.
2. Perform intracardiac perfusion with ice-cold PBS to rinse the blood out of the tissues. Alternatively, dissect tissues and rinse from blood in a petri dish with cold PBS, and then dry on Kimwipes.

Table 1
Components and concentrations of Internal Standards Mix 1: SPLASH® LIPIDOMIX®

Name	Vendor	Catalog number	Working concentration (ng/μL)
CE (18:1(d7))	Avanti Polar lipids	330707	350
Cholesterol(d7)	Avanti Polar lipids	330707	100
DG (15:0/18:1(d7))	Avanti Polar lipids	330707	10
LPC (18:1(d7))	Avanti Polar lipids	330707	25
LPE (16:0)(d7))	Avanti Polar lipids	330707	5
MG (18:1(d7))	Avanti Polar lipids	330707	2
PA (15:0/18:1(d7))	Avanti Polar lipids	330707	7
PC (15:0/18:1(d7))	Avanti Polar lipids	330707	160
PE (15:0/18:1(d7))	Avanti Polar lipids	330707	5
PG (15:0/18:1(d7))	Avanti Polar lipids	330707	30
PI (15:0/18:1(d7))	Avanti Polar lipids	330707	10
PS (15:0/18:1(d7))	Avanti Polar lipids	330707	5
SM (d18:1(d9)/18:1)	Avanti Polar lipids	330707	30
TG (15:0/18:1(d7)/15:0)	Avanti Polar lipids	330707	55

- Record whether tissues have been perfused (and for how long) or rinsed in PBS because this could affect the final results.
- Place tissues in aluminum foil or a labeled container. The container should be large enough that the tissue is not distorted by forcing it through the opening. If interested in preserving the anatomical structures, tissues should never be flash-frozen in a microcentrifuge tube, as they will take on the shape of the tube (*see Note 3*).
- Tissue should be flash-frozen as soon as possible after resection on dry ice. Do not over freeze as it causes cracks and makes it hard to cut the frozen sections.
- Frozen tissue should be stored at -80°C .

3.2 Collection of Biofluids: Plasma, Urine, and CSF

- For urine and cerebrospinal fluid (CSF), centrifuge to remove cells and other debris prior to freezing. Centrifuge in a benchtop microcentrifuge for 10 min at 21,000 RCF at 4°C . Transfer the liquid to a new microcentrifuge tube and store at -80°C until extraction.
- For plasma, blood should be collected in a potassium EDTA tube and kept on ice until separation (*see Note 4*). Generate plasma by centrifugation at 1000 RCF for 5 min at 4°C .

Table 2
Components and concentrations of Internal Standards Mix 2

Name	Vendor	Catalog number	Working concentration (ng/ μ L)
24-Hydroxycholesterol(d7)	Avanti Polar Lipids	7000018P	1
Arachidonic acid (d8)	Cayman Chemical Company	390010	10
BMP (14:0/14:0)	Avanti Polar Lipids	857131	5
Cer (d18:1/16:0(d7))	Avanti Polar Lipids	860676	1
CL (14:0/14:0/14:0/14:0)	Avanti Polar Lipids	710332P	10
GalCer (d18:1/15:0)	Cayman Chemical Company	24466	5
GB3 (d18:1/18:0(d3))	Cayman Chemical Company	24626	10
GlcCer (d18:1(d5)/18:0)	Avanti Polar Lipids	860638	1
GlcCer (d18:1/16:0(d3))	Cayman Chemical Company	24621	1
Glucosyl sphingosine(d5)	Avanti Polar Lipids	860636	1
GM1 (d18:1/17:0)	Avanti Polar Lipids	860094	0.5
GM2 (d18:1/18:0(d3))	Cayman Chemical Company	24849	1
GM3 (d18:1/18:0(d5))	Avanti Polar Lipids	860073	10
Hemi-BMP ((14:0/14:0) _{14:0})	Avanti Polar Lipids	857132	5
LacCer (d18:1/16:0(d3))	Cayman Chemical Company	24625	5
LysoGB3 (d18:1(d7))	Avanti Polar Lipids	860682	1
Sphingosine 1-phosphate d18:1(d7)	Cayman Chemical Company	10008121	10
Sphingosine d18:1(d7)	Cayman Chemical Company	22786	5
Sulfatide (d18:1/18:0(d3))	Cayman Chemical Company	24624	1

Carefully remove the plasma (upper layer) using a pipette, and transfer it to a fresh microcentrifuge tube, taking care not to disturb the interface between layers. Store at -80°C until extraction.

- It is preferred to use plasma rather than serum for lipid and metabolite analysis (*see* **Note 5**).

Table 3
Components and concentrations of Internal Standards Mix 3: deuterated primary COX and LOX LCMS mixture

Name	Vendor	Catalog number	Working concentration (ng/ μ L)
12-HETE-d8	Cayman Chemical Company	19228	1
15-HETE-d8	Cayman Chemical Company	19228	1
5-HETE-d8	Cayman Chemical Company	19228	1
6-keto-PGF1-alpha-d4	Cayman Chemical Company	19228	1
PGD-d4	Cayman Chemical Company	19228	1
PGE2-d4	Cayman Chemical Company	19228	1
PGF2-alpha-d4	Cayman Chemical Company	19228	1
TXB2-d4	Cayman Chemical Company	19228	1

3.3 Sample Preparation: Lipid and Metabolite Extraction from Brain Tissue

1. Before the extraction process, it is crucial to randomize your samples in terms of their groups. To achieve this, use block randomization method (*see Note 6*).
2. To obtain precise measurements for normalization, weigh the tissue while it is still frozen and document the weight. During this process, it is essential to keep the tissues on dry ice to prevent them from thawing. In situations where weighing tissues is impractical, such as with small brain sections, proceed directly to the subsequent step. However, remember to reserve an aliquot for protein measurements following homogenization.
3. Transfer tissue samples into the 2 mL homogenizer tubes containing Lysing Matrix D (*see Note 7*). Tubes and samples should be kept on dry ice to maintain frozen state.
4. Prepare extraction solvent: to ice-cold MS-grade methanol, add 5 μ L of each internal standard mixture per mL of methanol. Prepare fresh on the day of use in 40 mL glass vial (or larger) and store on ice.

Table 4
Components and concentrations of Internal Standards Mix 4: labeled amino acids standards

Name	Vendor	Catalog number	Working concentration (pmol/ μ L)
Alanine-d4	Cambridge Isotope Laboratories	NSK-A	500
Arginine-13C5d4	Cambridge Isotope Laboratories	NSK-A	500
Aspartate-d3	Cambridge Isotope Laboratories	NSK-A	500
Citrulline-d2	Cambridge Isotope Laboratories	NSK-A	500
Glutamate-d3	Cambridge Isotope Laboratories	NSK-A	500
Glycine-15N13C2	Cambridge Isotope Laboratories	NSK-A	2500
Leucine-d3	Cambridge Isotope Laboratories	NSK-A	500
Methionine-d3	Cambridge Isotope Laboratories	NSK-A	500
Ornithine-d2	Cambridge Isotope Laboratories	NSK-A	500
Phenylalanine-13C6	Cambridge Isotope Laboratories	NSK-A	500
Tyrosine-13C6	Cambridge Isotope Laboratories	NSK-A	500
Valine-d8	Cambridge Isotope Laboratories	NSK-A	500

5. To each tissue sample in homogenizer tube, add a volume of ice-cold extraction solvent equivalent to 20 times the weight of the tissue (*see Note 8*). Continue to maintain the sample tubes on dry ice, even after the solvent is added.
6. Place the block-randomized sample tubes in the FastPrep-24TM 5G bead beating grinder and lysis system with CoolPrepTM adapter 24 \times 2 mL tube holder loaded with dry ice pellets to maintain low temperature (*see Note 9*).
7. Homogenize the tissues for 40 s at a speed of 6 m/s. Samples should be a slurry with no visible tissue clumps. If clumps are visible, repeat this homogenization procedure until a homogeneous slurry is achieved.

Table 5
Components and concentrations of Internal Standards Mix 5: labeled carnitines standards

Name	Vendor	Catalog number	Working concentration (pmol/ μ L)
Acetylcarnitine-d3	Cambridge Isotope Laboratories	NSK-B	38
Butyrylcarnitine-d3	Cambridge Isotope Laboratories	NSK-B	7.6
Carnitine-d9	Cambridge Isotope Laboratories	NSK-B	152
Isovalerylcarnitine-d9	Cambridge Isotope Laboratories	NSK-B	7.6
Myristoylcarnitine-d9	Cambridge Isotope Laboratories	NSK-B	7.6
Octanoylcarnitine-d3	Cambridge Isotope Laboratories	NSK-B	7.6
Palmitoylcarnitine-d3	Cambridge Isotope Laboratories	NSK-B	15.2
Propionylcartinine-d3	Cambridge Isotope Laboratories	NSK-B	7.6

Table 6
Components and concentrations of Internal Standards Mix 6

Name	Vendor	Catalog number	Working concentration (ng/ μ L)
Anserine-d4	C/D/N Isotopes Inc	D-7865	5
Carnosine-d4	Cayman Chemical Company	26781	1
Creatinine-d3	Cayman Chemical Company	16763	1

8. Optional: Take a 15 μ L aliquot for protein measurement using a BCA protein assay kit (especially important if you could not weigh the tissue).
9. Centrifuge in a benchtop microcentrifuge for 10 min at 21,000 RCF at 4 °C (leaving the beads in the tube) (*see Note 10*).
10. Transfer the methanol supernatant to a new microcentrifuge tube, and store it in the freezer at -20 °C for 1 h. This will promote additional protein precipitation (*see Note 11*).
11. Centrifuge in a benchtop microcentrifuge for 10 min at 21,000 RCF at 4 °C.

12. Transfer 100 μL of the methanol supernatant into 96-well LCMS plate with silanized conical glass inserts. Seal with a PTFE/silicone cap mat (*see Note 12*).
13. If interested in separating glucosyl from galactosyl sphingolipids, take a 50 μL aliquot from the methanol extract, evaporate it under a nitrogen stream for 1 h, and resuspend it in 50 μL of mobile phase A consisting of acetonitrile/isopropyl alcohol/water 92.5/5/2.5 (vol/vol/vol) with 5 mM ammonium formate and 0.5% formic acid (*see Note 13*).
14. Proceed to analyze the sample on the LCMS, or store the plate at $-80\text{ }^{\circ}\text{C}$ until analysis (*see Note 14*).

3.4 Sample Preparation: Lipid and Metabolite Extraction from Biofluids

1. This extraction method is suitable for plasma, serum, urine, and CSF.
2. Prior to extraction, it is important to ensure that samples are randomized with respect to groups. To achieve this, use block randomization method (*see Note 6*).
3. Prepare the extraction solvent by adding 10 μL of each internal standard mixture per mL of ice-cold MS-grade methanol. For CSF samples, adjust the internal standard concentration by adding only 2 μL of each mixture per mL of methanol to the extraction solvent. This modification accounts for the lower lipid content of CSF compared to plasma. Prepare the extraction solvent fresh on the day of use in 40 mL glass vial (or larger), and store it on ice until extraction.
4. Thaw the frozen samples on ice, and vortex thoroughly to ensure homogeneity prior to aliquoting. Transfer 10 μL of the thawed and vortexed sample into a new microcentrifuge tube (*see Note 15*).
5. For plasma, serum, and urine, add 200 μL of extraction solvent to each 10 μL sample aliquot. For CSF, add only 100 μL of extraction solvent to each 10 μL sample aliquot.
6. Vortex for 5 min using a rack vortexer.
7. Centrifuge in a benchtop microcentrifuge for 10 min at 21,000 RCF at $4\text{ }^{\circ}\text{C}$. Transfer the methanol supernatant to a new microcentrifuge tube (*see Note 16*).
8. Place samples in the freezer at $-20\text{ }^{\circ}\text{C}$ for 1 h to allow further precipitation of proteins.
9. Centrifuge in a benchtop microcentrifuge for 10 min at 21,000 RCF at $4\text{ }^{\circ}\text{C}$.
10. Transfer the methanol supernatant into 96-well LCMS plate with silanized conical glass inserts. Seal with a PTFE/silicone cap mat (*see Note 12*).

11. If interested in separating glucosyl from galactosyl sphingolipids, take a 50 μL aliquot from the methanol extract, evaporate it under a nitrogen stream for 1 h, and resuspend it in 50 μL of mobile phase A consisting of acetonitrile/isopropyl alcohol/water 92.5/5/2.5 (vol/vol/vol) with 5 mM ammonium formate and 0.5% formic acid (*see Note 13*).
12. Proceed to analyze the sample on the LCMS, or store the plate at $-80\text{ }^\circ\text{C}$ until analysis (*see Note 14*).

3.5 Multiplexed Lipidomics Assay in Positive Ionization Mode

1. Prepare mobile phase A: acetonitrile/water 60/40 (vol/vol) with 10 mM ammonium formate and 0.1% formic acid.
2. Prepare mobile phase B: isopropyl alcohol/acetonitrile 90/10 (vol/vol) with 10 mM ammonium formate and 0.1% formic acid.
3. Create the positive mode electrospray ionization mass spectrometry method using the following parameters: curtain gas at 40 psi; collision gas set at 9; ion spray voltage at 2000 V; temperature at $250\text{ }^\circ\text{C}$; ion source Gas 1 at 40 psi; ion source Gas 2 at 70 psi; entrance potential at 10 V; and collision cell exit potential at 15 V. Acquire data in MRM mode with the precursor/product ions and CE values reported in Table 7.
4. Use a dedicated ACQUITY Premier BEH C18 1.7 μm , $2.1 \times 100\text{ mm}$ LC column. For the LC analysis, inject 1 μL of the sample using a flow rate of 0.25 mL/min at $55\text{ }^\circ\text{C}$. Set the gradient program: 0.0–8.0 min from 45% B to 99% B, 8.0–9.0 min at 99% B, 9.0–9.1 min to 45% B, and 9.1–10.0 min at 45% B.
5. Before starting the LCMS acquisition of a sample sequence, equilibrate the LCMS system by injecting three MS-grade methanol blanks.
6. To test the suitability of the LCMS system, prepare a system suitability solution by diluting all internal standard mixtures in MS-grade methanol at 1:100 ratio.
7. Inject the system suitability solution three times consecutively to ensure system stability and reproducibility.
8. Before proceeding, ensure that the retention times and the peak areas are reproducible across the triplicate injections of the system suitability solution by monitoring the following internal standards: PC (15:0/18:1(d7)), LPC (18:1(d7)), cholesterol(d7), and CE (18:1(d7)) (*see Note 17*).
9. Before running the sample sequence, equilibrate the LC system by making two injections of a pooled sample extract.
10. Run the sample sequence in a block-randomized order (*see Note 18*).
11. Quantify the area ratios of endogenous lipids and surrogate internal standards (Table 7) using SCIEX OS 3.1.

Table 7
Acquisition parameters for lipid analysis in positive ionization mode

Name	Q1	Q3	CE (V)	Internal standard
1-O-Palmitoyl-Cer (d18:1/18:0)	786.8	502.5	35	TG (15:0/18:1(d7)/15:0)
24-Hydroxycholesterol(d7)	392.30	374.50	20	
24-Hydroxycholesterol	385.3	367.3	20	24-Hydroxycholesterol(d7)
3-O-SulfoLacCer (d18:1/18:0)	970.8	548.5	61	Glucosyl sphingosine(d5)
4-beta-Hydroxycholesterol	420.3	385.3	15	Glucosyl sphingosine(d5)
7-keto-Cholesterol	401.3	383.3	15	Glucosyl sphingosine(d5)
Anandamide	348.4	62.1	23	LPC (18:1(d7))
CE (16:1)	640.6	369.3	26	CE (18:1(d7))
CE (18:1(d7))	675.2	369.4	26	
CE (18:1)	668.6	369.3	26	CE (18:1(d7))
CE (18:2)	666.6	369.3	26	CE (18:1(d7))
CE (20:4)	690.6	369.3	26	CE (18:1(d7))
CE (20:5)	688.6	369.3	26	CE (18:1(d7))
CE (22:6)(OH)	730.6	369.2	25	CE (18:1(d7))
CE (22:6)	714.6	369.3	26	CE (18:1(d7))
CE HETE	706.6	369.2	25	CE (18:1(d7))
CE HODE	682.6	369.2	25	CE (18:1(d7))
CE HpODE	698.6	369.2	25	CE (18:1(d7))
CE oxoHETE	704.6	369.2	25	CE (18:1(d7))
CE oxoODE	680.6	369.2	25	CE (18:1(d7))
Cer (d16:1/16:0)	510.5	236.3	40	Cer (d18:1/16:0(d7))
Cer (d16:1/18:0)	538.6	236.3	40	Cer (d18:1/16:0(d7))
Cer (d16:1/22:0)	594.6	236.3	40	Cer (d18:1/16:0(d7))
Cer (d16:1/24:0)	622.6	236.3	40	Cer (d18:1/16:0(d7))
Cer (d16:1/24:1)	620.6	236.3	40	Cer (d18:1/16:0(d7))
Cer (d16:1/26:0)	650.6	236.3	40	Cer (d18:1/16:0(d7))
Cer (d16:1/26:1)	648.6	236.3	40	Cer (d18:1/16:0(d7))
Cer (d18:0/16:0)	540.6	266.3	40	Cer (d18:1/16:0(d7))
Cer (d18:0/18:0)	568.7	266.3	40	Cer (d18:1/16:0(d7))
Cer (d18:0/24:0)	652.9	266.3	40	Cer (d18:1/16:0(d7))
Cer (d18:0/24:1)	650.9	266.3	40	Cer (d18:1/16:0(d7))

(continued)

Table 7
(continued)

Name	Q1	Q3	CE (V)	Internal standard
Cer (d18:1/16:0(d7))	545.5	271.4	40	
Cer (d18:1/16:0) phosphate	618.6	264.3	40	Cer (d18:1/16:0(d7))
Cer (d18:1/16:0)	538.5	264.3	40	Cer (d18:1/16:0(d7))
Cer (d18:1/18:0)	566.6	264.3	40	Cer (d18:1/16:0(d7))
Cer (d18:1/22:0)	622.6	264.3	40	Cer (d18:1/16:0(d7))
Cer (d18:1/23:0)	636.6	264.3	40	Cer (d18:1/16:0(d7))
Cer (d18:1/24:0)	650.6	264.3	40	Cer (d18:1/16:0(d7))
Cer (d18:1/24:1)	648.6	264.3	40	Cer (d18:1/16:0(d7))
Cer (d18:1/26:0)	678.6	264.3	40	Cer (d18:1/16:0(d7))
Cer (d18:1/26:1)	676.6	264.3	40	Cer (d18:1/16:0(d7))
Cer (d18:2/16:0)	536.5	262.3	40	Cer (d18:1/16:0(d7))
Cer (d18:2/18:0)	564.6	262.3	40	Cer (d18:1/16:0(d7))
Cer (d18:2/22:0)	620.6	262.3	40	Cer (d18:1/16:0(d7))
Cer (d18:2/24:0)	648.6	262.3	40	Cer (d18:1/16:0(d7))
Cer (d18:2/24:1)	646.6	262.3	40	Cer (d18:1/16:0(d7))
Cer (d18:2/26:0)	676.6	262.3	40	Cer (d18:1/16:0(d7))
Cer (d18:2/26:1)	674.6	262.3	40	Cer (d18:1/16:0(d7))
Cholesterol	369.3	369.3	10	Cholesterol(d7)
Cholesterol(d7)	411.3	376.2	10	
Cholesteryl hexoside	566.6	369.3	17	CE (18:1(d7))
Cholic acid	426.3	355.3	20	CE (18:1(d7))
Coenzyme Q10	863.6	197.2	35	CE (18:1(d7))
Coenzyme Q10_	880.7	197.2	35	CE (18:1(d7))
Coenzyme Q10_H2	882.7	197.2	35	CE (18:1(d7))
Coenzyme Q9	795.6	197.2	35	CE (18:1(d7))
Coenzyme Q9_	812.9	197.2	35	CE (18:1(d7))
Coenzyme Q9_H2	814.9	197.2	35	CE (18:1(d7))
Corticosterone	347.1	329.1	35	CE (18:1(d7))
Cortisol	363.3	121.2	35	CE (18:1(d7))
Cortisone	361.2	163.2	35	CE (18:1(d7))
Desmosterol	367.5	147.1	30	Cholesterol(d7)

(continued)

Table 7
(continued)

Name	Q1	Q3	CE (V)	Internal standard
DG (15:0/18:1(d7))	605.6	346.5	30	
DG (16:0_18:1)	612.4	313.3	30	DG (15:0/18:1(d7))
DG (16:0_20:4)	634.5	313.3	30	DG (15:0/18:1(d7))
DG (16:0_22:5)	660.6	313.3	30	DG (15:0/18:1(d7))
DG (16:0_22:6)	658.5	313.2	30	DG (15:0/18:1(d7))
DG (18:0_18:1)	640.4	341.3	30	DG (15:0/18:1(d7))
DG (18:0_20:4)	662.5	341.3	30	DG (15:0/18:1(d7))
DG (18:0_22:6)	686.6	341.3	30	DG (15:0/18:1(d7))
DG (18:1/18:1)	638.4	339.3	30	DG (15:0/18:1(d7))
DG (18:1_20:3)	662.6	339.3	30	DG (15:0/18:1(d7))
DG (18:1_20:4)	660.5	339.3	30	DG (15:0/18:1(d7))
DG (18:1_20:5)	658.6	339.3	30	DG (15:0/18:1(d7))
DG (18:1_22:5)	686.6	339.3	30	DG (15:0/18:1(d7))
DG (18:1_22:6)	684.6	339.3	30	DG (15:0/18:1(d7))
DG (18:2_20:4)	658.5	337.2	30	DG (15:0/18:1(d7))
DG (18:2_22:6)	682.6	337.3	30	DG (15:0/18:1(d7))
Deoxycholic acid	410.3	357.3	20	Glucosyl sphingosine(d5)
GB3 (d18:1/16:0)	1025	520.5	40	GB3 (d18:1/18:0(d3))
GB3 (d18:1/18:0(d3))	1056	551.6	40	
GB3 (d18:1/18:0)	1053	548.6	40	GB3 (d18:1/18:0(d3))
GB3 (d18:1/24:0)	1137	632.6	40	GB3 (d18:1/18:0(d3))
GB3 (d18:1/24:1)	1135	630.6	40	GB3 (d18:1/18:0(d3))
GlcCer (d18:1(d5)/18:0)	733.6	269.3	45	
GlcCer (d18:1/16:0(d3))	703.7	264.3	51	
Glucosyl sphingosine(d5)	467.2	287.2	30	
GM1 (d18:1/16:0)	760.1	366.2	15	Glucosyl sphingosine(d5)
Hex sphingosine d18:1	462.3	282.3	30	Glucosyl sphingosine(d5)
Hex2 sphingosine d18:1	624.4	282.3	30	Glucosyl sphingosine(d5)
Hex2Cer (d18:1/16:0)	862.6	264.3	40	LacCer (d18:1/16:0(d3))
Hex2Cer (d18:1/18:0)	890.7	264.3	40	LacCer (d18:1/16:0(d3))
Hex2Cer (d18:1/24:0)	974.8	264.3	40	LacCer (d18:1/16:0(d3))

(continued)

Table 7
(continued)

Name	Q1	Q3	CE (V)	Internal standard
Hex2Cer (d18:1/24:1)	972.7	264.3	40	LacCer (d18:1/16:0(d3))
Hex2Cer (d18:2/16:0)	860.6	262.3	40	LacCer (d18:1/16:0(d3))
Hex2Cer (d18:2/18:0)	970.7	262.3	40	LacCer (d18:1/16:0(d3))
Hex2Cer (d18:2/24:0)	972.7	262.3	40	LacCer (d18:1/16:0(d3))
HexCer (d18:1/16:0)	700.6	264.3	40	GlcCer (d18:1(d5)/18:0)
HexCer (d18:1/18:0)	728.6	264.3	40	GlcCer (d18:1(d5)/18:0)
HexCer (d18:1/22:0)	784.7	264.4	40	GlcCer (d18:1(d5)/18:0)
HexCer (d18:1/24:0)	812.7	264.3	40	GlcCer (d18:1(d5)/18:0)
HexCer (d18:1/24:1)	810.7	264.3	40	GlcCer (d18:1(d5)/18:0)
LacCer (d18:1/16:0(d3))	865.6	264.3	40	
LPC (16:0)	496.3	184.1	40	LPC (18:1(d7))
LPC (16:1)	494.5	184.1	40	LPC (18:1(d7))
LPC (18:0)	524.3	184.1	40	LPC (18:1(d7))
LPC (18:1(d7))	529.3	184.1	40	
LPC (18:1)	522.3	184.1	40	LPC (18:1(d7))
LPC (18:2)	520.3	184.1	40	LPC (18:1(d7))
LPC (20:4)	544.3	184.1	40	LPC (18:1(d7))
LPC (22:6)	568.3	184.1	40	LPC (18:1(d7))
LPC (24:0)	608.5	184.1	40	LPC (18:1(d7))
LPC (24:1)	606.5	184.1	40	LPC (18:1(d7))
LPC (26:0)	636.5	104.1	40	LPC (18:1(d7))
LPC (26:1)	634.5	104.1	40	LPC (18:1(d7))
LysoSM d18:1	465.5	184.1	40	LPC (18:1(d7))
LysoGB3 (d18:1(d7))	793.5	289.3	46	
LysoGB3 (d18:1)	786.6	282.3	46	LysoGB3 (d18:1(d7))
LysoGB4 (d18:1)	990.6	264.3	52	LysoGB3 (d18:1(d7))
MG (16:0)	348.3	239.3	22	MG (18:1(d7))
MG (16:1)	346.3	237.3	22	MG (18:1(d7))
MG (18:0)	376.3	267.3	22	MG (18:1(d7))
MG (18:1(d7))	381.3	272.5	22	
MG (18:1)	374.3	265.3	22	MG (18:1(d7))

(continued)

Table 7
(continued)

Name	Q1	Q3	CE (V)	Internal standard
MG (20:4)	396.3	287.3	22	MG (18:1(d7))
N-Palmitoyl-O-phosphocholineserine	509.5	184.1	40	LPC (18:1(d7))
Oleoylethanolamine	326.3	62.1	23	LPC (18:1(d7))
Palmitoylethanolamine	300.3	62.1	23	LPC (18:1(d7))
PC (15:0/18:1(d7))	754.6	184.1	40	
PC (16:0/5:0(CHO))	594.5	184.1	40	LPC (18:1(d7))
PC (16:0/9:0(CHO))	650.4	184.1	40	LPC (18:1(d7))
PC (16:0/9:0(COOH))	666.4	184.1	40	LPC (18:1(d7))
PC (18:0/20:4(OH))	826.6	184.1	40	PC (15:0/18:1(d7))
PC (18:0/20:4(OOH))	842.6	184.1	40	PC (15:0/18:1(d7))
PC (34:1)	760.6	184.1	40	PC (15:0/18:1(d7))
PC (34:2)(OH)	774.6	184.1	40	PC (15:0/18:1(d7))
PC (36:1)	788.6	184.1	40	PC (15:0/18:1(d7))
PC (36:2)	786.6	184.1	40	PC (15:0/18:1(d7))
PC (36:4)	782.6	184.1	40	PC (15:0/18:1(d7))
PC (38:4)	810.6	184.1	40	PC (15:0/18:1(d7))
PC (38:6)(OH)	822.6	184.1	40	PC (15:0/18:1(d7))
PC (38:6)	806.6	184.1	40	PC (15:0/18:1(d7))
PC (40:5)	836.6	184.1	40	PC (15:0/18:1(d7))
PC (40:6)(OH)	850.6	184.1	40	PC (15:0/18:1(d7))
PC (40:6)	834.6	184.1	40	PC (15:0/18:1(d7))
PC (O-16:0/0:0)	482.3	184.1	40	LPC (18:1(d7))
PC (O-16:0/2:0)	524.3	184.2	40	LPC (18:1(d7))
PC (O-18:0/0:0)	510.3	184.1	40	LPC (18:1(d7))
PC (O-18:0/2:0)	552.5	184.1	40	LPC (18:1(d7))
PC (P-16:0/0:0)	480.3	184.1	40	LPC (18:1(d7))
PC (P-18:0/0:0)	508.3	184.1	40	LPC (18:1(d7))
PCp (34:0)	746.6	184.1	40	PC (15:0/18:1(d7))
PCp (34:1)	744.6	184.1	40	PC (15:0/18:1(d7))
PCp (34:2)	742.6	184.1	40	PC (15:0/18:1(d7))
PCp (34:3)	740.6	184.1	40	PC (15:0/18:1(d7))

(continued)

Table 7
(continued)

Name	Q1	Q3	CE (V)	Internal standard
PCp (36:2)	770.6	184.1	40	PC (15:0/18:1(d7))
PE (15:0/18:1(d7))	711.6	570.5	40	
PE (18:0/20:4(OH))	784.5	643.4	40	PE (15:0/18:1(d7))
PE (18:0/20:4(OOH))	800.5	659.4	40	PE (15:0/18:1(d7))
PE (34:1)	718.6	577.6	40	PE (15:0/18:1(d7))
PE (36:1)	746.6	605.5	40	PE (15:0/18:1(d7))
PE (36:2)	744.6	603.5	40	PE (15:0/18:1(d7))
PE (36:4)	740.6	599.5	40	PE (15:0/18:1(d7))
PE (38:4)	768.6	627.5	40	PE (15:0/18:1(d7))
PE (38:5)	766.6	625.5	40	PE (15:0/18:1(d7))
PE (38:6)	764.6	623.5	40	PE (15:0/18:1(d7))
PE (38:6)OH	780.6	639.5	40	PE (15:0/18:1(d7))
PE (40:4)	796.6	655.5	40	PE (15:0/18:1(d7))
PE (40:5)	794.6	653.5	40	PE (15:0/18:1(d7))
PE (40:6)	792.6	651.5	40	PE (15:0/18:1(d7))
PE (40:6)OH	808.6	667.5	40	PE (15:0/18:1(d7))
PE (40:7)	790.6	649.5	40	PE (15:0/18:1(d7))
Sitosterol	397.5	161.2	30	Cholesterol(d7)
Sitosteryl hexoside	594.6	397.4	17	CE (18:1(d7))
SM (d18:1(d9)/18:1)	738.7	184.1	40	
SM d32:1	675.6	184.1	40	SM (d18:1(d9)/18:1)
SM d34:1	703.6	184.1	40	SM (d18:1(d9)/18:1)
SM d34:2	701.6	184.1	40	SM (d18:1(d9)/18:1)
SM d36:1	731.6	184.1	40	SM (d18:1(d9)/18:1)
SM d36:2	729.6	184.1	40	SM (d18:1(d9)/18:1)
SM d36:3	727.6	184.1	40	SM (d18:1(d9)/18:1)
SM d40:1	787.6	184.1	40	SM (d18:1(d9)/18:1)
SM d41:1	801.7	184.1	40	SM (d18:1(d9)/18:1)
SM d42:1	815.7	184.1	40	SM (d18:1(d9)/18:1)
SM d42:2	813.7	184.1	40	SM (d18:1(d9)/18:1)
Sphinganine 1-phosphate d18:0	382.3	266.3	25	Sphingosine 1-phosphate d18:1(d7)

(continued)

Table 7
(continued)

Name	Q1	Q3	CE (V)	Internal standard
Sphinganine d18:0	302.2	284.3	20	Sphingosine d18:1(d7)
Sphingosine 1-phosphate d18:1	380.3	264.3	25	Sphingosine 1-phosphate d18:1(d7)
Sphingosine 1-phosphate d18:1(d7)	387.3	271.3	25	
Sphingosine d16:1	272.2	254.3	20	Sphingosine d18:1(d7)
Sphingosine d17:1	286.2	268.3	20	Sphingosine d18:1(d7)
Sphingosine d18:1	300.2	282.3	20	Sphingosine d18:1(d7)
Sphingosine d18:1(d7)	307.3	289.3	20	
Sphingosine d18:2	298.2	280.3	20	Sphingosine d18:1(d7)
TG (15:0/18:1(d7)/15:0)	829.8	570.8	40	
TG (18:0_36:1)	906.8	605.5	40	TG (15:0/18:1(d7)/15:0)
TG (18:0_36:2)	904.7	603.4	40	TG (15:0/18:1(d7)/15:0)
TG (18:0_36:3)	902.7	601.4	40	TG (15:0/18:1(d7)/15:0)
TG (18:1_34:2)	874.7	575.4	40	TG (15:0/18:1(d7)/15:0)
TG (18:1_34:3)	872.7	573.4	40	TG (15:0/18:1(d7)/15:0)
TG (18:1_34:4)	870.6	571.3	40	TG (15:0/18:1(d7)/15:0)
TG (18:1_36:0)	900.7	601.4	40	TG (15:0/18:1(d7)/15:0)
TG (18:1_38:2)	930.8	631.5	40	TG (15:0/18:1(d7)/15:0)
TG (20:4_32:1)	870.6	549.3	40	TG (15:0/18:1(d7)/15:0)
TG (20:4_34:0)	900.6	579.3	40	TG (15:0/18:1(d7)/15:0)
TG (20:4_34:1)	898.6	577.3	40	TG (15:0/18:1(d7)/15:0)
TG (20:4_34:2)	896.6	575.3	40	TG (15:0/18:1(d7)/15:0)
TG (20:4_34:3)	894.6	573.3	40	TG (15:0/18:1(d7)/15:0)
TG (20:4_36:0)	928.8	607.5	40	TG (15:0/18:1(d7)/15:0)
TG (20:4_36:1)	926.7	605.4	40	TG (15:0/18:1(d7)/15:0)
TG (20:4_36:2)	924.7	603.4	40	TG (15:0/18:1(d7)/15:0)
TG (20:4_36:3)	922.7	601.4	40	TG (15:0/18:1(d7)/15:0)
TG (20:4_36:4)	920.7	599.4	40	TG (15:0/18:1(d7)/15:0)
TG (20:4_36:5)	918.6	597.3	40	TG (15:0/18:1(d7)/15:0)
TG (20:4_38:1)	954.7	633.4	40	TG (15:0/18:1(d7)/15:0)
TG (20:4_38:2)	952.7	631.4	40	TG (15:0/18:1(d7)/15:0)
TG (20:4_38:3)	950.7	629.4	40	TG (15:0/18:1(d7)/15:0)
TG (22:6_36:2)	948.7	603.4	40	TG (15:0/18:1(d7)/15:0)

(continued)

Table 7
(continued)

Name	Q1	Q3	CE (V)	Internal standard
TG (22:6_36:3)	946.7	601.4	40	TG (15:0/18:1(d7)/15:0)
TG (22:6_36:4)	944.7	599.4	40	TG (15:0/18:1(d7)/15:0)
TG (22:6_38:1)	978.7	633.4	40	TG (15:0/18:1(d7)/15:0)
TG (22:6_38:2)	976.7	631.4	40	TG (15:0/18:1(d7)/15:0)
TG (54:6) [NL-22:6]	896.8	551.5	40	TG (15:0/18:1(d7)/15:0)
TG (54:7) [NL-20:5]	894.8	575.5	40	TG (15:0/18:1(d7)/15:0)
TG (54:7) [NL-22:6]	894.8	549.5	40	TG (15:0/18:1(d7)/15:0)
TG (56:6) [NL-20:4]	924.8	603.5	40	TG (15:0/18:1(d7)/15:0)
TG (56:6) [NL-22:5]	924.8	577.5	40	TG (15:0/18:1(d7)/15:0)
TG (56:7) [NL-20:4]	922.8	601.5	40	TG (15:0/18:1(d7)/15:0)
TG (56:7) [NL-20:5]	922.8	603.5	40	TG (15:0/18:1(d7)/15:0)
TG (56:7) [NL-22:5]	922.8	575.5	40	TG (15:0/18:1(d7)/15:0)
TG (56:7) [NL-22:6] OH	938.8	577.5	40	TG (15:0/18:1(d7)/15:0)
TG (56:7) [NL-22:6]	922.8	577.5	40	TG (15:0/18:1(d7)/15:0)
TG (56:8) [NL-20:4]	920.8	599.5	40	TG (15:0/18:1(d7)/15:0)
TG (56:8) [NL-20:5]	920.8	601.5	40	TG (15:0/18:1(d7)/15:0)
TG (56:8) [NL-22:6]	920.8	575.5	40	TG (15:0/18:1(d7)/15:0)
TG (56:9) [NL-22:6]	918.8	573.5	40	TG (15:0/18:1(d7)/15:0)
TG (O-50:1) [NL-16:0]	836.8	563.5	40	TG (15:0/18:1(d7)/15:0)
TG (O-50:1) [NL-18:1]	836.8	537.5	40	TG (15:0/18:1(d7)/15:0)
TG (O-50:2) [NL-16:1]	834.8	563.5	40	TG (15:0/18:1(d7)/15:0)
TG (O-50:2) [NL-18:1]	834.8	535.5	40	TG (15:0/18:1(d7)/15:0)
TG (O-50:2) [NL-18:2]	834.8	537.5	40	TG (15:0/18:1(d7)/15:0)
TG (O-52:0) [NL-16:0]	866.8	593.5	40	TG (15:0/18:1(d7)/15:0)
TG (O-52:1) [NL-16:0]	864.8	591.5	40	TG (15:0/18:1(d7)/15:0)
TG (O-52:1) [NL-18:1]	864.8	565.5	40	TG (15:0/18:1(d7)/15:0)
TG (O-52:2) [NL-16:0]	862.8	589.5	40	TG (15:0/18:1(d7)/15:0)
TG (O-52:2) [NL-18:1]	862.8	563.5	40	TG (15:0/18:1(d7)/15:0)
TG (O-54:2) [NL-18:1]	890.8	591.5	40	TG (15:0/18:1(d7)/15:0)
TG (O-54:3) [NL-18:1]	888.8	589.5	40	TG (15:0/18:1(d7)/15:0)
TG (O-54:4) [NL-18:2]	886.8	589.5	40	TG (15:0/18:1(d7)/15:0)
TG (O-54:4) [NL-18:2]	886.8	589.5	40	TG (15:0/18:1(d7)/15:0)

3.6 Multiplexed Lipidomics Assay in Negative Ionization Mode

1. Prepare mobile phase A: acetonitrile/water 60/40 (vol/vol) with 10 mM ammonium acetate.
2. Prepare mobile phase B: isopropyl alcohol/acetonitrile 90/10 (vol/vol) with 10 mM ammonium acetate.
3. Create the negative mode electrospray ionization mass spectrometry method using the following parameters: curtain gas at 40 psi; collision gas set at 9; ion spray voltage at -2000 V; temperature at 450 °C; ion source Gas 1 at 40 psi; ion source Gas 2 at 70 psi; entrance potential at -10 V; and collision cell exit potential at -15 V. Acquire data in MRM mode with the precursor/product ions and CE values reported in Table 8.
4. Use a dedicated ACQUITY Premier BEH C18 1.7 μm , 2.1×100 mm LC column. For the LC analysis, inject 1 μL of the sample using a flow rate of 0.25 mL/min at 55 °C. Set the gradient program: 0.0 – 8.0 min from 45% B to 99% B, 8.0 – 9.0 min at 99% B, 9.0 – 9.1 min to 45% B, and 9.1 – 10.0 min at 45% B.
5. Before starting the LCMS acquisition of a sample sequence, equilibrate the LCMS system by injecting three MS-grade methanol blanks.
6. To test the suitability of the LCMS system, prepare a system suitability solution by diluting all internal standard mixtures in MS-grade methanol at 1:100 ratio.
7. Inject the system suitability solution three times consecutively to ensure system stability and reproducibility.
8. Before proceeding, ensure that the retention times and the peak areas are reproducible across the triplicate injections of the system suitability solution by monitoring the following internal standards: BMP (14:0/14:0), LPE (18:1(d7)), PA (15:0/18:1(d7)), PE (15:0/18:1(d7)), PG (15:0/18:1(d7)), PI (15:0/18:1(d7)), PS (15:0/18:1(d7)), and GM3 (d18:1)/18:0(d5) (*see* Note 17).
9. Before running the sample sequence, equilibrate the LC system by making two injections of a pooled sample extract.
10. Run the sample sequence in a block-randomized order (*see* Note 18).
11. Quantify the area ratios of endogenous lipids and surrogate internal standards (Table 8) using SCIEX OS 3.1.

3.7 Multiplexed Metabolomics Assay

1. Prepare mobile phase A: water with 10 mM ammonium formate and 0.1% formic acid.
2. Prepare mobile phase B: acetonitrile with 0.1% formic acid.
3. Create a positive mode electrospray ionization mass spectrometry method using the following parameters: curtain gas at

Table 8
Acquisition parameters for lipid analysis in negative ionization mode

Name	Q1	Q3	CE (V)	Internal standard
12-HETE	319.2	179.1	-22	12-HETE-d8
12-HETE-d8	327.2	184.1	-22	
13-HODE	295.2	195.1	-21	12-HETE-d8
14(15)-EpETE	317.2	207.1	-22	12-HETE-d8
14,15-DiHETE	335.2	207.1	-22	12-HETE-d8
15-deoxy-PGJ2	315.2	271.1	-20	12-HETE-d8
15-HETE	319.2	219.1	-22	15-HETE-d8
15-HETE-d8	327.2	226.1	-22	
15-keto-PGF2-alpha	351.2	113.1	-35	6-keto-PGF1-alpha-d4
16(17)-EpDPE	343.2	233.2	-22	15-HETE-d8
17(18)-EpETE	317.2	259.2	-22	15-HETE-d8
17,18-DiHETE	335.2	247.2	-22	15-HETE-d8
17-HDoHE	343.2	281.3	-22	15-HETE-d8
5-HEPE	317.2	115.1	-22	5-HETE-d8
5-HETE	319.2	115.1	-21	5-HETE-d8
5-HETE-d8	327.2	116.1	-22	
6-keto-PGF1-alpha	369	163	-20	6-keto-PGF1-alpha-d4
6-keto-PGF1-alpha-d4	373	167	-20	
8-HETE	319.2	155.1	-22	5-HETE-d8
9-HODE	295.2	171.1	-21	5-HETE-d8
Arachidonic acid (d8)	311.3	267.1	-19	
Arachidonic acid	303.2	259.1	-19	Arachidonic acid (d8)
BMP (14:0/14:0)	665.3	227.2	-50	
BMP (16:0_18:1)	747.5	255.4	-50	BMP (14:0/14:0)
BMP (16:0_20:4)	769.5	255.4	-50	BMP (14:0/14:0)
BMP (16:0_22:6)	795.5	255.4	-50	BMP (14:0/14:0)
BMP (16:1/16:1)	717.5	253.1	-50	BMP (14:0/14:0)
BMP (18:0_18:1)	775.5	281.4	-50	BMP (14:0/14:0)
BMP (18:0_20:4)	797.5	283.4	-50	BMP (14:0/14:0)
BMP (18:0_22:6)	823.5	283.4	-50	BMP (14:0/14:0)
BMP (18:1/18:1)	773.5	281.3	-50	BMP (14:0/14:0)

(continued)

Table 8
(continued)

Name	Q1	Q3	CE (V)	Internal standard
BMP (20:4/20:4)	817.5	303.3	-50	BMP (14:0/14:0)
BMP (22:6/22:6)	865.5	327.3	-50	BMP (14:0/14:0)
Cholesterol sulfate	465.3	96.7	-50	Arachidonic acid (d8)
CL (14:0/14:0/14:0/14:0)	619.5	227.2	-50	
CL (72:6/18:2)	725.7	279.2	-50	CL (14:0/14:0/14:0/14:0)
CL (72:7/18:2)	724.7	279.2	-50	CL (14:0/14:0/14:0/14:0)
CL (72:8/18:2)	723.7	279.3	-50	CL (14:0/14:0/14:0/14:0)
CL (74:9/18:2)	736.7	279.2	-50	CL (14:0/14:0/14:0/14:0)
DHA	327.2	229.1	-19	Arachidonic acid (d8)
EPA	301.3	257.1	-19	Arachidonic acid (d8)
GD1a/b (d34:1)	903.5	290.1	-50	GM3 (d18:1/18:0(d5))
GD1a/b (d36:1)	917.5	290.1	-50	GM3 (d18:1/18:0(d5))
GD1a/b (d38:1)	931.5	290.1	-50	GM3 (d18:1/18:0(d5))
GD3 (d34:1)	720.5	290.1	-50	GM3 (d18:1/18:0(d5))
GD3 (d36:1)	734.5	290.1	-50	GM3 (d18:1/18:0(d5))
GD3 (d38:1)	748.5	290.1	-50	GM3 (d18:1/18:0(d5))
GM1 (d18:1)/17:0)	1530.8	290.1	-80	
GM1 (d34:1)	1516.7	290.1	-80	GM1 (d18:1)/17:0)
GM1 (d36:1)	1544.7	290.1	-80	GM1 (d18:1)/17:0)
GM1 (d38:1)	1572.7	290.1	-80	GM1 (d18:1)/17:0)
GM2 (d18:1)/18:0(d3))	1385.7	290.1	-80	
GM2 (d34:1)	1354.7	290.1	-80	GM2 (d18:1/18:0(d3))
GM2 (d36:1)	1382.7	290.1	-80	GM2 (d18:1/18:0(d3))
GM2 (d38:1)	1410.7	290.1	-80	GM2 (d18:1/18:0(d3))
GM3 (d18:1)/18:0(d5))	1184.8	290.1	-65	
GM3 (d34:1)	1151.7	290.1	-65	GM3 (d18:1/18:0(d5))
GM3 (d36:1)	1179.8	290.1	-65	GM3 (d18:1/18:0(d5))
GM3 (d38:1)	1207.8	290.1	-65	GM3 (d18:1/18:0(d5))
GQ1b (d34:1)	796.5	290.1	-55	GM3 (d18:1/18:0(d5))
GQ1b (d36:1)	805.4	290.1	-55	GM3 (d18:1/18:0(d5))
GQ1b (d38:1)	814.4	290.1	-55	GM3 (d18:1/18:0(d5))

(continued)

Table 8
(continued)

Name	Q1	Q3	CE (V)	Internal standard
GT1a/b (d34:1)	1049.3	290.1	-35	GM3 (d18:1/18:0(d5))
GT1a/b (d36:1)	1063.3	290.1	-35	GM3 (d18:1/18:0(d5))
GT1a/b (d38:1)	1077.3	290.1	-35	GM3 (d18:1/18:0(d5))
Hemi-BMP ((14:0/14:0)_14:0)	875.5	227.3	-50	
Hemi-BMP ((18:1/18:1)_16:0)	1011.7	281.3	-50	Hemi-BMP ((14:0/14:0)_14:0)
Hemi-BMP ((18:1/18:1)_18:0)	1039.7	281.3	-50	Hemi-BMP ((14:0/14:0)_14:0)
Hemi-BMP ((18:1/18:1)_18:1)	1037.7	281.3	-50	Hemi-BMP ((14:0/14:0)_14:0)
Hemi-BMP ((20:4/20:4)_16:0)	1055.8	303.3	-50	Hemi-BMP ((14:0/14:0)_14:0)
Hemi-BMP ((20:4/20:4)_18:0)	1183.8	303.3	-50	Hemi-BMP ((14:0/14:0)_14:0)
Hemi-BMP ((20:4/20:4)_18:1)	1181.8	303.3	-50	Hemi-BMP ((14:0/14:0)_14:0)
Hemi-BMP ((20:4/20:4)_20:4)	1103.8	303.3	-50	Hemi-BMP ((14:0/14:0)_14:0)
Hemi-BMP ((22:6/22:6)_16:0)	1103.7	327.3	-50	Hemi-BMP ((14:0/14:0)_14:0)
Hemi-BMP ((22:6/22:6)_18:0)	1131.7	327.3	-50	Hemi-BMP ((14:0/14:0)_14:0)
Hemi-BMP ((22:6/22:6)_18:1)	1129.7	327.3	-50	Hemi-BMP ((14:0/14:0)_14:0)
Linoleic acid	279.2	261.3	-20	Arachidonic acid (d8)
Linolenic acid	277.2	277.2	-20	Arachidonic acid (d8)
LPA (16:0)	409.3	255.3	-50	LPE (18:1(d7))
LPA (18:0)	423.3	283.3	-50	LPE (18:1(d7))
LPA (18:1)	421.3	281.3	-50	LPE (18:1(d7))
LPE (16:0)	452.2	255.3	-50	LPE (18:1(d7))
LPE (18:0)	480.31	283.3	-50	LPE (18:1(d7))
LPE (18:1(d7))	485.3	288.3	-50	
LPEp (16:0)	436.3	196.1	-50	LPEp (18:1(d7))
LPEp (18:0)	464.3	196.1	-50	LPEp (18:1(d7))
LPEp (18:1(d7))	485.3	196.1	-50	
LPEp (18:1)	462.3	196.1	-50	LPEp (18:1(d7))
LPG (16:0)	483.3	255.3	-50	LPE (18:1(d7))
LPG (18:0)	511.3	283.3	-50	LPE (18:1(d7))
LPG (18:1)	509.3	281.3	-50	LPE (18:1(d7))
LPG (20:4)	531.3	303.3	-50	LPE (18:1(d7))
LPG (22:6)	555.3	327.3	-50	LPE (18:1(d7))

(continued)

Table 8
(continued)

Name	Q1	Q3	CE (V)	Internal standard
LPI (16:0)	571.3	241.1	-50	LPE (18:1(d7))
LPI (18:0)	599.3	241.1	-50	LPE (18:1(d7))
LPS (16:0)	496.3	255.3	-50	LPE (18:1(d7))
LPS (18:0)	524.3	283.3	-50	LPE (18:1(d7))
LPS (18:1)	522.3	281.3	-50	LPE (18:1(d7))
LPS (20:4)	544.3	303.3	-50	LPE (18:1(d7))
LPS (22:6)	568.3	327.3	-50	LPE (18:1(d7))
LTB4	335	195	-22	PGE2-d4
Oleic acid	281.2	263.3	-20	Arachidonic acid (d8)
PA (15:0/18:1(d7))	666.52	241.3	-50	
PA (16:0_18:1)	673.5	255.3	-50	PA (15:0/18:1(d7))
PA (18:0_18:1)	701.5	283.3	-50	PA (15:0/18:1(d7))
PA (18:0_20:4)	723.5	283.3	-50	PA (15:0/18:1(d7))
PA (18:0_22:6)	747.5	283.3	-50	PA (15:0/18:1(d7))
PA (18:1/18:1)	699.5	281.3	-50	PA (15:0/18:1(d7))
PA (20:4/20:4)	743.5	327.3	-50	PA (15:0/18:1(d7))
PA (22:6/22:6)	791.5	327.3	-50	PA (15:0/18:1(d7))
Palmitic acid	255.1	255.2	-20	Arachidonic acid (d8)
Palmitoleic acid	253.1	253.3	-20	Arachidonic acid (d8)
PE (15:0/18:1(d7))	709.6	241.3	-50	PE (15:0/18:1(d7))
PE (O-16:0/20:4)	724.5	303.2	-50	PE (15:0/18:1(d7))
PE (O-16:0/22:6)	748.5	327.2	-50	PE (15:0/18:1(d7))
PE (O-18:0/20:4)	752.6	303.2	-50	PE (15:0/18:1(d7))
PE (O-18:0/22:6)	776.6	327.2	-50	PE (15:0/18:1(d7))
PE (P-16:0/20:4)	722.6	303.3	-50	PE (15:0/18:1(d7))
PE (P-16:0/20:5)	720.6	301.3	-50	PE (15:0/18:1(d7))
PE (P-16:0/22:4)	750.6	331.3	-50	PE (15:0/18:1(d7))
PE (P-16:0/22:6)	746.6	327.3	-50	PE (15:0/18:1(d7))
PE (P-18:0/18:1)	728.6	281.3	-50	PE (15:0/18:1(d7))
PE (P-18:0/18:2)	726.6	279.2	-50	PE (15:0/18:1(d7))
PE (P-18:0/20:4)	750.6	303.3	-50	PE (15:0/18:1(d7))

(continued)

Table 8
(continued)

Name	Q1	Q3	CE (V)	Internal standard
PE (P-18:0/20:5)	748.6	301.3	-50	PE (15:0/18:1(d7))
PE (P-18:0/22:6)	774.6	327.3	-50	PE (15:0/18:1(d7))
PE (P-18:0/22:6)OH	790.6	343.3	-50	PE (15:0/18:1(d7))
PE (P-18:1/20:4)	748.5	303.3	-50	PE (15:0/18:1(d7))
PE (P-18:1/22:6)	772.5	327.3	-50	PE (15:0/18:1(d7))
PEth (16:0_18:1)	772.5	255.1	-50	PE (15:0/18:1(d7))
PEth (18:1/18:1)	773.6	281.2	-50	PE (15:0/18:1(d7))
PG (15:0/18:1(d7))	740.6	241.3	-50	
PG (16:0_18:1)	747.5	255.3	-50	PG (15:0/18:1(d7))
PG (16:0_20:4)	769.5	255.3	-50	PG (15:0/18:1(d7))
PG (16:0_22:6)	795.5	255.3	-50	PG (15:0/18:1(d7))
PG (18:0_18:1)	775.5	281.3	-50	PG (15:0/18:1(d7))
PG (18:0_20:4)	797.5	283.3	-50	PG (15:0/18:1(d7))
PG (18:0_22:6)	823.5	283.3	-50	PG (15:0/18:1(d7))
PG (18:1/18:1)	773.4	281.4	-50	PG (15:0/18:1(d7))
PGD2	351.2	233.1	-16	PGE2-d4
PGE2 and PGD2	351.2	189.1	-25	PGE2-d4
PGE2	351.2	175.1	-25	PGE2-d4
PGE2-d4	355.2	193.1	-22	
PGF2-alpha	353.2	193.1	-34	PGF2-alpha-d4
PGF2-alpha-d4	357	197	-35	
PGJ2	333.2	271.1	-22	PGF2-alpha-d4
PI (15:0/18:1(d7))	828.6	241.3	-50	
PI (16:0_18:1)	835.6	255.3	-50	PI (15:0/18:1(d7))
PI (16:0_20:4)	857.6	255.3	-50	PI (15:0/18:1(d7))
PI (16:0_22:6)	881.6	255.3	-50	PI (15:0/18:1(d7))
PI (18:0_18:1)	863.6	283.3	-50	PI (15:0/18:1(d7))
PI (18:0_20:4)	885.6	283.3	-50	PI (15:0/18:1(d7))
PI (18:0_22:6)	909.6	283.3	-50	PI (15:0/18:1(d7))
PI (18:1/18:1)	861.6	281.3	-50	PI (15:0/18:1(d7))
PI (20:4/20:4)	905.6	303.3	-50	PI (15:0/18:1(d7))

(continued)

Table 8
(continued)

Name	Q1	Q3	CE (V)	Internal standard
PS (15:0/18:1(d7))	753.6	241.3	-50	
PS (16:0_18:1)	760.6	255.3	-50	PS (15:0/18:1(d7))
PS (16:0_20:4)	782.6	255.3	-50	PS (15:0/18:1(d7))
PS (16:0_22:6)	806.6	255.3	-50	PS (15:0/18:1(d7))
PS (18:0_18:1)	788.6	283.3	-50	PS (15:0/18:1(d7))
PS (18:0_20:4)	810.6	283.3	-50	PS (15:0/18:1(d7))
PS (18:0_22:6)	834.6	283.3	-50	PS (15:0/18:1(d7))
PS (18:1/18:1)	786.6	281.3	-50	PS (15:0/18:1(d7))
PS (22:6/22:6)	878.5	327.3	-50	PS (15:0/18:1(d7))
Sphingosine 1-phosphate (d18:1(d7))	385.3	79.2	-50	
Sphingosine 1-phosphate (d18:1)	378.3	79.2	-50	Sphingosine 1-phosphate (d18:1(d7))
Stearic acid	283.2	265.3	-20	Arachidonic acid (d8)
Sulfatide (d34:1)	778.5	97	-150	Sulfatide (d18:1/18:0(d3))
Sulfatide (d36:1(OH))	822.6	97	-150	Sulfatide (d18:1/18:0(d3))
Sulfatide (d36:1)	806.6	97	-150	Sulfatide (d18:1/18:0(d3))
Sulfatide (d42:1(OH))	906.7	97	-150	Sulfatide (d18:1/18:0(d3))
Sulfatide (d42:1)	890.7	97	-150	Sulfatide (d18:1/18:0(d3))
Sulfatide (d42:2(OH))	904.7	97	-150	Sulfatide (d18:1/18:0(d3))
Sulfatide (d42:2)	888.7	97	-150	Sulfatide (d18:1/18:0(d3))
Sulfatide (d18:1/18:0(d3))	809.6	97	-150	
TXB2	369.2	169.1	-22	TXB2-d4
TXB2-d4	373	173	-22	

40 psi; collision gas at 9; ion spray voltage at 1600 V; the temperature at 350 °C; ion source Gas 1 at 30 psi; ion source Gas 2 at 50 psi; entrance potential at 10 V; and collision cell exit potential at 10 V. Acquire data in MRM mode with the precursor/product ions and CE values reported in Table 9.

- For the LC analysis, use an ACQUITY Premier BEH amide 1.7 μm , 2.1 \times 150 mm LC column. Inject 1 μL of the sample using a flow rate of 0.40 mL/min at 40 °C. Program the gradient as follows: 0.0–1.0 min at 95% B; 1.0–7.0 min to 50% B; 7.0–7.1 min to 95% B; and 7.1–10.0 min at 95% B.

Table 9**Acquisition parameters for metabolite analysis in positive ionization mode**

Name	Q1	Q3	CE(V)	Internal standard
1-Methylhistidine	170	124	20	Phenylalanine-13C6
1-Methylnicotinamide	137	94	20	Phenylalanine-13C6
1-Methylxanthine	167	110	30	Phenylalanine-13C6
1-Methylxanthosine	299	187.1	30	Phenylalanine-13C6
2-Aminobenzoic acid	138.1	92	20	Phenylalanine-13C6
3-Hydroxybutyric acid	105	87	20	Phenylalanine-13C6
3-Hydroxykynurenine	225.1	179.1	15	Phenylalanine-13C6
3-Hydroxy-N6,N6,N6-Trimethyllysine	205.2	128.1	25	Phenylalanine-13C6
3-Hydroxytyrosol	137.1	119	20	Phenylalanine-13C6
3-Methoxytyramine	168.1	151.1	25	Phenylalanine-13C6
3-Methoxytyrosine	212.1	166.1	20	Phenylalanine-13C6
3-Methylxanthine	167	69	30	Phenylalanine-13C6
3-Methylxanthosine	299.1	187.1	30	Phenylalanine-13C6
4-Hydroxyproline	132	68.1	20	Phenylalanine-13C6
4-Trimethylammoniobutanal	130.1	71.1	20	Phenylalanine-13C6
5-Glutamylalanine	219.1	90.1	12	Phenylalanine-13C6
5-Hydroxyindoleacetic acid	192.07	146.1	20	Phenylalanine-13C6
5-Hydroxytryptophan	221.1	175	20	Phenylalanine-13C6
5'-Methylthioadenosine	298	136	20	Phenylalanine-13C6
6-Aminouracil	128	85	19	Phenylalanine-13C6
7-alpha-Hydroxy-3-oxo-4-cholestenoate	431.3	395.3	15	Phenylalanine-13C6
7-Methylguanine	166.1	124.1	25	Phenylalanine-13C6
7-Methylguanosine	298	166	20	Phenylalanine-13C6
7-Methylxanthine	167.1	69	30	Phenylalanine-13C6
7-Methylxanthosine	299.2	167.1	30	Phenylalanine-13C6
8-Hydroxy-deoxyguanosine	284.1	140	20	Phenylalanine-13C6
8-Hydroxyguanosine	300	168	20	Phenylalanine-13C6
9-Hexadecenoylcarnitine	398.3	85	35	Isovalerylcarnitine-d3
Acetylcarnitine	204.1	85	25	Acetylcarnitine-d3
Acetylcarnitine-d3	207.14	85	25	
Adenine	136.1	119	30	Phenylalanine-13C6

(continued)

Table 9
(continued)

Name	Q1	Q3	CE(V)	Internal standard
Adenosine diphosphate ribose	560.1	136.1	30	Phenylalanine-13C6
Adenosine	268.15	136.1	27	Phenylalanine-13C6
Adenosylcobalamin	801.5	676.3	31	Phenylalanine-13C6
AICA-riboside	259	110	20	Phenylalanine-13C6
Alanine	90.1	44.2	20	Alanine-d4
Alanine-d4	94.08	48.1	25	
Allantoin	159.1	116	25	Phenylalanine-13C6
Alpha-tocopherol	431.4	165.1	20	Phenylalanine-13C6
Anserine	241.2	109.2	25	Anserine-d4
Anserine-d4	245.2	109.2	25	
Arabitol	153.1	153.1	10	Phenylalanine-13C6
Arginine	175.12	70	27	Arginine-13C5d4
Arginine-13C5d4	180.1	75	27	
Ascorbate	177	95	20	Phenylalanine-13C6
Asparagine	133.06	74.1	15	Aspartic acid-d3
Aspartic acid	134.1	74.1	18	Aspartic acid-d3
Aspartic acid-d3	137.1	75.1	18	
Asymmetric dimethylarginine	203.15	70.3	40	Arginine-13C5d4
Betaine	118.1	59.1	20	Phenylalanine-13C6
Bilirubin	585.3	299.1	20	Phenylalanine-13C6
Butyrobetaine	146.1	87	20	Phenylalanine-13C6
Butyrylcarnitine	232.2	85	30	Butyrylcarnitine-d3
Butyrylcarnitine-d3	235.16	85	30	
Cadaverine	102.9	86.1	14	Phenylalanine-13C6
cADPRibose	542.1	136.1	30	Phenylalanine-13C6
Caffeine	195.1	138	20	Phenylalanine-13C6
Capsaicin	306.2	137.1	20	Phenylalanine-13C6
Carnitine	162.1	103.1	20	Carnitine-d9
Carnitine-d9	171.16	85	20	
Carnosine	227.2	110.1	28	Carnosine-d4
Carnosine-d4	231.1	110.1	25	

(continued)

Table 9
(continued)

Name	Q1	Q3	CE(V)	Internal standard
Choline	104	60	21	Phenylalanine-13C6
Citrulline	176.1	113.1	12	Citrulline-d2
Citrulline-d2	178.11	115.1	12	
Cotinine	177.1	80	32	Phenylalanine-13C6
Creatine	132	90	18	Phenylalanine-13C6
Creatinine	114	44.1	22	Creatinine-d3
Creatinine-d3	117	86	15	
Curcumin	369	177	30	Phenylalanine-13C6
Cyanocobalamin	678.5	997.5	28	Phenylalanine-13C6
Cystathionine	223.1	134	15	Phenylalanine-13C6
Cysteine	122.03	76.02	15	Phenylalanine-13C6
Cysteinylglycine	179.1	162.2	15	Phenylalanine-13C6
Cystine	241	74	25	Phenylalanine-13C6
Cytosine	112.1	94.9	25	Phenylalanine-13C6
Decanoylcarnitine	316.2	85	35	Octanoylcarnitine-d3
Demethoxycurcumin	339.1	255.2	25	Phenylalanine-13C6
Deoxyadenosine	252.1	136	20	Phenylalanine-13C6
Deoxyguanosine	268.1	152	20	Phenylalanine-13C6
Deoxyinosine	253	137	20	Phenylalanine-13C6
Dimethylethanolamine	90	72	15	Phenylalanine-13C6
Dimethylglycine	104.02	58	21	Phenylalanine-13C6
Dodecanoylcarnitine	343.3	85	30	Octanoylcarnitine-d3
Dopa	198	152	20	Alanine-d4
Dopamine 3-o-sulfate	234	137.1	15	Alanine-d4
Dopamine 4-o-sulfate	234.1	137.2	15	Alanine-d4
Dopamine	154	137	13	Alanine-d4
Epinephrine	166	107	20	Phenylalanine-13C6
Ergothioneine	230.1	127	22	Phenylalanine-13C6
Ethanolamine	62	44.2	12	Phenylalanine-13C6
Formylanthranilic acid	166	120	16	Phenylalanine-13C6
Gamma-aminobutyric acid	104.1	87	13	Phenylalanine-13C6

(continued)

Table 9
(continued)

Name	Q1	Q3	CE(V)	Internal standard
Gamma-Glutamylcysteine	251.1	122.02	15	Phenylalanine-13C6
Glucosamine	180	162	20	Phenylalanine-13C6
Glucose	202.8	202.8	10	Phenylalanine-13C6
Glutamate-d3	151	133.1	20	
Glutamic acid	148.06	84.04	20	Glutamate-d3
Glutamine	147.08	84	15	Glutamate-d3
Glutathione disulfide	613.2	355.1	25	Phenylalanine-13C6
Glutathione	308.1	179.1	17	Phenylalanine-13C6
Glycerophosphocholine	258.1	104	16	Phenylalanine-13C6
Glycine	76.04	30	25	Glycine-15N13C2
Glycine-15N13C2	78.0	32.0	25	
Guanine	152.2	110	20	Phenylalanine-13C6
Guanosine	284.1	152	20	Phenylalanine-13C6
Hexanoylcarnitine	260.2	85	35	Isovalerylcarnitine-d3
Histamine	112.09	95	20	Phenylalanine-13C6
Histidine	156.08	110.07	16	Arginine-13C5d4
Homocarnosine	241.1	110.1	25	Phenylalanine-13C6
Homocysteine	136.12	90.1	17	Phenylalanine-13C6
Homoserine	120.15	56.2	24	Phenylalanine-13C6
Hydroxybutyrylcarnitine	248.2	85	30	Propionylcartinine-d3
Hydroxyhexanoylcarnitine	276.2	85	30	Propionylcartinine-d3
Hydroxyisovaleroyl carnitine	262.2	85	30	Propionylcartinine-d3
Hydroxypropionylcarnitine	234.1	85	30	Propionylcartinine-d3
Hypoxanthine	137.2	118.8	20	Phenylalanine-13C6
Imidazoleacetic acid	127	81	20	Phenylalanine-13C6
Indole	118	91	20	Phenylalanine-13C6
Inosine	269.1	137.01	20	Phenylalanine-13C6
Isoleucine	132.1	86.01	15	Leucine-d3
Isovalerylcarnitine	246.2	85	33	Isovalerylcarnitine-d3
Isovalerylcarnitine-d3	255.2	85	30	
Kynurenic acid	190.05	116	36	Phenylalanine-13C6

(continued)

Table 9
(continued)

Name	Q1	Q3	CE(V)	Internal standard
Kynurenine	209	146	25	Phenylalanine-13C6
Leucine	132.1	86.01	15	Leucine-d3
Leucine-d3	135.1	89.1	15	
Linoleyl carnitine	424.3	85	45	Palmitoylcarnitine-d3
LPC (18:1(d7))	529.3	184.1	40	
Lysine	147.11	84	20	Arginine-13C5d4
Mannitol	183	69	20	Phenylalanine-13C6
Mannose	202.81	202.81	15	Phenylalanine-13C6
Melatonin	233.1	174.1	20	Phenylalanine-13C6
Methionine S-oxide	166.05	74.02	20	Methionine-d3
Methionine	150.06	104.05	10	Methionine-d3
Methionine-d3	153.07	107	20	
Methylcobalamin	673	971.5	42	Phenylalanine-13C6
Myristoylcarnitine	372	85	40	Myristoylcarnitine-d9
Myristoylcarnitine-d9	381.36	85	35	
N,N'-Bis (gamma-glutamyl) cystine	499.1	453.1	15	Phenylalanine-13C6
N1-Acetylspermidine	188.2	171	19	Phenylalanine-13C6
N1-Acetylpermine	245.2	100.1	22	Phenylalanine-13C6
N1-N12-Diacetylpermine	287.2	100.1	22	Phenylalanine-13C6
N1-N8-Diacetylpermidine	230.5	100.2	19	Phenylalanine-13C6
N6,N6,N6-Trimethyllysine	189.2	84.1	20	Phenylalanine-13C6
N-Acetylalanine	160.1	72.1	18	Phenylalanine-13C6
N-Acetylaspartic acid	176.1	176.1	10	Phenylalanine-13C6
N-Acetylcysteine	163	121.2	15	Phenylalanine-13C6
N-Acetylglutamic acid	189	130	20	Phenylalanine-13C6
N-Acetylneuraminic acid	310.1	274	15	Phenylalanine-13C6
N-Acetylputrescine	131.1	114	12	Phenylalanine-13C6
N-Acetylserine	148	106	14	Phenylalanine-13C6
NAD	664.1	428.2	24	Phenylalanine-13C6
N-Alpha-acetyllysine	189	84	18	Phenylalanine-13C6
Niacinamide	123.1	80	24	Phenylalanine-13C6

(continued)

Table 9
(continued)

Name	Q1	Q3	CE(V)	Internal standard
Nicotinamide mononucleotide	335.2	123.1	30	Phenylalanine-13C6
Nicotinamide riboside	255	123	30	Phenylalanine-13C6
Nicotinic acid	124.1	78	30	Phenylalanine-13C6
Nitrotyrosine	227.1	210	12	Phenylalanine-13C6
Nonanoylcarnitine	302.2	85	30	Octanoylcarnitine-d3
Norepinephrine	152	107	15	Phenylalanine-13C6
Octanoylcarnitine	288.2	85	33	Octanoylcarnitine-d3
Octanoylcarnitine-d3	291.2	85	33	
Ornithine	133	70	15	Ornithine-d2
Ornithine-d2	135.1	117.2	15	
Palmitoylcarnitine	400	85	40	Palmitoylcarnitine-d3
Palmitoylcarnitine-d3	403.4	85	40	
Paraxanthine	181.1	124	24	Phenylalanine-13C6
Phenylalanine	166.1	120.1	18	Phenylalanine-13C6
Phenylalanine-13C6	172.1	126.1	18	
Piperanine	288.2	135.2	33	Phenylalanine-13C6
Piperine	286.1	201.1	20	Phenylalanine-13C6
Piperonaline	342.1	229.2	23	Phenylalanine-13C6
Piperyline	272.2	201.1	28	Phenylalanine-13C6
Proline	116	70.1	20	Phenylalanine-13C6
Propionylcarnitine	218.1	85	20	Propionylcartinine-d3
Propionylcartinine-d3	221.15	85	20	
Putrescine	89	72	20	Phenylalanine-13C6
Pyridoxamine	169	152	20	Phenylalanine-13C6
Pyroglutamic acid	130	84	15	Phenylalanine-13C6
S-Adenosylhomocysteine	385.1	136	20	Methionine-d3
S-Adenosylmethionine	399	250	21	Methionine-d3
Sarcosine	90.04	44.1	20	Phenylalanine-13C6
Serine	106	60	16	Phenylalanine-13C6
Serotonin	177	160	15	Phenylalanine-13C6
Spermidine	146.16	72	17	Phenylalanine-13C6

(continued)

Table 9
(continued)

Name	Q1	Q3	CE(V)	Internal standard
Spermine	203.1	129.1	15	Phenylalanine-13C6
Sphingosine d18:1(d7)	307.3	289.3	20	
Stearoylcarnitine	428.4	85	35	Palmitoylcarnitine-d3
Sucrose	364.8	202.8	35	Phenylalanine-13C6
Taurine	126.02	80	25	Phenylalanine-13C6
Tetrahydrocurcumin	355	137.1	24	Phenylalanine-13C6
Theobromine	181	138.3	25	Phenylalanine-13C6
Theophylline	181.13	124	20	Phenylalanine-13C6
Thiamine	265	122	25	Phenylalanine-13C6
Threonine	120	74	13	Phenylalanine-13C6
Trigonelline	138.1	94.1	20	Phenylalanine-13C6
Trimethylamine-N-oxide	76.08	58.07	20	Phenylalanine-13C6
Tryptophan	205.1	146.2	20	Phenylalanine-13C6
Tyrosine	182.1	136	15	Tyrosine-13C6
Tyrosine-13C6	188.1	142.1	24	
Uracil	113	70	23	Phenylalanine-13C6
Ureidopropionic acid	133	115	20	Phenylalanine-13C6
Uric acid	169.1	141	20	Phenylalanine-13C6
Uridine	245	113	18	Phenylalanine-13C6
Valerobetaine	160	101.1	21	Phenylalanine-13C6
Valine	118.1	55	20	Valine-d8
Valine-d8	126	80.1	20	
Xanthine	153	110	20	Phenylalanine-13C6
Xanthosine	285	153	20	Phenylalanine-13C6

5. Before starting the LCMS acquisition of a sample sequence, equilibrate the LCMS system by injecting three MS-grade methanol blanks.
6. To test the suitability of the LCMS system, prepare a system suitability solution by diluting all internal standard mixtures in MS-grade methanol at 1:100 ratio.
7. Inject the system suitability solution three times consecutively to ensure system stability and reproducibility.

8. Before proceeding, ensure that the retention times and the peak areas are reproducible across the triplicate injections of the system suitability solution by monitoring the following internal standards: Carnitine-d9 and Phenylalanine-13C6 (*see Note 17*).
9. Before running the sample sequence, equilibrate the LC system by making two injections of a pooled sample extract.
10. Run the sample sequence in a block-randomized order (*see Note 18*).
11. Quantify the area ratios of endogenous metabolites and surrogate internal standards (Table 9) using SCIEX OS 3.1.

3.8 Multiplexed Glucosyl- and Galactosyl- Sphingolipids Assay

1. Prepare mobile phase A: acetonitrile/isopropyl alcohol/water 92.5/5/2.5 (vol/vol/vol) with 5 mM ammonium formate and 0.5% formic acid.
2. Prepare mobile phase B: acetonitrile/isopropyl alcohol/water 2.5/5/92.5 (vol/vol/vol) with 5 mM ammonium formate and 0.5% formic acid.
3. Create a positive mode electrospray ionization mass spectrometry method using the following parameters: curtain gas at 40 psi; collision gas at 9 psi; ion spray voltage at 2250 V; temperature at 450 °C; ion source Gas 1 at 40 psi; ion source Gas 2 at 70 psi; entrance potential at 10 V; and collision cell exit potential at 15 V. Acquire data in MRM mode with the precursor/product ions and CE values reported in Table 10.
4. For the LC analysis, use a HALO HILIC 2.0 μm , 3.0 \times 150 mm LC column. Inject 1 μL of the sample using a flow rate of 0.48 mL/min at 45 °C. Program the gradient as follows: 0.0–2 min at 0% B, 2.1 min at 5% B, 4.5 min at 15% B; hold to 6.0 min at 15% B and up to 100% B at 6.1 min and hold to 7.0 min, drop back to 0% B at 7.1 min, and hold to 8.5 min.
5. Before starting the LCMS acquisition of a sample sequence, equilibrate the LCMS system by injecting three blanks of acetonitrile/isopropyl alcohol/water 92.5/5/2.5 (vol/vol/vol) with 5 mM ammonium formate and 0.5% formic acid (mobile phase A).
6. To test the suitability of the LCMS system, prepare a system suitability solution by diluting all internal standard mixtures at a 1:100 ratio into acetonitrile/isopropyl alcohol/water 2.5/5/92.5 (vol/vol/vol) with 5 mM ammonium formate and 0.5% formic acid (mobile phase A).
7. Inject the system suitability solution three times consecutively to ensure system stability and reproducibility.
8. Before proceeding, ensure that the retention times and the peak areas are reproducible across the triplicate injections of the system suitability solution by monitoring the following

Table 10**Acquisition parameters for analysis of glucosyl- and galactosyl-sphingolipid species**

Name	Q1	Q3	CE(V)	Internal standard
Cholesteryl glucoside	566.6	369.3	30	GlcCer (d18:1(d5)/18:0)
Galactosyl sphingosine d16:1	434.2	254.3	30	Glucosyl sphingosine(d5)
Galactosyl sphingosine d18:0	464.2	284.3	30	Glucosyl sphingosine(d5)
Galactosyl sphingosine d18:1	462.2	282.3	30	Glucosyl sphingosine(d5)
Galactosyl sphingosine d18:2	460.2	280.3	30	Glucosyl sphingosine(d5)
Galactosyl sphingosine d20:1	490.2	310.3	30	Glucosyl sphingosine(d5)
GalCer (d18:1/15:0)	686.3	264.3	45	
GalCer (d18:1/16:0)	700.6	264.3	45	GalCer (d18:1/15:0)
GalCer (d18:1/18:0)	728.6	264.3	45	GalCer (d18:1/15:0)
GalCer (d18:1/20:0)	756.6	264.3	45	GalCer (d18:1/15:0)
GalCer (d18:1/22:0)	784.7	264.3	45	GalCer (d18:1/15:0)
GalCer (d18:1/22:1)	782.7	264.3	45	GalCer (d18:1/15:0)
GalCer (d18:1/23:0)	798.8	264.3	45	GalCer (d18:1/15:0)
GalCer (d18:1/24:0)	812.7	264.3	45	GalCer (d18:1/15:0)
GalCer (d18:1/24:1)	810.7	264.3	45	GalCer (d18:1/15:0)
GlcCer (d18:1(d5)/18:0)	733.6	269.3	45	
GlcCer (d18:1/16:0(d3))	703.6	264.3	45	
GlcCer (d18:1/16:0)	700.6	264.3	45	GlcCer (d18:1(d5)/18:0)
GlcCer (d18:1/18:0)	728.6	264.3	45	GlcCer (d18:1(d5)/18:0)
GlcCer (d18:1/20:0)	756.6	264.3	45	GlcCer (d18:1(d5)/18:0)
GlcCer (d18:1/22:0)	784.7	264.3	45	GlcCer (d18:1(d5)/18:0)
GlcCer (d18:1/22:1)	782.7	264.3	45	GlcCer (d18:1(d5)/18:0)
GlcCer (d18:1/23:0)	798.8	264.3	45	GlcCer (d18:1(d5)/18:0)
GlcCer (d18:1/24:0)	812.7	264.3	45	GlcCer (d18:1(d5)/18:0)
GlcCer (d18:1/24:1)	810.7	264.3	45	GlcCer (d18:1(d5)/18:0)
GlcCer (d18:2/16:0)	698.6	262.3	45	GlcCer (d18:1(d5)/18:0)
GlcCer (d18:2/18:0)	726.6	262.3	45	GlcCer (d18:1(d5)/18:0)
Glucosyl sphingosine d16:1	434.2	254.3	30	Glucosyl sphingosine(d5)
Glucosyl sphingosine d18:0	464.2	284.3	30	Glucosyl sphingosine(d5)
Glucosyl sphingosine d18:1	462.2	282.3	30	Glucosyl sphingosine(d5)
Glucosyl sphingosine d18:2	460.2	280.3	30	Glucosyl sphingosine(d5)

(continued)

Table 10
(continued)

Name	Q1	Q3	CE(V)	Internal standard
Glucosyl sphingosine d20:1	490.2	310.3	30	Glucosyl sphingosine(d5)
Glucosyl sphingosine(d5)	467.2	287.3	30	
Lactosyl sphingosine d16:1	596.4	236.3	30	Glucosyl sphingosine(d5)
Lactosyl sphingosine d18:1	624.4	264.3	30	Glucosyl sphingosine(d5)
Lactosyl sphingosine d18:2	622.4	262.3	30	Glucosyl sphingosine(d5)
Lactosyl sphingosine d20:1	652.4	292.3	30	Glucosyl sphingosine(d5)
Sitosteryl glucoside	594.6	397.4	30	GlcCer (d18:1(d5)/18:0)
Sphinganine 1-phosphate d18:0	382.3	266.3	25	Sphingosine 1-phosphate d18:1(d7)
Sphinganine d18:0	302.3	284.3	25	Sphingosine d18:1(d7)
Sphingosine 1-phosphate d18:1	380.3	264.3	25	Sphingosine 1-phosphate d18:1(d7)
Sphingosine 1-phosphate d18:1(d7)	387.3	271.3	25	
Sphingosine d16:1	272.3	254.3	25	Sphingosine d18:1(d7)
Sphingosine d18:1	300.3	282.3	25	Sphingosine d18:1(d7)
Sphingosine d18:1(d7)	307.3	289.3	25	
Sphingosine d18:2	298.3	280.3	25	Sphingosine d18:1(d7)
Sphingosine d20:1	328.3	310.3	25	Sphingosine d18:1(d7)
alpha-GalCer (d18:1/16:0)	700.6	264.3	45	GalCer (d18:1/15:0)
alpha-GalCer (d18:1/18:0)	728.6	264.3	45	GalCer (d18:1/15:0)
alpha-GalCer (d18:1/20:0)	756.6	264.3	45	GalCer (d18:1/15:0)
alpha-GalCer (d18:1/22:0)	784.7	264.3	45	GalCer (d18:1/15:0)
alpha-GalCer (d18:1/22:1)	782.7	264.3	45	GalCer (d18:1/15:0)
alpha-GalCer (d18:1/23:0)	798.8	264.3	45	GalCer (d18:1/15:0)
alpha-GalCer (d18:1/24:0)	812.7	264.3	45	GalCer (d18:1/15:0)
alpha-GalCer (d18:1/24:1)	810.7	264.3	45	GalCer (d18:1/15:0)

internal standards: GlcCer (d18:1(d5)/18:0) and glucosyl sphingosine(d5) (*see Note 17*).

9. Before running the sample sequence, equilibrate the LC system by making two injections of a pooled sample extract.
10. Run the sample sequence in a block-randomized order (*see Note 18*).
11. Quantify the area ratios of endogenous glucosyl- or galactosyl-sphingolipids and surrogate internal standards (Table 10) quantified using SCIEX OS 3.1 (Sciex).

4 Notes

1. While the FastPrep-24™ 5G bead beating grinder and lysis system (MP Biomedicals) are our recommended systems for tissue homogenization, any system specifically designed for tissue homogenization can be used. The system should be able to completely homogenize the tissue into a slurry. It is important to use beads that are inert and preloaded tubes to avoid contamination of samples by environmental lipids.
2. Standard pipette tips and other liquid handling tools are appropriate for this protocol. Unlike many lipid extraction protocols that use strong organic solvents which are not compatible with standard biological liquid handling tools, the solvents used in this method can be safely used with polypropylene labware.
3. This protocol is applicable for analyzing lipids and metabolites from the whole brain, hemibrain, dissected brain regions, punches from cryosectioned brains, and powdered/crushed frozen brain. With some modifications, this protocol can also be adapted for the analysis of lipids and metabolites from various other animal tissues and cells [9].
4. To prevent interference with LCMS analysis, use potassium EDTA as an anticoagulant for plasma samples. Avoid anticoagulants containing lithium, citrate, or heparin.
5. It is preferred to use plasma rather than serum for lipid and metabolite analysis. Serum is obtained by allowing blood to coagulate at room temperature, which can lead to enzymatic reactions that alter the actual physiological concentration of lipids and metabolites. Therefore, higher levels of certain lipids and metabolites in serum could be an artifact of *ex vivo* enhancement. Furthermore, it has been demonstrated that chelating metals with EDTA can help to quench some enzymes that may alter the physiological concentration.
6. To reduce the effect of bias introduced during sample preparation or instrumental analysis, samples should be randomized during extraction and LCMS analysis, preferably using block randomization. For further information on block randomization, refer to [16].
7. For samples weighing up to 75 mg, 2 mL homogenizer tubes are suitable. However, larger samples require a larger volume of extraction solvent. In this case, we recommend using Lysing Matrix D, 15 mL tubes preloaded with zirconium-silicate beads to homogenize larger tissue samples.
8. Through our experience, we have found that the optimal ratio of extraction solvent to brain tissue is 20:1. For every gram of tissue, it is recommended to use 20 mL of extraction solvent.

This allows for the scalability of the procedure from small brain regions to whole brains. For example, a 20 mg dissected region of mouse brain would require 400 μL of extraction solvent, while a 400 mg whole mouse brain would require 8 mL of extraction solvent. It is important to note that when preparing the extraction solvent, 5 μL of each internal standard mix per mL of methanol should be used, regardless of the sample weight. This ensures that the appropriate amount of internal standards can be detected during LCMS analysis.

9. When using the 15 mL tubes for larger samples, use Teen-Prep™ adapter 12 \times 15 mL tube holder on FastPrep-24.
10. When using the 15 mL tubes for larger samples, centrifuge the sample for 20 min at 3800 RCF at 4 °C in a tabletop centrifuge with swinging-bucket rotor.
11. For larger samples, when using 15 mL tubes, transfer 1 mL of the methanol supernatant to a new microcentrifuge tube, and place it in the freezer at -20 °C for 1 h to allow for additional protein precipitation.
12. If your autosampler does not have a deep well MTP carrier, you may use standard glass LCMS vials with total recovery inserts.
13. After lipid extraction with methanol, it is important to evaporate the methanol and resuspend the analytes in a weaker solvent, such as acetonitrile/isopropyl alcohol/water 92.5/5/2.5 (vol/vol/vol) with 5 mM ammonium formate and 0.5% formic acid (mobile phase A). This is because methanol is a stronger solvent than the mobile phase used in HILIC LCMS analysis. Failure to properly resuspend the analytes can cause them to smear on the LC column, resulting in lost chromatographic resolution and low or lost signal in the analysis.
14. If final extracts are stored at -80 °C, they must be warmed and agitated before LCMS analysis. Let them come to room temperature on the benchtop, and then place them on a gentle plate vortexer for several minutes before analysis.
15. If the sample volume is limited, such as in the case of mouse CSF, a 2 μL sample can be combined with 8 μL of MS-grade water to obtain a total volume of 10 μL .
16. This centrifugation and removal of supernatant from the pellet is critical for plasma and serum but is optional for CSF and urine due to their lower protein content.
17. The retention times and peak areas should have an intra-assay coefficient of variation of $\leq 5\%$ and an inter-assay coefficient of variation of $\leq 10\%$. If the system suitability test fails to meet these criteria, troubleshooting of the LCMS system may be

necessary. Common solutions for troubleshooting include changing the LC column, checking for leaks, cleaning the ionization source, and cleaning the optics of the mass spectrometer.

18. When analyzing extracts from different sample matrices (e.g., from both brain and plasma), it is recommended to run all samples from one matrix first as one block, followed by all samples from another matrix as another block. At the start of each block, it is advised to make two injections of sample extract from that matrix to equilibrate the system prior to beginning actual sample analysis.

References

1. Wishart DS, Feunang YD, Marcu A, Guo AC, Liang K, Vazquez-Fresno R, Sajed T, Johnson D, Li C, Karu N, Sayeeda Z, Lo E, Assempour N, Berjanskii M, Singhal S, Arndt D, Liang Y, Badran H, Grant J, Serra-Cayuela A, Liu Y, Mandal R, Neveu V, Pon A, Knox C, Wilson M, Manach C, Scalbert A (2018) HMDB 4.0: the human metabolome database for 2018. *Nucleic Acids Res* 46(D1): D608–D617. <https://doi.org/10.1093/nar/gkx1089>
2. Piomelli D, Astarita G, Rapaka R (2007) A neuroscientist's guide to lipidomics. *Nat Rev Neurosci* 8(10):743–754. <https://doi.org/10.1038/nrn2233>
3. Johnson CH, Ivanisevic J, Siuzdak G (2016) Metabolomics: beyond biomarkers and towards mechanisms. *Nat Rev Mol Cell Biol* 17(7):451–459
4. Wenk MR (2005) The emerging field of lipidomics. *Nat Rev Drug Discov* 4(7):594–610. <https://doi.org/10.1038/nrd1776>
5. Alarcon-Barrera JC, Kostidis S, Ondo-Mendez A, Giera M (2022) Recent advances in metabolomics analysis for early drug development. *Drug Discov Today* 27(6): 1763–1773
6. Logan T, Simon MJ, Rana A, Cherf GM, Srivastava A, Davis SS, Low RLY, Chiu CL, Fang M, Huang F, Bhalla A, Llapashtica C, Prorok R, Pizzo ME, Calvert MEK, Sun EW, Hsiao-Nakamoto J, Rajendra Y, Lexa KW, Srivastava DB, van Lengerich B, Wang J, Robles-Colmenares Y, Kim DJ, Duque J, Lenser M, Earr TK, Nguyen H, Chau R, Tsogtbaatar B, Ravi R, Skuja LL, Solanoy H, Rosen HJ, Boeve BF, Boxer AL, Heuer HW, Dennis MS, Kariolis MS, Monroe KM, Przybyla L, Sanchez PE, Meisner R, Diaz D, Henne KR, Watts RJ, Henry AG, Gunasekaran K, Astarita G, Suh JH, Lewcock JW, DeVos SL, Di Paolo G (2021) Rescue of a lysosomal storage disorder caused by Grn loss of function with a brain penetrant progranulin biogenic. *Cell* 184(18): 4651–4668. <https://doi.org/10.1016/j.cell.2021.08.002>
7. Root J, Mendsaikhan A, Nandy S, Taylor G, Wang M, Araujo LT, Merino P, Ryu D, Holler C, Thompson BM, Astarita G, Blain J-F, Kukar T (2023) Granulins rescue inflammation, lysosome dysfunction, and neuropathology in a mouse model of progranulin deficiency. *bioRxiv:2023.2004.2017.536004*. <https://doi.org/10.1101/2023.04.17.536004>
8. Rhinn H, Tatton N, McCaughey S, Kurnellas M, Rosenthal A (2022) Progranulin as a therapeutic target in neurodegenerative diseases. *Trends Pharmacol Sci* 43(8):641–652
9. Zhao Z, Xu Y (2010) An extremely simple method for extraction of lysophospholipids and phospholipids from blood samples. *J Lipid Res* 51(3):652–659
10. Wang J, Bhalla A, Ullman JC, Fang M, Ravi R, Arguello A, Thomsen E, Tsogtbaatar B, Guo JL, Skuja LL, Dugas JC, Davis SS, Poda SB, Gunasekaran K, Costanzo S, Sweeney ZK, Henry AG, Harris JM, Henne KR, Astarita G (2020) High-throughput liquid chromatography-tandem mass spectrometry quantification of Glycosaminoglycans as biomarkers of Mucopolysaccharidosis II. *Int J Mol Sci* 21(15):5449. <https://doi.org/10.3390/ijms21155449>
11. Ullman JC, Arguello A, Getz JA, Bhalla A, Mahon CS, Wang J, Giese T, Bedard C, Kim DJ, Blumenfeld JR, Liang N, Ravi R, Nugent AA, Davis SS, Ha C, Duque J, Tran HL, Wells RC, Lianoglou S, Daryani VM, Kwan W, Solanoy H, Nguyen H, Earr T, Dugas JC,

- Tuck MD, Harvey JL, Reyzer ML, Caprioli RM, Hall S, Poda S, Sanchez PE, Dennis MS, Gunasekaran K, Srivastava A, Sandmann T, Henne KR, Thorne RG, Di Paolo G, Astarita G, Diaz D, Silverman AP, Watts RJ, Sweeney ZK, Kariolis MS, Henry AG (2020) Brain delivery and activity of a lysosomal enzyme using a blood-brain barrier transport vehicle in mice. *Sci Transl Med* 12(545). <https://doi.org/10.1126/scitranslmed.aay1163>
12. Nugent AA, Lin K, van Lengerich B, Lianoglou S, Przybyla L, Davis SS, Llapashtica C, Wang J, Kim DJ, Xia D, Lucas A, Baskaran S, Haddick PCG, Lenser M, Earr TK, Shi J, Dugas JC, Andreone BJ, Logan T, Solanoy HO, Chen H, Srivastava A, Poda SB, Sanchez PE, Watts RJ, Sandmann T, Astarita G, Lewcock JW, Monroe KM, Di Paolo G (2020) TREM2 regulates microglial cholesterol metabolism upon chronic phagocytic challenge. *Neuron* 105(5): 837–854. <https://doi.org/10.1016/j.neuron.2019.12.007>
 13. Crotty GF, Maciuca R, Macklin EA, Wang J, Montalban M, Davis SS, Alkabsh JI, Bakshi R, Chen X, Ascherio A, Astarita G, Huntwork-Rodriguez S, Schwarzschild MA (2020) Association of caffeine and related analytes with resistance to Parkinson disease among LRRK2 mutation carriers: a metabolomic study. *Neurology* 95(24):e3428–e3437. <https://doi.org/10.1212/WNL.0000000000010863>
 14. Bhalla A, Ravi R, Fang M, Arguello A, Davis SS, Chiu CL, Blumenfeld JR, Nguyen HN, Earr TK, Wang J, Astarita G, Zhu Y, Fiore D, Scarce-Levie K, Diaz D, Cahan H, Troyer MD, Harris JM, Escolar ML (2020) Characterization of fluid biomarkers reveals lysosome dysfunction and neurodegeneration in neurodegenerative MPS II patients. *Int J Mol Sci* 21(15): 5188. <https://doi.org/10.3390/ijms21155188>
 15. Andreone BJ, Przybyla L, Llapashtica C, Rana A, Davis SS, van Lengerich B, Lin K, Shi J, Mei Y, Astarita G, Di Paolo G, Sandmann T, Monroe KM, Lewcock JW (2020) Alzheimer’s-associated PLCgamma2 is a signaling node required for both TREM2 function and the inflammatory response in human microglia. *Nat Neurosci* 23(8): 927–938. <https://doi.org/10.1038/s41593-020-0650-6>
 16. Burger B, Vaudel M, Barsnes H (2020) Importance of block randomization when designing proteomics experiments. *J Proteome Res* 20(1):122–128



Neuropathological Assessment as an Endpoint in Clinical Trial Design

Steve M. Gentleman and Alan King Lun Liu

Abstract

Different neurodegenerative conditions can have complex, overlapping clinical presentations that make accurate diagnosis during life very challenging. For this reason, confirmation of the clinical diagnosis still requires postmortem verification. This is particularly relevant for clinical trials of novel therapeutics where it is important to ascertain what disease- and/or pathology-modifying effects the therapeutics have had. Furthermore, it is important to confirm that patients in the trial had the correct clinical diagnosis as this will have a major bearing on the interpretation of trial results. Here we present a simple protocol for pathological assessment of neurodegenerative changes.

Key words Clinical trial, Neurodegeneration, Postmortem, Diagnosis, Neuropathology

1 Introduction

Examination of postmortem human brain tissue has been key to many of the major advances in our understanding of neurodegenerative disorders over the past 30 years. The detection of the new variant Creutzfeldt-Jakob disease in the 1990s [1], the identification of the multiple molecular mechanisms underlying different frontotemporal dementias [2], and the emergence of new disease entities, such as chronic traumatic encephalopathy [3], and aging-related tau astroglial pathology (ARTAG) [4] have all been due to observations made on examination of autopsy brains. Postmortem examination is also crucial for clinical audit when the clinical diagnosis is not straightforward. For example, the most common cause of parkinsonism is idiopathic Parkinson's disease, but there are several other disorders, such as multiple system atrophy (MSA) and progressive supranuclear palsy (PSP), which can also present in this way. These disorders have different cellular and molecular mechanisms of pathogenesis, and it is sometimes only by postmortem examination that the correct diagnosis can be confirmed. With

increasing life expectancy, a further complication is the fact that many elderly patients may have more than one disease pathology which may make their clinical presentation very difficult to interpret [5]. These problems with clinical diagnostic accuracy have been highlighted recently in relation to immunotherapy trials for Alzheimer's disease. Autopsy studies revealed that a proportion of people enrolled on the trial, which was specifically based on removal of A β peptide, did not actually have Alzheimer's disease [6]. For all of these reasons, we feel that postmortem follow-up is essential for clinical trials, and we present here a protocol for assessment of neurodegenerative changes which is based on what we routinely use in the Parkinson's UK tissue bank (the Parkinson's UK Brain Bank, <https://www.parkinsons.org.uk/content/parkinsons-uk-brain-bank>).

2 Materials

Brain donations can be made in several different ways. A hospital postmortem can be requested by a physician after the death of an inpatient, particularly if there is uncertainty over diagnosis. However, for research purposes, many brain tissue banks will prospectively consent patients who have expressed a wish to donate their brain (UK Brain Banks Network, <https://www.mrc.ac.uk/research/facilities-and-resources-for-researchers/brain-banks/>; the Parkinson's UK Brain Bank). The prospective nature of this consenting process usually facilitates a more rapid retrieval of tissue when the patient dies because the next of kin and/or the attending healthcare professionals are aware of the patient's wishes and will inform the tissue banks soon after death. Ideally, a similar premortem prospective consent procedure should be included in clinical trial designs.

3 Methods

When a brain donation is received the protocol for neuropathological assessment entails tissue dissection, sampling, preparation, sectioning, staining, and examination. In some cases, donations will be of whole fixed brains, but, if possible, fresh brains should be bisected, and frozen tissue should be retained from one half of the brain. This tissue is not only useful for research purposes but will aid in the biochemical and genetic workup of the case.

3.1 *Macroscopic Dissection (Fresh Tissue)*

1. Weigh the whole brain.
2. Aliquot cerebrospinal fluid, measure pH, and store at -80°C .

3. Separate the brain stem and cerebellum from the cerebrum by cutting through the midbrain at the level of the oculomotor nerve (CNIII).
4. Bisect the cerebrum along the longitudinal fissure. Place one hemisphere into 4% paraformaldehyde (10% neutral buffered formalin) solution for subsequent diagnostic examination.
5. Bisect the brain stem in the midsagittal plane, and fix the half contralateral to the fixed cerebral hemisphere.
6. Coronally slice the unfixed hemisphere at 1 cm intervals with the first cut made at the level of the mammillary body. Dissect each slice into 2 cm² blocks using a grid system, photograph the dissected slice with each block having a unique grid coordinate, flash freeze, and store at -80 °C.
7. Separate the cerebellum from the brain stem by cutting the three cerebellar peduncles. Slice the cerebellum in the sagittal plane. Slice the brain stem in the horizontal plane. Photograph, flash freeze, and store at -80 °C.

3.2 Macroscopic Dissection (Fixed Tissue)

Tissue should be fixed in the 4% paraformaldehyde (10% neutral buffered formalin) solution for a minimum of 3 weeks before dissection (Fig. 1).

1. Examine the meninges for evidence of infection and fibrosis.
2. Examine the cortical gyration pattern, and determine if there is a global or any regional atrophy.
3. Examine the basal blood vessels.
4. Determine if there is any uncal indentation or tonsillar prominence suggestive of raised intracranial pressure in vivo.
5. Coronally slice the cerebral hemisphere at the level of the mammillary body.
6. Make coronal slices of the anterior and posterior cerebrum using a 1 cm cut guide.
7. Separate the cerebellum from the brain stem by cutting the three cerebellar peduncles.
8. Slice the cerebellum at 0.5 cm intervals in the sagittal plane.
9. Slice the brain stem at 0.5 cm intervals in the horizontal plane.

3.3 Tissue Sampling and Preparation

The following anatomical areas are sampled for diagnostic assessment:

1. Superior and middle frontal gyrus at level of genu of corpus callosum.
2. Anterior cingulate gyrus at level of nucleus accumbens.
3. Nucleus accumbens.

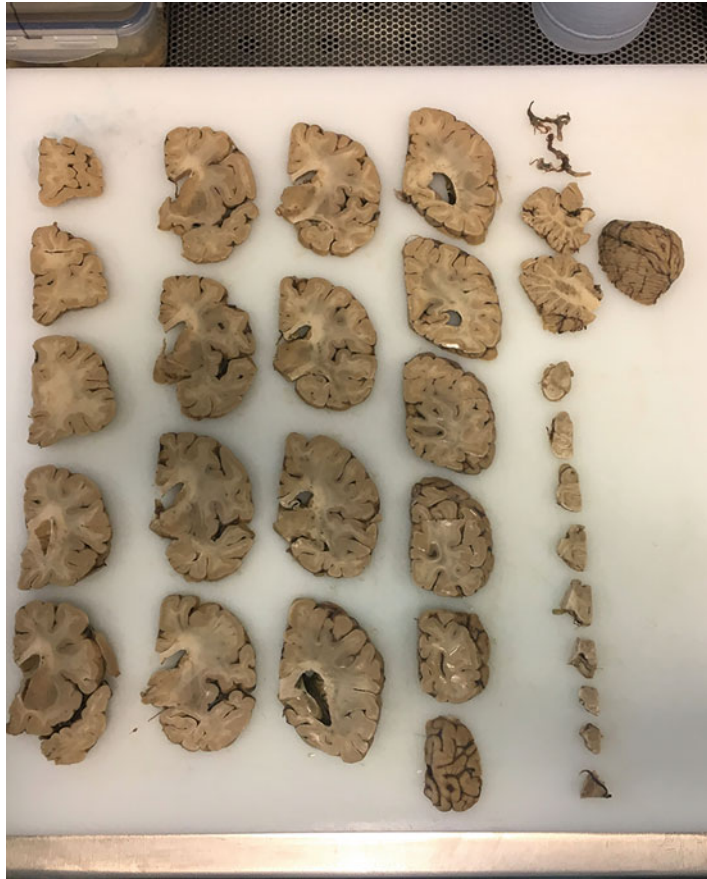


Fig. 1 Completed dissection of a single hemisphere and contralateral hemi-brain stem/cerebellum prior to tissue sampling

4. Superior temporal gyrus at level of mammillary body.
5. Basal ganglia at level of anterior commissure (containing the nucleus basalis of Meynert).
6. Hypothalamus at level of mammillary body.
7. Amygdala.
8. Thalamus to include subthalamic nucleus.
9. Anterior hippocampus.
10. Posterior hippocampus at level lateral geniculate nucleus.
11. Precentral gyrus (primary motor cortex).
12. Occipital cortex to include calcarine fissure.
13. Inferior parietal lobule.
14. Cerebellum to include folia and dentate nucleus.
15. Midbrain at level of oculomotor nerve (containing substantia nigra).

16. Pons to include locus coeruleus.
17. Medulla to include inferior olive and dorsal motor nucleus of the vagus.

The selected blocks of tissue are placed in processing cassettes for paraffin wax embedding. Following embedding 6–8 μm sections are cut for staining.

3.4 *Histological Staining*

A section from each block is stained with hematoxylin and eosin (H&E), and a consecutive section is stained with cresyl violet and luxol fast blue (CV/LFB).

1. Deparaffinize and rehydrate sections by immersing in: (a) xylene [3×5 min] (in a fume hood), (b) 100% industrial methylated spirit (IMS) [2×5 min], (c) 90% IMS [5 min], (d) 70% IMS [5 min], (e) distilled water [5 min].

H&E Staining

2. Immerse in filtered Mayer's hematoxylin [5 min].
3. Wash in running tap water (or Scott's tap water substitute) for blueing of sections.
4. Check sections under the microscope, and briefly differentiate in 1% acid-alcohol if necessary.
5. Nuclei should be a deep blue color with the vesicular nuclei showing a well-marked chromatin pattern. The background should show only weak residual hematoxylin coloration.
6. If the staining is too pale or too dark, immerse in hematoxylin or acid-alcohol again, respectively, for as long as necessary.
7. Immerse in filtered 1% eosin [5 min].
8. Wash briefly (as this will bleach the eosin stain) in running tap water.
9. If the stain is too dark, it can be bleached by washing for longer. If too pale, immerse the sections in 1% eosin again for as long as necessary.
10. Dehydrate by immersing briefly (as this also will bleach the eosin stain) in (a) 70% IMS, (b) 90% IMS, and finally wash in 100% IMS (2×5 min).
11. Clear by immersing in xylene [3×5 mins] (in fume hood).
12. Mount sections in distrene-plasticizer-xylene (DPX; a xylene-based mountant), in the fume hood.

The result of this protocol is that the nuclei are stained blue, cytoplasmic constituents are stained red to pink, and red blood cells are stained red to orange.

CV/LFB Staining

1. Immerse into luxol fast blue solution (0.1% wt/vol LFB, 0.05% vol/vol acetic acid in 100% IMS/methanol) overnight in 60 °C oven.
2. On the second day, immerse in 100% IMS/ethanol (2 × 5 min).
3. Wash in running tap water (5 min).
4. Differentiate in saturated lithium carbonate solution (1–2 min) until gray and white matter can be distinguished macroscopically.
5. Rinse in running tap water.
6. Immerse in 0.1% cresyl violet solution in 60 °C oven (20 min).
7. Immerse in 0.25% acid-alcohol (acetic acid in 95% IMS) until Nissl substance is clearly stained with low level of background.
8. Follow steps 10–12 as above.

The result of this protocol is that neurons are stained purple and myelin/white matter is stained blue.

3.5 Immunocytochemistry

For the pathological changes in the brain to be staged, immunocytochemical staining is required. The key antibodies for this assessment are against hyper-phosphorylated tau, A β peptide, α -synuclein (α SN, Fig. 2), and TDP-43. There are a variety of commercial antibodies available, and each will require individual staining protocol optimization. The anatomical areas that require immunostaining for each of these antibodies are detailed in Table 1.

1. Dewax and rehydrate tissue sections as described above.
2. Immerse in 1% hydrogen peroxide (H₂O₂)/phosphate-buffered saline (PBS, pH 7.4) for 30 min at room temperature for quenching of endogenous peroxidase activity.
3. Wash in distilled water (5 min).
4. Carry out antigen retrieval procedures (if necessary):
 - *Heat-induced antigen retrieval*: e.g., place sections in pressure cooker in 0.01 M sodium citrate buffer (pH 6) (25 min) or microwave in 1 mM EDTA buffer (pH 8) (20 min) or steamer in 0.01 M sodium citrate buffer (20 min).
 - Place in 80% formic acid (10 min) [essential for anti- α SN and anti-A β antibodies].
5. Wash in distilled water (5 min).
6. Wash in PBS (3 × 5 min).
7. Incubation with primary antibodies (diluted in 0.3% Triton X-100 in PBS) at 4 °C overnight (example of antibodies used is listed in Table 2).
8. Wash in PBS (3 × 5 min).

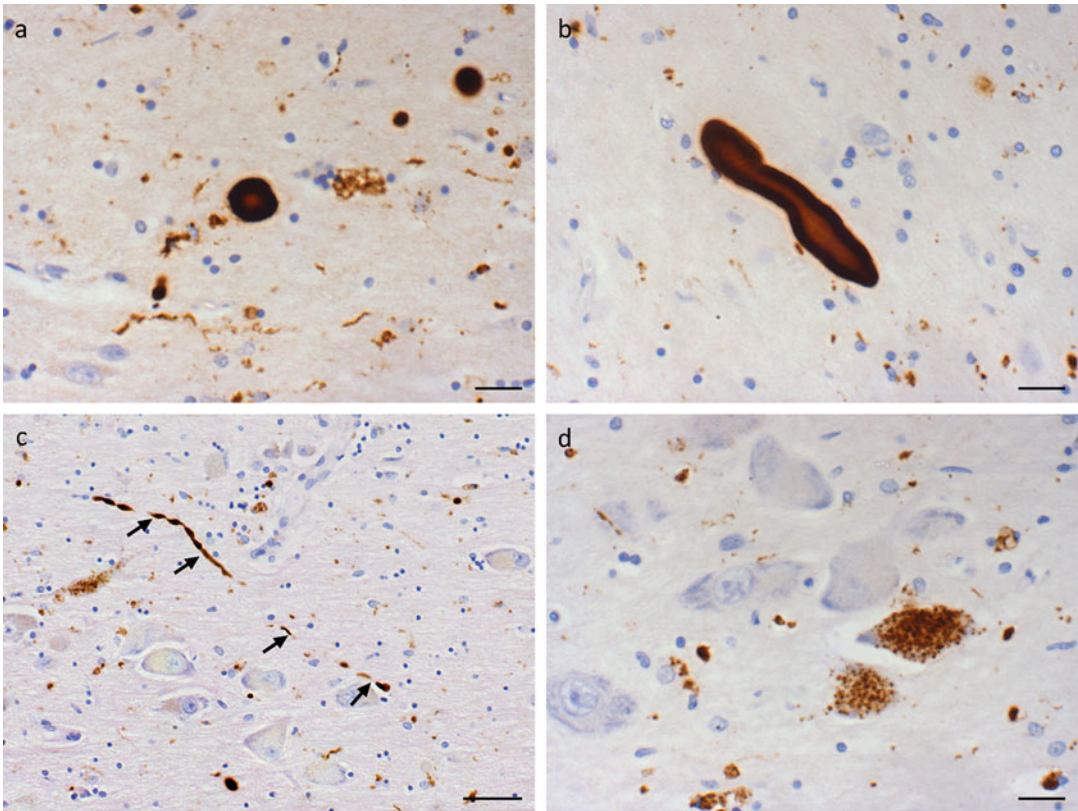


Fig. 2 Examples of α SN-immunopositive pathological structures. (a) and (b) Extracellular Lewy body-like inclusions. (c) α SN-immunopositive Lewy neurites (arrows). (d) Granular cytoplasmic staining within magnocellular neurons. Scale bars = 20 μ m (a, b, d); 50 μ m (c)

9. Incubation with biotinylated secondary antibodies (diluted in 0.3% Triton X-100/PBS) (1 h).
10. Signal amplification with avidin-biotin complex (ABC) (as per manufacturer's protocol).
11. Wash in PBS (3×5 min).
12. Visualization with 3'3-diaminobenzidine (DAB) (5 minutes).
13. Wash in distilled water (2×5 min).
14. Counterstaining with Meyer's hematoxylin (5 min).
15. Rinsing in running tap water.
16. Dehydration and clearing as described above and sections coverslipped with DPX.

3.6 Pathology Staging

The standard protocol for the reporting of microscopic neurodegenerative pathology is constantly evolving, but the current protocol most widely used is that of the National Institute on Aging-Alzheimer's Association [7]. This is reported in the ABC format

Table 1
H&E and immunocytochemistry to be carried out on sections from the different anatomical blocks

Block #	Anatomical area	H&E	Tau	A β	α SN	TDP-43
1	Frontal cortex	x	x	x	x	x
2	Cingulate cortex	x			x	
3	Ant basal ganglia	x				
4	Sup temporal gyrus	x	x	x	x	
5	Basal ganglia	x	x	x	x	
6	Hypothalamus	x				
7	Amygdala	x	x	x	x	x
8	Thalamus	x				
9	Ant hippocampus	x	x	x	x	
10	Post hippocampus	x	x	x	x	x
11	Precentral gyrus	x				
12	Occipital cortex	x	x	x		
13	Parietal cortex	x	x	x		
14	Cerebellum	x		x	x	
15	Midbrain	x	x	x	x	
16	Pons	x	x	x	x	
17	Medulla	x	x	x	x	

with the A relating to assessment of A β spread [8], B relating to tau pathology (*Braak tau staging*) [9], and C the assessment of neuritic plaques (CERAD score). For Lewy body-related α SN pathology, the staging of the BrainNet Europe consortium and McKeith criteria are used to classify pathology into the brain stem, limbic, or neocortical subtypes [10, 11]. TDP-43 is used to screen for other rarer neurodegenerative disorders.

Vascular pathology is assessed using H&E- and LFB/CV-stained sections as per the VCING protocol [12]. ARTAG pathology is assessed as per Kovacs et al. [4].

Acknowledgments

The authors would like to thank Parkinson's UK, registered charity 258197, for their continual support as well as the donors and family for their invaluable donation of brain tissue to the Parkinson's UK tissue bank.

Table 2
Examples of antibodies used for neuropathological assessment

Antibody	Host	Clonality	Immunogen	Company	Catalogue number	Pretreatment
Alpha-synuclein (clone 42)	Mouse	Monoclonal (IgG ₁)/ clone 42	Rat synuclein-1 aa. 15–123	BD transduction laboratories	610,787	10 mins 80% formic acid
Amyloid-beta	Mouse	Monoclonal (IgG _{2b})/ clone 4G8	β amyloid aa 17–24	Covance (signet)	800,704/800705/ 800706	10 mins 80% formic acid
Tau (phospho-PHF-tau pSer202 + Thr205)	Mouse	Monoclonal (IgG ₁)/ clone AT8	Partially purified human PHF-tau	Pierce Thermo Scientific	MNI020	Nil

References

1. Will RG, Ironside JW, Zeidler M et al (1996) A new variant of Creutzfeldt-Jakob disease in the UK. *Lancet* 347(9006):921–925. [https://doi.org/10.1016/s0140-6736\(96\)91412-9](https://doi.org/10.1016/s0140-6736(96)91412-9)
2. Lashley T, Rohrer JD, Mead S, Revesz T (2015) Review: an update on clinical, genetic and pathological aspects of frontotemporal lobar degenerations. *Neuropathol Appl Neurobiol* 41(7):858–881. <https://doi.org/10.1111/nan.12250>
3. McKee AC, Stein TD, Kiernan PT, Alvarez VE (2015) The neuropathology of chronic traumatic encephalopathy. *Brain Pathol* 25(3):350–364. <https://doi.org/10.1111/bpa.12248>
4. Kovacs GG, Ferrer I, Grinberg LT et al (2016) Aging-related tau astroglialopathy (ARTAG): harmonized evaluation strategy. *Acta Neuropathol* 131(1):87–102. <https://doi.org/10.1007/s00401-015-1509-x>
5. Attems J (2017) The multi-morbid old brain. *Acta Neuropathol* 134(2):169–170. <https://doi.org/10.1007/s00401-017-1723-9>
6. Buckland GR, Harrison CH, Love S et al (2016) Topographical distribution of A beta removal resulting from A beta immunotherapy in Alzheimer's disease. In: *Neuropathology and applied neurobiology*, vol 42. Wiley-Blackwell, Hoboken, p 16
7. Montine TJ, Phelps CH, Beach TG et al (2012) National Institute on Aging-Alzheimer's Association guidelines for the neuropathologic assessment of Alzheimer's disease: a practical approach. *Acta Neuropathol* 123(1):1–11. <https://doi.org/10.1007/s00401-011-0910-3>
8. Thal DR, Rüb U, Orantes M, Braak H (2002) Phases of A beta-deposition in the human brain and its relevance for the development of AD. *Neurology* 58(12):1791–1800. <https://doi.org/10.1212/wnl.58.12.1791>
9. Braak H, Alafuzoff I, Arzberger T, Kretzschmar H, Del Tredici K (2006) Staging of Alzheimer disease-associated neurofibrillary pathology using paraffin sections and immunocytochemistry. *Acta Neuropathol* 112(4):389–404. <https://doi.org/10.1007/s00401-006-0127-z>
10. Alafuzoff I, Ince PG, Arzberger T et al (2009) Staging/typing of Lewy body related alpha-synuclein pathology: a study of the BrainNet Europe Consortium. *Acta Neuropathol* 117(6):635–652. <https://doi.org/10.1007/s00401-009-0523-2>
11. Mckeith D, Lowe J, Kaufer DI (2005) Diagnosis and management of dementia with Lewy bodies: third report of the DLB diagnosis and management of dementia with Lewy bodies third report of the DLB consortium. *Neurology* 65(September 2004):1863–1972. <https://doi.org/10.1212/01.wnl.0000187889.17253.b1>
12. Skrobot OA, Attems J, Esiri M et al (2016) Vascular cognitive impairment neuropathology guidelines (VCING): the contribution of cerebrovascular pathology to cognitive impairment. *Brain* 139(11):2957–2969. <https://doi.org/10.1093/brain/aww214>



Noninvasive Visualization of Amyloid-Beta Deposits in Alzheimer's Amyloidosis Mice via Fluorescence Molecular Tomography Using Contrast Agent

Wuwei Ren and Ruiqing Ni

Abstract

Alzheimer's disease is pathologically featured by the accumulation of amyloid-beta ($A\beta$) plaque and neurofibrillary tangles. Compared to small animal positron emission tomography, optical imaging features nonionizing radiation, low cost, and logistic convenience. Optical detection of $A\beta$ deposits is typically implemented by 2D macroscopic imaging and various microscopic techniques assisted with $A\beta$ -targeted contrast agents. Here, we introduce fluorescence molecular tomography (FMT), a macroscopic 3D fluorescence imaging technique, convenient for in vivo longitudinal monitoring of the animal brain without the involvement of cranial window opening operation. This chapter aims to provide the protocols for FMT in vivo imaging of $A\beta$ deposits in the brain of rodent model of Alzheimer's disease. The materials, stepwise method, notes, limitations of FMT, and emerging opportunities for FMT techniques are presented.

Key words Alzheimer's disease, Amyloid-beta, Animal model, Fluorescence molecular tomography, In vivo imaging

1 Introduction

Alzheimer's disease (AD) is pathologically featured by the accumulation of amyloid-beta ($A\beta$) plaque and neurofibrillary tangles. Positron emission tomography (PET) using $A\beta$ imaging tracers such as [^{18}F]florbetapir, [^{18}F]florbetaben, and [^{18}F]flutemetamol has demonstrated its clinical utility and has been widely applied in preclinical studies in animal models [1]. Compared to small animal PET, optical imaging features nonionizing radiation, low cost, and logistic convenience [2, 3]. Optical detection of $A\beta$ deposits is typically implemented by 2D macroscopic imaging and various microscopic techniques assisted with $A\beta$ -targeted contrast agents [4]. Light-sheet microscopy, confocal microscopy, large-field multifocal illumination microscopy, multiphoton microscopy, and optical projection tomography have demonstrated their usefulness in

detecting A β deposits at a μ m spatial resolution in either low-scattering media or cortical regions of mouse/rat brain [5–9]. In contrast, traditional macroscopic imaging techniques, such as in vivo fluorescence reflectance imaging (FRI), provide a fast and convenient preview tool with large field-of view (FOV) but, nevertheless, are limited to a 2D view due to heavy light scattering [4]. One of the promising techniques balancing the penetration depth and spatial resolution is optoacoustic tomography, which offers volumetric visualization of the whole animal brain at a 20–100 micron resolution [10, 11]. Nevertheless, currently available contrast agents for optoacoustic imaging are under development and often feature relatively lower sensitivity compared with those in fluorescence detection [12]. Here, we introduce fluorescence molecular tomography (FMT), a large-FOV and 3D fluorescence imaging technique, which leverages advances of computational imaging and richness of the developed A β -targeted fluorescence probes. Similar to FRI, FMT is one of the noncontact macroscopic imaging method and is also convenient for in vivo longitudinal monitoring of the animal brain without the involvement of cranial window opening operation.

FMT is capable of visualizing fluorescence distribution in 3D in tissue by using a raster scanning method and a model-based reconstruction algorithm [13]. More specifically, a free-space near-infrared laser beam scans the surface of the object in a point-by-point raster scan pattern. The fluorescence emitting contrast agent is administered before the measurement and excited for each laser point. Next, the 2D fluorescence images are acquired as the raw data for reconstruction [14, 15]. Image reconstruction is crucial for recovering the 3D fluorescence distribution from a 2D image stack. A classic reconstruction framework consists of forward modeling and inversion [16]. In the first step of forward modeling, diffuse light propagation is simulated via various numerical methods, e.g., finite element methods (FEM) and Monte Carlo methods [17], which can virtually predict the measurement on the boundary of the object. The second step, inversion, treats FMT reconstruction as an optimization problem and seeks an optimal solution for the unknown fluorescence distribution. FMT is commonly used for in vivo tumor imaging in small animal models [18]. For the application in AD animal models, an FMT/X-ray computed tomography (XCT) multimodal imaging method has been applied to visualize A β deposits using A β fibril-binding oxazine-derivative AOI987 in APP/PS1 mice of AD amyloidosis [19]. A similar multimodal design combining FMT and magnetic resonance imaging (MRI) has further demonstrated the capacity of FMT in mapping A β deposits by using A β fibril-binding curcumin-derivative CRANAD-2 in arcA β mice of AD amyloidosis [20]. We have summarized a typical workflow of in vivo FMT brain imaging for visualizing A β deposits in rodent models of AD amyloidosis in

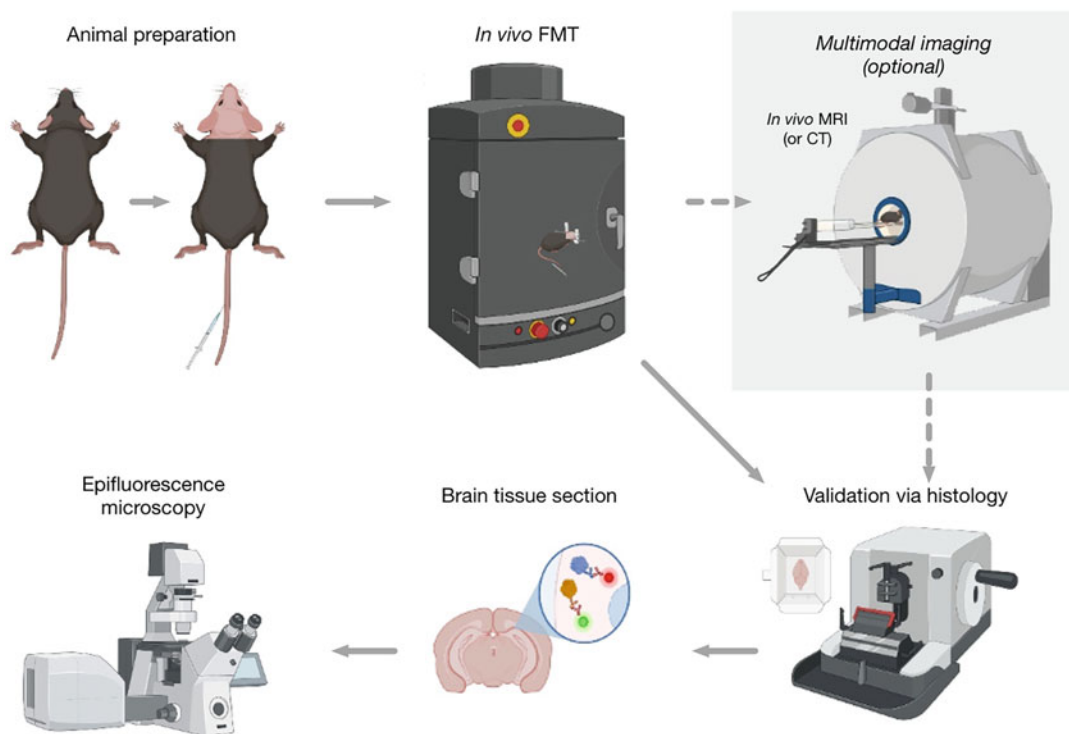


Fig. 1 A typical workflow of in vivo FMT brain imaging for visualizing amyloid-beta deposits in rodent models of AD amyloidosis. Sequential MRI or CT scan can also be incorporated in a FMT imaging experiment

Fig. 1. A multimodal module (e.g., by combining computed tomography (CT) or MRI) can be optionally integrated into the FMT protocol to provide structural reference for more accurate analysis of the regional A β -targeted fluorescence signal (Fig. 1, upper right).

The purpose of this chapter is to describe the methodology of FMT in vivo imaging of A β deposits in the brain of mouse/rat model of AD amyloidosis. The materials, detailed protocol, and notes are presented. We also discussed the considerations in animal models and contrast agents, along with the limitations and emerging opportunities for FMT techniques (created with BioRender.com).

2 Materials

2.1 Animal Models

See Note 1.

2.2 Anesthesia

1. Inhalational anesthesia system (with face mask) and induction chamber.
2. Isoflurane liquid (Piramal Pharma Limited).
3. Oxygen and air supply.

2.3 *Materials for Animal Preparation*

1. Ophthalmic ointment, e.g., Lacrinorm 0.2% ophthalmic gel (Bausch & Lomb AG).
2. Cannulation tubes and needle for intravenous injection (for mouse, 0.28 mm ID, Smiths Medical ASD, Inc., USA).
3. Tissue glue.
4. Warming pad for tail vein injection.
5. Vaseline[®].
6. PhysioSuite[®] system including rectal probe, sensor clip for physiological monitoring.
7. Electrical shaver (for removal of hair over the head).
8. Shaving cream for epilation of hair over the head.
9. Cotton tips.
10. Holder with a stereotactic frame.
11. Recovery chamber.
12. Ringer solution.

2.4 *A β Targeting Fluorescent Contrast Agent (See Note 2)*

1. A β binding fluorescence emitting contrast agents such as AOI987 [9], CRANAD-2 [21], luminescent conjugated oligothioflavins [7], etc. (review [22]).
2. Saline or other solvents suitable for intravenous injection for dilution of contrast agent.

2.5 *Fluorescent Molecular Tomography*

1. FMT system (*see Note 3*).
Available commercial FMT systems include IVIS Spectrum (PerkinElmer, MA, US), U-OI (MILabs, Netherlands), and InSyTe FLECT/CT (TriFoil imaging, CA, US). One may also develop a homebuilt FMT prototype as referred in [23].
2. Light source and emission filters (*see Note 4*).
3. Detector (*see Note 5*).
4. Sample stage and animal holder and warming system during imaging (*see Note 6*).
5. Control software (*see Note 7*).
6. Image reconstruction software (*see Note 8*).
7. Data analysis software (*see Note 9*).

3 Methods

3.1 *Animal Preparation, Inhalational Anesthesia, and Physiological Monitoring*

1. Weigh the animal using a balance, and calculate the injection volume of contrast agent (predefined concentration based on the affinity of contrast agent). Keep the injection volume below the approved volume for intravenous injection.
2. Induction of anesthesia is performed in an induction chamber using isoflurane 4–5% in a mixture of oxygen (200 mL/min)

and air (800 ml/min). Maintenance anesthesia (1–2% isoflurane in a mixture of oxygen (100 mL/min) and air (400 mL/min)) during preparation is supplied through a face mask and adjusted using an isoflurane evaporator. The depth of anesthesia is monitored by the absence of reflexes (e.g., toe pinch test) and assessment of muscle tone (e.g., test rigidity by pulling lower limb). The respiratory frequency is assessed visually.

3. Ophthalmic ointment is applied to the eyes of the animal.
4. Before the FMT imaging experiment, the fur over the animal head is gently trimmed with an electrical shaver for ca. 10 min to improve the image quality of both excitation and fluorescence images. Epilation of hair over the head is performed using shaving cream. Clean the shaved region with water and cotton tips.
5. Cannulation of the tail vein is performed for intravenous administration. For this, the tail is warmed using water at a maximum of 42 °C. The cannula is used for immediate administration and then removed after injection. Tissue glue is applied to the needle site to ensure that it is stable.
6. Transfer the animal to the custom-made (or commercial) animal holder in the FMT and fixed with a stereotactic frame. Heating support of the holder is essential to maintain the animal temperature at 36.5 ± 0.5 °C. Maintenance anesthesia is supplied through a face mask and adjusted using an isoflurane evaporator.
7. Measurement of the animal body temperature is performed with a rectal probe inserted with Vaseline[®]. The heart rate, pulse distention, and arterial oxygen saturation are monitored with a hind paw sensor clip (PhysioSuite[®] system). Dehydration is also checked during the experiments by visual inspection.

3.2 Data Acquisition

1. Make sure that calibration has been performed before in vivo FMT imaging (*see Note 10*).
2. Check if the charged-couple device (CCD) and complementary metal oxide semiconductor (CMOS) camera are cooled down (if needed, *see Note 5*).
3. Select the volume of interest (VOI) and design the illumination pattern (*see Note 11*).
4. Record a white-light image of the animal head as an anatomical reference. One can also capture the 3D surface of the animal head if the FMT system allows.
5. Select the wavelengths of the excitation laser and the emission filter according to the injection of the fluorescence contrast agent (*see Note 4*).

6. Capture a pair of excitation and emission images at each illumination point if raster scanning is used (in the case of structural illumination, the image pair should be recorded for each illumination pattern.). Some commercial FMT systems can perform this step automatically. The laser power and exposure time of the detector are tuned to improve the signal-to-noise ratio and avoid signal saturation in raw images.
7. Record preinjection images.
8. Intravenous injection of contrast agent via tail vein in the animal.
9. Record the postinjection images at defined time points to obtain the time curve of fluorescence intensity (e.g., 10, 20, 40, 60, and 90 min, depending on the kinetics of the contrast agent). The duration of the animal under anesthesia needs to be complied with approved license.
10. Repeat the previous **steps 8 and 9** if multiwavelength data acquisition is needed.
11. Once all raw images are collected, transfer the animal to the recovery chamber, and supply with water (and food pallet). To facilitate the recovery and avoid dehydration of the animal, intraperitoneal injection of Ringer solution (e.g., 200 μ L for mouse) can be performed.
12. Return the animal to its cage when the animal fully recovers.

3.3 Data Analysis

1. Semiquantitative preview in 2D. Before FMT reconstruction, it is highly recommended to first evaluate the quality of the raw images, i.e., the image pairs at excitation and emission wavelengths. This evaluation step is typically implemented by dividing the sum of all emission images by the sum of all excitation images [23], which serves as a semiquantitative preview of the real 3D distribution of fluorophores. The resulting image is equivalent to a fluorescence image using a wide-field illumination method.
2. Quantitative evaluation of the 3D fluorophore distribution (Fig. 2). After proper calibration of the system, FMT can provide quantitative and 3D information on the fluorophore distribution in mice. The raw image pairs at excitation and emission wavelengths are used as the input. Through reconstruction software, 3D FMT images are generated and analyzed. The structural information, such as anatomical images from the object acquired by CT and magnetic resonance imaging or surface geometry of the object, can significantly improve the image quality of FMT reconstruction [20, 24, 25].
3. Kinetics analysis and spectra unmixing (Fig. 3). In a longitudinal study or a kinetics study, where FMT measurements are

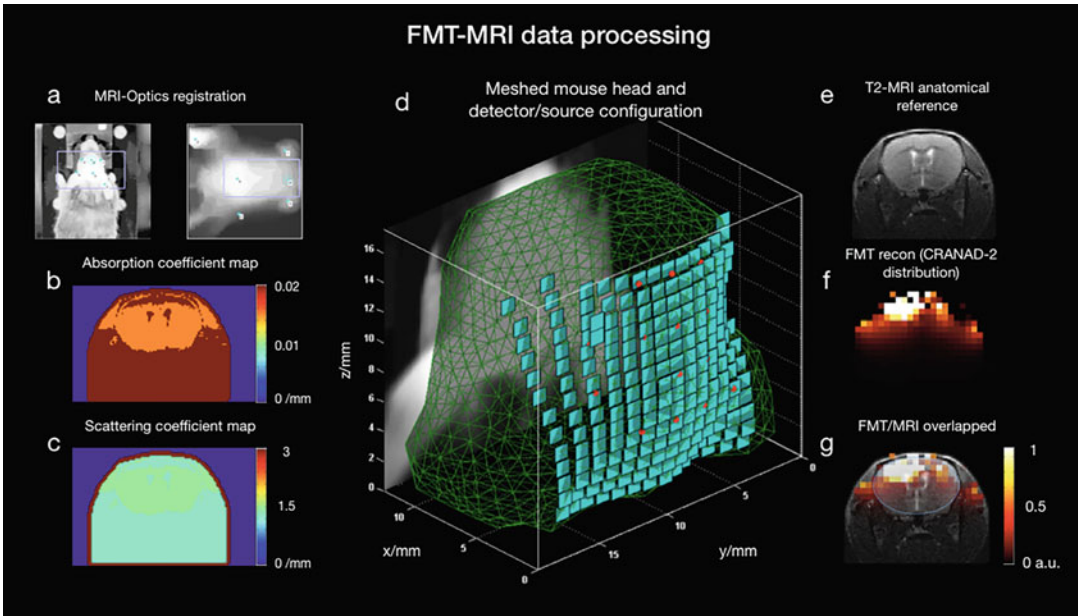


Fig. 2 An example of FMT reconstruction procedure. A FEM-based reconstruction algorithm is used to recover the 3D distribution of fluorophore. The MRI image serves as the structural reference. (With permission from Ref. [20] © The Optical Society)

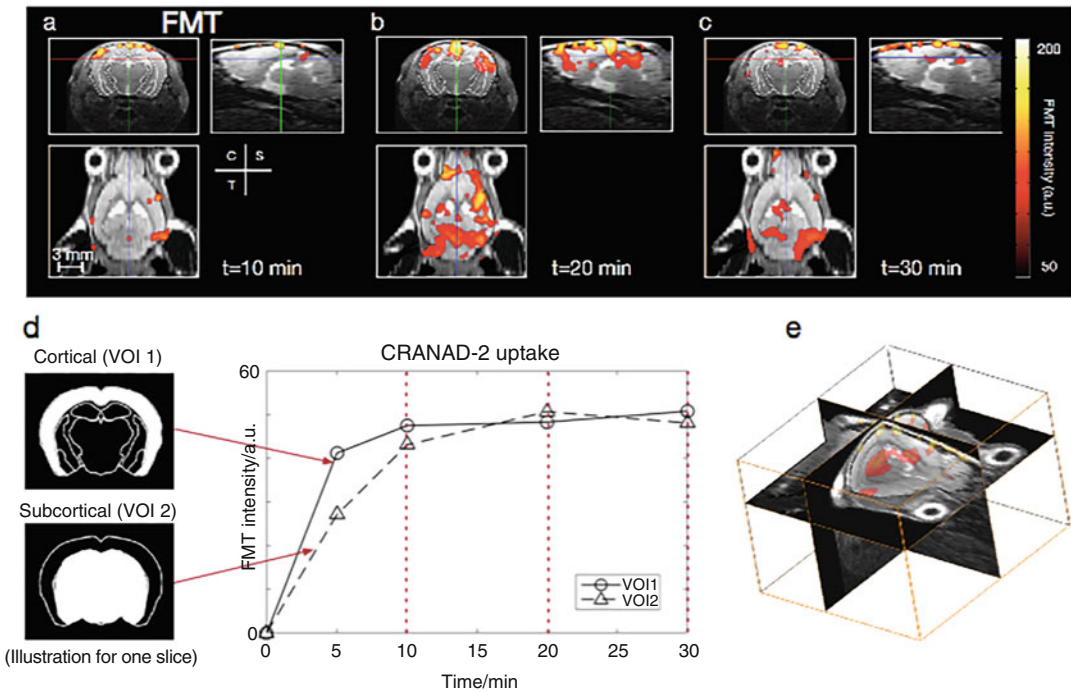


Fig. 3 An example of FMT kinetics data analysis. The time course of CRANAD-2 fluorescence intensity in different VOIs of the brain is visualized. (With permission from Ref. [20] © The Optical Society)

taken multiple times, FMT reconstruction should also be repeated correspondingly. One strategy to shorten the FMT measurements is by acquiring one group of excitation images at the beginning and only acquiring emission images for the rest of the time. The excitation images can be used multiple times during reconstruction [20]. If there is more than one contrast agent used in the experiment, spectral unmixing should be performed [26].

4 Notes

1. Animal model: animal models with cerebral A β plaque pathology (review of rodent models of AD [27]). Mouse models: e.g., single-transgenic APP/PS1 model, arcA β model, APP^{NL-G-F} knock-in model, multi-transgenic 5 \times FAD model, adeno-associated viral (AAV) vector model, and A β fibril-injected mouse model. Rat models: e.g., TgF344-AD model, McGill-R-Thy1-APP model, and adeno-associated viral (AAV) vector model. Different animal models demonstrate a distinct level and time course of A β accumulation in the brain. Therefore, the age of the animal model needs to be carefully selected based on the characteristics of each line. In addition, the cerebral A β load is known to differ between male and female transgenic models. Therefore, the use of balanced sex in the control and diseased groups during study design is needed. The ARRIVE guidelines (Animal Research: Reporting of In Vivo Experiments) [28] need to be followed for reporting. Please refer to the pathological characterization for each model to decide the age and group size of model to be studied. Alternatively, ketamine is usually used for murine anesthesia with other anesthetics which does not require inhalational system.
2. Contrast agent: A β detecting contrast agents have a wide affinity range from nM to mM. The signal-to-noise ratio of the acquired fluorescence images will need to be optimized based on the choice of contrast agent given that the signal will plateau after reaching a high concentration. In addition, some of the contrast agents are water soluble, such as AOI987 and luminescent conjugated oligothiophene, which makes them more convenient to administer intravenously. Some contrast agents, such as CRANAD-2, require a specific dilution procedure involving DMSO and Kolliphor EL. Moreover, depending on the kinetics of the contrast agent, different time to peak is expected.
3. FMT system: there are several commercially available in vivo imaging systems that can perform FMT. Among those, the IVIS Spectrum (PerkinElmer, MA, US) is one of the most

widely used FMT systems, as this device incorporates 2D and 3D optical imaging functions in one platform. Other commercial systems include U-OI (MILabs, Netherlands), InSyTe FLECT/CT (TriFoil imaging, CA, US), and former FMT series (FMT1000, FMT2000, and FMT4000, PerkinElmer, MA, US). Laboratory FMT prototypes have been reviewed in [23]. Interestingly, most commercial FMT systems can be optionally integrated with a CT scanner, which reflects the requirement for both molecular and structural information in many practical preclinical applications.

4. The selection of the wavelength of the excitation light source and emission filters is highly important and relevant to the fluorescence contrast agent. The FMT system, whether it is a commercial system or a laboratory prototype, is typically equipped with multiple wavelengths for both the light source and filters. One should carefully optimize the combination of the excitation/emission pair by checking the specifications of the FMT system and the absorption/emission spectrum of the fluorescence contrast agent. In the case of A β imaging using contrast agent CRANAD-2, the maximum values of absorption and emission upon interacting with A β aggregates appear at 640 nm and 715 nm, respectively; hence, the light source and emission filter need to be close to those values [20]: for example, an excitation laser with a 670 nm wavelength, bandpass filters with central frequencies of 660 ± 13 nm and 720 ± 13 nm for excitation and emission procedures, respectively [20].
5. Detector: the detector is responsible for collecting both excitation and fluorescence photons. The available detector types for a FMT system include photomultiplier tubes (PMTs), CCD camera, and sCMOS camera. Early contact-mode FMT employs single-pixel PMTs connected with optical fibers, while most commercial FMT systems and laboratory prototypes utilize a noncontact mode where a CCD/sCMOS camera is typically used. The detection sensitivity plays a critical role in capturing fluorescence in deep brain regions or at low concentrations of contrast agents. Decreasing the temperature of the camera can significantly improve the signal-to-noise ratio and suppress dark-current noise; thus, cooling is typically applied for a CCD/sCMOS camera in a FMT system.
6. Animal holder: during an FMT experiment, the imaging object (mouse/rat) is placed on a sample stage and stabilized with an animal holder (connected with face mask for inhalation anesthesia). Each FMT system might have a different design for both the sample stage and animal holder. In many commercial FMT systems, the sample stage is height-adjustable, which might lead to a change in the FOV and spatial resolution. A

properly designed animal holder should reduce the movement of the animal and provide good image quality during FMT experiments, especially for some kinetics studies lasting for hours. In a multimodal FMT framework, the animal holder should also be compatible with other imaging modalities, such as CT and MRI [29]. It is essential to maintain the stable physiological condition of animals via monitoring and heating supply in the animal holder.

7. Data acquisition: the FMT data acquisition procedure requires a controlling software installed in the FMT system. The controlling software configures the experimental environment to ensure an effective FMT experiment. Important configuration parameters are the number/positions of excitation sources, filter wavelength selection for excitation/fluorescence detection, laser power, exposure time of the camera, etc. In some FMT systems, the configuration of parameterization can also be passed to the subsequent reconstruction software, which can highly improve the reconstruction quality [14].
8. Image reconstruction: image reconstruction plays a pivotal role in FMT measurement, for both commercial and homebuilt system. Typically, the reconstruction software is composed of two parts, namely, forward modeling and inversion [16]. The forward modeling is equivalent to an optical simulator, which is capable of simulating light propagation in biological tissues. Most of these simulators rely on the physics model of the diffusion eq. (DE) and are solved numerically via the finite element method (FEM). Two popular FEM-based simulators are TOAST++ [30] and NIRFAST [31], both of which provide user-friendly interfaces and are suitable for the redevelopment of new FMT reconstruction algorithms. Other more complicated simulators are based on Monte Carlo methods, such as mesh-based Monte Carlo (MMC) [32] and Monte Carlo eXtreme (MCX) [33], which are more accurate than FEM-based modeling in low-scattering regions but require more computational power. Regarding the inversion procedure, most FMT reconstruction is treated as a problem of solving a large-scale linear equation. Due to light scattering, the system matrix of the linear equation is highly ill-posed and sensitive to noise. To remedy the ill-posedness of FMT inversion, different regularization methods have been applied [34]. Structural information obtained from CT and MRI can be integrated into the FMT reconstruction algorithm under a Bayesian framework [24, 35], and by using deep learning-based methods [36].
9. Data analysis softwares: most commercial FMT systems integrate data analysis and image reconstruction into a single software. Data analysis software can typically provide fluorescence

quantification by selecting a VOI in 3D. CT and MRI images feature high spatial resolution, which provides localization information for FMT reconstruction. Therefore in the case of multimodal imaging, one can use data analysis software to register FMT reconstruction with structural imaging data from CT and MRI [14, 20, 37]. If the FMT system allows multispectral measurement, spectral unmixing should be performed in reconstructed FMT results and not in the raw data [26].

10. Phantom: many commercial FMT systems provide their own phantoms for system calibration. The phantoms are usually composed of polydimethylsiloxane (PDMS) mixed with additives such as carbon powder and titanium dioxide (TiO_2) to generate absorption and scattering optical properties similar to biological tissues. There are also commercially available phantoms for system calibration (e.g., www.ino.ca). Recent reviews provide the criteria for designing a tissue-mimicking phantom [38], and the standardization in fluorescence imaging [39]. For quantitative analysis of the results, one should obtain a linear relationship between the concentration of fluorescent contrast agent and reconstructed fluorescence intensity in 3D via a phantom experiment.
11. VOI analysis: VOI typically covers the whole brain region of the mouse/rat. Most commercial FMT systems employ point-by-point raster scans as an illumination method, although structural illumination has been used in some laboratory prototype FMT systems [40]. For raster scanning, the number and density of illumination points influence the FMT reconstruction. A recommended distance between two adjacent illumination points is 0.5–1 mm. The captured VOI should allow an extra 5–10 mm space outside the illumination area. As the state-of-the-art FMT spatial resolution is approximately 1 mm, increasing the number and density of the illumination points will also increase the computational load during reconstruction, which is unnecessary in this case. The theory of optimizing the illumination pattern during FMT can be found in [41, 42]. Cerebellum is commonly chosen as reference brain regions for in vivo $\text{A}\beta$ imaging studies in animal models of AD amyloidosis given the low $\text{A}\beta$ load in this region.
12. Limitation of FMT technique: FMT is a highly sensitive and noninvasive 3D imaging technique, which is suitable for longitudinal investigation of the development of $\text{A}\beta$ pathology as well as monitoring of the treatment targeted at reducing $\text{A}\beta$. Despite the advantages of the technique, FMT is limited in spatial resolution (ca. 1 mm, similar to that of PET). Both the lateral and axial resolution of FMT may be deteriorated for fluorophores distributed in deep brain regions, which is related to the reconstruction algorithm applied.

13. Opportunities and advances in FMT technique: due to its noninvasive nature, 3D macroscopic fluorescence is a highly valuable and attractive method, especially for brain imaging of proteinopathies such as tau deposits and alpha-synuclein inclusions [43], as well as neuroinflammation assisted with contrast agents [44]. In addition, several technical advancements in FMT imaging will further improve the spatial resolution, sensitivity, and imaging speed of this modality.
 - (1) Usage of the near-infrared (NIR)-II window contrast agents: most current FMT systems focus on the first near-infrared (NIR-I) window, which ranges from 760 nm to 900 nm. Recently, fluorescence imaging in the second near-infrared (NIR-II) window (900–1800 nm) has gained popularity due to less light scattering in tissue and better visualization of fluorescence signals seated in deep tissue [45]. Although NIR-II FMT has been proposed previously, its reconstruction theory is still based on the same mathematical model of NIR-I light propagation and has not yet shown significant improvement in image quality [46]. Novel FMT reconstruction algorithms that accounts of NIR-II light propagation in a low-scattering medium will be helpful to break the bottleneck of low resolution in NIR-I window-based FMT imaging. Regarding the fluorescence probes, a few new NIR-II A β targeting fluorescence imaging contrast agents have been developed and applied in APP/PS1 mouse model of AD amyloidosis [47].
 - (2) Time-of-flight detection of light: currently continuous-wave (CW)-mode FMT is widely used for both laboratory prototypes and commercial systems, in which the camera of the system detects both excitation and fluorescence photons in a CW mode. This is mainly due to the technical maturity and high signal-to-noise ratio of CW light detection approach [23]. Compared with CW mode, a time-of-flight detector measures the arrival time of single photons, which in turn can estimate tissue optical properties and fluorescence distribution with a higher precision [48]. Emerging single-photon avalanche diode (SPAD) technology can facilitate picosecond time-resolved detection and holds promise for next-generation FMT with higher spatial resolution and larger penetration depth [25, 49].

References

1. Perani D, Iaccarino L, Jacobs AH (2019) Application of advanced brain positron emission tomography-based molecular imaging for a biological framework in neurodegenerative proteinopathies. *Alzheimers Dement (Amst)* 11:327–332. <https://doi.org/10.1016/j.dadm.2019.02.004>
2. Noltes ME, van Dam GM, Nagengast WB, van der Zaag PJ, Slart RHJA, Szymanski W et al (2021) Let's embrace optical imaging: a growing branch on the clinical molecular imaging tree. *Eur J Nucl Med Mol Imaging* 48:4120–4128. <https://doi.org/10.1007/s00259-021-05476-z>
3. Rodriguez-Vieitez E, Ni R, Gulyás B, Tóth M, Häggkvist J, Halldin C et al (2015) Astrocytosis precedes amyloid plaque deposition in Alzheimer APP^{swe} transgenic mouse brain: a correlative positron emission tomography and in vitro imaging study. *Eur J Nucl Med Mol Imaging* 42:1119–1132. <https://doi.org/10.1007/s00259-015-3047-0>
4. Yan C, Dai J, Yao Y, Fu W, Tian H, Zhu WH et al (2023) Preparation of near-infrared AIEgen-active fluorescent probes for mapping amyloid-beta plaques in brain tissues and living mice. *Nat Protoc* 18:1316–1336. <https://doi.org/10.1038/s41596-022-00789-1>
5. Nguyen D, Uhlmann V, Planchette AL, Marchand PJ, Van De Ville D, Lasser T et al (2019) Supervised learning to quantify amyloidosis in whole brains of an Alzheimer's disease mouse model acquired with optical projection tomography. *Biomed Opt Express* 10:3041–3060. <https://doi.org/10.1364/BOE.10.003041>
6. Pansieri J, Josserand V, Lee S-J, Rongier A, Imbert D, Sallanon MM et al (2019) Ultraviolet-visible-near-infrared optical properties of amyloid fibrils shed light on amyloidogenesis. *Nat Photonics* 13:473–479. <https://doi.org/10.1038/s41566-019-0422-6>
7. Calvo-Rodriguez M, Hou SS, Snyder AC, Dujardin S, Shirani H, Nilsson KPR et al (2019) In vivo detection of tau fibrils and amyloid β aggregates with luminescent conjugated oligothiophenes and multiphoton microscopy. *Acta Neuropathol Commun* 7:171. <https://doi.org/10.1186/s40478-019-0832-1>
8. Ni R, Chen Z, Gerez JA, Shi G, Zhou Q, Riek R et al (2020) Detection of cerebral tauopathy in P301L mice using high-resolution large-field multifocal illumination fluorescence microscopy. *Biomed Opt Express* 11:4989–5002. <https://doi.org/10.1364/BOE.11.049899>
9. Ni R, Chen Z, Deán-Ben XL, Voigt FF, Kirschenbaum D, Shi G et al (2022) Multiscale optical and optoacoustic imaging of amyloid- β deposits in mice. *Nat Biomed Eng*. <https://doi.org/10.1038/s41551-022-00906-1>
10. Razansky D, Klohs J, Ni R (2021) Multi-scale optoacoustic molecular imaging of brain diseases. *Eur J Nucl Med Mol Imaging*. <https://doi.org/10.1007/s00259-021-05207-4>
11. Wang LV, Yao J (2016) A practical guide to photoacoustic tomography in the life sciences. *Nat Methods* 13:627–638. <https://doi.org/10.1038/nmeth.3925>
12. Hou SS, Yang J, Lee JH, Kwon Y, Calvo-Rodriguez M, Bao K et al (2023) Near-infrared fluorescence lifetime imaging of amyloid-beta aggregates and tau fibrils through the intact skull of mice. *Nat Biomed Eng* 7:270–280. <https://doi.org/10.1038/s41551-023-01003-7>
13. Ntziachristos V, Tung CH, Bremer C, Weissleder R (2002) Fluorescence molecular tomography resolves protease activity in vivo. *Nat Med* 8:757–760. <https://doi.org/10.1038/nm729>
14. Ren W, Isler H, Wolf M, Ripoll J, Rudin M (2020) Smart toolkit for fluorescence tomography: simulation, reconstruction, and validation. *IEEE Trans Biomed Eng* 67:16–26. <https://doi.org/10.1109/TBME.2019.2907460>
15. Stuker F, Ripoll J, Rudin M (2011) Fluorescence molecular tomography: principles and potential for pharmaceutical research. *Pharmaceutics* 3:229–274. <https://doi.org/10.3390/pharmaceutics3020229>
16. Arridge SR, Schotland JC (2009) Optical tomography: forward and inverse problems. *Inverse Probl* 25:Art1230. <https://doi.org/10.1088/0266-5611/25/12/123010>
17. Arridge SR, Dehghani H, Schweiger M, Okada E (2000) The finite element model for the propagation of light in scattering media: a direct method for domains with nonscattering regions. *Med Phys* 27:252–264
18. Liu X, He X, Yan Z, Lu H (2015) 4-D reconstruction of fluorescence molecular tomography using re-assembled measurement data. *Biomed Opt Express* 6:1963–1976. <https://doi.org/10.1364/BOE.6.001963>
19. Hyde D, de Kleine R, MacLaurin SA, Miller E, Brooks DH, Krucker T et al (2009) Hybrid FMT-CT imaging of amyloid-beta plaques in

- a murine Alzheimer's disease model. *Neuro-Image* 44:1304–1311
20. Ren W, Li L, Zhang J, Vaas M, Klohs J, Ripoll J et al (2022) Non-invasive visualization of amyloid-beta deposits in Alzheimer amyloidosis mice using magnetic resonance imaging and fluorescence molecular tomography. *Biomed Opt Express* 13:3809–3822. <https://doi.org/10.1364/BOE.458290>
 21. Ni R, Villosio A, Dean-Ben XL, Chen Z, Vaas M, Stavakis S et al (2021) In-vitro and in-vivo characterization of CRANAD-2 for multi-spectral optoacoustic tomography and fluorescence imaging of amyloid-beta deposits in Alzheimer mice. *Photo-Dermatology* 23:100285. <https://doi.org/10.1016/j.pacs.2021.100285>
 22. Peng C, Wang X, Li Y, Li HW, Wong MS (2019) Versatile fluorescent probes for near-infrared imaging of amyloid- β species in Alzheimer's disease mouse model. *J Mater Chem B* 7:1986–1995. <https://doi.org/10.1039/c9tb00161a>
 23. Darne C, Lu YJ, Sevcik-Muraca EM (2014) Small animal fluorescence and bioluminescence tomography: a review of approaches, algorithms and technology update. *Phys Med Biol* 59:R1–R64
 24. Ren W, Ji B, Guan Y, Cao L, Ni R (2022) Recent technical advances in accelerating the clinical translation of small animal brain imaging: hybrid imaging, deep learning, and Transcriptomics. *Front Med (Lausanne)* 9:771982. <https://doi.org/10.3389/fmed.2022.771982>
 25. Ren W, Jiang J, Costanzo Mata AD, Kalyanov A, Ripoll J, Lindner S et al (2020) Multimodal imaging combining time-domain near-infrared optical tomography and continuous-wave fluorescence molecular tomography. *Opt Express* 28:9860–9874. <https://doi.org/10.1364/OE.385392>
 26. Arranz A, Rudin M, Zaragoza C, Ripoll J (2015) Fluorescent molecular tomography for in vivo imaging of mouse atherosclerosis. *Methods Mol Biol* 1339:367–376. https://doi.org/10.1007/978-1-4939-2929-0_27
 27. Götz J, Bodea LG, Goedert M (2018) Rodent models for Alzheimer disease. *Nat Rev Neurosci (Nature Publishing Group)* 19:583–598
 28. Percie du Sert N, Hurst V, Ahluwalia A, Alam S, Avey MT, Baker M et al (2020) The ARRIVE guidelines 2.0: updated guidelines for reporting animal research. *PLoS Biol* 18: e3000410. <https://doi.org/10.1371/journal.pbio.3000410>
 29. Stuker F, Baltes C, Dikaiou K, Vats D, Carrara L, Charbon E et al (2011) Hybrid small animal imaging system combining magnetic resonance imaging with fluorescence tomography using single photon avalanche diode detectors. *IEEE Trans Med Imaging* 30:1265–1273. <https://doi.org/10.1109/tmi.2011.2112669>
 30. Schweiger M, Arridge S (2014) The Toast++ software suite for forward and inverse modeling in optical tomography. *J Biomed Opt* 19. <https://doi.org/10.1117/1.JBO.19.4.040801>
 31. Dehghani H, Eames ME, Yalavarthy PK, Davis SC, Srinivasan S, Carpenter CM et al (2008) Near infrared optical tomography using NIRFAST: algorithm for numerical model and image reconstruction. *Commun Numer Methods Eng* 25:711–732. <https://doi.org/10.1002/cnm.1162>
 32. Zhang Y, Fang Q (2022) BlenderPhotonics: an integrated open-source software environment for three-dimensional meshing and photon simulations in complex tissues. *J Biomed Opt* 27. <https://doi.org/10.1117/1.JBO.27.8.083014>
 33. Fang QQ, Boas DA (2009) Monte Carlo simulation of photon migration in 3D turbid media accelerated by graphics processing units. *Opt Express* 17:20178–20190. <https://doi.org/10.1364/Oe.17.020178>
 34. Dehghani H, Srinivasan S, Pogue BW, Gibson A (2009) Numerical modelling and image reconstruction in diffuse optical tomography. *Philos Trans A Math Phys Eng Sci* 367:3073–3093. <https://doi.org/10.1098/rsta.2009.0090>
 35. Ren W, Cui S, Alini M, Grad S, Zhou Q, Li Z et al (2021) Noninvasive multimodal fluorescence and magnetic resonance imaging of whole-organ intervertebral discs. *Biomedical Opt Express* 12. <https://doi.org/10.1364/boe.421205>
 36. Smith JT, Ochoa M, Faulkner D, Haskins G, Intes X (2022) Deep learning in macroscopic diffuse optical imaging. *J Biomed Opt* 27. <https://doi.org/10.1117/1.JBO.27.2.020901>
 37. Ale A, Ermolayev V, Herzog E, Cohrs C, de Angelis MH, Ntziachristos V (2012) FMT-XCT: in vivo animal studies with hybrid fluorescence molecular tomography-X-ray computed tomography. *Nat Methods* 9:615–620. <https://doi.org/10.1038/nmeth.2014>
 38. Hacker L, Wabnitz H, Pifferi A, Pfefer TJ, Pogue BW, Bohnediek SE (2022) Criteria for the design of tissue-mimicking phantoms for the standardization of biophotonic

- instrumentation. *Nat Biomed Eng* 6:541–558. <https://doi.org/10.1038/s41551-022-00890-6>
39. Koch M, Symvoulidis P, Ntziachristos V (2018) Tackling standardization in fluorescence molecular imaging. *Nat Photonics* 12: 505–515. <https://doi.org/10.1038/s41566-018-0221-5>
 40. Angelo JP, Chen SJ, Ochoa M, Sunar U, Gioux S, Intes X (2018) Review of structured light in diffuse optical imaging. *J Biomed Opt* 24:1–20. <https://doi.org/10.1117/1.JBO.24.7.071602>
 41. Liu Y, Ren W, Ammari H (2019) Robust reconstruction of fluorescence molecular tomography with an optimized illumination pattern. *arXiv:1910.01480*. <https://doi.org/10.48550/arXiv.1910.01480>
 42. Dutta J, Ahn S, Joshi AA, Leahy RM (2010) Illumination pattern optimization for fluorescence tomography: theory and simulation studies. *Phys Med Biol* 55:2961–2982. <https://doi.org/10.1088/0031-9155/55/10/011>
 43. Vagenknecht P, Luzgin A, Ono M, Ji B, Higuchi M, Noain D et al (2022) Non-invasive imaging of tau-targeted probe uptake by whole brain multi-spectral optoacoustic tomography. *Eur J Nucl Med Mol Imaging*. <https://doi.org/10.1007/s00259-022-05708-w>
 44. Ni R, Vaas M, Ren W, Klohs J (2018) Noninvasive detection of acute cerebral hypoxia and subsequent matrix-metalloproteinase activity in a mouse model of cerebral ischemia using multispectral-optoacoustic-tomography. *Neurophotonics* 5:015005. <https://doi.org/10.1117/1.NPh.5.1.015005>
 45. Feng Z, Tang T, Wu T, Yu X, Zhang Y, Wang M et al (2021) Perfecting and extending the near-infrared imaging window. *Light Sci Appl* 10:197. <https://doi.org/10.1038/s41377-021-00628-0>
 46. Cai M, Zhang Z, Shi X, Hu Z, Tian J (2020) NIR-II/NIR-I fluorescence molecular tomography of heterogeneous mice based on Gaussian weighted neighborhood fused lasso method. *IEEE Trans Med Imaging* 39:2213–2222. <https://doi.org/10.1109/tmi.2020.2964853>
 47. Miao J, Miao M, Jiang Y, Zhao M, Li Q, Zhang Y et al (2023) An Activatable NIR-II fluorescent reporter for in vivo imaging of amyloid- β plaques. *Angew Chem Int Ed* 62:e202216351. <https://doi.org/10.1002/anie.202216351>
 48. Ban HY, Barrett GM, Borisevich A, Chaturvedi A, Dahle JL, Dehghani H et al (2022) Kernel flow: a high channel count scalable time-domain functional near-infrared spectroscopy system. *J Biomed Opt* 27. <https://doi.org/10.1117/1.JBO.27.7.074710>
 49. Bruschini C, Homulle H, Antolovic IM, Burri S, Charbon E (2019) Single-photon avalanche diode imagers in biophotonics: review and outlook. *Light Sci Appl* 8. <https://doi.org/10.1038/s41377-019-0191-5>



Brain Banking in Dementia Studies

Ahmet Turan Isik, Derya Kaya, and Murat Gokden

Abstract

It is now well-established practice in dementia that one clinical entity may be caused by various neurodegenerative disorders, each with different histopathological findings, whereas neuropathologically confirmed patients may have different, unusual, and atypical clinical manifestations.

This inconsistency in dementia patients leads to neuropathological examination of cases, and neuropathological examination seems to be an inevitable part of dementia practice, at least until all clinical entities are properly identified for humans.

Additionally, the development of disease-modifying therapies and confirmation of the actual accurate diagnosis of the neurodegenerative disease that the drug is thought to modify or act upon are of great importance for neuropathological evaluation in brain banks.

Neuropathological processes coexisting among patients diagnosed with established clinical criteria or international guidelines have provided a new perspective in the context of drug development.

Here, we review our routinely used methodology in the context of the brain banking process.

Key words Neuropathological examination, Neurodegenerative, Brain, Postmortem, Dissection

1 Introduction

We live in a century where the legal, ethical, and social implications of postmortem brain tissues and strategies for improving collaborations of brain bank networks are discussed. In addition, the brain bank is a powerful resource for new discoveries at the frontiers of neuroscience, through the concerted efforts of researchers, clinicians, patients, donors, and the general public [1].

It may be remarked that the first brain banking studies started in the eighteenth century when anatomists such as William Hunter archived nearly 50 brain samples due to the difficulties in brain protection [2].

After the French Revolution of 1789, the derelict bodies of the poor receiving state medical care became the source of 150 years of archiving human tissues in Europe, including the brain, giving a chance for a systematic and relatively logical approach [3].

It was not before 1792 when Philippe Pinel changed the treatment of the mentally ill drastically and described the term “dementia.” He fought for removing the shackles in “madmen” and relieving mentally ill people to get air and liberty as he did in his 34-year-old male patient, whose brain he investigated and came up with two macroscopic findings: increased water in the brain and thinning of the cerebral cortex.

Dealing with chains led to the development of the concept of dementia as one of the listed mental illnesses [4].

Nearly a century after Pinel’s findings, Dr. Alois Alzheimer reported the findings of his famous patient, Auguste Deter. He described the microscopic findings of tangles and senile plaques of “a presenile form of dementia” in 1906 [5]. Hence, within a period of 2400 years, humanity passed through Hippocrates’s extracerebral accumulation of water, to Pinel’s “dementia,” and eventually to Alzheimer’s presenile dementia. Today, brain banks have been established in many countries in order to demystify the brain and its diseases.

In this review, we would like to share with you our standard methodology for neuropathological examination on the basis of our brain bank, which is Turkey’s first brain tissue banking experience, which was officially established in 2015 in the Unit for Aging Brain and Dementia in the Department of Geriatric Medicine, Dokuz Eylul University Medical School, Izmir, for research purposes [6].

2 Materials and Methods

2.1 *Clinical Assessment*

Clinical diagnosis of the patients is made according to the updated/latest diagnostic criteria or international guidelines. For research purposes, our brain bank prospectively consents patients who had at least 1 year of clinical follow-up, comprehensive geriatric assessment, and brain imaging and who underwent neuropsychological testing at their initial visit in our Unit for Aging Brain and Dementia, unlike the studies that included brain donors despite the lack of regular clinical follow-up. The legal representatives/next of kin (NOK) contact our service, which is open for 24 h, including weekends and holidays, immediately after the death. The legal representatives/NOK receive an autopsy report with a conclusive diagnosis of their family member’s neurodegenerative disease.

2.2 *Radiological Assessment*

All the cases had neuroimaging, including brain magnetic resonance imaging (MRI) and computerized tomography. All the brain MRIs were performed with at least 1.5 Tesla MRI machines.

2.3 **Neuropathological Evaluation**

When a donor is deceased, it is critical to remove the brain and other organs/tissues as soon as possible to minimize autolysis and subsequent interference with the ancillary studies. Generally, a timeframe for the autopsy in less than 24 h from death is acceptable, while longer than 30 h is not preferable [7, 8]. In our cases, the brains are removed within less than 12 h after death.

2.3.1 *During the Performance of the Autopsy*

1. Cerebrospinal fluid (CSF) is obtained through a transcallosal puncture with a syringe before the brain is removed.
2. Blood samples are obtained through the internal carotid arteries in brain-only autopsies and from the aorta or heart in full autopsies.
3. Weighing the brain fresh and without the dura is done after removal.
4. Pictures of the outer surfaces of the brain from superior, lateral, and basal views aid future examination and the extent and pattern of involvement of any atrophy.
5. A variety of protocols have been developed and are tailored to the needs of the research team and the circumstances of the institution and community. The protocols can be relatively simple or extremely detailed, again depending on the research objectives as well as the sources. For example, a protocol published and used by Columbia University, New York City, NY [7], requires sampling of up to 150 regions from the fresh half of the brain, while protocols developed for the extraction of brains in distant regions require splitting initially. The brain is divided into right and left hemispheres, with one half being fixed while the other half is frozen for easy transport and keeping simple for remote participants (Washington University in St. Louis, St. Louis, MO; personal communication). In such remote operations, it is important to provide detailed instructions and the preferred types of containers and ice packs to maintain uniformity and avoid misunderstandings and errors that may affect tissue quality. A number of protocols and experiences of leading institutions that have established these operations and accumulated considerable experience have been published [7–12].

2.3.2 *In Practice*

1. It is typical that one half of the brain is fixed in the midsagittal plane and the other half is frozen or fresh tissue is triaged.
2. Tissue is frozen at -80°C and triaged for ancillary studies such as Western blot, in situ hybridization, and DNA and RNA analysis.
3. Tissue saving for electron microscopic studies can also be done at this time. It is essential, however, that the protocol, processing, and neuropathologic evaluation be performed by a central

laboratory in a uniform manner so that a certain level of standard and uniformity is maintained, and the results are comparable for appropriate interpretation and statistical analysis.

4. The other half of the brain is typically fixed in 10–15% formalin, and the internal carotid artery and vertebral artery are initially perfused or not, which helps deliver the formalin deeper into the tissue more quickly and typically takes 1–2 weeks or 7–10 days. It shortens the fixation time.
5. Both the fresh and fixed hemispheres are cut in the coronal/frontal planes and are extensively sampled, typically resulting in 15–20 sections, but can be over 40 sections from the fixed tissue in some protocols [12], depending on the protocol, as outlined in the aforementioned publications, targeting the critical areas involved in a variety of neurodegenerative diseases, so that a comprehensive workup can be performed.
6. Removal of the spinal cord in its total length is also important, especially in cases that may have a motor neuron disease component, such as amyotrophic lateral sclerosis (ALS) and ALS-frontotemporal lobar degeneration (ALS-FTLD).

2.3.3 A Basic Panel of Histochemical and Immunohistochemical Stains Are Utilized

1. Specifically for dementia workup, a silver impregnation technique such as Bielschowsky or Gallyas helps evaluate axonal population and identify pathologic processes, such as neurofibrillary tangles, diffuse, primitive, and neuritic plaques and any other abnormal accumulations/inclusions such as Pick bodies and argyrophilic grains.
2. Immunohistochemical staining protocols for postmortem brain tissue have been described in detail [9], although automated systems and expanded immunohistochemical antibody panels are widely available currently.
3. Our core work consists of antibodies targeting pathological protein aggregations using phosphorylated tau (including 3R and 4R), alpha-synuclein, TDP-43, and beta-amyloid and ubiquitin and others such as p62, FUS, and neurofilament protein. Neu-N, among others, was included based on the results of initial assessments. These identify neuropathologic findings associated with major dementing neurodegenerative diseases such as Alzheimer's disease, Parkinson's disease and dementia with Lewy bodies/Parkinson's disease dementia, frontotemporal lobar degeneration and its subtypes, and other entities that result in cognitive/memory problems, such as primary age-related tauopathy (PART) [13], cerebral age-related TDP-43 with sclerosis (CART) [14], and limbic-predominant age-related TDP-43 leukoencephalopathy (LATE) [15].
4. Prion disease, despite its relatively rapid course of dementia, can also masquerade as a neurodegenerative disease or may

coexist with it. Therefore, appropriate testing and investigation, especially in older adults, should be considered [16].

5. Evaluation for other commonly coexisting pathologies, namely, arteriosclerotic disease, i.e., atherosclerosis and arteriolosclerosis (small vessel disease) [17] and hippocampal sclerosis [18], and cerebral amyloid angiopathy (CAA) and other vasculopathies, such as cerebral autosomal dominant arteriopathy with subcortical infarcts and leukoencephalopathy (CADASIL), is also performed.

Interpretation and recording of findings in a standard systematic manner according to published consensus criteria facilitate uniformity of diagnoses and data analysis. These include, but are not limited to, National Institute on Aging-Alzheimer's Association (NIA-AA) guidelines [19], Thal phases of amyloid deposition [20], the Consortium to Establish a Registry for Alzheimer's Disease (CERAD) [21], Braak staging [22], FTLN classification [23], Dementia with Lewy Bodies Consortium [24], Modified Boston Criteria for CAA [25], and small vessel disease (arteriolosclerosis) [26], as well as evaluating white matter changes [27].

3 Discussion

Diagnosis of neurodegenerative diseases such as Alzheimer's disease (AD), Lewy bodies and dementia (DLB), vascular dementia (VaD), Parkinson's disease (PD), frontotemporal lobar degeneration (FTLD), and others are currently based on established clinical criteria, which are far from making a definitive diagnosis, because they are characterized by a complex set of neuropathological features, often with marked overlapping pathologies [28] as seen in Fig. 1 [6]. Also, it is well-known that there is only a moderate relationship between some clinical diagnoses and subsequent neuropathological diagnoses [6, 29].

Brain bank and subsequent histopathological evaluation of the human brain in a systematic manner in large groups have had an important role in advancing our understanding of the pathogenesis of neurodegenerative diseases and age-related changes in the brain, while providing additional opportunities to other researchers who can use this material and data [7]. The postmortem brain examination performed in the brain banks, established with these purposes, provides the accurate diagnosis of the participant whom the clinicians followed longitudinally with all available clinical, neuropsychological, radiological, and biomarker data, giving the chance to correlate all these data with the neuropathological findings [30] since no fluid and imaging biomarker is currently able to provide a definitive diagnosis [6]. For example, provided that dementia with Lewy bodies is the second most common dementia and it has been

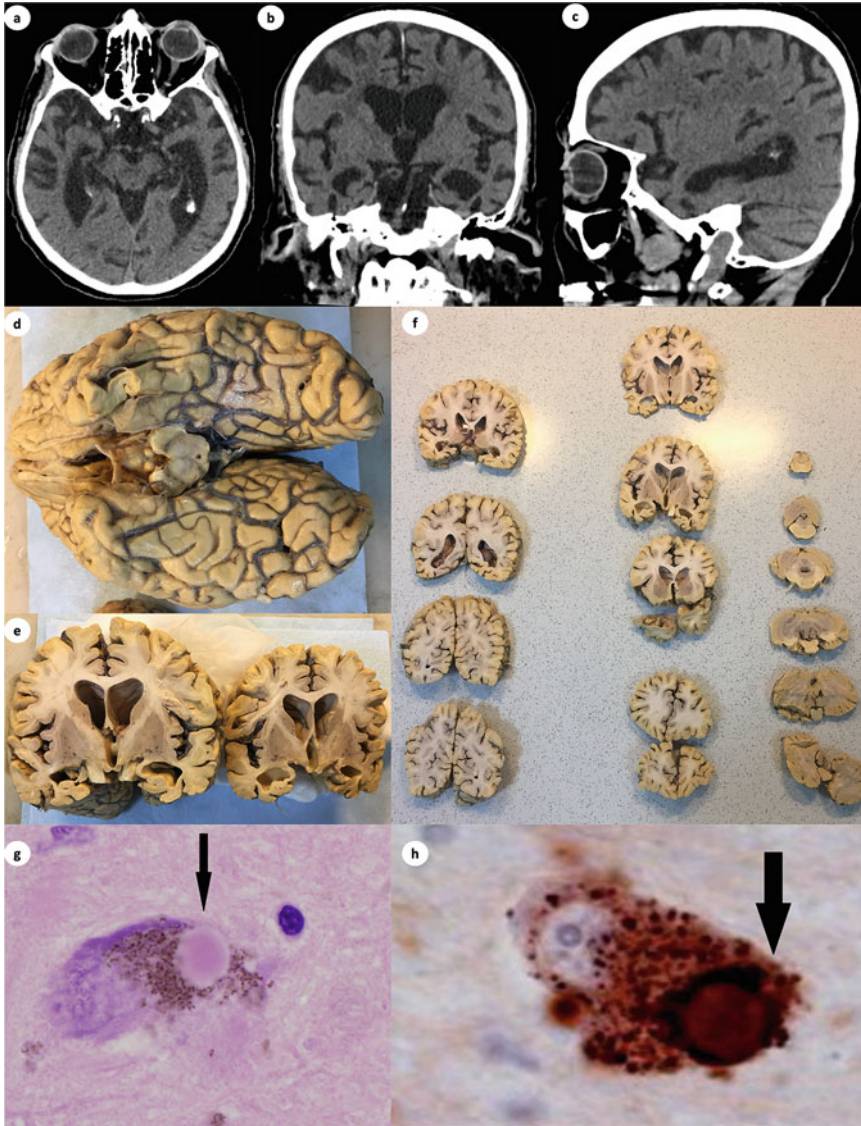


Fig. 1 A male patient [6] (age at diagnosis, 88, and age at death, 91) was admitted to our clinic with forgetfulness, fluctuating cognition, neuroleptic sensitivity, organized visual hallucination, and postural hypotension and diagnosed and followed as DLB. His brain computerized tomography (CT): (a) axial, (b) coronal, and (c) sagittal CT images show enlargement of the subarachnoid spaces, and dilatation of the ventricular system and reduction in size of both hippocampal bodies. Macroscopic dissection samples: (d–f). Microscopy: (g) typical view of a pigmented neuron with classical Lewy body, H&E stain, and (h) α -synuclein positivity of the Lewy body, α -synuclein stain. The neuropathologic findings were compatible with AD (A1, B2, C2) and DLB.

reported that one in three cases may be missed, the disease remains still under-recognized or misdiagnosed [31]. This could be the most straightforward and most compelling reason for the need of brain banks in dementia studies.

In addition, the treatment failure rate in AD, the most common neurodegenerative disease worldwide, was reported as high as 99% in placebo-controlled studies [32]. Lessons learned from neuropathological assessments regarding the failure of drugs in the disease have led the studies to include participants diagnosed with AD with biomarker support [33]. The presence of comorbid neuropathologies in the setting of AD neuropathology was another essential lesson learned [34]. Nonetheless, potential agents with various mechanisms under investigation and recent advancements make us hopeful for the near future.

In brief, until the accurate antemortem diagnosis of all the neurodegenerative diseases has been established by either clinical, pathophysiological, genetical, or with biomarkers, the neuropathological examination will be essential for the identification of unusual, atypical, and strange cases, for the development of successful treatment modalities such as disease-modifying therapies or for the confirmation of the actual underlying disease that the disease-modifying treatment had been thought to target.

References

1. Dedova I, Harding A, Sheedy D, Garrick T, Sundqvist N, Hunt C, Gillies J, Harper CG (2009) The importance of brain banks for molecular neuropathological research: The New South Wales Tissue Resource Centre experience. *Int J Mol Sci* 10:366–384
2. Teacher JH (1900) Catalogue of the anatomical and pathological preparations of Dr William Hunter. James MacLehose and Sons, Hunterian Museum, Glasgow, pp 318–319
3. Gere C (2005) History of neuroscience: a brief history of brain archiving. *IBRO History of neuroscience*
4. *Nosographie philosophique, ou la méthode de l'analyse appliquée à la médecine* (2 volumes) (1798)
5. Alzheimer A (1907) Über eine eigenartige Erkrankung der Hirnrinde. *Allg Zschr Psychiatr Psych gerichtl Med* 64:146–148
6. Isik AT, Danyeli AE, Kaya D, Soysal P, Karabay N, Gokden M (2020) The importance of brain banking for dementia practice: the first experience of Turkey. *Cell Tissue Bank* 21: 367–375
7. Vonsattel JPG, del Amaya MP, Keller CE (2008) Twenty-first century brain banking. Processing brains for research: the Columbia University methods. *Acta Neuropathol* 115: 509–532
8. Poloni TE, Medici V, Carlos AF, Davin A, Ceretti A, Mangieri M, Cassini P, Vaccaro R, Zaccaria D, Abbondanza S, Bordoni M, Fantini V, Fogato E, Cereda C, Ceroni M, Guaita A (2020) Abbiategrosso brain bank protocol for collecting, processing and characterizing aging brains. *J Vis Exp* 160(e60296): 1–25
9. Waldvogel HJ, Curtis MA, Baer K, Rees MI, Faull RLM (2006) Immunohistochemical staining of post-mortem adult human brain sections. *Nat Protoc* 1:2719–2732
10. Grinberg LT, de Lucena Ferretti RE, Farfel JM, Leite R, Pasqualucci CA, Rosemberg S, Nitrini R, Saldiva PHN, Filho WJ, Brazilian Aging Brain Study Group (2007) Brain bank of the Brazilian aging brain study group – a milestone reached and more than 1,600 collected brains. *Cell Tissue Bank* 8:151–162
11. Cairns NJ, Taylor-Reinwalda L, Morrisa JC, and the Alzheimer's Disease Neuroimaging Initiative (2010) Autopsy consent, brain collection, and standardized neuropathologic assessment of ADNI participants: the essential role of the neuropathology core. *Alzheimers Dement* 6:274–279
12. Beach TG, Adler CH, Sue LI, Serrano G, Shill HA, Walker DG, Lue LF, Roher AE, Dugger BN, Maarouf C, Birdsill AC, Intorcchia A, Saxon-Labelle M, Pullen J, Scroggins A, Filon J, Scott S, Hoffman B, Garcia A, Caviness JN, Hentz JG, Driver-Dunckley E, Jacobson SA, Davis KJ, Belden CM, Long KE, Malek-Ahmadi M, Powell JJ, Gale LD, Nicholson LR, Caselli RJ, Woodruff BK, Rapsack SZ,

- Ahern GL, Shi J, Burke AD, Reiman EM, Sabagh MN (2015) Arizona study of aging and neurodegenerative disorders and brain and body donation program. *Neuropathology* 35: 354–389
13. Crary JF, Trojanowski JQ, Schneider JA, Abisambra JF, Abner EL, Alafuzoff I, Arnold SE, Attems J, Beach TG, Bigio EH, Cairns NJ, Dickson DW, Gearing M, Grinberg LT, Hof PR, Hyman BT, Jellinger K, Jicha GA, Kovacs GG, Knopman DS, Kofler J, Kukull WA, Mackenzie IR, Masliah E, McKee A, Montine TJ, Murray ME, Neltner JH, Santa-Maria I, Seeley WW, Serrano-Pozo A, Shelanski ML, Stein T, Takao M, Thal DR, Toledo JB, Troncoso JC, Vonsattel JP, White CL 3rd, Wisniewski T, Woltjer RL, Yamada M, Nelson PT (2014) Primary age-related tauopathy (PART): a common pathology associated with human aging. *Acta Neuropathol* 128:755–766
 14. Cykowski MD, Powell SZ, Schulz PE, Takei H, Rivera AL, Jackson RE, Roman G, Jicha GA, Nelson PT (2017) Hippocampal sclerosis in older patients: practical examples and guidance with a focus on cerebral age-related TDP-43 with sclerosis. *Arch Pathol Lab Med* 141: 1113–1126
 15. Nelson PT, Dickson DW, Trojanowski JQ, Jack CR Jr, Boyle PA, Arfanakis K, Rademakers R, Alafuzoff I, Attems J, Brayne C, Coyle-Gilchrist ITS, Chui HC, Fardo DW, Flanagan ME, Halliday G, Hokkanen SRK, Hunter S, Jicha GA, Katsumata Y, Kawas CH, Keene CD, Kovacs GG, Kukull WA, Levey AI, Makinejad N, Montine TJ, Murayama S, Murray ME, Nag S, Rissman RA, Seeley WW, Sperling RA, White CL III, Yu L, Schneider JA (2019) Limbic-predominant age-related TDP-43 encephalopathy (LATE): consensus working group report. *Brain* 142:1503–1527
 16. Peden AH, Kanguru L, Ritchie DL, Smith C, Molesworth AM (2019) Study protocol for enhanced CJD surveillance in the 65+ years population group in Scotland: an observational neuropathological screening study of banked brain tissue donations for evidence of prion disease. *BMJ Open* 9(10):e033744
 17. Nelson PT, Trojanowski JQ, Abner EL, Al-Janabi OM, Jicha GA, Schmitt FA, Smith CD, Fardo DW, Wang WX, Kryscio RJ, Neltner JH, Kukull WA, Cykowski MD, Van Eldik LJ, Ighodaro ET (2016) “New old pathologies”: AD, PART, and cerebral age-related TDP-43 with sclerosis (CARTS). *J Neuropathol Exp Neurol* 75:482–498
 18. Hatanpaa KJ, Raisanen JM, Herndon E, Burns DK, Foong C, Habib AA, White CL III (2014) Hippocampal sclerosis in dementia, epilepsy, and ischemic injury: differential vulnerability of hippocampal subfields. *J Neuropathol Exp Neurol* 73:136–142
 19. Montine TJ, Phelps CH, Beach TG, Bigio EH, Cairns NJ, Dickson DW, Duyckaerts C, Frosch MP, Masliah E, Mirra SS, Nelson PT, Schneider JA, Thal DR, Trojanowski JQ, Vinters HJ, Hyman BT (2012) National Institute on Aging–Alzheimer’s Association guidelines for the neuropathologic assessment of Alzheimer’s disease: a practical approach. *Acta Neuropathol* 123:1–11
 20. Thal DR, Rüb U, Orantes M, Braak H (2002) Phases of A β -deposition in the human brain and its relevance for the development of AD. *Neurology* 58:1791–1800
 21. Mirra SS, Heyman A, McKeel D, Sumi SM, Crain BJ, Brownlee LM, Vogel FS, Hughes JP, van Belle G, Berg L (1991) The Consortium to Establish a Registry for Alzheimer’s Disease (CERAD). Part II. Standardization of the neuropathologic assessment of Alzheimer’s disease. *Neurology* 41:479–486
 22. Braak H, Braak E (1991) Neuropathological staging of Alzheimer-related changes. *Acta Neuropathol* 82:239–259
 23. Mackenzie IR, Neumann M, Bigio EH, Cairns NJ, Alafuzoff I, Kril J, Kovacs GG, Ghetti B, Halliday G, Holm IE, Ince PG, Kamphorst W, Revesz T, Rozemuller AJM, Kumar-Singh S, Akiyama H, Baborie A, Spina S, Dickson DW, Trojanowski JQ, Mann DMA (2010) Nomenclature and nosology for neuropathologic subtypes of frontotemporal lobar degeneration: an update. *Acta Neuropathol* 119:1–4
 24. McKeith IG, Dickson DW, Lowe J, Emre M, O’Brien JT, Feldman H, Cummings J, Duda JE, Lippa C, Perry EK, Aarsland D, Arai H, Ballard CG, Boeve B, Burn DJ, Costa D, Del Ser T, Dubois B, Galasko D, Gauthier S, Goetz CG, Gomez-Tortosa E, Halliday G, Hansen LA, Hardy J, Iwatsubo T, Kalara RN, Kaufer D, Kenny RA, Korczyn A, Kosaka K, VMY L, Lees A, Litvan I, Londos E, Lopez OL, Minoshima S, Mizuno Y, Molina JA, Mukaetova-Ladinska EB, Pasquier F, Perry RH, Schulz JB, Trojanowski JQ, Yamada M, Consortium on DLB (2005) Diagnosis and management of dementia with Lewy bodies: third report of the DLB consortium. *Neurology* 65:1863–1872
 25. Greenberg SM, Charidimou A (2018) Diagnosis of cerebral amyloid Angiopathy Evolution of the Boston criteria. *Stroke* 49:491–497
 26. Smallwood A, Oulhaj A, Joachim C, Christie S, Sloan C, Smith AD, Esiri M (2012) Cerebral subcortical small vessel disease and its relation to cognition in elderly subjects: a pathological

- study in the Oxford Project to Investigate Memory and Ageing (OPTIMA) cohort. *Neuropathol Appl Neurobiol* 38:337–343
27. Love S, Miners SJ (2015) White matter hypoperfusion and damage in dementia: post-mortem assessment. *Brain Pathol* 25:99–107
 28. Murphy DD, Ravina B (2003) Brain banking for neurodegenerative diseases. *Curr Opin Neurol* 16:459–463
 29. Nelson PT, Jicha GA, Kryscio RJ, Abner EL, Schmitt FA, Cooper G, Xu LO, Smith CD, Markesbery WR (2010) Low sensitivity in clinical diagnoses of dementia with Lewy bodies. *J Neurol* 257:359–366
 30. Franklin EE, Perrin RJ, Vincent B, Baxter M, Morris JC, Cairns NJ (2015) Brain collection, standardized neuropathologic assessment, and comorbidity in ADNI participants. *Alzheimers Dement* 11:815–822
 31. Thomas AJ, Taylor JP, McKeith I, Bamford C, Burn D, Allan L, O'Brien J (2017) Development of assessment toolkits for improving the diagnosis of the Lewy body dementias: feasibility study within the DIAMOND Lewy study. *Int J Geriatr Psychiatry* 32:1280–1304
 32. Cummings J, Feldman HH, Scheltens P (2019) The “rights” of precision drug development for Alzheimer’s disease. *Alzheimers Res Ther* 11:76
 33. Cummings J (2018) Lessons learned from Alzheimer disease: clinical trials with negative outcomes. *Clin Transl Sci* 11:147–152
 34. Rabinovici GD, Carrillo MC, Forman M, DeSanti S, Miller DS, Kozauer N, Petersen RC, Randolph C, Knopman DS, Smith EE, Isaac M, Mattsson N, Bain LJ, Hendrix JA, Sims JR (2016) Multiple comorbid neuropathologies in the setting of Alzheimer’s disease neuropathology and implications for drug development. *Alzheimers Dement (N Y)* 3:83–91

Part VI

Digital Biomarkers and In Silico Methods



Chapter 18

Speech-Based Digital Biomarkers for Alzheimer's Research

Simona Schäfer, Janna Herrmann, Sol Tovar, Nicklas Linz,
and Johannes Tröger

Abstract

Digital biomarkers are of growing interest in the field of Alzheimer's Disease (AD) research. Digital biomarker data arising from digital health tools holds various potential benefits: more objective and more accurate assessment of patients' symptoms and remote collection of signals in real-world scenarios but also multimodal variance for prediction models of individual disease progression. Speech can be collected at minimal patient burden and provides rich data for assessing multiple aspects of AD pathology including cognition. However, the operations around collecting, preparing, and validly interpreting speech data within the context of clinical research on AD remains complex and sometimes challenging. Through a dedicated pipeline of speech collection tools, preprocessing steps and algorithms, precise qualification and quantification of an AD patient's pathology can be achieved from their speech. The aim of this chapter is to describe the methods that are needed to create speech collection scenarios that result in valuable speech-based digital biomarkers for clinical research.

Key words Cognition, Digital biomarkers, Alzheimer's disease, Speech biomarkers

1 Introduction

Alzheimer's disease (AD) clinical trials are the slowest and most expensive clinical trials among neuropsychological indications [1], and with 99.6% they have an exceptionally high failure rate [2]. Regarding the reasons for the high failure rate, inadequate or ineffective endpoint design was identified as one of the problems [3]. An accurate classification of disease stage and progression is an essential step to make AD clinical trials more efficient. This especially applies to the detection of early and asymptomatic disease stages, since modern clinical trials have shifted their focus to the earlier phases of the disease and mostly include prodromal or preclinical AD patients [4]. Hence, a new framework for detecting different AD stages that meets contemporary requirements could improve the success rate of AD clinical trials.

Biomarkers that sensitively, reliably, and validly detect disease status and progression provide a valuable option that could support (1) patient selection, (2) classification of disease stage, (3) clarification of drugs' mechanism of action, and (4) measurement of treatment response, as well as (5) appropriate dose selection [3]. Therefore biomarkers are an important tool to overcome recent barriers to AD clinical trial success.

In recent years, increasing interest has been directed toward the exploration of noninvasive biomarkers. Speech analysis has become a research tool, as well as a diagnostic resource, for measuring multiple pathological aspects of AD such as cognition, late-life depression, apathy, and other psychiatric symptoms.

Just as traditional "fluid" biomarkers that assess pathogenetic hallmarks of AD, digital speech biomarkers (SBs) measure indicators of normal biological processes, pathogenic processes, or responses to an exposure or intervention. In particular, SBs that target cognition can provide meaningful insights into disease-related pathological changes, since progressive cognitive decline is the cardinal behavioral symptom in AD [5]. Whereas classical neuropsychological tests often have sufficient psychometric properties to measure cognitive decline in dementia, they are less suitable or not applicable at all to decentralized remote clinical trials, as they require physical presence of clinicians. The benefit of speech-based digital biomarkers is that they can easily be deployed remotely over low-tech immersive frontends such as standard telephones, supporting robust decentralized trials. Additionally, SBs are a promising solution, as they can be carried out automatically and thus enable scalable and cost-efficient outreach for trial inclusion, thereby saving time and reducing bias through more representative trial populations. Moreover, the assessment can be carried out at home and is thus particularly convenient, which results in lower burden on sites and patients during the trials. The scalability of speech biomarkers facilitates screening and prescreening scenarios as well and thus supports trial enrichment by preselecting more appropriate participants, making AD clinical trials more efficient by reducing time and costs that are caused by high screen-outs [1]. SBs' noninvasiveness provides unique advantages beyond CSF- or blood-based biomarkers. They are collected using a digital sensing product, so SBs can also be referred to as digital biomarkers. Since the sensing product captures speech (e.g., using a microphone), they qualify as digital speech biomarkers (sometimes also called voice biomarkers) [6].

When referring to SBs, it is important to carefully consider the technical framework that a specific SB is embedded into, as given by its intended use. Depending on this framework, use-case-specific sensor setups need to be evaluated as part of the SB evaluation (e.g., lower audio sampling rate for a telephone-based deployment compared to an app-based usage) [7]. From a conceptual/clinical point

of view, it is important to define how speech readouts connect to a concept of interest (e.g., a symptom or syndrome) and eventually a meaningful aspect of health. This conceptual framework ultimately also drives the validation efforts. Conceptually, an SB often does not measure the capability of a human being to talk and use language but rather uses speech as a medium to measure language-distant pathogenic processes such as, e.g., breathiness in spoken language due to asthma or other respiratory diseases.

As far as SBs for cognition are concerned, in some cases, an SB measures language as a cognitive function, and therefore the medium (speech) overlaps directly with the concept of interest (speech/language capabilities; for an overview see [6]). In addition, SBs can focus on other aspects of neurocognition that are impaired in AD such as learning and memory, executive function, or processing speed, which are related to everyday functionalities (remembering and knowing some facts, planning of activities, following a conversation) that are meaningful to the patient but are not necessarily related to speech. Based on the cognitive domains that are targeted, the use of different speech tasks and a different analysis can be useful (for an explanation of different tasks and their analyses, see Subheading 3 “Methods”).

2 Materials

Speech biomarkers need to be embedded in a technical system that allows the capture and interpretation of speech data (for an overview see Fig. 3). One such system would need to be configurable to meet the demands for the planning, management, and (remote) execution of different studies in the field of medicine and pharmacy. It would be an additional benefit if the system can be easily implemented in third-party systems to be used together with other tools that are required for the study. The platform would consist of at least two components: one interface for the study team for the organization of the study and one for the participants where assessments can be performed.

2.1 Components

Interface for the Study Team The expert/clinician-facing frontend typically is a central space where studies can be planned, participants can be registered, assessments can be set up using different implemented language tasks, participants' assessment dates can be scheduled, and the final results including patients' adherence can be viewed. There are no specific requirements for the hardware that should be used. However, it makes sense to use an interface that every clinician probably has available anyway, such as a password-protected web page that can be accessed with different devices.

Interface for the Participants While the organization of a study does not require specific technology, the collection of speech data demands a technology that has an appropriate sensor, which would be a microphone. Depending on the study population, disease, affinity with technology of the participants, and disabilities, the most fitting data collection component can be chosen. In general, two setups would be possible: (1) interfaces with a screen (app assessment for smartphone or tablets, computer-based assessment) or (2) phone call.

1. Interfaces with a screen: in the computer or smartphone-based assessment, participants are guided through the tasks via instructions on the screen. This allows the performing of speech tasks that rely on visual stimuli (such as describing a picture). When designing an app or web page for studies in AD trials, the vast age range, diseases, and tech-savviness of participants need to be considered including the following aspects:
 - (a) Technology and user interfaces often make use of *symbols*, *icons*, etc. to increase usability. Unfortunately, many of these symbols originate in younger generations, and their understanding often requires a cultural homogeneity, which can lead to difficulties in understanding across different cultures and generations [8]. To overcome this, the usage of icons should be reduced to a minimum, and instead, buttons have text describing their action.
 - (b) Kilian et al. point out that by simplifying the knowledge presented, the usability of a system can be improved—especially for the elderly as cognitive performance slows down with age [9]. In order to minimize the cognitive load of the participant, the flow through the app should be as simple and linear as possible. Beyond the actual assessment, the login should also be made as easy as possible. One possibility would be to use a QR code—no need for participants to remember a complex username and password combination. The assessments could be used in-clinic and remotely at home. Remote assessments reduce the burden and allow to conduct study protocols with higher assessment frequencies (e.g., weekly). If the recording device has a sufficient microphone quality (considering sampling rate and bit depth), which is true for almost any currently used device, the generated speech data has solid audio quality. Otherwise, usage of a headset can be considered.
2. Phone call: in addition to the app or computer-based assessments, a phone-based administration (which can be carried out using an ordinary landline telephone) is also possible, which

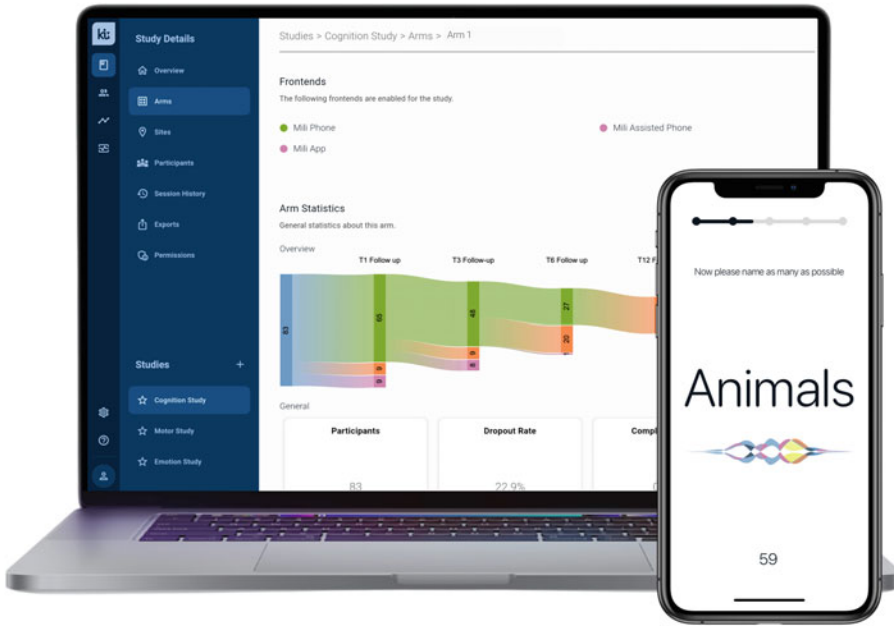


Fig. 1 Example of the speech data collection platform “Mili” (ki:elements GmbH)

allows less tech-savvy persons to access the assessment. Of course, the presentation of visual stimuli is not possible. Phone calls can be carried out fully automated, which requires the interaction of the participant with a phone bot that provides the task instructions or alternatively—and especially for people with higher degrees of disabilities—in an assisted phone call, where a study team member carries out the assessment. Even when a landline phone is used, the audio quality of the assessment is sufficient for analysis (Fig. 1).

2.2 Environment

While speech biomarkers can be administered at home or in-clinic, they require a silent environment with minimal background noise (*see Note 1*), so that the sound signal can be picked up and processed properly. Participants should be free from any disturbance and should wear their hearing or vision aids if needed. If a smartphone or tablet is used, the device should be charged and needs to be set to a volume that allows the participant to hear acoustic stimuli (*see Note 2*).

3 Methods

3.1 Selection of Speech Tasks

To use speech biomarkers to measure cognition, a speech protocol has to be set up that elicits speech from the patient. As mentioned in the introduction, the context of a task significantly determines the demands on the speaker. Hence, the features that can be derived as

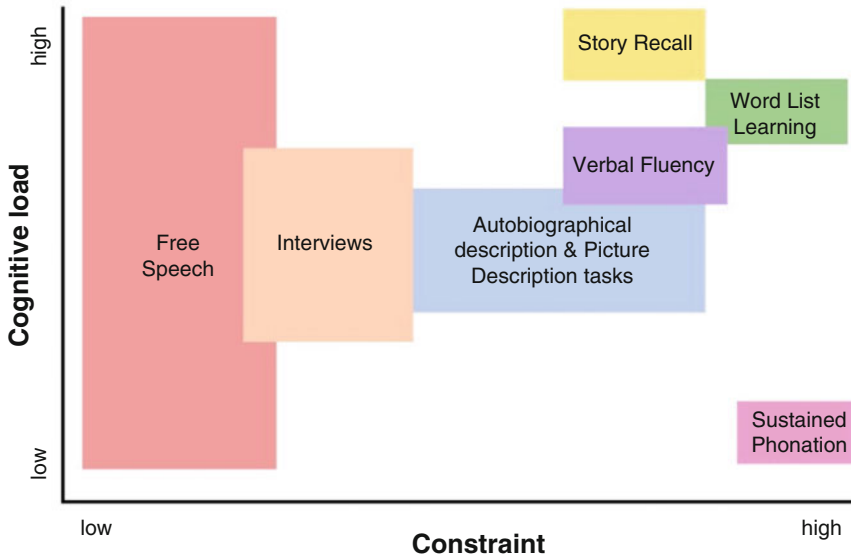


Fig. 2 Speech tasks sorted by level of constraints and cognitive load that is induced by the task

well as the analysis and interpretation of the results depend on the verbal content and the constraints of the given task. A pause, for example, cannot be interpreted on its own, without knowledge of the context, as it does not contain any data on its own.

Tasks can be classified according to the extent of their constraints on a continuum from very constrained tasks to free speech (see Fig. 2). An example of a very constrained task would be reading aloud a given sentence. Semantics, syntax, and pragmatics are already predetermined in this task and thus cannot be analyzed in any meaningful way. In this task, however, articulation skills could be tested. A pause in this task would possibly indicate respiratory problems. The fewer constraints a task has, the more levels of speech can be considered for a meaningful analysis. A pause in a free speech task could be interpreted as a hesitation or as word-finding difficulties. In addition, the restriction of the task itself can also influence speech production, since a higher cognitive load is already given to complete the task. The influence of cognitive load can affect the performance differently depending on the disease.

For the assessment of AD, cognitive functions including memory, executive functions, and processing speed are eligible. Accordingly, tasks must be selected that can capture this. For the assessment of memory functions, the patient would need a task that provides some sort of memory stimuli that is presented to them and that needs to be recalled verbally. In this case, features could be derived that allow to trace back different memory processes by analyzing *how* the items are recalled to reproduce the cognitive manipulation that the patient undertakes. For this analysis, a speech biomarker could analyze the semantic relationships between individual items to examine whether they have been

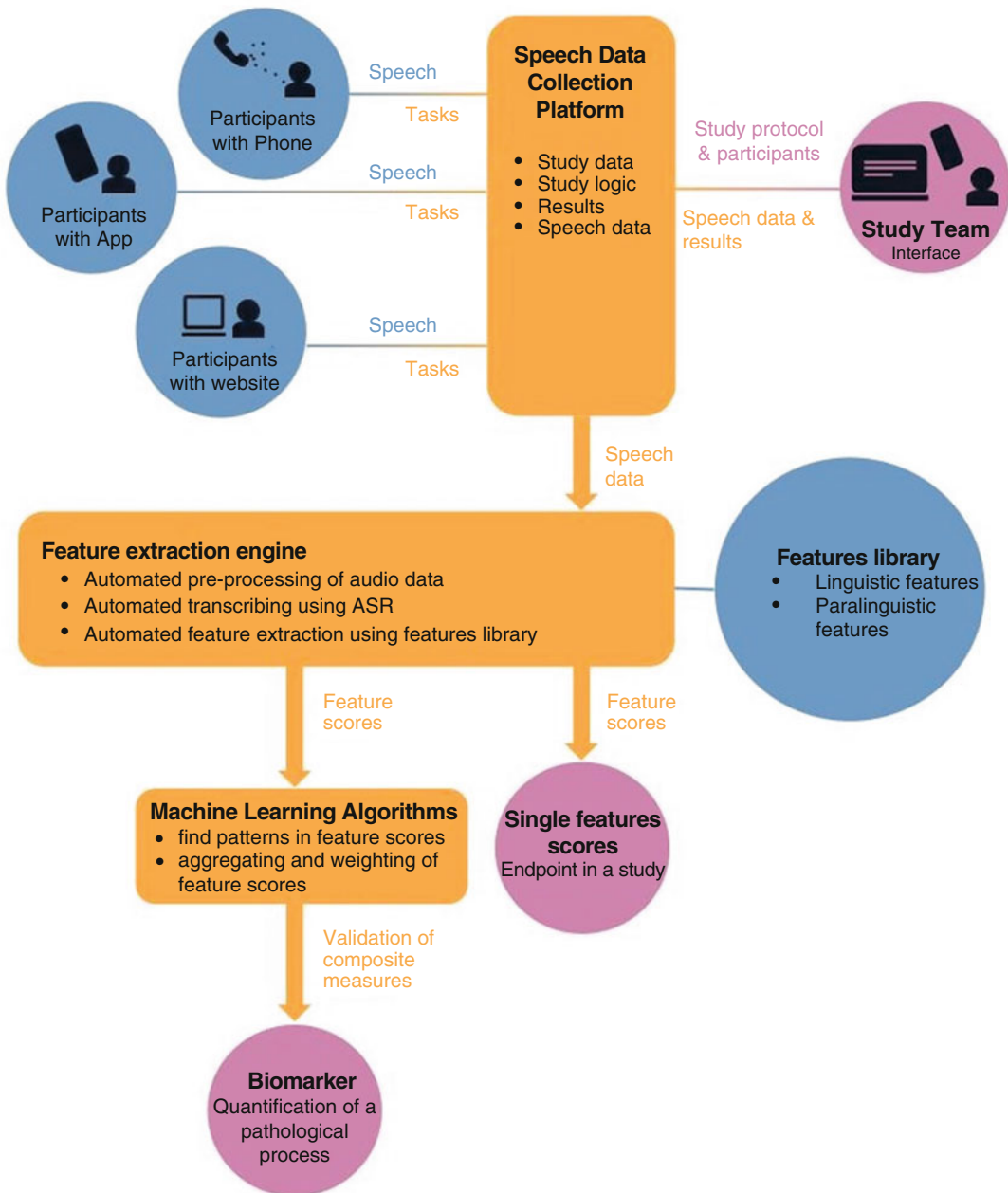


Fig. 3 Schematic overview of the interplay of the described materials and methods

organized by the patient, or it could be examined whether specific word properties have an advantage to be recalled correctly. Many more characteristics of memory impairment have been identified that can be captured using specific features.

For the assessment of executive functions, a task needs to be administered that requires the patient to use some sort of cognitive control functions. There are several verbal tasks that can be used for

Table 1
Overview of speech tasks suitable for AD cognitive assessment

Speech tasks	Cognitive domain	Description	Possible features
Verbal fluency	Executive functions	Participants are presented with a category and should name as many items out of this category as possible. Typically the “animal” version is administered, which requires participants to name as many animals as they can think of in 1 min (<i>see Note 3</i>).	Number of words, semantic, and temporal clusters
Word and story recall	Memory	Participants are presented with verbal material (either words or a story) and should immediately recall the story/word list. Word list tests repetitively present the same word list on several successive trials, which allows learning the list. After each trial there is an immediate recall trial. After all trials are performed, there is a delay of 30 min, followed by a delayed recall trial.	Number of correctly recalled items, proportion of primacy and recency items, learning slopes
Picture description	Language, executive Functions	A picture is presented to the participant that represents a complex visual scene with several persons and actions. The participant should describe the picture as detailed as possible. A time limit can be applied.	Filler words, part-of-speech proportions, hesitation rate, repetitions
Interviews	Language, memory, executive functions, processing speed	Interviews are a semi-constrained task. The interviewer asks specific, standardized questions and the participant answers them. Speech features derived from interview contributions of the participant correlate significantly with PET-tau values.	Filler words, part-of-speech proportions, hesitations rate, repetitions, length of an utterance

this. For example, verbal fluency tasks require the participant to actively retrieve words from the semantic lexicon. Performance in this task depends on strategy use and mental flexibility, which can be assessed using clustering and switching features, which are known to be altered in AD [10]. Further features can be analyzed and have been examined previously [11]. Table 1 provides an overview of speech tasks that are suitable for assessment of cognitive impairment in AD and some features that can be derived from these tasks.

3.2 Practical Implications for the Assessment

For the assessment to be performed correctly, the background must be quiet. If a disruption happens during the assessment that interferes with the recording (background noise, someone speaks in between, instructions were not understood), the possibility should be implemented to redo the assessment (*see Note 4*). However, when redoing an assessment, practice effects have to be considered, since a second administration could lead to a significant learning effect (e.g., starting with all trials from a word list task, a second time allows the participant to have the learning twice).

To allow the study team to decide whether an assessment should be repeated, an online quality analysis comes in handy. The quality analysis can provide a first impression whether the audio data that were collected fulfill basic quality criteria including background noise or the length of an audio file (e.g., if the task is timed for 1 min, and the audio file only contains 10 s, the quality control analysis should indicate that the task has not passed the quality analysis).

3.3 Speech Analysis

The voice data that is generated is typically evaluated with the help of machine learning artificial intelligence. Speech data can be analyzed on a linguistic level (*what* is said; what words are used, how the sentence is structured, etc.) and on an acoustic level (*how* something is said; pitch, intonation, etc.). For the linguistic analysis, recorded speech is often transcribed as a preparation using automatic speech recognition. From the transcripts, several different features reflecting structure, sentiment, semantic, or cohesiveness of language can be derived. For the acoustic analysis, no transcript is needed. Features can be extracted directly from the audio recording. However, the audio recording might require some preprocessing and cleaning before features are extracted. Typical preprocessing steps involve the cutting of the audio to the relevant parts or the decomposition of the audio recording into single frequencies. Since these process steps are typically applied to all audio data, it often makes sense in practical applications to automate the preprocessing and feature extraction. Such an engine in combination with a features library will then provide ready-to-use feature values whenever an audio file is entered.

Feature values in themselves provide a measure, yet it is usually a specific pattern of different features that collectively present as deviating from the norm or a control group that allow association with a particular pathology (such as AD). Since a large number of features are also often extracted, it is generally useful to aggregate them. This is typically done using machine learning algorithms that support the search for a pattern or the weighting and aggregation of the values into a clinically meaningful composite (which requires a clinical anchor). A clinically meaningful score that captures a relevant concept of a given disease qualifies as a biomarker which can be used to characterize a pathological process, including the

detection of a disease or monitoring of the disease progress (*see Note 5*). One example for a speech-based biomarker that can be used in Alzheimer's is the ki:elements speech biomarker for cognition, which provides a score for processing speed, episodic memory, and executive functions based on a 10–15-min speech assessment [12].

4 Notes

1. A general concern in speech biomarkers is that the signal that is recorded needs to have sufficient audio quality to not distort the analysis and lead to incorrect results. A separate room or a headset can be useful to reduce the background noise. Although controlling the environment is difficult in a remote setting, the study team can check the quality of the recording in the Interface for the Study Team and can offer a retesting (whereby practice effects should be considered).
2. To avoid that the assessment is interrupted due to technical difficulties that arise from the selected device, the risk should be minimized by setting up the device correctly.
3. In some cases it may happen that not all words are picked up by the automatic speech recognition, which can lead to slightly distorted results.
4. A software bug can result in the interruption of the assessment, a missing analysis, or a wrong result. Sometimes the problem resolves itself, if the app is started new. Otherwise the app support needs to be contacted.
5. In general, whereas digital biomarkers, typically complex algorithms which take many data sources in order to make a binary patient assessment, may be highly predictive or prognostic, they are often difficult for the patient, care partner, or clinician to interpret in a way that is meaningful and translational. Interpretation and scoring aids such as norms from a clinical and a healthy population provided by the developers may be useful.

References

1. Malzbender K, Lavin-Mena L, Hughes L, Bose N, Goldman D, Patel D (2020) Key barriers for clinical trials for Alzheimer's disease. White Pap. – USC Schaeffer Cent
2. Cummings JL, Morstorf T, Zhong K (2014) Alzheimer's disease drug-development pipeline: few candidates, frequent failures. *Alzheimers Res. Ther.* 6(4):37. <https://doi.org/10.1186/alzrt269>
3. Yiannopoulou KG, Anastasiou AI, Zachariou V, Pelidou S-H (2019) Reasons for failed trials of disease-modifying treatments for alzheimer disease and their contribution in recent research. *Biomedicines* 7(4):97. <https://doi.org/10.3390/biomedicines7040097>
4. Khoury R, Ghossoub E (2019) Diagnostic biomarkers of Alzheimer's disease: A state-of-the-art review. *Biomark. Neuropsychiatry* 1:

100005. <https://doi.org/10.1016/j.bionps.2019.100005>
5. Jack CR et al (2013) Tracking pathophysiological processes in Alzheimer's disease: an updated hypothetical model of dynamic biomarkers. *Lancet Neurol.* 12(2):207–216. [https://doi.org/10.1016/S1474-4422\(12\)70291-0](https://doi.org/10.1016/S1474-4422(12)70291-0)
 6. Robin J, Simpson W, Kaufman LD (2020) Tracking changes in cognition in Mild Cognitive Impairment and Alzheimer's Disease over a 6-month period using a speech-based digital biomarker. Presented at the ICSTM 16th Annual Scientific Meeting
 7. Tröger J, Linz N, König A, Robert P, Alexandersson J (2018) Telephone-based dementia screening I: automated semantic verbal fluency assessment. Proceedings of the 12th EAI International Conference on Pervasive Computing Technologies for Healthcare, pp 59–66. [Online]. Available: <https://dl.acm.org/doi/10.1145/3240925.3240943>
 8. M. Antona and C. Stephanidis, Eds., Universal access in human-computer interaction: universal access to information and knowledge (Part 2) 2014
 9. Holzinger A, Searle G, Nischelwitzer A (2007) On Some Aspects of Improving Mobile Applications for the Elderly. In: Stephanidis C (ed) Universal Access in Human Computer Interaction. Coping with Diversity, vol 4554. Springer Berlin Heidelberg, Berlin, Heidelberg, pp 923–932. https://doi.org/10.1007/978-3-540-73279-2_103
 10. Tröger J et al (2019) Exploitation vs. exploration-computational temporal and semantic analysis explains semantic verbal fluency impairment in Alzheimer's disease. *Neuropsychologia* 131:53–61. <https://doi.org/10.1016/j.neuropsychologia.2019.05.007>
 11. König A et al (2018) Use of speech analyses within a mobile application for the assessment of cognitive impairment in elderly people. *Curr. Alzheimer Res.* 15(2):120–129. <https://doi.org/10.2174/1567205014666170829111942>
 12. Tröger J et al (2022) Validation of the remote automated ki:e speech biomarker for cognition in mild cognitive impairment: verification and validation following DiME V3 framework. *Digit. Biomark.* 6(3):107–116. <https://doi.org/10.1159/000526471>



cCOG Web-Based Cognitive Assessment Tool

Hanneke F. M. Rhodius-Meester, Teemu Paajanen, and Jyrki Lötjönen

Abstract

Cognitive testing is an essential part of clinical diagnostics and clinical trials in Alzheimer's disease. Digital cognitive tests hold a great opportunity to provide more versatile and cost-efficient patient pathways through flexible testing including at home. In this work, we describe a web-based cognitive test, cCOG, that can be used in screening, differential diagnosis, and monitoring the progression of neurodegenerative diseases.

Key words Cognitive testing, Alzheimer's disease, Neurodegenerative diseases, Digital biomarkers

1 Introduction

To provide adequate care and appropriate treatment, timely and accurate diagnosis of neurodegenerative disorders is essential. Timely diagnosis of Alzheimer's disease (AD) combined with adequate management can support cognition, delay institutionalization, and lead to socioeconomic benefits even with existing treatment options but becomes even more critical when disease-modifying treatments are more widely available [1]. Knowledge on diagnosis and future perspectives, focusing on the patient and caregiver, are essential for empowerment of patients. Yet, to date, patients experience on average 3 years of cognitive complaints prior to referral to the memory clinic, leading to stress and anxiety and leaving a high number of diagnoses undetected [2, 3]. Patients struggle whether or not to visit their general practitioner (GP), and some might fear the burdensome of cognitive testing; and GPs struggle with which patients to refer to memory clinics [4]. Whereas at the memory clinic, the challenge of differential diagnosis results in clinicians struggling with determining the correct workup, leading to unwarranted practice variation and suboptimal diagnostic accuracy [5].

The field is in the dawn of major changes due to developments in blood-based and digital biomarkers, in artificial intelligence (AI), and in disease-modifying treatments [6, 7]. The transformation of the patient journey is crucial to prepare for a future with optimal dementia diagnostics and monitoring, solving current challenges and using novel opportunities [8]. To ensure that our healthcare system provides an adequate and timely diagnosis and care for all patients, just spending more money and increasing capacity is not the solution. The COVID pandemic has shown the rigidity and inadequacy of our current healthcare system, as well as the need for digital cognitive testing [9]. The solution is to use our resources smarter and apply novel digital tools for dementia screening and diagnostics [10]. This is crucial also in the light of clinical trials and eventually disease-modifying treatment. This means improved participant selection (screening and diagnostics) and monitoring disease progression (outcome measures). For example, tools are needed to identify AD cases in a cost-effective way, avoiding unnecessary CSF or amyloid-PET testing. Digital tools can aid in this difficult challenge, separating AD from other dementias, such as vascular dementia, frontotemporal dementia, and dementia with Lewy bodies (DLB) [11–13]. Despite intense developments, AI, remote testing, and digital tools are not comprehensively validated and implemented in memory clinics, let alone used at the GP or at home [14, 15]. In a recent European survey, stakeholders are overall clearly positive toward AI and use of digital tools yet point out too many hurdles have to be taken for them to use AI or digital tools in their daily practice [16].

Cognitive testing with pen and paper tests is still the norm both in screening tests and neuropsychological assessments. Neuropsychological assessment is too broad and time-consuming for screening cognitive problems and requires trained neuropsychologists to assess and interpret the test results. Short paper and pencil-based cognitive screening tests such as Mini-Mental State Examination, Montreal Cognitive Assessment, and the CERAD cognitive battery have proved to be accurate in detection of dementia disorders. However, web-based cognitive testing provides several advantages as compared to paper and pencil tests, such as enhanced precision of measurements and standardizing measurements between hospitals. Web-based tests may increase the availability of testing and help to reduce costs at the same time [17, 18]. In addition digitized results can be more easily integrated to electronic patient data platforms [19]. Web-based cognitive tests have been found to be promising in measuring cognition in general population [20] and in detecting mild cognitive impairment (MCI) and dementia [21, 22]. However, test performance can vary depending on test devices [20, 23, 24]. Also retest reliability of self-administered cognitive tests and their correlation to the traditional neuropsychological tests vary [20, 22, 25]. Finally, online cognitive testing at home can provide

a less stressful environment for patients and enable more flexible and cost-efficient patient pathways for clinics and pharma companies.

Despite clear benefits and potential of web-based cognitive tests, they are clearly underutilized in clinical settings. We therefore developed in an European project, a web-based self-administrable cognitive test tool, cCOG, designed for early detection of neurodegenerative disorders. Different tasks of cCOG were developed based on traditional cognitive tests to maintain the internal validity and to support clinicians to interpret the results. As a result, cCOG shows high correlation with standard neuropsychological tests which represent the gold standard of cognitive assessment. cCOG can be applied as a cognitive screening tool in clinics and clinical trial settings, but also as a follow-up tool to detect individual-level cognitive change in a standardized manner.

2 Materials

2.1 Test Subjects

The cCOG test can be executed on a standard personal computer (PC), laptop, or tablet with an Internet connection and a web browser (*see Note 1*). A touch screen, external mouse, or a laptop mouse can be used as a pointing device. When the test is done at home, the test subject should also have an email account because the test is launched from an email link.

As in any cognitive testing, the test subject should not be tired, his/her mood should be within normal variation, and there should not be external distractors or interruption during the session. It is instructed to reserve about 20 minutes in a quiet environment for doing the test. It is recommended that the questionnaire on symptoms is filled together with their closest one.

2.2 Healthcare Specialists

The administration tools for healthcare specialists are available through a web portal. The administrator of the clinic can invite new healthcare specialist users to the portal.

3 Methods

cCOG is composed of three questionnaires and six cognitive tasks. cCOG measures episodic memory (word list learning and delayed recall), attention and reaction time (choice reaction time test), visual search, processing speed and executive function (modified versions of Trail Making A and B tests, TMT-A and TMT-B), and visual object perception (fragmented letters test). cCOG has been shown to provide valuable information for detection of cognitive problems and for differential diagnostics [12, 13] (*see Note 2*). Next, the cCOG test is described in detail.

Questionnaire pretest: the questionnaire reminds a test subject that he/she should be alert enough for doing the test and has enough time. If not, the test is recommended to be done another time. If a healthcare specialist has not entered the age, sex, and education years for the subject when creating a test invite, those will be asked directly from the subject.

Questionnaire on symptoms: the questionnaire is designed to evaluate whether the subject has symptoms that are especially typical in dementia with Lewy bodies. The questions address the following areas:

1. Motor problems.
2. Visual hallucinations.
3. REM sleep behavioral disorders.
4. Fluctuation in alertness.
5. Constipation.
6. Urinary retention.
7. Orthostatic hypotension.

Next, the cognitive test starts. Each task is first briefly introduced in writing, and then a short video follows showing what a test subject is supposed to do.

Task 1 (episodic memory, learning): The test subject is asked to remember 12 words shown one by one (Fig. 1). For each word, a written word and its picture is presented. After the words have been shown, the subject is asked to type as many words as she/he can remember. The same list of words is shown three times but each time in a random order (*see Note 3*).

Task 2 (choice reaction time): In this choice reaction time test, stimuli are letters indicating the directions right and left to which the subject should react by pressing the arrow buttons as quickly as possible. The subject is supposed to press the right and left arrow buttons when she/he sees the letter “R” (right) or “L” (left). The letters used depend on the language used in the test.

Task 3 (fragmented letters): The test subject is shown 20 letters with incomplete shape and asked to type the corresponding letter (Fig. 2).

Task 4 (modified Trail Making Test A): The numbers from 1 to 24 are shown in random locations on the screen. The subject is asked to select the numbers in ascending order as quickly as possible. The task ends when the subject reaches number 12.

Task 5 (modified Trail Making Test B): The subject must again select numbers in order, but this time each number is presented both in a circle and a square (Fig. 3). Altogether 48 stimuli are shown on the screen. The subject is asked to select the numbers in ascending order but alternating between circles and squares. The sequence is started from the number 1 within a circle, then number

Task 1/6



DRUM

Fig. 1 Episodic memory task: learning

Task 3/6



Fig. 2 Fragmented letters task

Task 5/6

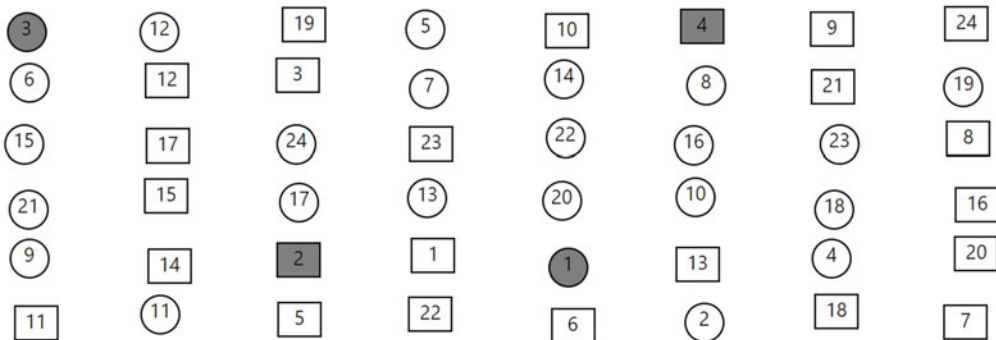


Fig. 3 Modified Trail Making Test B task

2 within a square, then number 3 within a circle, and so on. The subject is supposed to continue alternating as quickly as possible until she/he reaches number 12.

Task 5 (episodic memory – delayed recall): After the delay, the subject is asked to recall and type the words from Task 1.

Questionnaire post-test.: The questionnaire checks whether the test subject had any issues during the test. The subject is asked about the level of concentration, distractions, possible help obtained during the test, the place where the test was done, and the device used.

cCOG Administration Tools

Proper administration tools are necessary for healthcare professionals to efficiently administer a clinical trial or the use in clinical practice. This section describes the main functionalities of the cCOG portal for healthcare professionals.

Defining organization settings: The general settings for the organization, e.g., for a memory clinic, are defined first, but many of these settings can be personalized for each test subject. If a test subject does the test at home, she/he receives an email containing a link to the test. In the settings, an organization can define:

- The content of the invitation and reminder emails.
- The time when the link expires and when the reminder email is sent.
- The default language of the test (*see Note 4*).
- The schedule for automatically sent invites for follow-up tests (if activated).

Inviting a new subject: New test subjects can be created in the cCOG portal. Invites can be sent immediately or scheduled for the future, and they can be sent directly to the patient or clinic. If the test is done in the clinic, it is not necessary to send any invites, but the test can be started from the portal. One can deviate from the general organization settings if desired, e.g., change the language of the test.

Managing existing subjects: The test subjects of the organization can be filtered based on their status, e.g., whether she/he has done the test, failed in completing the test, or the test has been scheduled for the future.

Reviewing results After a test subject has completed the cCOG test, the report and additional information are available in the portal. The report contains results for each task (learning, delayed recall, modified Trail Making A and B, reaction time, and fragmented letters) and the overall score called global cognitive score (Fig. 4). The black ring shows the value measured from the test subject, and the green and purple bars denote the distribution of

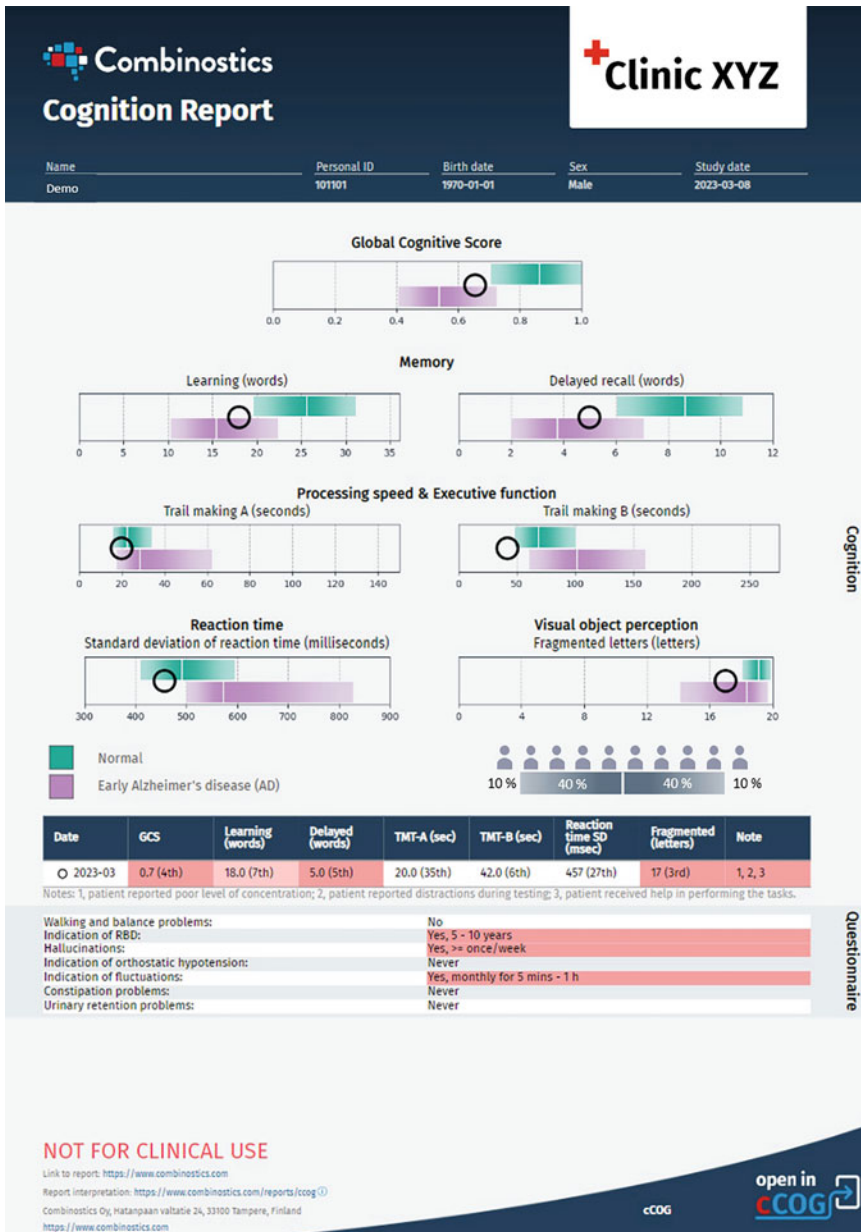


Fig. 4 cCOG report (Percentile for a test result value is the share of people in a population having a smaller value)

values in cognitively normal and mild Alzheimer’s disease patients, respectively, when normalized for age, sex, and education years. The bars show the range within which 80% of people in the corresponding diagnostic group fall. In other words, the left edge of the bar indicates the test result value for the 10th percentile and the right edge for the 90th percentile. The white vertical bar in the

middle shows the median value (50th percentile) for the corresponding diagnostic group.

The values of test result and their percentiles are shown in the table. If the value falls between 0–5th and 5–10th percentile for the learning, delayed recall, or fragmented letters test, the value is highlighted in a red or a light red color, respectively. The values between 95–100th and 90–95th are highlighted consequently for modified TMT-A, TMT-B, and reaction time tests. The final column, *Notes*, indicates if a test subject reported something that might impact the test results. The number 1 denotes poor concentration, 2 distractions during testing, and 3 help obtained in doing the tasks, e.g., tips for remembering the words (*see Note 6*).

The results from the questionnaire on symptoms are shown in the bottom. If a test subject reports symptoms, the values are highlighted in red.

4 Notes

1. The screens of mobile phones are often too small for the modified Trail Making B test making the reliable selection of correct items challenging on the screen.
2. In [12], cCOG was shown to separate cognitively normal people from mild cognitive impairment (MCI) with area under the curve, $AUC = 0.84$, while the performance was $AUC = 0.75$ for MMSE and $AUC = 0.77$ for a combination of paper and pencil tests used in clinical practice (MMSE, RAVLT/CERAD wordlist, TMT-A, TMT-B, categorical verbal fluency, and forward and backward digit span tests) in the same population. Consequently, $AUC = 0.92$, $AUC = 0.84$, and $AUC = 0.91$ were reported for cCOG, MMSE, and combination of clinical cognitive tests, respectively, in separating cognitively normal people from early dementia cases ($MMSE = 27.2 \pm 1.9$). In [13], cCOG was tested in differential diagnostics of Alzheimer's disease (AD), dementia with Lewy bodies (DLB), and cognitively normal people (CN). The combination of the questionnaire on symptoms and cognitive tests produced the following performance: $AUC = 0.94$ for DLB vs. CN, $AUC = 0.87$ for AD vs. DLB, and $AUC = 0.88$ for AD vs. CN. Nearly 90% of test subjects did the test at home.
3. cCOG contains six wordlists which are gone through sequentially for each test subject. Each list contains words from corresponding categories, e.g., one word for furniture, one for body parts, etc. To minimize the learning effect, the numbers in the modified trail making tests are also shown in a random order on the screen.

4. cCOG supports currently (4/2023) the following languages: English, German, Italian, Dutch, Swedish, and Finnish.
5. If a test subject fails to complete the test or does not do the test within given time (despite of reminders), it is worth of contacting her/him and check the reason before sending a new invite.
6. A test subject can report three different types of help received in typing the words/letters, in understanding the instructions, and/or in doing the tasks, e.g., received tips about the words to be remembered. If an assistant does not help in remembering the words, the help in typing or understanding instructions does not impact the results, and the value is not highlighted in red.

References

1. Pouryamout L, Dams J, Wasem J, Dodel R, Neumann A (2012) Economic evaluation of treatment options in patients with Alzheimer's disease: a systematic review of cost-effectiveness analyses. *Drugs* 72:789–802
2. Lang L, Clifford A, Wei L, Zhang D, Leung D, Augustine G et al (2017) Prevalence and determinants of undetected dementia in the community: a systematic literature review and a meta-analysis. *BMJ Open* 7:e011146
3. van den Dungen P, van Marwijk HW, van der Horst HE, Moll van Charante EP, Macneil Vroomen J, van de Ven PM et al (2012) The accuracy of family physicians' dementia diagnoses at different stages of dementia: a systematic review. *Int J Geriatr Psychiatry* 27:342–354
4. Krolak-Salmon P, Maillet A, Vanacore N, Selbaek G, Rejdak K, Traykov L et al (2019) Toward a sequential strategy for diagnosing Neurocognitive disorders: a consensus from the “act on dementia” European joint action. *J Alzheimers Dis* 72:363–372
5. de Wilde A, Ossenkoppele R, Pelkmans W, Bouwman F, Groot C, van Maurik I et al (2019) Assessment of the appropriate use criteria for amyloid PET in an unselected memory clinic cohort: the ABIDE project. *Alzheimers Dement* 15:1458–1467
6. Lam J, Mattke S (2021) Memory care approaches to better leverage capacity of dementia specialists: a narrative synthesis. *Neurodegenerative disease management* 11:239–250
7. Herring WL, Gould IG, Fillit H, Lindgren P, Forrestal F, Thompson R et al (2021) Predicted lifetime health outcomes for Aducanumab in patients with early Alzheimer's disease. *Neurology and therapy* 10(2): 919–940
8. Getsios D, Blume S, Ishak KJ, Maclaine G, Hernandez L (2012) An economic evaluation of early assessment for Alzheimer's disease in the United Kingdom. *Alzheimers Dement* 8: 22–30
9. van Maurik IS, Bakker ED, van den Buuse S, Gillissen F, van de Beek M, Lemstra E et al (2020) Psychosocial effects of Corona measures on patients with dementia, mild cognitive impairment and subjective cognitive decline. *Front Psych* 11:585686
10. Lam J, Hlávka J, Mattke S (2019) The potential emergence of disease-modifying treatments for Alzheimer disease: the role of primary care in managing the patient journey. *Journal of the American Board of Family Medicine: JABFM* 32:931–940
11. Tolonen AFM, Rhodius-Meester H, Bruun M, Koikkalainen J, Barkhof F, Lemstra A et al (2018) Data-driven differential diagnosis of dementia using multiclass disease state index classifier. *Front Aging Neurosci* 10:111
12. Rhodius-Meester HFM, Paajanen T, Koikkalainen J, Mahdiani S, Bruun M, Baroni M et al (2020) cCOG: a web-based cognitive test tool for detecting neurodegenerative disorders. *Alzheimers Dement (Amst)* 12:e12083
13. van Gils AM, van de Beek M, van Unnik A, Tolonen A, Handgraaf D, van Leeuwenstijn M et al (2022) Optimizing cCOG, a web-based tool, to detect dementia with Lewy bodies. *Alzheimers Dement (Amst)* 14:e12379
14. Tsoy E, Zygouris S, Possin KL (2021) Current state of self-administered brief computerized

- cognitive assessments for detection of cognitive disorders in older adults: a systematic review. *J Prev Alzheimers Dis* 8:267–276
15. Aslam RW, Bates V, Dundar Y, Hounsoume J, Richardson M, Krishan A et al (2018) A systematic review of the diagnostic accuracy of automated tests for cognitive impairment. *Int J Geriatr Psychiatry* 33:561–575
 16. van Gils A, van der Flier WM, Rhodius-Meester HFM (2021) Assessing the views of professionals, patients, and care partners concerning the use of computer tools in memory clinics: international survey study. *J Med Internet Res* 5:e31053
 17. Wild K, Howieson D, Webbe F, Seelye A, Kaye J (2008) Status of computerized cognitive testing in aging: a systematic review. *Alzheimers Dement* 4:428–437
 18. Casaletto KB, Heaton RK (2017) Neuropsychological assessment: past and future. *J Int Neuropsychol Soc* 23:778–790
 19. Bilder RM, Reise SP (2019) Neuropsychological tests of the future: how do we get there from here? *Clin Neuropsychol* 33:220–245
 20. Mielke MM, Machulda MM, Hagen CE, Edwards KK, Roberts RO, Pankratz VS et al (2015) Performance of the CogState computerized battery in the Mayo Clinic Study on aging. *Alzheimers Dement* 11:1367–1376
 21. Mackin RS, Insel PS, Truran D, Finley S, Flenniken D, Nosheny R et al (2018) Unsupervised online neuropsychological test performance for individuals with mild cognitive impairment and dementia: results from the Brain Health Registry. *Alzheimers Dement (Amst)* 10:573–582
 22. Morrison GE, Simone CM, Ng NF, Hardy JL (2015) Reliability and validity of the Neuro-Cognitive Performance Test, a web-based neuropsychological assessment. *Front Psychol* 6:1652
 23. Ruggeri K, Maguire A, Andrews JL, Martin E, Menon S (2016) Are we there yet? Exploring the impact of translating cognitive tests for dementia using mobile technology in an aging population. *Front Aging Neurosci* 8:21
 24. Wallace SE, Donoso Brown EV, Fairman AD, Beardshall K, Olexovich A, Taylor A et al (2017) Validation of the standardized touchscreen assessment of cognition with neurotypical adults. *NeuroRehabilitation* 40:411–420
 25. Morrison RL, Pei H, Novak G, Kaufer DI, Welsh-Bohmer KA, Ruhmel S et al (2018) A computerized, self-administered test of verbal episodic memory in elderly patients with mild cognitive impairment and healthy participants: a randomized, crossover, validation study. *Alzheimers Dement (Amst)* 10:647–656



In Silico Models to Validate Novel Blood-Based Biomarkers

Angélique Sadlon

Abstract

Biological validation of preliminary findings is a key prerequisite in biomarker discovery. In recent years, the development of advanced large-scale sequencing technologies combined with high-throughput computational analysis methods led to the extraction of considerable amount of data from healthy and diseased tissues. Stored in large open-access repositories, these data can be accessed and interrogated by researchers aiming at understanding the biological rationale behind their results. These so called in silico analyses, in opposite to in vitro analyses, have gained increasing importance in recent years, becoming a major component of research projects and publications. However, making sense of the large amount of data available can be challenging and may lead to a misinterpretation of the data. To reduce the dimensionality of this data, recent years have seen the development of statistical methods and advanced graph analytics which help researchers summarize the available data and draw appropriate conclusions. In this chapter we will describe three in silico methods to investigate the biological underpinnings of a panel of seven blood-based biomarkers of Alzheimer's disease.

Key words In silico analysis, Functional enrichment analysis, Omics, Graph analytics, Network analysis

1 Introduction

Biomarkers are measurable characteristics of physiological and pathological states, which have become the cornerstone in the screening, diagnosis, and risk stratification of diseases as well as in the monitoring of therapies [1]. Biomarker discovery and development are lengthy and costly processes, and only a minority of biomarkers will be implemented in clinical practice [2]. Consequently, exploring the biological plausibility behind preliminary findings is an essential prerequisite before progressing to the next stages.

Recently, advanced large-scale sequencing technologies have helped gathering considerable amount of biological data from healthy and diseased tissues. Stored in large open-source databases, these data can be leveraged by researchers to test hypothesis,

explore biological correlates underlying clinical conditions, and most importantly, make sense of findings by linking these to underlying biological processes. These so called *in silico* models, in opposite to *in vitro* models, have become essential components of research projects. In recent years, the number of databases and bioinformatics resources to conduct *in silico* analysis has risen exponentially, each providing various data types (e.g., DNA, RNA, and protein sequence data, gene expression data, methylation data) from healthy tissues (e.g., the Genotype-Tissue Expression (GTEx) project [3]), diseased tissues (e.g., The Cancer Genome Atlas for cancer tissues [4]), or both (e.g., Gene Expression Omnibus—GEO [5]). Additionally, research institutes such as the National Center for Biotechnology Information (NCBI), the Broad Institute, and the European Bioinformatics Institute provide a large palette of tools and resources to compare, process, analyze, and visualize omics data. In parallel, annotation databases such as the Gene Ontology (GO) [6], REACTOME [7], or KEGG [8] map genes to biological or disease pathways allowing researchers to identify pathways or diseases potentially affected by the molecules under investigation.

With the accumulation of data to leverage, it has become essential to summarize the information and prioritize the data at hand, while reducing the noise. One frequently used technique is functional/pathway enrichment analysis, which applies statistical methods to explore whether a selected list of genes (for instance, genes found to be down- or upregulated in a particular condition) is enriched in gene sets of biological or disease pathways [9]. Last decades have observed a surge in functional enrichment analysis methods, available as tools accessible either online and/or as list of codes (grouped into packages) written for R or Python (e.g., WebGestalt [10], g:Profiler [11], DAVID [12], ToppGene [13], GOrilla [14], PANTHER [15], Enrichr [16]).

While validating findings using post hoc analyses has become a critical step in a growing number of research projects, the importance of visualizing these results is gaining increasing importance. Indeed, functional enrichment analysis results often provide a long list of prioritized biological functions, and interpreting these can be challenging. To reduce the dimensionality of the results, advanced visualization tools (e.g., EnrichmentMap [17], BiNGO [18], GOSim [19]) relying on graph analytics have been developed, many of which are implemented as packages in R or as stand-alone softwares developed for advanced visualization of biological data and networks (e.g., Cytoscape [20]).

In this chapter, we will describe three steps which allow researchers to efficiently mine relevant biological information in key databases, analyze and summarize the information, and eventually visualize their findings.

2 Materials

2.1 Computational Requirements

8 GB or RAM (required for Cytoscape).
Java Standard Edition to run Cytoscape.
Internet browser.

2.2 Programs Used

R, version >3.5. We used R Studio, an integrated development environment (IDE) for R. Details on how to install R and the R Studio desktop application can be found here: <https://posit.co/download/rstudio-desktop/>.

For this chapter, we have added comments to R codes to improve the understanding of the codes; these comments are marked with # and will appear in a different color from the code lines in a text editor (e.g. RStudio).

Cytoscape, version >3.7. This software offers a large range of apps, which can be installed according to the researcher's aims (*see* Subheading 2.3, Cytoscape Apps).

2.3 R Packages

ggplot2, *dplyr*, *tidyr*, *tidyverse*, *gprofiler2*, *purrr*, *grid*, *ggpubr*, *janitor*, *data.table*, *ggseg*, *ggseg3d*, *ggsegCampbell*, *gtable*, *ActivePathways*.

The packages can be installed using following **R commands** :

```
####--STEP1: install the packages which are not
yet installed--####
list.of.packages <- c("ggplot2", "dplyr", "tidyr",
"tidyverse", "gprofiler2", "purrr", "grid",
"ggpubr", "janitor", "data.table", "ggseg",
"ggseg3d", "ggsegCampbell", "gtable", "magrittr",
"ActivePathways")
new.packages <- list.of.packages[!(list.of.
packages %in% installed.packages()[,"Package"])
if(length(new.packages)) install.packages(new.
packages)

####--STEP2: load the packages--####
library(ggplot2)
library(dplyr)
library(tidyr)
library(tidyverse)
library(gprofiler2)
library(purrr)
library(grid)
library(ggpubr)
library(janitor)
library(data.table)
```



```
library(ggseg3d)
library(ggseg)
library(ggsegCampbell)
library(ActivePathways)
library(magrittr)
```

2.4 Cytoscape App

EnrichmentMap. Details on how to install the app can be found here:

<https://apps.cytoscape.org/apps/enrichmentmap>.

The chapter materials can also be found in the following GitHub repository:

https://github.com/ansmor/springer_chapter.

3 Methods

3.1 Experimental Design

For this tutorial, we will use the data from a 2022 systematic review of blood-based diagnostic biomarker panels for Alzheimer’s disease [21]. Among others, the authors described seven potential blood-based biomarkers (neurogranin (NRGN), synaptosome associated protein 25 (SNAP25), synaptotagmin-1 (SYT1), growth-associated protein 43 (GAP43), very low-density lipoprotein receptor (VLDLR), synaptopodin (SYNPO), and synaptophysin (SYP)) linked to synaptic dysfunction.

3.2 Genetic Landscape

A detailed description of each gene (e.g., genomic locations, functions, risk variants and genome-wide association studies results, involvement in pathways, and so on) can be found in GeneCards [22] (<https://www.genecards.org/>) (Fig. 1).

3.3 Blood-Based Biomarker Expression in the Brain

Before undertaking the functional enrichment analysis, we are interested in exploring these biomarkers’ expression in healthy brain tissues. A large palette of tools and database providing gene and protein expression is available (e.g., GTEx [3], the Human Protein Atlas [23]), some providing their own data, others providing curated or processed data from external resources. For this tutorial we will use the Human Protein Atlas protein expression profiles measured by immunohistochemistry; 15,318 genes (76% of all annotated genes) are covered (access date: 04.2023). The data can be downloaded on the HPA website (<https://www.proteinatlas.org/about/download>) and imported in R where we can obtain a brief overview of the brain expression data for the seven biomarkers. Here, we considered only data with an enhanced reliability score (i.e., one or more validated antibodies are targeting nonoverlapping sequences within the same gene).

SNAP25 Gene - Synaptosome Associated Protein 25
 Protein Coding (Updated: Jan 10, 2023 ; GC20P010198 ; GIFTS: 55)

Jump to section	Aliases	Disorders	Domains	Drugs	Expression	Function	Genomics	Localization	Orthologs
	Paralogs	Pathways	Products	Proteins	Publications	Sources	Summaries	Transcripts	Variants
Research Products	Antibodies Cell Lines	Assays Clones	Proteins Primers	Inhib. RNA Genotyping	CRISPR	Exp. Assays	miRNA	Drugs	Animal Models

Aliases for SNAP25 Gene

GeneCards Symbol: **SNAP25**
Synaptosome Associated Protein 25
 SNAP-25
 DJ1068F16.2
 BA416N4.2
 RIC-4
 RIC4
 SEC9
 SNAP

External Ids for SNAP25 Gene
 HGNC: 11132 NCBI Entrez Gene: 6616 Ensembl: ENSG00000132639 OMIM®: 600322 UniProtKB/Swiss-Prot: P60880

Previous HGNC Symbols for SNAP25 Gene
 SNAP

Previous GeneCards Identifiers for SNAP25 Gene
 GC20P010187, GC20P010194, GC20P010147, GC20P010151, GC20P010218, GC20P010177, GC20P010181, GC20P010184, GC20P010186, GC20P010189, GC20P010193

Summaries for SNAP25 Gene
Entrez Gene Summary for SNAP25 Gene
 Synaptic vesicle membrane docking and fusion is mediated by SNAREs (soluble N-ethylmaleimide-sensitive factor attachment protein receptors) located on the vesicle

Fig. 1 Screenshot of the GeneCards website for the *SNAP25* gene. The database provides detailed information on genomic locations, aliases, risk variants, functions, etc.

```
####--STEP1: read human protein atlas data "normal_tissue.tsv" from your current working directory--####
hpa<-data.table::fread("normal_tissue.tsv")
#clean columns names and filter for data with enhanced reliability score#
hpa<-hpa %>%
  janitor::clean_names() %>%
  filter(reliability=="Enhanced")

#see tissues and cell types which are available#
hpa.cell_types<-unique(hpa$cell_type)
hpa.tissues<-unique(hpa$tissue)
hpa.tissues
hpa.cell_types

#select brain tissues#
hpa.brain.tissues<-c("caudate","cerebellum","cerebral cortex","pituitary gland","choroid plexus")
hpa.brain.tissues

#extract cell types available from brain tissues#
```

```

hpa.brain.celltypes<-hpa %>%
  filter(tissue%in%hpa.brain.tissues) %>%
  distinct(cell_type) %>%
  pull(cell_type)

#get genes with low, high or medium expression in
the brain#
hpa.brain<-hpa %>%
  filter(tissue%in%hpa.brain.tissues) %>%
  filter(level=="High"|level=="Medium"|level=="-
Low") %>%
  distinct(gene_name) %>%
  pull(gene_name)

####--STEP2: analysis and visualisation of HPA
data--####
#create a vector with the biomarkers we are inter-
ested in#
biom<-c("NRGN","SNAP25", "SYT1", "GAP43", "VLDLR",
"SYNPO", "SYP")

#create the first graph showing the expression
profile by cell type#
gA<-hpa %>%
  filter(gene_name%in%biom) %>%
  filter(tissue%in%hpa.brain.tissues) %>%
  group_by(gene_name,cell_type, level) %>%
  summarise(N=n()) %>%
  ungroup() %>%
  add_row(gene_name=setdiff(biom,unique(.$gene_
name)),cell_type=unique(.$cell_type),level="Not
detected",N=1) %>%
  tidyr::complete(gene_name,cell_type) %>%
  replace_na(list(level="Not detected")) %>%
  mutate(level2=factor(level,levels=rev(c("Not de-
tected","Low","Medium","High")))) %>%
  ggplot(.,aes(x=gene_name,y=cell_type,fill=le-
vel2))+
  geom_tile(colour="black") +
  scale_fill_brewer(palette=2,direction=-1,
name="",na.value="grey90")+
  theme(axis.text.x=element_text(face="bold"))+
  theme_light()+
  theme(
  axis.ticks=element_line(size=0.4),
  plot.background=element_blank(),
  panel.border=element_blank(),
  axis.text.x=element_text(face="bold", angle=90,
vjust=1),

```

```

    plot.title.position = 'plot')+
    ylab("")+xlab("cell type")+
    ggtitle("A. Expression by brain cell type")
#show the graph#
gA

#create the second graph showing the expression by
brain regions#
#use the aseg (Automatic subcortical segmentation)
atlas to show the subcortical regions#
dfaseg<-aseg$data$region %>%
  as.data.frame(.) %>%
  'colnames<-'(c("region")) %>%
  mutate(region2=region) %>%
  mutate(region2=ifelse(region2=="cerebellum cor-
tex","cerebellum",region2))

data.aseg<-hpa %>%
  janitor::clean_names() %>% #nice function to
clean names
  filter(gene_name%in%biom) %>%
  filter(tissue%in%hpa.brain.tissues) %>%
  group_by(gene_name,tissue,level) %>%
  summarise(N=n()) %>%
  filter(level%in%c("Medium","High")) %>%
  distinct(gene_name,tissue) %>%
  group_by(gene_name,tissue) %>%
  summarise(N2=n()) %>%
  merge(.,dfaseg,by.x="tissue",by.y="region2",all.
y=T) %>%
  dplyr::select(-tissue) %>%
  ungroup() %>%
  tidyr::complete(gene_name,region) %>%
  filter(!is.na(gene_name)) %>%
  add_row(gene_name=biom,N2=NA,region=NA)

gB<-ggplot(data.aseg) +
  geom_brain(atlas = aseg,
             aes(fill = N2)) +
  scale_fill_viridis_c(option = "magma", direction
=1 ,na.value="grey90") +
  theme_void() +
  labs(title = "B. Detected expression in subcorti-
cal regions \n")+
  facet_wrap(~gene_name)+
  theme(legend.position = "none",
        plot.title.position = 'plot')
#show the graph#
gB

```

```

#use the Campbell atlas to show the cortical regions
(HPA only provides data for "cerebral cortex" and
does not specifies the regions (frontal, parietal,
etc...))
dfcampbell<-campbell$data$region %>%
  as.data.frame(.) %>%
  'colnames<-'(c("region")) %>%
  mutate(region2=region) %>%
  mutate(region2=ifelse(!is.na(region2),"cerebral
cortex",region2))

data.campbell<-hpa %>%
  filter(gene_name%in%biom) %>%
  filter(tissue%in%hpa.brain.tissues) %>%
  group_by(gene_name,tissue,level) %>%
  summarise(N=n()) %>%
  filter(level%in%c("Light","Medium","High")) %>%
  distinct(gene_name,tissue) %>%
  group_by(gene_name,tissue) %>%
  summarise(N2=n()) %>%
  ungroup() %>%
  tidyr::complete(gene_name,tissue) %>%
  merge(.,dfcampbell,by.x="tissue",by.y="region2",
all.y=T) %>%
  dplyr::select(-tissue) %>%
  ungroup() %>%
  filter(!is.na(gene_name)) %>%
  add_row(gene_name=setdiff(biom,unique(.$gene_
name)),N2=NA,region=unique(.$region)) %>%
  add_row(gene_name=biom,N2=NA,region=NA)

gC<-ggplot(data.campbell) +
  geom_brain(atlas = campbell, hemi="left", col-
our="white",
            aes(fill = N2)) +
  scale_fill_viridis_c(option = "magma", direction
=1 ,na.value="grey90") +
  theme_void() +
  labs(title = "C. Detected expression in cerebral
cortex \n")+
  facet_wrap(~gene_name)+
  theme(legend.position = "none")
#show the graph#
gC

#create the final graph (Figure 2 in this tutorial)#
ggarrange(gA, ggarrange(gB,gC,nrow=2),ncol=2)

```

After running the **R commands**, the summary graph shows that six biomarkers (all except VLDLR) are expressed in healthy brain

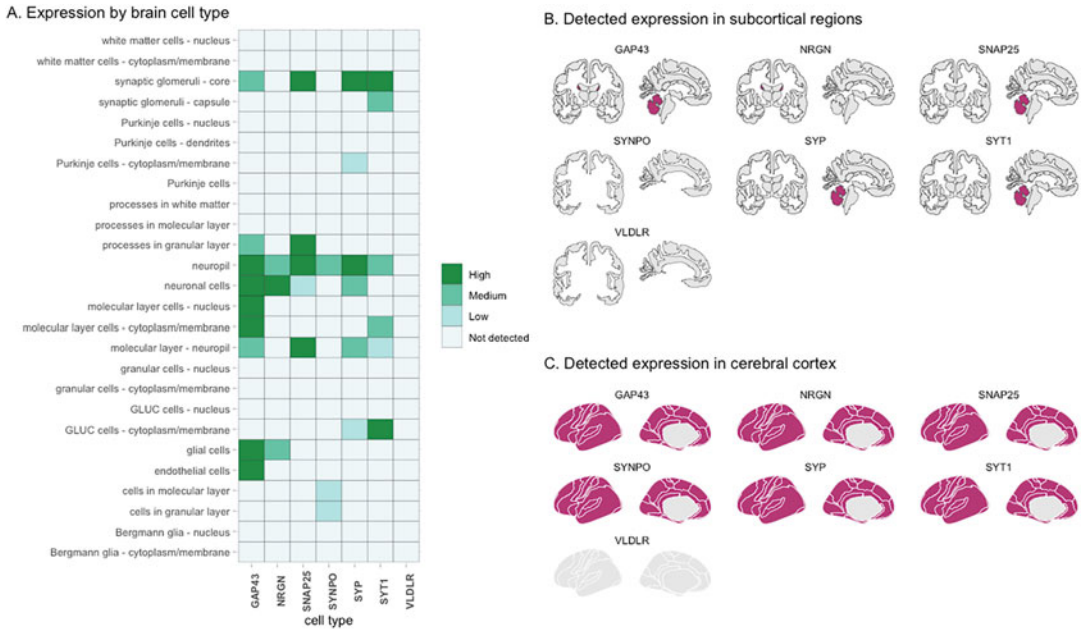


Fig. 2 Summary graph showing the seven biomarkers' expression in healthy brain tissues. *Panel A.* Expression by brain cell type. *Panel B.* Detected expression in subcortical regions using the aseg (automatic subcortical segmentation) atlas. Highlighted regions include caudate nucleus and cerebellum. *Panel C.* Detected expression in the cerebral cortex. The Campbell Atlas (1905) was used as an illustration (*note*, the Human Protein Atlas does not specify the cortical regions (i.e., frontal, parietal, etc.)). Other atlases can be found under: <https://github.com/ggseg/ggsegExtra>

tissues. All six biomarkers show a medium to high expression in the neuropil, while high expressions of GAP43 and neurogranin are found in neuronal cells. Using the *ggseg* package [24] (and dependencies, *ggseg3d* and *ggsegCampbell*), we can also efficiently visualize the cortical and subcortical brain regions in which at least mild expression of any of the six proteins is found (Fig. 2).

3.4 Functional Enrichment Analysis

The three main categories of functional enrichment analysis include overrepresentation analysis (ORA), functional class scoring (FCS), and pathway topology methods. In ORA, statistical tests such as Fisher's exact or chi-square tests are used to test whether *a priori* defined genes from a gene set (for instance, GO gene set "GO:0031547: brain-derived neurotrophic factor receptor signaling pathway") are more present ('overrepresented') within a set of interesting genes (in our case, the seven examined genes) than what would be expected by chance (taking into account a background set of genes—for instance, all the genes annotated in a species) (*see Note 1*) [31]. In FCS, gene expression data is used to rank pathways using a permutation method while in pathway topology-based methods, a score is assigned based on a gene's position and interactions with other genes in a pathway [9]. The choice regarding the type of functional enrichment analysis to use depends on the experimental design of the study, the data type available (gene expression

data versus list of significant genes, *see* **Note 2**), and the purpose. Here, we will use the ORA approach as implemented in *g:Profiler* [11]. This tool is available both online (<https://biit.cs.ut.ee/gprofiler/gost>) and in R.

In this tutorial, we use the *gprofiler2* [25] R package and provide a list of codes allowing for a smooth visualization of the results. The enrichment analysis is undertaken using the *gost* function which offers a wide range of advanced options to personalize the functional enrichment analysis: choice of multiple comparison testing methods (FDR, Benjamini Hochberg, *g:Profiler* own correction method called *g:SCS*), choice of annotation databases (we suggest choosing the database more relevant to your research question, *see* **Note 3**), choice of background gene list, and choice of genes to consider (annotation which was computationally identified vs manually curated). To reduce the noise and increase the specificity of the results, it is further recommended to filter for gene set sizes with a minimum of 2–5 and a maximum of 200–500 genes (*see* **Note 4**). The filtered annotation database can be submitted as GMT file (*see* **Note 5**). The annotation database (Gene Ontology in our case) in gmt format can be downloaded from <http://www.gsea-msigdb.org/gsea/msigdb/collections.jsp>. (Fig. 3). Once the file is downloaded, you can filter the gene sets by size using following R commands.

C5: ontology gene sets (browse 15937 gene sets)	Gene sets that contain genes annotated by the same ontology term. The C5 collection is divided into two subcollections, the first derived from the Gene Ontology resource (GO) which contains BP, CC, and MF components and a second derived from the Human Phenotype Ontology (HPO). details	Download GMT Files Gene Symbols NCBI (Entrez) Gene IDs JSON bundle
GO: Gene Ontology gene sets (browse 10532 gene sets)	All gene sets derived from Gene Ontology. details	Download GMT Files Gene Symbols NCBI (Entrez) Gene IDs JSON bundle
BP: subset of GO (browse 7751 gene sets)	Gene sets derived from the GO Biological Process ontology.	Download GMT Files Gene Symbols NCBI (Entrez) Gene IDs JSON bundle
CC: subset of GO (browse 1009 gene sets)	Gene sets derived from the GO Cellular Component ontology.	Download GMT Files Gene Symbols NCBI (Entrez) Gene IDs JSON bundle
MF: subset of GO (browse 1772 gene sets)	Gene sets derived from the GO Molecular Function ontology.	Download GMT Files Gene Symbols NCBI (Entrez) Gene IDs JSON bundle
HPO: Human Phenotype Ontology (browse 5405 gene sets)	Gene sets derived from the Human Phenotype ontology. details	Download GMT Files Gene Symbols NCBI (Entrez) Gene IDs JSON bundle

Fig. 3 Screenshot from the Human MSigDB Collections. Here we downloaded the *GO: Gene Ontology* gene sets. Two files are available depending on the format of your gene name (gene symbols: SNAP25 vs NCBI Entrez gene IDs: 6616). In this tutorial, our gene names are formatted as gene symbols

```

#define two functions to read and write the GMT
files: readGMT and writeGMT#
#these functions are available in a R package (rWikiPathways [26]) or can be defined separately here:#
####OPTION 1####
#download the rWikiPathways package - you will need
to install BiocManager first#
BiocManager::install("rWikiPathways")

####OPTION 2####
#define the two functions separately (without down-
loading the complete package)#
readGMT <- function(file) {
  x <- readLines(file)
  res <- strsplit(x, "\t")
  names(res) <- vapply(res, function(y) y[1], character(1))
  res <- lapply(res, "[", -c(1:2))
  wp2gene <- stack(res)
  wp2gene <- wp2gene[, c("ind", "values")]
  colnames(wp2gene) <- c("term", "gene")
  wp2gene[] <- lapply(wp2gene, as.character) #re-
place factors for strings
  return(wp2gene)
}

writeGMT <- function(df, outfile){
  # Assess and prep data frame
  df.len <- length(df)
  if(df.len < 2){
    stop("The input data frame must include at least
two columns.")
  } else if(df.len == 2){
    df$desc <- df[,1]
    df <- df[,c(1,3,2)]
  } else if(df.len > 3){
    id.cols <- names(df[,seq(1,df.len-2)])
    message(paste0("Concatenating the following
columns to use as Identifiers: ",paste(id.cols,
collapse = ", ")))
    df[,df.len+1] <- apply(df[,id.cols],1,paste,
collapse="%")
    df <- df[,!(names(df) %in% id.cols)]
    df <- df[,c(3,1,2)]
  }
  # Generate file
  genelists = lapply(unique(df[,1]), function(x){
    paste(df[df[,1]==x, 3], collapse = "\t")
  })
}

```



```

gmt = cbind(unique(df[,1]), df[!duplicated(df
[,1]),2], unlist(genelists))
write.table(gmt, outfile, sep = "\t", row.names =
FALSE,
           col.names = FALSE, quote = FALSE)
}

#read the downloaded gmt file (in our case called
#c5.go.v2023.1.Hs.symbols.gmt)#
#make sure to define the correct path for your file#
GeneSetsGOALL<-readGMT("c5.go.v2023.1.Hs.symbols.
gmt")
#show how many gene sets have been loaded#
length(unique(GeneSetsGOALL$term))

#remove gene set sizes <2 and >500#
#took about 22 sec on a Apple M1#
GeneSetsGOALL.sel<-GeneSetsGOALL %>%
  group_by(term) %>%
  mutate(N=n()) %>%
  filter(N>2&N<500) %>%
  rowwise() %>%
  mutate(genesetid=unlist(str_split(term,"%"))
[3]) %>%
  mutate(description=unlist(str_split(term,"%"))
[1]) %>%
  ungroup() %>%
  dplyr::select(description,gene) %>%
  as.data.frame(.)

#write the new gmt file (for future use)#
#takes about 30 sec on a Apple M1#
writeGMT(GeneSetsGOALL.sel,"GeneSetsGOALL.sel.
gmt")

#upload the new gmt file#
upload_GMT_file(gmtfile = "GeneSetsGOALL.sel.gmt")
#following message will pop up (the custom annota-
tion ID can be different)#
# Your custom annotations ID is gp__xOQr_REfT_1lE
# You can use this ID as an 'organism' name in all
the related enrichment tests against this custom
source.
# Just use: gost(my_genes, organism = 'gp__xOQr_-
REfT_1lE')
# [1] "gp__xOQr_REfT_1lE"

```

In this example, we run the functional enrichment using the Gene Ontology (GO) annotation database (molecular function (GO:MF), biological process (GO:BP), and cellular components (CC) annotations), applied the Benjamini Hochberg FDR correction ($FDR < 0.05$), and provided a list of genes with expression in the brain (using the HPA proteomics data) (*see Note 6*).

```
#REMINDER of vectors which have been defined in
previous steps#
#biom = vector of biomarkers we are interested in#
#hpa.brain = vector of genes found to be expressed
in the brain in the HPA#

#run the functional enrichment analysis, with the
organism ID defined previously (here: gp__xOQr_-
RefT_llE)#
enr<-gprofiler2::gost(query=biom, organism="gp__-
xOQr_REFt_llE", significant=TRUE,
                    user_threshold=0.05, evcodes=TRUE,
                    exclude_iea = FALSE, custom_bg =
hpa.brain,
                    correction_method="fdr")

class(enr) #enr is a list
#element of this list can be visualised as follows#
names(enr)
#the results are stored in the first element (called
"result")#
#we add those results in a dataframe, which we call
dfenr and add a column showing the database source #
(GO_BP, GO_CC or GO_MF)
dfenr<-as.data.frame(enr$result) %>%
  mutate(source=ifelse(term_name%like%"GOBP", "-
GO_BP",
                      ifelse(term_name%like
%"GOCC", "GO_CC", "GO_MF")))
#show the first 6 lines of the results#
head(dfenr)
#explore other information provided by gprofiler2#
colnames(dfenr)

#explore the results#
#number of significantly enriched pathways:
nrow(dfenr)

#the next lines will create a summary graph
(as shown in Figure 4)#
#graph 1: identify the annotations databases in
```

```

which significantly enriched pathways were found#
g1<-dfenr %>%
  group_by(source) %>%
  summarise(N=n()) %>%
  ggplot(.,aes(x=source,y=N,fill=source,label=N))+
  geom_bar(stat="identity",colour="black",width =
0.5)+
  scale_fill_brewer(palette=1,direction=1)+
  geom_text(vjust=1.4)+
  ggtitle("A. Database sources of significant path-
ways")+
  theme_bw()+
  theme(plot.title.position = 'plot')

#graph2: identify the number of enriched pathways
by genes
g2<-dfenr %>%
  group_by(intersection) %>%
  summarise(N=n()) %>%
  ggplot(.,aes(x=reorder(intersection,N),y=N,
fill=N, label=N)) +
  geom_bar(stat="identity",colour="black")+
  xlab("")+
  coord_flip()+
  scale_color_continuous()+
  ggtitle("B. Number of enriched pathways by genes/
intersections")+
  theme_bw()+
  geom_text(hjust=-0.3,size=2.5)+
  theme(plot.title.position = 'plot')+
  theme(axis.text.y= element_text(face="bold",
size=8),
  legend.position = "none")

#graph3: create a graph showing the size and dis-
tribution of the enriched pathways
mx<-max(dfenr$term_size)-10
q1<-round(as.numeric(quantile(dfenr$term_size,1/
4)),0)
q3<-round(as.numeric(quantile(dfenr$term_size,3/
4)),0)

txt1<-paste0("mean(SD): ", round(mean(dfenr$term_
size),0)," (",round(sd(dfenr$term_size),0),")")
txt2<-paste0("median[IQR]: ", round(median(dfenr
$term_size),0)," [",q1,"-",q3,"]")
txt3<-max(dfenr$term_size)
txt4<-min(dfenr$term_size)

```

```

dx <- density(dfenr$term_size)
xnew <- mx
approx(dx$x,dx$y,xout=max(dfenr$term_size))

g3<-dfenr %>%
  ggplot(.,aes(x=term_size))+
    geom_density(linewidth=0.5,fill="grey90",col-
our="black")+
    geom_vline(aes(xintercept=mean(term_size)),
              color="coral1", linetype="dashed",
linewidth=0.5)+
    geom_vline(aes(xintercept=median(term_size)),
              color="coral4", linetype="dashed",
linewidth=0.5)+
    xlab("gene set size")+
    labs(title="C. Summary statistics for the signif-
icant gene set sizes",
         subtitle = paste0("N total=", nrow
(dfenr),"\n",
                           txt1," ",txt2,"\n",
                           "max gs size =",txt3," ", "min gs
size =",txt4))+
    theme_bw()+
    theme(plot.title.position = 'plot',
          plot.subtitle = element_text(size=10))

#create a final graph
summary.graph<-ggpubr::ggarrange(g1,g2,g3,nrow=3,
ncol=1)
annotate_figure(summary.graph, top = text_grob
("gProfileR results",
                                color = "black",
face = "bold", size = 12),
                bottom = text_grob("Legend:
                                dark red dashed line=
median;
                                light red dashed line=
mean", color = "black",
                                hjust = 1, x = 1, face =
"italic", size = 8))

```

The analysis yielded a total of 49, 26, and 13 significant pathways from GO_BP, GO_CC, and GO_MF, respectively, and the median (IQR) gene set size was 30 [6–58] (Fig. 4).

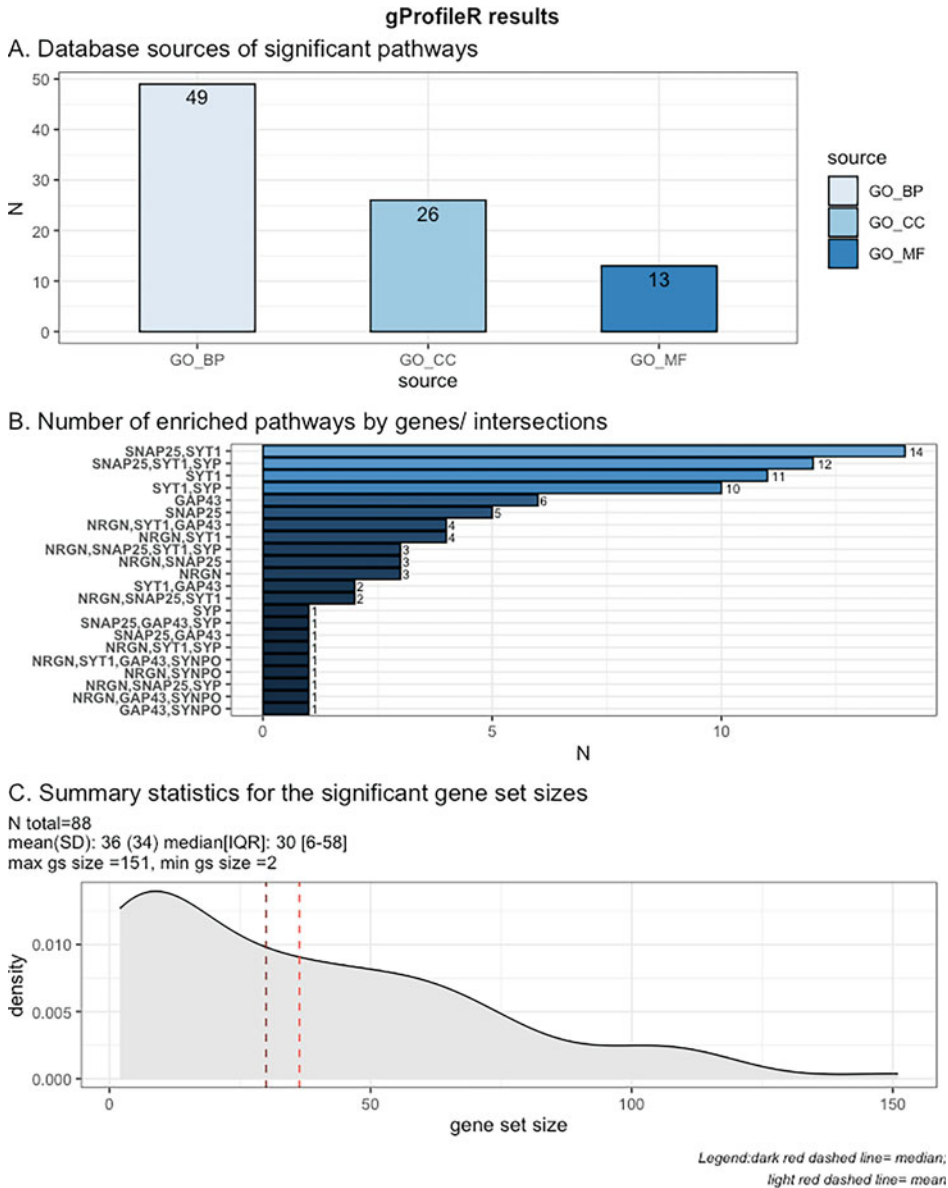


Fig. 4 Summary graph for the functional enrichment analysis conducted using g:Profiler in R. *Panel A.* Database sources of significant pathways (GO_BP = Gene Ontology Biological Process, GO_CC = Gene Ontology Cellular Component, GO_MF = Gene Ontology Molecular Function). *Panel B.* Number of significantly ($P_{FDR} < 0.05$) enriched pathways by genes/intersections. *Panel C.* Summary statistics for the significant gene set sizes

3.5 Network Analysis

In the above step, we found that the seven genes are overrepresented in 88 different pathways. Although these results already provide a first understanding of the functional pathways our seven genes are involved in, we would like to understand the relationships between these gene sets: *do they share common genes? Is there a*

biological function which plays a more central role and what is the position of a particular biological function among the enriched pathways? These questions can be answered using advanced graph analytics where enriched gene sets represent nodes and where edges (i.e., the connection between two nodes) represent the shared characteristics between the two nodes (for instance, the number of shared genes between two gene sets, measured by a similarity coefficient). In order to undertake this analysis, we will use *EnrichmentMap* [17], a widely used network-based visualization application, which is available as an add-on app in *Cytoscape*. If you run your functional enrichment analysis in the web-based *g:Profiler*, the results can be exported in a format allowing direct import into *EnrichmentMap*. As we used *g:Profiler* in R, we first need to prepare the dataset accordingly using the following R commands:

```
#define the columns needed to import the dataframe
in EnrichmentMap in Cytoscape#
col_oi_EM<-c("term_id", "term_name", "p_value", "F-
DR", "origin", "Gene")
#create the dataframe#
dfenr_cyto<-dfenr %>%
  mutate(origin=1, FDR=p_value) %>%
  rename(Gene=intersection) %>%
  select(all_of(col_oi_EM))
#save the dataframe#
write.table(dfenr_cyto, file="dfenr_cyto.txt",
sep="\t", row.names=FALSE, quote = FALSE)
```

In *Cytoscape*, open the *EnrichmentMap* app in the **Apps** tab. This will prompt a window **Create Enrichment Map**. Using the + button, you can load the result file you have just created in R and define your network's parameters as follows: **Name** = enter the name of your network; **Analysis Type** = chose **Generic/gProfiler/Enrichr**; **Enrichments** = click on the ... button, this opens a window where you can select the result file to load; **FDR q-value cutoff** = 0.05 (the *g:Profiler* output only includes q-values <0.05). Once we have entered those parameters, we click on **Build**. The network is created.

3.5.1 Style

We can adapt the network style in the **Style** tab in *Cytoscape* (label A in Fig. 5). We are interested in adapting the nodes' sizes (larger nodes reflecting larger gene sets sizes), the nodes' colors (different color depending on which gene of interest is enriched in the gene set), the nodes' labels (lower case), and the edges width. To do so, we create a file in R which includes all the attributes necessary to adapt the style. After exporting the node table (label B in Fig. 5) using the **Export Table to File** option (label C in Fig. 5), we create the attribute file using following R commands :

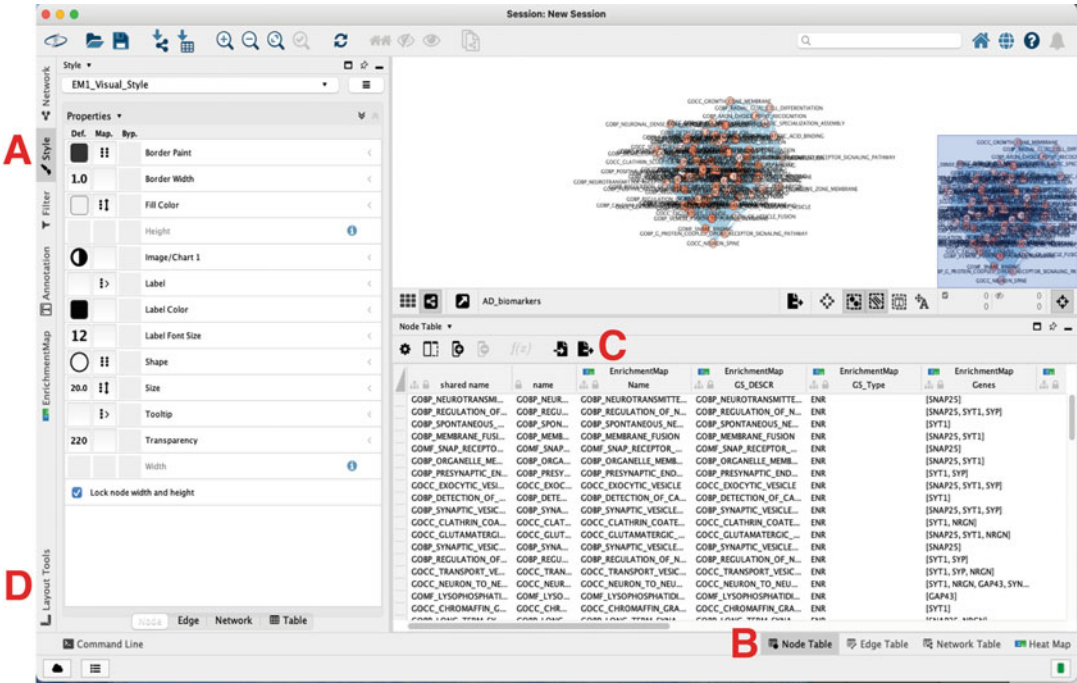


Fig. 5 Styling options in the Cytoscape environment. The style can be adjusted under the Style tab (*label A*). To export the node table, the Node Table tab (*label B*) followed by the option Export Table to File (*label C*) should be selected. A further style adjustment can be undertaken using the Layout Tools (*label D*). The graphical panel at the top right shows the default network

```
#read the exported node file from Cytoscape (called
"AD_biomarkers_default_node.csv"#
cyto<-read.csv("AD_biomarkers_default_node.csv",
sep=",",header=TRUE)
#make node names lowercase#
cyto$transf.name<-tolower(cyto$EnrichmentMap..
GS_DESCR)
#add colours column#
dfcolours<-data.frame(
  colours=sample(colors(),length(unique(cyto$En-
richmentMap..Genes))),
  intersection=unique(cyto$EnrichmentMap..Genes)
)%>%
mutate(intersection=gsub(",","|",intersection))
)%>%
rowwise() %>%
mutate(colours=ifelse(length(grep("\\|",inter-
section))>0,"multi",intersection))
#add to main dataframe#
cyto2<-cyto %>%
```

```

merge(.,dfenr %>% dplyr::select(term_id,term_
size),by.y="term_id",by.x="shared.name",all.x=T)
#add a column gs size which can be used to change the
size of the nodes#
cyto3<-cyto2%>%
  mutate(gs_cat=cut(term_size, breaks=c
(0,5,10,20,50,100,200))) %>%
  mutate(shared.name=paste0("\",name, "\")) %>%
  merge(.,dfcolours,by.y="intersection",by.x="En-
richmentMap..Genes",all.x=T) %>%
  relocate(c(name,transf.name,gs_cat,colours,
term_size))
#write the file#
write.table(cyto3,file="nodes_attributes.txt",
sep="\t",row.names=FALSE,quote=FALSE)

```

The file can be imported in Cytoscape as follows: **File > Import > Table from file**. After selecting the attributes file, a window will pop up where you can load the file (Fig. 6). The node table now includes the additional columns *term size*, *gs_cat*, and *colours* which can be used to adapt the style of our nodes in the **Style tab** using the *Fill Color*, *Shape*, *Size*, and *Edge* options (Fig. 7).

3.5.2 Layout and Network Density

Should the network be too dense, the Node Cutoff Q value and Edge Cutoff Similarity value can be used to remove less significant nodes and connections with less similarity, respectively.

3.5.3 Clustering into Biological Functions

Finally, the labels show that many gene sets share similar biological function (e.g., binding of neurotransmitter vesicle to the synaptic membrane). We can group these nodes into cluster of similar functions. To do so, we can either use the AutoAnnotate [27] app in Cytoscape or define the clusters manually. To perform the latter, node names can be exported into a text editor (for instance, Excel), categorized into biological functions, and then exported as a csv document. To create the file, we used the following **R commands**:

```

#we use the previously created cyto3 dataframe and
save the gene set names#
write.csv(cyto3$transf.name,file="cluster.txt",
quote=FALSE,row.names = FALSE)
#we open the file in excel or any tabular text
editor and manually identify clusters of similar
biological function and then reload the file in R#
cluster<-read.table("cluster.txt",sep="\t",
fill=T,header=T) %>% magrittr::set_colnames(.,c
("transf.name","cluster"))

```

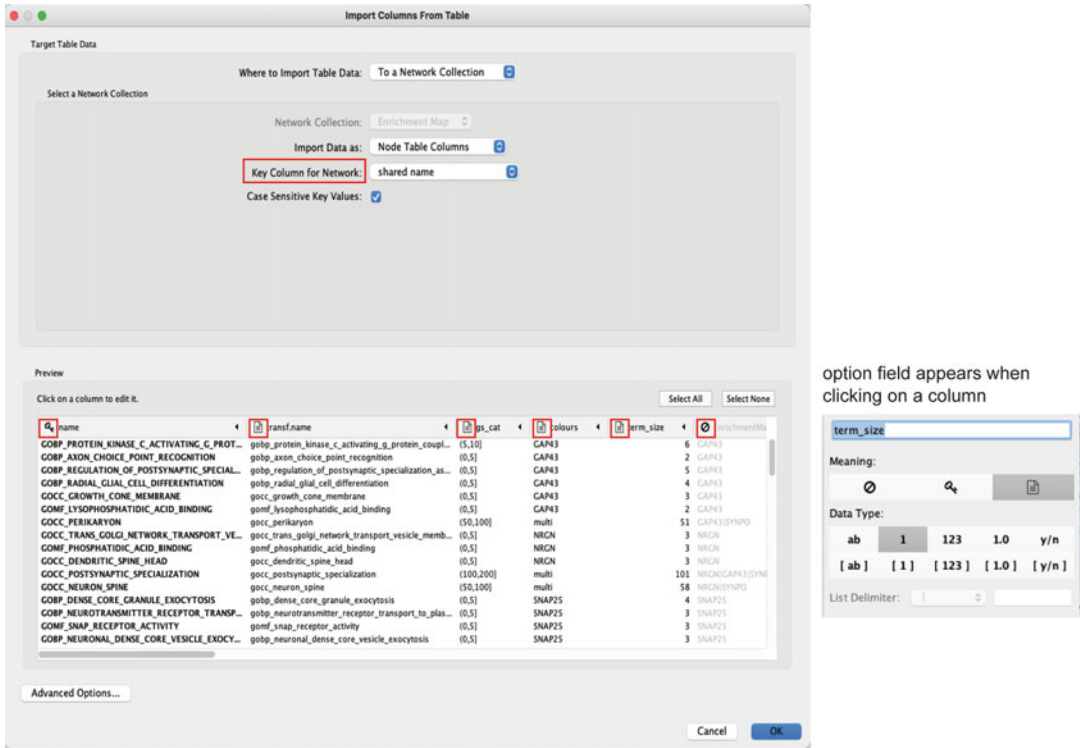



Fig. 6 Importing the attribute file in Cytoscape. The attribute file can be imported using *File > Import > Table from file*. Once the file is chosen, the columns to import can be selected. We recommend first selecting “Select None” and then only selecting the columns of interest. The column type (attribute vs key column) can be selected by clicking on a column. It is important to select the correct “key column” otherwise the import will fail

```
#and add the cluster to the main dataframe#
cyto4<-cyto3 %>%
  merge(.,cluster,by.x="transf.name",all.x=T)
#save the file to be exported into Cytoscape#
write.table(cyto4,file="cytoscape_cluster.txt",
  sep="\t",row.names=FALSE,quote=FALSE)
```

For this tutorial, we identified 12 biological functions. We can now import the cluster file into Cytoscape using the same approach as above (**File > Import > Table from file**). Then, in the **Layout** tab, the option *Group Attribute Layout* should be selected. This will arrange the nodes by cluster (in a circle format). Within each cluster, we can further adjust the layout in the **Layout** tab using the Prefuse Force-Directed Layout based on the similarity coefficient. Nodes can be further moved manually to improve the clarity of the graph. Finally, we can add circles and annotations for each cluster using the **Annotation** tab (Fig. 8).

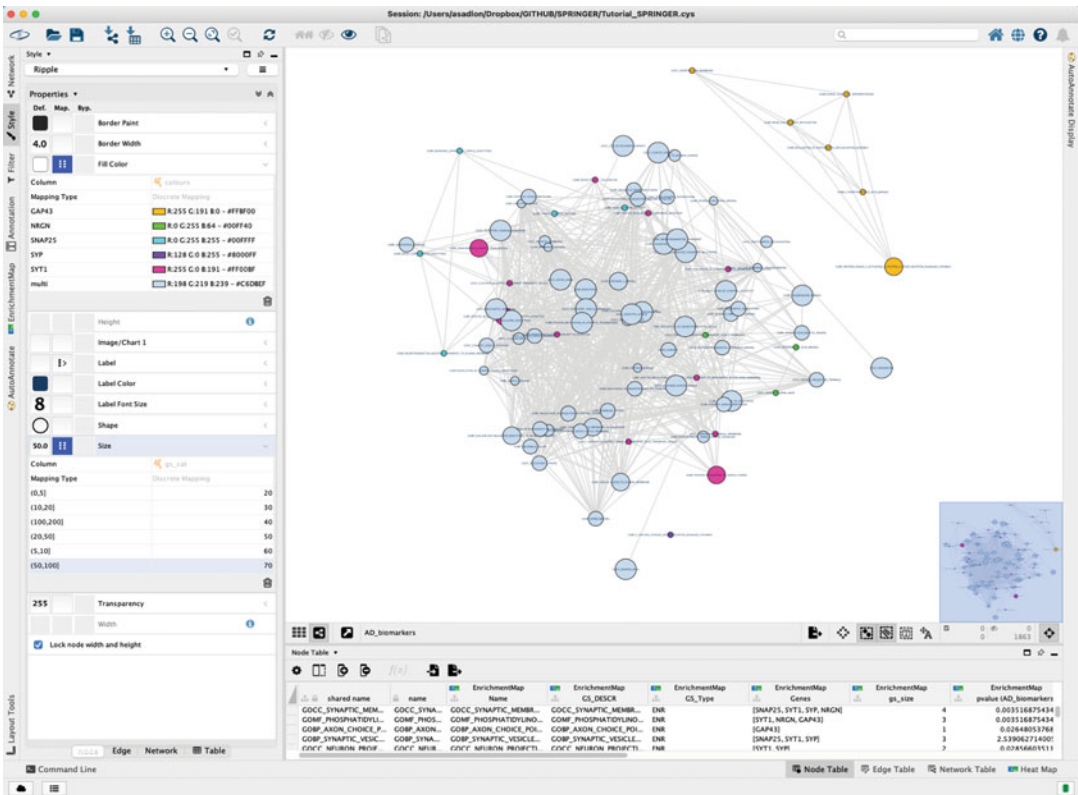


Fig. 7 Example of style adaptation in Cytoscape. Additional adaptations can be made according to your taste (both in the *Node* and *Edge* tabs in the *Style* section)

3.6 Final Remarks

After this tutorial you should be able to conduct a post hoc in silico analysis using open access databases. Our analysis shows that six out of seven blood-based biomarkers of synaptic dysfunction in AD show medium to high expression in the neuropil in healthy individuals. Our findings highlight that, in addition to participating in biological pathways related to synaptic function, several of these biomarkers are involved in calcium and lipid-dependent signaling. Finally, our results confirm that these biomarkers play a key role in learning and memory.

4 Notes

1. The choice of the background genes is essential. As an example, if you are interested in testing the role of a selected list of genes in biological pathways in the brain, you should only consider genes expressed in the brain as background genes and not the total number of genes (or proteins) annotated in a species [9]. A customized list of genes can be added using the *custom_bg* option in the *gost* function in *g:Profiler*.

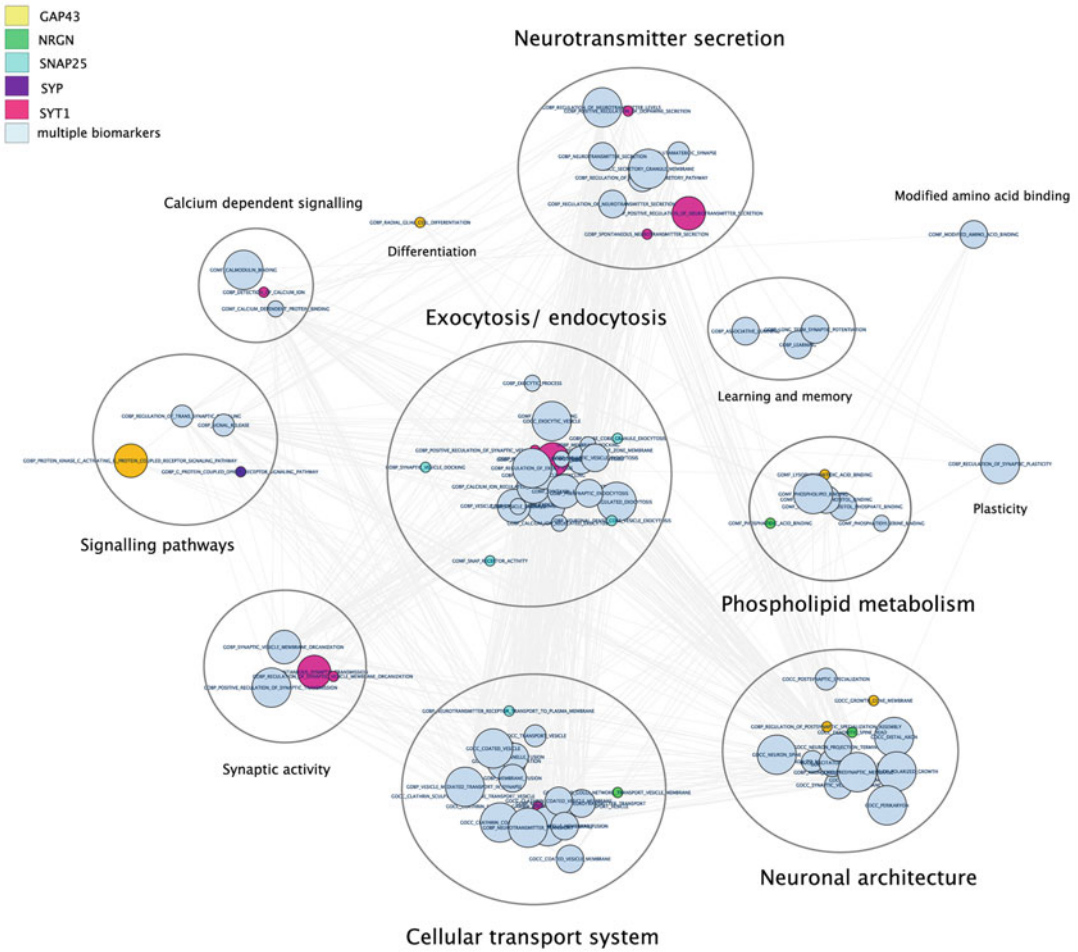


Fig. 8 Example of enrichment map for the seven blood-based biomarkers

2. Depending on the experimental design, the gene list can contain additional information, such as an effect size, a direction of change (upregulated or downregulated), or a *p*-value. Overrepresentation analysis does not consider gene ranking, while, for instance, gene set enrichment analysis (GSEA), a functional class scoring approach, uses ranked gene list [28]. In ORA, only genes passing a threshold in the experimental design (for instance, $P_{FDR} < 0.05$) are considered, while in GSEA, all genes are considered.
3. Each functional annotation database (e.g., KEGG, REACTOME, Gene Ontology) has its own classification and hierarchical structure resulting in different annotations and gene mapping. It is therefore important to choose the source wisely, depending on the biological question under investigation. Some annotation databases are more specific to biological or functional pathways, other to diseases, enzymatic pathways, or

regulatory motifs [29]. It is also common to include different annotation databases when performing a functional enrichment analysis.

4. Gene sets can be very large (i.e., contain >5000 genes) and are not very informative. Small gene set sizes (<2–5 genes) reduce the statistical power. It is therefore common practice to include only gene sets of a minimum size (2–5 as a cutoff) and maximum size (200–500) to reduce the noise of the data and improve the specificity of the data [30].
5. We highly recommend checking when the database was last updated and be cautious about outdated databases. In gprofiler2, this can be undertaken using following **R command**:

```
get_version_info(organism = hsapiens)
```

Updated gene sets from various databases can also be found on the Bader Lab, University of Toronto. http://download.baderlab.org/EM_Genesets/.

6. g:Profiler provides a large palette of input options as well as output information. A detailed description can be found here: <https://biit.cs.ut.ee/gprofiler/page/apis>.

References

1. Califf RM (2018) Biomarker definitions and their applications. *Exp Biol Med* (Maywood) 243:213–221. <https://doi.org/10.1177/1535370217750088>
2. Ioannidis JPA, Bossuyt PMM (2017) Waste, leaks, and failures in the biomarker pipeline. *Clin Chem* 63:963–972. <https://doi.org/10.1373/clinchem.2016.254649>
3. GTEx Consortium (2013) The genotype-tissue expression (GTEx) project. *Nat Genet* 45:580–585. <https://doi.org/10.1038/ng.2653>
4. Weinstein JN, Collisson EA, Mills GB et al (2013) The cancer genome atlas pan-cancer analysis project. *Nat Genet* 45:1113–1120. <https://doi.org/10.1038/ng.2764>
5. Barrett T, Troup DB, Wilhite SE et al (2011) NCBI GEO: archive for functional genomics data sets – 10 years on. *Nucleic Acids Res* 39: D1005–D1010. <https://doi.org/10.1093/nar/gkq1184>
6. Harris MA, Clark J, Ireland A et al (2004) The gene ontology (GO) database and informatics resource. *Nucleic Acids Res* 32:D258–D261. <https://doi.org/10.1093/nar/gkh036>
7. Jassal B, Matthews L, Viteri G et al (2020) The reactome pathway knowledgebase. *Nucleic Acids Res* 48:D498–D503. <https://doi.org/10.1093/nar/gkz1031>
8. Kanehisa M, Goto S (2000) KEGG: Kyoto encyclopedia of genes and genomes. *Nucleic Acids Res* 28:27–30. <https://doi.org/10.1093/nar/28.1.27>
9. Wijesooriya K, Jadaan SA, Perera KL et al (2022) Urgent need for consistent standards in functional enrichment analysis. *PLoS Comput Biol* 18:e1009935. <https://doi.org/10.1371/journal.pcbi.1009935>
10. Liao Y, Wang J, Jaehnig EJ et al (2019) WebGestalt 2019: gene set analysis toolkit with revamped UIs and APIs. *Nucleic Acids Res* 47:W199–W205. <https://doi.org/10.1093/nar/gkz401>
11. Raudvere U, Kolberg L, Kuzmin I et al (2019) G:profiler: a web server for functional enrichment analysis and conversions of gene lists (2019 update). *Nucleic Acids Res* 47: W191–W198. <https://doi.org/10.1093/nar/gkz369>
12. Sherman BT, Hao M, Qiu J et al (2022) DAVID: a web server for functional enrichment analysis and functional annotation of gene lists (2021 update). *Nucleic Acids Res*

- 50:W216–W221. <https://doi.org/10.1093/nar/gkac194>
13. Chen J, Bardes EE, Aronow BJ, Jegga AG (2009) ToppGene suite for gene list enrichment analysis and candidate gene prioritization. *Nucleic Acids Res* 37:W305–W311. <https://doi.org/10.1093/nar/gkp427>
 14. Eden E, Navon R, Steinfeld I et al (2009) GOrilla: a tool for discovery and visualization of enriched GO terms in ranked gene lists. *BMC Bioinformatics* 10:48. <https://doi.org/10.1186/1471-2105-10-48>
 15. Mi H, Ebert D, Muruganujan A et al (2021) PANTHER version 16: a revised family classification, tree-based classification tool, enhancer regions and extensive API. *Nucleic Acids Res* 49:D394–D403. <https://doi.org/10.1093/nar/gkaal106>
 16. Chen EY, Tan CM, Kou Y et al (2013) Enrichr: interactive and collaborative HTML5 gene list enrichment analysis tool. *BMC Bioinformatics* 14:128. <https://doi.org/10.1186/1471-2105-14-128>
 17. Merico D, Isserlin R, Stueker O et al (2010) Enrichment map: a network-based method for gene-set enrichment visualization and interpretation. *PLoS One* 5:e13984. <https://doi.org/10.1371/journal.pone.0013984>
 18. Maere S, Heymans K, Kuiper M (2005) BiNGO: a Cytoscape plugin to assess overrepresentation of gene ontology categories in biological networks. *Bioinformatics* 21:3448–3449. <https://doi.org/10.1093/bioinformatics/bti551>
 19. Fröhlich H, Speer N, Poustka A, Beißbarth T (2007) GOSim – an R-package for computation of information theoretic GO similarities between terms and gene products. *BMC Bioinformatics* 8:166. <https://doi.org/10.1186/1471-2105-8-166>
 20. Shannon P, Markiel A, Ozier O et al (2003) Cytoscape: a software environment for integrated models of biomolecular interaction networks. *Genome Res* 13:2498–2504. <https://doi.org/10.1101/gr.1239303>
 21. Hardy-Sosa A, León-Arcia K, Llibre-Guerra JJ et al (2022) Diagnostic accuracy of blood-based biomarker panels: a systematic review. *Front Aging Neurosci* 14
 22. Stelzer G, Rosen N, Plaschkes I et al (2016) The GeneCards suite: from gene data mining to disease genome sequence analyses. *Curr Protoc Bioinformatics* 54:1.30.1–1.30.33. <https://doi.org/10.1002/cpbi.5>
 23. Thul PJ, Lindskog C (2018) The human protein atlas: a spatial map of the human proteome. *Protein Sci* 27:233–244. <https://doi.org/10.1002/pro.3307>
 24. Mowinckel AM, Vidal-Piñeiro D (2020) Visualization of brain statistics with R packages ggseg and ggseg3d. *Adv Methods Pract Psychol Sci* 3:466–483. <https://doi.org/10.1177/2515245920928009>
 25. Kolberg L, Raudvere U, Kuzmin I et al (2020) gprofiler2 – an R package for gene list functional enrichment analysis and namespace conversion toolset g:profiler. *F1000Research* 9:709
 26. Slenter DN, Kutmon M, Hanspers K et al (2018) WikiPathways: a multifaceted pathway database bridging metabolomics to other omics research. *Nucleic Acids Res* 46:D661–D667. <https://doi.org/10.1093/nar/gkx1064>
 27. Kucera M, Isserlin R, Arkhangorodsky A, Bader GD (2016) AutoAnnotate: a Cytoscape app for summarizing networks with semantic annotations. *F1000Res* 5:1717. <https://doi.org/10.12688/f1000research.9090.1>
 28. Subramanian A, Tamayo P, Mootha VK et al (2005) Gene set enrichment analysis: a knowledge-based approach for interpreting genome-wide expression profiles. *Proc Natl Acad Sci U S A* 102:15545–15550. <https://doi.org/10.1073/pnas.0506580102>
 29. Gable AL, Szklarczyk D, Lyon D et al (2022) Systematic assessment of pathway databases, based on a diverse collection of user-submitted experiments. *Brief Bioinform* 23:bbac355. <https://doi.org/10.1093/bib/bbac355>
 30. Mooney MA, Wilmot B (2015) Gene set analysis: a step-by-step guide. *Am J Med Genet B Neuropsychiatr Genet* 168:517–527. <https://doi.org/10.1002/ajmg.b.32328>
 31. Da Wei Huang, Brad T. Sherman, Richard A. Lempicki (2009) Bioinformatics enrichment tools: paths toward the comprehensive functional analysis of large gene lists. *Nucleic Acids Res* 37(1):1–13. <https://doi.org/10.1093/nar/gkn923>

INDEX

A

- Alzheimer's disease (AD)..... 4, 15, 37,
49, 67, 75, 90, 107, 125, 143, 165, 177, 196,
222, 262, 271, 290, 299, 311, 324
- Amyloid 4, 15, 37, 68, 75,
90, 126, 165, 179, 196, 269, 291, 312
- Amyloid-beta (AB)..... 55, 126,
128–132, 269, 271, 273
- Amyloid PET..... 98, 165–172, 174, 312
- Animal model..... 177, 271–273, 278, 281
- Ascorbate (Asc) 132, 134, 248
- Astrocytosis..... 199–202

B

- Beta-amyloid 37, 67, 68,
75, 169, 269, 290
- Biomarkers..... 5, 15, 52, 69, 75, 90,
106, 126, 143, 165, 196, 222, 291, 300, 321
- Blood-based biomarker..... 6, 11, 68, 70,
166, 300, 324, 341, 342
- Brain..... 4, 20, 37, 49, 67, 79,
89, 105, 116, 144, 165, 177, 196, 222, 261, 272,
287, 324

C

- ¹¹C-deuterium-L-deprenyl (¹¹C-DED) 199–202,
204–207, 209–213
- Centiloids 172, 173
- Cerebrospinal fluid (CSF) 4, 6–11, 18,
38–44, 50–52, 54, 57, 60–62, 64, 68, 94, 126,
129, 143, 144, 147, 148, 151, 154–156, 165,
166, 172, 174, 201, 204, 225, 228, 258, 289, 312
- Choline (Chol)..... 117, 123, 125,
126, 129–131, 133, 249
- Clinical trial 68, 100, 134, 166,
173, 186, 196, 262, 299, 300, 312, 313, 316
- Cognition 24, 109, 179, 292,
300–302, 308, 311, 312
- Cognitive testing..... 6, 169, 311–313
- Cohort studies..... 16–18
- Connectome 96, 97, 99, 144, 154
- ¹¹C-Pittsburgh compound B (¹¹C-PiB)..... 166,
168, 169, 201, 202, 204, 206–208, 211, 213

- Creatine (Cr)..... 117, 122, 125,
126, 133, 249

D

- Dementia 4, 15, 67, 90, 106,
125, 165, 177, 196, 222, 288, 300, 312
- Diagnosis 4, 5, 8–10, 24,
38, 52, 68, 75, 99, 112, 126, 129, 131, 132, 143,
166, 172, 174, 196–198, 204, 261, 262, 288,
291–293, 311, 312, 321
- Diffusion tensor imaging (DTI) 105–112,
144–146, 152–154
- Diffusion-weighted imaging (DWI) 105, 111, 201
- Digital biomarkers..... 100, 300, 308, 312
- Direct MS analysis..... 76, 78, 81–82, 84
- Dissection 262–264, 292
- Drug development 15, 185, 222
- Drug discovery..... 15

E

- Early and targeted treatment and prevention of
neurodegeneration 4–5
- Early diagnosis of Alzheimer's disease and dementia 9
- Early perfusion amyloid PET imaging..... 167
- Environment..... 76, 123, 157,
197, 280, 302, 308, 313, 323, 338

F

- ¹⁸F-fluorodeoxyglucose (18F-FDG) 200–202,
204, 206–208, 211, 213
- Fluorescence molecular tomography 272
- Functional connectivity 90, 92, 94,
96, 97, 144, 154–157, 161, 180
- Functional enrichment analysis 322, 324,
325, 330, 336, 337, 343
- Functional magnetic resonance imaging
(fMRI)..... 89–100, 144, 145

G

- γ-aminobutyric acid (GABA)..... 122, 123, 132, 133
- Gas chromatography (GC)..... 76, 78, 82

Genetics 7, 8, 15, 16, 18,
 19, 21, 22, 24, 25, 98, 157, 177, 178, 181, 182,
 262, 324
 Glucose 123, 126, 134,
 196, 200–202, 207, 250
 Glutamate (Glu) 125, 132, 133
 Glutamate + Glutamine (Glx) 117, 126, 131–132
 Glutamine (Gln) 132
 Glutathione (GSH) 20, 132, 133, 250
 Graph analytics 322, 337
 Graph theory 97, 153

H

High throughput N-glycomics 38

I

Imaging biomarkers 100, 291
 Immunoassay 9
 In silico analysis 322, 341
 Intrinsic connectivity network (ICN) 90, 96
 In vivo imaging 185, 273, 278

K

18-kDa Translocator Protein (TSPO) 178–183,
 185, 186, 199

L

Lifestyle 16, 17, 19–24
 Lipidomics 221, 222, 224, 231, 240
 Lipids 16, 20, 22, 25,
 79, 84, 116, 133, 169, 221, 222, 224–226, 228,
 231, 232, 240, 241, 257, 258

M

Magnetic resonance imaging (MRI) 24, 105,
 118, 123, 125, 127, 132, 143–161, 174, 180,
 186, 197, 203–210, 212, 213, 272, 273, 277,
 280, 281, 288
 Magnetic resonance spectroscopy (MRS) 116–134
 Major tract 106, 109
 MALDI MS 50, 55, 58, 59, 61
 Mass spectrometry (MS) 9, 38, 39,
 47, 50, 56, 58, 60–62, 64, 65, 76, 78, 81, 82, 231,
 240, 246
 Metabolomics 17, 76–78,
 80–84, 221, 222, 224, 240
 Microglial activation 99, 128, 177–184
 Mild cognitive impairment (MCI) 5, 7–9, 19,
 24, 38, 52, 67, 83, 106, 107, 110, 125–133, 165,
 174, 186, 204, 205, 312, 318
 Multitracer PET imaging 201, 202, 204
 Myoinositol (mI) 117, 126, 133

N

N-acetylaspartate (NAA) 117, 122–129,
 131, 133
 Network analysis 336–340
 Neurodegeneration 5, 7–9, 16,
 18, 49, 68, 90, 126, 131, 132, 167, 177, 180,
 185, 196, 197
 Neurodegenerative 9, 11, 16,
 17, 19, 24, 37, 90, 122, 132, 134, 177, 184, 185,
 196–199, 201, 202, 261, 262, 267, 268, 288,
 290, 291, 293, 311, 313
 Neurodegenerative diseases 9, 17, 18, 24,
 26, 37, 122, 177, 184, 185, 196–199, 201, 202,
 288, 290, 291, 293
 Neuroinflammation 177–185,
 196–199, 202, 282
 Neuropathological examination 288, 293
 Neuropathology 183, 293
 N-glycan 37–40, 45–47,
 49–53, 57, 58, 60–62

O

Omics 16, 322

P

Phosphorylated-tau (phospho-tau) 68
 Plasma 7–9, 20, 68–71, 83,
 184, 185, 198, 201, 202, 225, 226, 228, 257–259
 Population-based 6, 18, 21, 26, 128
 Positron emission tomography (PET) 4, 6, 10,
 11, 21, 68, 89, 126, 128, 129, 131, 132, 134,
 148, 165–174, 177–186, 196–209, 211–214,
 271, 281
 Post mortem 168, 177, 179,
 181, 183, 185, 186, 261, 262, 287, 290, 291
 Protocol 50, 52, 58, 68–70,
 80, 82, 84, 92, 124, 168, 207, 211, 212, 222,
 257, 262, 264, 266–268, 273, 289, 290, 302

R

Resting state 89–100, 145, 154
 ROI-based analysis 144, 150

S

Scalable diagnostic technologies 6
 Speech biomarkers 300–302, 304, 308
 Structural and functional connectivity 110,
 144, 179
 Structural connectivity 110, 111, 153,
 154, 179, 180
 Subjective cognitive impairment and mild cognitive
 impairment 107, 112

T

Tau 4, 6, 16, 67, 68, 75,
 90, 98, 99, 126, 129, 130, 132, 166, 168, 169,
 179, 180, 182, 196, 197, 200, 201, 261, 266,
 268, 269, 282, 290

U

Ultra-high field 92
 Ultrahigh performance liquid chromatography
 (UHPLC) 46, 78

V

Voxel-based morphology (VBM) 144,
 150–152, 157, 207, 212

W

White matter 24, 94, 105–112,
 125, 130, 131, 144–147, 153, 154, 158, 169,
 170, 179, 186, 199, 202, 208, 266, 291